

Advances in Optical Technologies

Silicon Photonics

Guest Editors: Pavel Cheben, Richard Soref,
David Lockwood, and Graham Reed





Silicon Photonics

Advances in Optical Technologies

Silicon Photonics

Guest Editors: Pavel Cheben, Richard Soref,
David Lockwood, and Graham Reed



Copyright © 2008 Hindawi Publishing Corporation. All rights reserved.

This is a special issue published in volume 2008 of “Advances in Optical Technologies.” All articles are open access articles distributed under the Creative Commons Attribution License, which permits unrestricted use, distribution, and reproduction in any medium, provided the original work is properly cited.

Editor-in-Chief

H. John Caulfield, Fisk University and Alabama A&M University Research Institute, USA

Associate Editors

Mustafa A. G. Abushagur, USA

Partha P. Banerjee, USA

Ralph Barry Johnson, USA

Steve Blair, USA

Maria Luisa Calvo, Spain

Pierre Chavel, France

Michael A. Fiddy, USA

Patti Gillespie, USA

Richard B. Hoover, USA

Mark A. Kahan, USA

Liren Liu, China

Mikhail Noginov, USA

Mikhail P. Petrov, Russia

Joseph Rosen, Israel

Colin J. R. Sheppard, Singapore

Theo Tschudi, Germany

Cardinal Warde, USA

Leonid P. Yaroslavsky, Israel

Contents

Silicon Photonics, Pavel Cheben, Richard Soref, David Lockwood, and Graham Reed
Volume 2008, Article ID 510937, 2 pages

The Achievements and Challenges of Silicon Photonics, Richard Soref
Volume 2008, Article ID 472305, 7 pages

Synthesis of Planar Reflective Gratings for Silicon Interconnects, Ronald Millett, Jamie Ramsey, Przemek Bock, Julie Nkanta, Henry Schriemer, Trevor J. Hall, and Serge Bidnyk
Volume 2008, Article ID 315724, 8 pages

High-Speed Near Infrared Optical Receivers Based on Ge Waveguide Photodetectors Integrated in a CMOS Process, Gianlorenzo Masini, Subal Sahni, Giovanni Capellini, Jeremy Witzens, and Cary Gunn
Volume 2008, Article ID 196572, 5 pages

Light Emission from Rare-Earth Doped Silicon Nanostructures, J. Li, O. H. Y. Zalloum, T. Roschuk, C. L. Heng, J. Wojcik, and P. Mascher
Volume 2008, Article ID 295601, 10 pages

Development of Silicon Photonics Devices Using Microelectronic Tools for the Integration on Top of a CMOS Wafer, J. M. Fedeli, L. Di Cioccio, D. Marris-Morini, L. Vivien, R. Orobtschouk, P. Rojo-Romeo, C. Seassal, and F. Mandorlo
Volume 2008, Article ID 412518, 15 pages

Developments in Gigascale Silicon Optical Modulators Using Free Carrier Dispersion Mechanisms, Juthika Basak, Ling Liao, Ansheng Liu, Doron Rubin, Yoel Chetrit, Hat Nguyen, Dean Samara-Rubio, Rami Cohen, Nahum Izhaky, and Mario Paniccia
Volume 2008, Article ID 678948, 10 pages

Photonic Integration on the Hybrid Silicon Evanescent Device Platform, Hyundai Park, Alexander W. Fang, Di Liang, Ying-Hao Kuo, Hsu-Hao Chang, Brian R. Koch, Hui-Wen Chen, Matthew N. Sysak, Richard Jones, and John E. Bowers
Volume 2008, Article ID 682978, 17 pages

Subwavelength Grating Structures in Silicon-on-Insulator Waveguides, J. H. Schmid, P. Cheben, S. Janz, J. Lapointe, E. Post, A. Del ge, A. Densmore, B. Lamontagne, P. Waldron, and D.-X. Xu
Volume 2008, Article ID 685489, 8 pages

Hybrid Silicon Photonics for Low-Cost High-Bandwidth Link Applications, B. Jonathan Luff, Dazeng Feng, Daniel C. Lee, Wei Qian, Hong Liang, and Mehdi Asghari
Volume 2008, Article ID 245131, 6 pages

On-Chip All-Optical Switching and Memory by Silicon Photonic Crystal Nanocavities, Masaya Notomi, Takasumi Tanabe, Akihiko Shinya, Eiichi Kuramochi, and Hideaki Taniyama
Volume 2008, Article ID 568936, 10 pages

Optical Filters Utilizing Ion Implanted Bragg Gratings in SOI Waveguides, M. P. Bulk, A. P. Knights, P. E. Jessop, P. Waugh, R. Loiacono, G. Z. Mashanovich, G. T. Reed, and R. M. Gwilliam
Volume 2008, Article ID 276165, 6 pages

Tuning of the Optical Properties in Photonic Crystals Made of Macroporous Silicon, Heinz-S. Kitzerow, Heinrich Matthias, Stefan L. Schweizer, Henry M. van Driel, and Ralf B. Wehrspohn
Volume 2008, Article ID 780784, 12 pages

Silicon-Based Light Sources for Silicon Integrated Circuits, L. Pavesi
Volume 2008, Article ID 416926, 12 pages

Stress Induced Effects for Advanced Polarization Control in Silicon Photonics Components, D.-X. Xu, W. N. Ye, S. Janz, A. Del age, P. Cheben, B. Lamontagne, E. Post, and P. Waldron
Volume 2008, Article ID 689715, 10 pages

Silicon Photonic Biosensors for Lab-on-a-Chip Applications, Kirill Zinoviev, Laura G. Carrascosa, Jos e S anchez del R o, Borja Sep lveda, Carlos Dom nguez, and Laura M. Lechuga
Volume 2008, Article ID 383927, 6 pages

Silicon Nanocrystals: Fundamental Theory and Implications for Stimulated Emission, V. A. Belyakov, V. A. Burdov, R. Lockwood, and A. Meldrum
Volume 2008, Article ID 279502, 32 pages

Quantum Electrodynamical Modeling of Silicon-Based Active Devices, Shouyuan Shi, Brandon Redding, Tim Creazzo, Elton Marchena, and Dennis W. Prather
Volume 2008, Article ID 615393, 11 pages

Three-Dimensional Silicon-Germanium Nanostructures for CMOS Compatible Light Emitters and Optical Interconnects, L. Tsybeskov, E.-K. Lee, H.-Y. Chang, B. V. Kamenev, D. J. Lockwood, J.-M. Baribeau, and T. I. Kamins
Volume 2008, Article ID 218032, 16 pages

A New Approach of Electronics and Photonics Convergence on Si CMOS Platform: How to Reduce Device Diversity of Photonics for Integration, Kazumi Wada
Volume 2008, Article ID 807457, 7 pages

Slow Light with Photonic Crystals for On-Chip Optical Interconnects, Sean P. Anderson, Ashutosh R. Shroff, and Philippe M. Fauchet
Volume 2008, Article ID 293531, 12 pages

Editorial

Silicon Photonics

Pavel Cheben,¹ Richard Soref,² David Lockwood,¹ and Graham Reed³

¹ *Institute for Microstructural Sciences, National Research Council of Canada, Ottawa, ON, Canada K1A 0R6*

² *Air Force Research Laboratory, Sensors Directorate, Electromagnetics Technology Division, Hanscom Air Force Base, Massachusetts 01731, USA*

³ *Department of Electronic Engineering, School of Electronics and Physical Sciences, University of Surrey, Guildford, Surrey GU2 7XH, UK*

Correspondence should be addressed to Pavel Cheben, pavel.cheben@nrc-cnrc.gc.ca

Received 17 June 2008; Accepted 25 June 2008

Copyright © 2008 Pavel Cheben et al. This is an open access article distributed under the Creative Commons Attribution License, which permits unrestricted use, distribution, and reproduction in any medium, provided the original work is properly cited.

With the goal of developing photonic components that are factory-compatible with silicon microelectronic integrated circuits and optical integrated circuits, silicon photonics has been the subject of intense research activity in both industry and academia. Silicon is an excellent material for confining and manipulating light at the submicrometer scale, and possesses the added advantage of leveraging the enormous manufacturing infrastructure developed by the silicon microelectronics industry. Silicon optoelectronic integrated devices have the potential to be miniaturized and mass-produced at affordable cost for many applications and markets, including telecommunications, optical interconnects, medical screening, and biological and chemical sensing. Recent developments in diverse areas, such as light sources, modulators, switches, detectors, photonic crystals, waveguide structures, resonators, sensors, and various sub-systems, indicate that Si photonics is an extremely active, and now, firmly established research field.

The aim of this special issue is to document some of the remarkable recent progress in silicon photonics from academic and industrial viewpoints and thereby point to future trends in this rapidly evolving field. All the articles in this issue are invited review or invited research papers by leading authorities and research groups in this field from universities, industry and government laboratories.

The invited papers of this special issue are the following.

“The achievements and challenges of silicon photonics” by R. Soref.

“Synthesis of planar reflective gratings for silicon interconnects” by R. Millett et al.

“High-speed near infrared optical receivers based on Ge waveguide photodetectors integrated in a CMOS process” by G. Masini et al.

“Light emission from rare-earth doped silicon nanostructures” by J. Li et al.

“Development of silicon photonics devices using micro-electronic tools for the integration on top of a CMOS wafer” by J. M. Fedeli et al.

“Developments in gigascale silicon optical modulators using free carrier dispersion mechanisms” by J. Basak et al.

“Photonic integration on hybrid silicon evanescent device platform” by H. Park et al.

“Subwavelength grating structures in silicon-on-insulator waveguides” by J. H. Schmid et al.

“Hybrid silicon photonics for low-cost high-bandwidth link applications” by B. Jonathan Luff et al.

“On-chip all-optical switching and memory by silicon photonic crystal nanocavities” by M. Notomi et al.

“Optical filters utilizing ion implanted Bragg gratings in SOI waveguides” by M. P. Bulk et al.

“Tuning of the optical properties in photonic crystals made of macroporous silicon” by H.-S. Kitzerow et al.

“Silicon-based light sources for silicon integrated circuits” by L. Pavesi.

“Stress induced effects for advanced polarization control in silicon photonics components” by D.-X. Xu et al.

“Silicon photonic biosensors for “lab-on-a-chip” applications” by K. Zinoviev et al.

“Silicon nanocrystals: fundamental theory and implications for stimulated emission” by V. A. Belyakov et al.

“Quantum electrodynamic modeling of silicon-based active devices” by S. Shi et al.

“Three-dimensional silicon-Germanium nanostructures for CMOS compatible light emitters and optical interconnects” by L. Tsybeskov et al.

“A new approach of electronics and photonics convergence on Si CMOS platform” by K. Wada.

“Slow light with photonic crystals for on-chip optical interconnects” by S. P. Anderson et al.

We thank the contributors for their very positive response to our request for papers and for providing informative overviews of their respective topics and new insights into forthcoming developments. We hope that this special issue will prove valuable to those working in silicon photonics and will help in advancing research in this field.

Pavel Cheben
Richard Soref
David Lockwood
Graham Reed

Review Article

The Achievements and Challenges of Silicon Photonics

Richard Soref

Sensors Directorate, Air Force Research Laboratory, AFRL/RYPH, 80 Scott Drive, Hanscom AFB, MA 01731, USA

Correspondence should be addressed to Richard Soref, richard.soref@hanscom.af.mil

Received 22 November 2007; Accepted 15 May 2008

Recommended by Pavel Cheben

A brief overview of silicon photonics is given here in order to provide a context for invited and contributed papers in this special issue. Recent progress on silicon-based photonic components, photonic integrated circuits, and optoelectronic integrated circuits is surveyed. Present and potential applications are identified along with the scientific and engineering challenges that must be met in order to actualize applications. Some on-going government-sponsored projects in silicon optoelectronics are also described.

Copyright © 2008 Richard Soref. This is an open access article distributed under the Creative Commons Attribution License, which permits unrestricted use, distribution, and reproduction in any medium, provided the original work is properly cited.

1. INTRODUCTION

We are fortunate in this special issue to have authoritative invited papers written by key contributors to the field silicon-based photonics. It is a pleasure for me to be in the company of these leaders as I write this introductory article. The forward-looking papers here highlight the “technical momentum” that has built up in silicon photonics. They describe discoveries in science and technology that are being made worldwide at an increased rate thanks to the ramped-up investment by industry, universities, and governments [1, 2]. Transitions from “lab-to-fab” are taking place for commercial and military uses. Products are being developed (Luxtera, Kotura, SiLight). This is the beginning of optoelectronic (OE) manufacturing on a much wider scale [3]. My mission here is to give a context or background for the papers. I will review recent achievements in Si-based photonic integrated circuits (PICs) and optoelectronic integrated circuits (OEICs). I will pinpoint important challenges for the emerging OE industry, and I will identify applications that will be actualized if and when those challenges are met.

2. RECENT PROJECTS

Several new and on-going programs related to PICs and OEICs are described in this section. PICs are important in their own right, but the main driver today of the Si photonics field is the quest for low-cost large-scale-integrated OEICs manufactured in state-of-the-art high-volume silicon CMOS foundries (silicon fabs). Potentially, these chips have vast and

highly significant applications which, if implemented, would make those circuits pervasive in our planet.

The essential role that silicon nanophotonics will play in the future is highlighted in a new 2007 initiative on ultraperformance nanophotonic intrachip communication (UNIC) sponsored by the US Defense Advanced Research Projects Agency. The goal is to demonstrate low-power, high-bandwidth, low-latency intrachip photonic communication networks designed to enable chip multiprocessors with hundreds or thousands of compute cores to realize extremely high computational efficiency; a goal that embodies the convergence of computation and communication envisioned by Lionel C. Kimerling. The optoelectronic UNIC project poses a major challenge to the technical community because it will require revolutionary rather than evolutionary advances in science, devices, circuits, and computing systems.

An important investigation of nanoscale devices was made at the March 19-20, 2007 workshop on “very large-scale photonic integration” sponsored by the US National Science Foundation and chaired by Ronging Hui, Usha Varney, and Thomas Koch. Nanophotonic strategies for VLSI were explored, but the path to mass production was not clear. Corporations and universities now engaged in the fledgling OE industry need a cost-effective way to demonstrate and optimize their individual OE prototype chips. For that reason, I and other workshop participants recommended that a government-sponsored national CMOS-photonics User Facility should be set up in the United States to establish a cost-shared “photonics-ready” silicon foundry that will provide application-specific OEIC prototypes for users

throughout the technical community. The proposed user fab would rely upon the SOI photonic-component manufacturing “libraries” that are being developed at BAE Systems, Luxtera, and elsewhere. Both BAE and Luxtera are currently “on track” with their Phase II milestones for DARPA EPIC [1] (www.darpa.mil/MTO/Programs/epic/index.html). I am aware that “serious” OE programs are starting up in France, South Korea, and China, but I don’t have much information on those efforts.

The basic motivation for OE is to attain electronic drivers and controllers that are intimately integrated with their laser diodes, modulators, amplifiers and photodetectors. The larger OE goal is to create greatly improved devices, subsystems, and systems. Silicon of course is not the only OE medium, and silicon OE is currently struggling with the issue of on-chip light sources, a problem solved years ago by the III-V semiconductor laser industry. That is why OE based upon GaAs and InP is likely in the near term to give Si OE strong competition in “small-scale” integration situations, for example, in InP-based 1.55 μm transceivers (Infinera Corporation, Sunnyvale, Calif., USA) where III-V lasers and photodetectors can be integrated monolithically. However, two key advantages of silicon appear in the bigger picture: the very low chip costs that high-volume Si OE production will ultimately give, and the very high level of functionality that Si OE will eventually provide sophistication derived from hundreds or thousands of photonic components integrated on-chip with perhaps a million transistors.

Some of the cutting-edge research topics in Si photonics are nanophotonics, plasmonics [4], photonic crystals, nanomembranes, SiGeSn alloys, commercial manufacturing methods, nonlinear optics, nanoelectrooptical mechanics, and microfluidics. The papers presented at the IEEE LEOS 4th International Conference on Group IV Photonics (Tokyo, September 19-21 2007) give a good indication of the present R&D thrusts of silicon photonics (<http://www.ieee.org/organizations/society/leos/LEOSCONF/GFP2007/index.html>).

The sessions there deal with the Japanese MARAI optical interconnection project, waveguides and filters, OE and III-V hybrid integration, MOEMs and 3D structures, modulators and switches, disruptive materials and process technologies, nonlinear optics and active functions, slow-light devices and passive photonic crystals, light-source materials, light-source devices and structures, and detectors.

The new thrust in group IV nanomembranes, catalyzed by a 2008 AFOSR multiuniversity research initiative (ONR BAA Announcement Number 07-036, Research Opportunity number 10) can yield single-crystal membranes of Si or Ge or layered Group IV heterostructures whose thickness is, for example, in the 5 to 500 nm range. Such membranes could be deployed in flexible intelligent photonics and more generally in all of the applications areas listed below in Section 5.

3. THE LIGHT-SOURCE CHALLENGE

An optical network, whether fiber-optic or on-chip, requires light sources, and an Si OEIC or PIC is incomplete without sources. Because bulk crystalline silicon has inefficient electroluminescence, light sources have been critical issues

for silicon photonics since its inception. For these reasons, the creation of practical silicon light sources is a major, ongoing R&D focus.

Off-chip light sources can be thought of as a “photon supply” or “optical power supply” for the chip. In a particular subsystem or application, the decision about whether to locate the light source on- or off-chip is “situational,” depending upon factors such as heat sinking, average power consumption, energy dissipated per bit per second, cost, and size. Both on- and off-chip solutions have been proposed for intrachip interconnects. The preferred light source is usually (but not always) a laser. The case of a spectroscopic laboratory on a chip [5, 6] presents an exception to the “rule” of laser. There, a spectrally broad source like an on-chip light-emitting diode would be optimum, although a WDM laser array could serve also.

Silicon Raman lasers and amplifiers are certainly useful in silicon photonics, but intense optical pumping is required for these on-chip devices (it takes a laser to make a Raman laser) so the pump is likely to be off-chip and capable of pumping several on-chip gain devices.

Significant Si-based sources are beginning to emerge due to hard work by the technical community. We can divide these sources into those that will be available in five years and those emerging in a year or two. Regarding the integration of on-chip sources, the categories are monolithic and hybrid. These terms are a bit vague: I will interpret the word “monolithic” to mean “entirely within group IV” and “hybrid” to mean “silicon plus III-V” or silicon plus “other” (in other words, heterogeneous integration).

The III-V/Si hybrid source technique of John Bower’s group at UCSB is a very potent short-term solution that provides on-chip evanescently coupled lasers-on-SOI, amplifiers, photodetectors, and modulators created by low-temperature bonding of the PIN III-V components to the top surfaces of the waveguided silicon network. The remaining questions about these hybrids are in the areas of manufacturing and economics. Will the hybrids be viable in a CMOS Fab and will the yields be high? The answers are not known yet.

The US Air Force Office of Scientific Research has a multiuniversity research initiative on electrically pumped silicon-based lasers, an effort in its second year (see http://www.mphotonics.mit.edu/about_mphc/MURI/siliconlasers.php and http://www.asu.edu/news/stories/200603/20060310_MURI.htm). The lasers of the MIT team are either extrinsic or intrinsic. A quantum dot or nanocrystal gain medium within Si is extrinsic, while a tensile-Ge gain medium within an Si/Ge/Si heterostructure is intrinsic. The Arizona State University team utilizes an intrinsic “all in group IV” approach employing intersubband emission in Ge/SiGeSn multiquantum-well structures for the far infrared, and band-to-band emission in GeSn/SiGeSn or Ge/SiGeSn heterostructures for the near/mid infrared. The MIT and ASU intrinsic lasers appear to be CMOS manufacturable. The five-year MURI results will be very important to the SiOE industry if the resulting lasers have adequate efficiency and intensity.

4. THE HIGH-VOLUME CHALLENGE

Job creation and an expanded economic infrastructure will be triggered by sustained growth of the “nacent” silicon optoelectronics industry, growth that would be supported by long-term high-volume markets. A strong industry would provide optoelectronic “hardware for the information age,” thereby benefiting a global society that values “bits more than things” [7]. We examine high-volume SiOE markets in this section.

Which devices will likely be purchased at the rate of ten million units per year? The answer according to the MIT CTR consortium [7] is the transceiver, a Si-based send-and-receive optoelectronic chip. Two fast chips interconnected by a fiber create a duplex fiber-optic communication link that, with near-future technology, is capable of transmitting data at rate anywhere from 1 Gbps up to 100 Gbps, depending upon the sophistication of the chip constituents. If the chip can be manufactured to sell at a price of one dollar per Gbps or less, and if the chip will draw less than 1 mW/Gbps of power, then the transceiver will probably meet the needs of several major markets including: broadband core-, metro- and access-networks (fiber to the home, internet box, Ethernet LAN, FTTH), supercomputers, high-performance computers, enterprise networks, data centers (active cables as computer patch cords; optical interconnects for cabinet to cabinet, board to board, chip to board, and chip to chip), avionics-automotive-shipboard (communication and control links for aircraft, cars and ships), and microwave photonics (optical control of a phased-array antennas). Potentially, there are also huge, pervasive markets for “nanotransceivers” found inside new computer chips where waveguides link CPU cores.

Optics will replace copper if and only if the optics has compelling advantages. If SiOE research and development succeed in making on-chip optical linkages sufficiently fast, small, efficient, cheap, and reliable, then “long” copper paths would be replaced and many millions of such OE chips would appear in next-generation personal computers, notebooks, and gaming boxes (Playstation, Nintendo).

In addition to the DARPA effort mentioned above, the optical interconnect MIRAI project sponsored by Japan’s MITI is making a major R&D investment in the intrachip area [8]. The main objective is ultrafast on-chip global interconnects having a total path length of 5 to 30 mm. A second goal is optical clock distribution. Their optical interconnect approach is quite pragmatic and “wavelength agnostic”; whatever wavelength and technology are cost-effective and work well are appropriate. They will use an off-chip light source (or an off-chip WDM laser array) emitting in the 800 nm range, together with SiON waveguides and Si photodiodes. Modulation will be accomplished by poled PLZT films.

I will conclude this section with some speculations about chip-scale 1550-nm global interconnects and the “not-yet-born” nanolasers that will be necessary to produce them. There are many feasible architectures for an SOI waveguided optical network that gives communication among multiple processor cores on a computer chip. I will illustrate here the

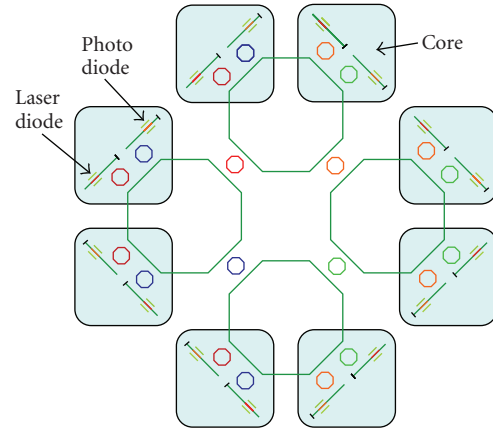


FIGURE 1: Top view of proposed SOI waveguided intrachip photonic interconnect system for global communication among eight cores.

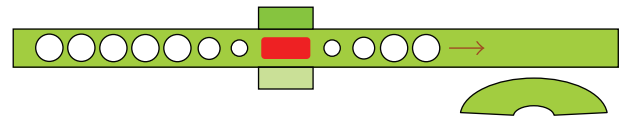


FIGURE 2: Structure of the strip-waveguided group IV nanolasers and nanophotodetectors used in Figure 1.

example of a reconfigurable broadcast network for eight-core interconnection. The four-ring layout of Figure 1 is similar to the WDM- and switched-network geometries that I presented in slides at the high-speed interconnect workshop [9]. In Figure 1, the green octagons are made from Si strip waveguides. Each bus-coupled circular ring (red, orange, green, blue) in Figure 1 is a reconfigurable optical add-drop multiplexer (ROADM) that can be electrically tuned over eight laser wavelengths around 1550-nm. Each PIN laser diode and photodiode in Figure 1 (integrated in a silicon strip waveguide shown as a green line) would use tensile Ge as the gain medium [10]. In [1, Figure 5], I suggested that a carrier-injected lateral superlattice formed within a germanium PIN-diode microring could be the heart of a 1550-nm laser. To attain a smaller-than-ring mode volume in a laser resonator, the Ge nanolasers and the nanoscale Ge photodetectors presented here in Figure 1 would each have an inline Fabry-Perot cavity created by a pair of 1D photonic crystal (PC) “mirrors” in a silicon strip (photonic wire) waveguide as illustrated in the enlarged top view of Figure 2. The resonator, consisting of one or two PC point defects, would have a mode volume of approximately $(\lambda/2n)^3$.

The tapered hole-diameter mirrors in Figure 2 minimize out-of-plane loss and maximize Q as discussed in a “nanolink” patent application [11]. The reflectors in Figure 2 consist of a row of air columns and are equivalent to a set of deeply etched rectangular slots in the SOI strip (a tapered Bragg mirror).

As shown in the detailed views of Figure 3, the tensile-Ge or GeSn parallelepiped (an ultrasmall bulk crystal) is grown selectively within an Si strip trench to form a P-Si/I-Ge/N-Si heterodiode, forward- or reverse-biased, as needed.

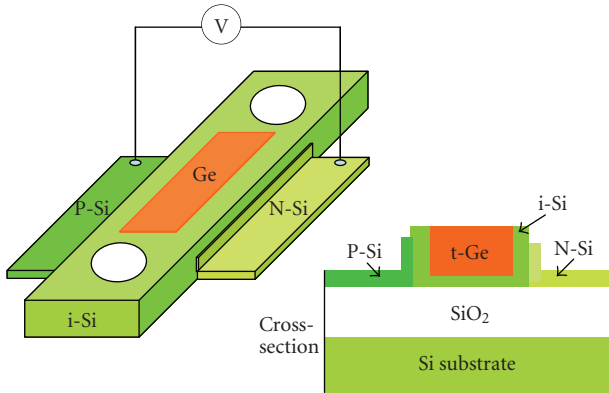


FIGURE 3: Closeup views of the Figure 2 resonant lateral PIN Ge-in-Si (or GeSn-in-Si) heterodiode laser (and photodetector) used in the Figure 1 nanophotonic system.

The lateral P-type and N-type silicon “wings” bracketing the Ge create a localized rib waveguide within the strip waveguide, a rib that does not disturb the fundamental guided mode. Addressing the ROADMs in Figure 1 will be discussed elsewhere. Thermal stability is a challenge for any of the resonant devices discussed in this paper.

5. THE DREAM AND CHALLENGE OF HIGH-IMPACT APPLICATIONS

I believe that “well-developed” Si-OEICs will have major impact on global society and commerce. Generally speaking, the Si OE application areas are optical interconnects, sensor technologies for the visible and near-, mid-, and far-infrared [5, 12, 13], signal processing functions, imaging, displays, energy conversion, illumination, optical storage, and gaming. If I look inside of these eight categories, I can identify specific high-impact cases. These are the challenges and opportunities for those of us involved in Si OE:

- interconnects*: all of the transceiver applications listed above in the high-volume section, electrooptically switched (reconfigured) optical networks;
 - sensors*: infrared spectrometer-on-a-chip, photonic laboratory-on-a-chip for sensing chemical and biological agents, lab-on-a-chip for environmental monitoring or process control or medical diagnosis;
 - signal processing*: wireless mobile multifunction “phone-like” device, optical time-delay beam-steerer for a phased-array microwave antenna, RF-optical receivers for RF spectrum analysis, ultrafast analog-to-digital converters, reconfigurable wavelength-division multiplexers and demultiplexers, reconfigurable optical filters, electronic warfare processors, photonically enhanced microwave and millimeter-wave circuits, optical buffer memories, electrooptical logic that operates on phase-coherent light beams, quantum communication-cryptography-metrology-computing, photonic testing of electronic ICs, bionic
- signal processors; neural network processors; data-fusion chips using inputs from several sensors;
 - imaging*: focal-plane-array imager with integral read-out: infrared-to-visible image converter chip;
 - displays*: chip-scale electrooptical display with integral scanning;
 - energy*: highly efficient group IV photovoltaic solar cells with integral signal processing—perhaps with thin-film supercapacitors for energy storage;
 - illumination*: efficient group IV solid-state lighting devices;
 - optical storage*: read/write chips for ultradense CDs and atom-scale memories;
 - gaming*: ultrafast graphic computation chips for Nintendo and Playstation.

I feel that nonlinear optical effects in group IV PCs and photonic-wire devices will have applications in signal processing. These NLO effects encompass all-optical modulation, all-optical wavelength conversion, electrooptically tuned resonator wavelength conversion, four wave mixing, broadband parametric gain, all-optical signal regeneration, electromagnetically induced transparency, Pockels-effect polymer/Si self-phase modulation, cross-phase modulation, stimulated-Raman slow-light delay lines, temporal pulse compression, and soliton generation. Many of these apply to optical networks.

6. RECENT ACHIEVEMENTS

This section contains a brief sketch of results achieved during the past six months. Most of results streaming out of Europe, North America, and Asia pertain to 1550 nm, but we are beginning to witness progress at longer wavelengths, highlighted here in Sections 6.2 and 6.3. In 2005, I proposed that silicon-integrated optoelectronics could be migrated into the wide, longwave infrared region that stretches from 1.6 to 200 μm . That migration will require innovative components whose dimensions are scaled-up from 1550 nm [12]. In a recent 2008 talk [5], I suggest that the time is ripe for chip-scale LWIR integration.

6.1. Results at 1550 nm

Modeling of an n+-doped layer of tensile Ge [10] predicts strong 1550-nm luminescence because the As doping populates the lower-energy L conduction valley, thereby transferring electrons from “excited L” into the Γ valley that sits at higher energy. Thus strong radiative recombination is obtained. I do not know whether the amount of electron-hole injection in a PNN⁺ diode will be adequate compared to that of a PIN diode. With regard to Sn-alloy emission experiments, the SiGeSn photoluminescence results of ASU [15, 16] are precursors of their electroluminescence studies. Their new SiSn alloy [16] is predicted to have a direct bandgap at 1460 nm when Si_{0.65}Sn_{0.35} is grown lattice-matched upon Ge_{0.88}Sn_{0.12}-buffered silicon.

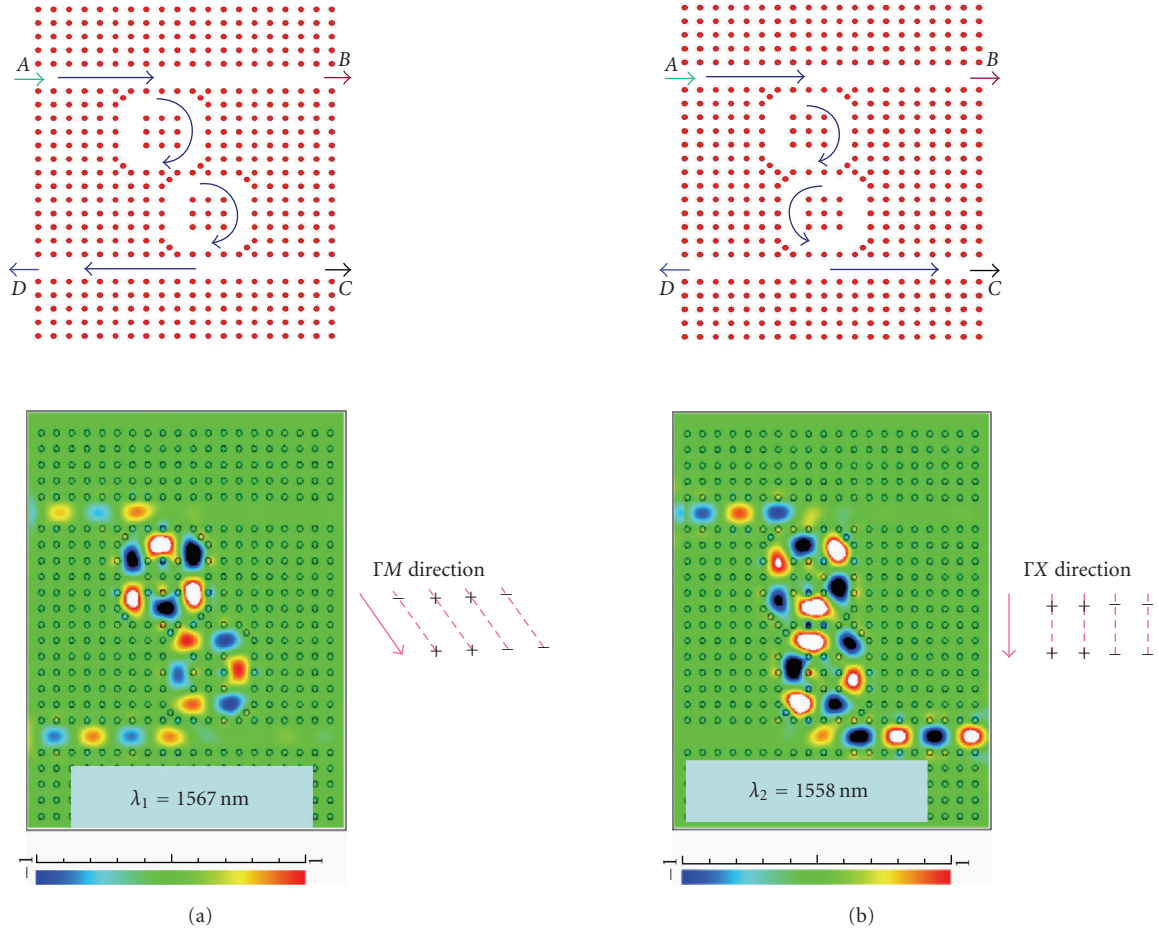


FIGURE 4: Two designs for an SOI photonic-crystal dual-ring-resonator wavelength-division add-drop multiplexer optimized for (a) backward dropping, (b) forward dropping. (Illustrations taken from [18]).

On the topic of PCs, the first photonic crystal in a film of crystal Ge has been reported [17]. Strong luminescence from a point-defect resonant cavity in a 2D PC slab of GeOI was attained. On the topic of microring resonators, considerable progress has been made as evidenced by an experimental SOI photonic-wire fifth-order filter [14]. An alternative to the SOI strip ring has now surfaced in the form of the SOI 2D photonic-crystal ring resonator (PCRR) presented in [18, 19]. As shown in Figure 4, the dual-ring PCRR has a property not found in photonic-wire rings. It can drop a resonant wavelength in either the forward or the backward direction [18]. Also, the PCRR diameter can be made smaller than that of the microwire without suffering size-dependent losses like those present in the microwire resonators.

6.2. Results at the near and mid infrared

The 3.39 μm midinfrared silicon Raman amplifier reported by Bahram Jalali's group at UCLA represents an important migration of silicon photonics into the 3 to 5 μm atmospheric-transmission window [20]. The room temperature electrically pumped germanium MIS-diode laser developed in the group of Chee-Wee Liu appears to be

a world first [21]. This novel tunneling-injection device utilizes an unstrained bulk Ge crystal with a strip-shaped metal-insulator gate on the Ge top surface, plus a contact on the bottom Ge surface. This multimode laser has output lines from 1600 nm to 2140 nm, and there are temporal instabilities in the laser output associated with local heating under the gate.

I propose improvements to this MIS laser diode laser that would reduce indirect-bandgap effects and would increase infrared mode confinement under the gate without relying upon heating. Since the direct-gap wavelength of a $\text{Ge}_{1-x}\text{Sn}_x$ crystal film moves from 1550 nm in pure Ge to 1900 nm as 5% Sn is added to Ge, and since GeSn can be grown directly upon Si, the improved MIS laser would employ a $\sim 1 \mu\text{m}$ -high nearly direct GeSn stripe mesa waveguide upon a thin Si substrate. The emission wavelength would be in the 1900 to 2100 nm range. A multi-quantum-well GeSn/Ge active region would lase closer to 1600 nm.

As GeSn technology becomes mature, I feel that several practical GeSn/Si PIN laser diodes and photo diodes will be invented whose wavelengths-of-operation are from 1.8 to 2.5 μm . At these near/mid-IR wavelengths, the attenuation of a glass optical fiber is too large for meter-scale transmission,

but the high-speed GeSn-transceiver fiber-optic links would work well over a few cm and fluoride fiber could serve for multimeter links.

6.3. Results at the far infrared

ASU researchers have demonstrated a relaxed-crystal SiGeSn buffer on silicon, offering a template for subsequent MQW epitaxy. This provides a real-world basis for design studies. A quantum-cascade laser design of a strain-free Ge/SiGeSn MQW lattice-matched to the ternary buffer was recently presented by Sun et al. [22]. This conduction intersubband device, a unique advance in Group IV technology, was predicted to have 120 cm^{-1} of gain at the $49 \mu\text{m}$ wavelength.

Because the deposited material $\text{Ge}_{0.23}\text{Sb}_{0.07}\text{S}_{0.70}$ has mid IR and far IR transparency, as well as CMOS compatibility, the low-loss GeSbS waveguides announced by the MIT group [23] appear to be good candidates for silicon-based LWIR on-chip networks.

7. OVERVIEW OF THIS SPECIAL ISSUE

As I read through the invited papers, I was impressed by their depth, diversity, timeliness, and innovation. The main themes of this issue are efficient silicon light sources (Gaburro et al.), optical switching and memory in photonic crystal nanocavities (Notomi et al.), macroporous silicon photonic crystals (Kitzerow et al.), hybrid evanescent III-V integration (Park et al.), light emitters in 3D Si/SiGe nanostructures (Lockwood et al.), chip-scale silicon photonic biosensors (Carracosa et al.), reflective gratings for photonic interconnects (Bidnyk et al.), high-speed waveguided Ge integrated photodetectors (Masini et al.), rare-earth doped silicon nano-emitters (Li et al.), foundry tools for photonic integration on CMOS (Fedeli et al.), gigascale silicon optical modulators (Basak et al.), sub-wavelength grating structures in SOI (Schmid et al.), low-cost silicon photonic links (Luff et al.), ion-implanted optical Bragg filters in SOI (Knights et al.), polarization control via stress induction (Xu et al.), electromagnetic modeling of silicon lasers (Prather et al.), engineering of material-photon interaction (Wada), and active photonic crystal devices for interconnects (Fauchet). The advances reported here lift silicon-integrated photonics to a higher level of capability and lay a foundation for further progress. These advances will help silicon reach preeminence in microphotonics.

ACKNOWLEDGMENT

The author wishes to thank AFOSR/NE, Dr. Gernot Pomrenke program manager, for sponsorship of his inhouse basic research at Hanscom AFB.

REFERENCES

- [1] R. Soref, "The past, present, and future of silicon photonics," *IEEE Journal on Selected Topics in Quantum Electronics*, vol. 12, no. 6, pp. 1678–1687, 2006.

- [2] R. Soref, "Introduction: the opto-electronic integrated circuit," in *Silicon Photonics: The State of the Art*, G. T. Reed, Ed., John Wiley & Sons, Chichester, UK, 2008.
- [3] R. Soref, "The impact of silicon photonics," *IEICE Transactions on Electronics*, vol. E91-C, no. 2, pp. 129–130, 2008.
- [4] AFOSR Plasmonic MURI, <http://www.plasmonmuri.caltech.edu/>.
- [5] R. A. Soref, "Toward silicon-based longwave integrated optoelectronics (LIO)," in *Silicon Photonics III*, vol. 6898 of *Proceedings of SPIE*, pp. 1–13, San Jose, Calif, USA, January 2008.
- [6] B. Momeni, J. Huang, M. Soltani, et al., "Compact wavelength demultiplexing using focusing negative index photonic crystal superprisms," *Optics Express*, vol. 14, no. 6, pp. 2413–2422, 2006.
- [7] L. C. Kimerling, "MIT communications technology roadmap," Second Annual Meeting, Cambridge, Mass, USA, September 2007. <http://mph-roadmap.mit.edu/>.
- [8] K. Ohashi, "MIRAI's optical interconnection project and its related topics," in *Proceedings of the 4th IEEE International Conference on Group IV Photonics (GFP '07)*, Tokyo, Japan, September 2007.
- [9] R. A. Soref, "Requirements and technology for silicon photonic interconnects," in *Proceedings of the 17th Annual IEEE LEOS Workshop on Interconnections within High-Speed Digital Systems*, Santa Fe, NM, USA, May 2006.
- [10] J. Liu, X. Sun, D. Pan, et al., "Tensile-strained, n-type Ge as a gain medium for monolithic laser integration on Si," *Optics Express*, vol. 15, no. 18, pp. 11272–11277, 2007.
- [11] R. A. Soref, "Semiconductor photonic nano communication link: apparatus and method," US patent application serial numbers 11/801-766 and 11/801-767, April 2007.
- [12] R. A. Soref, S. J. Emelett, and W. R. Buchwald, "Silicon waveguided components for the long-wave infrared region," *Journal of Optics A*, vol. 8, no. 10, pp. 840–848, 2006.
- [13] R. A. Soref, Z. Qiang, and W. Zhou, "Far infrared photonic crystals operating in the Reststrahl region," *Optics Express*, vol. 15, no. 17, pp. 10637–10648, 2007.
- [14] F. Xia, M. Rooks, L. Sekaric, and Y. Vlasov, "Ultra-compact high order ring resonator filters using submicron silicon photonic wires for on-chip optical interconnects," *Optics Express*, vol. 15, no. 19, pp. 11934–11941, 2007.
- [15] R. Soref, J. Kouvetakis, and J. Menendez, "Advances in SiGeSn/Ge technology," in *Materials Research Society Symposium Proceedings*, vol. 958, pp. 13–24, Warsaw, Poland, 2007.
- [16] R. Soref, J. Kouvetakis, J. Tolle, J. Menendez, and V. D'Costa, "Advances in SiGeSn technology," *Journal of Materials Research*, vol. 22, no. 12, pp. 3281–3291, 2007.
- [17] M. El Kurdi, S. David, X. Checoury, et al., "Two-dimensional photonic crystals with pure germanium-on-insulator," *Optics Communications*, vol. 281, no. 4, pp. 846–850, 2008.
- [18] Z. Qiang, W. Zhou, and R. A. Soref, "Optical add-drop filters based on photonic crystal ring resonators," *Optics Express*, vol. 15, no. 4, pp. 1823–1831, 2007.
- [19] Z. Qiang, W. Zhou, and R. A. Soref, "Diffraction-limited ultra-small photonic-crystal ring resonators with low loss," in *Proceedings of the 20th IEEE Annual Meeting of the Lasers and Electro-Optics Society (LEOS '07)*, pp. 54–55, Lake Buena Vista, Fla, USA, October 2007.
- [20] V. Raghunathan, D. Borlaug, R. R. Rice, and B. Jalali, "Demonstration of a mid-infrared silicon Raman amplifier," *Optics Express*, vol. 15, no. 22, pp. 14355–14362, 2007.
- [21] T.-H. Cheng, P.-S. Kuo, C. T. Lee, M. H. Liao, T. A. Hung, and C. W. Liu, "Electrically pumped Ge laser at room

- temperature,” in *Proceedings of the IEEE International Electron Devices Meeting (IEDM '07)*, pp. 659–662, Washington, DC, USA, December 2007.
- [22] G. Sun, H. H. Cheng, J. Menéndez, J. B. Khurgin, and R. A. Soref, “Strain-free Ge/GeSiSn quantum cascade lasers based on *L*-valley intersubband transitions,” *Applied Physics Letters*, vol. 90, no. 25, Article ID 251105, 3 pages, 2007.
- [23] J. Hu, V. Tarasov, N. Carlie, et al., “Si-CMOS-compatible lift-off fabrication of low-loss planar chalcogenide waveguides,” *Optics Express*, vol. 15, no. 19, pp. 11798–11807, 2007.

Research Article

Synthesis of Planar Reflective Gratings for Silicon Interconnects

Ronald Millett, Jamie Ramsey, Przemek Bock, Julie Nkanta, Henry Schriemer, Trevor J. Hall, and Serge Bidnyk

School of Information Technology and Engineering, University of Ottawa, Ottawa, Canada ON K1N 6N5

Correspondence should be addressed to Ronald Millett, rmillett@site.uottawa.ca

Received 29 November 2007; Accepted 13 March 2008

Recommended by Pavel Cheben

The design and simulations of planar reflective gratings for building optical interconnects in silicon-on-insulator (SOI) were studied for a range of silicon core thicknesses of 0.1 to 10 μm . The verticality of the grating facets has been shown to be the main contributing factor to the cumulative crosstalk in thick silicon cores. The dispersion property of the slab was found to limit the minimal thickness of the core for polarization-insensitive gratings. The effects of polarization-dependent confinement on optical crosstalk were studied. The findings were used to design and simulate a polarization-insensitive 18-channel coarse wavelength division demultiplexer (CWDM) with a free spectral range of over 600 nm. The CWDM demultiplexer uses a 1.7 μm silicon core and combines a shallow-etch tapered rib structure and multimode silicon channels to produce box-like passbands for integrated receiver applications. The diffraction grating was constructed using double astigmatic point design with phase-corrected grating facets to reduce astigmatism. Optical properties of the planar gratings have been simulated using quasivectorial diffraction grating theory. The simulation results confirm that there is high diffraction efficiency and low optical crosstalk over the entire range of operation. Applications of planar silicon gratings to the synthesis of silicon interconnects are discussed.

Copyright © 2008 Ronald Millett et al. This is an open access article distributed under the Creative Commons Attribution License, which permits unrestricted use, distribution, and reproduction in any medium, provided the original work is properly cited.

1. INTRODUCTION

Over the past several decades, data transfer rates over electronic interconnects have been increasing exponentially following Moore's law. The clock speed of silicon-based electronic processors has reached microwave frequencies of over 4 GHz causing severe problems with the signal integrity of electronic interconnects. At these frequencies, traditional stripline interconnects suffer from a fundamental cross-coupling penalty and large radiation losses. The research in silicon photonics has been driven primarily by the objective of overcoming the limitations of stripline interconnects. Recently, several key elements, including silicon lasers, modulators, and photodetectors, have been realized in silicon using low-cost CMOS-compatible processes [1, 2]. Further research in silicon-on-insulator (SOI) shows promise for implementing additional key functionality—demultiplexing—to enable wavelength division multiplexing and transferring data over multiple channels. The high index contrast of SOI waveguides also permits smaller

device footprints compared to more weakly guided material systems.

Due to performance limitations, arrayed waveguide grating- (AWG-) based demultiplexers in SOI have not been able to compete effectively with silica-based AWGs. Porting AWG technology directly from silica to SOI has been a challenge, mainly due to high waveguide propagation losses, limited spectral range, strong polarization dependence, and poor optical crosstalk arising from phase noise in the delay line region of SOI-based AWGs [3]. In order to overcome AWG limitations in SOI, several research groups have explored the possibility of using planar reflective gratings as an alternative to AWGs. To generate diffraction, planar reflective gratings, also known as Echelle gratings, rely on the optical properties of a 2D silicon slab as opposed to a phase array of waveguides in AWGs. SOI-based planar reflective gratings have now been realized with SOI core thicknesses of 0.22 μm [4], 3 μm [5], and 5 μm [6]. These initial studies are very promising and demonstrate that on-chip insertion

losses of less than 2 dB are readily achievable in both thin and thick core SOI-based planar gratings [4, 5].

In this paper, we theoretically explore the optical properties of planar reflective grating demultiplexers based on silicon cores of various thicknesses. We show that the thickness of the silicon core layer has a profound effect on the polarization and crosstalk performance of the SOI grating. The results of our findings were used to synthesize a polarization-insensitive 18-channel coarse wavelength division demultiplexer (CWDM) with box-like responses based on a planar reflective grating. The device combines a shallow-etch tapered rib structure and multi-mode silicon channels. The grating was optimized to reduce aberration effects. The polarization-insensitive performance of the demultiplexer was confirmed using quasi-vectorial diffraction theory. Applications of planar reflective gratings to building silicon interconnects are discussed.

2. PLANAR REFLECTIVE GRATING DESIGN

The success of AWGs in meeting the requirements of the multichannel demultiplexer market has been largely due to the silica platform where AWGs can be fabricated using shallow etched waveguides in a relatively simple fabrication process. In spite of a considerably smaller footprint, the fabrication of planar reflective gratings in silica was more complex compared to AWGs and required additional research into controlling the verticality and smoothness of the reflective facets. Contrary to silica, there are a number of well-established processes for producing deep, smooth, and highly vertical-etched structures in SOI. One of the key advantages of planar grating devices compared to free-space bulk gratings is that they are lithographically produced and any grating shape is readily achievable. Techniques for etching silicon have benefited from recent advancements in the fabrication of microelectromechanical systems. Planar reflective gratings in SOI have the potential for monolithic integration with large-scale electronic-integrated circuits.

An SOI-based planar grating uses a variety of input and output structures, as shown in Figure 1. In a rib-waveguide SOI structure, the fundamental mode of the waveguide is asymmetrically positioned below the center of the slab core. In order to improve the waveguide-to-slab coupling, the input waveguide is usually tapered at the entrance to the slab region. In the slab, the light remains confined in the vertical direction but expands horizontally until it encounters a series of reflectors. The grating not only diffracts but also refocuses the light into the output waveguides, as shown in Figure 1.

The lithographic approach to making planar gratings carries little design restrictions on the shape of the launching mode or the shapes of the diffracting elements. Such flexibility in planar grating design has recently resulted in the successful demonstration of planar gratings with facet widths varying from 4 to 1000 μm [4, 7]. Diffractive elements in SOI can be created by either a single dielectric-to-metal interface [5], a reflective dielectric stack [8], or using total-internal reflection facets [6].

The first planar reflective gratings were realized using the Rowland configuration [9]. Research into novel grating

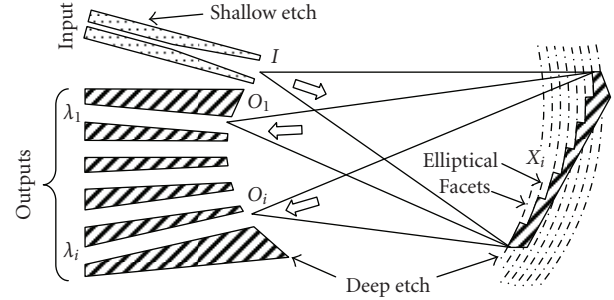


FIGURE 1: Architecture of the planar reflective grating in a silicon-on-insulator optical interconnect. A shallow etch (0.5 μm) defines the input structure, whereas a deep etch (1.7 μm) defines the output waveguides and grating facets.

designs has since yielded a methodology for eliminating the aberration effects caused by grating facets [10]. Subsequently, a mechanism of compensating for the dispersion of the refractive index of glass has been discovered, resulting in the successful demonstration of interleavers [7].

A comparative analysis of both planar reflective gratings and arrayed waveguide gratings recently performed by Cheben found that the traditional scalar approach to the simulation of planar gratings is unable to reconcile simulated and measured data [11]. Numerical difficulties posed by the large number of diffraction orders, deep triangular grooves with high blaze angles, and small wavelength-to-grating pitch ratios have made the calculation of diffraction efficiency one of the most intractable problems of electromagnetic theory.

Until a decade ago, simple relationships between fundamental grating parameters, such as diffraction order, diffraction angle, resolving power, Rowland circle radius, grating pitch, were deemed sufficient to model planar reflective gratings. The linear dispersion strength of a planar grating can be readily computed through the angle of incidence, α , and reflected angle, α' [12]:

$$L \frac{\partial \alpha'}{\partial \lambda} = L \frac{\sin \alpha + \sin \alpha'}{\lambda \cos \alpha'} \left[1 - \frac{\lambda}{n} \frac{\partial n}{\partial \lambda} \right], \quad (1)$$

where L is the length of the slab region. Theoretically, it is possible to use infinite permutations of diffraction angles and slab lengths to produce gratings with almost identical characteristics. However, in practice, researchers have realized that theoretically equivalent gratings can exhibit vastly different performance characteristics.

Vector diffraction theories that replaced the traditional scalar approach revealed that the shape and metallization of the grating facets affect both the grating efficiency and polarization sensitivity. Del age and Dossou [13] solved Maxwell's equations in proximity to the grating facets using a finite-element method and matched their numerical solution near the grating surface to a Rayleigh expansion. Their work showed that metallization had a profound impact on the absolute and relative grating efficiencies of both TE and TM polarized light.

The design of planar gratings in SOI requires careful studies on the effects of silicon core thickness and grating verticality on the polarization dependence and optical crosstalk. Particular consideration should be given to the selection of diffraction angles for the planar grating in SOI.

3. POLARIZATION DEPENDENCE OF PLANAR GRATINGS

The polarization dependence of the wavelength (PDW) has different origins in AWGs and planar reflective gratings. PDW in an SOI-based AWG is predominantly caused by waveguide birefringence in the phase array region. Contributing factors to the waveguide birefringence include waveguide cross-section variations and stress. Both of these factors can be used to eliminate modal birefringence in SOI-ridge waveguides [14]. Consequently, the selection of proper waveguide dimensions and cladding layers is essential for improving the PDW performance of AWGs.

Contrary to AWGs, the PDW of SOI planar waveguide gratings depends only on birefringence of the slab and not the waveguides. The geometry of waveguides can be selected independently, thus providing additional design flexibility in optimizing other planar lightwave circuit subcomponents, such as fiber-to-waveguide mode converters and bend waveguide regions.

The modes of an asymmetric slab waveguide can be found using analytical expressions that assume that the waveguide is infinite in the transverse direction [15]. The three layers of the infinite asymmetric slab waveguide are a cladding layer of air ($n_0 = 1$), a core layer of silicon ($n_1 = 3.48$), and a substrate layer of SiO_2 ($n_2 = 1.445$). The thickness of the cladding and substrate layers are assumed to be infinite in these calculations, a good approximation due to the strong modal confinement in the high-index silicon core. The equations for the TM mode are found using the duality relationships between TE and TM electric and magnetic fields. The computation was performed for a wavelength of $1.55 \mu\text{m}$.

The results of the effective index computations are shown in Figure 2 (left axis). The effective index of the fundamental slab mode in a silicon core has been found to depend strongly on the core thickness, due to the high index contrast of SOI. The birefringence of the slab waveguide becomes greater as the core thickness decreases, with only the TE mode propagating at core thicknesses of $< 0.12 \mu\text{m}$. In silica, researchers have found a way of eliminating the slab birefringence through a use of a compensator region [16]. In SOI, the amount of birefringence is orders of magnitude larger.

Polarization compensation in SOI is possible for a range of core thicknesses using, for example, the approach described in [16]. The difficulty associated with this approach is that a large mode profile mismatch between the slab and compensator regions can excite undesirable higher modes. This problem has been solved by Cheben et al. using silicon-oxide-silicon compensators that can provide

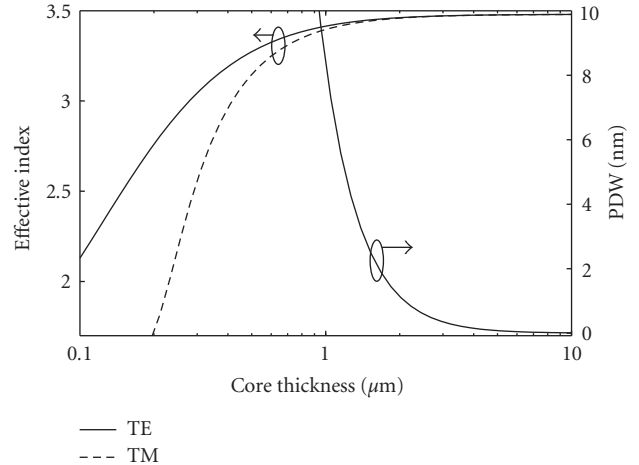


FIGURE 2: (i) Dependence of the effective refractive index of the fundamental mode on the core thickness of the slab for TE- and TM-polarized lights (left axis); and (ii) polarization dependence of the wavelength as a function of the slab thickness (right axis).

sufficiently strong birefringence correction with minimal field profile mismatch [17, 18].

The present manuscript is limited only to the consideration of planar gratings containing no polarization compensators. The design and architecture of compensators is a subject of our present research in this field. A strong slab birefringence has a profound effect on the optical properties of silicon interconnects based on planar reflective gratings. In Figure 2 (right axis), we have computed the amount of PDW that is caused by slab birefringence. The data clearly shows that, in devices with a silicon core thickness of $< 1 \mu\text{m}$ ($\text{PDW} = \lambda \cdot \Delta n / n > 10 \text{ nm}$), it is not possible to achieve polarization-independent performance for most practical applications. In a different approach, it has been suggested that the polarization diversity scheme can potentially be applied to overcome the polarization dependence of reflective interconnects [19]. This, however, would likely lead to doubling the number of optical and electronic subcomponents and would also require integrating polarization splitters and combiners. The complexity of the polarization diversity scheme will likely outweigh the benefits of silicon photonic integration for the majority of applications that require polarization insensitivity.

In addition to PDW, SOI-based devices also experience polarization-dependent loss (PDL). Nanometer-scale sidewall roughness is the prime cause of polarization-dependent waveguide loss in silicon waveguides [20]. In AWGs, PDL primarily arises from different waveguide propagation losses associated with the two polarizations in the phase array region. Planar reflective gratings, in contrast, require no phase-array waveguides, but rather a slab region that can be made polarization-insensitive. However, PDL does arise due to the presence of nonreflecting sidewalls between adjacent grating facets. The approach to reduce this source of PDL will be discussed later in this manuscript.

4. OPTICAL CROSSTALK

Optical crosstalk also has different origins for AWGs and planar reflective gratings. In AWGs, the theoretical crosstalk limit depends on the number of waveguides (the Gaussian field truncation) and waveguide phase errors. The Gaussian field truncation can be overcome by merely increasing the number of waveguides in the phase array region. However, controlling the phase noise in SOI waveguides is very challenging. Even nanometer-scale variations in the waveguide geometry leads to severe phase distortions. Phase error noise in SOI typically results in optical crosstalk values unsuitable for most applications [3]. This limitation underscores the difficulty of implementing the AWG architecture in SOI.

Planar reflective gratings offer the unique possibility of overcoming the crosstalk limitations of the SOI platform. The optical crosstalk of planar reflective gratings is not degraded by waveguide geometry phase errors since diffraction occurs in the slab region. The slab region typically has a high refractive index and thickness uniformity. The two main contributors to optical crosstalk in planar gratings are grating anomalies and facet verticality. A numerical model which simulates the spectral characteristics of the demultiplexer including grating anomalies due to the pixilation effect, random stage movement error, and gain error has already been established and discussed in the literature [21]. In this study, we primarily examine the effects of grating verticality on the cumulative optical crosstalk.

In a multichannel demultiplexer, the cumulative optical crosstalk arising from a grating facet tilted by θ degrees from the vertical can be computed by considering the phase distortion of the mode reflected from the facet. For the TE mode (and similarly for the TM mode) the mode reflected from a tilted interface, $\mathbf{E}_{\text{tilted}}$, is given by the input fundamental slab mode, \mathbf{E}_{slab} , multiplied by a phase-shifting factor

$$\mathbf{E}_{\text{tilted}} = \mathbf{E}_{\text{slab}} e^{i2\beta y \tan \theta}, \quad (2)$$

where y is the coordinate in the growth direction and β is the slab mode propagation constant. Crosstalk originates from the fact that the reflected mode does not perfectly couple with the fundamental slab mode, and the uncoupled portion of the light can contribute to the crosstalk. Assuming that all fields are normalized, the amount of cumulative crosstalk can be estimated by calculating the coupling loss between the reflected mode and the fundamental slab mode (wavelength dependence is implicit):

$$\eta_{\text{TE}} = 1 - \left| \frac{1}{2} \int_{-\infty}^{\infty} E_{y,\text{slab}} H_{x,\text{tilted}}^* dx \right|^2, \quad (3)$$

$$\eta_{\text{TM}} = 1 - \left| \frac{1}{2} \int_{-\infty}^{\infty} E_{x,\text{slab}} H_{y,\text{tilted}}^* dx \right|^2.$$

This gives the worst case crosstalk estimate, as some of the reflected mode may couple to radiation modes and not contribute to the crosstalk. In multichannel planar grating demultiplexers, the spectral response from each channel, including side-lobes and other crosstalk limiting features,

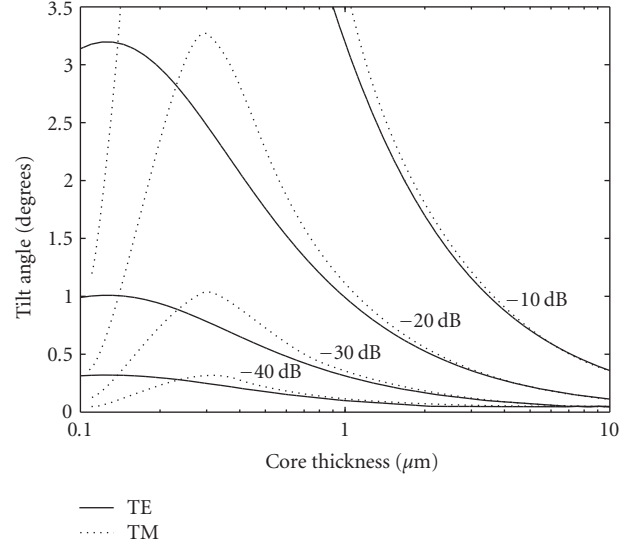


FIGURE 3: Cumulative optical crosstalk as a function of silicon core thickness and facet tilt angle (relative to vertical) for different isolation requirements. In order to achieve -30 dB isolation in $1.7\text{-}\mu\text{m}$ -thick silicon slab, the verticality of facets should be controlled to within ± 0.4 degree.

is very similar if channels are spectrally shifted by the amount of channel spacing and overlaid [12]. Higher-order slab modes have different propagation constants and will generally diffract at different angles, focusing at spatially different locations along the Rowland circle, resulting in “ghost peaks” appearing in the other channels. Effectively, each channel will experience crosstalk from a different spectral window coming from every other channel. Thus, the cumulative optical crosstalk can be estimated by either adding together crosstalks in different spectral windows from all the channels, or alternatively performing a spectral integral of crosstalk coming from a single channel, as given by the above formulas.

The results of our simulations are shown in Figure 3. Each curve shows the maximum vertical tilt angle of the grating permissible for a given silicon core thickness so as to maintain a particular amount of cumulative crosstalk, from -10 dB to -40 dB. From Figure 3, silicon cores with a thickness of $\sim 0.3\text{ }\mu\text{m}$ are capable of withstanding the largest grating facet tilt with the smallest amount of crosstalk. For thicker silicon cores, crosstalk values become unacceptable even for relatively vertical grating facets (e.g., crosstalk $\eta_{\text{TE}} \approx \eta_{\text{TM}} = -15$ dB for core thickness of $5\text{ }\mu\text{m}$ and a tilt angle of $\theta = 0.5^\circ$).

Figure 3 also shows the polarization dependence of the cumulative crosstalk. For thinner cores ($< 0.2\text{ }\mu\text{m}$), TM-polarized light is more sensitive to the facet tilt angle, while for larger core thicknesses TE-polarized light is more sensitive. For reflective gratings with thick cores ($> 10\text{ }\mu\text{m}$), the TE- and TM-polarized modes are both equally highly sensitive to the tilt angle. These results can be explained by examining the confinement of the optical mode. As the optical power in the mode becomes more diffuse in the

vertical direction, the edges of the modal field experience a greater phase shift according to (2), and the mode will become more sensitive to grating verticality. The peaks in Figure 3 occur at core thicknesses where the TE or TM mode is the most vertically confined.

Figure 4 shows the confinement in the silicon core of the TE- and TM-polarized mode. For thinner cores, where the modes are only weakly guided, the TM mode is much less confined than the TE mode, resulting in a greater sensitivity to the tilt angle. As the core thickness increases, the TM-polarized light becomes more confined than TE-polarized light, and hence less sensitive to the tilt angle. At core thicknesses above $1\ \mu\text{m}$, both TE- and TM-polarized modes are almost entirely confined in the core, and the width of the mode field in the vertical direction increases as the core thickness increases. This results in a high sensitivity to the tilt angle at large values of the core thickness.

It is advantageous to use the thinnest possible core that provides acceptable PDW values (see Figure 2). Thus, the selection of the core thickness has to be done in conjunction with a specific application. Irrespective of the core thickness, the ability to etch nearly vertical grating facets is essential in minimizing the insertion loss and reducing the optical crosstalk of planar reflective gratings.

5. CWDM DEMULTIPLEXER DESIGN

We have applied our findings to design an SOI-based CWDM demultiplexer suited for use in integrated receiver applications. The CWDM grid is made up of 18 wavelengths defined within a range of 1270 nm to 1610 nm, spaced by 20 nm [22]. CWDM can support various topologies of interconnects—hubbed rings, point-to-point, and passive optical networks with transmission distances of up to 50 km. The CWDM receivers often require larger bandwidths that can capture all the specified bitrates and protocols. We assume that our CWDM demultiplexer is used in conjunction with wavelength agnostic PINs or avalanche photodiode detectors (APDs) that operate over the entire ITU CWDM band.

On the transmitter side, polarization control is not necessary since laser diodes are strongly polarized. However, on the receiver side, the incoming signal polarization is not known a priori, consequently, receiver demultiplexers should be sufficiently polarization insensitive. From Figure 2, it is apparent that to have sufficiently low polarization dependence ($\text{PDW} < 2\ \text{nm}$) in a planar reflective grating containing no polarization compensators, the silicon core thickness should be no less than $1.7\ \mu\text{m}$. On the other hand, for the best crosstalk performance, Figure 3 suggests that the core thickness is as small as possible. Therefore, to construct the CWDM receiver, we selected the nominal core thickness of $1.7\ \mu\text{m}$.

The rib waveguide geometry was chosen to be single mode according to the modified criterion of Soref et al. [23]. Single-mode operation was confirmed with a full-vectorial finite-element method. The nominal ridge width was chosen to be $1.5\ \mu\text{m}$ with a ridge depth of $0.5\ \mu\text{m}$. The TM mode profile for this structure, generated using finite-element analysis, is shown in Figure 5.

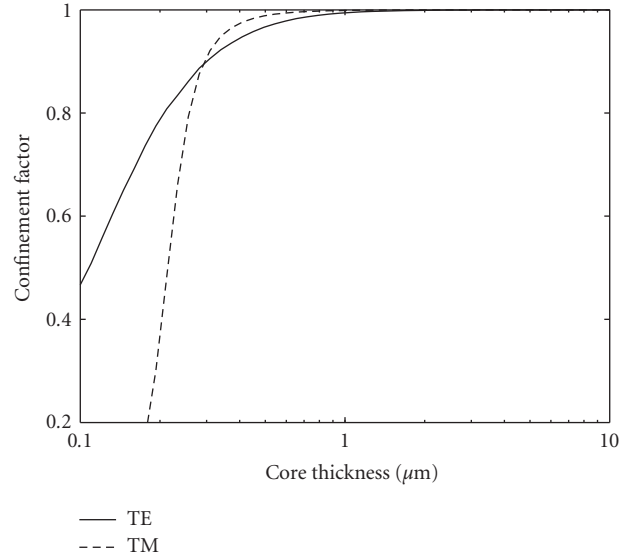


FIGURE 4: Confinement factor in the core layer of TE- and TM-polarized lights versus thickness of the core layer.

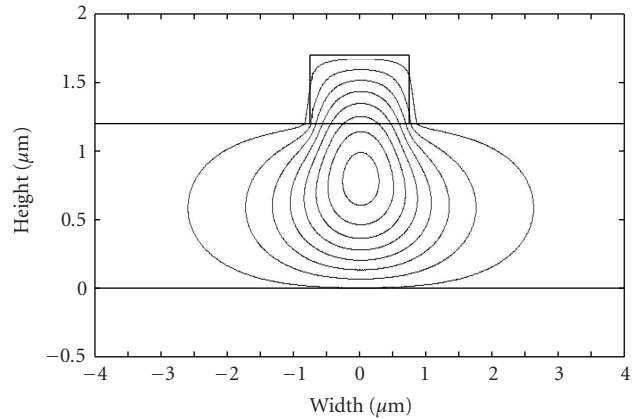


FIGURE 5: The TM mode profile of the input rib waveguide of the CWDM demultiplexer. Birefringence of the waveguide does not contribute to the polarization dependence of a planar reflective grating.

The high-contrast silicon slab considered here supports a large number of higher-order modes. Consequently, special consideration should be given to the design of the input taper to prevent higher-order mode excitation. If higher-order modes are unintentionally excited, it will inevitably lead to the presence of ghost peaks in the output guides even if the grating facets are perfectly vertical. To overcome the higher-order mode excitation, the input waveguide incorporates a linear taper that adiabatically increases the rib width from $1.5\ \mu\text{m}$ to $4\ \mu\text{m}$ over a length of $2000\ \mu\text{m}$. The length of the slab region was chosen to be $6200\ \mu\text{m}$. The slab length is selected to achieve sufficient linear dispersion (as given by (1)) to accommodate the width and separation between the output waveguides.

The selection of the diffraction grating order is dictated by the requirements imposed by the free spectral range (FSR) of the device. In general, the overlap between different orders is determined by

$$(N + 1)\lambda_1 = N\lambda_2. \quad (4)$$

In order to accommodate all 18 channels spaced at 20 nm, as required for a CWDM receiver, $\Delta\lambda = \lambda_2 - \lambda_1$ should be more than 400 nm. Such a wide-free spectral range demands the diffraction order to be $N = 1$, yielding a free spectral range of over 600 nm. While low-diffraction order devices are easily achievable using the planar reflective grating technology, realizing such wide-free spectral range device using the AWG architecture would require an impractically large phase array region that would have severe crosstalk limitations in SOI.

The Rowland circle configuration was chosen as a zero-order approximation to the position of refractive elements and the plane of the input and output waveguides. The first-order correction was obtained through the use of standard double-astigmatic point improvement to the position of the grating facets [11]. In our case, we chose 1270 nm and 1610 nm as astigmatic wavelengths to compensate for the reduced diffraction efficiency in the end channels. The energy of light diffracted by the grating was optimized by selecting a blaze wavelength of 1440 nm.

Careful consideration should be given to the selection of diffraction angles for the planar grating in SOI. Traditionally, planar reflective gratings in SOI have been selected to have incident and reflected angles of around 40 degrees [4, 6]. However, building a wide-free spectral range CWDM demultiplexer at such large diffracting angles would lead to suboptimally shaped grating facets that are susceptible to corner rounding and polarization dependence. While it is possible to remove reflective material from the nonreflective facets to improve the grating efficiency, this would require additional postprocessing steps such as selective metal etch removal.

The reduction in the planar grating diffraction efficiency due to corner rounding is approximately equal to the ratio between the size of the round corner and the size of the reflective portion of the facet. It is advantageous to have the size of the reflective facet much larger compared to the corner rounding. Furthermore, the ratio of the reflective to nonreflective facet has been shown to be the key for overcoming PDL in planar reflective gratings [24]. Consequently, the diffraction angle should be low enough to produce sufficiently wide reflecting facets for ease of manufacturing, while keeping the size of the nonreflecting facets small enough to eliminate corner rounding and polarization effects.

Our analysis of the grating parameters yielded a value of 3.5 degrees for the angle of diffraction. At this diffraction angle, an average size of the reflective facet is $3 \mu\text{m}$ while the nonreflecting sidewall is only $0.2 \mu\text{m}$. This results in the aspect ratio of the reflecting to nonreflecting facet of 15 : 1, putting a limit of -0.3 dB on the maximum diffraction efficiency loss due to corner rounding. The total number of facets was chosen to be 600. This ensured that well over

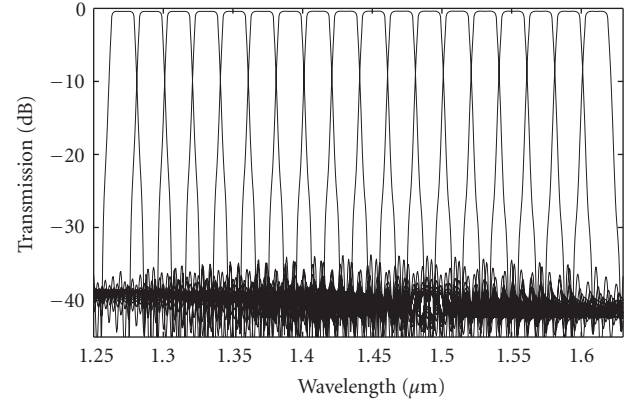


FIGURE 6: Transmission spectra of an 18-channel CWDM demultiplexer for TM polarization. No decrease in the diffraction efficiency was observed for the end channels. Optical crosstalk of better than -35 dB was achieved.

99% of the light from the input waveguide is captured by the grating. Each grating facet was chosen to be an elliptical shape to further reduce aberration effects. Details of aberration reduction are described in [10].

To achieve a box-like channel profile for the CWDM demultiplexer, the output waveguides are formed using a $1.7\text{-}\mu\text{m}$ -deep etch with a waveguide width of $8 \mu\text{m}$ and a separation between waveguides of approximately $4 \mu\text{m}$ (see Figure 1). This output waveguide structure can support a large number of modes. Since the proposed device is specifically designed for use in receiver applications, we assume that the active area of the photodetector is sufficiently large to absorb all of the light in the multimode guide.

To simulate the grating performance, we used a full-vectorial finite-element method to compute the modes of input and output guides. An asymptotic approximation for Hankel functions of large argument was then used to obtain the intensity on the grating facets. This approximation was used once again to obtain the reflected field $\Theta(\lambda)$ on the plane of the output waveguide structures. The demultiplexer transmission intensity at a specific wavelength was obtained by a convolution of the diffracted light with the intensity profile of each individual mode $\phi_i(\lambda)$ in each output multimode output waveguide:

$$T(\lambda) = \sum_i \langle \Theta(\lambda) | \phi_i(\lambda) \rangle. \quad (5)$$

The results of our simulation are shown in Figure 6 for TM polarization. It is worth pointing out that the diffraction efficiency at the end channels is as strong as the efficiency of the central channels. This was possible by our selection of the blaze wavelength of the planar grating to be in the middle of the free spectral range, and the use of the end wavelengths for astigmatic points. Crosstalk values of better than -35 dB have been computed for all 18 channels. The 0.5-dB spectral width of an individual channel was estimated to be 16 nm. Considering that this device has a projected PDW of 2 nm due to the slab birefringence, centering the wavelength between the two extreme polarizations can potentially yield

15 nm of useful bandwidth for each individual channel. Such wide spectral passbands can be useful for transmitting large-bandwidth data while still allowing for the temperature drift of the demultiplexer and the transmitter laser diodes. This work confirms that planar reflective gratings in SOI can be used to achieve both wide-free spectral range and polarization-insensitive performance.

Multiplexing and demultiplexing light is only one of many possible applications of planar reflective gratings in silicon interconnects. Planar reflective gratings can also be used in add-drop filters, repeaters, dispersion compensators, and gain equalizers. Because of their reflective nature, planar gratings can be very effective in stabilizing laser sources through wavelength locking. Additional applications of planar gratings will likely be found in optical clocking through the use of time domain to frequency domain interferometry in silicon interconnects.

6. SUMMARY

In summary, we have investigated the optical properties of planar reflective gratings for building optical interconnects in silicon on insulator for various silicon core thicknesses. We have shown that the dispersion of the slab can be controlled through the core thickness selection to produce polarization-insensitive gratings. The verticality of the grating facets has been found to be the main contributing factor to the cumulative crosstalk in thick silicon cores. Our findings were applied towards the design and simulation of an 18-channel coarse wavelength division demultiplexer that has both a wide-free spectral range and polarization-insensitive performance. These results demonstrate that planar reflective gratings can become an essential element in building many silicon photonics applications.

REFERENCES

- [1] A. W. Fang, H. Park, O. Cohen, R. Jones, M. J. Paniccia, and J. E. Bowers, "Electrically pumped hybrid AlGaInAs-silicon evanescent laser," *Optics Express*, vol. 14, no. 20, pp. 9203–9210, 2006.
- [2] H. Park, A. W. Fang, R. Jones, et al., "A hybrid silicon evanescent photodetector," in *Proceedings of the 65th Annual Device Research Conference (DRC '07)*, pp. 185–186, South Bend, Ind, USA, June 2007.
- [3] W. Bogaerts, P. Dumon, D. Van Thourhout, et al., "Compact wavelength-selective functions in silicon-on-insulator photonic wires," *IEEE Journal on Selected Topics in Quantum Electronics*, vol. 12, no. 6, pp. 1394–1401, 2006.
- [4] J. Brouckaert, W. Bogaerts, P. Dumon, D. Van Thourhout, and R. Baets, "Planar concave grating demultiplexer fabricated on a nanophotonic silicon-on-insulator platform," *Journal of Lightwave Technology*, vol. 25, no. 5, pp. 1269–1275, 2007.
- [5] S. Bidnyk, D. Feng, A. Balakrishnan, et al., "Silicon-on-insulator-based planar circuit for passive optical network applications," *IEEE Photonics Technology Letters*, vol. 18, no. 22, pp. 2392–2394, 2006.
- [6] W. Wang, Y. Tang, Y. Wang, et al., "Etched-diffraction-grating-based planar waveguide demultiplexer on silicon-on-insulator," *Optical and Quantum Electronics*, vol. 36, no. 6, pp. 559–566, 2004.
- [7] S. Bidnyk, A. Balakrishnan, A. Del age, et al., "Novel architecture for design of planar lightwave interleavers," *Journal of Lightwave Technology*, vol. 23, no. 3, pp. 1435–1440, 2005.
- [8] J. Brouckaert, W. Bogaerts, P. Dumon, et al., "Planar concave grating demultiplexer with distributed bragg reflection facets," in *Proceedings of the 4th IEEE International Conference on Group IV Photonics*, pp. 1–3, Tokyo, Japan, September 2007.
- [9] H. W. Yen, H. R. Friedrich, R. J. Morrison, and G. L. Tangonan, "Planar Rowland spectrometer for fiber-optic wavelength demultiplexing," *Optics Letters*, vol. 6, no. 12, pp. 639–641, 1981.
- [10] S. Bidnyk, A. Balakrishnan, A. Del age, et al., "Planar comb filters based on aberration-free elliptical grating facets," *Journal of Lightwave Technology*, vol. 23, no. 3, pp. 1239–1243, 2005.
- [11] P. Cheben, "Wavelength dispersive planar waveguide devices: echelle gratings and arrayed waveguide gratings," in *Optical Waveguides: From Theory to Applied Technologies*, M. L. Calvo and V. Lakshminarayanan, Eds., chapter 5, CRC Press, London, UK, 2007.
- [12] S. Bidnyk, A. Balakrishnan, M. Pearson, M. Gao, and T. Hall, "Configurable coarse wavelength division demultiplexers based on planar reflective gratings," *Optics Communications*, vol. 262, no. 1, pp. 82–86, 2006.
- [13] A. Del age and K. Dossou, "Polarisation dependent loss calculation in echelle gratings using finite element method and Rayleigh expansion," *Optical and Quantum Electronics*, vol. 36, no. 1–3, pp. 223–238, 2004.
- [14] D.-X. Xu, P. Cheben, D. Dalacu, et al., "Eliminating the birefringence in silicon-on-insulator ridge waveguides by use of cladding stress," *Optics Letters*, vol. 29, no. 20, pp. 2384–2386, 2004.
- [15] S. L. Chuang, *Physics of Optoelectronic Devices*, Wiley-Interscience, New York, NY, USA, 1995.
- [16] J. J. He, E. S. Koteles, L. Erickson, B. Lamontagne, and A. Del age, "Optical grating-based device having a slab waveguide polarization compensating region," US patent 5937113, 1999.
- [17] P. Cheben, D.-X. Xu, S. Janz, A. Del age, and D. Dalacu, "Birefringence compensation in silicon-on-insulator planar waveguide demultiplexers using a buried oxide layer," in *Photonics Packaging and Integration III*, vol. 4997 of *Proceedings of SPIE*, pp. 181–189, San Jose, Calif, USA, January 2003.
- [18] P. Cheben, D.-X. Xu, S. Janz, and A. Del age, "Scaling down photonic waveguide devices on the SOI platform," in *VLSI Circuits and Systems*, vol. 5117 of *Proceedings of SPIE*, pp. 147–156, Maspalomas, Spain, May 2003.
- [19] W. Bogaerts, D. Taillaert, P. Dumon, E. Pluk, D. Van Thourhout, and R. Baets, "A compact polarization-independent wavelength duplexer using a polarization-diversity SOI photonic wire circuit," in *Proceedings of the Optical Fiber Communication and the National Fiber Optic Engineers Conference (OFC/NFOEC '07)*, pp. 1–3, Anaheim, Calif, USA, March 2007, paper OTuM2.
- [20] D. K. Sparacin, S. J. Spector, and L. C. Kimerling, "Silicon waveguide sidewall smoothing by wet chemical oxidation," *Journal of Lightwave Technology*, vol. 23, no. 8, pp. 2455–2461, 2005.
- [21] J.-J. He, B. Lamontagne, A. Del age, L. Erickson, M. Davies, and E. S. Koteles, "Monolithic integrated wavelength demultiplexer based on a waveguide Rowland circle grating in InGaAsP/InP," *Journal of Lightwave Technology*, vol. 16, no. 4, pp. 631–637, 1998.
- [22] International Telecommunication Union, ITU-T Recommendation G.694.2, 2002.

- [23] R. A. Soref, J. Schmidtchen, and K. Petermann, "Large single-mode RIB waveguides in GeSi-Si and Si-on-SiO₂," *IEEE Journal of Quantum Electronics*, vol. 27, no. 8, pp. 1971–1974, 1991.
- [24] S. Bidnyk, A. Balakrishnan, and M. Pearson, "Planar waveguide reflective diffraction grating," US patent 7151635, 2006.

Research Article

High-Speed Near Infrared Optical Receivers Based on Ge Waveguide Photodetectors Integrated in a CMOS Process

Gianlorenzo Masini, Subal Sahni, Giovanni Capellini, Jeremy Witzens, and Cary Gunn

Luxtera, Inc., Carlsbad, CA 92011, USA

Correspondence should be addressed to Gianlorenzo Masini, gmasini@luxtera.com

Received 2 December 2007; Revised 8 March 2008; Accepted 4 April 2008

Recommended by Pavel Cheben

We discuss our approach to monolithic intergration of Ge photodetectors with CMOS electronics for high-speed optical transceivers. Receivers based on Ge waveguide photodetectors achieve a sensitivity of -14.2 dBm (10^{-12} bit error rate (BER)) at 10 Gbps and 1550 nm.

Copyright © 2008 Gianlorenzo Masini et al. This is an open access article distributed under the Creative Commons Attribution License, which permits unrestricted use, distribution, and reproduction in any medium, provided the original work is properly cited.

1. INTRODUCTION

Monolithic integration of optical components on an Si platform has been pursued for a long time for its potential advantages over hybrid approaches: lower assembly cost, compactness, channel count, scalability to high-volume production. Integration in a CMOS platform, in particular, is very attractive because of the very low cost-per-unit attainable with this technology.

Several optical building blocks have been demonstrated already on Si: waveguides [1], high-speed modulators [2], photodetectors [3], and complete transceiver systems have been demonstrated as well by Luxtera with its recently introduced 40 Gbps (4 channel, 10 Gbps each) monolithic optical transceiver built on an Si CMOS platform [4].

While waveguiding and modulation can be done in Si and do not require the integration of new materials in the CMOS process, photodetection at long wavelengths (1.3 μm and 1.55 μm) requires either Germanium or a III-V compound such as InGaAs. The former is preferred over the latter due to its better compatibility with the Si technology in terms of lattice structure and parameter and contamination concerns. Germanium on Si photodetectors has been demonstrated by several research groups with high responsivity and speed and relatively low dark current [5–8], however, none of the published devices is integrated in a CMOS process along with standard Si transistors.

In this paper, we first describe our approach to integration of a Ge module for photodetectors in LuxG, Luxtera's

optical-enabled CMOS process based on Freescale's hip7_soi, then we introduce the world's first monolithic high-speed optical receiver based on Ge waveguide photodetectors.

2. TECHNOLOGY

SiGe alloys are commonly found in today's Si technologies both bipolar, as the base layer in heterojunction bipolar transistors (HBTs) [9], and CMOS, as channel "stressors" for p-channel field effect transistors [10]. Unfortunately, the absorption coefficient of the low-Ge-content alloys used in these applications is too weak to be useful for efficient photodetection at 1.5 μm . On the contrary, pure Ge shows very high absorption coefficient up to 1.55 μm , thanks to the direct transitions occurring at the gamma point of its band structure at energies above 0.8 eV. While the use of 100% Ge fet is envisioned as a solution to address the mobility degradation induced by the extreme gate length scaling dictated by the ITRS roadmap [11], several issues remain to be solved before the first product based on this technology faces high volume production, with gate oxide formation and leakage reduction being, probably, the most formidable [12]. Luckily enough, the use of 100% Ge for photodetectors does not imply the formation of a high quality, chemically compatible, high-K, ultrathin dielectric, as it is the case for fets, and the leakage attainable by Ge on Si diodes is high but still compatible with high-speed receivers operation [13].

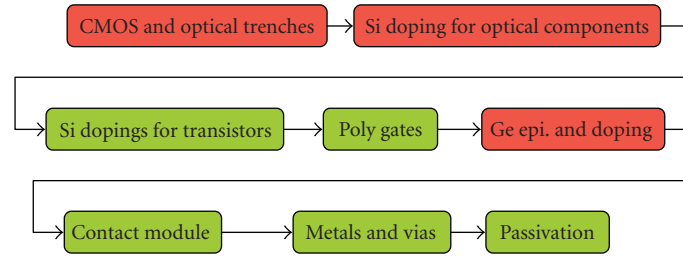


FIGURE 1: LuxG process flow.

Ge can be epitaxially grown on Si, despite the large difference in lattice parameter (4%), using buffering techniques [14]. The buffer is used to plastically relax the strain induced by the lattice mismatch, usually through controlled creation of dislocations, therefore allowing a layer-by-layer, flat, film growth. Among the different approaches found in literature, the low-temperature buffering technique introduced in [15] is very attractive for integration in a CMOS process since it does not require thick (and long) growths thus simplifying the insertion of the Ge film in the limited headroom allowed to a CMOS fet. Ge films grown using this technique have been shown to have less than 10^7 cm^{-2} dislocation density, improving consistently after thermal cycling [16], though the high temperature required by the latter limits its use in a CMOS flow. Ge epitaxy in a CVD environment is, usually, naturally selective to oxide thus allowing for selective deposition in the areas where the detector has to be fabricated using a hard mask. Selectivity can be improved by adding HCl to the gas flow. When it comes to choose the insertion point of the Ge epitaxy step within a CMOS process, several factors must be considered: the temperature profile of the process, the possibility to contact the Ge device using the standard Si contact module, the salicide sensitivity to thermal treatments, the availability of a clean Si surface, the presence of dielectric films, and their interaction on the selective growth of Ge. All these requirements may differ among different technology nodes and need to be carefully evaluated to ensure a seamless integration. LuxG, the Ge-enabled Luxtera process, integrates the Ge epitaxy step at the end of the front-end processing and before the contact module (see Figure 1). Epitaxy is performed in an RPCVD reactor for 8" wafers using GeH_4 and hydrogen as the carrier gas.

While forcing the detector to share the same contact module of a transistor greatly simplifies its integration, it also constraints the maximum thickness that can be used for the Ge epitaxy to a fraction of a micron. This fact rules out the possibility to integrate surface illuminated detectors which, given the penetration depth of $1.5 \mu\text{m}$ light in Ge, require an absorption length (i.e., thickness) larger than 2 micron. Waveguide photodetectors can be used, instead, since absorption in these devices occurs along propagation of the optical beam parallel to the growth surface (see Figure 2), thus transforming the thickness constraint in a waveguide length requirement. Waveguide photodetectors have other advantages over surface illuminated ones, the most relevant being the decoupling of light absorption and photocarrier drift directions which allows for independent optimization

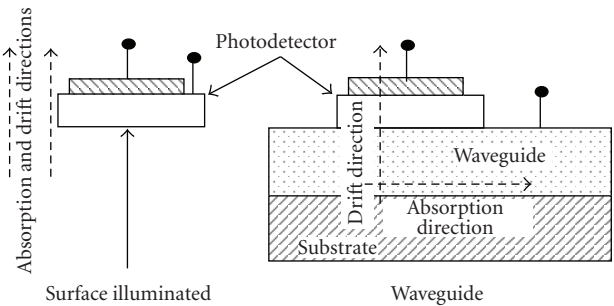


FIGURE 2: Absorption and drift directions are decoupled in a waveguide photodetector allowing to independently optimize efficiency and speed.

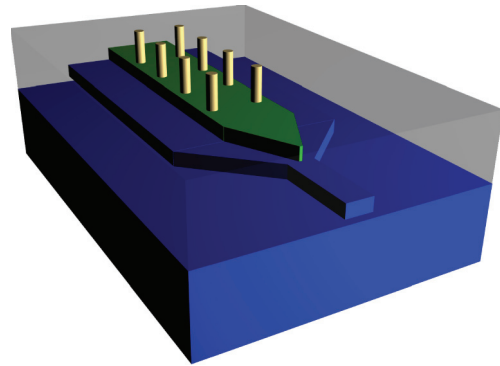


FIGURE 3: 3D view of an LuxG PIN waveguide photodetector.

of absorption on one side and collection efficiency and speed on the other.

3. LuxG WAVEGUIDE PHOTODETECTORS

LuxG waveguide photodetectors have a p-i-n structure in which both anode and cathode are formed on Ge by ion implantation. While other contact configurations, such as the heterojunction one with one electrode on Ge and the other on Si, have been explored, the homojunction one proved best in terms of responsivity and speed, at the cost of a higher leakage. A pictorial view of an LuxG waveguide photodetector is shown in Figure 3. Light coupling from the

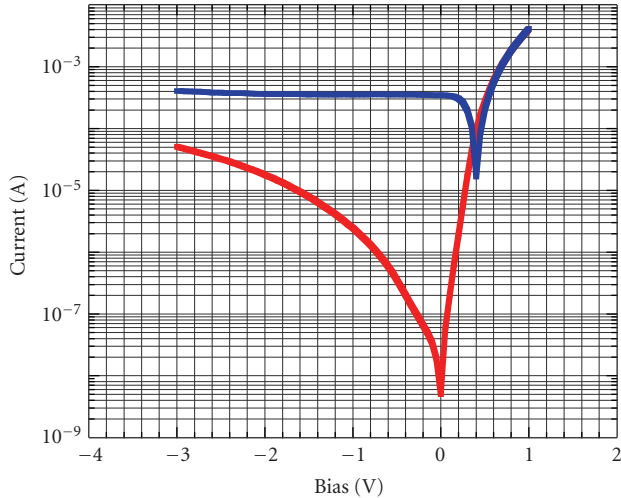


FIGURE 4: Current-voltage characteristics of an LuxG PIN waveguide photodetector in the dark (red) and under illumination at a wavelength of 1550 nm (blue).

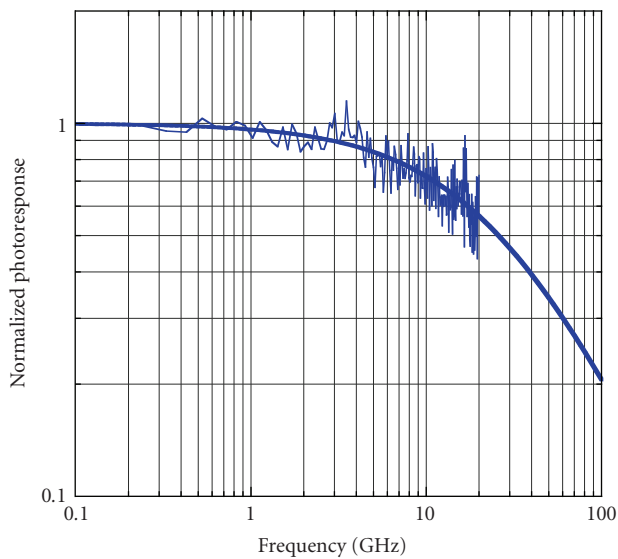


FIGURE 5: Frequency response of an LuxG PIN waveguide photodetector at a wavelength of 1550 nm and 1V reverse bias. An optical bandwidth of 26 GHz is extrapolated from the single-pole fit.

Si waveguide is facilitated by the higher refractive index of Ge and total absorption at 1550 nm occurs in $28 \mu\text{m}$ which is the detector length. A typical current/voltage characteristic in the dark and under illumination is shown in Figure 4. At a typical operating voltage of 1V reverse bias, the dark current is $3 \mu\text{A}$ and the responsivity is 0.85 A/W . Note that the responsivity at short circuit is 99% of that achieved in reverse bias thus allowing efficient operation at 0V, when very high-speed operation is not required as an example for power monitor applications. The relatively high dark current of the Ge detector is due to the presence of defects in the film and at the Si/Ge interface originated by the lattice mismatch.

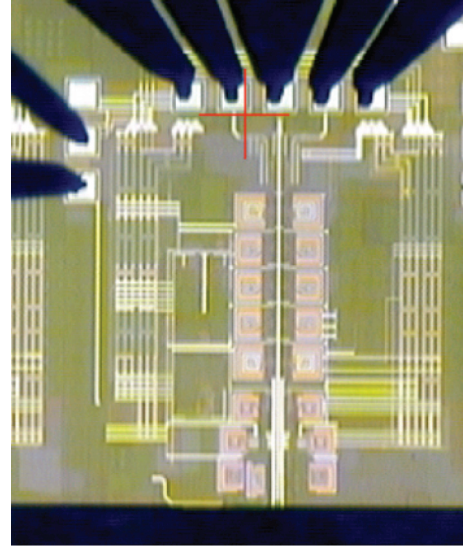


FIGURE 6: Optical microscope picture of a TIA-LA with LuxG waveguide photodetectors during waferscale test.

Frequency response at 1V reverse bias is reported in Figure 5 showing an optical bandwidth in excess of 20 GHz with a well-behaved, single-pole, roll-off.

4. LuxG HIGH-SPEED OPTICAL RECEIVER

LuxG waveguide photodetectors have been monolithically integrated with a full TIA-LA (transimpedance amplifier-limiting amplifier) CMOS receiver. The TIA is implemented using a three stages classic feedback architecture with peaking inductors to enhance the high-frequency response, and the LA is a 5-stage differential amplifier also using hybrid resistive-inductive loading. More details on the TIA-LA design can be found in [17]. The TIA was designed for use with a standard stand-alone, surface-illuminated detector which has a much higher capacitance than a waveguide integrated one. The potential sensitivity enhancement achievable by increasing the transimpedance gain of the TIA and enabled by the smaller photodetector capacitance (estimated to be between 10 and 15 fF) was, therefore, not exploited in this experiment. A picture of the full receiver during waferscale test is shown in Figure 6: the RF probes used to pick up the high speed signal are visible in the top part of the picture while the electrodes used to bias the TIA-LA and the detector are on the left. The light was coupled by means of a grating coupler from a fiber array, partially visible in the bottom part of the picture, to an Si waveguide feeding the photodetector. A typical eye diagram at 10 Gbps is shown in Figure 7. The TIA-LA power supply voltage was 1.4V while the detector was biased at 0.3V. Power level at the detector was -10.5 dBm . The measured bit error rate as a function of the optical power at the detector is shown in Figure 8 indicating a sensitivity of -14.2 dBm . The input signal for this experiment was a 10 Gbps, 2^7 PRBS (pseudo-random binary sequence).

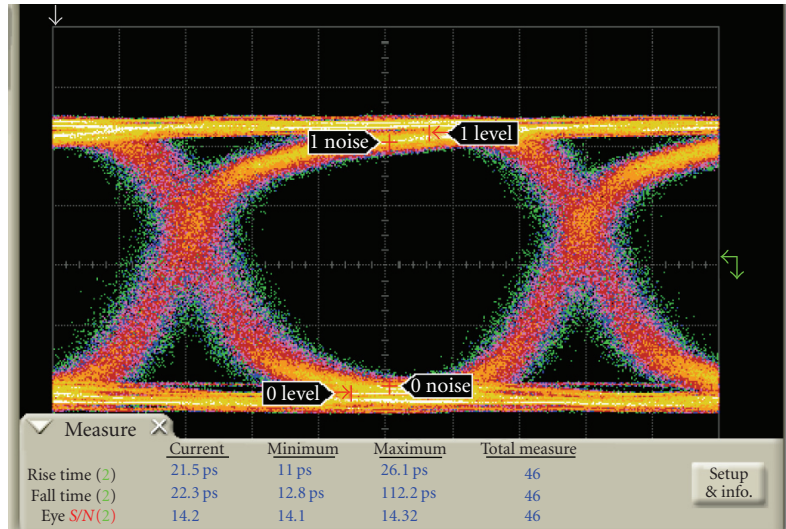


FIGURE 7: Typical eye diagram at 10 Gbps.

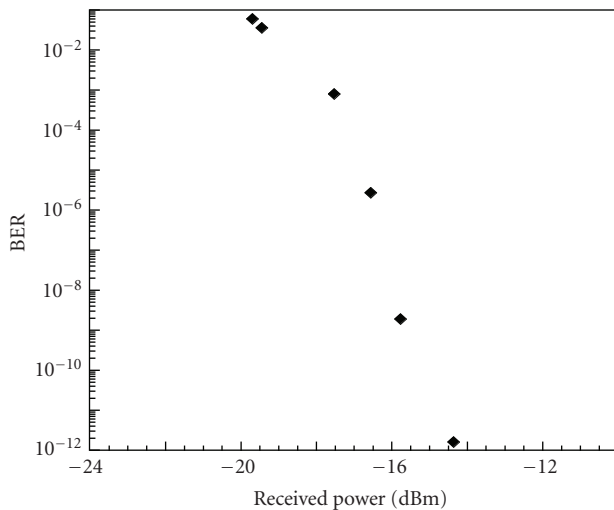


FIGURE 8: Bit error rate as a function of optical power for the 10 Gbps monolithic receiver as measured during waferscale test. Light wavelength is 1550 nm.

5. CONCLUSIONS

In this paper, we discuss our approach to monolithic integration of near infrared Ge waveguide photodetectors in a CMOS process. Waveguide detectors with 0.85 A/W responsivity at 1550 nm and speed in excess of 20 GHz are shown. A monolithic CMOS receiver using Ge waveguide photodetectors and operating at 10 Gbps with a sensitivity better than -14 dBm is also demonstrated.

ACKNOWLEDGMENT

This work was partially supported by the Microsystems Technology Office at DARPA under Contract no. HR0011-05-9-0004.

REFERENCES

- [1] K. K. Lee, D. R. Lim, L. C. Kimerling, J. Shin, and F. Cerrina, "Fabrication of ultralow-loss Si/SiO₂ waveguides by roughness reduction," *Optics Letters*, vol. 26, no. 23, pp. 1888–1890, 2001.
- [2] A. Liu, L. Liao, D. Rubin, et al., "High-speed optical modulation based on carrier depletion in a silicon waveguide," *Optics Express*, vol. 15, no. 2, pp. 660–668, 2007.
- [3] G. Masini, L. Colace, G. Assanto, H.-C. Luan, and L. C. Kimerling, "High-performance p-i-n Ge on Si photodetectors for the near infrared: from model to demonstration," *IEEE Transactions on Electron Devices*, vol. 48, no. 6, pp. 1092–1096, 2001.
- [4] A. Narasimha, B. Analui, E. Balmater, et al., "A 40-Gb/s QSFP optoelectronic transceiver in a 0.13 μ m CMOS Silicon-on-Insulator technology," in *Proceedings of the Optical Fiber Communication Conference and Exposition (OFC '08)*, San Diego, Calif, USA, February 2008.
- [5] M. Morse, O. Dosunmu, G. Sarid, and Y. Chetrit, "Performance of Ge-on-Si p-i-n photodetectors for standard receiver modules," *IEEE Photonics Technology Letters*, vol. 18, no. 23, pp. 2442–2444, 2006.
- [6] D. Ahn, C. Hong, J. Liu, et al., "High performance, waveguide integrated Ge photodetectors," *Optics Express*, vol. 15, no. 7, pp. 3916–3921, 2007.
- [7] L. Vivien, M. Rouvière, J.-M. Fédéli, et al., "High speed and high responsivity germanium photodetector integrated in a Silicon-On-Insulator microwaveguide," *Optics Express*, vol. 15, no. 15, pp. 9843–9848, 2007.
- [8] G. Mascini, L. Colace, G. Assanto, H.-C. Luan, K. Wada, and L. C. Kimerling, "High responsivity near infrared Ge photodetectors integrated on Si," *Electronics Letters*, vol. 35, no. 17, pp. 1467–1468, 1999.
- [9] D. J. Friedman, M. Meghelli, B. D. Parker, et al., "SiGe BiCMOS integrated circuits for high-speed serial communication links," *IBM Journal of Research and Development*, vol. 47, no. 2-3, pp. 259–282, 2003.
- [10] T. Ghani, M. Armstrong, C. Auth, et al., "A 90 nm high volume manufacturing logic technology featuring novel 45 nm gate length strained silicon CMOS transistors," in *Proceedings of 49th IEEE International Electron Devices Meeting (IEDM '03)*, pp. 978–980, Washington, DC, USA, December 2003.

-
- [11] http://www.itrs.net/Links/2006Update/FinalToPost/07_FEP2006Update.pdf.
 - [12] H. Shang, M. M. Frank, E. P. Gusev, et al., "Germanium channel MOSFETs: opportunities and challenges," *IBM Journal of Research and Development*, vol. 50, no. 4-5, pp. 377–386, 2006.
 - [13] S. J. Koester, J. D. Schaub, G. Dehlinger, and J. O. Chu, "Germanium-on-SOI infrared detectors for integrated photonic applications," *IEEE Journal on Selected Topics in Quantum Electronics*, vol. 12, no. 6, pp. 1489–1502, 2006.
 - [14] G. Masini, L. Colace, and G. Assanto, "Germanium thin films on silicon for detection of near-infrared light," in *Thin Films Handbook*, H. S. Nalwa, Ed., p. 237, Academic Press, Boston, Mass, USA, 2001.
 - [15] L. Colace, G. Masini, F. Galluzzi, et al., "Metal-semiconductor-metal near-infrared light detector based on epitaxial Ge/Si," *Applied Physics Letters*, vol. 72, no. 24, pp. 3175–3177, 1998.
 - [16] L. Colace, G. Masini, G. Assanto, H.-C. Luan, K. Wada, and L. C. Kimerling, "Efficient high-speed near-infrared Ge photodetectors integrated on Si substrates," *Applied Physics Letters*, vol. 76, no. 10, pp. 1231–1233, 2000.
 - [17] B. Analui, D. Guckenberger, D. Kucharski, and A. Narasimha, "A fully integrated 20-Gb/s optoelectronic transceiver implemented in a standard 0.13- μm CMOS SOI technology," *IEEE Journal of Solid-State Circuits*, vol. 41, no. 12, pp. 2945–2955, 2006.

Research Article

Light Emission from Rare-Earth Doped Silicon Nanostructures

J. Li, O. H. Y. Zalloum, T. Roschuk, C. L. Heng, J. Wojcik, and P. Mascher

Department of Engineering Physics and Centre for Emerging Device Technologies, McMaster University, Hamilton, ON, Canada L8S 4K1

Correspondence should be addressed to P. Mascher, mascher@mcmaster.ca

Received 5 December 2007; Accepted 27 March 2008

Recommended by D. Lockwood

Rare earth (Tb or Ce)-doped silicon oxides were deposited by electron cyclotron resonance plasma-enhanced chemical vapour deposition (ECR-PECVD). Silicon nanocrystals (Si-ncs) were formed in the silicon-rich films during certain annealing processes. Photoluminescence (PL) properties of the films were found to be highly dependent on the deposition parameters and annealing conditions. We propose that the presence of a novel sensitizer in the Tb-doped oxygen-rich films is responsible for the indirect excitation of the Tb emission, while in the Tb-doped silicon-rich films the Tb emission is excited by the Si-ncs through an exciton-mediated energy transfer. In the Ce-doped oxygen-rich films, an abrupt increase of the Ce emission intensity was observed after annealing at 1200°C. This effect is tentatively attributed to the formation of Ce silicate. In the Ce-doped silicon-rich films, the Ce emission was absent at annealing temperatures lower than 1100°C due to the strong absorption of Si-ncs. Optimal film compositions and annealing conditions for maximizing the PL intensities of the rare earths in the films have been determined. The light emissions from these films were very bright and can be easily observed even under room lighting conditions.

Copyright © 2008 J. Li et al. This is an open access article distributed under the Creative Commons Attribution License, which permits unrestricted use, distribution, and reproduction in any medium, provided the original work is properly cited.

1. INTRODUCTION

The realization of integrated silicon photonics requires the development of several fundamental components including light sources, modulators, amplifiers, and detectors [1, 2]. To achieve silicon-based light sources has always been the most challenging task, with the first optically pumped silicon Raman laser being reported only very recently [3]. It is well known that bulk silicon is a poor light emitter due to its indirect bandgap and the presence of nonradiative recombination pathways [4]. Many approaches have been attempted to overcome these obstacles and achieve efficient emission from silicon. One of the most promising solutions is to introduce impurities such as rare-earth elements into materials. Of the rare-earth elements, Er has attracted the most extensive attention because of the coincidence between its intra-4f transition at 1535 nm and the transparency window used for telecommunications [5]. However, the demand to realize full-color light emission from silicon structures can extend technology interests to many other rare-earth elements such as Tb and Ce which

usually emit green and ultraviolet/blue light, respectively [6].

Luminescence from rare-earths has been studied extensively since it was discovered at the beginning of the 20th century [7]. Today various rare-earth doped materials are playing important roles in many areas such as displays, solid-state lasers, detectors, and data storage [8–12]. Recently, there have arisen enormous demands to develop optical sources and amplifiers compatible with silicon ULSI technology leading to a large increase in the interest for one specific type of material: rare-earth doped silicon-based materials [6].

Rare-earth elements make up the sixth row of the periodic table and have a partially filled 4f shell. Optically active rare-earth ions often exist as trivalent and are formed by losing one 4f electron and both 6s electrons. Luminescence from these ions is mainly attributed to their intra-4f or 5d-4f transitions. Intra-4f transitions are relatively independent of the host material, since the 4f states are shielded from outside interaction by 5d states. Note that intra-4f transitions for free ions are parity forbidden but are partially allowed

through the mixing of opposite parity wave functions when rare-earth ions are embedded in a host material. As a result, they have very long luminescence lifetimes and weak oscillator strengths. In contrast, 5d-4f transitions are very sensitive to the surrounding ligands because 5d states are directly exposed to the local environment. Thus, changes in the spectral shapes, peak positions, and intensities may suggest the evolution of the matrix structure. Additionally, since 5d-4f transitions are parity permitted, they have very short luminescence lifetimes and strong oscillator strengths [13].

There are two major obstacles that have to be overcome in order to achieve efficient emission from rare-earth doped silicon oxides: inefficient excitation of intra-4f transitions from rare-earth ions and low solubility of optically active rare-earth ions in silicon-based hosts.

Emissions from rare-earth ions often originate from the intra-4f transitions which are only partially parity allowed. As a result, many rare-earth ions suffer from constraints on excitation wavelengths and their low absorption cross-sections of pump photons. For example, Er ions embedded in silica can only be directly excited at several specific wavelengths including 488, 514, 800, 980, and 1480 nm and the absorption cross-section is as low as 10^{-21} to 10^{-20} cm² [5]. Various sensitizers such as Yb ions, silicon nanocrystals (Si-ncs), silver, and organic complexes have been found to be able to enhance rare-earth emission significantly through a dipole-dipole Forster-Dexter coupling process [14].

One structure receiving particular attention is Er-doped silicon-rich silicon oxide (SRSO). The Si-ncs precipitated upon annealing can be considered as three-dimensionally confined structures. The “bandgap” (energy difference between the highest occupied molecularorbital (HOMO) and the lowest unoccupied molecular orbital (LUMO)) of these structures increases with a decrease in size due to quantum confinement effects [15]. It was demonstrated that Er emission can be enhanced significantly through exciton-mediated energy transfer between Si-ncs and Er [16].

Great efforts have been made to understand the physics of the Er:Si-ncs system. The sensitization mechanism is now relatively well understood at the phenomenological level. After a Si-nc absorbs a photon, a bound exciton is generated in the Si-nc. The exciton may recombine nonradiatively by transferring energy to a nearby Er ion, putting the ion into an excited state. The Er ion then decays to the ground state by emitting a photon of 1.54 μm [14]. According to the generalized rate-equation analysis by Kenyon et al. [17], this sensitization process is strongly dependent on the distance between the Si-nc and Er ion. The Er luminescence is thus limited by the low number of Er ions coupled to the Si-ncs, which is due to the low Si-ncs density and the short interaction distance.

Since Si-ncs have a high absorption cross-section and efficiently transfer energy to Er ions, the excitation cross-section of Er ions can be increased by up to 10^4 times [16]. Furthermore, the absorption band of Si-ncs covers the whole visible spectrum and the utilization of broad band excitation sources becomes possible. The successful excitation of Er in SRSO using a broad band visible excitation source, such

as a commercial camera flashgun or blue LED has been demonstrated [18, 19].

In principle, an analogous excitation mechanism can operate in SRSO films doped with other rare-earths as long as the “bandgap” of Si-ncs wide enough to ensure energy transfer to the rare-earth ions [20]. In the present work, we demonstrate that by using a 325 nm He-Cd laser the Tb emission can be excited efficiently in both SRSO and oxygen-rich silicon oxides (ORSO) through different excitation processes.

The solubility of optically active rare-earth ions in various silicon materials is universally low due to the mismatch of ionic radii and the strong covalent bonding of the matrix network. Above the critical concentrations, rare-earth ions tend to form precipitates, which results in severe luminescence quenching through ion-ion interaction or by forming an optically inactive phase [6]. It is very difficult to incorporate high concentrations of optically active rare-earths in silicon materials through equilibrium techniques such as the sol-gel method [21]. Low temperature techniques, such as ion implantation or plasma enhanced chemical vapor deposition (PECVD), are able to increase the solubility limit by an order of magnitude, an effect attributed to the lower diffusivity of the dopant ions. Particularly, electron cyclotron resonance (ECR)-PECVD can generate a uniform distribution of rare-earth doping throughout the entire film thickness with low defect concentrations due to the low ion energy [22].

Over the past few years, we have been conducting extensive studies on achieving highly efficient light emission from rare-earth doped silicon nanostructures formed in thin films prepared by ECR-PECVD. It was found that Er emission properties are highly dependent on the details of Si-ncs and Er concentrations. The Er emission intensities can be enhanced greatly by optimizing deposition parameters and postdeposition thermal annealing conditions [23, 24].

In this paper, we report on studies of SRSO and ORSO doped with Tb or Ce. We show successful in situ incorporation of high concentrations of rare-earth elements. The dependence of the emission properties on rare-earth dopant concentration, silicon/oxygen ratio, and annealing temperature was investigated. The emission intensities from the rare-earths were optimized. An interpretation of the excitation mechanisms and the correlation between optical properties and structural evolution is suggested.

2. EXPERIMENTAL DETAILS

Tb or Ce doped silicon oxides were prepared in a custom-designed ECR-PECVD system (Figure 1). Ar and O₂ plasma gases were introduced from the upper dispersion ring. Silane (SiH₄) gas diluted in Ar was used as the Si source and volatile metal-organic precursors served as the rare-earth sources. Tb(tmhd)₃ or *tris* (2,2,6,6-teramethyl-3,5-heptanedionato)-Tb(III), and Ce(tmhd)₃ or *tris* (2,2,6,6-teramethyl-3,5-heptanedionato)-Ce(III) were used as the Tb and Ce sources, respectively. The rare-earth sources were contained in a manifold which can be heated up to 200 °C to sublime the precursor inside. Ar carrier gas then transports

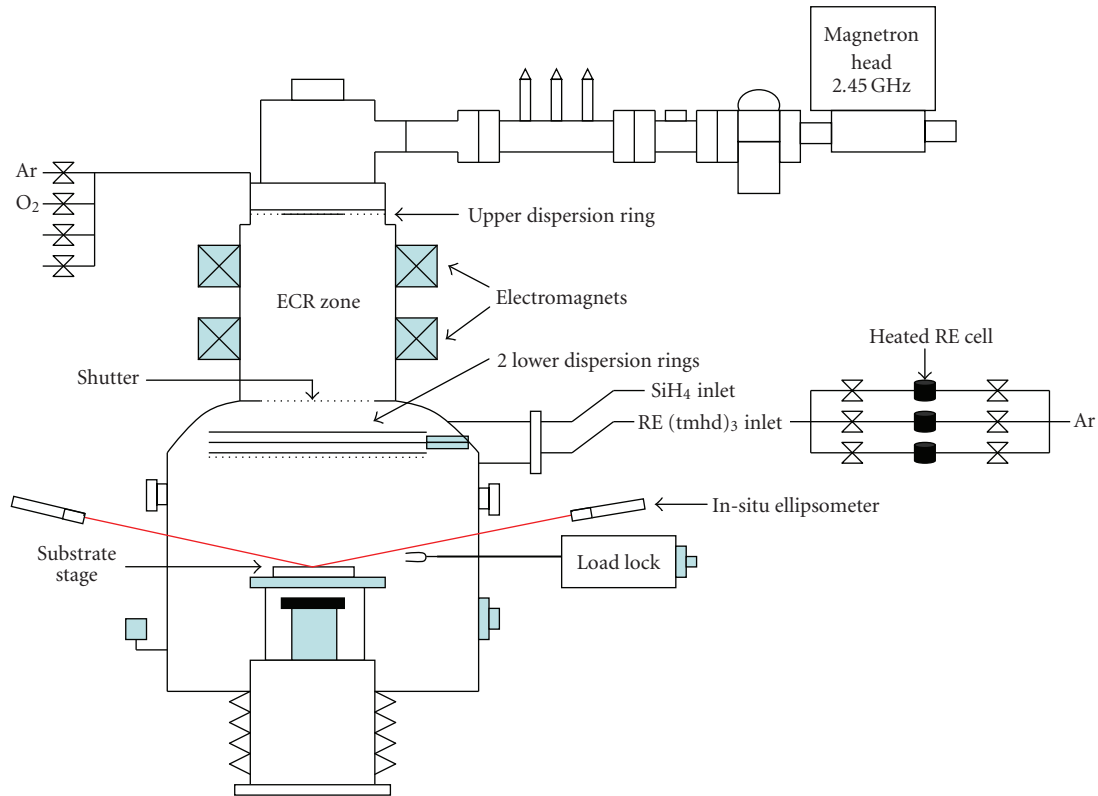


FIGURE 1: ECR-PECVD system.

the rare-earth precursor through a transmission line after which it is introduced in the chamber alongside the SiH_4 through the lower dispersion ring. This multidopant delivery system allows the incorporation of up to three types of rare-earth elements simultaneously. The temperatures of three rare-earth manifold containers, the rare-earth dispersion ring, and the transmission lines are independently controlled by five Eurotherm temperature controllers. All of the gas flow rates can be controlled independently using a central mass flow controller panel. The base pressure of the system was 1×10^{-7} Torr and the deposition pressure was between 2 and 5 mTorr.

Rare-earth doped silicon oxide films were deposited on n-type (100) silicon wafers which sit on the substrate stage located in the reaction chamber. In the present study, the stage temperature was 350°C , but it could be varied from room temperature to 800°C . The film thickness was monitored during the deposition by an in situ ellipsometer operating at 632.8 nm. Several deposition parameters including rare-earth cell temperature, SiH_4 and O_2 gas flows, and microwave power were varied to achieve different Si, O, and rare-earth content. A summary of the deposition parameters and their values in this study are given in Table 1. Two types of mass flow controller were used for different samples, therefore, there are two types of flow rate units employed as indicated in Table 1. Each sample contains only one type of rare-earth dopant. The thicknesses of all the samples were remeasured after the deposition through ellipsometry and

vary from 800–1100 Å. All PL intensities discussed in this report were normalized to 1000 Å, assuming that PL intensity increases linearly with thickness.

The compositions of the samples were determined quantitatively through Rutherford backscattering spectrometry (RBS) using a 1.0 MeV He^+ beam confirming the successful incorporation of rare-earth elements into the thin films. Figure 2 shows the RBS spectrum of an as-deposited Ce-doped sample containing 32 at.% Si and 1.0 at.% Ce. The energies related to the surface Ce, Ar, Si, and O atoms are as indicated. The signal from O sits on the signal from Si in the substrate and depresses the signal from Si in the film. Si, O, and Ce all exhibit a uniform concentration distribution throughout the film thickness. Trace amounts of Ar are also observed in the spectrum. The majority of Ar can be removed from the film during annealing. In the present study, the Si content varies from 32 to 40 at.%, Tb 0.1 to 0.8 at.%, and Ce 0.01 to 1.0 at.%.

All the films were annealed in a quartz tube furnace under flowing N_2 for 1 hour. The annealing temperature varied from 800 to 1200°C . The luminescence properties of the films were analyzed by single wavelength laser-excited PL spectroscopy. The excitation source was a 17 mW He-Cd laser operating at 325 nm. The PL from the films was detected by a spectrometer employing a charge-coupled device array; these PL spectra were corrected for system response and optics transmission and subsequently converted to normalized photon flux. A full description of the CCD-based

TABLE 1: Summary of the deposition parameters and their values for the depositions in this study.

Dopant type	RE concentration [at.%]	Si concentration [at.%]	Forwarded power [W]	Reflected power [W]	SiH ₄ flow rate	O ₂ flow rate	Ar flow rate	RE cell temp [°C]
Tb	0.4 ⁽²⁾	32	420	10	7	24	20	160
	0.8 ⁽²⁾	32	420	10	7	24	30	160
	0.1 ⁽²⁾	36	608	7	20	60	25	160
	0.2 ⁽²⁾	38	327	27	20	56	25	156
	0.3 ⁽²⁾	36	500	5	20	56	25	153
Ce	0.01 ⁽²⁾	33	510	5	11	78	12	100
	0.1 ⁽³⁾	32	507	7	4	40	25	180
	1.0 ⁽³⁾	32	509	7	2	30	10	200
	0.04 ⁽²⁾	40	515	5	25	70	12	161

⁽²⁾ The sample was deposited using mass flow controller 1, the corresponding flow rate unit is mV.

⁽³⁾ The sample was deposited using mass flow controller 2, the corresponding flow rate unit is sccm.

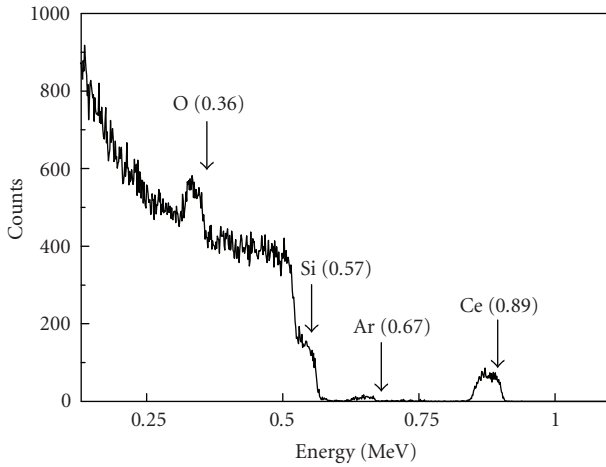


FIGURE 2: RBS measurement of a Ce:ORSO sample containing 32 at.% Si and 1.0 at.% Ce. The surface energies of Ce, Ar, Si, and O are indicated by arrows.

PL system and the data correction methodology is given elsewhere [25]. All the measurements were performed at room temperature. The formation of Si-ncs in the Tb doped silicon-rich film was studied by a JEOL 2010F Field Emission Gun Transmission Electron Microscope operating at 200 keV.

3. RESULTS AND DISCUSSION

3.1. Tb doped oxygen-rich silicon oxides (Tb:ORSO)

The Tb:ORSO samples have a constant Si content of 32 at.% and varying Tb content of 0.4 and 0.8 at.%, respectively. Figure 3 shows the PL spectra of the 0.4 at.% Tb sample as-deposited and annealed at various temperatures. Four strong distinct sharp bands were observed sitting on a weak broad band for all annealing temperatures. According to the energy level diagram of Tb³⁺ ions shown in Figure 4 [adapted from [26]], the four bands centered at 487, 546, 588, and 620 nm are related to ⁵D₄ – ⁷F_{*j*} (*j* = 6, 5, 4, 3) intra-4f transitions

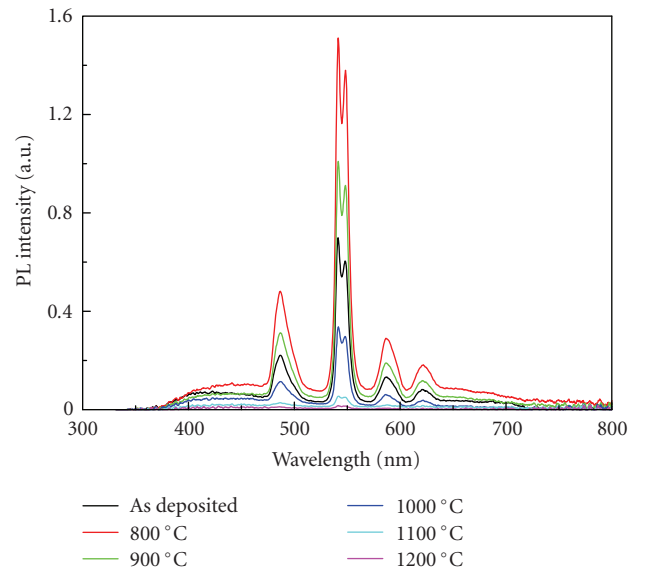


FIGURE 3: PL spectra of the Tb:ORSO samples containing 0.4 at.% Tb, as deposited and annealed at different temperatures in the range of 800–1200 °C.

of Tb³⁺. The 546 nm band is split into two peaks, centered at 542 and 548 nm, due to the Stark splitting of the matrix. The emissions from the ⁵D₃ state are absent due to the cross-relaxation effect [27]. The observed emission spectra resemble those of Tb doped SiO₂ fabricated by conventional PECVD [28]. The peak around 546 nm has been confirmed to originate from Tb³⁺ using PL decay measurements [29]. The corresponding lifetime was around 1.3 ms. There are no appreciable changes in the peak positions and spectral widths with annealing temperature.

The weak broadband emission ranging from 400 to 700 nm is usually attributed to oxide defects in the matrix [30]. If that were indeed the case, the corresponding emission should decrease after annealing at 800 °C, since the defects in SiO₂ tend to reduce during annealing process.

However, in this study the emission became stronger after annealing at 800°C. In addition, this unidentified emission and the Tb emission have a similar dependence on annealing temperature. Therefore, we suggest that the origin is related to the optically active Tb³⁺ sites.

It is important to note that the 325 nm (3.8 eV) excitation is not resonant with any optical absorption band of Tb³⁺, so the observation of the strong Tb emission from the film implies the presence of a highly efficient indirect excitation process. In general, there are two types of indirect excitation mechanisms: carrier-mediated excitation and dipole-dipole Forster-Dexter coupling [6]. A previous investigation on Tb-doped silicon oxynitrides by Jeong et al. has suggested that Tb³⁺ ions can be excited efficiently by a 325 nm excitation source through carrier recombination processes [31]. The 325 nm source is able to excite carriers into extended above-band-gap states, because the bandgap of silicon oxynitride is only between 3.5 to 4 eV for the samples they considered [32]. However, for the films considered here, this process is less possible, because the bandgap of SiO₂ is as large as 8 eV. In oxygen-rich films, it is expected that no or very few Si_{nc}s exist. Based on this assumption, the presence of alternate sensitizers has to be considered.

One possible sensitizer is the organic molecule introduced during the deposition from the metal organic precursor Tb(tmhd)₃. It was found that some rare-earth chelates have broad absorption bands and high absorption coefficients and can serve as sensitizers to efficiently excite rare-earth ions. Many rare-earth chelates have been synthesised to exploit the effect [14]. To the best of our knowledge, however, there have been no reports on the sensitizing effect of the Tb(tmhd)₃ molecules employed in the present study. Further studies on the absorption properties of the sensitizer clearly are necessary.

Figure 5 shows the 546 nm peak intensities of various samples as a function of annealing temperature between 800 and 1200°C. The intensities generally decrease with an increase of the annealing temperature. In comparison to the as-deposited sample, the significant enhancement of the Tb emission after annealing at 800°C can be attributed to the reduction of defects and the activation of optically active Tb³⁺ sites. The decrease of the Tb emission at annealing temperatures higher than 800°C can be explained by the reduction of both optically active Tb sites and available sensitizers. X-ray absorption fine structure (XAFS) analysis has confirmed that there are two types of Tb sites existing in Tb-doped SiO₂:Tb coordinated with two oxygen atoms (Tb-2O) or six oxygen atoms (Tb-6O), with the formation of the latter being related to the enhancement of Tb emission [33]. At annealing temperatures higher than 800°C, Tb ions achieve enough energy to diffuse and form clusters. So the number of oxygen atoms associated with each Tb ion is reduced, which may lead to the transformation from Tb-6O to Tb-2O and results in the decrease of Tb emission. Another possibility that cannot be excluded is that the organic molecules become more unstable and begin to dissociate at higher annealing temperatures. As a result, the available sensitizers may reduce significantly and also lead to the decrease of Tb emission.

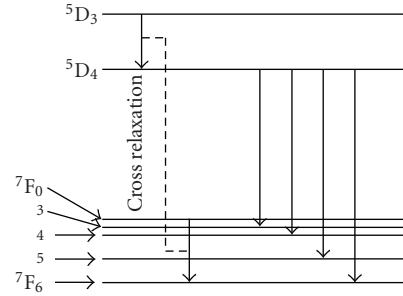


FIGURE 4: The electronic energy levels of Tb³⁺ [adapted from [26]].

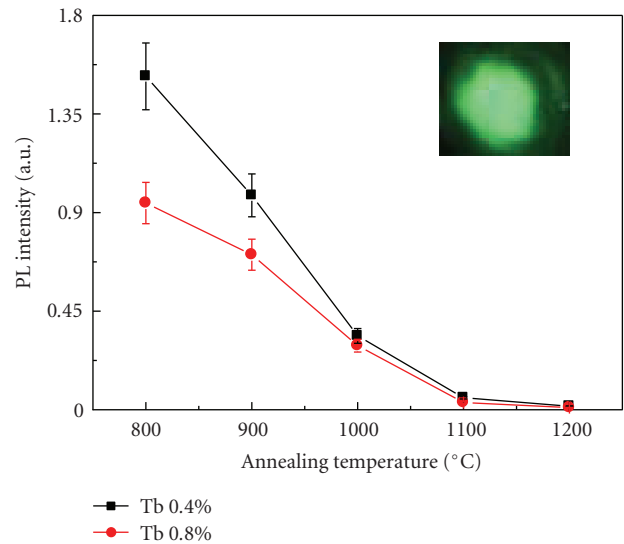


FIGURE 5: PL intensity of Tb³⁺ at 546 nm from two Tb:ORSO samples as a function of annealing temperature. The inset shows an image of strong green Tb emission from the 0.4 at.% Tb sample after annealing at 800°C taken by camera.

Since a previous study on Tb doped SiO₂ showed that the lifetime of Tb emission still remains almost constant at concentration as high as 2.7 at.% [29], our observation of the decrease of the emission intensity at high Tb concentration might not be due to ion-ion interaction and is possibly attributable to the trend to form clusters which leads to the reduction of optically active Tb-6O sites or the exhaustion of available sensitizers.

In this study, the strongest Tb emission was observed from the 0.4 at.% Tb sample annealed at 800°C. The inset of Figure 5 shows the corresponding picture taken with a camera. The emission was quite strong and can be easily observed under bright room lighting conditions.

3.2. Tb-doped silicon-rich silicon oxide (Tb:SRSO)

The Tb:SRSO samples have a constant Si content of 36 at.% and varying Tb content of 0.1, 0.2, and 0.3 at.%, respectively. Figure 6 shows the PL spectra of the 0.3 at.% Tb sample as-deposited and annealed at various temperatures. A broad emission band centered at 650 nm was observed from the

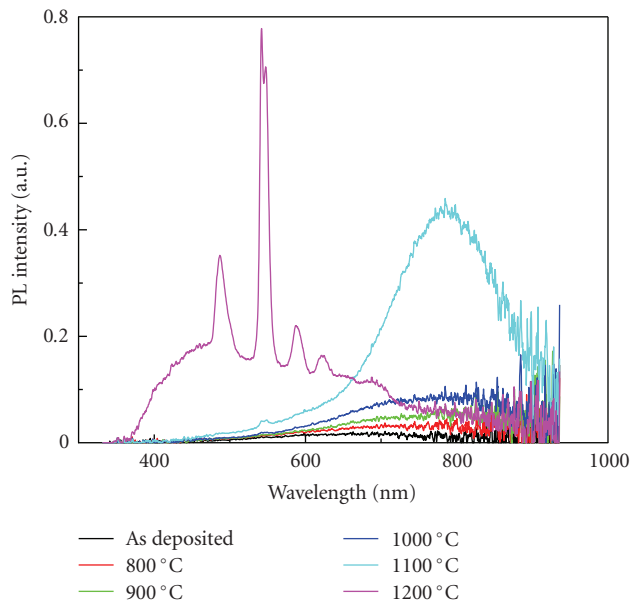


FIGURE 6: PL spectra of the Tb:SRSO samples containing 0.3 at.% Tb, as-deposited or annealed at various temperatures in the range of 800–1200°C.

as-deposited sample. Annealing at temperatures between 800 and 1100°C results in an increase in its intensity with a red shift of the peak position. This is characteristic of Si-ncs emission. The enhancement of the emission intensity indicates the formation of more Si-ncs, while the red shift of the peak suggests the growth of the Si-ncs sizes.

A weak emission band peaking at 546 nm emerged after annealing at 1100°C. After annealing at 1200°C, the Si-ncs emission decreases abruptly. At the same time, the four sharp peaks centered at 487, 546, 588, and 620 nm become dominant. Both the weak 546 nm peak observed after annealing at 1100°C and the four strong sharp peaks observed after annealing at 1200°C originate from intra-4f transitions of Tb^{3+} ions.

As mentioned in the previous section, the 325 nm excitation is not resonant with any absorption band of Tb^{3+} ions and the observation of Tb emission indicates the existence of (an) indirect excitation mechanism(s). The simultaneous quenching of the Si-ncs emission and the increase of the Tb emission intensity after annealing at 1200°C suggests the efficient energy transfer from Si-ncs to Tb^{3+} ions. Here, we attribute the observed Tb emission to the exciton energy transfer process. This mechanism may appear questionable, since the PL of Si-ncs after annealing at 1200°C is peaking around 800 nm (1.55 eV), while at least 2.5 eV (488 nm) energy is required to excite Tb^{3+} . However, it has been suggested that when the sizes of Si-ncs reduce to less than 3 nm, the infrared PL of Si-ncs is due to the recombination of the excitons trapped in oxygen-related localized states. Therefore, the actual “bandgap” of an Si-nc might be much higher than that indicated by its emission wavelength [15]. Figure 7 shows a high-resolution transmission electron microscopy (HR-TEM) image of a

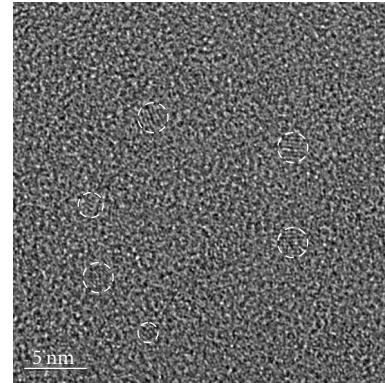


FIGURE 7: HR-TEM image of a Tb:SRSO sample containing 0.3 at.% Tb annealed at 1100°C.

Tb:SRSO sample containing 0.3 at.% Tb annealed at 1100°C. The clear lattice fringes shown in the circle areas reveal the formation of Si-ncs. The sizes of Si-ncs are around 2 nm. The “bandgap” of a 2 nm Si-nc can be as high as 2.5 eV as a result of quantum confinement effects [15], which is sufficient for the excitation of Tb^{3+} .

Although the organic sensitizer-Tb (tmhd)₃ may also be present in the silicon-rich samples, the absence of the Tb emission from the samples as-deposited and after annealing between 800 and 1200°C indicates that the corresponding excitation is not very efficient. One possible explanation is that the Si-ncs are dominant in the absorption of excitation photons due to their relatively high absorption coefficient [6]. In particular, the organic sensitizers are less likely to be responsible for the strong Tb emission after annealing at 1200°C, since the Tb emission intensity of the silicon-rich sample containing 0.3 at.% Tb is 50 times higher than that of the oxygen-rich sample containing 0.4 at.% Tb after annealing at the same temperature.

Figure 8 shows the emission intensities of Si-ncs in the samples with various Tb concentrations as a function of annealing temperature. The Si-ncs emission was observed to decrease with the increase of Tb concentration at annealing temperatures greater than 900°C. Although Tb emission was only appreciable from the samples annealed at 1100 and 1200°C, this decrease is indicative that the energy transfer between Si-ncs and Tb^{3+} ions is also occurring at 1000°C, thereby suppressing the Si-ncs PL. The inset of Figure 8 shows that after annealing at 1200°C, the intensity of the Tb^{3+} 546 nm emission increases with the Tb concentration, which can be explained by an increase of optically active Tb^{3+} sites.

3.3. Ce-doped oxygen-rich silicon oxides (Ce:ORSO)

The Ce:ORSO samples have a constant Si content of 32 at.% and varying Ce contents of 0.01, 0.1, and 1.0 at.%, respectively. Figure 9 shows the PL spectra of the 1.0 at.% Ce sample as-deposited or after annealing at 800 and 1200°C, respectively. All spectra show an intense broad peak with a pronounced shoulder at longer wavelengths. The main peaks

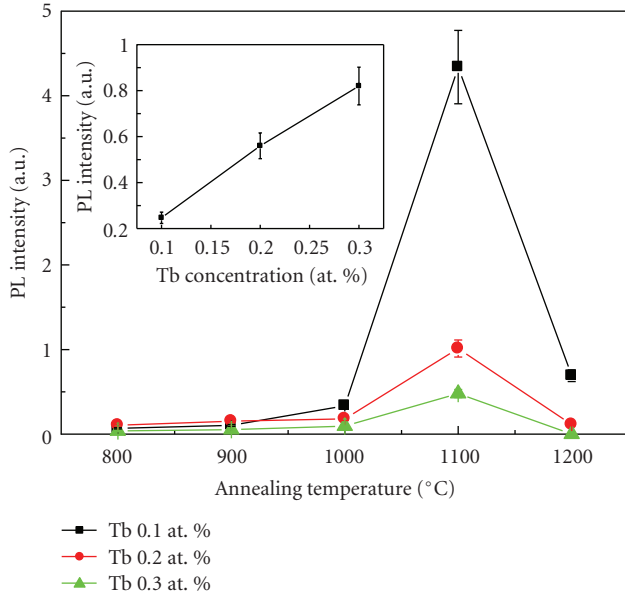


FIGURE 8: PL peak intensities of Si-ncs from the Tb:SRSO samples with various Tb concentrations as a function of annealing temperature. The inset shows the PL intensity of Tb^{3+} at 546 nm from Tb:SRSO samples after annealing at 1200°C as a function of Tb concentration.

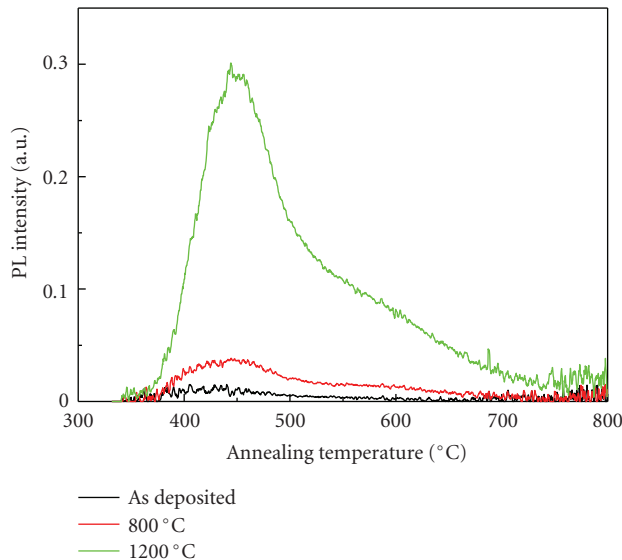


FIGURE 9: PL spectra of a Ce:ORSO sample containing 1.0 at.% Ce, as-deposited or after annealing at 800 and 1200°C, respectively.

were observed at 400, 422, and 460 nm from the samples as-deposited or annealed at 800 and 1200°C, respectively. The other two samples containing 0.01 and 0.1 at.% Ce have similar spectral shapes and peak positions.

Cerium can exist in both trivalent and tetravalent forms when embedded in the host materials by losing two 6s electrons and either one or two 4f electrons. Ce^{4+} is optically inactive due to the lack of 4f electrons. Although the 4f states are shielded by 5s and 5p states, the 5d states into which the

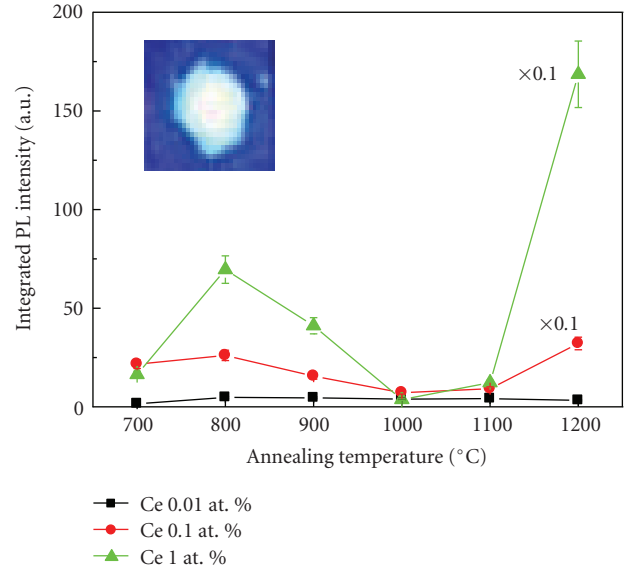


FIGURE 10: Integrated PL intensities in the range of 350–700 nm from the Ce:ORSO samples with various Ce concentrations as a function of annealing temperature. The inset shows an image of strong blue emission from the 1.0 at.% Ce sample after annealing at 1200°C taken by camera.

4f electron will be excited are exposed to the surrounding ligands. As previously discussed, the PL properties of Ce ions are highly dependent on the surrounding environment. Therefore, the changes in the spectral shapes, peak positions, and intensities strongly suggest the evolution of the film structure [13].

Unlike Tb, Ce^{3+} usually has a broad absorption band around 330 nm. The observed emissions originate from 5d-4f transitions of the Ce^{3+} in the films. Similar PL features have been observed from Ce doped SiO_2 prepared by the sol-gel method [34]. As the films were deposited under oxygen-rich conditions, most of the Ce ions exist as quadrivalent and possibly in the form of CeO_2 . Since the Ce^{4+} ions are the dominant species in the as-deposited samples and only few optically active Ce^{3+} ions exist, the corresponding emission intensity is low.

Figure 10 shows the integrated normalized PL intensity in the range of 350–700 nm for the above three Ce:ORSO samples as a function of annealing temperature. At all of annealing temperatures—except for 700 and 1000°C—the PL intensity increases with increasing Ce concentration. And a similar dependence of the PL intensities on annealing temperatures was observed despite of the Ce concentrations. The PL intensities increase with annealing temperature up to 800°C and then decrease with annealing temperature up to 1000°C. At 1100°C, the intensities begin to increase again and reach the greatest value at 1200°C.

When annealed in an inert ambient at 700 and 800°C, the increase in emission intensities can be attributed to the increasing Ce^{3+}/Ce^{4+} ratio. Previous studies on CeO_2 have shown that at high temperatures, crystallized stoichiometric CeO_2 tends to form Ce_6O_{11} in order to lower the O/Ce

ratio through the migration of oxygen vacancies [35]. It appears that under these conditions, Ce^{3+} ions are more stable than Ce^{4+} ions. Furthermore, due to the concentration difference between the film and surrounding environment, some oxygen may be released from the film during the annealing process, which possibly leads to a local oxygen deficiency facilitating the deoxidization of Ce^{4+} ions.

It was reported that Ce^{3+} can form two types of optical centers depending on whether their surrounding environment was composed mainly of Ce^{4+} or Ce^{3+} ions. The former were observed to exhibit a shorter emission wavelength than the latter [36]. Our results are consistent with this finding, with a red shift of emission wavelength being observed for samples after annealing at 800°C or greater.

The decrease in emission intensity between anneals from 800 to 1000°C can be attributed to the clustering of Ce^{3+} ions leading to a quenching of the luminescence as this quenching is more profound in the samples with greater Ce concentrations. At these temperatures, the SiO_x matrix begins to form a more uniform and stable structure. Correspondingly, the number of nonbridging oxygen (NBO) defects is reduced significantly. As the temperature further increases, more Ce^{3+} ions form clusters to share the limited amount of NBO, and emissions from the Ce^{3+} ions are quenched by transferring their energy to other Ce^{3+} ions in the vicinity [37].

Several groups have observed similar UV/blue light emission from $\text{CeO}_x/\text{SiO}_x$ or CeO_x/Si films annealed at 1000°C or greater in inert or reducing ambients [35, 38, 39]. However, the origin of the emission still remains controversial. Morshed et al. [35] observed the emission from CeO_2/Si films after rapid thermal annealing in Ar at 1000°C peaking at 400 nm. This emission was attributed to the formation of Ce_6O_{11} around the CeO_2/Si interface. Choi et al. [38] observed a weak 388 nm emission from a CeO_x/Si film and an intense 358 nm emission from $(\text{CeO}_x + \text{Si})/\text{Si}$ and $(\text{CeO}_x + \text{Si})/\text{SiO}_x/\text{Si}$ films after annealing in N_2 at 1100°C. Significant diffusion of Si from the substrate into CeO_2 and the formation of two cerium silicate phases, $\text{Ce}_2\text{Si}_2\text{O}_7$ and $\text{Ce}_{4.667}(\text{SiO}_4)_3\text{O}$, at the interface were observed. The 358 nm emission was attributed to $\text{Ce}_2\text{Si}_2\text{O}_7$ phase, and the weak 388 nm emission to the $\text{Ce}_{4.667}(\text{SiO}_4)_3\text{O}$ phase. Kępiński et al. [39] observed emission peaking at 400 nm from $\text{CeO}_2/\text{SiO}_2$ samples subjected to anneal in H_2 at 1050 and 1100°C and assigned it to an unidentified cerium silicate with some structural similarity to tetragonal $\text{Ce}_2\text{Si}_2\text{O}_7$ silicate. Therefore, in our study, the abrupt increase of the emission intensity at annealing temperatures greater than 1100°C may also suggest the formation of Ce silicate. At this high temperature, Ce^{3+} ions may acquire enough energy to interact with the surrounding Si and O atoms and reorganize to form a more stable structure.

A detailed study of the effects of high-temperature annealing on the structural evolution of these samples is in progress. Preliminary results from Fourier transform infrared spectroscopy show the emergence of new sharp absorption bands after the sample was annealed at 1200°C, similar to the peaks characteristic of $\text{Ce}_2\text{Si}_2\text{O}_7$ silicate, while

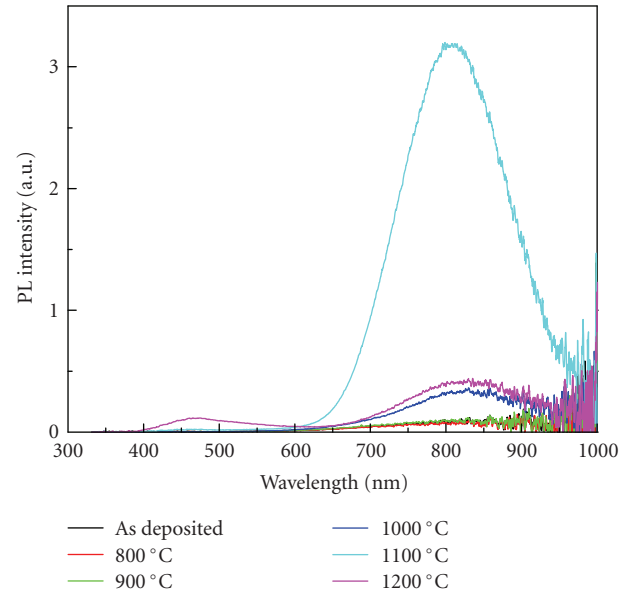


FIGURE 11: PL spectra of a Ce:SRSO sample containing 0.04 at.% Ce, as-deposited or annealed at various temperatures in the range of 800–1200°C.

there are still differences in both numbers and positions of absorption bands between them (data not shown).

The greatest intensity was observed from the 1.0 at.% Ce sample subjected to a 1200°C anneal which has the highest Ce concentration in the samples we studied. The inset of Figure 10 shows the emission picture taken by a camera. The Ce emission from this sample was 230 times greater than that of the as-deposited sample. In fact, after annealing at 800 or 1200°C, both the 0.1% Ce and 1.0% Ce samples exhibit such strong emissions that they can be easily observed under very bright room lighting condition. Considering that the excitation power is as low as 17 mW, the emission intensities are quite outstanding.

3.4. Ce-doped silicon-rich silicon oxide (Ce:SRSO)

The Ce:SRSO sample has Si and Ce content of 40 and 0.04 at.%, respectively. Figure 11 shows the PL spectra of the sample as deposited or annealed at various temperatures. There is no appreciable emission from the as-deposited sample. After annealing at 800°C, the sample shows a broad emission band centered at 800 nm, the emission intensity of which increases with annealing temperature until 1100°C. After annealing at 1200°C, the emission decreases by a factor of 8 and another weak broad emission band centered at 450 nm emerges.

It is evident that the 800 nm emission originates from the precipitated Si-ncs upon annealing. We attribute the 450 nm emission to the Ce^{3+} ions in the film. The enhancement of the Si-ncs emission intensity with annealing temperature indicates the formation of more Si-ncs in the same manner as was observed in Tb:SRSO samples. The absence of Ce emission at annealing temperatures lower than 1200°C is also

possibly due to the competition between Si-ncs and Ce ions in the absorption of excitation photons.

4. CONCLUSIONS

Rare-earth (Tb or Ce) doped silicon oxides (silicon-rich or oxygen-rich) were deposited by ECR-PECVD. The successful in situ incorporation of high concentrations of optically active rare-earth ions was demonstrated. The dependence of the PL properties on Si/O ratio, doping concentration, and annealing temperature was investigated.

Green Tb emission was observed in both oxygen-rich and silicon-rich samples. The excitation wavelength is not resonant with any optical absorption band of Tb³⁺. We propose that in oxygen-rich films, the organic ligands introduced from the deposition process may serve as the sensitizers to excite Tb emission while Si-ncs serve as the sensitizers in silicon-rich films.

Violet/blue Ce emission was observed in both oxygen-rich and silicon-rich films. An abrupt increase of Ce emission intensity in oxygen-rich films after annealing at 1200°C is possibly due to the formation of Ce silicate. In silicon-rich films, the Ce emission was absent at annealing temperatures lower than 1200°C.

It was found that by choosing appropriate compositions and annealing temperatures, the Ce and Tb PL intensities can be enhanced significantly. The highest Ce PL intensity was observed from the sample containing 32 at.% Si and 1.0 at.% Ce annealed at 1200°C which has the highest Ce concentration in the samples we examined. The highest Tb PL intensity was observed from the sample containing 32 at.% Si and 0.4 at.% Tb annealed at 800°C. Those emissions were very bright and can be easily observed under room lighting condition.

ACKNOWLEDGMENTS

The authors would like to acknowledge Dr. W. Lennard and J. Hendriks, both at the University of Western Ontario, for their expert help in RBS measurements, J. Garrett and G. Pearson at McMaster University for technical support in annealing, and J. Huang and F. Pearson at McMaster University for TEM analysis. We thank H. (Charlie) Zhang for many hours of film depositions. This work has been cofunded by the Ontario Photonics Consortium (OPC), Ontario Centres of Excellence (OCE), Centre for Photonics Fabrication Research (CPFR), and Canadian Institute for Photonic Innovation (CIPI). We are grateful for financial and technical support from Group IV Semiconductor Inc. (Kanata, Ontario) and Johnsen-Ultravac (Burlington, Ontario).

REFERENCES

- [1] G. T. Reed and A. P. Knights, *Silicon Photonics: An Introduction*, John Wiley & Sons, New York, NY, USA, 2004.
- [2] D. J. Lockwood, *Light Emission in Silicon: From Physics to Devices*, Academic Press, New York, NY, USA, 1998.
- [3] A. Liu and M. Paniccia, "Advances in silicon photonic devices for silicon-based optoelectronic applications," *Physica E*, vol. 35, no. 2, pp. 223–228, 2006.
- [4] S. Ossicini, L. Pavesi, and F. Priolo, *Light Emitting Silicon for Microphotonics*, Springer, Berlin, Germany, 2003.
- [5] P. G. Kik and A. Polman, "Erbium-doped optical-waveguide amplifiers on silicon," *MRS Bulletin*, vol. 23, no. 4, pp. 48–54, 1998.
- [6] A. J. Kenyon, "Recent developments in rare-earth doped materials for optoelectronics," *Progress in Quantum Electronics*, vol. 26, no. 4-5, pp. 225–284, 2002.
- [7] G. H. Dieke, *Spectra and Energy Levels of Rare-Earth Ions in Crystals*, John Wiley & Sons, New York, NY, USA, 1968.
- [8] A. Yoshida, Y. Nakanishi, and A. Wakahara, "Light emission from rare-earth-implanted GaN expected for full-color display," in *Smart Materials, Structures, and Systems*, vol. 5062 of *Proceedings of SPIE*, pp. 18–19, San Diego, Calif, USA, October 2003.
- [9] N. D. Vieira Jr., I. M. Ranieri, L. V. G. Tarelho, et al., "Laser development of rare-earth doped crystals," *Journal of Alloys and Compounds*, vol. 344, no. 1-2, pp. 231–239, 2002.
- [10] J. K. Sahu, Y. Jeong, D. J. Richardson, and J. Nilsson, "A 103 W erbium-ytterbium co-doped large-core fiber laser," *Optics Communications*, vol. 227, no. 1–3, pp. 159–163, 2003.
- [11] B. V. Shul'gin, V. L. Petrov, V. A. Pustovarov, et al., "Scintillation neutron detectors based on ⁶Li-silica glass doped with cerium," *Physics of the Solid State*, vol. 47, no. 8, pp. 1412–1415, 2005.
- [12] L. Galambos, S. S. Orlov, L. Hesselink, Y. Furukawa, K. Kitamura, and S. Takekawa, "Doubly doped stoichiometric and congruent lithium niobate for holographic data storage," *Journal of Crystal Growth*, vol. 229, no. 1–4, pp. 228–232, 2001.
- [13] M. Gaft, R. Reisfel, and G. Panczer, *Morden Luminescence Spectroscopy of Minerals and Materials*, Springer, Berlin, Germany, 2005.
- [14] A. Polman and F. C. J. M. van Veggel, "Broadband sensitizers for erbium-doped planar optical amplifiers: review," *Journal of the Optical Society of America B*, vol. 21, no. 5, pp. 871–892, 2004.
- [15] M. V. Wolkin, J. Jorne, P. M. Fauchet, G. Allan, and C. Delerue, "Electronic states and luminescence in porous silicon quantum dots: the role of oxygen," *Physical Review Letters*, vol. 82, no. 1, pp. 197–200, 1999.
- [16] A. J. Kenyon, "Erbium in silicon," *Semiconductor Science and Technology*, vol. 20, no. 12, pp. R65–R84, 2005.
- [17] A. J. Kenyon, M. Wojdak, I. Ahmad, W. H. Loh, and C. J. Oton, "Generalized rate-equation analysis of excitation exchange between silicon nanoclusters and erbium ions," *Physical Review B*, vol. 77, no. 3, Article ID 035318, 9 pages, 2008.
- [18] A. J. Kenyon, P. F. Trwoga, C. W. Pitt, and G. Rehm, "The origin of photoluminescence from thin films of silicon-rich silica," *Journal of Applied Physics*, vol. 79, no. 12, pp. 9291–9300, 1996.
- [19] J. Lee, J. H. Shin, and N. Park, "Optical gain at 1.5 μm in nanocrystal Si-sensitized Er-doped silica waveguide using top-pumping 470 nm LEDs," *Journal of Lightwave Technology*, vol. 23, no. 1, pp. 19–25, 2005.
- [20] S.-Y. Seo and J. H. Shin, "Enhancement of the green, visible Tb³⁺ luminescence from Tb-doped silicon-rich silicon oxide by C co-doping," *Applied Physics Letters*, vol. 84, no. 22, pp. 4379–4381, 2004.

- [21] A. Vedda, N. Chiodini, D. Di Martino, et al., "Rare-earth aggregates in sol-gel silica and their influence on optical properties," *Physica Status Solidi C*, vol. 2, no. 1, pp. 620–623, 2005.
- [22] M. Flynn, J. Wojcik, S. Gujrathi, E. Irving, and P. Mascher, "The impact of deposition parameters on the optical and compositional properties of Er doped SRSO thin films deposited by ECR-PECVD," in *Proceedings of the Materials Research Society Symposium*, vol. 866, pp. 163–167, San Francisco, Calif, USA, March 2005.
- [23] D. E. Blakie, O. H. Y. Zalloum, J. Wojcik, E. J. Irving, A. P. Knights, and P. Mascher, "Coupled luminescence centres in erbium-doped silicon rich silicon oxide thin films," in *Photonics North*, vol. 6343 of *Proceedings of SPIE*, p. 11 pages, Quebec City, Canada, June 2006.
- [24] C. L. Heng, O. H. Y. Zalloum, T. Roschuk, D. Blakie, J. Wojcik, and P. Mascher, "Photoluminescence study of an Er-doped Si-rich SiO_x film," *Electrochemical and Solid-State Letters*, vol. 10, no. 7, pp. K20–K23, 2007.
- [25] O. H. Y. Zalloum, M. Flynn, T. Roschuk, J. Wojcik, E. Irving, and P. Mascher, "Laser photoluminescence spectrometer based on charge-coupled device detection for silicon-based photonics," *Review of Scientific Instruments*, vol. 77, no. 2, Article ID 023907, 8 pages, 2006.
- [26] S. P. Depinna and D. J. Dunstan, "Frequency-resolved spectroscopy and its application to the analysis of recombination in semiconductors," *Philosophical Magazine B*, vol. 50, no. 5, pp. 579–597, 1984.
- [27] M. Gaft, R. Reisfeld, and G. Pancezer, *Luminescence Spectroscopy of Minerals and Materials*, Springer, New York, NY, USA, 2005.
- [28] M. Yoshihara, A. Sekiya, T. Morita, et al., "Rare-earth-doped SiO_2 films prepared by plasma-enhanced chemical vapour deposition," *Journal of Physics D*, vol. 30, no. 13, pp. 1908–1912, 1997.
- [29] H. Amekura, A. Eckau, R. Carius, and Ch. Buchal, "Visible photoluminescence from Tb^{3+} ions implanted into a SiO_2 film on Si at room temperature," in *Proceedings of the International Conference on Ion Implantation Technology (IIT '99)*, vol. 2, pp. 925–928, Kyoto, Japan, June 1999.
- [30] A. Polman, D. C. Jacobson, A. Lidgard, J. M. Poate, and G. W. Arnold, "Photoluminescence and structural characterization of MeV erbium-implanted silica glass," *Nuclear Instruments and Methods in Physics Research B*, vol. 59-60, part 2, pp. 1313–1316, 1991.
- [31] H. Jeong, S.-Y. Seo, and J. H. Shin, "Excitation mechanism of visible, Tb^{3+} photoluminescence from Tb-doped silicon oxynitride," *Applied Physics Letters*, vol. 88, no. 16, Article ID 161910, 3 pages, 2006.
- [32] B. Stannowski, J. K. Rath, and R. E. I. Schropp, "Growth process and properties of silicon nitride deposited by hot-wire chemical vapor deposition," *Journal of Applied Physics*, vol. 93, no. 5, pp. 2618–2625, 2003.
- [33] H. Ofuchi, Y. Imaizumi, H. Sugawara, H. Fujioka, M. Oshima, and Y. Takeda, "Fluorescence XAFS study on local structures around Tb ions implanted in SiO_2 on Si," *Nuclear Instruments and Methods in Physics Research B*, vol. 199, pp. 231–234, 2003.
- [34] G. Q. Xu, Z. X. Zheng, W. M. Tang, and Y. C. Wu, "Luminescence property of Ce^{3+} -doped silica decorated with S^{2-} and Cl^- anions," *Journal of Luminescence*, vol. 126, no. 2, pp. 475–480, 2007.
- [35] A. H. Morshed, M. E. Moussa, S. M. Bedair, R. Leonard, S. X. Liu, and N. El-Masry, "Violet/blue emission from epitaxial cerium oxide films on silicon substrates," *Applied Physics Letters*, vol. 70, no. 13, pp. 1647–1649, 1997.
- [36] G. E. Malashkevich, E. N. Poddenezhny, I. M. Melnichenko, and A. A. Boiko, "Optical centers of cerium in silica glasses obtained by the sol-gel process," *Journal of Non-Crystalline Solids*, vol. 188, no. 1-2, pp. 107–117, 1995.
- [37] H. Bi, W. Cai, H. Shi, B. Yao, and L. Zhang, "Effects of annealing and Al co-doping on the photoluminescence of Ce^{3+} -doped silica prepared by a sol-gel process," *Journal of Physics D*, vol. 33, no. 19, pp. 2369–2372, 2000.
- [38] W. C. Choi, H. N. Lee, Y. Kim, H. M. Park, and E. K. Kim, "Luminescence from the thermally treated cerium oxide on silicon," *Japanese Journal of Applied Physics*, vol. 38, no. 11, pp. 6392–6393, 1999.
- [39] L. Kepiński, M. Wołczyk, and M. Marchewka, "Structure evolution of nanocrystalline CeO_2 supported on silica: effect of temperature and atmosphere," *Journal of Solid State Chemistry*, vol. 168, no. 1, pp. 110–118, 2002.

Research Article

Development of Silicon Photonics Devices Using Microelectronic Tools for the Integration on Top of a CMOS Wafer

J. M. Fedeli,¹ L. Di Cioccio,¹ D. Marris-Morini,² L. Vivien,² R. Orobtcchouk,³ P. Rojo-Romeo,⁴ C. Seassal,⁴ and F. Mandorlo^{1,4}

¹CEA-Leti, MINATEC, 17 rue des Martyrs, 38054 Grenoble, France

²Institut d'Electronique Fondamentale, Université Paris-Sud XI, UMR8622, CNRS, Bat. 220, 91405 Orsay Cedex, France

³Institut des Nanotechnologies de Lyon, Université de Lyon, INL-UMR5270, CNRS, INSA de Lyon, 69621 Villeurbanne, France

⁴Institut des Nanotechnologies de Lyon, Université de Lyon, INL-UMR5270, CNRS, Ecole Centrale de Lyon, 69134 Ecully, France

Correspondence should be addressed to J. M. Fedeli, jean-marc.fedeli@cea.fr

Received 6 December 2007; Accepted 13 March 2008

Recommended by Pavel Cheben

Photonics on CMOS is the integration of microelectronics technology and optics components to enable either improved functionality of the electronic circuit or miniaturization of optical functions. The integration of a photonic layer on an electronic circuit has been studied with three routes. For combined fabrication at the front end level, several building blocks using a silicon on insulator rib technology have been developed: slightly etched rib waveguide with low (0.1 dB/cm) propagation loss, a high speed and high responsivity Ge integrated photodetector and a 10 GHz Si modulators. Next, a wafer bonding of silicon rib and stripe technologies was achieved above the metallization layers of a CMOS wafer. Last, direct fabrication of a photonic layer at the back-end level was achieved using low-temperature processes with amorphous silicon waveguide (loss 5 dB/cm), followed by the molecular bonding of InP dice and by the processing in microelectronics environment of InP μ sources and detector.

Copyright © 2008 J. M. Fedeli et al. This is an open access article distributed under the Creative Commons Attribution License, which permits unrestricted use, distribution, and reproduction in any medium, provided the original work is properly cited.

1. INTRODUCTION

Silicon-based photonics has generated an increasing interest in the recent year, mainly for optical telecommunications or for optical interconnects in microelectronic circuits. The development of elementary components (I/O couplers, modulators, passive functions, and photodetectors) has achieved such a performance level that the integration challenge of silicon photonics with microelectronics has been discussed [1] in the literature and products have been announced in the near future [2]. The rationale of silicon photonics is the reduction of the cost of photonic systems through the integration of photonic components and an integrated circuit (IC) on a common chip, or in the longer term, the enhancement of IC performance with the introduction of optics inside a high-performance chip. To achieve such a high level of photonic function integration, the light has to be strongly confined in submicron waveguides with a medium ($\Delta n \sim 0.5$) to large ($\Delta n \sim 2$) refractive index contrast

between the core and the cladding. Most of these studies have relied on the use of SOI substrates because they are accepted for CMOS technology. When one wants to integrate a CMOS circuit with some photonic functions in order to build a photonic integrated circuit on CMOS (PICMOS), the question of how to combine the photonic with the electronic parts is raised. The goal of this paper is to illustrate some routes and challenges of PICMOS in conjunction with presenting some technical achievements of our laboratories.

In the world of silicon photonics, different approaches of integration have been developed. The stand-alone one was pioneered by Bookham. It is comparable to silica on silicon technology, which today is in production whereby the silicon substrate acts only as a convenient and cheap substrate, but with the difference that the waveguiding layer is made on silicon. This technology, with waveguide dimensions typically in the μm range, is used by Kotura for their different products and also by INTEL for the demonstration of silicon building blocks. The rationale of highly integrated photonics

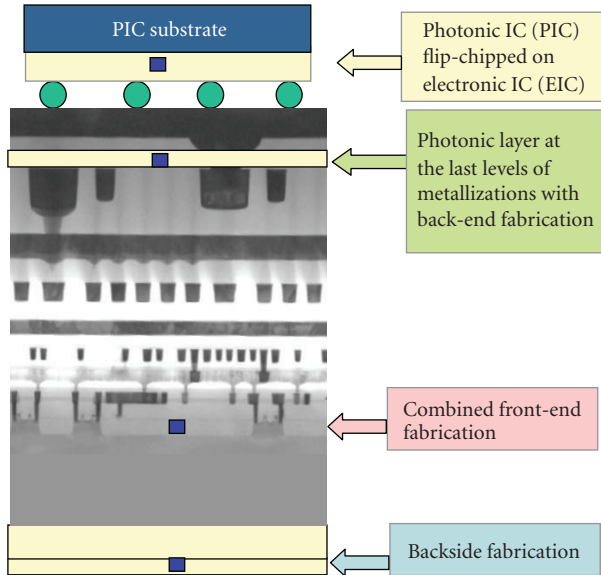


FIGURE 1: Integration routes.

is the reduction of the cost and the increase of performances by merging the photonics and the control electronics part. Different integration technology routes are presented in Figure 1. Each one has its own merit and will be discussed in the next sections. One can fabricate a photonic only integrated circuit (PIC) and connect the electronic and the photonic part either by state of the art flip-chip technique or by full wafer copper bonding which is in development. Fabrication of a photonic layer at the back side of the electric integrated circuit (EIC) can be envisaged and developed. However, connections through the substrate (100 to 200 μm thick typically) limits the frequency operation to MHz range. In this paper, deeper integration is considered with operation in the GHz domain with the EIC:

- (i) a combined front-end fabrication: the photonic devices are at the transistor level which corresponds to the “full” integration;
- (ii) the second route is often called 3D integration and relies on wafer bonding where a fully or partially processed photonic wafer is mounted on an almost finished CMOS wafer;
- (iii) the third approach is to fabricate the optical layer with back-end technology at the metallization levels.

2. COMBINED FABRICATION

The integration of optical functions which are compatible with microelectronic process technologies presents new and interesting potentialities for integrated circuits. However, a monolithic integration of dissimilar functions still remains a difficult technological challenge. The company Luxtera chooses the combined front-end fabrication route for the production of 10 Gb/s transceiver. The chip is fabricated almost completely within a freescale 0.13 μm CMOS wafer

fabrication and the electronic driver circuit are directly integrated aside the photonic circuits. With a combined integration scheme, the new components (waveguides and optoelectronic components) can be fabricated at the beginning of the IC process at the transistor level. Starting with the substrate, photonics components need a separation of larger than 1 μm between the waveguide core (thickness between 200 nm and 400 nm for a submicron waveguide) and the silicon substrate to avoid light leakage. On the contrary, CMOS technologies are based on either a bulk-type substrate or an SOI-type with thin buried oxide (BOX) and silicon layer (150 nm Si on 400 nm BOX decreasing to 60 nm Si on 150 nm BOX). As the thickness of the BOX is defined by the photonic parts, either a modified CMOS technology has to be developed using an SOI substrate with at least 1 μm thick BOX and a 200 nm thick silicon layers, localized thick BOX substrates under the photonic components can be used. An analysis of the process steps for both technologies reveals that high temperatures ($\approx 1000^\circ\text{C}$) are necessary for the STI, implant activation as well as for the optimization of waveguide losses. Medium temperature ($\approx 700^\circ\text{C}$) steps are used for gate oxide, implant anneal, and for active photonic layers like SiGe/Si and Ge epitaxy, and lower temperature for metallizations on both. So mixing steps for the electronic and the photonic parts in order to avoid redundant steps is possible on an optical SOI substrate, leading to a photonic SOI technology (PSOI). For this goal, we developed a SOI technology with 1 μm BOX and 400 nm silicon thickness.

2.1. Passive circuitry

Passive optical circuits need low-loss optical structures to get enough optical power at each output to ensure light detection with an acceptable bit error rate. Strong light confinement is obtained either by partial etching of the silicon film leading to rib geometry or by full etching of the silicon film down to the buried oxide to get strip geometry. The highest compactness is achieved with single-mode strip waveguides which require a width smaller than 500 nm for height lower than 220 nm and allow very low crosstalk between waveguides distant from 1 μm . However, the main limitation is the difficulty to reduce propagation loss due to the side-wall roughness induced by the lithography and etching processes. Slightly etched submicron rib SOI waveguides are much less sensitive to scattering losses due to low interaction between optical mode and side-wall roughness [3]. Propagation losses as low as 0.1 dB/cm have been obtained using processes steps to reduce the roughness. These processes consist in a 10 nm thermal oxidation at 1100 $^\circ\text{C}$, followed by a desoxidation, and followed again by a second oxidation. Vacuum hydrogen annealing can also be used to reconstruct the silicon edges before thermal oxidation. The height and width of the rib waveguides were 380 nm and 1 μm , respectively, and the etching depth was 70 nm. However, with a constant thickness of 380 nm, different pairs of width and etching depth can lead to monomode operation.

Compact 90 $^\circ$ turns using slightly etched SOI rib waveguides can be made by etching silicon down to the BOX to obtain a mirror facet at the angle between two perpendicular

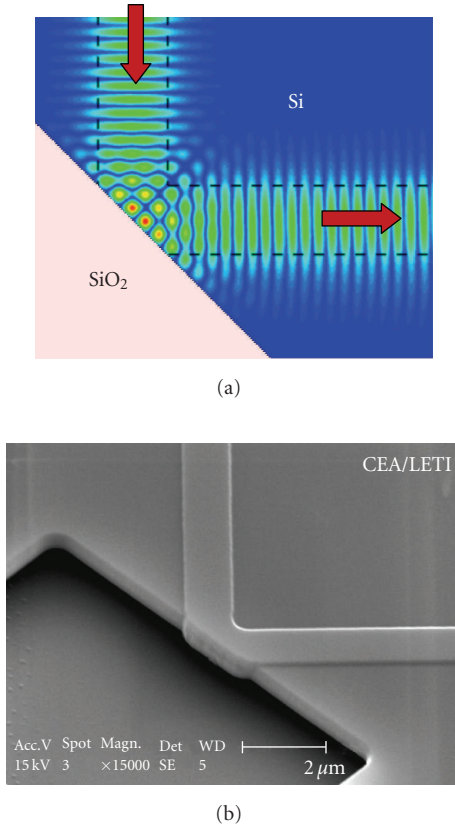


FIGURE 2: Etched mirror for 90° turn of rib waveguides: FDTD calculation of the field amplitude and scanning electron microscope (SEM) view after removal of the silicon oxide.

waveguides (Figure 2). The theoretical loss determined from three dimensional finite difference time domain (3D-FDTD) numerical calculations is 0.1 dB, and the measured value is under 0.5 dB. The main issue to overcome for lowering this loss relies on the ability to etch anisotropically and without roughness the 380 nm down to the box. Low loss and compact T-splitters can be made by collecting the light in two waveguides after it has diffracted in a wider slab region (Figure 3). It occupies an area of $8\ \mu\text{m}$ per $16\ \mu\text{m}$ and is much more compact than a rib MMI splitter ($118 \times 13\ \mu\text{m}$). 3D-FDTD simulations give excess losses lower than 0.2 dB at $1.31\ \mu\text{m}$ for each branch, which is confirmed experimentally with a measured value of 0.5 dB. Furthermore, a broadband efficiency, ranging at least from $1.3\ \mu\text{m}$ to $1.6\ \mu\text{m}$, is obtained as well as temperature independence.

Shallow single-mode SOI rib microwaveguides are a promising solution for photonic integrated circuits, especially if an optical distribution to a large number of outputs is required. Experimental demonstrations of a 1 to 16 optical distribution [4] and an optical division equivalent to optical distribution from one input to 1024 output points [5, 6] have been demonstrated.

The interface between nanophotonic devices and a single-mode fiber is a real challenge due to their optical mode mismatch. In order to inject light anywhere on an optical circuit and to test optically the wafer, we developed

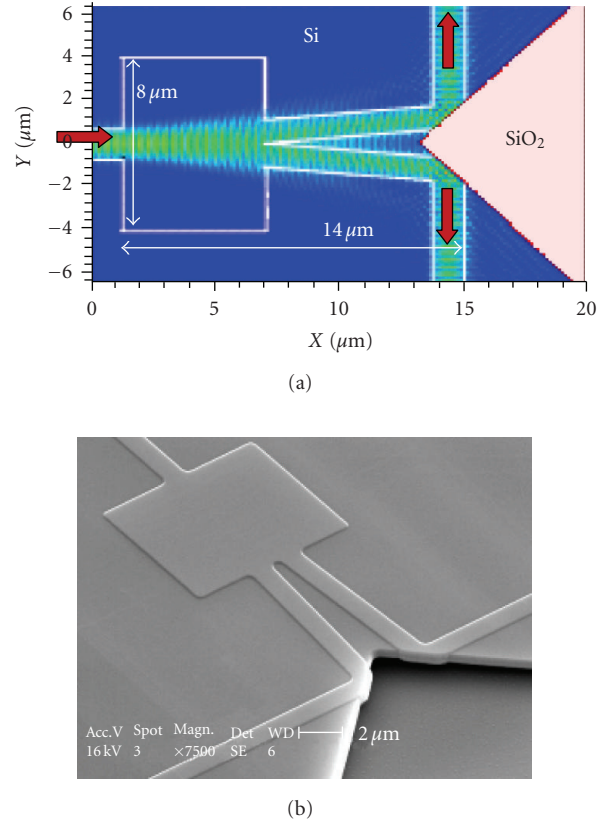


FIGURE 3: T-splitter for rib waveguides: 3D-FDTD calculation of the field amplitude and SEM view after removal of the silicon oxide.

diffraction grating couplers using etched grooves of the same depth than the rib etching on the top of the silicon layer. The surface gratings have been fabricated (Figure 4) and characterized for the +1 diffraction order at an operating wavelength of $1.31\ \mu\text{m}$ for the TE polarization. At the resonant angle, a coupling efficiency higher than 60% has been measured under the grating. The resonance angle and the wavelength tolerances have been evaluated to 3° and 20 nm, respectively. The grating coupler is followed by a taper, and about 80% (loss < 1 dB) of the input power at $1.31\ \mu\text{m}$ is coupled into submicron rib waveguides [7]. By engineering further, the grating (silicon thickness, etching depth, etc.) insertion lower than 1 dB in the 1530–1560 nm wavelength range can be achieved.

2.2. Modulated source

With the combined fabrication route, integration of a light source is the weak point. Silicon sources have to be proven and get sufficient maturity. Integration of InP components before the metallization is not thermally compatible. So before any integration of the source, a continuous external light source can be coupled via an input-output coupler (surface grating or edge coupler) to the waveguide circuitry of the circuit. To make the silicon photonics worthwhile, the optical signal has to be encoded to ensure information

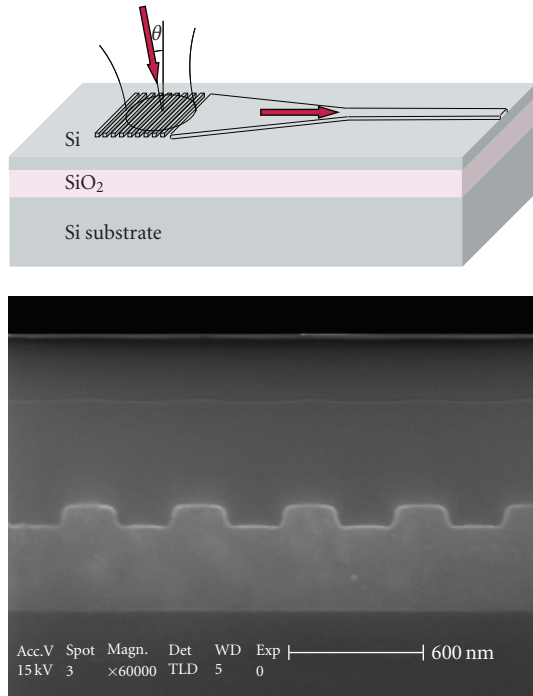


FIGURE 4: Scanning electron microscope view of a surface 1D grating.

transmission at frequencies larger than 10 GHz. Impressive progresses have been obtained in the recent years on several ways investigated for high-speed optical modulation in Si or Si-based devices: electro-optical effects in strained silicon [8] or SiGe superlattices [9], quantum confined Stark effect in silicon-germanium/germanium quantum wells [10, 11], Franz Keldysh effect in GeSi diode, [12], carrier concentration variations in silicon [13–18]. The mainly used possibility to make a high-speed optical modulator is to use index variations by free-carrier concentration variations. A lot of silicon-based optical modulators made for several years are based on free-carrier concentration variation using injection, accumulation, or depletion of carriers. Each structure is integrated in an SOI rib waveguide and the refractive index variation induces a phase shift of the guided wave. An interference device such as a Mach-Zehnder interferometer, Fabry-Perot microcavity, or microring resonator is used to convert the phase modulation into an intensity one. The best published results are summarized in Table 1.

For several years, vertical carrier depletion structures have been proposed by IEF [18, 19], using either SiGe/Si modulation doped quantum wells or all Si structures, placed in the intrinsic region of a PIN diode and integrated in an SOI rib microwaveguide. Holes introduced by thin highly-doped P+ layers in the Si barriers are confined in the intrinsic region of the pin diode at the equilibrium state. When a reverse bias is applied to the diode, the electrical field sweeps the carriers out of the active region due to band bending. Hole concentration variations are responsible for refractive index variations. The intrinsic response time allows operation at frequencies higher than 10 GHz. The

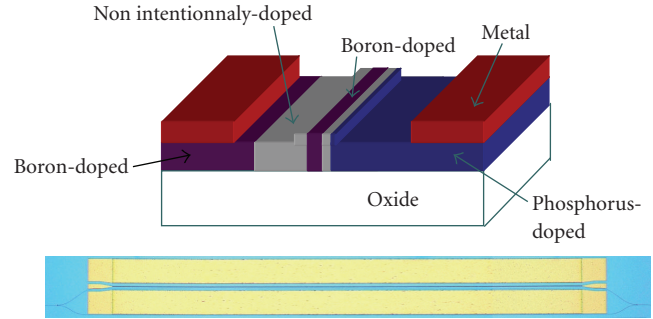


FIGURE 5: Cross section of the phase shifter structure integrated into a rib silicon-on-insulator waveguide and optical microscope view of the modulator.

performance of the modulators is also dependant on the access resistance, in series with the reverse-bias pin diode capacitor. The challenge is to get low optical losses and low RC constants in Mach-Zehnder or Fabry-Perot interferometer configurations. The variation of the effective index due to carrier depletion has been measured at $\text{few} \cdot 10^{-4}$ at $1.55 \mu\text{m}$ for a 0 V to 6 V reverse voltage bias variation. After optimization of such structure, the obtained factor of merit ($L_{\pi} \cdot V_{\pi}$) is lower than 1.3. This vertical approach of depletion modulator was followed recently by Liu et al. [16] and Gardes et al. [17] and the 40 Gb/s operation obtained proves the high frequency capacity of the depletion solution. However, the fabricated modulator of this kind requires numerous doped epitaxy and implantation steps and it would be a real challenge for a combined fabrication.

So in the aim of reducing the complexity of the fabrication, we proposed hereafter a structure based on a horizontal pin diode which has a simpler technological process without any epitaxial steps. The optical loss is reduced as the optical mode has a weak interaction with the P+ and N+ doped regions of the diode. A good overlap between the carrier density variation zone and the guided mode is obtained leading to high effective index change. In comparison with vertical diodes [15–18], the capacitance of the diode is reduced, that is favourable to high-speed operation and low electrical power dissipation.

A schematic view of the device cross-section is shown in Figure 5. The silicon rib waveguide width is 660 nm, the rib height is 400 nm, and the etching depth is 100 nm leading to a single mode propagation of the guided mode at $1.55 \mu\text{m}$ wavelength. A P+ doped layer (10^{18}cm^{-3}) is inserted in the intrinsic region of the pin diode which acts as a source of holes. The P and N doped regions of the pin diode have doping concentrations close to 10^{18}cm^{-3} . Metallic contacts are deposited on both sides of the waveguide, a few microns apart to reduce optical loss.

The silicon modulator is based on an asymmetric Mach-Zehnder interferometer (Figure 5). The phase shifter is inserted in both arms over a length of 4 mm, and electrodes are used to bias one arm. Waveguide splitters are star couplers with a reduced area ($10 \times 2 \mu\text{m}^2$). To ensure high-frequency operation, RC time constants have to be

TABLE 1: State of the art of silicon-based optical modulators.

Modulator type	λ (μm)	$V_{\pi}L_{\pi}$ (V \cdot cm)	Bandwidth or time constant	Extinction ratio (dB)	Insertion loss (dB)	Labs
Franz Keldysh effect in Ge diode	1.647	no		7.5	2.5	S. Jongthammanurak, Group IV photonics, ottawa (2006)
Quantum confined Stark effect (QCSE) in Ge/SiGe quantum wells	1.55 at 90°C	no		Absorption coefficient contrast >3		Kuo and al, IEEE JSTQE, 12 (6) p1503 (2006)
Carrier injection in lateral PIN diode	1.55		12.5 Gbit/s	>9		Q. Xu et al., Optics express, 15 (2) p 430 (2007)
		7.7	1 GHz			A. Liu et al., nature 427, 615–618 (2004)
MOS capacitance	1.55	3.3	10 Gbit/s	3.8	10	L. Liao et al., optics express 13, 3129–3135 (2005)
Carrier depletion (vertical PN diode)	1.55	4	30 GHz (40 Gbit/s)		7	Liu and al optics express, 15 (2) p660, (2007)
Carrier depletion (Doped modulation of vertical Si PIN diode)	1.31 1.55	3.1 (exp)	Time constant \sim 1ps (Theory)			D. Marris-Morini et al., optics express, 14 (22) 10838 (2006)
Carrier depletion (Doped modulation of all Si lateral PIN diode)	1.55	5	10 GHz		5	This work
Carrier depletion (Doped modulation of all Si lateral PN diode)	1.55	3	9 GHz	6	3	T. Pinguet Group IV photonics Tokyo 2007
Carrier depletion (four terminal p ⁺ pnn ⁺ vertical device)	1.55	2.5 (theory) birefringence free	Time constant <7 ps (Theory)		2	F. Y. Gardes et al., optics express 13 (22), 8845–8854, (2005)

minimized. The capacitance of the device was evaluated using small-signal simulations. The diode capacitance per unit length varies from 2.3 to $1.8 \cdot 10^{-16}$ F/ μm for reverse biases from 0 V to -10 V. To ensure operating frequency above 10 GHz, the serial resistance of the device should be lower than 70 Ω/mm . Doped regions and silicide are thus used to form ohmic contacts and to achieve such a low resistance. Coplanar waveguide electrodes are designed to obtain characteristic impedance around 50 ohms taking into account the capacitance of the pin diode.

The modulator was fabricated on an undoped 200 mm SOI substrate with a 1 μm thick buried oxide (BOX) layer, a 400 nm crystalline silicon film, and a 100 nm silica hard mask on top. A 100 nm-wide slit is etched in the hard mask using 193 nm deep-UV lithographic patterning and reactive ion plasma etching. Double ion implantation and annealing are then performed to obtain a thin slit doped layer on the whole thickness. Waveguides are patterned with DUV lithography and HBr etching. Implantation for N⁺ and P⁺ area are performed followed by another annealing. It is worth

to note that these implantation steps could be common to the source and drain fabrication. Finally, Ti/TiN/AlCu/Ti/TiN metal stack was deposited onto the wafer and electrodes were patterned and etched down to the SiO₂ layer. The used processes are fully compatible with SOI CMOS technology and could be transferred in high-volume microelectronic manufacturing.

The experimental setup uses a tunable laser around 1550 nm. A linearly polarized light beam is coupled into the waveguide using a polarization-maintaining lensed-fiber. The output light is collected by an objective and focused on an IR detector. Electrical probes are used to bias the diode. Very low values of the reverse current ($-2 \mu\text{A}$ at -10 V) have been measured that ensures low electrical power dissipation in DC configurations. The insertion loss was measured at about 5 dB. DC extinction ratio is around 14 dB from 0 to -10 V. To evaluate the modulation phase efficiency, a figure of merit is usually defined as the product $V_{\pi}L_{\pi}$, where V_{π} and L_{π} are the applied voltage and the length required to obtain a π phase shift of the guided wave, respectively. The

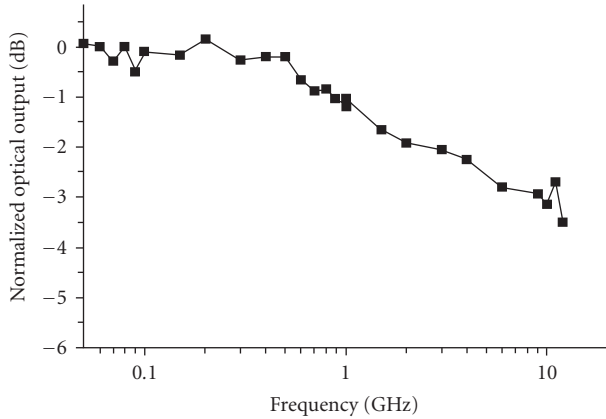


FIGURE 6: Normalized optical response of the Si modulator integrated in rib SOI waveguide with optical 3 dB-bandwidth of about 10 GHz.

obtained value $V_{\pi}L_{\pi}$ is equal to $5 \text{ V}\cdot\text{cm}$. The normalized optical response of the modulator is reported in Figure 6 for a DC bias of -5 V . A 3 dB cutoff frequency of $\sim 10 \text{ GHz}$ is measured on a Mach-Zehnder interferometer using 4 mm-long phase shifters.

Several ways improvement can be considered. Design optimizations of the RF travelling wave and optical waveguide are required to increase the modulation bandwidth to some tens of GHz. Progress in modulation efficiency are also possible: $V_{\pi}L_{\pi}$ product as low as $1 \text{ V}\cdot\text{cm}$ is theoretically predicted with the proposed structure, thanks to the good overlap between the optical mode and the doped region in the middle of the waveguide where carrier depletion occurs. The proposed structure has a large potential for the realization of high performances integrated high-speed modulators. Optical loss is reduced as the rib waveguide is not entirely doped, and the reduced-capacitance is favourable for high speed and low electrical power consumption. The fabrication can be combined with processing steps of CMOS transistors.

2.3. Germanium photodetectors

High-speed photodetector is one of the key building blocks and a large wavelength range of detection from 850 nm to telecom standards ($1.55 \mu\text{m}$) is necessary. These components have been available for several years from the III/V semiconductor technology on InP and GaAs wafers. Nevertheless, the integration of these devices on large wafers within the mainstream silicon technology requires hybrid integration approach [20, 21]. The used material requires high absorption for broadband telecommunication wavelengths. Within the group IV material, silicon is transparent at the telecommunication wavelengths ($\lambda > 1.2 \mu\text{m}$) making it unsuitable for photodetection from $1.31 \mu\text{m}$ to $1.55 \mu\text{m}$. While pure Germanium is a promising candidate as a broadband photodetector. Furthermore, germanium has a direct energy bandgap of 0.8 eV and is compatible with the CMOS technology.

Despite large lattice mismatch between Ge and Si, which is about 4.2%, previous works have shown that epitaxial growth of high-quality germanium layers on silicon can be achieved using reduced pressure chemical vapor deposition (RP-CVD) or ultrahigh-vacuum chemical vapor deposition (UHV-CVD). The germanium film was grown by RP-CVD on SOI substrates. After the growth of a thin buffer layer (50 nm) at low temperature (400°C), a Ge layer in the range of about 300 nm is typically grown at 700°C . The first layer enables to avoid three dimensional growths. After a thermal annealing at 750°C of the stack, the threading dislocations density is in the range of $5\cdot 10^6/\text{cm}^2$. Spectroscopic ellipsometry measurements confirmed the absence of silicon diffusion as the thickness values of the various layers are close to the nominal ones.

The measured Ge layer absorption coefficients are close to $10\,000 \text{ cm}^{-1}$ and 5000 cm^{-1} at $1.31 \mu\text{m}$ and $1.55 \mu\text{m}$, respectively. The strain-induced Ge bandgap narrowing allows detection to $1.6 \mu\text{m}$ with fairly large internal quantum efficiency. Hall measurements indicated that the layer was P-type, with a hole mobility close to $1300 \text{ V}\cdot\text{cm}^{-2}\cdot\text{s}^{-1}$ and a residual carrier density smaller than 10^{16} cm^{-3} . Pump-probe experiments using a femtosecond laser have been carried out and have shown carrier lifetimes much higher than carrier collection times. Then the recombination rate of the photogenerated carriers is very low.

Much work has been focused on vertical illumination Ge photodetectors and impressive results with frequency up to 39 GHz have been obtained [22–24]. We focused mainly on integrated photodetectors coupled to a silicon rib waveguide. We investigated different technology schemes for the integration of Ge photodetectors with the silicon rib waveguides described in Section 2.1. The introduction of the germanium absorbing layer has been considered by a direct coupling of the light from the SOI waveguide into germanium. 3D FDTD simulation shows that in this case 95% of the light was absorbed in $4 \mu\text{m}$ length PD (Figure 7) leading to short photodetectors with possible reduced capacitance in the 10 fF range. However, this increased efficiency is balanced by the need of etching a recess in the 380 nm thick waveguide. For reliability of the process and due to the needed tolerance of the partial etching of silicon, the recess was etched with a SiO_2 mask to a safe $60 \text{ nm} \pm 10 \text{ nm}$ thickness. Selective epitaxy was performed and filled the recess without any cavity between the output of the waveguide and the germanium layer. A SiO_2 cladding was deposited after germanium annealing before the fabrication of diodes (Figure 8). Three kinds of diodes have been studied: a metal-Schottky-metal (MSM), a lateral PIN, and a vertical PIN.

The MSM structure needs an intrinsic Germanium and the formation of Schottky contacts on the Germanium surface. The surface contacts were dry etched in the SiO_2 before used in microelectronics. I–V curve for different designs showing the nonlinear behavior of Schottky contacts were obtained. The electrode spacing is $1 \mu\text{m}$. Figure 9 presents optical and electron scanning microscope views of the integrated photodetector. The measured dark current for such a photodetector is rather high, that is, $30 \mu\text{A}/\mu\text{m}$ at 6 V. That is

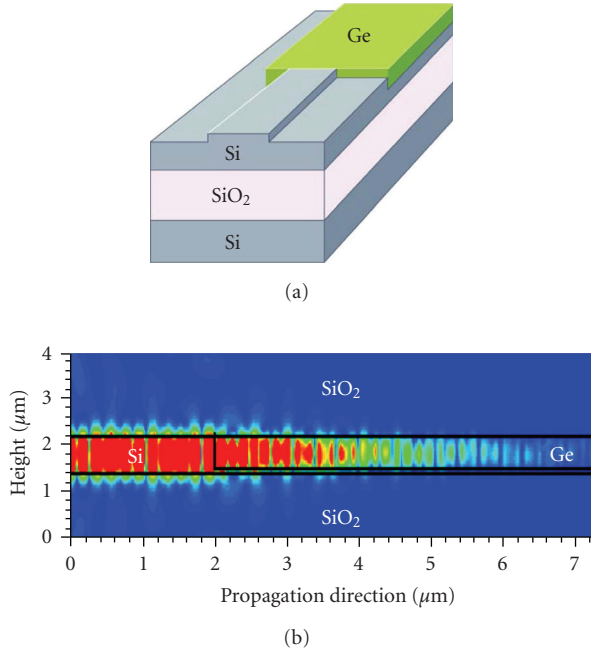


FIGURE 7: Ge photodetector integrated into a rib silicon-on-insulator waveguide and a 3D-FDTD calculation of the electric field profile amplitude in a longitudinal cross section of the photodetector.

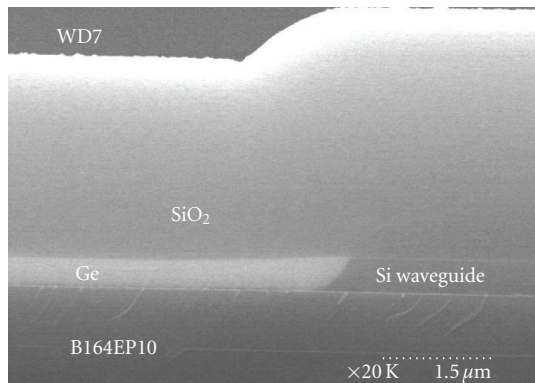


FIGURE 8: RP-CVD germanium epitaxy in a recess at the output of a silicon rib waveguide.

mainly due to the Schottky barrier height, the dislocations in Ge layer and the metallic contacts. The responsivity of the $10\mu\text{m}$ long integrated Ge on Si photodetector is as high as 1 A/W at $1.55\mu\text{m}$ wavelength [25]. Bandwidth characterizations of MSM Ge on Si photodetectors have been carried out using two kinds of experimental setup at $\lambda = 1.55\mu\text{m}$: time response measurements and opto-RF measurements. The normalized responses at 6V bias obtained for both experiments at $1.55\mu\text{m}$, are reported in Figure 10. With opto-RF experiments, the -3 dB bandwidth is close to 25 GHz at 6V bias. For time response experiments, the convolution between a Gaussian profile which characterizes the acquisition system response and a double exponential response give an intrinsic response time of the

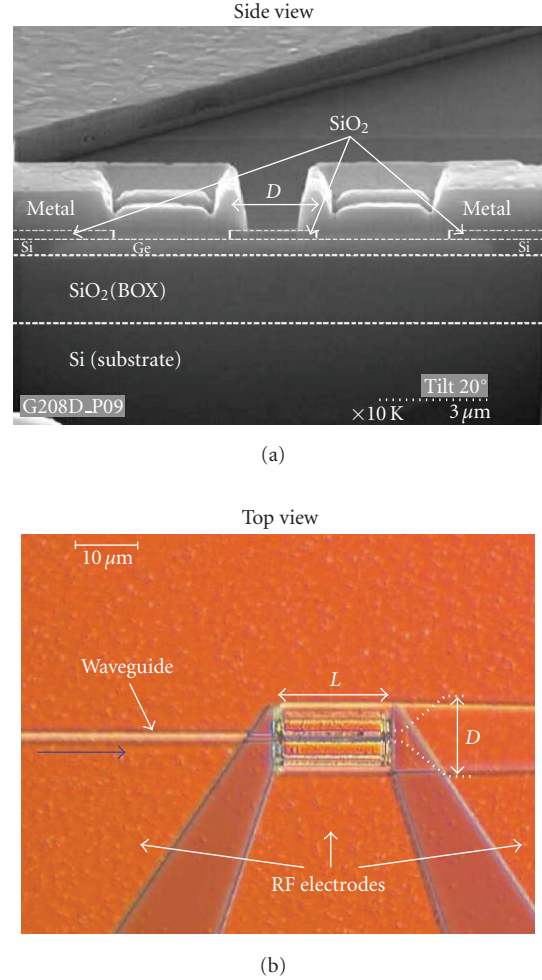


FIGURE 9: Optical microscope (Top view) and Scanning electron microscope (side view) images of the Ge on Si MSM photodetector integrated in slightly etched SOI rib waveguide.

Ge on Si photodetector of about 19 picoseconds, which corresponds on a cutoff frequency of about 23.5 GHz at 6V bias (Figure 10).

The fabrication of vertical PIN photodiode relies on selective epitaxy of in situ P doped layer, followed by intrinsic germanium and N doped layer. P doping with Boron during RP-CVD epitaxy was achieved with $1 \cdot 10^{19}\text{ at/cm}^3$. In situ, N doping epitaxy with a steep profile is a challenge as phosphorus is migrating easily. Deposition of N doped polysilicon on top of the intrinsic Ge is an alternative way. However, epitaxy with a high $1.5 \cdot 10^{19}\text{ at/cm}^3$ doping level, leading to $1.3\text{ m}\Omega\cdot\text{cm}$ resistivity, has been performed for upper contact of the photodetector. In order to contact the P layer at the bottom of the Ge layers, precise etching of Ge for bottom contacting is mandatory for submicron devices. With an AMAT centura machine using RIE etching with Cl_2 gazes, a steep profile ($> 80^\circ$) was achieved without any roughness. An SiO_2 cladding was then deposited and opened for contacting the P and N area. The Ti/TiN/AlCu metallization completed the formation of the pads (Figure 11). Depending

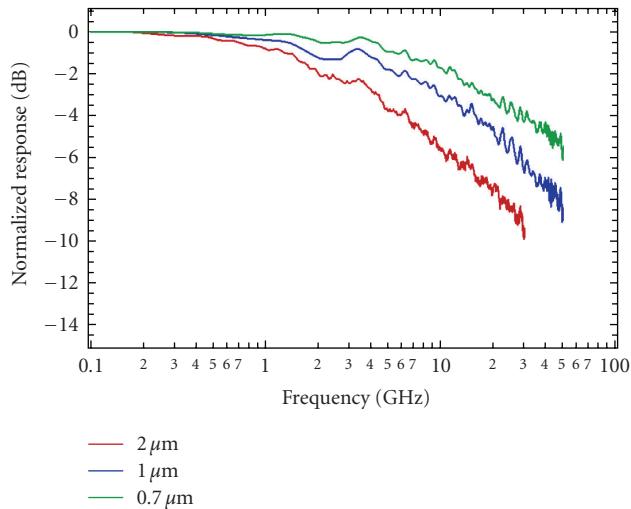


FIGURE 10: Normalized opto-RF responses at 6 V bias obtained for separation of $2\ \mu\text{m}$ (red), $1\ \mu\text{m}$ (blue), $0.7\ \mu\text{m}$ (green).

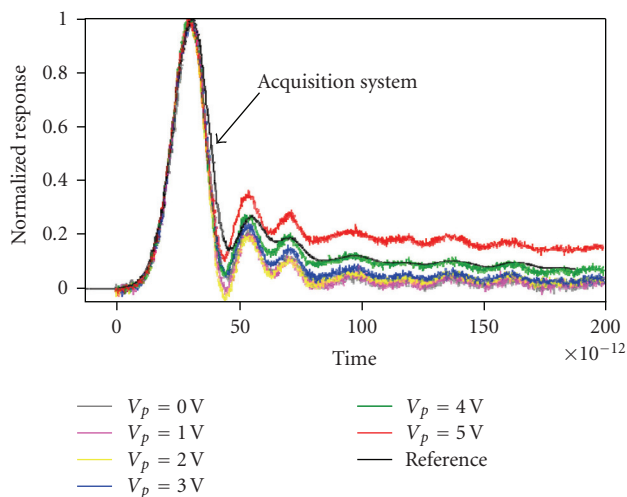


FIGURE 11: Femtosecond pulse response of an integrated vertical PIN.

of the length of the photodiodes, the dark current is in the nA range. The bandwidth exceeded 35 GHz which was the limit of our test equipment (Figure 11).

2.4. Light generation

As efficient modulators can be performed, a CW light source is needed. Different options are followed: light is coming from an external InP laser connected with I/O couplers to the passive circuitry of the chip. This required efficient couplers and expensive packaging. In a second option [2], the laser source is flip-chipped and the emitted light is collected vertically via a surface grating coupler. Compared to the first option, the packaging is reduced and the integration is increased. The third option would be to process InP source after transistor fabrication, but it is rather difficult due to

thermal budgets needed for the combined fabrication. The Graal option would be to process a silicon source. Despite the fact that $\text{SiO}_x\text{-Er}$ layers are a good candidate for such silicon lasers, amplification and lasing have still to be demonstrated in an efficient way. So for a combined fabrication, light generation is really an issue with poor integration.

In conclusion, the results described here above show that a large variety of passive photonic devices except sources can be implemented on SOI substrate by means of CMOS technology. However, as the microelectronic process is very mature, the introduction of a new photonic part in a large CMOS foundry requires a lot of effort for changing the process. Low and medium scale IC foundries are more suitable to accept such modifications as they can differentiate their process and address new markets. However, this combined fabrication is fixed for one CMOS technology and not compatible with other CMOS technologies (SiGe, sSOI, GOI, etc.). As an example, a typical 130 nm CMOS technology ready for 10 G components may be not suitable for 40 G devices.

3. SOI PHOTONICS AND CMOS WAFER BONDING

Using the wafer bonding technique, one can introduce a photonic layer at some level in the processing steps of CMOS. Since the first metal layers are too densely packed and thin, introduction at the upper metal layers must be considered. For example, after the fabrication of metal 4 in advanced MOS process, the planarized surface has been coated with a deposited oxide. On another substrate, a photonic part is fabricated with silicon waveguides and electro-optical components. After cladding with oxide and planarisation of the optical wafer with CMP, perfect cleaning of both wafers facilitates their molecular bonding at room temperature. However, one of the flaws with this approach lies in the alignment between the electrical and the photonic parts which today can be as much as $\pm 2\ \mu\text{m}$. Therefore, the design rules for the subsequent metal layers have to take this alignment margin into account. After bonding, grinding and chemical etching of the backside of the Si optical wafer a flat surface of thermal oxide remains on the top of the PICMOS circuit. Some subsequent process steps are needed to electrically connect the electrical and photonic parts which involve etching through the top layer to contact the electrical circuit below. This technique is often called 3D heterogeneous integration because the CMOS part is separated from the photonic part without any silicon surface waste at the transistor level. With this approach, any microelectronics technologies can be used for the electrical parts and III-V components can be embedded in the photonic layer.

We have performed two demonstrations of this concept in collaboration with TRACIT Technology. On SOITEC optical SOI, we have processed a silicon rib network with cavities filled with Ge. After an SiO_2 cladding deposition, the optical wafer was carefully polished and bonded to a CMOS wafer before substrate removal (Figure 13). An SEM cross-cut observation revealed no interface between the two SiO_2

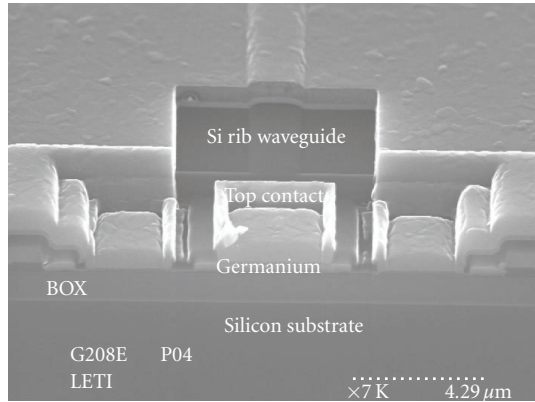


FIGURE 12: SEM view of a PIN vertical PD.

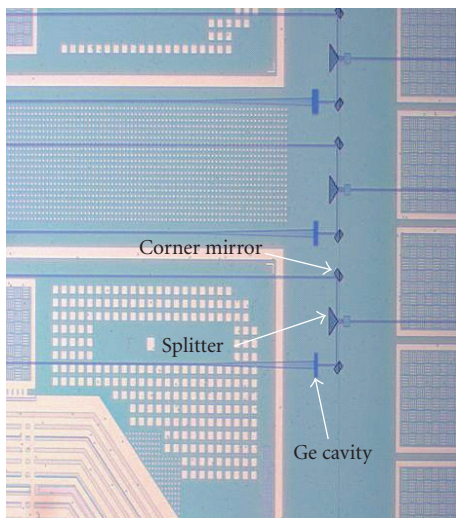


FIGURE 13: Rib waveguides with splitters, corner mirrors, rectangular cavities filled with germanium on a CMOS at level M4.

layers and no degradation of either the metal or the photonic layers (Figure 14).

This wafer bonding technique is a very promising way to integrate a photonic layer into a CMOS technology. The wafer bonding technique is mature and the intraconnections (3D techniques) are well addressed by the electronics community. The PIC can use all the components for the combined fabrication and integrate InP sources by die to wafer bonding. The EIC can use any new electronics technology and can be tested before the wafer bonding as well as the PIC. However, the main challenge that needs to be faced is the bonding cost issue compared to the combined fabrication.

4. HETEROGENEOUS INTEGRATION

As long as temperature is constrained so that it must not exceed 400°C , a photonic layer can be defined above the transistors and the dielectric/metallic levels. The obvious way to introduce such a photonic layer is to treat it as an

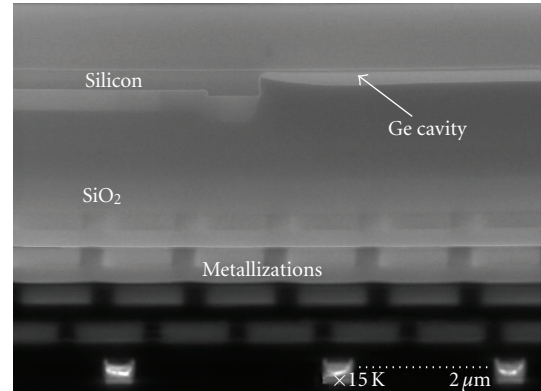


FIGURE 14: Cross-cut of a CMOS wafer with metal levels and a bonded photonic layer with rib waveguides and rectangular cavities filled with germanium.

additional metallic layer on top of most of the layers that have been used for the electrical interconnect. For the passive circuitry, we developed hydrogenated amorphous silicon layer which have a high contrast index. For the active parts, such as the introduction of copper for electrical interconnect, new materials like low temperature III–V compounds can be introduced on the wafers in a dedicated part of the CMOS clean room. After a CMP planarization and surface preparation, QD or MQW layers on top of an InP substrate are bonded on the wafers without precise alignment to fabricated aSi waveguides. The InP substrate of these die is then removed by chemical etching and further processing steps are performed which lead to sources and detectors connected to the metallic interconnects of the integrated circuit.

4.1. Amorphous silicon waveguide fabrication

As the area of a CMOS circuit can range from 1 cm^2 to 2 cm^2 , increasing the refractive index contrast between the cladding and the guiding medium leads to more compact devices. With silicon oxide and silicon films, this is achieved with a value of 2, however, the losses have to be minimized. As with monocrystalline silicon on SOI, the high index difference allows the simultaneous use of refractive compact components and photonic crystal components for wavelength functionality. Amorphous silicon films were deposited by a capacitively coupled plasma reactor, with an RF excitation frequency (13.56 MHz). The power can be tuned from 30 to 1200 W and the operating pressure can be varied from 0.2 mtorr to few torr. All films were deposited at temperatures lower than 400°C to avoid damage to the interconnect layers. TEOS was used as precursor for oxide deposition and silane/ H_2 mixture for the amorphous silicon. Sheet optical guided losses at the full after level during process were measured using a prism coupling technique (METRICON 5010) at $1.3\ \mu\text{m}$ and $1.55\ \mu\text{m}$. By optimizing the H_2 /Silane ratio in the deposition chamber, silicon films with losses as low as 0.2 dB/cm at $1.55\ \mu\text{m}$ after 350°C annealing were deposited on silicon wafers covered with

1 μm TEOS. DUV 193 nm or 248 nm lithography with or without hard mask and HBr silicon etching were used to define the waveguide and basic passive functions for optical links (Figure 15). A thick 1 μm SiO_2 TEOS oxide was deposited to provide an upper cladding. Measurements were performed at a spectral range between 1.25 to 1.65 μm . Results are compared to previous SOI waveguides data [26]. The propagation losses decrease when the width of the waveguide increases and for a guide of width 500 nm (limits to have a monomode waveguide), there is only a dip towards the wavelength of 1380 nm. The losses are comparable to that of an SOI waveguide. We can notice that for this a:Si waveguide, the losses are, respectively, equal to 5 and 4 dB/cm for the wavelengths of 1300 and 1550 nm. We can consider that these losses are essentially due to the diffraction phenomenon due to the side wall roughness of the waveguide. For the waveguide of 800 nm width, the losses become very weak, lower than one dB/cm for wavelengths close to 1300 nm, and tend toward the values of a planar waveguide for both types of waveguides (with or without thermal annealing of 350°C), this shows that the material has a good stability in time. Experimental results of the basic building blocks obtain on the amorphous silicon are in a good agreement with those of the SOI technology. The μbends of 2 μm radius exhibited only negligible losses (0.04 dB/ μbend) for all the spectral range. Measurements on a very compact size of $2 \times 4.2 \mu\text{m}^2$ MMI devices give an extra losses of 1 dB at $\lambda = 1.3 \mu\text{m}$ (the design wavelength), a spectral range at 1 dB of 500 nm and the imbalance

between the two output is lower than 0.5 dB for all the spectral range. The most important features for amorphous silicon circuitry is the easy possibility to pile up layers and, therefore, to open new designs concepts or to ease designs such as crossings or coupling. As an example, in Figure 16, a aSi surface gratings is formed on top a aSi/SiO₂ Bragg mirrors for an increase in the coupling efficiency with a fiber.

4.2. Die to wafer bonding of InP sources

Even with the latest development on active silicon photonics, III–V components remain more efficient for light-matter interaction. However, the cost of wafers and processing on small diameter wafers leads to rather expensive components. Integration of InP components coupled to passive optical functions on top of a CMOS requires a new approach which is different from the flip-chip solution. The first issue would be to enable integration of InP-based laser heterostructures on top of an IC. Another objective was to be able to process the InP-based components in the same way as the CMOS transistors in order to reduce the cost of the introduction of III–V components. As passive components can be efficiently developed with SiN or Si technology, only the active components require an InP technology. One should note that photonic sources or other active devices should exhibit low power consumption, and a small footprint, and should also operate at high speed. For all of these reasons, the needed devices should be as small and integrated as possible. This means that the InP-based components occupy a very small surface on a large CMOS circuit. Therefore,

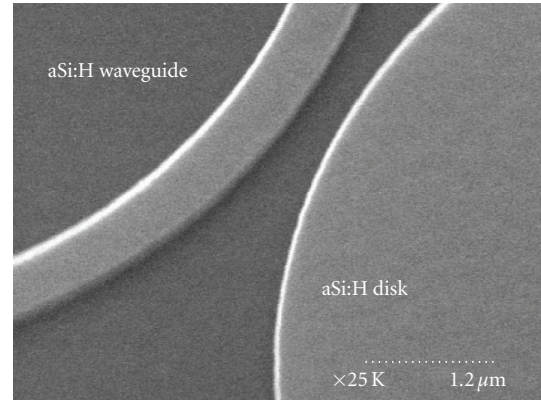


FIGURE 15: Amorphous Si waveguide with resonating disk.

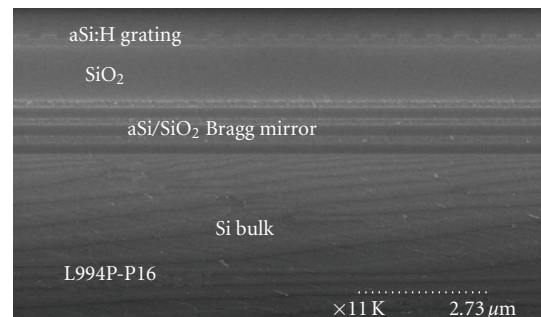


FIGURE 16: Cross-cut of an amorphous Si gratings on top of a Bragg mirror made of an:Si/SiO₂ alternate layers.

our approach consists of dicing an InP wafer with all the heteroepitaxial layers, bonding the die to the required places, removing the back of the InP die in order to only leave the active thin films attached to the CMOS wafer, thus enabling processing of InP components on a dedicated 200 or 300 mm fabrication line. To mount the die, molecular bonding was selected because good bonding quality can be achieved without any additional adhesive materials [22, 23]. In fact, the presence of the bonding material could inhibit efficient optical coupling. Furthermore, molecular bonding satisfies the requirements better in term of thermal conductivity and dissipation, transparency at the device working wavelengths and mechanical resistance.

Surface morphology and chemistry are critical to the bonding quality. Prior to bonding the die, the surfaces must be flat and uniform. The required flatness and uniformity can be obtained by use of CMP. The additional role of CMP polishing is to adjust the thickness of the silicon dioxide cladding layer in order to satisfy the optical coupling conditions. The surfaces were carefully cleaned and hydrated in the chemical solution and bonding can occur spontaneously when the prepared wafers are made of silicon. A complete physical model of such a molecular bonding was proposed and presented by Stengl et al. [27] and Gósele et al. [28]. As these materials are of dissimilar nature, one possible way

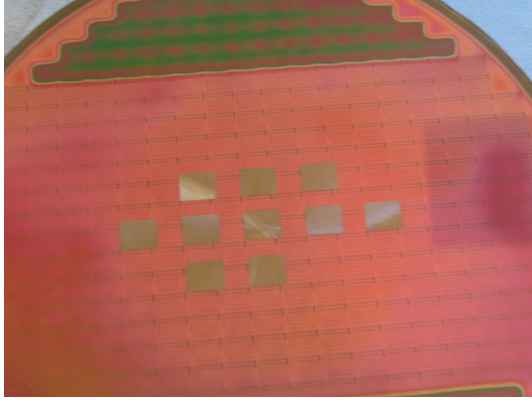


FIGURE 17: Silicon wafer with InP-bonded dice after InP substrate removal.

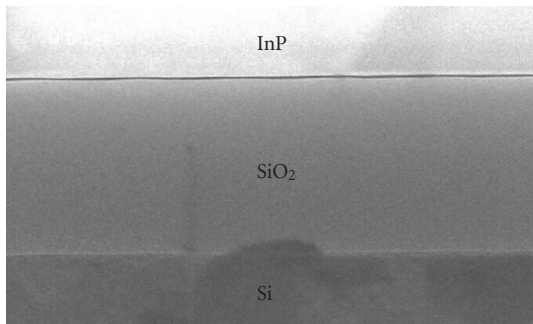


FIGURE 18: SEM cross-cut at the bonding level.

to achieve their assembly is to deposit a silicon dioxide or a silicon nitride layer on each surface.

Using this molecular bonding approach, we have successfully performed the heterogeneous integration of 50 mm InP wafers on silicon and also InP die containing an epitaxial layer stack with multiple quantum wells (MQWs). The CMOS wafer with SiO₂ top cladding was polished to reach a low roughness, cleaned in deionized water, and then dried. A silicon dioxide layer is deposited and then processed on InP (100) epitaxial substrate using electron cyclotron resonance plasma. Thanks to this preparation, the bonding of the both InP/SiO₂ and CMOS/SiO₂ wafers is similar to that achieved for Si/SiO₂ on Si/SiO₂ bonding. Further details on InP-on-Silicon wafer bonding have been described elsewhere [26]. The dice were obtained by mechanical dicing of 360 μm thick InP substrate containing an epitaxial heterostructure and a thin silicon dioxide layer. The smallest die size we have bonded is 1 × 1 mm². A pick and place apparatus can be used to mount the InP die onto the silicon substrate. The bonding itself occurs spontaneously at room temperature; however, an annealing at 200 °C for several hours reinforces adhesion. Mechanically thinning the die down to 20 μm was performed after bonding without degrading the remaining bonded material quality. Next, the remaining InP substrate and the sacrificial InGaAs layer can be chemically and selectively backetched. We mounted the 360 μm thick InP dice including MQW on the optical

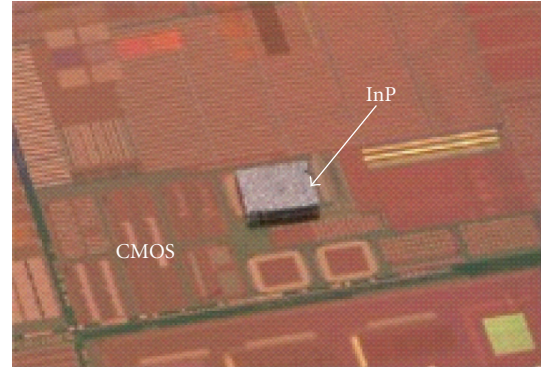


FIGURE 19: 1.2 × 1.2 mm², 200 μm thick InP die-bonded on an optical layer on a CMOS substrate.

layer transferred onto a 200 mm diameter CMOS processed wafer [29] as shown in Figure 19. The InP dice were placed on specific locations where InP devices are needed. The additional postbonding technological steps such as polishing show that the assembled InP dice on the Si substrate can endure many kinds of mechanical maltreatment without debonding. The bond strength between the die and the substrate was measured using die shear testing equipment. The obtained shear strength is of 5 MPa ± 1.4 MPa for 1 mm², 360 μm thick InP dice. Using this approach in another experiment, InAs_{0.65}P_{0.35} 6 nm thick single quantum well (SQW) confined between 120 nm thick InP barriers were deposited locally on the 200 mm wafer and this resulted as a localized epitaxy of II–V material.

4.3. Fabrication of InP microsources with microelectronics tools

The concept chosen was to define a cavity in the III–V material which is evanescently coupled to silicon waveguides located underneath. Whispering gallery modes (WGMs) of microdisks resonators are efficient solutions for low threshold microlaser fabrication. The concept chosen was to define a cavity in the III–V material which is evanescently coupled to underneath silicon waveguides. Whispering gallery modes (WGMs) of microdisks resonators are efficient solutions for photon confinement as they exhibit low mode volumes and high-quality factors. In a previous paper [30], the coupling of such μdisks to silicon waveguides has been described so we have only reported the main results here. The active heterostructure with MQW was designed to emit at 1.5 μm and was grown by molecular beam epitaxy (MBE) on a 2-inch InP wafer. After molecular bonding, 5 μm diameter microdisks were patterned with alignment accuracy better than ± 200 nm to the waveguides by reactive ion etching, using a CH₄:H₂ plasma. The quality of the final devices relies heavily on two main parameters: the ability to control the silica bonding thickness between the microdisk and the waveguide, and the ability to align properly the microdisk with the collecting waveguides. Figure 20 presents a top view of a final device. In the injection axis, the pumping light was generated by a pulsed 780 nm laser diode (duty-cycle of 10%

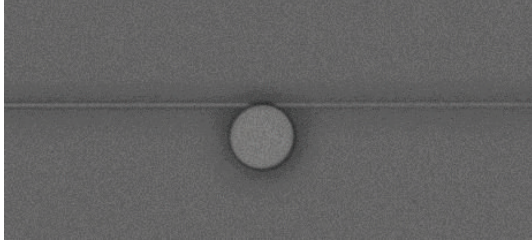


FIGURE 20: SEM top view of an InP μ disc perfectly aligned to a silicon waveguide.

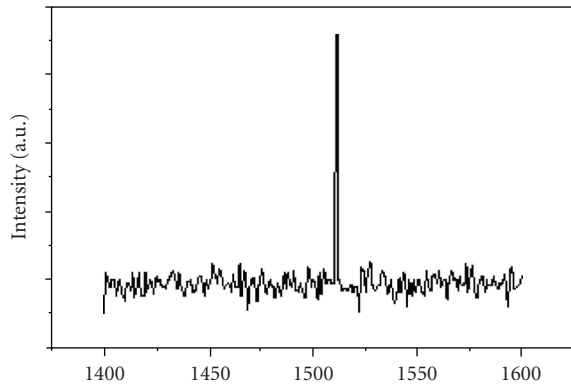


FIGURE 21: Spectrum of the guided light collected at the cleaved facet.

with a repetition rate of 200 nanoseconds), and focused onto the sample by using a $\times 10$ IR microscope objective lens. The guided light was collected by a $\times 20$ IR microscope objective lens, with the signal coming from a cleaved facet of the sample which was partially analyzed by the spectrometer, and partially used to display an IR image. Analysis of the radiated light from a coupled microdisk shows that laser emission is maintained although light coupling into a waveguide induces additional losses. The spectral analysis of the guided light (Figure 21) reveals the same spectral features as the radiated light in terms of wavelength and linewidth. With 300 nm separation of the μ disc to the silicon waveguide, the coupling efficiency is higher than 40%.

Fabrication of an electrically driven μ laser was then studied and consists in μ disks with a vertical P-I-N junction.

Two technologies were considered. The first one followed during the PICMOS project was to process samples with conventional InP technology after the ebeam lithography of the μ disk aligned to the silicon waveguide. This led to the first lasing device on silicon [31, 32], then to the first μ lasing device coupled to a silicon waveguide [33], and finally to the demonstration of a full link in silicon [34, 35]. The second one developed in this paper concerns the fabrication of the μ disk using 200 mm microelectronics tools at CEA-LETI.

To process a vertical InP PIN diode (Figure 28) in the form of a μ disk connected at the bottom level and at the top level in the center, optimization of the main parameters design was necessary (Figure 22). The electromagnetic properties of a microdisk were first analytically calculated

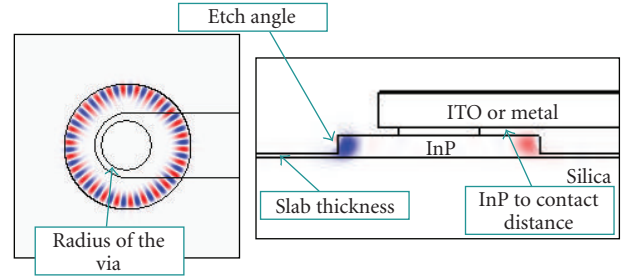


FIGURE 22: Main parameters for the design of the microlaser coupled to a silicon waveguide.

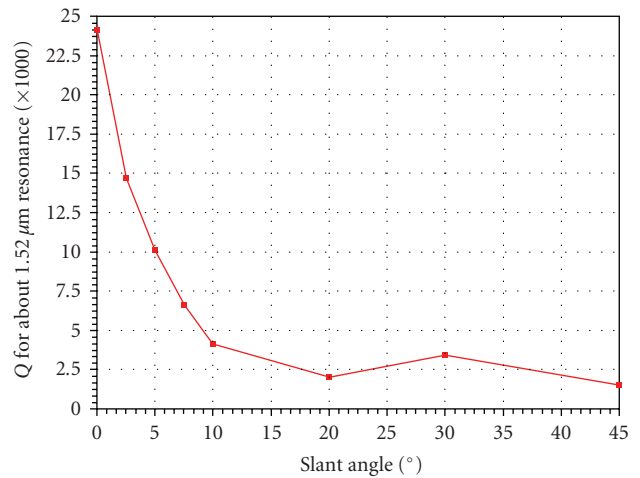


FIGURE 23: Evolution of Q for the 1.5 μ m nearest mode for a 2.5 μ m radius InP μ disk (0.545 μ m thick) in silica with a 100 nm slab.

in an approximate 2D approach and afterwards precised with 3D FDTD. Figure 23 reported the sharp decrease of the quality factor with the increase of the slope edge for a disk with a slab. The mode is attracted in the slab region where it leaks. This gives a challenge for the etching of InP stack. We studied also the geometrical properties of the top contact, keeping in mind that high-quality factors must be achieved. Top contact that can be made of metal or ITO (Indium Tin Oxide), has a major influence on the laser behavior: a too small contact results in inefficient electrical injection while a too large one strengthen optical losses due to metal or ITO absorption. The thickness of the InP-doped slab which is mandatory for defining the bottom contact is the result of a partial etch of the membrane constituting the microdisk. Too low, the contact is poor, but the quality factor is high. Too high, the contacts are good, but the quality factor decreases as the confinement is reduced. The process started by a contamination analysis of the 200 mm wafers after the bonding step and the InP substrate removal as it was not performed in the same clean room. Then a special decontamination of the rear face of the wafers was performed, in order to avoid any contamination of the chucks of the clean rooms equipment. An SiO_2 hard mask of 100 nm was deposited by PECVD. Microdisks were defined with 248 nm DUV lithography. A special attention has to be

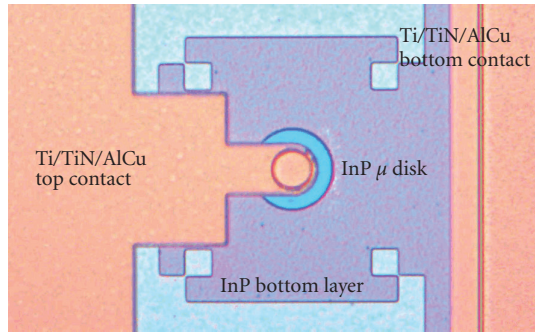


FIGURE 24: Optical top view of a micro disk.

made on the focus, due to the presence of the dice on limited area of the wafer. The hard mask is then etched with InP as stopping layer. The partial etching was performed with ICP equipment using HBr reactive ion etching. A second lithography step followed by an InP etching defined the slab necessary for the bottom contact. Then $1.5\ \mu\text{m}$ SiO_2 TEOS, that is, a low index and electrical isolating material, was deposited in place of the BCB used for planarization in the PICMOS demonstration. Chemical mechanical polishing (CMP) was then performed to get a planar surface with $400\ \text{nm}$ separation with the upper surface of the InP disk. This distance between the membrane, where modes are propagating and the absorbing contacts were optimized for ITO contacts to get the highest Q. However, higher value could be useful with more absorbing material. As the P contact requires very high doping, which increases optical absorption, the studied structures use a tunnel junction to get two N contacts. Even if gold-based contacts have well known properties on InP, CMOS processes are not compatible with such a metal (except for back-end metallization) because of contamination risks. Ti/TiN/AlCu contacts were an alternative solution since we can get a low resistive contact. TLM measurements were performed on a trial InP wafer with a $500\ \text{nm}$ thick $5 \cdot 10^{18}\ \text{cm}^{-3}$ N+Si doped layer and showed that the contacts were ohmic types. So top and bottom electrodes were formed by opening the SiO_2 to the bottom and upper InP N-doped surface and by patterning the electrodes after the Ti/TiN/AlCu deposition. Figure 24 shows the final device. Light emission in continuous wave (CW) electrical injection at room temperature was observed, but optical characterization proved that no structure was lasing, even in pulsed mode. The electrical threshold was determined to $0.7\ \text{V}$. Emitting light is possible under electric power as high as $150\ \text{mW}$, without reducing too much the light power. Maximum light emission is obtained at $30\ \text{mW}$. Lateral roughness and the etching slant are two critical parameters to get efficient resonators. Considering the real slab thickness that was $400\ \text{nm}$ for a membrane of $1\ \mu\text{m}$, FDTD proved that these first samples with 45° slanted edges could not get higher quality factors than 500 what is too low to reach lasing mode.

Some devices with large area were tested as photodetectors (Figure 28), even their shapes did not match with a beam coming from a fiber vertically to the substrate. With

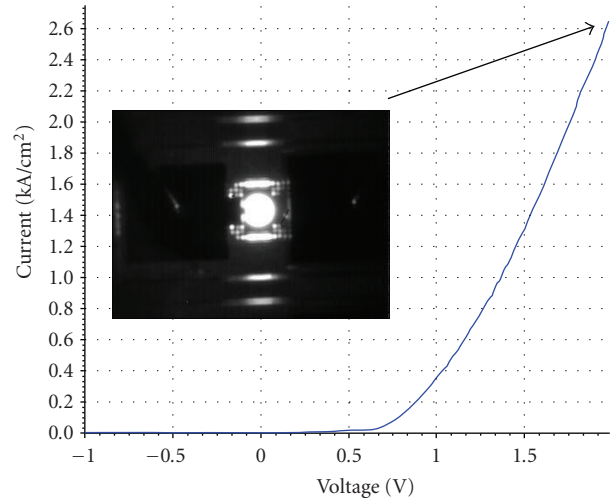


FIGURE 25: PIN characteristic for Ti/TiN/AlCu contacts.

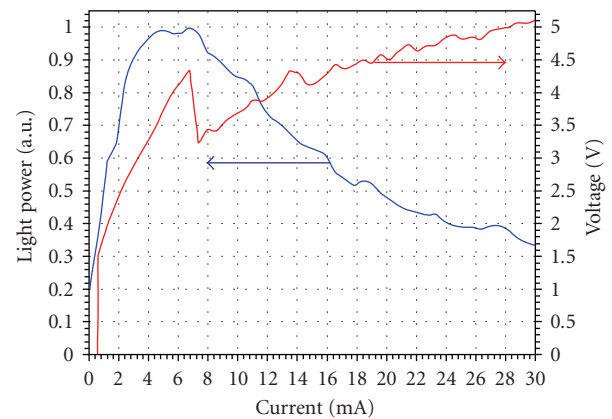


FIGURE 26: Light power emission at room temperature (in blue) and voltage (in red).

the cross-cut of Figure 27, the TiAlCu were contacted with P and N-type layers, giving a PIN diode without the tunnel junction. The dark current at $-1\ \text{V}$ was quite low ($1\ \text{nA}$) for a surface of $900\ \mu\text{m}^2$. This low value can be explained by passivation of the slanted edges with HBr etching. With a surface illumination at $1.55\ \mu\text{m}$, the sensitivity was measured in the range of $10\ \text{mA/W}$. This resulted from the very thin absorption layer. So by changing the active layers to more absorbing ones like InGaAs with a thickness up to $1\ \mu\text{m}$, the sensitivity can be largely improved to the A/W range, while keeping low dark current. So, arrays of III-V photodetectors can be processed on $200\ \text{mm}$ wafers with microelectronics' tools.

Therefore, basic elementary building blocks for the demonstration of a laser source coupled to a silicon waveguide and photodetectors have been demonstrated and fabrication is possible on a $200\ \text{mm}$ Si fabrication line. However, more studies such as optimization of the etching process, investigations of temperature dependency, power

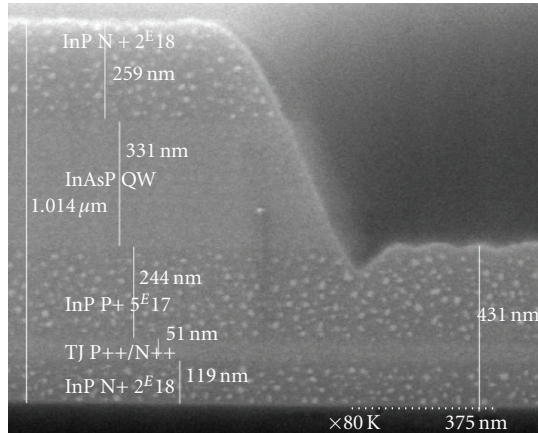


FIGURE 27: SEM slice view of a micro disk.

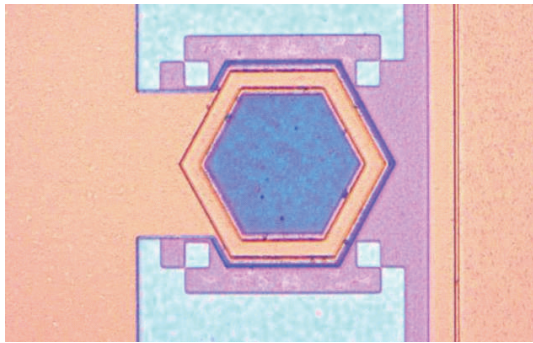


FIGURE 28: Hexagon used for photodetection.

range, and so on have to be performed before they can be used in applications.

5. CONCLUSION

Several different approaches for making the integration of a photonic layer on a CMOS circuit have been reported: the hybridization of photonics on top of a CMOS, a combined fabrication at the front end level, the wafer bonding of SOI photonic circuit at the back-end level, and an embedded photonic layer between metallization have all been performed and some results have been presented. These different approaches lead to different technologies with their own merits and drawbacks. Depending of the applications and the associated volumes of fabrication, the system designers would be able to choose the best way to make their desired system if the necessary building blocks were available. We have presented for each approach some technology routes to the achievement of these building blocks: for combined fabrication, a silicon rib technology was developed with low 0.1 dB/cm losses, 35 GHz Ge photodetectors, and 10 GHz Si modulators. A wafer bonding of an SOI wafer with silicon rib waveguide and cavities filled with Ge or with photonic crystals was achieved above metallization of a CMOS wafer. With the back-end level approach, direct fabrication of a photonic layer was achieved with low-temperature processes.

Low-temperature waveguide technologies with amorphous silicon (loss 5 dB/cm) were developed. The molecular bonding of InP dice and the fabrication of InP microdisks using microelectronics tools base demonstrate that III-V μ sources can be developed on silicon substrates. A 40% coupling was achieved to a stripe silicon waveguide, but only LED mode was demonstrated with electrical injection, due to poor InP etching. Clearly, the improvement and development of such photonics building blocks need to be carried on for the development of photonic integrated CMOS chip (PICMOS).

ACKNOWLEDGMENTS

This paper summarizes the work of numerous other fellows who could not be all cited and the authors wanted to acknowledge them. The CMOS wafers used for technology demonstration were provided by STMicroelectronics. This work is supported by the European community projects FP6-2002-IST-1-002131-PICMOS and FP6-RII3-CT-2004-50623 MNTEurope and by the French RMNT programs "CAURICO" and "HETEROPT." The authors thank Suzanne Laval, Eric Cassan, Paul Crozat, and Juliette Mangeney from IEF for fruitful discussions. They also acknowledge the staff of the 200 mm clean rooms of the LETI for the fabrication of high-quality optical structures.

REFERENCES

- [1] G. T. Reed, "The optical age of silicon," *Nature*, vol. 427, no. 6975, pp. 595–596, 2004.
- [2] G. Nunn, "CMOS photonics," in *Proceedings of the IEEE SOI Conference (SOI '06)*, Niagara Falls, NY, USA, October 2006.
- [3] S. Lardenois, D. Pascal, L. Vivien, et al., "Low-loss submicrometer silicon-on-insulator rib waveguides and corner mirrors," *Optics Letters*, vol. 28, no. 13, pp. 1150–1152, 2003.
- [4] L. Vivien, S. Lardenois, D. Pascal, et al., "Experimental demonstration of a low-loss optical *H*-tree distribution using silicon-on-insulator microwaveguides," *Applied Physics Letters*, vol. 85, no. 5, pp. 701–703, 2004.
- [5] D. Marris, L. Vivien, D. Pascal, et al., "Experimental demonstration of 1 to 1024 optical division using slightly etched rib silicon-on-insulator waveguides," in *Proceedings of the 2nd IEEE International Conference on Group IV Photonics*, pp. 204–206, Antwerp, Belgium, September 2005.
- [6] D. Marris, L. Vivien, D. Pascal, et al., "Ultralow loss successive divisions using silicon-on-insulator microwaveguides," *Applied Physics Letters*, vol. 87, no. 21, Article ID 211102, 3 pages, 2005.
- [7] L. Vivien, D. Pascal, S. Lardenois, et al., "Light injection in SOI microwaveguides using high-efficiency grating couplers," *Journal of Lightwave Technology*, vol. 24, no. 10, pp. 3810–3815, 2006.
- [8] R. S. Jacobsen, K. N. Andersen, P. I. Borel, et al., "Strained silicon as a new electro-optic material," *Nature*, vol. 441, no. 7090, pp. 199–202, 2006.
- [9] P. Yu, J. Wu, and B.-F. Zhu, "Enhanced quantum-confined Pockels effect in SiGe superlattices," *Physical Review B*, vol. 73, Article ID 235328, 7 pages, 2006.
- [10] Y.-H. Kuo, Y. K. Lee, Y. Ge, et al., "Strong quantum-confined Stark effect in germanium quantum-well structures on silicon," *Nature*, vol. 437, no. 7063, pp. 1334–1336, 2005.

- [11] J. E. Roth, O. Fidaner, R. K. Schaevitz, et al., "Optical modulator on silicon employing germanium quantum wells," *Optics Express*, vol. 15, no. 9, pp. 5851–5859, 2007.
- [12] J. Liu, D. Pan, S. Jongthammanurak, S. Wada, L. C. Kimerling, and J. Michel, "Design of monolithically integrated GeSi electroabsorption modulators and photodetectors on an SOI platform," *Optics Express*, vol. 15, no. 2, pp. 623–628, 2007.
- [13] Q. Xu, S. Manapatruni, B. Schmidt, J. Shakya, and M. Lipson, "12.5 Gbit/s carrier-injection-based silicon micro-ring silicon modulators," *Optics Express*, vol. 15, no. 2, pp. 430–436, 2007.
- [14] B. Schmidt, Q. Xu, J. Shakya, S. Manapatruni, and M. Lipson, "Compact electro-optic modulator on silicon-on-insulator substrates using cavities with ultra-small modal volumes," *Optics Express*, vol. 15, no. 6, pp. 3140–3148, 2007.
- [15] L. Liao, D. Samara-Rubio, M. Morse, et al., "High speed silicon Mach-Zehnder modulator," *Optics Express*, vol. 13, no. 8, pp. 3129–3135, 2005.
- [16] A. Liu, L. Liao, D. Rubin, et al., "High-speed optical modulation based on carrier depletion in a silicon waveguide," *Optics Express*, vol. 15, no. 2, pp. 660–668, 2007.
- [17] F. Y. Gardes, G. T. Reed, N. G. Emerson, and C. E. Png, "A sub-micron depletion-type photonic modulator in silicon on insulator," *Optics Express*, vol. 13, no. 22, pp. 8845–8854, 2005.
- [18] D. Marris-Morini, X. L. Roux, L. Vivien, et al., "Optical modulation by carrier depletion in a silicon PIN diode," *Optics Express*, vol. 14, no. 22, pp. 10838–10843, 2006.
- [19] D. Marris, E. Cassan, and L. Vivien, "Response time analysis of SiGe/Si modulation-doped multiple-quantum-well structures for optical modulation," *Journal of Applied Physics*, vol. 96, no. 11, pp. 6109–6112, 2004.
- [20] G. Roelkens, D. Van Thourhout, R. Baets, R. Nötzel, and M. Smit, "Laser emission and photodetection in an InP/InGaAsP layer integrated on and coupled to a silicon-on-insulator waveguide circuit," *Optics Express*, vol. 14, no. 18, pp. 8154–8159, 2006.
- [21] J. Bourckaert, G. Roelkens, D. Van Thourhout, and R. Baets, "Compact InAlAs-InGaAs metal-semiconductor-metal photodetectors integrated on silicon-on-insulator waveguides," *IEEE Photonics Technology Letters*, vol. 19, no. 19, pp. 1484–1486, 2007.
- [22] M. Jutzi, M. Berroth, G. Wöhl, M. Oehme, and E. Kasper, "Ge-on-Si vertical incidence photodiodes with 39-GHz bandwidth," *IEEE Photonics Technology Letters*, vol. 17, no. 7, pp. 1510–1512, 2005.
- [23] M. Rouvière, L. Vivien, X. Le Roux, et al., "Ultrahigh speed germanium-on-silicon-on-insulator photodetectors for 1.31 and 1.55 μm operation," *Applied Physics Letters*, vol. 87, no. 23, pp. 231109–231111, 2005.
- [24] D. Ahn, C.-Y. Hong, J. Liu, et al., "High performance, waveguide integrated Ge photodetectors," *Optics Express*, vol. 15, no. 7, pp. 3916–3921, 2007.
- [25] L. Vivien, M. Rouvière, J.-M. Fédéli, et al., "High speed and high responsivity germanium photodetector integrated in a silicon-on-insulator microwaveguide," *Optics Express*, vol. 15, no. 15, pp. 9843–9848, 2007.
- [26] R. Orobtschouk, N. Schnell, T. Benyattou, and J. M. Fedeli, "Compact building block for optical link on SOI technology," in *Proceedings of the 12th European Conference on Integrated Optics (ECIO '05)*, pp. 221–224, Grenoble, France, April 2005.
- [27] R. Stengl, T. Tan, and U. Gösele, "A model for the silicon wafer bonding process," *Japanese Journal of Applied Physics*, vol. 28, no. 10, pp. 1735–1741, 1989.
- [28] U. Gösele, Y. Bluhm, G. Kästner, et al., "Fundamental issues in wafer bonding," *Journal of Vacuum Science & Technology A*, vol. 17, no. 4, pp. 1145–1152, 1999.
- [29] M. Kostrzewa, L. Di Cioccio, J. M. Fedeli, et al., "Die-to-wafer molecular bonding for optical interconnects and packaging," in *Proceedings of the 15th Microelectronics and Packaging Conference and Exhibition (EMPC '05)*, Brugge, Belgium, June 2005.
- [30] U. Gösele, Q.-Y. Tong, A. Schumacher, et al., "Wafer bonding for microsystems technologies," *Sensors and Actuators A*, vol. 74, no. 1–3, pp. 161–168, 1999.
- [31] J. Van Campenhout, P. Rojo-Romeo, D. Van Thourhout, et al., "An electrically driven membrane microdisk laser for the integration of photonic and electronic ICs," in *Proceedings of the 18th Annual Meeting of the IEEE Lasers & Electro-Optics Society (LEOS '05)*, p. PD 1.7, Sydney, Australia, October 2005.
- [32] P. Rojo-Romeo, J. Van Campenhout, P. Regreny, et al., "Heterogeneous integration of electrically driven microdisk based laser sources for optical interconnects and photonic ICs," *Optics Express*, vol. 14, no. 9, pp. 3864–3871, 2006.
- [33] J. Van Campenhout, P. Rojo-Romeo, P. Regreny, et al., "Electrically pumped InP-based microdisk lasers integrated with a nanophotonic silicon-on-insulator waveguide circuit," *Optics Express*, vol. 15, no. 11, pp. 6744–6749, 2007.
- [34] P. R. A. Binetti, J. Van Campenhout, X. J. M. Leijtens, et al., "An optical interconnect layer on silicon," in *Proceedings of the 13th European Conference on Integrated Optics (ECIO '07)*, pp. 1–3, Copenhagen, Denmark, April 2007.
- [35] D. Van Thourhout, J. Van Campenhout, P. Rojo-Romeo, et al., "PICMOS—a photonic interconnect layer on CMOS," in *Proceedings of the 33rd European Conference and Exhibition on Optical Communication (ECOC '07)*, Berlin, Germany, September 2007.

Research Article

Developments in Gigascale Silicon Optical Modulators Using Free Carrier Dispersion Mechanisms

Juthika Basak,¹ Ling Liao,¹ Ansheng Liu,¹ Doron Rubin,² Yoel Chetrit,² Hat Nguyen,¹
Dean Samara-Rubio,¹ Rami Cohen,² Nahum Izhaky,² and Mario Paniccia¹

¹Intel Corporation, 2200 Mission College Blvd, SC12-326, Santa Clara, CA 95054, USA

²Intel Corporation, S. B. I. Park Har Hotzvim, Jerusalem 91031, Israel

Correspondence should be addressed to Juthika Basak, juthika.basak@intel.com

Received 6 December 2007; Accepted 15 April 2008

Recommended by Graham Reed

This paper describes the recent advances made in silicon optical modulators employing the free carrier dispersion effect, specifically those governed by majority carrier dynamics. The design, fabrication, and measurements for two different devices are discussed in detail. We present an MOS capacitor-based modulator delivering 10 Gbps data with an extinction ratio of ~4 dB and a pn-diode-based device with high-speed transmission of 40 Gbps and bandwidth greater than 30 GHz. Device improvements for achieving higher extinction ratios, as required for certain applications, are also discussed. These devices are key components of integrated silicon photonic chips which could enable optical interconnects in future terascale processors.

Copyright © 2008 Juthika Basak et al. This is an open access article distributed under the Creative Commons Attribution License, which permits unrestricted use, distribution, and reproduction in any medium, provided the original work is properly cited.

1. INTRODUCTION

Over the past few years, the demands for high-performance computers, ever increasing instructions per cycle and high-energy efficiency, have fuelled the rapid development of multicore and many core microprocessors. With the recent advent of quad-core processors into the market [1, 2], coupled with the laboratory demonstration of a teraflop processor containing 80 cores [3], the need for interconnects supporting gigascale and terascale I/O has become imperative. Although present implementations of chip to chip copper interconnects are being pushed to deliver gigascale bandwidths with the design of transceivers that use active or passive equalizers [4, 5], this is unlikely to be a frequency scalable option.

On a parallel front, optical technology has been successfully deployed in long-haul fiber communications for more than two decades now. Individual components targeted toward these applications have been developed to the extent of delivering bandwidths as large as 40 Gbps [6, 7]. Multiple channels of such high bandwidth transmitted together using wavelength division multiplexing (WDM) is capable of terascale data rates. It would therefore seem intuitive to extensively employ similar optical technology in short reach applications such as rack to rack and board to board

communications. However, this approach has not gathered momentum and the primary reason has been the high costs of materials such as III-V semiconductors and lithium niobate, which are inherently suited for photonic applications. Thus, developing a cost-effective optical technology has become essential for its adoption in the computer industry.

Interest in silicon photonics has been spurred predominantly by the low cost of silicon. In addition, its high volume manufacturability and the potential of electronics and photonics integration in the all pervasive microelectronics applications have added a further boost to this field. Silicon photonics is now being enabled by the successful demonstration of the requisite building blocks on silicon such as fast silicon optical modulators [8–13], SiGe photodetectors [14–16], silicon Raman lasers [17, 18], silicon optical amplifiers [19–22], silicon wavelength converters [23–25], and hybrid silicon lasers [26]. A high speed silicon photonic transceiver circuit which monolithically integrates all of these functionalities would be the ultimate culmination point expected to provide a low-cost solution for future optical interconnects.

Silicon optical modulators are one of the key building blocks which have been extensively studied. High-speed data transmission at 10 Gb/s [9–11], 30 Gb/s [12], and 40 Gb/s [13] has been demonstrated using silicon modulators with

different device configurations. Combining these gigascale silicon modulators with recently developed hybrid silicon lasers [26] and using WDM, one could create a single chip that can transmit data at Tb/s data rate for future high performance computing applications and mega data centers.

Unlike today's commercially available optical modulators which use III-V semiconductors [27] or LiNbO₃ [28], achieving modulation in crystalline silicon is challenging due to the fact that it exhibits no linear electro-optic (Pockels) coefficient and has a very weak Franz-Keldysh effect [29, 30]. It has been very recently shown that strained silicon possesses the Pockels effect [31], but the measured electro-optic coefficient is relatively small (an order of magnitude smaller than that for LiNbO₃). It has also been shown that strained Ge/SiGe quantum well structures have relatively strong electro-optic absorption due to the quantum-confined Stark effect [32], making it possible for optical modulation. However, critical strain engineering is needed and high-speed optical modulator performance has yet to be demonstrated for the Ge quantum well system. Silicon also exhibits an appreciable thermo-optic efficient ($\sim 2 \times 10^{-4}/\text{K}$) [33]. However, the thermo-optic modulator is not suitable for high-speed applications because of its inherently slow response.

The most effective way of performing fast optical modulation in silicon is via the free carrier plasma dispersion effect. This effect relates the variation in the concentration of electrons (ΔN_e) and holes (ΔN_h) in a semiconductor to changes in the absorption coefficient ($\Delta\alpha$) and refractive index (Δn). This effect has been mathematically described by the Drude-Lorenz equations [33] and further refined experimentally to give the following empirical relation at the wavelength of 1.55 μm :

$$\Delta n = -(8.8 \times 10^{-22} \Delta N_e + 8.5 \times 10^{-18} \Delta N_h^{0.8}), \quad (1)$$

$$\Delta\alpha = 8.5 \times 10^{-18} \Delta N_e + 6 \times 10^{-18} \Delta N_h. \quad (2)$$

The performance of modulators using free carrier plasma dispersion is determined by the speed and efficiency of carrier density modulation in the region of the traveling optical mode. Various device configurations have so far been proposed to achieve carrier density modulation in silicon. The first and most extensively investigated device configuration is the forward biased p-i-n diode modulator [34]. In this device, the free carrier density change in silicon is achieved through current injection and is primarily governed by minority carrier dynamics. The forward biased p-i-n diode approach in a resonant ring structure implementation has been demonstrated to give high modulation efficiency and, in turn, compact device sizes of $\sim 12 \mu\text{m}$ [35]. However, modulation speed in these devices is usually limited by the slow carrier generation and/or recombination processes, unless the carrier lifetime can be significantly reduced [36]. It is to be noted that a reduction in the carrier lifetime also results in a reduction in current injection as well as phase modulation and these tradeoffs need to be considered based on specific applications.

Contrary to the forward biased diode, the MOS capacitor [8, 9] and reverse biased pn junction [10, 12, 13, 37]

based modulators rely on electric field-induced majority carrier dynamics and do not suffer from inherent bandwidth limitations. However, the phase modulation in these devices is not as efficient due to smaller overlap between the charge modulation area and the optical mode. In addition, since these devices are limited by their resistance-capacitance (RC) time constants, reducing device parasitic effects is critical to exploit their high bandwidth characteristics.

This paper describes our efforts progressively toward developing a high-speed silicon optical modulator. We focus on the investigation of the phase modulator or phase shifter, as it is the key element of modulators that can be constructed based on various implementation configurations such as Mach-Zehnder interferometer (MZI) and microring resonators. Since the MZI modulator has a broad operation wavelength range and provides a good vehicle for the modulator characterization, we adopted the MZI configuration in all our approaches [33]. In addition, our devices were designed to operate in the push-pull configuration in order to achieve higher power efficiency. This paper is organized as follows. In Section 2, we present details of the MOS capacitor-based silicon modulator and demonstrate 10 Gbps operation with an extinction ratio of 4 dB. Section 3 describes further device development to achieve bandwidths greater than 10 Gbps and discusses the implementation of the silicon modulator based on a pn-diode. Here, we present experimental results of data transmission at 40 Gbps with a 3 dB bandwidth of >30 GHz. Section 4 concludes this paper.

2. MOS CAPACITOR-BASED SILICON MODULATOR

Carrier density modulation is obtained by driving an MOS capacitor into the accumulation mode of operation. A voltage applied across the capacitor can induce an accumulation of charges in the doped silicon near the center dielectric. This modifies the refractive index profile of silicon in the waveguide region and ultimately the optical phase of light passing through it, thus acting as a phase modulator. When placed in one or both arms of an MZI, this phase modulator(s) can change the relative phase difference between the light passing through the two paths. Interference of the outputs from the two arms causes the phase modulation to be converted into the desired optical intensity modulation.

2.1. Design and structure

Figure 1(a) shows the schematic of the cross-section of the designed silicon waveguide-based MOS capacitor phase shifter. It comprises of a 1.0 μm *n*-type-doped crystalline silicon layer (the epitaxial silicon layer of the SOI wafer) at the bottom and a 0.55 μm *p*-type-doped crystalline silicon on the top with a gate dielectric separating them. The 10.5 nm gate dielectric consists of a multilayer stack of silicon dioxide and nitride. A process called epitaxial lateral overgrowth (ELO) is used to grow the crystalline silicon on top of the gate dielectric [38]. This use of single crystalline silicon was a significant development toward reducing device transmission loss from its prototype version which had a polysilicon layer that gave much larger optical

loss due to defects in the material lattice [39]. The p-doping concentration in the ELO-silicon is $1 \times 10^{18}/\text{cm}^3$, while the n-dopant concentration in the SOI silicon is $2 \times 10^{17}/\text{cm}^3$. These doping concentrations were chosen to ensure high bandwidth performance but were not strictly optimized for minimum resistance.

To form the rib waveguide, the entire ELO-silicon, gate dielectric, and $\sim 0.1 \mu\text{m}$ of the SOI silicon are etched. This results in a waveguide rib height of $0.65 \mu\text{m}$ and waveguide slab thickness of $0.9 \mu\text{m}$. The rib width is $1.6 \mu\text{m}$ (measured at the middle of the rib height), and since the sidewalls of the waveguide rib are not entirely vertical, the gate dielectric width is $1.9 \mu\text{m}$. This yields a $1.6 \mu\text{m}$ by $1.6 \mu\text{m}$ waveguide with single-mode operation. In order to minimize the metal contact loss, it is necessary to place the contacts outside of the optical mode. To meet this requirement, two $\sim 3 \mu\text{m}$ wide polysilicon sections with high p-doping concentration and a $0.3 \mu\text{m}$ overlap with the top corners of the ELO-silicon rib (Figure 1(a)) are grown. Aluminum for contacting the p-region is subsequently placed on top of the polysilicon. This design ensures an Ohmic contact between the metal and the polysilicon as well as electrical connectivity between the polysilicon and the rib. The $1 \mu\text{m}$ wide oxide region between the two polysilicon regions shown in Figure 1(a) serves to isolate the contact metal from the rib as well as push the optical mode downwards, away from the lossy polysilicon. The aluminum contacts to the n-region are deposited on the slab, also far from the waveguide. The oxide regions underneath the polysilicon and on both sides of the rib ensure optical confinement and prevent optical field from penetrating into the contact areas. The scanning electron microscope (SEM) cross-sectional image of the fabricated device is shown in Figure 1(b).

The overall length of the MZI modulator is 15 mm, which includes the input and output waveguides, 3 dB directional coupler-based splitters, and two arms of straight waveguides of a nominally equal length of 13 mm. Each arm comprises of a 3.45 mm long high-doping, high-speed RF MOS capacitor phase shifter section, and two ~ 4.75 mm long lightly-doped, low-speed phase shifters that are driven with DC voltages to electrically bias the MZI at quadrature.

2.2. Optical performance

As mentioned earlier, the MOS capacitor device operates in accumulation mode, where the n-type silicon slab is grounded and a positive drive voltage, V_D , is applied to the p-type ELO-silicon causing a thin charge layer to accumulate on both sides of the gate dielectric. The resulting change in free carrier density causes a change in refractive index (n) of silicon in accordance with (1), which is manifested as a change in the effective refractive index of the optical mode (Δn_{eff}). The optical phase shift at the end of the capacitor depends on the magnitude of this voltage-induced Δn_{eff} , the device length L , and the optical wavelength λ and can be calculated as [33]

$$\Delta\phi = \frac{2\pi\Delta n_{\text{eff}}L}{\lambda}. \quad (3)$$

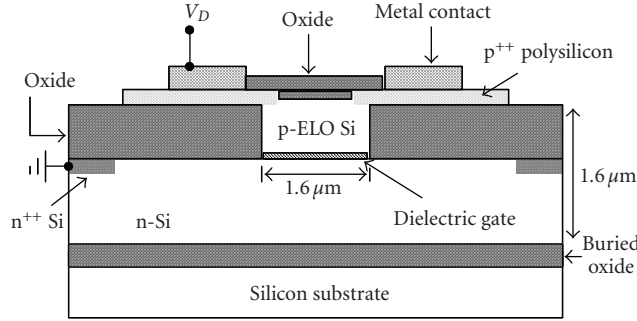
The Δn_{eff} is governed by device design parameters such as the waveguide dimensions and the position of the gate dielectric as they determine how effectively the accumulated charges overlap with the optical mode [8]. As a figure of merit for phase efficiency, the product $V_\pi L_\pi$ can be determined from the measured phase shift, where V_π and L_π are the voltage swing (beyond the flat-band voltage of 1.25 V) and device length required to achieve π radian phase shift. The goal is to minimize the $V_\pi L_\pi$ product to lower the required voltage drive and shorten the device length for a given phase shift. Smaller waveguide dimensions, though harder to fabricate, ensure stronger mode-charge interaction and hence higher phase efficiency. As an example, the phase shifter design of Figure 1 with waveguide dimensions of $1.6 \mu\text{m} \times 1.6 \mu\text{m}$ gives $V_\pi L_\pi$ of 3.3 V-cm, which is 50% smaller than the prototype of this device which had waveguide dimensions of $2.5 \mu\text{m} \times 2.3 \mu\text{m}$ and gave $V_\pi L_\pi$ of 7.8 V-cm.

The optical loss of the phase shifters is measured to be 10 dB/cm for the high-speed sections and 5.2 dB/cm for the low-speed sections. Optical measurements on the MZI modulator gives a total insertion loss of 19 dB comprising of 9 dB coupling loss and 10 dB on-chip loss, when the MZI is in the “on” state, which is defined here as the maximum optical output intensity of the MZI. Of the 10 dB on-chip loss, 3.5 dB is due to the high-speed (RF) sections, 2.5 dB due to the low-speed (bias) sections, and the remaining 4 dB is estimated to be due to a combination of voltage-induced free carrier absorption [40] and the unoptimized design of the splitters and bends. Optical coupling to the $1.6 \mu\text{m} \times 1.6 \mu\text{m}$ waveguides is done using a lensed single-mode fiber with approximately $3.3 \mu\text{m}$ spot size. The total coupling loss of 9 dB can be significantly reduced using one of the known waveguide mode converter techniques [41–43]. Although mode converters were not implemented with the MOS capacitor-based devices, we have extensively studied their performance and have achieved coupling loss as low as ~ 1.5 dB/facet for similar waveguide thickness [44].

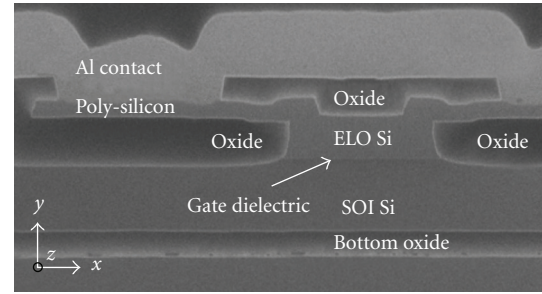
2.3. High-speed performance

The intrinsic bandwidth of the modulator was expected to be limited by the RC time constant. Since the capacitance of the device is proportional to its length, a shorter device would have a larger bandwidth. Therefore, in order to maintain the same phase shift as a 3.45 mm long RF phase shifter but simultaneously enhancing the bandwidth, the phase shifter is divided into eleven equal segments of $315 \mu\text{m}$ each and every segment driven by the same signal with a phase correlation determined by the group velocity of light. The impedance of these sections is measured as a function of frequency and is plotted in Figure 2. The reactance is modeled to be from a capacitance of 2.4 pF, while the resistance is measured as 6.5Ω . The RC cutoff frequency, $(2\pi RC)^{-1}$, can therefore be calculated to be 10.2 GHz.

High-speed operation of the modulator required the use of a low-impedance driver circuit. A custom IC was designed and manufactured using a 70 GHz-F_T SiGe HBT process, details of which can be found in [9]. It employs a



(a) Schematic of the device. The optical waveguide has dimensions of $1.6\ \mu\text{m} \times 1.6\ \mu\text{m}$. The highly doped (p++) polysilicon slabs are each $3\ \mu\text{m}$ wide and with an overlap of $0.3\ \mu\text{m}$ with the ELO silicon region. (The n-contacts are not shown here.)



(b) SEM of the device showing the optical waveguide, comprising of the *p*-type ELO-silicon and the *n*-type SOI silicon with the gate dielectric in the middle

FIGURE 1: Cross-section of the MOS capacitor-based silicon optical modulator.

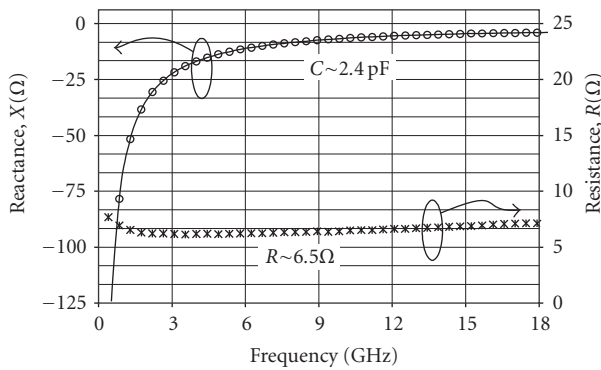


FIGURE 2: Impedance of a $315\ \mu\text{m}$ long phase-shift segment on the MOS capacitor-based modulator. Resistance is measured as $\sim 6.5\ \Omega$, while a modeled capacitance of $\sim 2.4\ \text{pF}$ fits the measured reactance, giving an RC cutoff of $10.2\ \text{GHz}$.

push-pull emitter-coupled logic (ECL) output stage which is wire-bonded directly to each of the 11 segments of the RF phase-shifter on each arm and has been indicated schematically in Figure 3. The driver operates from a single-ended power supply in the range from 3.3 to $3.9\ \text{V}$ and is targeted to deliver up to $1.6V_{\text{pp}}$ ($3.2V_{\text{pp}}$ differential) to each phase-shifter when operating at $8\ \text{Gbps}$. The data pulses delivered to each of the segments are delayed using internal transmission lines to match the optical group velocity across the modulator. A number of control settings are available to trade performance for power dissipation (from $2.7\ \text{W}$ to $3.9\ \text{W}$ depending on supply voltage, output swing, bit rate, and edge rate). Of this power, approximately 10% is dissipated in the modulator. Improved driver design and improved phase-shifter efficiency will lead to reduced power dissipation.

To characterize data transmission performance, a DC voltage of $-3.3\ \text{V}$ is applied to the *n*-type silicon slab. A DC voltage applied to the ELO-silicon rib of the low-speed phase sections sets the MZI at quadrature bias. The DC bias is chosen such that the entire AC swing of $1.4V_{\text{pp}}$ applied to the RF phase shifters is above the flat-band voltage [8].

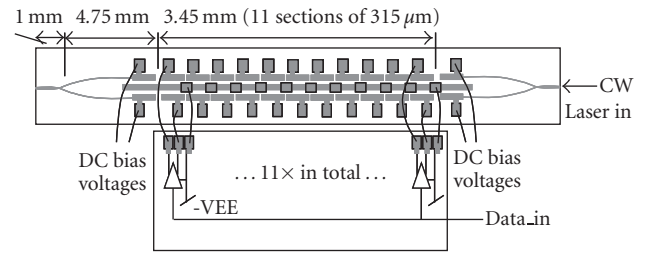


FIGURE 3: Schematic of the MZI-based modulator along with the driver inputs and wire-bonds.

This voltage swing, based on calculations for the device in Figure 3, should yield $0.15\ \pi$ radian phase shift in each MZI arm, enough to give a modulation extinction ratio (ER) of $4.2\ \text{dB}$. The modulator was tested at several data rates with a maximum at $10\ \text{Gbps}$. The resulting eye diagram for a $10\ \text{Gbps}$ $[2^{32} - 1]$ pseudorandom bit sequence (PRBS) input gives an ER of $3.8\ \text{dB}$ and is shown in Figure 4. The $20\text{--}80\%$ rise/fall time is measured to be $\sim 55\ \text{ps}$ and is not found to vary too much from measurements at lower data rates such as at $6\ \text{Gbps}$. Combined with the fact that the inherent bandwidth of the modulator was earlier estimated to be $\sim 10\ \text{GHz}$ from measurements of capacitance and resistance, it is evident that the inherent modulator bandwidth is not the limitation in these measurements. On the contrary, it is the $\sim 0.7\ \text{nH}$ inductance of the wirebonds and the slower slew rate of the driver circuit, corresponding only to $8\ \text{Gbps}$, that limit the demonstrated device bandwidth.

This MOS capacitor-based modulator is the first silicon modulator to reach the $10\ \text{GHz}$ bandwidth milestone. In addition, further improvements in phase efficiency, optical loss, as well as bandwidth are possible with optimization. Modeling and experimental studies show that reducing the waveguide dimensions and thinning down the gate dielectric could greatly improve the phase efficiency [45, 46]. A waveguide with dimensions of $1\ \mu\text{m} \times 1\ \mu\text{m}$ and a gate dielectric of $6\ \text{nm}$ is expected to give a $V_{\pi}L_{\pi}$ product as low as $0.68\ \text{V}\cdot\text{cm}$. Such a device would facilitate the use of a CMOS-based driver with drive voltages $< 1V_{\text{pp}}$ to obtain an ER as

high as 12 dB for a 0.25 cm long phase shifter length. By optimizing the doping profiles as well as the MZI splitter design, this small cross-section device can achieve 10 GHz modulation bandwidth with >12 dB ER and on-chip loss as little as 2 dB.

While the MOS capacitor-based modulator has the potential to realize several GHz of intrinsic bandwidth with reasonably low-optical loss, the device operation speed that can be experimentally demonstrated depends on the electrical drive design. As the capacitance of the MOS capacitor modulator is large (6–8 pF/mm), it requires very short device segments for high data rates if lumped drive is used. An alternative approach would be to use a traveling-wave electrode (transmission line) design. This approach not only addresses the RC speed limitation of lumped devices but also significantly reduces the frequency dependence of the power dissipation of the modulator. For the MOS capacitor-based modulator, however, its high capacitance makes matching the RF phase velocity and optical group velocity more challenging for high-speed operations. In addition, the RF loss of the transmission line would be large at high frequencies because of the large capacitance per unit length. Therefore, from the electrical drive circuitry point of view, it is critical to reduce device capacitance. With this in mind and with the aim of pushing up modulation speeds higher, we started exploring the pn-diode-based optical modulator design, which can potentially have a smaller capacitance. The following section describes the design and performance of the pn-diode-based modulator.

3. PN DIODE-BASED SILICON MODULATOR

This implementation of the modulator, also based on free carrier dispersion, produces a carrier modulation by operating a pn diode in reverse bias and hence in the carrier depletion mode. This modulator is also built in an MZI configuration but is an improvement over the MOS capacitor-based device in a couple of different ways. The dielectric layer between the two doped sections in the MOS capacitor is now replaced by the depletion width of the pn junction, and this leads to a reduction in the modulator capacitance and hence improved bandwidth. At the same time, the metal electrodes are now designed to operate as traveling wave electrodes and this eliminates the dependence of bandwidth on the RC time constant. Processing of this modulator also employs a simpler and more standard nonselective epitaxial silicon growth process instead of the ELO growth step required for the demonstrated version of the MOS capacitor-based device.

3.1. Design and structure

The phase shifter components of this silicon modulator are the reverse biased pn diodes embedded in the MZI arms. Figure 5(a) shows a schematic of the cross-sectional view of the phase shifter. It comprises of a *p*-type-doped crystalline silicon rib waveguide having a rib width of $\sim 0.6 \mu\text{m}$ and a rib height of $\sim 0.5 \mu\text{m}$ with an *n*-type-doped silicon cap layer. This thin cap layer which is $0.1 \mu\text{m}$ thick and $\sim 1.8 \mu\text{m}$ wide is

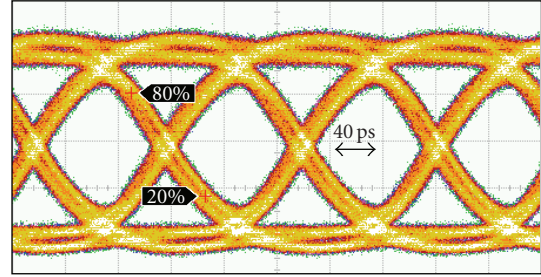
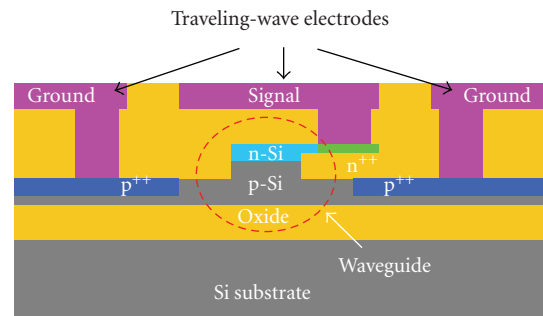
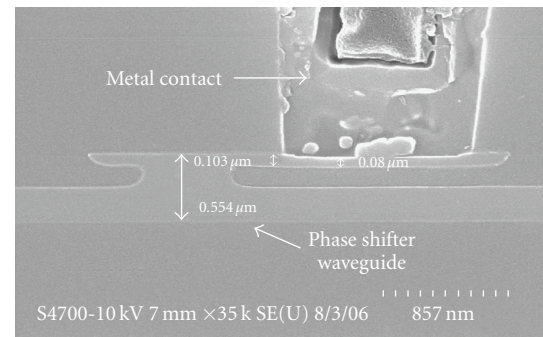


FIGURE 4: Optical eye diagram at 10 Gbps for the capacitor-based modulator copackaged with the custom designed driver. Measured ER = 3.8 dB.



(a) Schematic of the device. The optical waveguide has dimensions of $0.6 \mu\text{m} \times 0.6 \mu\text{m}$. The coplanar waveguide electrode has a signal metal width of $6 \mu\text{m}$ and signal-ground metal separation of $3 \mu\text{m}$



(b) SEM of the rib area showing the metal contact on the *n*-type silicon cap

FIGURE 5: Cross-section of the PN-diode-based silicon optical modulator.

formed using a nonselective epitaxial silicon growth process and is used for pn junction formation and electrical contact. Both modeling and experiments confirm that the $0.6 \mu\text{m}$ by $0.6 \mu\text{m}$ waveguide can support only a single TE mode for wavelengths around $1.55 \mu\text{m}$.

The *p*-doping concentration is $\sim 1.5 \times 10^{17} \text{ cm}^{-3}$, and the *n*-doping concentration varies from $\sim 3 \times 10^{18} \text{ cm}^{-3}$ near the top of the cap layer to $\sim 1.5 \times 10^{17} \text{ cm}^{-3}$ at the pn junction. To ensure good Ohmic contact between silicon and metal contacts, two slab regions $\sim 1 \mu\text{m}$ away from both sides of the rib edge and part of the thin cap layer starting $\sim 0.3 \mu\text{m}$ away

from the rib edge are heavily doped with a concentration of $\sim 1 \times 10^{20} \text{ cm}^{-3}$ of *p*- and *n*-type dopants, respectively. The process parameters described above have been designed to target the pn junction at approximately $0.4 \mu\text{m}$ above the buried oxide to enable optimal mode overlap with the depletion region. As the *n*-doping concentration is much higher than the *p*-doping concentration, carrier depletion under reverse bias occurs mainly in the *p*-type-doped region. This leads to better phase modulation efficiency because the hole density change results in a larger refractive index change as compared to the electron density change as indicated by (1).

Modeling shows that the high-speed performance of a pn-diode modulator is limited by the pn junction capacitance, silicon resistances, and the metal contact parasitics, and not by the carrier dynamics. To minimize the RC limitation of the frequency response of the modulator [47, 48], we designed a traveling wave electrode based on a coplanar waveguide structure as shown in Figure 5(a). The “signal” metal layer is $\sim 6 \mu\text{m}$ wide and is connected to the heavily doped *n*-type silicon region through a $1 \mu\text{m}$ contact. The separation between the signal and ground metal layers is $\sim 3 \mu\text{m}$ and the metal thickness is $\sim 1.5 \mu\text{m}$. The RF traveling wave coplanar waveguide and modulator optical waveguide are carefully designed so that both electrical and optical signals copropagate along the length of the phase shifter with similar speeds. In addition, it is necessary to keep the electrode capacitance small so that the RF loss of the electrodes is minimal. The single-sided asymmetric silicon cap layer design, also shown in Figure 5(a), is used to reduce the capacitance of the phase shifter. The transmission line loss, impedance, and phase velocity are calculated using a commercial software package HFSS, and details on this can be found in [49]. These parameters strongly depend on the metal trace dimensions as well as silicon doping concentration and profile. The cross-section SEM image of a fabricated pn diode phase shifter waveguide is shown in Figure 5(b).

3.2. Optical performance

As in the MOS capacitor-based modulator, the phase shift in the reverse biased pn junction is also given by (3). By changing the applied reverse bias voltage V across the diode, we can obtain a change in depletion width (W_D) according to the following equation [50]:

$$W_D = \left(\frac{2\epsilon_0\epsilon_r(V_{\text{Bi}} + V)}{eN_A} \right)^{1/2}, \quad (4)$$

where the condition of an asymmetrically doped pn junction has been assumed with the *n*-doping concentration much higher than the *p*-doping concentration. Here, ϵ_r is the low-frequency relative permittivity of silicon, N_A is the acceptor concentration, and V_{Bi} is the built-in voltage. Changing the depletion width of a pn junction is equivalent to changing the free carrier density, and hence a change in the refractive index Δn_{eff} . Because the depletion width is usually smaller than the waveguide height, the phase modulation efficiency

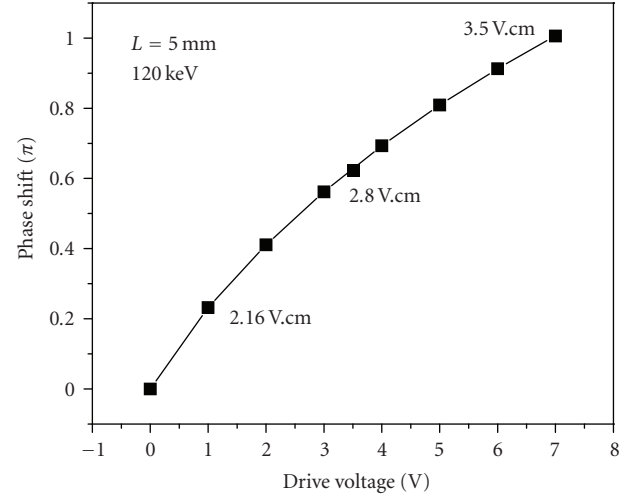


FIGURE 6: Nonlinear phase-shift versus drive voltage as modeled along with the phase efficiency values for the PN-diode-based modulator with a 5 mm long phase shifter at 1 V, 3.5 V, and 7 V.

strongly depends on the pn junction location relative to the guided mode center.

Similar to the MOS capacitor-based modulator, we define the figure of merit for phase efficiency as the $V_\pi L_\pi$ product, where V_π and L_π are the reverse bias voltage and device length required for achieving π -radian phase shift, respectively. The $V_\pi L_\pi$ dependence on junction position location is modeled to show that at 3.5 V drive, junction depths of 0.1, 0.2, and $0.3 \mu\text{m}$ from the top of the waveguide rib yield $V_\pi L_\pi$ values of 5.2, 3.1, and 2.8 V-cm, respectively. This marked dependence proves the importance of optimizing the *p*- and *n*-doping profiles to get maximum overlap between the free carrier density change and the optical mode. Figure 6 also shows the modeled phase shift versus the reverse bias for the device with a junction depth of $0.3 \mu\text{m}$ and with a length of 5 mm. It is clear from Figure 6 that the phase efficiency is not linearly dependent upon the voltage, and this is in accordance with the nonlinear dependence of W_D on the bias, as indicated in (4). A better phase efficiency is obtained for a smaller drive voltage. For example, $V_\pi L_\pi = 2.16 \text{ V-cm}$ for 1 V drive, while it is 2.8 V-cm for 3.5 V drive and 3.5 V-cm for 7 V drive.

Figure 7 shows the measured phase shift of the pn junction phase shifter as a function of the drive voltage for different phase shifter lengths. As the data shows, $\pi/2$ phase shift is achieved at 4 V bias for a phase shifter length of 5 mm, and hence the measured $V_\pi L_\pi$ is $\sim 4 \text{ V-cm}$. This measured phase efficiency is much smaller than the modeled results shown in Figure 6. We suspect this is mainly due to process variations in the pn junction location, causing it to be nonoptimal. We can also see that the measured phase shift is not linearly dependent on the drive voltage, which is qualitatively in agreement with our modeling. Figure 7 also shows the phase shift versus drive voltage for 1 mm and 3 mm phase shifters. As expected, they have the same phase efficiency of $\sim 4 \text{ V-cm}$.

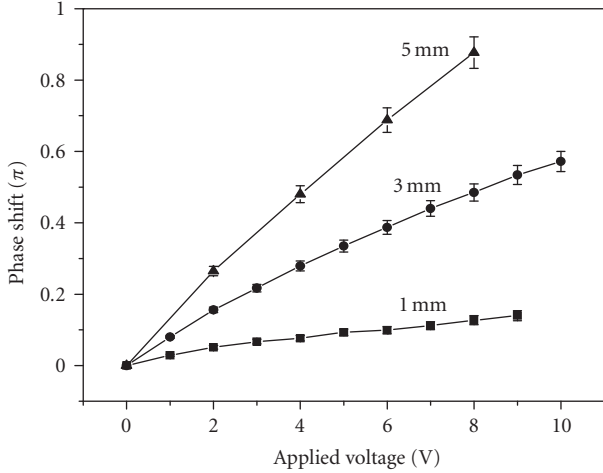


FIGURE 7: Measured phase shift versus applied voltage for MZIs with phase shifter lengths of 1 mm, 3 mm, and 5 mm. Phase efficiency for these devices is calculated as 4 V-cm.

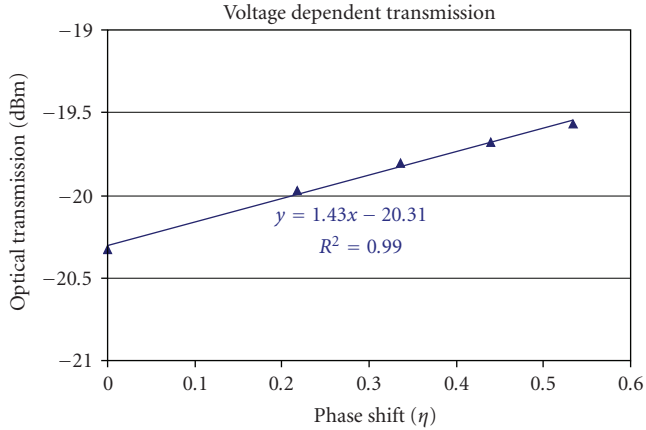


FIGURE 8: Measured change in optical transmission versus phase shift yields a voltage dependent gain of 1.43 dB/π.

The phase modulation is accompanied by optical absorption modulation, as can be seen in (2). Therefore, we expect a voltage induced gain in the phase shifter transmission which can introduce an optical field amplitude imbalance between the two arms of the MZI and potentially degrade the extinction ratio of the device. To quantify this effect, we measure the change in transmission for a straight phase shifter for different bias voltages and plot the optical transmission versus the phase shift. The results are given in Figure 8 which shows that the measured VDG is ~1.43 dB/π. This is in excellent agreement with our modeling. In spite of the VDG-induced arm imbalance, the DC extinction ratio of the MZI is measured to be >20 dB, as can be seen in Figure 9.

The total length of the MZI modulator is 8.25 mm. This includes the input and output waveguides, 2 MMI splitters, and the two straight arms of the MZI, each ~3 mm long, inclusive of a 1 mm long phase shifter. 1 × 2 multimode interference (MMI) couplers are used as the splitters in the MZI because the directional coupler-based splitter (used

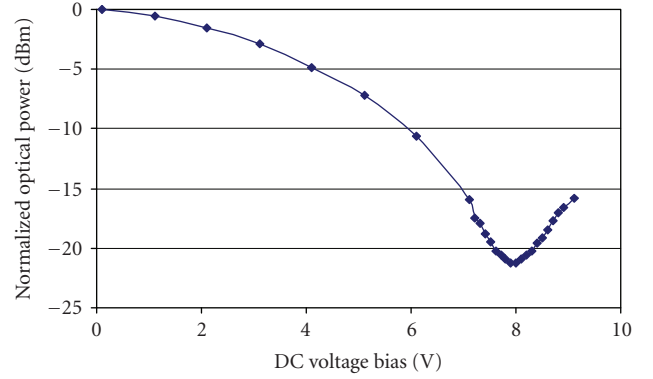


FIGURE 9: Transfer characteristics (optical power output versus bias voltage) for an MZI with phase shifter length of 5 mm. Measured DC extinction ratio >20 dB.

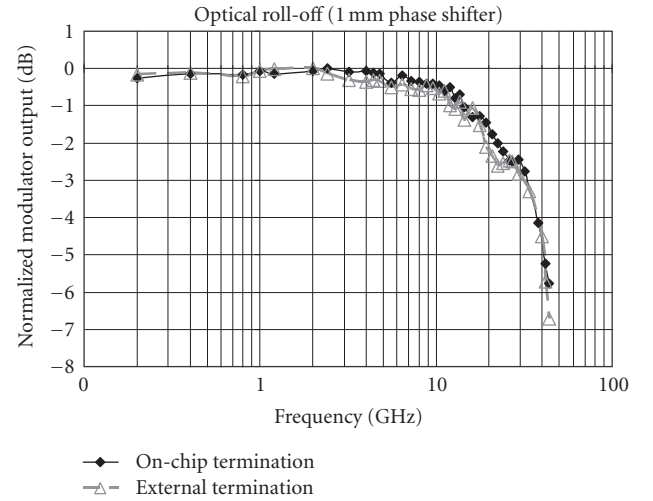
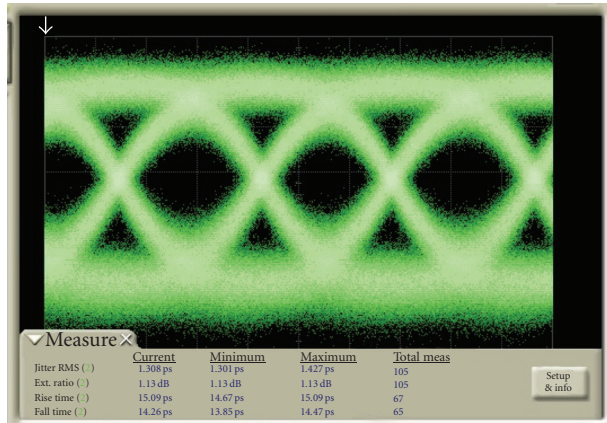


FIGURE 10: Frequency response measurements for an MZI with a 1 mm long phase shifter with on-chip and external termination, respectively, indicating a 3 dB roll-off at ~33 GHz.

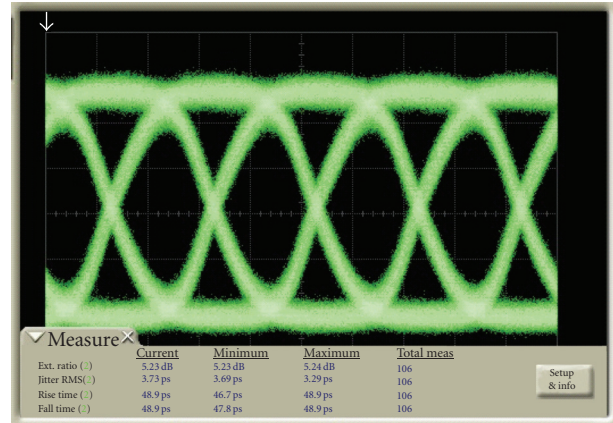
for the MOS capacitor device) for the small waveguide size used here requires very fine lithography resolution to keep excess optical loss at a minimum. The on-chip insertion loss is ~4 dB, when the MZI is in the “on” state, which is defined here as the maximum optical output intensity of the MZI. This on-chip insertion loss (excluding coupling loss) includes ~1 dB passive waveguide transmission loss, ~0.5 dB MMI coupler loss, and ~2.5 dB phase shifter loss, which can be attributed primarily to the dopants. The passive waveguide and phase shifter losses are measured using the well-known cutback method [33], and the MMI coupler loss is determined by comparing its transmission to that of straight reference waveguides.

3.3. High-speed performance

As described in Section 3.1, the metal electrodes have been designed to give high-bandwidth performance. Both modeling and measurements show that the capacitance of



(a) 1 mm phase shifter at 40 Gbps. Single-ended drive signal = $6.2 V_{pp}$ with DC bias of 3.1 V. Measured ER = 1.1 dB



(b) 3 mm phase shifter at 10 Gbps. Dual drive signal = $7.6 V_{pp}$ differential with DC bias of 2 V. Measured ER = 5.2 dB

FIGURE 11: Optical eye diagram of the PN-diode-based modulator.

this device is an order of magnitude smaller than the MOS capacitor-based modulator. However, it is imperative to ensure proper termination of the modulator transmission line in order to suppress the RF signal reflection from the end of the traveling-wave electrode. In our experiment, we have used two different approaches for device termination. One approach is to flip-chip bond the silicon MZI modulator chip to a printed circuit board (PCB) and surface mount external resistors on the PCB traces that are connected to the output end of the modulator electrode. The PCB is designed for high-speed performance with PCB traces having ~ 0.3 dB/cm RF loss and 50 ohm impedance at 40 GHz and is used with low RF loss connectors. The other approach for terminating the device is to monolithically integrate a thin-film resistor with the silicon modulator die. For our MZI devices, we used titanium nitride (TiN) as the resistor material.

The high-frequency performance of the silicon modulator has been characterized by measuring both its 3 dB frequency roll-off and data transmission capability. The MZI silicon modulator used for the high-speed experiments contains a 1 mm long phase shifter in each arm. The RF signal from either a signal generator or a pseudorandom bit sequence (PRBS) generator is amplified using a commercially available modulator driver. For single-ended drive, the amplified output of $6.2 V_{pp}$ is combined with $3.1 V_{DC}$ using a bias tee to ensure reverse bias operation for the entire AC voltage swing. (For dual drive, we use an RF signal of $\sim 7.6 V_{pp}$ differential with each arm biased at $\sim 2 V_{DC}$.) This DC-coupled signal is connected to the input of the traveling-wave electrode of one of the phase shifters via the PCB connector or a GSG probe with RF insertion loss of < 1 dB up to 50 GHz. The output of the electrode is terminated with a 14Ω load. A continuous-wave laser beam at ~ 1550 nm is coupled into the silicon modulator via a lensed fiber. The modulated optical output is collected using another lensed fiber and is connected to a 53 GHz digital communications analyzer (DCA) optical module.

For the optical frequency roll-off measurement, the signal generator is swept from 100 MHz to 44 GHz. The input drive signal is first measured as a function of frequency using a DCA electrical module with 63 GHz bandwidth. This DC-coupled RF signal is then applied to the modulator and the modulated optical signal is also measured as a function of frequency. To obtain the frequency response of the MZI modulator for a constant input drive voltage, the optical output is normalized by the measured input drive voltage for all frequencies. The results for the frequency roll-off measurements for both the devices packaged on a PCB as well as that with on-chip resistors are plotted in Figure 10, where we can see that both the devices have a 3-dB roll-off frequency of > 30 GHz.

The high-speed data transmission performance of the MZI modulator was measured using a PRBS source with $[2^{31}-1]$ pattern length as the RF input. The MZIs have been designed such that both arms can be driven in a push-pull configuration but can be driven more simply in the single-ended configuration as well. The high-speed testing of the device on the PCB was performed using a single-ended drive scheme, while the device with the on-chip termination was driven differentially. Figure 11(a) shows the eye diagram of the modulator optical output at a bit rate of 40 Gb/s. The ER is measured to be 1.1 dB with a rise/fall time of ~ 14 ps. The open eye diagram proves that the modulator is capable of transmitting data at 40 Gb/s, which is consistent with the 3 dB roll-off frequency of > 30 GHz.

Demonstration of such high-speed data transmission represents a significant leap in silicon modulator performance and is a testament to the success of the steps taken to extend the bandwidth beyond 10 Gbps. However, the demonstrated performance above is, by no means, the fundamental limit and there is a lot of room for improvement. For example, the ER can be significantly improved by optimizing the pn-junction location, which alone can lead to $\sim 30\%$ improvement in phase efficiency based on our simulation results.

Another approach toward increasing the ER is to increase the length of the phase shifter contained in the MZI. However, this comes with the trade-off of a larger RF signal attenuation, which limits the data rate to a lower value. Figure 11(b) shows the measured eye diagram at 10 Gbps for an MZI with a 3 mm phase shifter section, which gives an ER of ~ 5.2 dB for a $7.6 V_{pp}$ differential drive with each arm biased at $2 V_{DC}$. Increasing the data rate beyond 10 Gbps rapidly closes the eye due to insufficient bandwidth. One way to overcome the bandwidth limitation would be to break up the 3 mm phase shifter into three smaller segments of 1 mm each and drive every segment with the same signal. This configuration can be expected to give an ER of ~ 5 dB even for ~ 40 Gbps since the bandwidth is now determined by that of a 1 mm device, which has already been shown to be >30 GHz. This is identical to the approach taken for the MOS capacitor which has already been successfully demonstrated. Analogously, the total phase shifter length in the MZI can be further increased to 5 or even 10 mm to give larger extinction ratios, while still maintaining individual segment length at 1 mm. The limitations now become the optical loss, and the increase in driver and packaging complexity.

4. CONCLUSIONS

In this paper, we have presented two implementations of silicon optical modulators, both based on the free carrier plasma dispersion effect. One of them is based on an MOS capacitor operating in the accumulation mode, while the other incorporates a pn-diode operating in the carrier depletion mode. The MOS capacitor-based device was the world's first silicon optical modulator to give data transmission at 10 Gbps. Transmission line implementation of the pn-diode-based modulator helped us push the bandwidths even higher to demonstrate 40 Gbps data transmission and provide a more frequency scalable option for optical modulators. Several straightforward options have been suggested for improving the performance further in terms of the phase efficiency and the achievable extinction ratio. The developments in the silicon optical modulator described in this paper indicate that reaching the performance levels demonstrated so far by other materials is now a forthcoming reality, thus providing a huge impetus toward driving optical interconnects in future terascale microprocessors.

ACKNOWLEDGMENTS

The authors thank K. Callegari, J. Ngo, and J. Tseng for sample preparation; T. Luo for early work on RF characterization; Ulrich D. Keil and Thorkild Franck for driver circuit development for the MOS capacitor device; D. Li for data collection software; R. Gabay, A. Ugnitz, and G. Nutrica for device fabrication assistance; L. Kulig for material analysis; and M. Morse, T. Mader, S. Q. Shang, G. Sarid, T. Franck, R. Jones, D. D. Lu, H. Braunisch, G. T. Reed, and J. E. Bowers for useful discussions.

REFERENCES

- [1] http://www.intel.com/products/processor/core2XE/qc_prod_brief.pdf.
- [2] http://www.intel.com/products/processor/core2quad/prod_brief.pdf.
- [3] S. Vangal, J. Howard, G. Ruhl, et al., "An 80-Tile 1.28TFLOPS network-on-chip in 65 nm CMOS," in *Proceedings of the 54th IEEE International Solid-State Circuits Conference (ISSCC '07)*, pp. 98–589, San Francisco, Calif, USA, February 2007.
- [4] B. Casper, J. Jaussi, F. O'Mahony, et al., "A 20 Gb/s forwarded clock transceiver in 90 nm CMOS," in *Proceedings of IEEE International Solid-State Circuits Conference (ISSCC '06)*, pp. 263–272, San Francisco, Calif, USA, February 2006.
- [5] G. Balamurugan, J. Kennedy, G. Banerjee, et al., "A scalable 5–15 Gbps, 14–75 mW low power I/O transceiver in 65 nm CMOS," in *Proceedings of IEEE Symposium on VLSI Circuits (VLSIC '07)*, pp. 270–271, Kyoto, Japan, June 2007.
- [6] <http://www.cyooptics.com/dynContentFolder/LIM400.pdf>.
- [7] http://www.u2t.de/pdf/Preliminary_Datasheet_XPRV2022_V24.pdf.
- [8] A. Liu, R. Jones, L. Liao, et al., "A high-speed silicon optical modulator based on a metal-oxide-semiconductor capacitor," *Nature*, vol. 427, no. 6975, pp. 615–618, 2004.
- [9] L. Liao, D. Samara-Rubio, M. Morse, et al., "High speed silicon Mach-Zehnder modulator," *Optics Express*, vol. 13, no. 8, pp. 3129–3135, 2005.
- [10] A. Huang, C. Gunn, G.-A. Li, et al., "A 10 Gb/s photonic modulator and WDM MUX/DEMUX integrated with electronics in 0.13 μm SOI CMOS," in *Proceedings of IEEE International Solid-State Circuits Conference (ISSCC '06)*, pp. 922–929, San Francisco, Calif, USA, February 2006.
- [11] Q. Xu, S. Manipatruni, B. Schmidt, J. Shakya, and M. Lipson, "12.5 Gbit/s carrier-injection-based silicon micro-ring silicon modulators," *Optics Express*, vol. 15, no. 2, pp. 430–436, 2007.
- [12] A. Liu, L. Liao, D. Rubin, et al., "High-speed optical modulation based on carrier depletion in a silicon waveguide," *Optics Express*, vol. 15, no. 2, pp. 660–668, 2007.
- [13] A. Liu, L. Liao, D. Rubin, et al., "High-speed silicon modulator for future VLSI interconnect," in *OSA Topical Meeting on Integrated Photonics and Nanophotonics Research and Applications (IPNRA '07)*, Salt Lake City, Utah, USA, July 2007, paper IMD3.
- [14] S. J. Koester, G. Dehlinger, J. D. Schaub, J. O. Chu, Q. C. Ouyang, and A. Grill, "Germanium-on-insulator photodetectors," in *Proceedings of the 2nd IEEE International Conference on Group IV Photonics*, pp. 171–173, Antwerp, Belgium, September 2005.
- [15] M. Oehme, J. Werner, E. Kasper, M. Jutzi, and M. Berroth, "High bandwidth Ge *p-i-n* photodetector integrated on Si," *Applied Physics Letters*, vol. 89, no. 7, Article ID 071117, 3 pages, 2006.
- [16] T. Yin, R. Cohen, M. M. Morse, et al., "31 GHz Ge *n-i-p* waveguide photodetectors on silicon-on-insulator substrate," *Optics Express*, vol. 15, no. 21, pp. 13965–13971, 2007.
- [17] O. Boyraz and B. Jalali, "Demonstration of a silicon Raman laser," *Optics Express*, vol. 12, no. 21, pp. 5269–5273, 2004.
- [18] H. Rong, R. Jones, A. Liu, et al., "A continuous-wave Raman silicon laser," *Nature*, vol. 433, no. 7027, pp. 725–728, 2005.
- [19] A. Liu, H. Rong, M. Paniccia, O. Cohen, and D. Hak, "Net optical gain in a low loss silicon-on-insulator waveguide by stimulated Raman scattering," *Optics Express*, vol. 12, no. 18, pp. 4261–4268, 2004.

- [20] O. Boyraz and B. Jalali, "Demonstration of 11 dB fiber-to-fiber gain in a silicon Raman amplifier," *IEICE Electronics Express*, vol. 1, no. 14, pp. 429–434, 2004.
- [21] Q. Xu, V. R. Almeida, and M. Lipson, "Demonstration of high Raman gain in a submicrometer-size silicon-on-insulator waveguide," *Optics Letters*, vol. 30, no. 1, pp. 35–37, 2005.
- [22] R. Jones, H. Rong, A. Liu, et al., "Net continuous wave optical gain in a low loss silicon-on-insulator waveguide by stimulated Raman scattering," *Optics Express*, vol. 13, no. 2, pp. 519–525, 2005.
- [23] R. L. Espinola, J. I. Dadap, R. M. Osgood Jr., S. J. McNab, and Y. A. Vlasov, "C-band wavelength conversion in silicon photonic wire waveguides," *Optics Express*, vol. 13, no. 11, pp. 4341–4349, 2005.
- [24] K. Yamada, H. Fukuda, T. Tsuchizawa, T. Watanabe, T. Shoji, and S. Itabashi, "All-optical efficient wavelength conversion using silicon photonic wire waveguide," *IEEE Photonics Technology Letters*, vol. 18, no. 9, pp. 1046–1048, 2006.
- [25] H. Rong, Y.-H. Kuo, A. Liu, M. Paniccia, and O. Cohen, "High efficiency wavelength conversion of 10 Gb/s data in silicon waveguides," *Optics Express*, vol. 14, no. 3, pp. 1182–1188, 2006.
- [26] A. W. Fang, H. Park, O. Cohen, R. Jones, M. J. Paniccia, and J. E. Bowers, "Electrically pumped hybrid AlGaInAs-silicon evanescent laser," *Optics Express*, vol. 14, no. 20, pp. 9203–9210, 2006.
- [27] K. Tsuzuki, T. Ishibashi, T. Ito, et al., "A 40-Gb/s InGaAlAs-InAlAs MQW n-i-n Mach-Zehnder modulator with a drive voltage of 2.3 V," *IEEE Photonics Technology Letters*, vol. 17, no. 1, pp. 46–48, 2005.
- [28] K. Noguchi, O. Mitomi, and H. Miyazawa, "Millimeter-wave Ti:LiNbO₃ optical modulators," *Journal of Lightwave Technology*, vol. 16, no. 4, pp. 615–619, 1998.
- [29] R. A. Soref and J. P. Lorenzo, "All-silicon active and passive guided-wave components for $\lambda = 1.3$ and $1.6 \mu\text{m}$," *IEEE Journal of Quantum Electronics*, vol. 22, no. 6, pp. 873–879, 1986.
- [30] R. A. Soref and B. R. Bennett, "Electrooptical effects in silicon," *IEEE Journal of Quantum Electronics*, vol. 23, no. 1, pp. 123–129, 1987.
- [31] R. S. Jacobsen, K. N. Andersen, P. I. Borel, et al., "Strained silicon as a new electrooptic material," *Nature*, vol. 441, no. 7090, pp. 199–202, 2006.
- [32] Y.-H. Kuo, Y. K. Lee, Y. Ge, et al., "Strong quantum-confined Stark effect in germanium quantum-well structures on silicon," *Nature*, vol. 437, no. 7063, pp. 1334–1336, 2005.
- [33] G. T. Reed and A. P. Knights, *Silicon Photonics: An Introduction*, John Wiley & Sons, Chichester, UK, 2004.
- [34] C. K. Tang and G. T. Reed, "Highly efficient optical phase modulator in SOI waveguides," *Electronics Letters*, vol. 31, no. 6, pp. 451–452, 1995.
- [35] Q. Xu, B. Schmidt, S. Pradhan, and M. Lipson, "Micrometre-scale silicon electrooptic modulator," *Nature*, vol. 435, no. 7040, pp. 325–327, 2005.
- [36] F. Gan and F. X. Kärtner, "High-speed silicon electrooptic modulator design," *IEEE Photonics Technology Letters*, vol. 17, no. 5, pp. 1007–1009, 2005.
- [37] F. Y. Gardes, G. T. Reed, N. G. Emerson, and C. E. Png, "A sub-micron depletion-type photonic modulator in silicon on insulator," *Optics Express*, vol. 13, no. 22, pp. 8845–8854, 2005.
- [38] S. Pae, T. Su, J. P. Denton, and G. W. Neudeck, "Multiple layers of silicon-on-insulator islands fabrication by selective epitaxial growth," *IEEE Electron Device Letters*, vol. 20, no. 5, pp. 194–196, 1999.
- [39] L. Liao, D. R. Lim, A. M. Agarwal, X. Duan, K. K. Lee, and L. C. Kimerling, "Optical transmission losses in polycrystalline silicon strip waveguides: effects of waveguide dimensions, thermal treatment, hydrogen passivation, and wavelength," *Journal of Electronic Materials*, vol. 29, no. 12, pp. 1380–1386, 2000.
- [40] L. Liao, A. Liu, R. Jones, et al., "Phase modulation efficiency and transmission loss of silicon optical phase shifters," *IEEE Journal of Quantum Electronics*, vol. 41, no. 2, pp. 250–257, 2005.
- [41] V. R. Almeida, R. R. Panepucci, and M. Lipson, "Nanotaper for compact mode conversion," *Optics Letters*, vol. 28, no. 15, pp. 1302–1304, 2003.
- [42] G. Z. Masanovic, V. M. N. Passaro, and G. T. Reed, "Coupling to nanophotonic waveguides using a dual grating-assisted directional coupler," *IEEE Proceedings: Optoelectronics*, vol. 152, no. 1, pp. 41–48, 2005.
- [43] T. Tsuchizawa, K. Yamada, H. Fukuda, et al., "Microphotonic devices based on silicon microfabrication technology," *IEEE Journal on Selected Topics in Quantum Electronics*, vol. 11, no. 1, pp. 232–240, 2005.
- [44] A. Barkai, A. Liu, D. Kim, et al., "Efficient mode converter for coupling between fiber and micrometer size silicon waveguides," in *Proceedings of the 4th IEEE International Conference on Group IV Photonics*, pp. 49–51, Tokyo, Japan, September 2007.
- [45] A. Liu, D. Samara-Rubio, L. Liao, and M. Paniccia, "Scaling the modulation bandwidth and phase efficiency of a silicon optical modulator," *IEEE Journal on Selected Topics in Quantum Electronics*, vol. 11, no. 2, pp. 367–372, 2005.
- [46] L. Liao, A. Liu, R. Jones, et al., "Phase modulation efficiency and transmission loss of silicon optical phase shifters," *IEEE Journal of Quantum Electronics*, vol. 41, no. 2, pp. 250–257, 2005.
- [47] R. C. Alferness, "Waveguide electrooptic modulators," *IEEE Transactions on Microwave Theory and Techniques*, vol. 30, no. 8, pp. 1121–1137, 1982.
- [48] R. G. Walker, "High-speed III-V semiconductor intensity modulators," *IEEE Journal of Quantum Electronics*, vol. 27, no. 3, pp. 654–667, 1991.
- [49] <http://www.ansoft.com/>.
- [50] S. L. Chuang, *Physics of Optoelectronic Devices*, John Wiley & Sons, New York, NY, USA, 1995.

Review Article

Photonic Integration on the Hybrid Silicon Evanescent Device Platform

Hyundai Park,¹ Alexander W. Fang,¹ Di Liang,¹ Ying-Hao Kuo,¹ Hsu-Hao Chang,¹ Brian R. Koch,¹ Hui-Wen Chen,¹ Matthew N. Sysak,² Richard Jones,² and John E. Bowers¹

¹Department of Electrical and Computer Engineering, University of California, Santa Barbara, CA 93106, USA

²Intel Corporation, 2200 Mission College Blvd, SC12-326, Santa Clara, CA 95054, USA

Correspondence should be addressed to John E. Bowers, bowers@ece.ucsb.edu

Received 17 December 2007; Revised 25 January 2008; Accepted 12 March 2008

Recommended by D. Lockwood

This paper reviews the recent progress of hybrid silicon evanescent devices. The hybrid silicon evanescent device structure consists of III-V epitaxial layers transferred to silicon waveguides through a low-temperature wafer bonding process to achieve optical gain, absorption, and modulation efficiently on a silicon photonics platform. The low-temperature wafer bonding process enables fusion of two different material systems without degradation of material quality and is scalable to wafer-level bonding. Lasers, amplifiers, photodetectors, and modulators have been demonstrated with this hybrid structure and integration of these individual components for improved optical functionality is also presented. This approach provides a unique way to build photonic active devices on silicon and should allow application of silicon photonic integrated circuits to optical telecommunication and optical interconnects.

Copyright © 2008 Hyundai Park et al. This is an open access article distributed under the Creative Commons Attribution License, which permits unrestricted use, distribution, and reproduction in any medium, provided the original work is properly cited.

1. INTRODUCTION

Recent research in silicon photonics has been driven by the motivation to realize silicon optoelectronic integrated devices using large scale, low-cost, and highly accurate CMOS technology. Silicon is transparent at the 1.5 μm and 1.3 μm telecommunication wavelengths and has demonstrated low loss waveguide with losses in the range of 0.2 dB/cm \sim 1 dB/cm. The large index contrast of silicon waveguides with silicon dioxide cladding results in highly confined optical modes and reduction of waveguide bend radii leading to dense photonic integration. This has resulted in advances in passive devices such as compact filters [1], optical buffers [2], photonic crystals [3], and wavelength multiplexer/demultiplexers [4, 5].

It was only recently that silicon has been demonstrated as a high-speed modulator. Silicon-based modulators have been reported using free carrier plasma dispersion in Mach-Zehnder interferometer structure [6, 7], photonic crystals [8], and ring resonator structures [9]. Strained silicon has been shown to break the inversion symmetry of silicon allowing silicon to exhibit linear electro-optic refractive index modulation [10]. Recently, an electroabsorption mod-

ulator on silicon has been demonstrated based on the quantum confined stark effect in strained silicon germanium [11].

Light detection is another major research topic in silicon photonics. Strained germanium and silicon germanium push the absorption out to 1.55 μm wavelength and are attractive since it is compatible with CMOS processing capabilities [12, 13]. Integration of the photodetector with the receiver is critical for lower capacitance and higher sensitivity [14].

The indirect bandgap of silicon has been a key hurdle for achieving optical gain elements. Although Raman lasers and amplifiers [15–17], and optical gain in nanopatterned silicon have been observed [18], an electrically pumped silicon waveguide gain element has been an unsolved challenge.

An alternative to fabricating the gain element in silicon is to take prefabricated lasers and couple them to silicon waveguides. However, due to the tight alignment tolerances of the optical modes and the need to align each laser individually, this method has limited scalability, and it is difficult to envision die attaching more than a few lasers to each chip without prohibitive expense. Furthermore, the reflections at the chip interfaces limit the gain and spectral flatness that can be achieved.

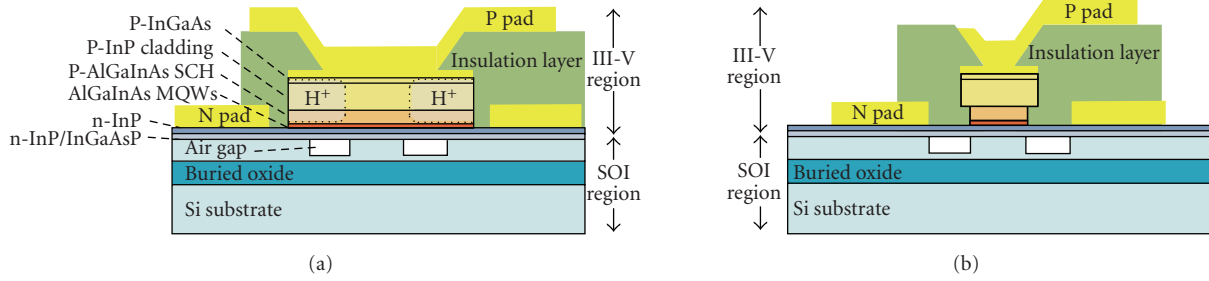


FIGURE 1: Hybrid silicon evanescent device cross-section structures: (a) a wide III-V mesa for amplifiers and lasers, (b) a narrow III-V mesa for detectors and modulators.

Epitaxial growth of III-V layers on silicon substrates has been investigated as well. The demonstrations include InGaAs quantum dot lasers [18] and InGaSb quantum well lasers [19] fabricated on silicon substrate. Those demonstrations have widened the possibility of building monolithically integrated on-chip laser sources on the silicon photonics platform. However, an efficient coupling scheme from the III-V lasers to the silicon waveguide needs to be developed since most of the lasing mode is in the III-V layers.

Recently, we have demonstrated a hybrid integration platform utilizing III-V epitaxial layers transferred to silicon to realize many types of photonic active devices through a single wafer bonding step. The wafer-bonded structure forms a hybrid waveguide, where its optical mode lies both in silicon and III-V layers. This structure enables the use of III-V layers for active light manipulation such as gain, absorption, and electro-optical effect for the amplifiers, lasers, detectors, and modulators. In this paper, we review the recent progress on hybrid silicon evanescent devices. In Section 2, the device structure and design issues are introduced. In Section 3, the device fabrication process is described. Section 4 presents the performance and characteristics of fabricated silicon evanescent devices. Finally, several potential future paths of this research are discussed in Section 5.

2. DEVICE PLATFORM

Figure 1 shows the general structure of hybrid silicon evanescent devices. The hybrid structure is comprised of a III-V region bonded to a silicon waveguide fabricated on a silicon-on-insulator wafer. The mesa structure formed on the III-V region enables the current flow through the multiple quantum well region. The general structure of III-V layers consists of a p-type contact layer, a p-type cladding, a p-type separated confinement heterostructure (SCH) layer, an undoped multiple quantum well layer, n-type contact layer, and n-type super lattices. Amplifiers and lasers have a wide III-V mesa ($12\ \mu\text{m} \sim 14\ \mu\text{m}$) for better heat conduction and mechanical strength (Figure 1(a)) while a narrow III-V mesa ($2\ \mu\text{m} \sim 4\ \mu\text{m}$) is chosen for detectors and modulators for high-speed operation with a reduced capacitance (Figure 1(b)). The optical mode in this hybrid waveguide lies both in the silicon waveguide and the multiple quantum well layers. The confinement factors in III-V and silicon regions of the hybrid waveguide can be manipulated

by changing the silicon waveguide dimensions. The quantum well confinement factor is a critical design parameter in order to achieve enough optical gain and absorption while the silicon confinement factor is an important parameter determining coupling efficiency when the device is integrated with silicon passive devices. Figure 2 shows three different mode profiles with three different waveguide widths. In general, the silicon confinement factor increases as the height or width of the silicon waveguide increases while the quantum well confinement factor decreases. The epitaxial structures and confinement factors for each device set will be specified in Section 4.

3. FABRICATION

3.1. Plasma assisted low-temperature wafer bonding

The transfer of the indium phosphide (InP)-based epitaxial layer structure to the silicon-on-insulator (SOI) substrate is a key step in the fabrication of this hybrid platform and has direct impact on the device performance, yield, and reliability. Due to the mismatch between the thermal expansion coefficient of silicon and indium phosphide ($\alpha_{\text{Si}} = 2.6 \times 10^{-6}/\text{K}$, $\alpha_{\text{InP}} = 4.8 \times 10^{-6}/\text{K}$), high-temperature ($>400^\circ\text{C}$) annealing steps are not desirable. Figure 3(a) shows a Nomarski photograph of the top surface of an InP die transferred to a silicon-on-insulator substrate at 600°C . Crosshatching can be seen for this high-temperature direct wafer bonding which can lead to degradation of material quality and scalability issues due to the accumulation of stress over larger sample sizes. In order to resolve this issue, low-temperature annealing is used with an oxygen plasma surface treatment to enable strong bonding [20]. An annealing temperature of 300°C is chosen to minimize bonding stress while still being able to convert the weak Hydrogen bonds formed by the room temperature bonding to strong covalent Si–O–In and Si–O–P bonds. Figure 3(b) shows a successful transfer of InP epitaxial layers to SOI with smooth device quality surface morphology and no interfacial voids.

Figure 4 is the schematic process flow of the oxygen plasma assisted low-temperature (300°C) wafer bonding. After rigorous sample cleaning and close microscopic inspection with 200x magnification, the native oxide on SOI and InP are removed in standard buffer HF solution (1HF : 7

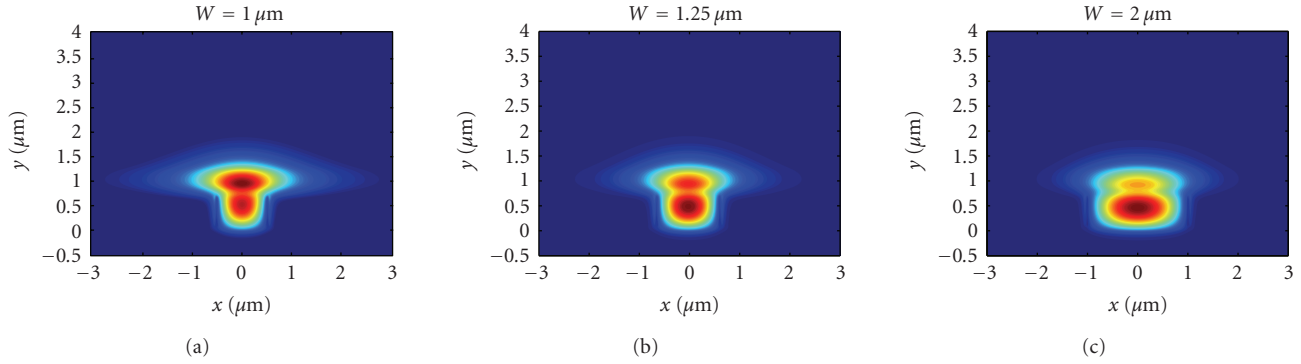


FIGURE 2: Mode profiles with different waveguide widths. Height of the silicon waveguide is fixed at $0.7 \mu\text{m}$.



FIGURE 3: Nomarski microscope images of the transferred III-V surface at bonding temperatures of (a) 600°C and (b) 300°C .

H_2O) and NH_4OH (39%), respectively, resulting in clean, hydrophobic surfaces. The samples then undergo an oxygen plasma surface treatment to grow an ultrathin layer of oxide ($<5 \text{ nm}$) [21] which leads to very smooth (rms roughness $<0.5 \text{ nm}$) hydrophilic surfaces, which is less sensitive to the microroughness as compared to hydrophobic bonding. The Si–O–Si bonds of the oxide (SOI side) are also found to be more strained than conventional oxides formed in standard RCA-1 cleaning process or other hydrophilic wet-chemical treatment, and have a higher readiness to break and form new bonds. O_2 energetic ion bombardment also acts as a final cleaning step to remove hydrocarbons and water-related species on the sample surface efficiently. The following deionized water dip further terminates the oxide surface by polar hydroxyl groups OH^- , forming bridging bonds between the mating surfaces to result in spontaneous bonding at room temperature [22]. To strengthen the bond, the bonded sample is placed in a conventional wafer bonding machine (Suss Bonder SB6E), where the samples are held together at a pressure of 1.5 MPa and a temperature of 300°C , under vacuum ($<4 \times 10^{-4} \text{ Torr}$) from 1 to 12 hours. The 300°C annealing process enhances out diffusion of molecules trapped at the interface and desorption of chemisorbed surface atoms, such as hydrogen, while activating the formation of covalent bonds to achieve higher bonding energy [20]. After annealing and cooling, the InP substrate is selectively removed in a $3\text{HCl} : 1\text{H}_2\text{O}$ solution at room temperature.

Figure 5 shows a 2-inch InP-based epitaxial wafer bonded on a SOI sample cleaved from a 6 inch SOI wafer. Smooth III-V morphology with no interfacial void is

achieved in the bonded area. The two defects on the left-hand side of the figure are due to wafer handling with tweezers and InP epitaxial surface defects that are $29 \mu\text{m}$ in diameter. Successful epitaxial transfer on 2 inch wafer demonstrates the scalability of this oxygen plasma-assisted low-temperature bonding process, which subsequently paves the way for mass production of the hybrid devices.

3.2. Silicon waveguide and III-V back-end processing

The general procedure of silicon waveguide formation on an SOI wafer and III-V back-end processing after wafer bonding process is as follows. The silicon waveguide is formed on the (100) surface of an undoped silicon-on-insulator (SOI) substrate using $\text{Cl}_2/\text{Ar}/\text{HBr}$ -based plasma reactive ion etching. The thickness of the buried oxide (BOX) is $1 \mu\text{m}$ for the devices reported in this paper. The III-V epitaxial layer is then transferred to the patterned silicon wafer through low-temperature oxygen plasma-assisted wafer bonding, which was described in Section 3.1. After removal of the InP substrate, mesa structures on III-V layers are formed by dry-etching the p-type layers using a $\text{CH}_4/\text{H}/\text{Ar}$ -based plasma reactive ion etch. Subsequent wet-etching of the quantum well layers to the n-type layers is performed using $\text{H}_3\text{PO}_4/\text{H}_2\text{O}_2$. Ni/AuGe/Ni/Au alloy contacts are deposited onto the exposed n-type InP layer. Pd/Ti/Pd/Au p-contacts are then deposited on the center of the mesas. For lasers and amplifiers, protons (H^+) are implanted on the two sides of the p-type mesa to create a $4 \mu\text{m}$ wide current channel and to prevent lateral current spreading, ensuring a large overlap between the carriers and the optical mode. Ti/Au probe pads are then deposited on the top of the mesa. Then, if necessary, the sample is diced into bars and each bar is polished.

4. DEVICE RESULTS

4.1. Silicon evanescent lasers

4.1.1. 1550 nm Fabry Perot lasers

The first demonstrated device using the silicon evanescent device platform was the Fabry-Perot (FP) hybrid silicon evanescent laser [23]. The cavity for these lasers was made by dicing the ends of the hybrid waveguide and polishing

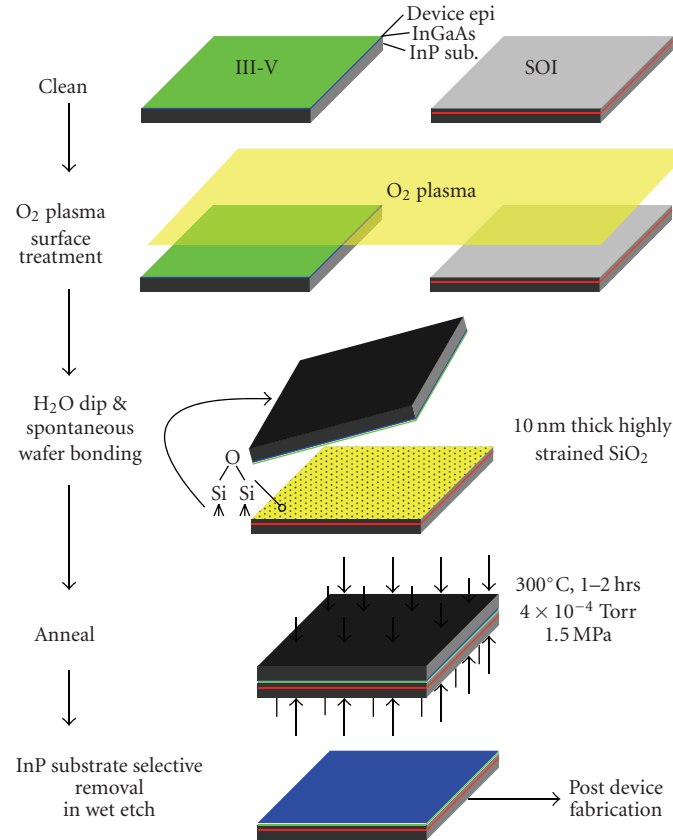


FIGURE 4: Oxygen plasma-assisted low-temperature wafer bonding process flow.

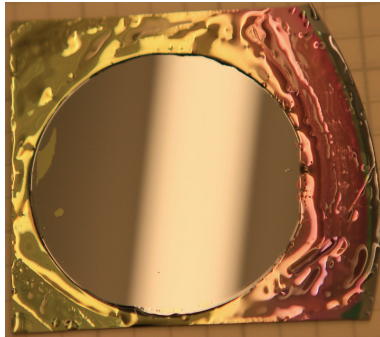


FIGURE 5: Photograph of a 2 inch III-V epitaxial transferred to an SOI sample after 300°C anneal for 2 hours and selective removal of the InP substrate. InP wafer sidewall is surrounded by Crystalbond™ wax to protect InP device layer from being etched laterally during the substrate removal step. The white region in the middle of the wafer is a reflection of the illuminator.

them to a mirror finish. The device presented here has two major changes from the first reported devices. First, the buried oxide thickness is reduced to 1 μm in order to reduce the thermal impedance of the device. Second, the III-V mesa was reduced to 12 μm in order to reduce the device series resistance as shown in Figure 1(a). The waveguide height, width, rib etch depth, and cavity length were 0.7 μm ,

2 μm , 0.5 μm , and 850 μm , respectively. The calculated confinement factors in the silicon and the quantum well region are 63% and 4%, respectively. The epitaxial structure of the lasers is specified in Table 1.

The continuous wave (CW) LI curve for this device is collected on one side with an integrating sphere as shown in Figure 6(a). In order to account for light exiting both sides of the cavity, the data is multiplied by two. It can be seen that the maximum laser output power, threshold, and differential efficiency at 15°C are 24 mW, 70 mA, and 16%, respectively. The device shows improvement in output power and differential efficiency while maintaining a similar threshold when compared to the first generation device. The maximum operating temperature is 45°C.

Figure 6(b) shows a set of pulsed single-sided output power as a function of applied current (1 kHz repetition rate, 0.1% duty cycle) for stage temperatures ranging from 15 to 50°C. The characteristic temperature (T_0) and an above threshold characteristic temperature (T_1) [24] are 60 K and 120 K, respectively. The thermal impedance of the laser is measured using a combination of two experiments. The first set of measurements is used to establish a baseline for the shift in lasing wavelength as a function of active region (stage) temperature ($d\lambda/dT$) as shown in Figure 7(a). Similar to the characteristic temperature measurement above, this experiment is performed pulsed to ensure that there is minimal device heating other than what is provided by

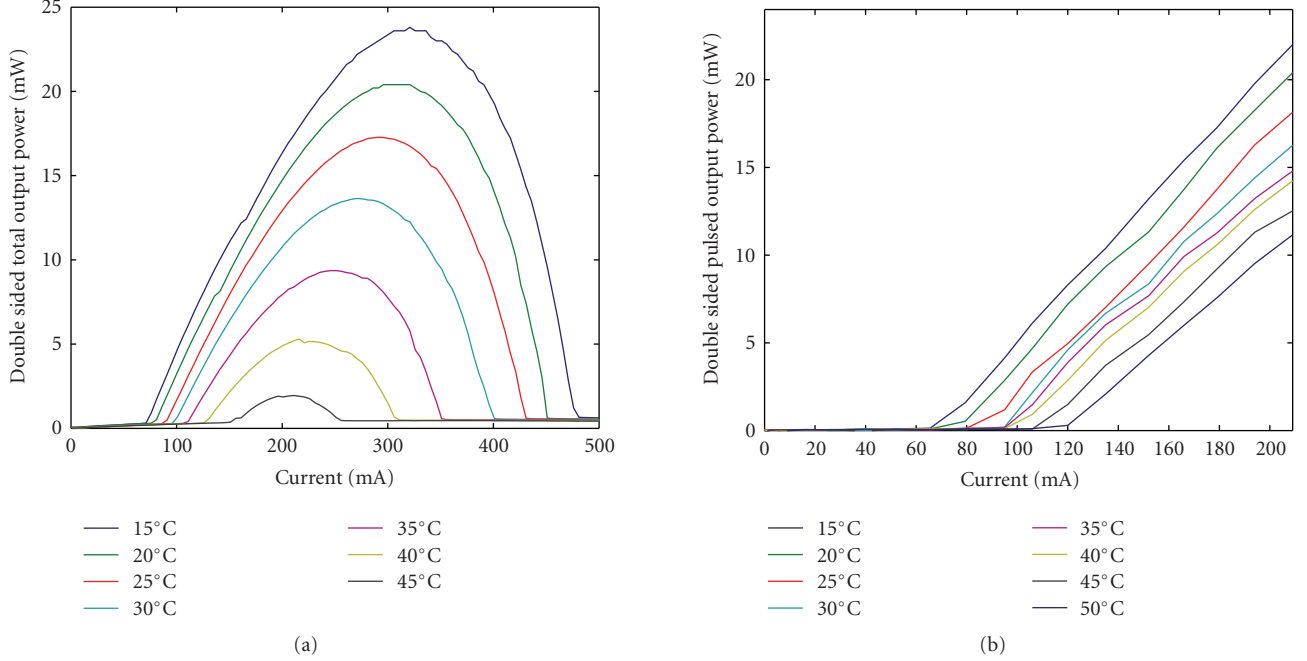


FIGURE 6: LI curves for a 1550 nm FP silicon evanescent laser (a) double-sided continuous wave output power, (b) double-sided pulsed output power.

TABLE 1: III-V epitaxial layer structure with a 1550 nm photoluminescence peak.

Name	Composition	Doping concentration	Thickness
P contact layer	P-type $\text{In}_{0.53}\text{Ga}_{0.47}\text{As}$	$1 \times 10^{19} \text{ cm}^{-3}$	$0.1 \mu\text{m}$
Cladding	P-type InP	$1 \times 10^{18} \text{ cm}^{-3}$	$1.5 \mu\text{m}$
SCH	P-type $\text{Al}_{0.131}\text{Ga}_{0.34}\text{In}_{0.528} \text{As}$, 1.3Q	$1 \times 10^{17} \text{ cm}^{-3}$	$0.25 \mu\text{m}$
Quantum wells	$\text{Al}_{0.089}\text{Ga}_{0.461}\text{In}_{0.45} \text{As}$, 1.3Q(9x)	undoped	10 nm
	$\text{Al}_{0.055}\text{Ga}_{0.292}\text{In}_{0.653} \text{As}$, 1.7Q(8x)	undoped	7 nm
N layer	N-type InP	$1 \times 10^{18} \text{ cm}^{-3}$	110 nm
Super lattice	N-type $\text{In}_{0.85}\text{Ga}_{0.15}\text{As}_{0.327}\text{P}_{0.673}$, 1.1Q(2x)	$1 \times 10^{18} \text{ cm}^{-3}$	7.5 nm
	N-type InP (2x)	$1 \times 10^{18} \text{ cm}^{-3}$	7.5 nm
N bonding layer	N-type InP	$1 \times 10^{18} \text{ cm}^{-3}$	10 nm

the temperature-controlled stage. The second measurement is performed CW, and is used to measure the shift in wavelength as a function of applied electrical power to the laser ($d\lambda/dP$) as shown in Figure 7(b). The thermal impedance Z_T is then given by (1)

$$Z_T = \left(\frac{d\lambda}{dT} \right)^{-1} \left(\frac{d\lambda}{dP} \right). \quad (1)$$

In both the $d\lambda/dT$ and $d\lambda/dP$ experiments, a single longitudinal mode in the laser spectrum is monitored. Combining the results from Figures 7(a) and 7(b), the laser thermal impedance is measured to be 42°C/W .

The thermal performance of the hybrid laser depends on several factors. These include the amount and location of heat that is generated, the thermal conductivity of the layers surrounding the heat sources, and the operating temperature of the laser active region. To model the temperature rise as a function of applied bias, we have employed a two-

dimensional finite element modeling technique. For the hybrid laser cross-section shown in Figure 1(a), there are six major sources of thermal energy. These include resistive heating in the p-cladding, the n-contact layer, the active region, and the p and n contacts, along with heat generated by the diode drop associated with the active region. More detailed information about the values used in the simulation can be found in [25].

A two dimensional temperature profile of the hybrid laser operating at 500 mA is shown in Figure 8(a). The dissipated electrical power and the predicted temperature rise in the laser active region are plotted as a function of applied current in Figure 8(b). The contribution of each layer to the total electrical power dissipation is also shown in the same figure. Combining the simulated temperature rise, the dissipated electrical power, and the output optical power, the thermal impedance of the laser is 43.5°C/W , which is within 5% of our initial experimental results.

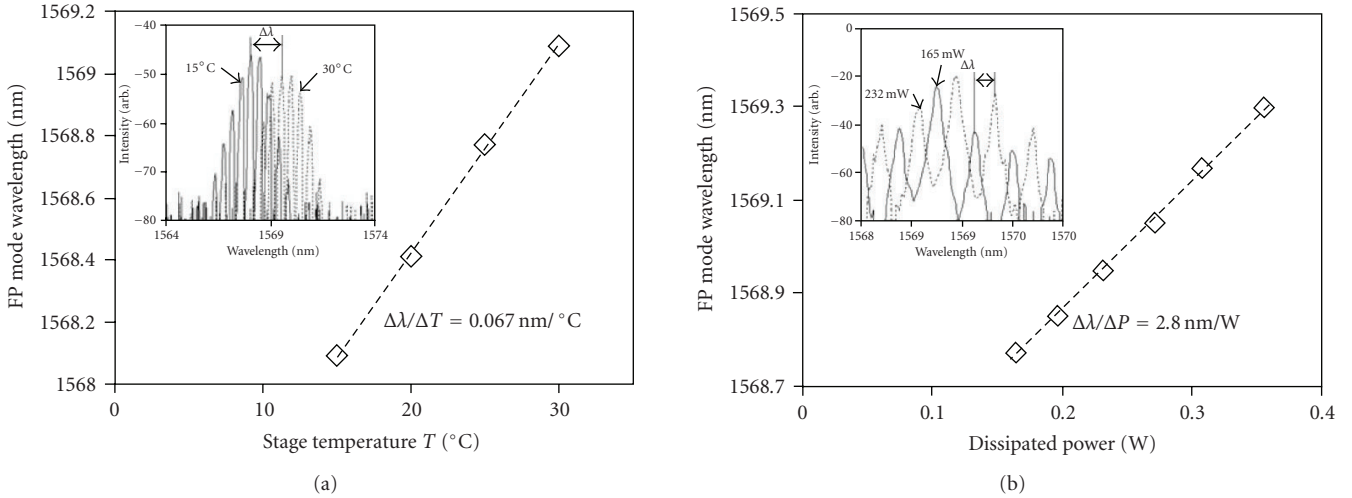


FIGURE 7: (a) Pulsed measurement results for the shift in lasing wavelength (single FP mode) as a function of stage temperature. The inset contains a laser output spectrum at 15°C and 30°C. (b) Results for the shift in lasing wavelength (single FP mode) as a function of dissipated power.

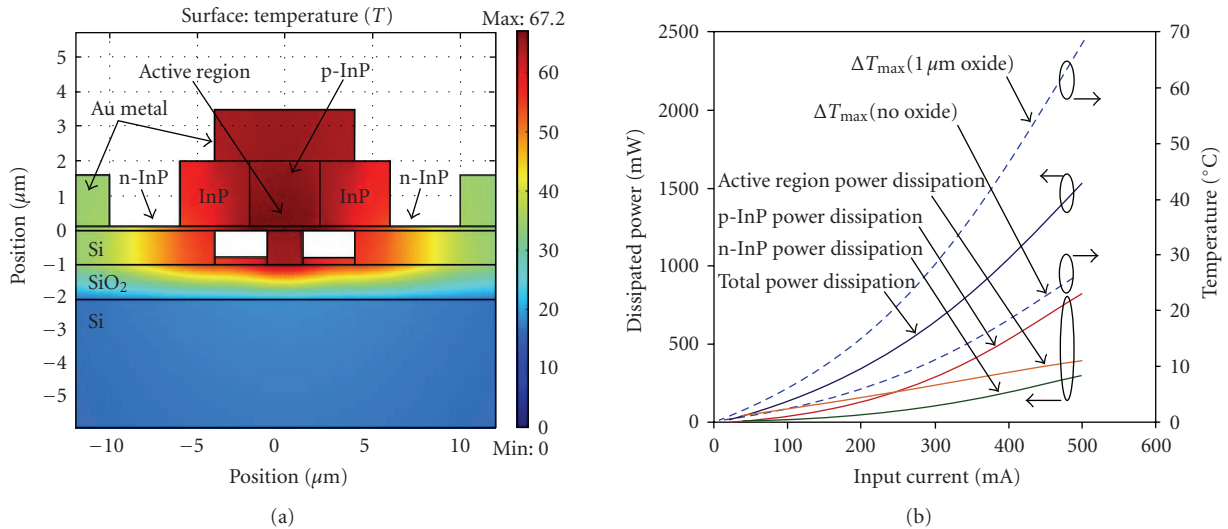


FIGURE 8: (a) Two-dimensional temperature profile in the hybrid laser at a bias current of 500 mA. (b) Theoretical predictions for the dissipated electrical power in the various laser sections along with the predicted temperature rise in the active region as a function of contact current.

To show the effect of the buried oxide on the thermal impedance, Figure 8(b) also includes a simulation of the temperature rise in the device when the buried oxide has been removed. Reducing the thickness of the BOX layer results in lowering the thermal impedance to 18°C/W. This illustrates how the high thermal conductivity of silicon should result in the very low thermal resistances of silicon photonic devices.

4.1.2. 1310 nm Fabry Perot lasers

1310 nm hybrid silicon lasers are also important for many data and telecommunication applications [26]. The epitaxial layer structure used here (Table 2) contains an electron

blocking layer between the quantum wells and the SCH layer for better injection efficiency [27]. The layer is designed to provide a high conduction band offset between the barrier and the SCH layer to prevent electrons from leaking out of the quantum well region while a valence band offset is kept low not to alter the hole flow into the quantum wells.

Lasers with fundamental transverse mode or with second-order transverse mode can be designed and fabricated. Figure 9(a) shows the simulated quantum well confinement factor as a function of silicon waveguide height while keeping the waveguide width and slab thickness at 2.5 μm and 0.2 μm, respectively. Quantum well confinement represents the mode overlap to the 4 μm wide quantum well at the center, where electrons and holes are injected. In the

TABLE 2: III-V epitaxial layer structure with a 1303 nm photoluminescence peak.

Name	Composition	Doping Concentration	Thickness
P contact layer	P-type $\text{In}_{0.53}\text{Ga}_{0.47}\text{As}$	$1 \times 10^{19} \text{ cm}^{-3}$	$0.1 \mu\text{m}$
Cladding	P-type InP	$1 \times 10^{18} \text{ cm}^{-3}$	$1.5 \mu\text{m}$
SCH	P-type $\text{Al}_{0.4055}\text{Ga}_{0.064}\text{In}_{0.5305} \text{As}$, 0.9Q	$1 \times 10^{17} \text{ cm}^{-3}$	$0.25 \mu\text{m}$
Electron blocking layer	$\text{Al}_{0.4764}\text{Ga}_{0.0189}\text{In}_{0.5047}\text{As}$	undoped	10 nm
Quantum wells	$\text{Al}_{0.055}\text{Ga}_{0.292}\text{In}_{0.653}\text{As}$, 1.0Q(9x)	undoped	10 nm
	$\text{Al}_{0.178}\text{Ga}_{0.1234}\text{In}_{0.0986}\text{As}$, 1.5Q(8x)	undoped	7 nm
N layer	N-type InP	$1 \times 10^{18} \text{ cm}^{-3}$	110 nm
Super lattice	N-type $\text{In}_{0.85}\text{Ga}_{0.15}\text{As}_{0.327}\text{P}_{0.673}$, 1.1Q(2x)	$1 \times 10^{18} \text{ cm}^{-3}$	7.5 nm
	N-type InP (2x)	$1 \times 10^{18} \text{ cm}^{-3}$	7.5 nm
N bonding layer	N-type InP	$1 \times 10^{18} \text{ cm}^{-3}$	10 nm

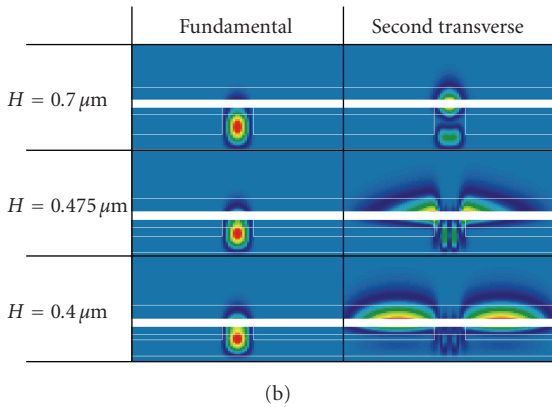
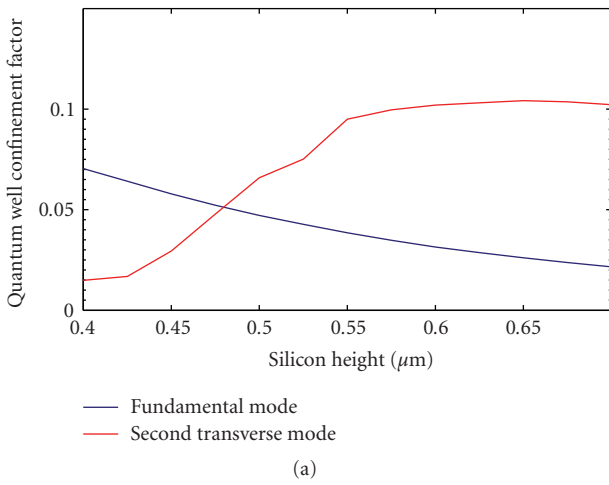


FIGURE 9: The confinement factor in III-V region simulation for different silicon waveguide height (a) confinement factor calculations for the fundamental mode and second transverse mode as a function of waveguide height (b) fundamental and second transverse modes for waveguide heights of 0.7, 0.475, and 0.4 μm . The image aspect ratio (Height:Width) is 4 : 1.

tall silicon height regime (right hand part in Figure 9(a)), a higher quantum well confinement factor for the second transverse mode exists. In the short silicon height regime (left-hand part in Figure 9(a)), the fundamental mode has a

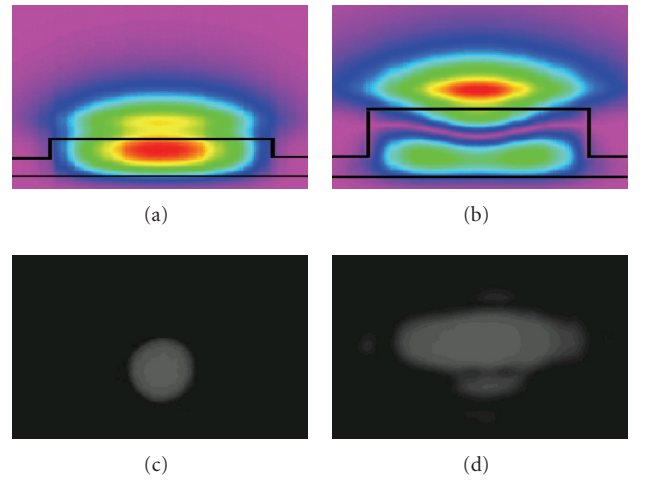


FIGURE 10: The simulated and measured lasing optical mode profiles (a) simulated optical mode for a waveguide height of 0.4 μm , (b) simulated optical mode for a waveguide height of 0.7 μm , (c) measured optical mode for a waveguide height of 0.4 μm , and (d) measured optical mode for a waveguide height of 0.7 μm .

higher quantum well confinement factor. Figure 9(b) shows the fundamental mode and second transverse mode with different waveguide heights illustrating the fundamental mode increasingly lies more in the III-V region as the silicon height decreases. The second transverse mode also undergoes an increase in III-V confinement factor but splits into two lateral lobes at lower silicon heights. This splitting reduces the modal overlap with the 4 μm wide excited quantum well region at the center.

Two different silicon waveguide heights of 0.4 μm and 0.7 μm have been chosen to study the lasing mode selection depending on different quantum well confinement factors. The width and slab height of the silicon waveguide is 2.5 μm and 0.2 μm , respectively. The device length is $\sim 850 \mu\text{m}$. Figures 10(a) and 10(b) show the simulated mode profiles with the largest quantum well confinement factor for waveguide heights of 0.4 μm and 0.7 μm , respectively. The measured lasing mode profiles in Figures 10(c) and 10(d) agree with the simulation results, indicating the quantum well confinement

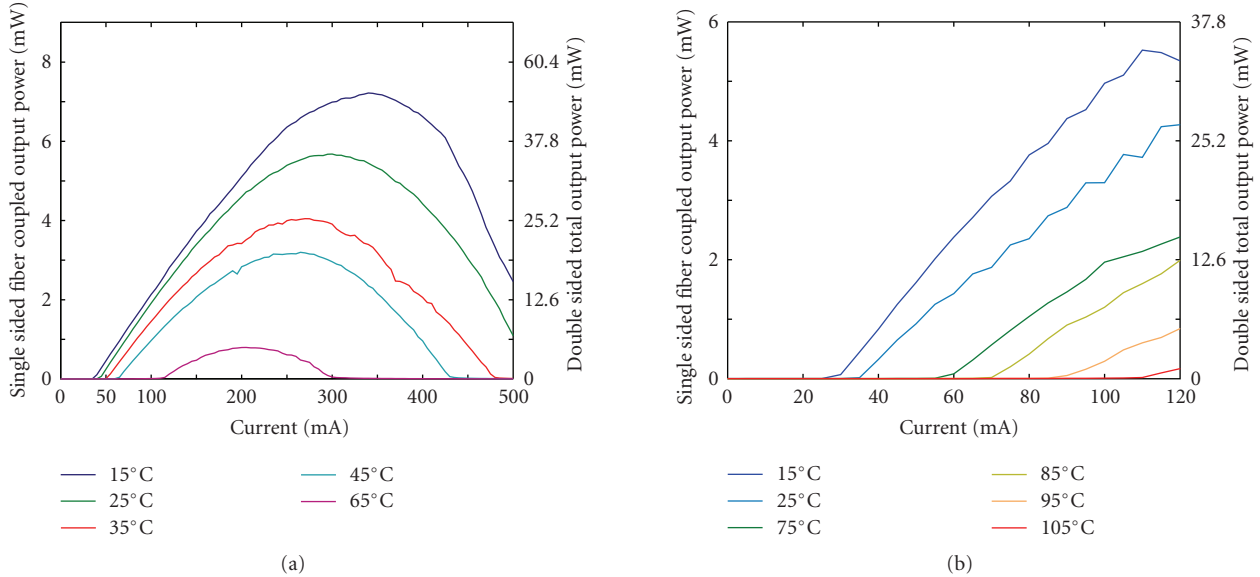


FIGURE 11: LI curves for 1310 nm FP silicon evanescent lasers (a) fundamental mode lasing device, (b) second transverse mode lasing device. The secondary y -axis represents the estimated total laser output power.

factor primarily determines the lasing mode and can be engineered by changing the silicon waveguide dimensions.

Figure 11 shows the measured single-sided fiber-coupled CW output power as a function of the injected current at different temperatures for two different lasers ($0.4\ \mu\text{m}$ and $0.7\ \mu\text{m}$ waveguide heights). The threshold current for both devices at 15°C is $30\ \text{mA}$. The output power at $100\ \text{mA}$ is $2.9\ \text{mW}$ and $5\ \text{mW}$ and its corresponding differential quantum efficiency is 2.5% and 8% for the fundamental mode and second transverse mode lasing devices, respectively. The estimated double-sided total output power is shown in the secondary y -axis taking account for the output power from the both facets and a coupling loss of $5\ \text{dB}$ between the device and the lensed fiber. The double sided total output power at $100\ \text{mA}$ is estimated to be $18\ \text{mW}$ and $31\ \text{mW}$, and its total differential quantum efficiency is 15% and 50% for the fundamental mode and second transverse mode lasing devices, respectively. The device lasing with second transverse mode ($0.7\ \mu\text{m}$ waveguide height) operates up to 105°C and has better performance than the device lasing with a fundamental mode primarily due to the higher quantum well confinement factor (10% versus 7%). Moreover, the overall performance of $1.3\ \mu\text{m}$ lasers is superior to $1.5\ \mu\text{m}$ lasers previously described because the carrier blocking layer is incorporated and because of the reduced intravalence band absorption and Auger scattering.

4.1.3. 1550 nm integrated racetrack laser and photodetectors

Figure 12(a) shows the layout of an integrated hybrid silicon evanescent racetrack laser and two photodetectors operating at $1550\ \text{nm}$ [28]. The same epitaxial structure described in Table 1 is used both for the laser and the detector. This laser

does not rely on facet dicing or polishing and can be tested on-chip with simple probing of the laser and photodetectors.

The waveguide height, width, and rib etch depth were $0.69\ \mu\text{m}$, $1.5\ \mu\text{m}$, and $0.5\ \mu\text{m}$, respectively. The scanning electron microscope (SEM) image of the fabricated devices is shown in Figure 12(b). It consists of a racetrack ring resonator with a straight waveguide length of $700\ \mu\text{m}$ and ring radii of 200 and $100\ \mu\text{m}$. A directional coupler is formed on the bottom arm by placing a bus waveguide $0.5\ \mu\text{m}$ away from the racetrack. Since clockwise and counterclockwise propagating modes of ring lasers are only weakly coupled, two $440\ \mu\text{m}$ long photodetectors are used to collect the laser power; the clockwise being collected at the left detector, and the counterclockwise being collected at the right detector. These photodetectors have the same waveguide structure as the hybrid laser, and the only difference being that they are reverse biased to collect photogenerated carriers.

To estimate the laser output power from the measured photocurrent, the responsivity of the detector is first measured by dicing and polishing a discrete detector in the same chip and launching laser light into the detector through a lensed fiber. The fiber coupled responsivity was measured to be $0.25\ \text{A/W}$ at $1580\ \text{nm}$. Taking into consideration the $\sim 30\%$ reflection off the waveguide facet and an estimated $5.25\ \pm 0.25\ \text{dB}$ coupling loss, the photodetector responsivity is estimated to be in the range of $1.25\text{--}1.11\ \text{A/W}$. This corresponds to an internal quantum efficiency of around 92% . A responsivity of $1.25\ \text{A/W}$ is used for laser power estimation such that the laser power values are on the conservative side. These measurement results are also consistent with the measured responsivity from stand alone photodetectors [29].

The total laser output power collected at both detectors as a function of current and temperature is shown in Figure 12(c) for a laser with a ring radius of $200\ \mu\text{m}$ and a coupler interaction length of $400\ \mu\text{m}$. The laser has a total

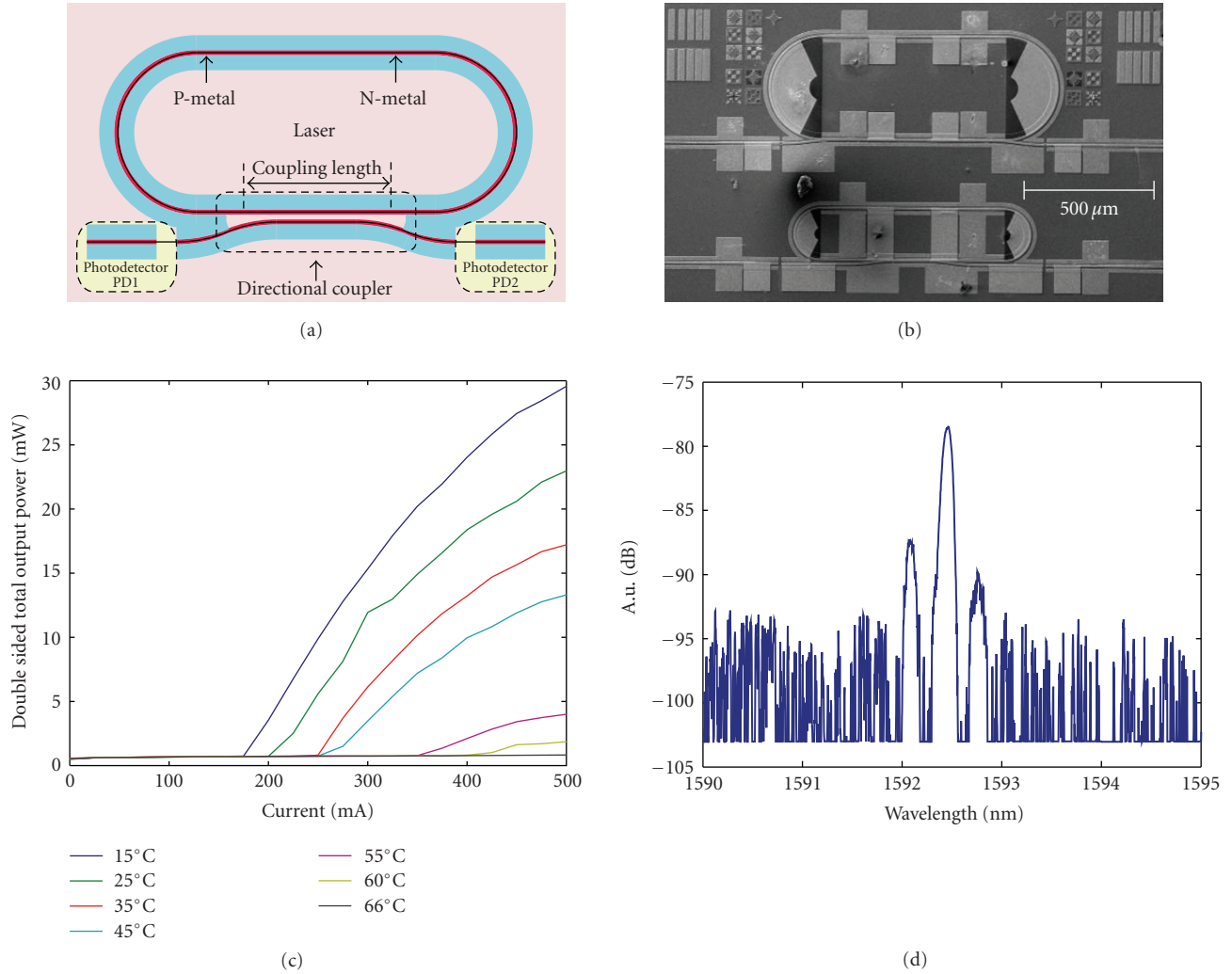


FIGURE 12: (a) The layout of the racetrack resonator and the photodetectors. (b) A top view SEM micrograph of two racetrack resonator lasers. The racetrack resonator lasers on the top and bottom have radii of 200 and 100 μm , respectively. (c) The LI curve for a laser with a bend radius, R , of 200 μm , and directional coupler coupling length, $L_{\text{interaction}}$, of 400 μm for various temperatures. (d) The spectrum for a laser with $R = 100 \mu\text{m}$ and $L_{\text{interaction}} = 400 \mu\text{m}$.

output power of 29 mW with a maximum lasing temperature of 60°C. The differential efficiency is 17% and the laser threshold is 175 mA at 15°C. The laser spectrum is shown in Figure 12(d) with its lasing peak in the range of 1592.5 nm.

Since the two modes of propagation are not coupled and are degenerate, mode competition is typical in such lasers with a ring cavity structure. Figure 13(a) shows the photocurrent measured separately from the left (PD1) and the right (PD2) detectors as a function of the laser drive current for a laser with a ring radius of 100 μm and a coupler interaction length of 100 μm . There are two distinct regions of operation above threshold: (1) unidirectional bistable (low-bias current), and (2) alternating oscillation (high-bias current). In the unidirectional bistable region, the laser is lasing in either one direction or the other and the laser output switches from one direction to the other direction as the laser diode current increase. At higher bias (>360 mA), the laser enter the alternating oscillation region, the output power

exhibit oscillatory behavior. The unidirectional bistability of the racetrack laser can be alleviated if one of the detectors is forward biased to inject light into the cavity (Figure 13(b)). The forward-biased photodetector acts as an ASE source, which increases the photon density of the clockwise mode, leading to greater simulated emission and mode selection. This shows that the lasing direction can be controlled by forward biasing one of the photodiodes; that is, lasing either clockwise or counterclockwise.

4.1.4. 1550 nm mode locked lasers

Silicon hybrid lasers can be mode locked at a variety of frequencies from 10 GHz to 40 GHz [30], for potential applications in optical pulse generation, OTDM, WDM, and regenerative all-optical clock recovery [31].

An FP ML-SEL is shown in Figure 14(a) and its test setup is shown in Figure 14(b). The 39.4 GHz FP ML-SEL had

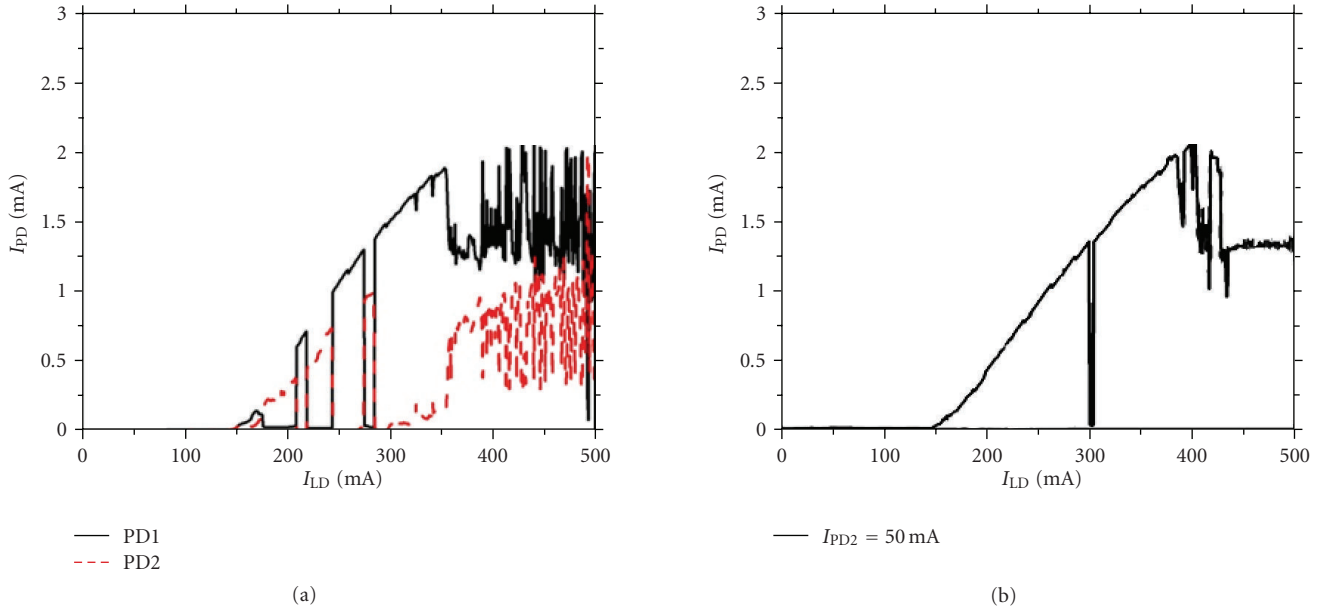


FIGURE 13: (a) L-I curves of CW and CCW direction, (b) L-I curve of CW direction when the PD2 is forward bias with 50 mA.

a total cavity length of $1060 \mu\text{m}$ and a saturable absorber (SA) length of $70 \mu\text{m}$. For all devices presented here, separate gain and SA sections were electrically isolated using proton implantation. Passive mode locking was achieved for a range of gain currents between 195 mA and 245 mA with similar output characteristics. For a gain current of 206 mA and a saturable absorber reverse bias voltage of 0.4 V, the pulse has a sech^2 shape with 4.2 picoseconds full width at half maximum (FWHM) pulsewidth, extinction ratio (ER) over 18 dB between the peak and null, peak power of 4.5 dBm in fiber, and FWHM optical spectral width of 0.9 nm. The time bandwidth product is 0.4, close to the transform limited value of 0.32 for sech^2 pulses, indicating minimal chirp. The laser was capable of stable mode locking for a range of gain currents between 195 mA and 245 mA with similar output characteristics.

By applying an RF signal to the saturable absorber section, hybrid mode locking occurs and the jitter of the pulses can be considerably reduced [32] without changing the pulsewidth or spectral width. To achieve subharmonic hybrid mode locking, a 20 GHz RF source with 17 dBm of RF input power is used. For these conditions, the absolute jitter of this laser is 1 picosecond and the locking range was 5 MHz. For all measurements in this paper, the jitter was evaluated by integrating two times the single-sideband noise from 1 kHz to 100 MHz offset from the carrier frequency.

Increasing the cavity length to 4.16 mm resulted in 10 GHz mode locking. The saturable absorber was $80 \mu\text{m}$ long and the cavity was divided into 4 equal length gain sections that can be biased differently depending on the application. The bias conditions used for pulse generation were as follows: Gain 1 and Gain 2 (adjacent to the saturable absorber) were biased together at 531 mA, Gain 3 was biased at 140 mA, Gain 4 at 149 mA, and the SA was biased with

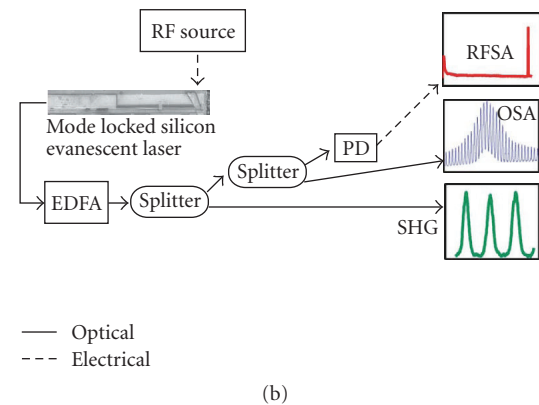
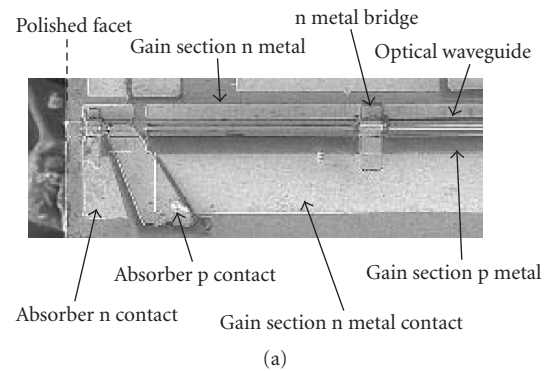


FIGURE 14: (a) Scanning electron micrograph of one end of an FP ML-SEL. (b) Schematic of the general experimental setup. For some measurements, more components were required as detailed in the references. EDFA = erbium doped fiber amplifier, SHG = second harmonic generation autocorrelator, OSA = optical spectrum analyzer, RFSAs = 41 GHz radio frequency spectrum analyzer, PD = 40 GHz photodetector.

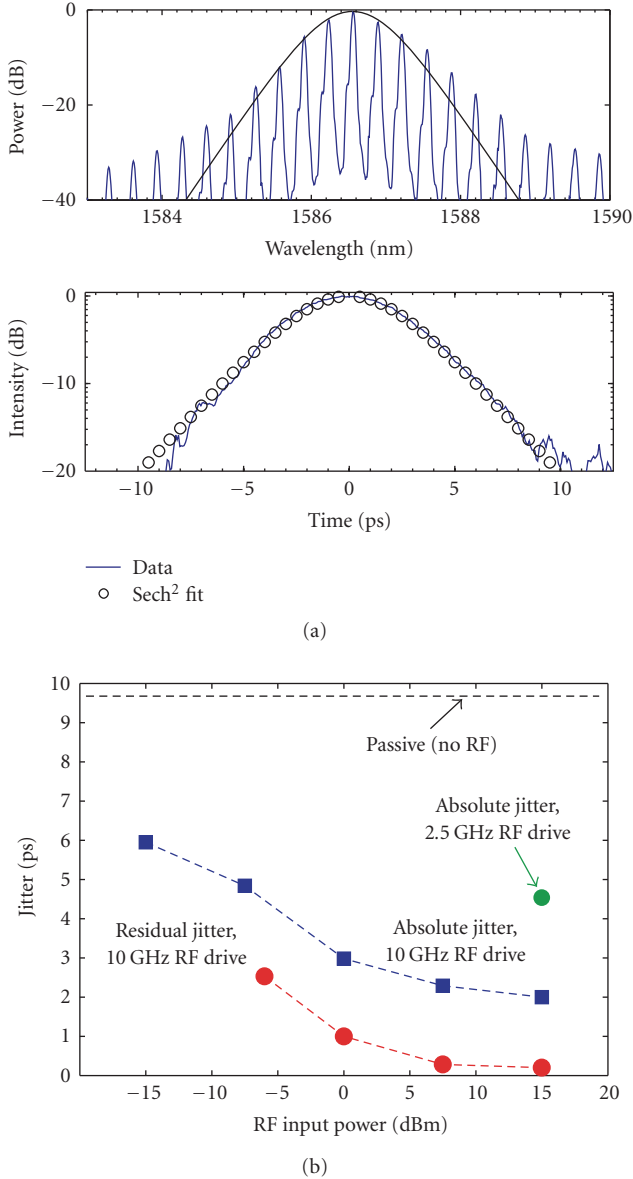


FIGURE 15: (a) Wavelength spectrum and autocorrelation trace of the 40 GHz FP ML-SEL output. The fit to the optical spectrum is the Fourier transform of the autocorrelation fit. (b) Jitter measurements for the 10 GHz FP ML-SEL versus the RF input power.

–2.3 V. The FWHM pulsewidth was 3.9 picoseconds with a sech² shape, the ER is over 18 dB, the peak power in fiber was 11.9 dBm, and the FWHM spectral width was 3.8 nm, containing 45 modes evenly spaced at 10.16 GHz. The time bandwidth product is 1.7, indicating significant chirping. Chirp can be reduced in future designs by incorporating passive silicon waveguide sections in the laser cavity with a shorter gain section [33]. This is fairly easy to do on this platform and is a potential advantage of the platform for lower repetition rate mode-locked lasers. Changing the SA bias between –0.5 and –2 V changes the output pulsewidth between 9 and 4 picoseconds, while the ER and output power

do not change significantly. Figure 15(b) shows results for passive and hybrid mode locking with different RF powers and RF injection frequencies. Also shown is the residual jitter, which is the jitter of the hybrid mode locked laser compared to that of the RF drive source. The minimum residual jitter is 199 femtoseconds with 15 dBm RF drive at 10.16 GHz. At this RF power, the locking range was 260 MHz.

Increasing the combined gain section bias currents to a total of 1 A generates over 100 optical modes with power levels within 10 dB of the peak mode power. If the modes have high enough quality, the single ML-SEL could be combined with an AWG and used as a multiple wavelength source for wavelength division multiplexing applications [34]. Across 100 modes, the linewidth was below 500 MHz and the OSNR was near 15 dB. The linewidths of these modes are too large for some applications, but for short reach applications the signal quality is sufficient. The mode quality can be improved by injecting a stable CW laser into the hybrid mode-locked laser, inducing optical injection locking [34]. In this case, the spectral width narrows to 30 modes within 10 dB, but the linewidth of each of these modes is reduced to that of the injected signal (<100 kHz). Also the OSNR is improved to over 25 dB for the majority of the modes. It is expected that better stabilization of the hybrid mode-locked laser through packaging would allow for a wider spectral width under optical injection locking, allowing for more high-quality modes to be generated.

A 30.4 GHz racetrack ML-SEL [31] is shown in Figure 16(a). A racetrack mode-locked laser has the advantage that its cavity is defined by lithography. Since the repetition rate is determined by the cavity length, this allows for the repetition rate to be precisely determined and repeated across different devices. Racetrack lasers can also be integrated monolithically with other components. This laser has a cavity length of 2.6 mm, an absorber length of 50 μ m, and 2 separate gain sections. The gain sections were biased together at 410 mA and the absorber was biased with –0.66 V. This resulted in Gaussian-shaped output pulses with 7.1 picoseconds FWHM pulsewidth, 0.5 nm FWHM spectral width, and approximately 10 dB ER. The time bandwidth product was 0.43. The peak power was 6.8 dBm onchip, determined from onchip photocurrent measurements.

With a 30.4 GHz, 13 dBm RF signal applied to the SA section, this laser had 364 femtoseconds of absolute jitter and 50 MHz locking range. The laser could also be synchronized to 30 Gbps optical input signals with average powers below 0 dBm in the input waveguide meaning that it can perform all-optical clock recovery. To test this application, we intentionally degraded a 30.4 Gbps return to zero 2³¹-1 pseudorandom bit stream by adding timing jitter and reducing the extinction ratio, and we used the racetrack ML-SEL to recover the clock all-optically [31]. The input ER was 3.8 dB and the input jitter was 14 picoseconds. The recovered clock had an ER of 10.4 dB and jitter of 1.7 picoseconds. The input data and output clock eye diagrams are shown in Figure 16(b). The device’s extreme regenerative capabilities and potential for integration with other components indicate that it could be used as part of a silicon integrated optical 3R regenerator.

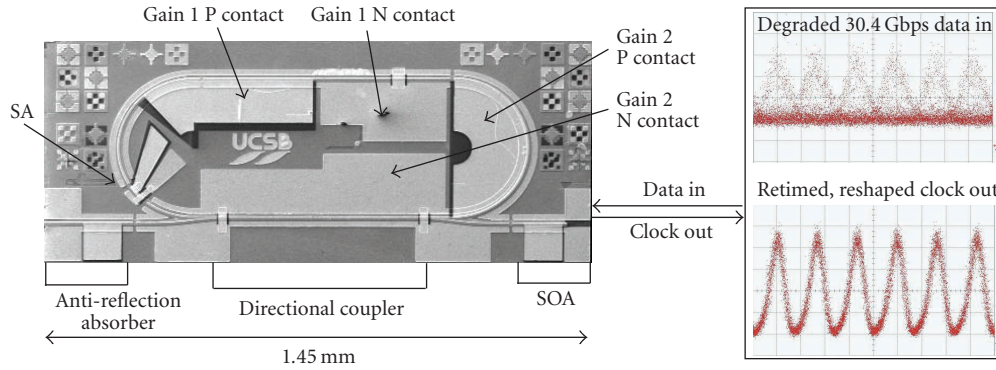


FIGURE 16: (a) SEM image of the 30.4 GHz racetrack ML-SEL. (b) Eye diagrams of the input data sent to the device and the regenerated, all-optically recovered clock.

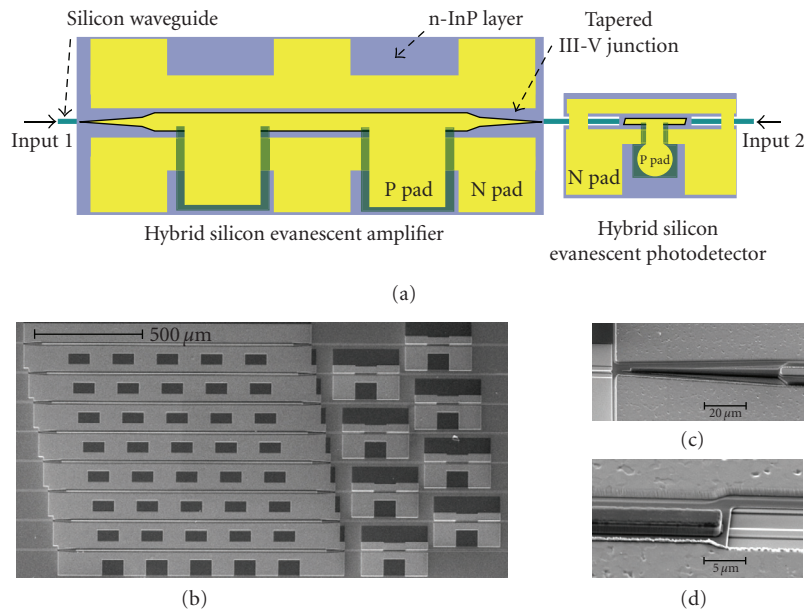


FIGURE 17: (a) Top view of the integrated device. (b) SEM image of eight fabricated devices. (c) Close view of the III-V taper of the amplifier. (d) Close view of the narrow III-V mesa of the detector.

4.2. Silicon evanescent amplifiers and photodetectors

Optical amplifiers are key components in realizing high levels of photonic integration as they compensate for optical losses from individual photonic elements. The hybrid silicon evanescent amplifier structure is similar to the offset quantum well structure which has typical quantum well confinement factor in the range of 2% to 4% and it is suitable for preamplifiers [35]. In this section, the integration of an amplifier and a detector for improved receiver sensitivity is discussed [36].

Figure 17(a) shows a device structure of the integrated device with an amplifier and a detector. At the transition between the passive silicon waveguide and the hybrid waveguide of the amplifier, the width of the III-V mesa is tapered from 0 μm to 4 μm over a length of 70 μm to increase the coupling efficiency and to minimize reflection. The width from 4 μm to 14 μm is tapered more abruptly over 5 μm

since III-V mesas wider than 4 μm do not laterally affect the optical mode. A 7° tilted abrupt junction is used between the passive silicon waveguide and the detector hybrid waveguide. The details of the epitaxial structure of the III-V layers are summarized in Table 1. The III-V mesa width of the amplifier is 14 μm. The III-V mesa width of the detector is 3 μm at the p cladding layer and 2 μm at the p SCH and the quantum well layers to reduce the capacitance of the device. The detector p and n pads are designed to be 100 μm apart from center to center to use a standard GSG RF probe for high-speed testing. The SEM image of the eight fabricated devices is shown in Figure 17(b), and the close view of the III-V amplifier taper and the III-V detector mesa are shown in Figures 17(c) and 17(d) respectively. The total length of the amplifier and the detector is 1.24 mm and 100 μm, respectively.

The internal quantum efficiency is measured to be around 50% at a reverse bias voltage of 2 V at 1550 nm as

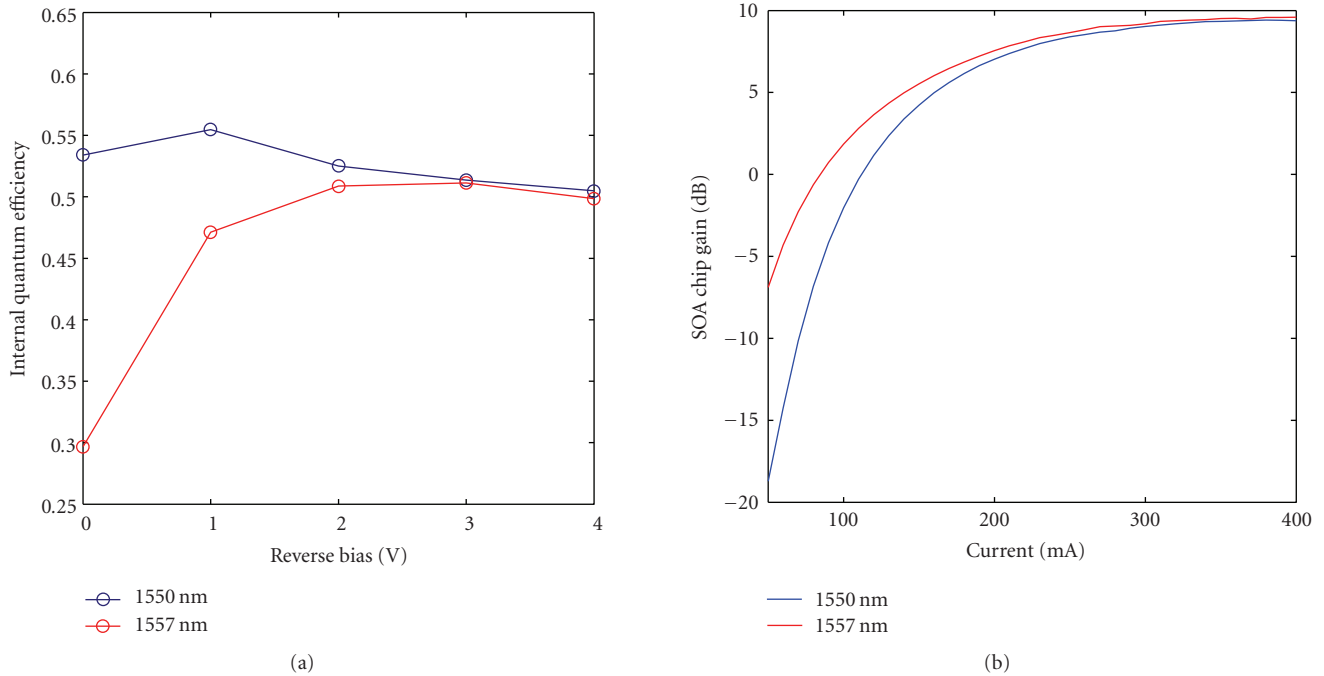


FIGURE 18: (a) Internal quantum efficiency of the detector. (b) Gain of the amplifier.

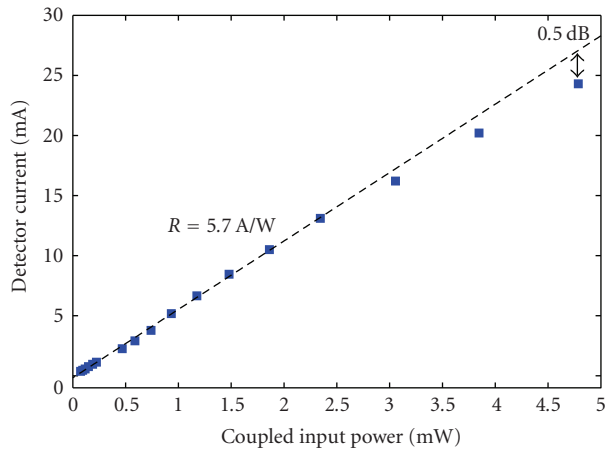


FIGURE 19: Saturation characteristics of the integrated optically preamplified receiver.

shown in Figure 18(a). The amplifier gain is also measured by taking photocurrent from the detector and the maximum gain is 9.5 dB at 300 mA as shown in Figure 18(b). The reflection from the III-V taper is estimated from the ripples at the ASE spectrum and it is less than 5×10^{-4} . The taper loss is estimated to be in the range of 0.6 dB to 1.2 dB by measuring the photocurrent from the reverse-biased amplifier [36]. Figure 19 shows the saturation characteristics of the integrated device. The overall responsivity is 5.7 A/W and the device is saturated by 0.5 dB at an output photocurrent of 25 mA. The device bandwidth is measured to be 3 GHz from the time domain impulse measurements even though the estimated RC limited bandwidth is 7.5 GHz.

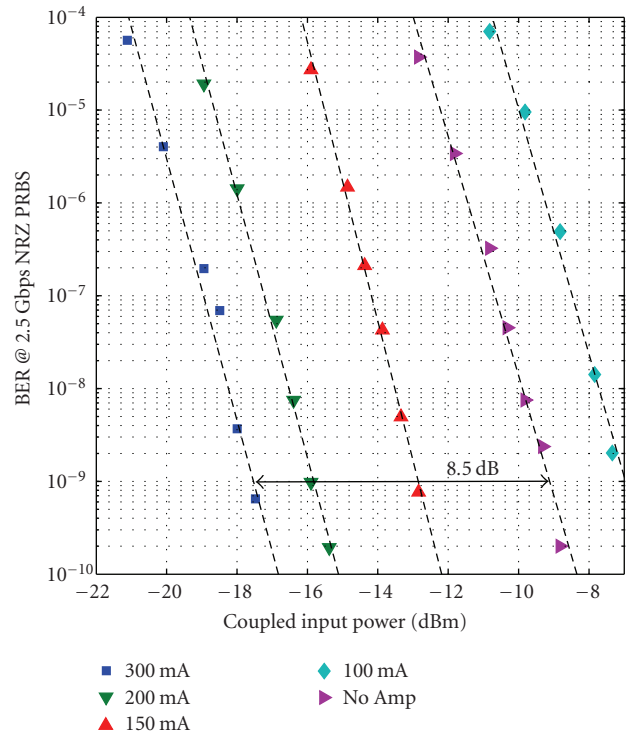


FIGURE 20: Optically preamplified receiver bit error rate curves measured with $2^{31}-1$ NRZ 2.5 Gbps transmissions with different amplifier gains.

The current bandwidth is limited by carrier trapping in the quantum wells. Higher bandwidth can be achieved by incorporating a thinner SCH layer and a bulk absorbing

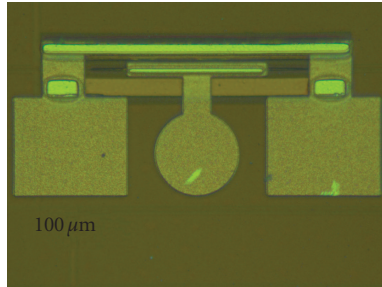


FIGURE 21: Photograph of the fabricated EAM modulator.

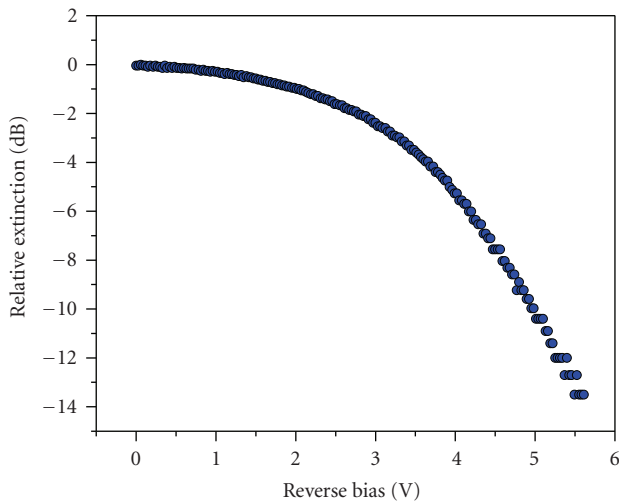


FIGURE 22: EAM extinction versus bias.

region or new quantum wells with small valence band offset. The bit error rate (BER) was measured with 2.5 Gbps NRZ $2^{31}-1$ pseudorandom bit sequence (PRBS) with different amplifier gains and the result is shown in Figure 20. The purple data points are baseline measurements without the amplification by launching the signal to input 2. The BER data at an amplifier current of 100 mA shows worse receiver sensitivity than the receiver sensitivity without amplification (baseline) because the amplifier is below transparency. Once the amplifier is driven beyond transparency, the power penalty becomes negative as shown in the three BER curves on the left side. At the maximum gain of 9.5 dB, the power penalty is -8.5 dB compared to the baseline and the receiver sensitivity at a BER of 10^{-9} is -17.5 dBm. The 1 dB difference between the gain and the measured power penalty is due to the ASE noise. Better sensitivities would be achievable with a good transimpedance amplifier and this device can be integrated with silicon passive wavelength demultiplexers for high-speed WDM receivers [37].

4.3. Silicon evanescent electroabsorption modulators

In this section, we review hybrid silicon evanescent electroabsorption modulators (EAMs). The modulator structure described here can be integrated with lasers, amplifiers, and photodetectors using quantum well intermixing [38]

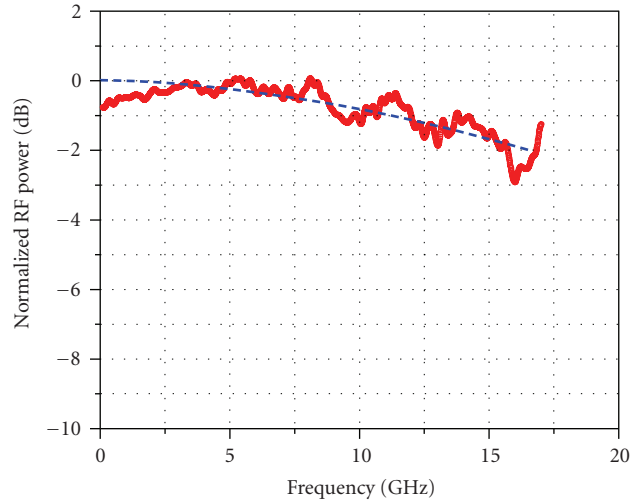


FIGURE 23: Measured small signal response (solid). Calculated response using an RC model (dashed line).

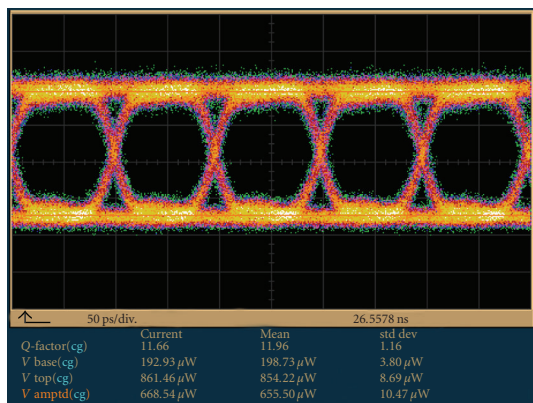
enabling integrated high-speed transmitters. The cross-sectional structure is shown in Figure 1(b) and the III-V epitaxial structure with photoluminescence at 1478 nm is summarized in Table 3. AlGaInAs is chosen as the multiple quantum well material because typically it has a large conduction band offset which provides a stronger carrier confinement and produces strong quantum confined Stark effect with higher extinction ratio [39, 40]. The silicon waveguide was fabricated with a height of $0.5 \mu\text{m}$ and a slab thickness of $0.3 \mu\text{m}$. The silicon waveguide has a width of $1.5 \mu\text{m}$ for passive segments and is tapered to $0.8 \mu\text{m}$ in the hybrid modulator region for a larger quantum well confinement factor. The width of the III-V mesa is $4 \mu\text{m}$ at the top InP cladding layer and $2 \mu\text{m}$ at the SCH and quantum well layers to reduce the capacitance of the device [40, 41]. The overall layout of the device is the same as the detector describe in the previous section except for the width of the III-V mesa is tapered from 0 to $2 \mu\text{m}$ over a length of $60 \mu\text{m}$ to increase the coupling efficiency and to minimize reflection as in the amplifiers. The hybrid EAM has a total length around $220 \mu\text{m}$ with $100 \mu\text{m}$ absorber and two $60 \mu\text{m}$ long tapers. The photograph of the fabricated device is shown in Figure 21.

Figure 22 shows the relative extinction at wavelength of 1550 nm under various reverse biases. More than 10 dB extinction can be achieved with a reverse bias voltage of 5 V. The device has a series resistance around 30Ω and capacitance of 0.1 pF measured from the impedance measurements resulting in a RC limited bandwidth of ~ 20 GHz. It matches with the measured small signal modulation response as shown in Figure 22.

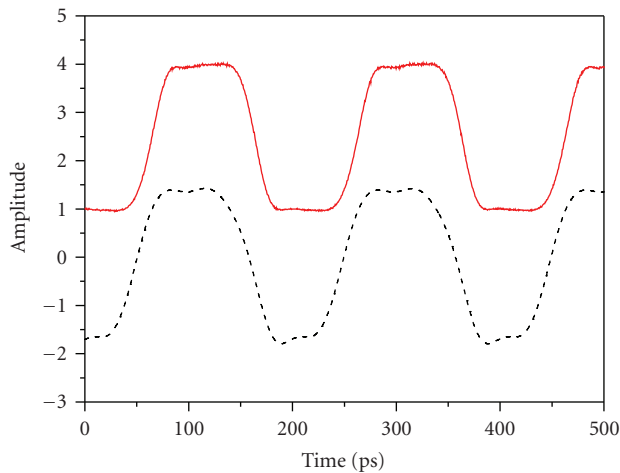
To investigate the performance of large signal modulation, the modulator is driven with a $2^{31}-1$ pseudorandom bit sequence (PRBS). The device is biased at -3 V with a peak-to-peak drive voltage of 3.2 V. The modulated light is collected with a lensed fiber and amplified with an EDFA. Figure 24(a) shows eye diagrams measured at nonreturn-to-zero (NRZ) 10 Gbps. The 10 Gbps signal has an extinction

TABLE 3: III-V epitaxial layer structure with a 1478 nm photoluminescence peak.

Name	Composition	Doping concentration	Thickness
P contact layer	P-type $\text{In}_{0.53}\text{Ga}_{0.47}\text{As}$	$1 \times 10^{19} \text{ cm}^{-3}$	0.1 μm
Cladding	P-type InP	$1 \times 10^{18} \text{ cm}^{-3}$	1.5 μm
SCH	P-type $\text{Al}_{0.160}\text{Ga}_{0.320}\text{In}_{0.520}\text{As}$, 1.3Q	$1 \times 10^{17} \text{ cm}^{-3}$	0.15 μm
Quantum wells	$\text{Al}_{0.200}\text{Ga}_{0.330}\text{In}_{0.470}\text{As}$, 1.19Q(11x)	Undoped	7 nm
	$\text{Al}_{0.080}\text{Ga}_{0.330}\text{In}_{0.590}\text{As}$, 1.55Q(10x)	Undoped	11 nm
SCH	$\text{Al}_{0.160}\text{Ga}_{0.320}\text{In}_{0.520}\text{As}$, 1.3Q	Undoped	0.1 μm
N layer	N-type InP	$1 \times 10^{18} \text{ cm}^{-3}$	110 nm
Super lattice	N-type $\text{In}_{0.85}\text{Ga}_{0.15}\text{As}_{0.327}\text{P}_{0.673}$, 1.1Q(2x)	$1 \times 10^{18} \text{ cm}^{-3}$	7.5 nm
	N-type InP (2x)	$1 \times 10^{18} \text{ cm}^{-3}$	7.5 nm
N bonding layer	N-type InP	$1 \times 10^{18} \text{ cm}^{-3}$	10 nm



(a)



(b)

FIGURE 24: (a) Measured 10G NRZ eye diagrams; (b) pulse train of drive signal (dashed) and optical modulated signal (solid). The drive signal has rise/fall time around 35 picoseconds. The modulated signal shows rising/falling times of about 27 picoseconds.

ratio of 6.3 dB, which is slightly lower than the DC extinction due to additional microwave voltage drop at cladding and ohmic contacts. The eye is clearly open with quality factor (Q factor) close to 12. The rise and fall times of the signal are

about 27 picoseconds, which is, as expected, faster than the driving signal as shown in Figure 24(b).

5. CONCLUSION

Recent progress of hybrid silicon evanescent devices has been reviewed in this paper. Discrete lasers, amplifiers, photodetectors, and electroabsorption modulators have been demonstrated. Racetrack lasers integrated with photodetectors, mode locked lasers, and photodetectors with preamplifiers have also been presented as examples of photonic integration with this hybrid device structure. These demonstrations show the potential for realizing active functionality on the silicon photonics platform. One of the important paths of this research is improving performance of individual devices, that is, device efficiency and thermal performance, in conjunction with studies on device reliability. Another path is the development of bonding of III-V materials to large size silicon wafers (>6 inch). The bonding process can be wafer scale or can be used for die attach. The optimum size of III-V material to use depends on the density of active devices required for the silicon wafer [42]. The hybrid silicon evanescent device platform provides a unique way to build photonic active devices on silicon, and those studies will expedite the applications of silicon photonic integrated circuits in optical telecommunications and optical interconnects.

ACKNOWLEDGMENTS

The authors would like to thank M. J. Paniccia, J. Shah, M. Haney, and W. Chang for insightful discussions and O. Cohen and O. Raday for silicon fabrication. This work was supported by DARPA/MTO and ARL under Awards W911NF-05-1-0175 and W911NF-04-9-0001 and by Intel Corporation.

REFERENCES

- [1] F. Xia, M. Rooks, L. Sekaric, and Y. Vlasov, "Ultra-compact high order ring resonator filters using submicron silicon photonic wires for on-chip optical interconnects," *Optics Express*, vol. 15, no. 19, pp. 11934–11941, 2007.

- [2] F. Xia, L. Sekaric, and Y. Vlasov, "Ultracompact optical buffers on a silicon chip," *Nature Photonics*, vol. 1, no. 1, pp. 65–71, 2007.
- [3] M. Lončar, T. Doll, J. Vučković, and A. Scherer, "Design and fabrication of silicon photonic crystal optical waveguides," *Journal of Lightwave Technology*, vol. 18, no. 10, pp. 1402–1411, 2000.
- [4] P. D. Trinh, S. Yegnanarayanan, F. Coppinger, and B. Jalali, "Silicon-on-insulator (SOI) phased-array wavelength multi/demultiplexer with extremely low-polarization sensitivity," *IEEE Photonics Technology Letters*, vol. 9, no. 7, pp. 940–942, 1997.
- [5] K. Jia, W. Wang, Y. Tang, et al., "Silicon-on-insulator-based optical demultiplexer employing turning-mirror-integrated arrayed-waveguide grating," *IEEE Photonics Technology Letters*, vol. 17, no. 2, pp. 378–380, 2005.
- [6] A. Liu, R. Jones, L. Liao, et al., "A high-speed silicon optical modulator based on a metal-oxide-semiconductor capacitor," *Nature*, vol. 427, no. 6975, pp. 615–618, 2004.
- [7] D. Marris-Morini, X. L. Roux, L. Vivien, et al., "Optical modulation by carrier depletion in a silicon PIN diode," *Optics Express*, vol. 14, no. 22, pp. 10838–10843, 2006.
- [8] Y. Jiang, W. Jiang, L. Gu, X. Chen, and R. T. Chen, "80-micron interaction length silicon photonic crystal waveguide modulator," *Applied Physics Letters*, vol. 87, no. 22, Article ID 221105, 3 pages, 2005.
- [9] Q. Xu, B. Schmidt, S. Pradhan, and M. Lipson, "Micrometre-scale silicon electro-optic modulator," *Nature*, vol. 435, no. 7040, pp. 325–327, 2005.
- [10] R. S. Jacobsen, K. N. Andersen, P. I. Borel, et al., "Strained silicon as a new electro-optic material," *Nature*, vol. 441, no. 7090, pp. 199–202, 2006.
- [11] J. E. Roth, O. Fidaner, R. K. Schaevitz, et al., "Optical modulator on silicon employing germanium quantum wells," *Optics Express*, vol. 15, no. 9, pp. 5851–5859, 2007.
- [12] D. Ahn, C.-Y. Hong, J. Liu, et al., "High performance, waveguide integrated Ge photodetectors," *Optics Express*, vol. 15, no. 7, pp. 3916–3921, 2007.
- [13] A. O. Splett, T. Zinke, B. Schueppert, et al., "Integrated optoelectronic waveguide detectors in SiGe for optical communications," in *Photodetectors and Power Meters II*, vol. 2550 of *Proceedings of SPIE*, pp. 224–234, San Diego, Calif, USA, July 1995.
- [14] G. Masini, G. Capellini, J. Witzens, and C. Gunn, "A four-channel, 10 Gbps monolithic optical receiver in 130 nm CMOS with integrated Ge waveguide photodetectors," in *Proceedings of the Optical Fiber Communication and the National Fiber Optic Engineers Conference (OFC/NFOEC '07)*, Anaheim, Calif, USA, March 2007, PDP 31.
- [15] R. Jones, H. Rong, A. Liu, et al., "Net continuous wave optical gain in a low loss silicon-on-insulator waveguide by stimulated Raman scattering," *Optics Express*, vol. 13, no. 2, pp. 519–525, 2005.
- [16] H. Rong, R. Jones, A. Liu, et al., "A continuous-wave Raman silicon laser," *Nature*, vol. 433, no. 7027, pp. 725–728, 2005.
- [17] O. Boyraz and B. Jalali, "Demonstration of a silicon Raman laser," *Optics Express*, vol. 12, no. 21, pp. 5269–5273, 2004.
- [18] S. G. Cloutier, P. A. Kossyrev, and J. Xu, "Optical gain and stimulated emission in periodic nanopatterned crystalline silicon," *Nature Materials*, vol. 4, no. 12, pp. 887–891, 2005.
- [19] Z. Mi, P. Bhattacharya, J. Yang, and K. P. Pipe, "Room-temperature self-organised $\text{In}_{0.5}\text{Ga}_{0.5}\text{As}$ quantum dot laser on silicon," *Electronics Letters*, vol. 41, no. 13, pp. 742–744, 2005.
- [20] D. Pasquariello and K. Hjort, "Plasma-assisted InP-to-Si low temperature wafer bonding," *IEEE Journal on Selected Topics in Quantum Electronics*, vol. 8, no. 1, pp. 118–131, 2002.
- [21] Y. C. Liu, L. T. Ho, Y. B. Bai, et al., "Growth of ultrathin SiO_2 on Si by surface irradiation with an O_2^+ Ar electron cyclotron resonance microwave plasma at low temperatures," *Journal of Applied Physics*, vol. 85, no. 3, pp. 1911–1915, 1999.
- [22] U. Gösele and Q.-Y. Tong, "Semiconductor wafer bonding," *Annual Review of Materials Science*, vol. 28, no. 1, pp. 215–241, 1998.
- [23] A. W. Fang, H. Park, O. Cohen, R. Jones, M. J. Paniccia, and J. E. Bowers, "Electrically pumped hybrid AlGaInAs-silicon evanescent laser," *Optics Express*, vol. 14, no. 20, pp. 9203–9210, 2006.
- [24] L. Coldren and S. Corzine, *Diode Lasers and Photonic Integrated Circuits*, John Wiley & Sons, New York, NY, USA, 1995.
- [25] M. N. Sysak, H. Park, A. W. Fang, et al., "Experimental and theoretical thermal analysis of a hybrid silicon evanescent laser," *Optics Express*, vol. 15, no. 23, pp. 15041–15046, 2007.
- [26] H.-H. Chang, A. W. Fang, M. N. Sysak, et al., "1310 nm silicon evanescent laser," *Optics Express*, vol. 15, no. 18, pp. 11466–11471, 2007.
- [27] Y.-A. Chang, T.-S. Ko, J.-R. Chen, et al., "The carrier blocking effect on 850 nm InAlGaAs/AlGaAs vertical-cavity surface-emitting lasers," *Semiconductor Science and Technology*, vol. 21, no. 10, pp. 1488–1494, 2006.
- [28] A. W. Fang, R. Jones, H. Park, et al., "Integrated AlGaInAs-silicon evanescent race track laser and photodetector," *Optics Express*, vol. 15, no. 5, pp. 2315–2322, 2007.
- [29] H. Park, A. W. Fang, R. Jones, et al., "A hybrid AlGaInAs-silicon evanescent waveguide photodetector," *Optics Express*, vol. 15, no. 10, pp. 6044–6052, 2007.
- [30] B. R. Koch, A. W. Fang, O. Cohen, and J. E. Bowers, "Mode-locked silicon evanescent lasers," *Optics Express*, vol. 15, no. 18, pp. 11225–11233, 2007.
- [31] B. R. Koch, A. W. Fang, H. N. Poulsen, et al., "All-optical clock recovery with retiming and reshaping using a silicon evanescent mode locked ring laser," in *Proceedings of the Optical Fiber Communication and the National Fiber Optic Engineers Conference (OFC/NFOEC '08)*, San Diego, Calif, USA, February 2008.
- [32] E. A. Avrutin, J. H. Marsh, and E. L. Portnoi, "Monolithic and multi-gigahertz mode-locked semiconductor lasers: constructions, experiments, models and applications," *IEEE Proceedings: Optoelectronics*, vol. 147, no. 4, pp. 251–278, 2000.
- [33] P. J. Delfyett, S. Gee, M.-T. Choi, et al., "Optical frequency combs from semiconductor lasers and applications in ultrawideband signal processing and communications," *Journal of Lightwave Technology*, vol. 24, no. 7, pp. 2701–2719, 2006.
- [34] M. Teshima, K. Sato, and M. Koga, "Experimental investigation of injection locking of fundamental and subharmonic frequency-modulated active mode-locked laser diodes," *IEEE Journal of Quantum Electronics*, vol. 34, no. 9, pp. 1588–1596, 1998.
- [35] H. Park, A. W. Fang, O. Cohen, R. Jones, M. J. Paniccia, and J. E. Bowers, "A hybrid AlGaInAs-silicon evanescent amplifier," *IEEE Photonics Technology Letters*, vol. 19, no. 4, pp. 230–232, 2007.
- [36] H. Park, Y.-H. Kuo, A. W. Fang, et al., "A hybrid AlGaInAs-silicon evanescent preamplifier and photodetector," *Optics Express*, vol. 15, no. 21, pp. 13539–13546, 2007.

- [37] R. Nagarajan, M. Kato, S. Hurtt, et al., "Monolithic, 10 and 40 channel InP receiver photonic integrated circuits with on-chip amplification," in *Proceedings of the Optical Fiber Communication and the National Fiber Optic Engineers Conference (OFC/NFOEC '07)*, Anaheim, Calif, USA, March 2007, PDP 32.
- [38] J. W. Raring, E. J. Skogen, L. A. Johansson, et al., "Demonstration of widely tunable single-chip 10-Gbps laser-modulators using multiple-bandgap InGaAsP quantum-well intermixing," *IEEE Photonics Technology Letters*, vol. 16, no. 7, pp. 1613–1615, 2004.
- [39] J. Shimizu, M. Aoki, T. Tsuchiya, et al., "Advantages of optical modulators with InGaAlAs/InGaAlAs MQW structure," *Electronics Letters*, vol. 38, no. 15, pp. 821–822, 2002.
- [40] H. Fukano, T. Yamanaka, M. Tamura, and Y. Kondo, "Very-low-driving-voltage electroabsorption modulators operating at 40 Gbps," *Journal of Lightwave Technology*, vol. 24, no. 5, pp. 2219–2224, 2006.
- [41] K. Kato, A. Kozen, Y. Muramoto, Y. Itaya, T. Nagatsuma, and M. Yaita, "110-GHz, 50%-efficiency mushroom-mesa waveguide p-i-n photodiode for a 1.55- μ m wavelength," *IEEE Photonics Technology Letters*, vol. 6, no. 6, pp. 719–721, 1994.
- [42] J. E. Bowers, A. W. Fang, H. Park, R. Jones, M. J. Paniccia, and O. Cohen, "Hybrid silicon evanescent laser in a silicon-on-insulator waveguide," in *Proceedings of the Optical Fiber Communication and the National Fiber Optic Engineers Conference (OFC/NFOEC '07)*, pp. 1–3, Anaheim, Calif, USA, March 2007, OTuK4.

Research Article

Subwavelength Grating Structures in Silicon-on-Insulator Waveguides

J. H. Schmid, P. Cheben, S. Janz, J. Lapointe, E. Post, A. Delâge, A. Densmore, B. Lamontagne, P. Waldron, and D.-X. Xu

Institute for Microstructural Sciences, National Research Council of Canada, Ottawa, ON, Canada K1A 0R6

Correspondence should be addressed to J. H. Schmid, jens.schmid@nrc-cnrc.gc.ca

Received 20 December 2007; Revised 24 April 2008; Accepted 28 May 2008

Recommended by Graham Reed

First implementations of subwavelength gratings (SWG) in silicon-on-insulator (SOI) waveguides are discussed and demonstrated by experiment and simulations. The subwavelength effect is exploited for making antireflective and highly reflective waveguide facets as well as efficient fiber-chip coupling structures. We demonstrate experimentally that by etching triangular SWGs into SOI waveguide facets, the facet power reflectivity can be reduced from 31% to <2.5%. Similar structures using square gratings can also be used to achieve high facet reflectivity. Finite difference time-domain simulations show that >94% facet reflectivity can be achieved with square SWGs for 5 μm thick SOI waveguides. Finally, SWG fiber-chip couplers for SOI photonic wire waveguides are introduced, including design, simulation, and first experimental results.

Copyright © 2008 J. H. Schmid et al. This is an open access article distributed under the Creative Commons Attribution License, which permits unrestricted use, distribution, and reproduction in any medium, provided the original work is properly cited.

1. INTRODUCTION

Subwavelength gratings (SWG) have been known and used for many years [1], most commonly as an alternative to antireflective (AR) coatings on bulk optical surfaces. The defining property of an SWG is a pitch that is sufficiently small to suppress all but the 0th order diffraction, the latter referring to the light that is reflected or transmitted according to Snell's law. According to the grating equation for normally incident light ($\sin\theta = m\lambda/\Lambda$, where θ is the angle of diffraction, λ is the wavelength of light, Λ is the grating pitch, and m is the diffraction order) diffraction is suppressed for $\Lambda < \lambda$, as the diffraction angle becomes imaginary for all orders m . Conceptually, the light propagating through a SWG structure "senses" the average optical properties of the SWG medium. The SWG can thus be represented as a locally homogeneous effective medium with optical properties determined by the grating geometry. The effect of a specific optical coating can be mimicked by an SWG with an appropriate modulation depth and duty cycle. Effective multilayer and gradient-index (GRIN) structures can also be obtained with SWGs. Low reflectivities on optical surfaces have been demonstrated with SWGs both by a single-layer AR effect as well as by a GRIN effect [2]. More recently,

SWG surface structures that exhibit very high reflectivity over a broad wavelength band have also been demonstrated [3, 4]. In this paper we discuss the first implementations of SWG structures in silicon-on-insulator (SOI) integrated planar waveguide circuits.

Integrated planar waveguide circuits are widely used in optical telecommunication systems, with arrayed waveguide grating (AWG) multiplexers being one of the most complex of such circuits [5]. Currently, these commercial waveguide devices are typically made from doped silica glass with a low refractive index contrast. The high-index contrast (HIC) SOI material system offers the potential of a significant size and cost reduction of integrated planar waveguide devices, including AWGs [6, 7]. In addition, new applications are emerging for miniaturized SOI waveguide devices. For example, we have recently demonstrated a compact high resolution microspectrometer [8] and highly sensitive photonic wire evanescent field sensors (PWEF) with a detection limit of ~ 20 fg of organic molecules [9, 10]. However, there are also fundamental challenges of the SOI material system related to the fixed value of the refractive indices of the constituent materials (Si and SiO_2). Since the SWG effect allows one to engineer artificial materials with intermediate effective indices simply by lithographic patterning, it has

the potential to circumvent this limitation. We demonstrate this on two specific examples, namely, the control of the Fresnel reflectivity of the waveguide facets and the fiber-to-chip coupling, both relying on the SWG effect.

The Fresnel reflectivity of a cleaved SOI waveguide facet is typically $\sim 30\%$, which is the reflectivity of the Si-air interface. This comparatively high facet reflectivity causes Fabry-Pérot cavity effects in SOI planar waveguide devices and also increases the fiber-chip coupling loss. Thus antireflective facets are often desirable. For some devices, for example, optical cavities, a facet reflectivity larger than 30% is required. Both AR and highly reflective (HR) facets can be achieved by the use of thin-film coatings; however, the use of optical coatings on facets has various drawbacks. For example, film deposition has to be carried out at the chip level after cleaving, requiring additional processing and precluding device testing at the wafer level. Thin film deposition processes can be complex, may reduce yield, and may require the use of expensive deposition equipment. Furthermore, optical coatings may become mechanically unstable under thermal cycling, leading to restrictions on device power and limitation of device lifetime.

A major problem in the design and fabrication of silicon microphotonic devices is the limited efficiency of optical coupling to silicon waveguides at the input/output interfaces. Due to the large mode size disparities, the light coupling between an optical fiber and a silicon waveguide with a small cross section is largely inefficient. Various solutions to this problem have been suggested, for example, three-dimensional mode size transformers, edge [11] and off-plane [12–15] grating couplers, inversely tapered waveguides [16] and GRIN planar waveguide lenses [17], each having some advantages and drawbacks. A comparative review of various coupling schemes is contained in [18]. For submicron silicon wire waveguides, inverse tapers have emerged as a particularly efficient coupling method. Demonstrated coupling losses of inverse tapers with a minimum width of $0.1\ \mu\text{m}$ reported in [16] are 6 dB and 3.3 dB for TE and TM polarized light, respectively. While this is a remarkable achievement, a further improvement of the total coupling efficiency is desirable. Furthermore, the coupling efficiency of inverse tapers is strongly dependent on the minimum taper width, a fact that results in tight fabrication tolerances for the taper width.

We have recently proposed the use of the SWG effect as a general tool for waveguide mode modifications, including light coupling between an optical fiber and high index contrast waveguides of submicrometer dimensions [19] and modification of facet reflectivity [20]. In this paper, we review our work but also provide new experimental and modeling results on the use of SWGs in SOI waveguides. All SWG patterns discussed here, both for facet reflectivity modification and for fiber-to-chip coupling enhancement, can be fabricated by standard lithography and vertical etching processes. This has two obvious advantages. First, devices can be processed at the wafer level before dicing; and second, shape control of the SWG is limited only by the resolution of the lithography and pattern transfer. To demonstrate the effects, we have carried out experiments on

SOI waveguides and compared the experimental results with reflectivity calculations using effective medium theory and finite difference time-domain (FDTD) simulations.

2. ANTIREFLECTIVE WAVEGUIDE FACETS

The AR effect of specific SWG structures on waveguide facets is analogous to the same effect on bulk optical surfaces. It can be described using the effective medium theory (EMT) [21]. According to EMT, a composite medium comprising two different materials interleaved at the subwavelength scale can be approximated as a homogeneous medium with a refractive index expressed as a power series in (Λ/λ) , where Λ is the pitch of the SWG and λ is the wavelength of the light. For the case of a one-dimensional surface grating, the first-order expressions for the anisotropic refractive index are given by

$$n_{\parallel} = (fn_1^2 + (1-f)n_2^2)^{1/2}, \quad (1a)$$

$$n_{\perp} = \left(\frac{f}{n_1^2} + \frac{(1-f)}{n_2^2} \right)^{-1/2}. \quad (1b)$$

Equations (1a) and (1b) refer to the case of the electric field of the incident light being parallel or perpendicular to the grooves (see Figure 1), respectively. In these equations, n_1 and n_2 are the refractive indices of the two media comprising the SWG, and f is the filling factor, defined as the fraction of material with index n_1 in a thin slice parallel to the surface, as shown in Figure 1. The equations above are valid in the limit $(\Lambda/\lambda) \rightarrow 0$. Figure 1 shows the geometry of SWGs with square and triangular shapes at a silicon-air interface ($n_1 = 3.5$, $n_2 = 1$). For square gratings (top left), the filling factor profile is a step function (left center panel). Using (1a) and (1b), the refractive index profile, which is also a step function, is obtained (bottom left). The effective index in the grating region is polarization dependent, as per (1a) and (1b). The TM mode has the electric field parallel to the grating grooves, corresponding to (1a) whereas the electric field of the TE mode is perpendicular to the grooves, corresponding to (1b). For triangular gratings (top right in Figure 1), the filling factor profile is a linearly decreasing function along the depth of the grating (center right). The corresponding effective index profiles are continuously decreasing functions across the grating region for both polarizations as shown in the bottom right panel of Figure 1.

The step function effective index profile of a square grating is equivalent to that of a single-layer coating on a silicon surface. The thickness of this effective layer is given by the modulation depth of the grating and the effective refractive index can be adjusted between the values of silicon and air by changing the duty cycle of the SWG. From thin film theory, the requirements for a single-layer interference AR coating for light crossing the boundary between two materials of reflective indices n_1 and n_2 at normal incidence are $n_f^{\text{AR}} = \sqrt{n_1 n_2}$ and $t = m\lambda/(4n_f^{\text{AR}})$ where n_f^{AR} is the film refractive index, t is the film thickness, and $m = 1, 3, 5, \dots$ is an odd integer. Thus an AR surface with a square SWG can be designed by choosing the effective refractive index for

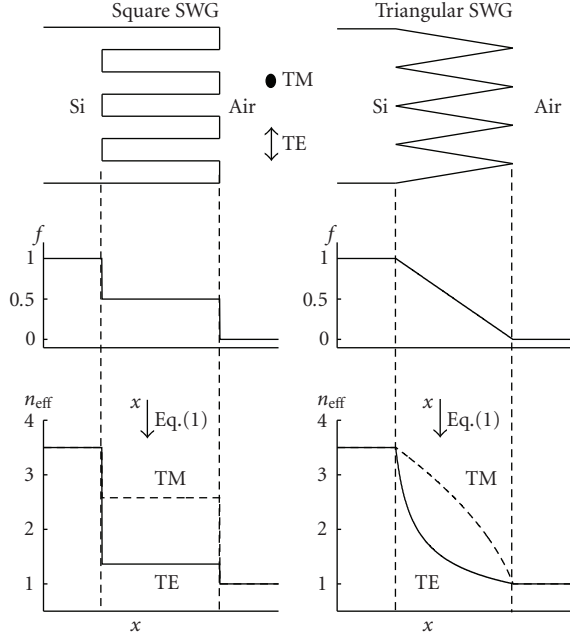


FIGURE 1: Effective medium theory applied to square and triangular SWGs on a Si-air interface. Top: schematic of the grating geometry. Center: filling factor corresponding to the square and triangular SWGs. Bottom: resulting effective refractive index profiles for light with the electric field along the grating grooves (TM, dashed curves) and perpendicular to the grating grooves (TE, solid curves).

a specific polarization in (1a) and (1b) equal to the required n_f^{AR} . This determines the filling factor and thus the duty cycle of the grating. The modulation depth is then determined by the condition above for the AR coating thickness t . In contrast to the square gratings, the antireflective properties of triangular gratings arise from the GRIN effect, as the effective refractive index varies continuously between the bulk values of the two media that comprise the grating, namely, Si and air.

Figure 2 shows the scanning electron microscope images of SOI ridge waveguide facets patterned with square and triangular SWGs. These structures were fabricated with a two-step patterning process on SOI substrates with a Si layer thickness of $1.5 \mu\text{m}$ and a buried oxide (BOX) layer thickness of $1 \mu\text{m}$, as described in [20]. Square and triangular facet patterns with various dimensions as well as flat reference facets were produced by electron beam lithography and reactive ion etching (RIE). The facet reflectivity was inferred from Fabry-Pérot (FP) transmission measurements on waveguides terminated with SWG facets, as shown schematically in Figure 3. The ridge waveguides have a width of $1.5 \mu\text{m}$, adiabatically tapered to a width of $4 \mu\text{m}$ near the facets. This increased waveguide width at the facet makes it possible to include 10 periods of the SWG with a pitch of $0.4 \mu\text{m}$. The etch depth for the shallow etch (defining the ridge waveguide) is $0.7 \mu\text{m}$, while the deep facet etch is terminated at the bottom oxide.

Transmittance of fabricated waveguides was measured as a function of wavelength near $\lambda = 1.55 \mu\text{m}$. Propagation

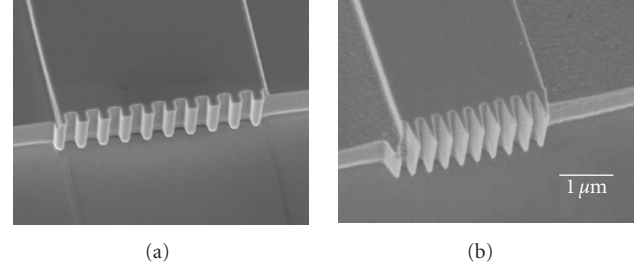


FIGURE 2: Scanning electron micrographs of SOI waveguide facets patterned with (a) square and (b) triangular SWGs.

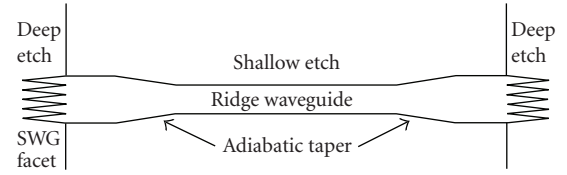


FIGURE 3: Schematic top view of a SOI ridge waveguide terminated at both ends with a SWG (not to scale), as used for waveguide transmission measurements described in the text.

loss was determined from the reference waveguides with flat facets to be 1.7 dB/cm for TE and 5.2 dB/cm for TM polarized light, using the Fabry-Pérot method. The Fresnel reflectivity of a material with the mode effective index was used as an approximation for the reference waveguide facet reflectivity. This value differs from the reflectivity of a Si-air interface by less than 0.5% for either polarization. The polarization dependence of the propagation loss is believed to be due to scattering loss from the etched sidewalls of the waveguides. The reproducibility of the loss measurement was found to be good with waveguide-to-waveguide fluctuations of the loss less than 0.5 dB/cm . A comparison of transmission spectra of waveguides with flat facets and with triangular and square SWG patterned facets is shown in Figure 4 for TE polarized light. The peak-to-peak grating modulation depth is 720 nm for the triangular SWG pattern and 270 nm for the square pattern which has a duty ratio of 61%. The amplitude of the FP fringes is reduced from 4.5 dB for the flat facets to approximately 0.3 dB and 0.5 dB for the triangular and square SWGs, respectively. Assuming the same propagation loss for all waveguides as obtained from the reference measurement on waveguides with flat facets, the power reflectivities of the triangular and square SWG facets are calculated to be 2.1% and 3.6%, respectively, from the amplitude of the observed FP fringes shown in Figure 4.

For triangular gratings, the facet reflectivity was measured as a function of the modulation depth of the SWG for both polarizations and compared with EMT theory for the equivalent grating on a bulk silicon surface. The results are shown in Figure 5. The EMT calculation was carried out by discretizing the continuous effective index profiles shown in Figure 1 (bottom right) in steps of 1 nm . The resulting discrete index profile for each polarization is the same as

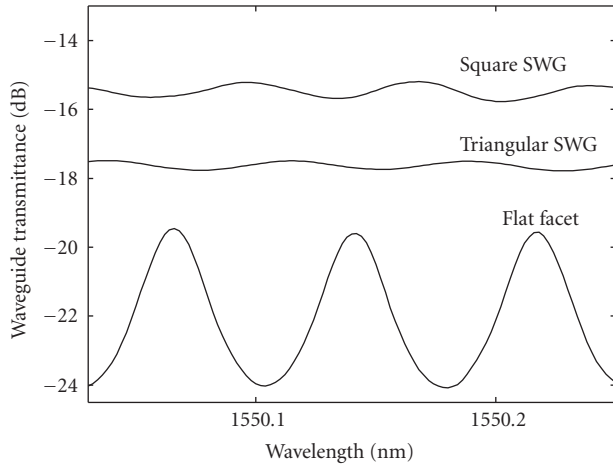


FIGURE 4: Fabry-Pérot fringes for the reference waveguide with flat facets and for the waveguides terminated with antireflective triangular or square SWG structures. The curves are offset for clarity.

that of a stack of 1 nm thick films. The reflectivity of the SWG is then calculated as the reflectivity of this equivalent thin film stack using standard thin film theory. There is good quantitative agreement of experiment and theory (see Figure 5). The reflectivity decreases substantially with the grating modulation depth, as the gradient-index section becomes more adiabatic. The minimum measured reflectivity of 2.0% for TE and 2.4% for TM polarization is obtained for a modulation depth of 720 nm, which is the maximum grating depth used in our experiments. The quoted values are an average over 4 measured samples. According to the EMT calculations, reflectivities below 1% can be achieved for SWG modulation depths of approximately 1 μm and 2.5 μm for TE and TM polarized light, respectively. Since the SWG profiles are defined lithographically, their shape and thus the effective index profile can be readily engineered for specific requirements (e.g., polarization properties), in a similar way as for bulk SWG surfaces [22].

For square SWGs (Figure 2, left), the lowest measured facet reflectivity was 3.6% for TE polarized light whereas the TM reflectivity of the same sample was 23%. Such a large polarization dependence is expected for square gratings. As discussed above, according to EMT, the square AR SWGs can be represented as a single-layer AR coating, the efficiency of which is known to be rather sensitive to the index of the layer. Since the effective index of the SWG is polarization dependent (Figure 1, bottom left), optimal AR performance can only be achieved for one polarization state for a particular SWG duty cycle. The strong polarization dependence of square SWG facets can potentially be exploited for making polarization selective waveguide elements.

3. WAVEGUIDE FACETS WITH HIGH REFLECTIVITY

Subwavelength gratings with high reflectivity have recently been demonstrated on optical surfaces as a replacement for the top distributed Bragg reflector in a vertical-cavity

surface emitting laser (VCSEL) [23]. In order to obtain the SWG effect, these gratings need to be separated from the substrate by a layer of low index material. This was achieved in a VCSEL device by fabricating a grating freely suspended above the substrate with an air gap of $\sim 1 \mu\text{m}$. A similar SWG structure can be envisioned for planar waveguide facets consisting of a row of vertical posts in front of a flat waveguide facet at a specific distance (equivalent to the air gap of the VCSEL structure). However, in such a structure there is no vertical mode confinement in the air gap, resulting in out-of-plane radiative loss as the light propagates in the air gap. For a SOI waveguide thickness of $\sim 1 \mu\text{m}$ or less, these radiative losses are prohibitive for practical devices, as we have found with three-dimensional FDTD simulations.

Interestingly though, FDTD simulations show that if a square grating is etched directly into the facet without a separating air gap, high reflectivities can also be obtained. The modeled structure is shown in Figure 6(a). It is a 7 μm wide Si slab waveguide ($n_{\text{Si}} = 3.476$) with SiO_2 lateral claddings ($n_{\text{SiO}_2} = 1.44$), terminated at the facet with a square grating. The grating period is 0.7 μm , the duty cycle is 54% and the grating modulation depth is 485 nm. The external medium is air ($n = 1$). A continuous-wave field excitation of a TE (electric field in the plane of the drawing) waveguide fundamental mode of free space wavelength $\lambda = 1550 \text{ nm}$ propagating in the waveguide towards the facet was assumed. The mesh size used was 10 nm and the simulation was run for a total of 10 000 time steps of $\Delta t = 2.2 \times 10^{-17}$ seconds. The calculated TE electric field map is shown in Figure 6(b). The excitation plane for the waveguide mode source is indicated in the figure by a blue line, including the mode propagation direction (arrow). It can be seen that the transmittance through the grating structure is efficiently suppressed, hence the mirror effect. Between the excitation plane and the facet, the forward propagating and the reflected light form a standing wave interference pattern. To the left of the excitation plane, the reflected mode propagates unperturbed in the waveguide. The facet reflectivity is calculated as an overlap integral of the reflected intensity profile in the waveguide region to the left of the excitation plane with the fundamental TE mode. A reflectivity value of 97% was obtained for this 2D structure. Figure 6(c) shows the simulation of light coupling from an external optical fiber to the Si waveguide. In this case, a light source with Gaussian intensity profile with a $1/e^2$ width of 10.4 μm (SMF-28 fiber mode), is located at the excitation plane (white line in Figure 6(c)). The calculated field in the waveguide reveals a strong transverse modulation with a period half of the grating pitch. This modulation persists almost unperturbed for several micrometers as the light propagates in the waveguide. Since the overlap integral of this modulated field with the fundamental mode of the waveguide is comparatively small, coupling from an external fiber to the waveguide is inefficient.

These markedly different grating properties for light propagating in opposite directions may seem surprising, but have a straightforward explanation. Obviously, diffraction is suppressed on the air side of the grating, since $\Lambda < \lambda_{\text{air}}$. However, the grating is not subwavelength for light coupled

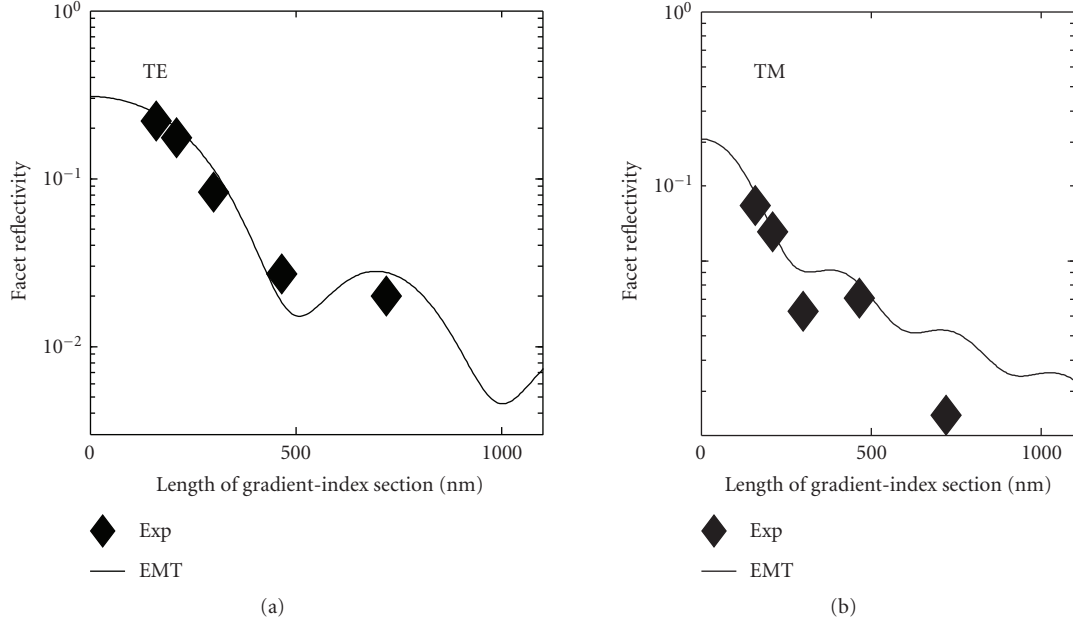


FIGURE 5: Experimental and theoretical results from effective medium theory for the reflectivity of facets with triangular SWGs as a function of the length of the gradient-index section (i.e., the grating modulation depth).

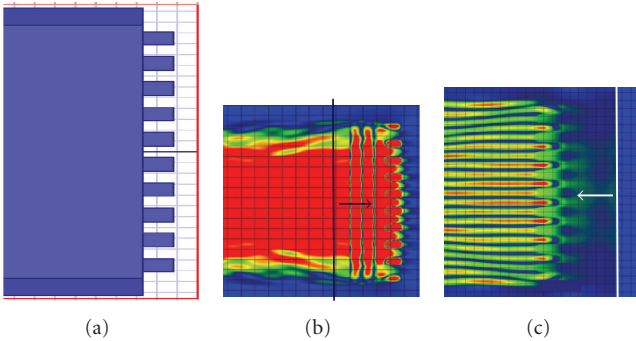


FIGURE 6: FDTD simulations of HR SOI facets. (a) Layout used for a typical simulation. The light and dark blue regions are the silicon waveguide core and SiO₂ lateral cladding, respectively. (b) Simulated TE field map for a waveguide mode launched at the plane indicated in the figure. (c) TE field map for an external optical fiber mode coupling into the waveguide.

into the Si waveguide, where the first diffraction order is not evanescent, since $\Lambda > \lambda_{Si}$. In our case $\Lambda = 700$ nm, $\lambda_{air} = 1.55$ μ m, and $\lambda_{Si} = \lambda_{air}/n_{Si} = 446$ nm. This is a fundamental difference between the HR gratings and the square AR gratings discussed in the previous section, which have a pitch of $\Lambda = 400$ nm and are thus subwavelength both in the Si and in air. It can be shown with rigorous coupled wave analysis (RCWA) that for a plane wave normally incident from inside the bulk Si on a surface grating with the same pitch and duty cycle as our HR facet gratings, both the diffraction efficiency and the transmittance are extremely small, while the specular (0th order) reflectivity is $>99.9\%$. Conversely, when the plane wave is incident on such a bulk

grating from the air to Si, the power diffracted into the +1 and -1 diffracted orders is approximately 98%, with $<2\%$ of light reflected or transmitted in 0th order. The intensity pattern in Figure 6(c) is thus a superposition of the -1 and +1 diffraction orders, while the 0th order is suppressed. This zero-order suppression effect is commonly employed in phase masks used in the fabrication of fiber-Bragg gratings [24].

The reflectance of HR gratings on waveguide facets can be estimated from measured FP fringes similar to the AR measurements discussed in the previous section. The most notable difference is that fiber-waveguide coupling is now largely inefficient due to the diffraction effect explained above. In fact, waveguides terminated with HR facets on both sides were found experimentally to have no measurable transmittance ($T < -60$ dB). To circumvent this problem and measure the internal (Si-air) facet reflectivity, we have used waveguides that are terminated with an HR grating on the output facet but with a regular flat facet having a Fresnel reflectivity of 31% on the input side. This way an asymmetric FP cavity is formed. As in the case of the AR facets, FP fringes can be observed in the transmission spectra of these waveguides. In Figure 7, the spectrum of such an asymmetric cavity waveguide is compared to that of a reference waveguide terminated on both ends with flat facets. The measured peak-to-peak fringe modulations are 6.4 dB and 4.2 dB for the respective waveguides. Using a simple Fabry-Pérot model for the asymmetric cavity, this corresponds to an HR facet reflectivity of 75%, clearly demonstrating the validity of the HR grating concept. However, since this reflectivity is significantly lower than the best results of our 2D FDTD simulations, full 3D FDTD simulations of the HR facet structures were carried out. These simulations

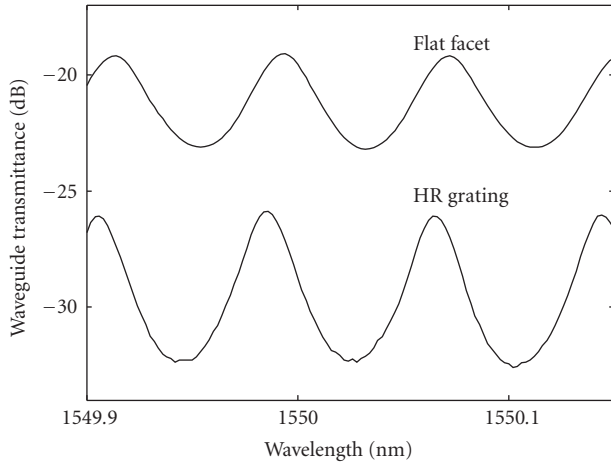


FIGURE 7: Measured Fabry-Pérot fringes in the transmission spectrum of a waveguide with an HR grating on the output facet. A reference waveguide with flat facets is also shown. The curves are offset for clarity.

reveal a strong dependence of the expected reflectivity on mode confinement. For the $1.5\ \mu\text{m}$ thick SOI waveguides with the $0.7\ \mu\text{m}$ pitch gratings used in our experiments, the highest reflectivity obtained in the 3D FDTD simulations is 80%, in good agreement with the measurement. For thicker waveguides with the same facet grating dimensions the achievable reflectivity increases significantly. For example, 94% reflectivity is expected for $5\ \mu\text{m}$ thickness according to the 3D FDTD simulations. Physically, the reason for the mode size effect is the dependence of the grating reflectivity on the incident angle. With RCWA we find that the grating reflectivity for plane waves drops from $>99.9\%$ to 81% when the angle of incidence is increased from 0° to 10° . Therefore, the larger range of incident angles contained in a smaller, more localized mode, results in a lower reflectivity.

4. FIBER-TO-CHIP COUPLERS

An original application of SWGs for fiber-to-waveguide coupling and mitigating losses due to the mode size mismatch of optical fibers and submicron SOI waveguides has been proposed recently [19]. The principle of this fiber-chip coupler is based on a gradual modification of the waveguide mode effective index by the SWG effect. The idea is illustrated in a schematic side view of a coupler structure in Figure 8. The waveguide mode effective index is altered by chirping the SWG duty ratio $r(z) = a(z)/\Lambda$, where $a(z)$ is the length of the waveguide core segment. Unlike in the case of the AR and HR SWG structures discussed above, where the direction of light propagation is orthogonal to the grating vector, here they are colinear, that is, the light propagates along the grating. Nevertheless, EMT applies to these structures in a similar way. The effective index of the mode in the SWG coupling structure increases with the grating duty ratio. The duty ratio and hence the volume fraction of the Si waveguide core is modified such that at one end of the coupler the effective index is matched to the SOI waveguide while at the other

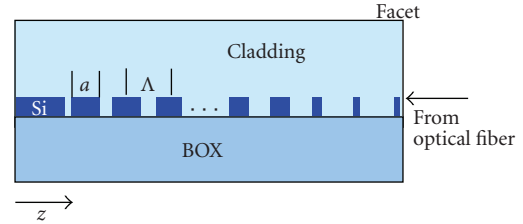


FIGURE 8: Schematic of an SWG fiber-to-waveguide coupler, side view.

end, near the chip facet, it matches that of the optical fiber. We have demonstrated the proposed principle on various SWG coupling structures [19], using two-dimensional FDTD calculations for an SOI waveguide with Si core thickness of $0.3\ \mu\text{m}$ with SiO_2 cladding. Efficiencies as large as 76% (1.35 dB loss) and a negligible return loss ($-35\ \text{dB}$, or 0.03%) were calculated for coupling from a standard optical fiber (SMF-28, mode field diameter $10.4\ \mu\text{m}$) using a $50\text{-}\mu\text{m}$ -long SWG coupler. Further loss reduction can be expected by advanced design, including parabolic width tapering and chirping the SWG pitch. The coupling efficiency tolerance to misalignment is high. Transverse misalignment of $\pm 2\ \mu\text{m}$ results in an excess coupling loss of only 0.5 dB. The angular misalignment tolerance is also large, with only 0.24 dB loss penalty for angular misalignment of ± 2 degrees. We have also demonstrated the reduction of the coupler length down to $10\ \mu\text{m}$ and found an excess loss of 0.6 dB compared to the $50\ \mu\text{m}$ long coupler discussed above. Unlike waveguide grating couplers based on diffraction, the SWG mechanism is nonresonant, and hence intrinsically wavelength insensitive.

First SWG waveguide couplers for SOI photonic wires (PWs) have recently been fabricated in our lab. The dimensions of the PWs are $0.45\ \mu\text{m}$ (width) \times $0.26\ \mu\text{m}$ (height). Such thin PW waveguides have been shown to provide the maximum sensitivity for evanescent field waveguide-based biosensors [9]. The coupler structures were fabricated on SOI substrates from SOITEC with an Si layer and BOX thickness of $0.26\ \mu\text{m}$ and $2\ \mu\text{m}$, respectively. Electron beam lithography with a chemically amplified negative resist (NEB 22 A3) was used to define both waveguides and SWG couplers in a single step. The pattern was then etched through the Si layer to the BOX with inductively coupled plasma RIE. After the resist mask was stripped, a $2\ \mu\text{m}$ thick upper cladding layer of SU-8 resist with a refractive index of $n = 1.58$ was deposited on the sample using a standard spin and bake procedure. The samples were then cleaved and polished as necessary to obtain good facet quality. The ideal SWG coupler structure described above requires a specific duty cycle at the facet; however, for cleaving and polishing the facet some tolerance in the exact position of the facet with respect to the pattern is required. Therefore, the SWG was extended with constant grating parameters for $400\ \mu\text{m}$ beyond the ideal position of the facet. This allows the final position of the fabricated facet to be within this distance from the end of the coupler structure. SEM images of a fabricated coupler structure are shown in Figure 9. On the left side, the part of the SWG joining the PW waveguide is shown.

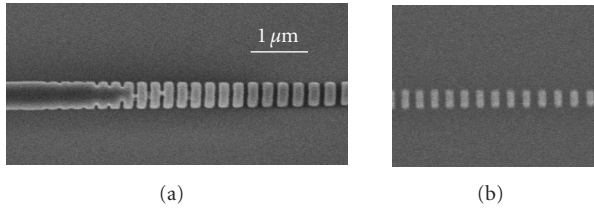


FIGURE 9: SEM micrographs of a fabricated SOI photonic wire waveguide with an SWG coupler (top view). (a) The SWG coupler joining the photonic wire waveguide. (b) Mid-section of the SWG coupler.

The pitch of the grating is $0.2\ \mu\text{m}$ and the smallest gaps are nominally $50\ \text{nm}$. Due to the proximity effect in the e-beam lithography, the grating gaps become successively more closed as the waveguide, which is written with a higher e-beam dose, is approached. Within a distance of a few periods of the SWG from the waveguide, the grating is essentially a subwavelength sidewall grating. This gradual closing of the gaps may in fact be beneficial to the performance of the coupler, as it reduces the small discontinuity in the effective mode index as the waveguide transforms into an SWG, making the transition more adiabatic. Figure 9(b) shows the same coupler at a position closer to the facet. Here the fabricated structure shows little deviation from the design except for some corner rounding. To increase the effective index gradient along the SWG coupler, the width of the SWG segments is tapered from $0.45\ \mu\text{m}$ at the waveguide to $0.2\ \mu\text{m}$ at the facet.

Samples with SWG couplers of varying lengths and taper widths have been fabricated. Two identical couplers are connected via S-shaped PW waveguides for transmission measurements. The S-shape helps to reduce the amount of scattered light reaching the photodetector, as the latter is laterally offset from the light source. The SWG couplers are compared with inverse tapers of similar dimensions, as well as untapered waveguides. The inverse taper couplers are adiabatically tapered waveguides that reach a specific minimum width at the facet [16]. Coupling loss was inferred from measurements of the waveguide transmittance at a wavelength $\lambda = 1.55\ \mu\text{m}$ using an erbium doped fiber amplified spontaneous emission (ASE) source with $50\ \text{mW}$ output power. An indium gallium arsenide photo diode was used as a detector. Coupling loss values were estimated from the measured waveguide transmittance by correcting for the photonic wire propagation loss, which was determined using the cut back method on comparable samples to be $9.1\ \text{dB/cm}$ and $6.5\ \text{dB/cm}$ for TE and TM polarization, respectively. The lowest coupling loss for the SWG couplers of $6.5\ \text{dB}$ and $4\ \text{dB}$ for TE and TM polarization, respectively, was obtained for a width of $0.2\ \mu\text{m}$. The corresponding values for straight waveguides with a width of $0.45\ \mu\text{m}$ are $18\ \text{dB}$ and $11\ \text{dB}$. The coupling loss of our first coupler is comparable to the loss of inverse couplers as reported in [16] ($6.0\ \text{dB}$ and $3.3\ \text{dB}$ loss for TE and TM polarization, respectively), but is achieved for a two times larger width. A wider taper width implies improved fabrication tolerance to width

fluctuations. We expect the loss can be reduced by further improvements in our design and fabrication, using a thicker box and/or a wider taper width. Our experiments provide a first verification of the proposed SWG coupler concept. Also, the SWG principle experimentally demonstrated in this paper can be generalized to other types of waveguide modifications including effective index changes and mode transformations, opening new possibilities for engineering of waveguide properties at the subwavelength scale.

5. SUMMARY AND CONCLUSIONS

We have reviewed our work in implementing first SWG structures in SOI waveguides. Three types of structures have been discussed, namely, AR and HR waveguide facets and fiber-chip couplers, all fabricated using standard fabrication techniques. The AR facets were demonstrated exploiting either a GRIN effect from triangular SWGs or a single-layer AR effect from square SWGs. The GRIN AR structures were found to be particularly efficient, with measured facet reflectivities below 2.5% for both polarizations. These experimental results are in good agreement with EMT calculations. A minimum reflectivity of 3.6% for the TE mode is reported for square SWGs, including highly polarization selective properties. HR facets employ a very similar structure to that of square AR SWG waveguide facets but with different grating parameters. The $0.7\ \mu\text{m}$ pitch of the HR grating is large enough that the ± 1 orders of diffraction are allowed in the Si, but are evanescent in air. For light incident from the air, such gratings act as a zero-order suppressed phase mask. In the opposite direction (light incident from the waveguide), high specular reflectivity is observed. We have measured up to 75% reflectivity for facets in $1.5\ \mu\text{m}$ thick SOI waveguides, in good agreement with 3D FDTD simulations. The FDTD simulations predict that reflectivities in excess of 95% can be achieved for SOI waveguides with a thickness of $5\ \mu\text{m}$ or more. Finally, the principle, design and first experimental results on SWG fiber-chip couplers were reviewed. Coupling losses on the order of $\sim 1\ \text{dB}$ can be achieved with these structures according to FDTD simulations and losses of $6.5\ \text{dB}$ and $4\ \text{dB}$ for TE and TM polarized light, respectively, have been demonstrated experimentally. The first results suggest that the SWG couplers may outperform inverse taper fiber-chip couplers in terms of fabrication robustness, compactness, and tolerance to misalignment.

REFERENCES

- [1] H. Kikuta, H. Toyota, and W. Yu, "Optical elements with subwavelength structured surfaces," *Optical Review*, vol. 10, no. 2, pp. 63–73, 2003.
- [2] W. H. Southwell, "Pyramid-array surface-relief structures producing antireflection index matching on optical surfaces," *Journal of the Optical Society of America A*, vol. 8, no. 3, pp. 549–553, 1991.
- [3] C. F. R. Mateus, M. C. Y. Huang, Y. Deng, A. R. Neureuther, and C. J. Chang-Hasnain, "Ultrabroadband mirror using low-index cladded subwavelength grating," *IEEE Photonics Technology Letters*, vol. 16, no. 2, pp. 518–520, 2004.

- [4] P. Cheben, S. Janz, D.-X. Xu, B. Lamontagne, A. Del age, and S. Tanev, "A broad-band waveguide grating coupler with a subwavelength grating mirror," *IEEE Photonics Technology Letters*, vol. 18, no. 1, pp. 13–15, 2006.
- [5] P. Cheben, "Wavelength dispersive planar waveguide devices: echelle and arrayed waveguide gratings," in *Optical Waveguides: From Theory to Applied Technologies*, M. L. Calvo and V. Lakshminarayanan, Eds., chapter 5, CRC Press, London, UK, 2007.
- [6] P. Cheben, D.-X. Xu, S. Janz, and A. Del age, "Scaling down photonic waveguide devices on the SOI platform," in *VLSI Circuits and Systems*, vol. 5117 of *Proceedings of SPIE*, pp. 147–156, Maspalomas, Spain, May 2003.
- [7] S. Janz, P. Cheben, A. Del age, et al., "Silicon-based integrated optics: waveguide technology to microphotonics," in *Proceedings of the Materials Research Society Symposium (MRS '04)*, vol. 832, pp. 3–14, Boston, Mass, USA, November-December 2004, F1.1.
- [8] P. Cheben, J. H. Schmid, A. Del age, et al., "A high-resolution silicon-on-insulator arrayed waveguide grating microspectrometer with sub-micrometer aperture waveguides," *Optics Express*, vol. 15, no. 5, pp. 2299–2306, 2007.
- [9] A. Densmore, D.-X. Xu, P. Waldron, et al., "A silicon-on-insulator photonic wire based evanescent field sensor," *IEEE Photonics Technology Letters*, vol. 18, no. 23, pp. 2520–2522, 2006.
- [10] A. Densmore, D.-X. Xu, S. Janz, et al., "Spiral-path high-sensitivity silicon photonic wire molecular sensor with temperature-independent response," *Optics Letters*, vol. 33, no. 6, pp. 596–598, 2008.
- [11] G. Z. Masanovic, V. M. N. Passaro, and G. T. Reed, "Dual grating-assisted directional coupling between fibers and thin semiconductor waveguides," *IEEE Photonics Technology Letters*, vol. 15, no. 10, pp. 1395–1397, 2003.
- [12] F. Van Laere, T. Claes, J. Schrauwen, et al., "Compact focusing grating couplers for silicon-on-insulator integrated circuits," *IEEE Photonics Technology Letters*, vol. 19, no. 23, pp. 1919–1921, 2007.
- [13] J. Schrauwen, F. Van Laere, D. Van Thourhout, and R. Baets, "Focused-ion-beam fabrication of slanted grating couplers in silicon-on-insulator waveguides," *IEEE Photonics Technology Letters*, vol. 19, no. 11, pp. 816–818, 2007.
- [14] G. Roelkens, D. Van Thourhout, and R. Baets, "High efficiency silicon-on-insulator grating coupler based on a poly-silicon overlay," *Optics Express*, vol. 14, no. 24, pp. 11622–11630, 2006.
- [15] B. Wang, J. Jiang, and G. P. Nordin, "Embedded slanted grating for vertical coupling between fibers and silicon-on-insulator planar waveguides," *IEEE Photonics Technology Letters*, vol. 17, no. 9, pp. 1884–1886, 2005.
- [16] V. R. Almeida, R. R. Panepucci, and M. Lipson, "Nanotaper for compact mode conversion," *Optics Letters*, vol. 28, no. 15, pp. 1302–1304, 2003.
- [17] A. Del age, S. Janz, B. Lamontagne, et al., "Monolithically integrated asymmetric graded and step-index couplers for microphotonic waveguides," *Optics Express*, vol. 14, no. 1, pp. 148–161, 2006.
- [18] J. K. Doyle and A. P. Knights, "Design and simulation of an integrated fiber-to-chip coupler for silicon-on-insulator waveguides," *IEEE Journal on Selected Topics in Quantum Electronics*, vol. 12, no. 6, pp. 1363–1370, 2006.
- [19] P. Cheben, D.-X. Xu, S. Janz, and A. Densmore, "Subwavelength waveguide grating for mode conversion and light coupling in integrated optics," *Optics Express*, vol. 14, no. 11, pp. 4695–4702, 2006.
- [20] J. H. Schmid, P. Cheben, S. Janz, J. Lapointe, E. Post, and D.-X. Xu, "Gradient-index antireflective subwavelength structures for planar waveguide facets," *Optics Letters*, vol. 32, no. 13, pp. 1794–1796, 2007.
- [21] S. M. Rytov, "Electromagnetic properties of a finely stratified medium," *Soviet Physics JETP*, vol. 2, no. 3, pp. 466–475, 1956.
- [22] D. H. Raguin and G. M. Morris, "Analysis of antireflection-structured surfaces with continuous one-dimensional surface profiles," *Applied Optics*, vol. 32, no. 14, pp. 2582–2598, 1993.
- [23] M. C. Y. Huang, Y. Zhou, and C. J. Chang-Hasnain, "A surface-emitting laser incorporating a high-index-contrast subwavelength grating," *Nature Photonics*, vol. 1, no. 2, pp. 119–122, 2007.
- [24] K. O. Hill, B. Malo, F. Bilodeau, D. C. Johnson, and J. Albert, "Bragg gratings fabricated in monomode photosensitive optical fiber by UV exposure through a phase mask," *Applied Physics Letters*, vol. 62, no. 10, pp. 1035–1037, 1993.

Research Article

Hybrid Silicon Photonics for Low-Cost High-Bandwidth Link Applications

B. Jonathan Luff, Dazeng Feng, Daniel C. Lee, Wei Qian, Hong Liang, and Mehdi Asghari

Kotura Inc., 2630 Corporate Place, Monterey Park, CA 91754, USA

Correspondence should be addressed to B. Jonathan Luff, jluff@kotura.com

Received 22 December 2007; Accepted 27 March 2008

Recommended by D. Lockwood

Current discrete optical solutions for high data-rate link applications, even with potentially high manufacturing volumes, are too costly. Highly integrated, multifunction modules are a key part of the solution, reducing size and cost while providing improved reliability. Silicon, with its proven manufacturability and reliability, offers a solid foundation for building a cost-efficient path to successful products. In this paper, recent work on the development of silicon photonic enabling components for multichannel high data-rate links is presented.

Copyright © 2008 B. Jonathan Luff et al. This is an open access article distributed under the Creative Commons Attribution License, which permits unrestricted use, distribution, and reproduction in any medium, provided the original work is properly cited.

1. INTRODUCTION

High-speed consumer connections are becoming more prevalent due to the introduction of newer services such as online video, HDTV, IPTV, and the increase of personalized data content. This is leading to significant connectivity bottlenecks in the network infrastructure of, for example, datacenters, campus networks, and storage area networks. Internet exchanges and network centers have expanded to as many as 100 000 optical fibers routing traffic at speeds of 10 Gbps. The availability of cost-effective interface solutions operating at data rates of multiples of 10 Gbps or above over a single fiber will enable the proliferation of these new services by greatly reducing the wiring complexity, instrumentation, and operating cost in high-capacity fiber-optic networks. In this paper, we discuss the development of components based on a silicon photonics hybrid platform that will create a compact and low-cost solution for multiple channel transmission over single mode fiber. Initial work focuses on a 10 channel/10 Gbps per channel solution, but extension of channel count and/or modulation speed is envisioned, enabling aggregate data rates of up to 1 Tbps for a 25 channel, 40 Gbps solution.

The approach is illustrated in Figure 1. On the transmit (Tx) side of the link, light at multiple wavelengths from

a hybridized laser array is multiplexed onto a single fiber. After transmission over the fiber, the light is coupled onto the receiver (Rx) chip where the wavelength channels are demultiplexed and detected using a hybridized photodiode array. The silicon platform is able to support the formation of low-loss RF traces onchip to enable space-efficient positioning of driver and receiver electronics. Transimpedance amplifiers (TIAs) may also be hybridized onchip if that is appropriate to a particular packaging solution. Laser diode output power monitoring may be accomplished by hybridized back-facet monitor photodiodes. Alternatively, as illustrated in Figure 1, the silicon photonics platform offers the option of front-facet monitoring through the fabrication of tap coupler and the hybridization of PIN photodiodes [1]. It is also possible to monolithically fabricate monitor diodes in silicon using defect engineering [2]. A useful function that may be included in future devices is per channel variable attenuation, a well-established monolithic functional element in silicon technology [3].

The refractive index of silicon is similar to that of active materials such as GaAs and InP, facilitating efficient coupling between silicon waveguides, and hybridized active devices such as lasers and photodetectors. For powered devices such as lasers, the high thermal conductivity of silicon enables efficient heat removal and good equalization of temperature across a chip.

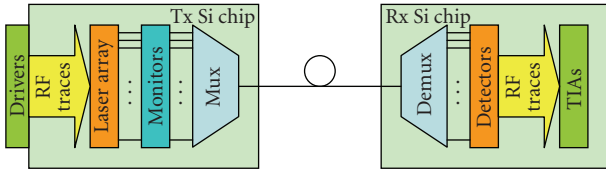


FIGURE 1: Multichannel optical transmission link.

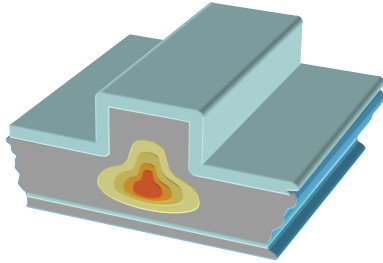


FIGURE 2: Silicon-on-insulator waveguide structure.

The basic silicon-on-insulator (SOI) waveguide ridge structure used in this work is shown in Figure 2. Vertical confinement is provided by the buried layer of oxide inside the wafer (SOI) and a top layer of oxide deposited on the waveguide during fabrication. Lateral confinement is provided by the ridge structure. Such waveguides can be designed to be single mode based on correct choice of ridge height and width.

The manufacturing process for the basic waveguide is based on pattern definition by an appropriate masking layer and subsequent photolithography. RIE etch is used to achieve the required topology. Following the removal of the masking layer, an oxide cladding layer is deposited followed by a protective nitride thin film.

A key challenge for a Si photonics platform is coupling light efficiently on and off the chip. The large index of Si drives small waveguide dimensions, which enables highly compact structures, but in turn can cause high beam divergence off chip and high mode mismatch to other optical components such as fibers. Although not implemented for the devices described in this paper, the Si photonics platform enables the fabrication of three dimensional tapers (Figure 3) that can significantly reduce fiber coupling loss to standard single-mode fiber. If necessary, taper structures can also be used to improve coupling efficiency to hybridized optical components.

2. SILICON MUX AND DEMUX

Silicon-based multiplexers and demultiplexers are the critical passive elements in a multichannel link system using a single fiber. The key challenges are the design and fabrication of low loss, low crosstalk, and small footprint devices. The echelle grating-based design (Figure 4) is favored for use in the link architecture because of its much smaller footprint compared to, for example, an arrayed waveguide grating (AWG) design [4]. A wavelength channel spacing of 20

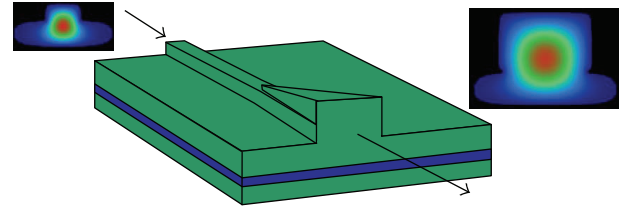


FIGURE 3: 3D mode transforming taper.

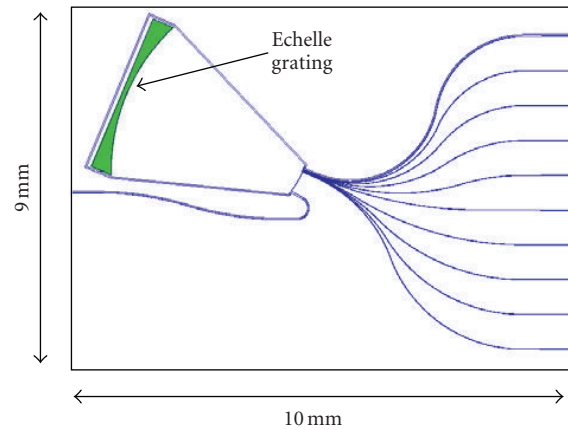


FIGURE 4: 10-channel echelle grating demultiplexer in silicon.

nm was chosen for fabrication of a demonstration device. This channel spacing is typically used in coarse wavelength division multiplexing (CWDM) systems, and will ensure sufficient passband width to accommodate the spectral deviation of laser wavelength and filter passband position due to temperature and polarization variations.

The loss of echelle grating arises mainly from nonvertical grating facets and facet roughness. It is difficult to make both a smooth and vertical grating facet because of fabrication limitations. Grating performance variation due to wall roughness and verticality are shown in Figures 5(a) and 5(b), respectively. For this work, the roughness of the grating facets is estimated from SEM measurements as ~ 11 nm, and the verticality as ~ 1.5 degrees. Projected process developments are likely to improve these values to ~ 7 nm and 0.5 degrees, respectively.

Another important factor influencing the loss of the mux and demux element is the rounding of the grating teeth element within the echelle grating design. This can be reduced with better photolithographic tools and etching processes as indicated in Figure 6.

Nonguided stray light and scattered light from the rough grating facet can generate high optical crosstalk in an echelle grating. To reduce crosstalk and enhance performance, proprietary absorber structures were utilized.

To make the silicon demux polarization independent, a relatively large silicon waveguide core size is used (waveguide height and waveguide width are both $\sim 3 \mu\text{m}$). The buried oxide thickness is approximately $0.4 \mu\text{m}$. The drawback of using large area waveguides is that the minimum waveguide bending radius for single mode operation is large (~ 5 mm)

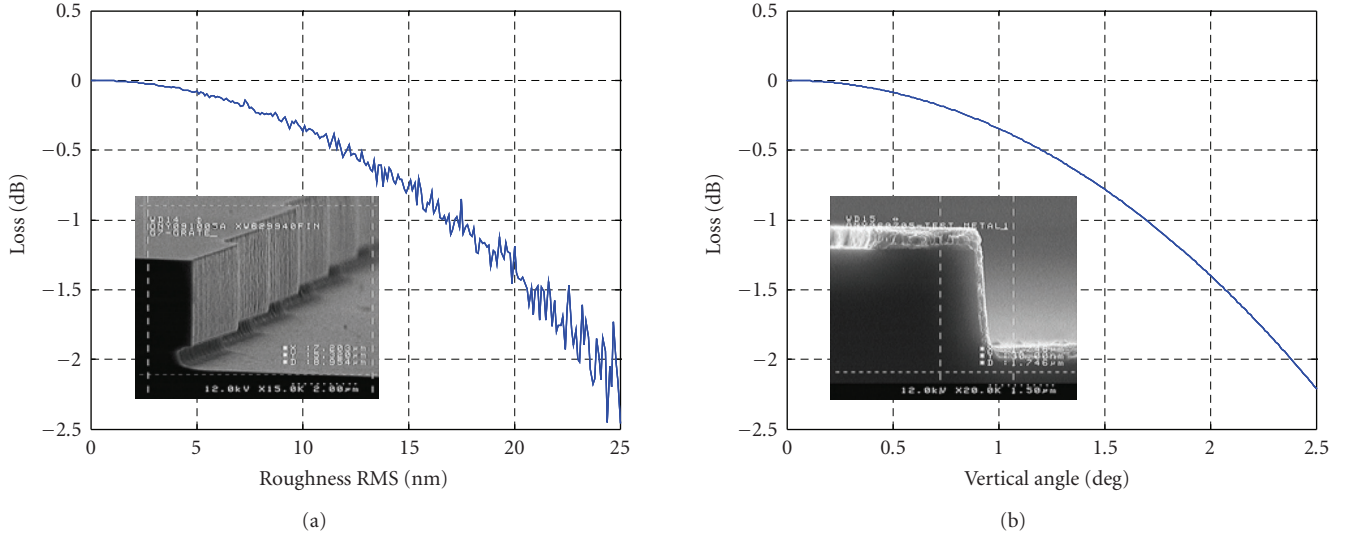


FIGURE 5: Effect of grating wall roughness (a) and verticality (b) on grating insertion loss.

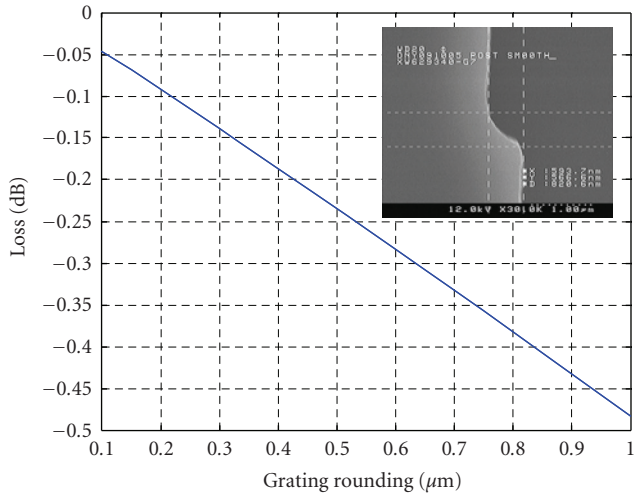


FIGURE 6: Effect of grating teeth roundness on insertion and anticipated potential improvement.

and although the echelle grating itself can be very small, the waveguide fan-in and fan-out can take up much of the available space because of the bend radius limitation. For this work, sharp waveguide bends using a deep-etched multimode curved waveguide with tapered transitions into the bend to maintain power in the fundamental mode were used. Using this method, the bending radius was reduced to approximately 0.25 mm so that the overall silicon mux and demux footprints were reduced to $<1 \text{ cm}^2$ for 10-channel devices with 20 nm channel spacing. Because the outputs of the receive waveguides in the architecture of Figure 1 can be coupled directly to hybridized photodiodes, for the demux design a flat-top output spectrum was produced by using multimode output waveguides. Measured transmission spectra from fabricated multiplexer and demultiplexer devices are shown in Figure 7.

The mux demonstrated 6.5 dB insertion loss over the passband of 6.4 nm; PDL was $<0.5 \text{ dB}$. Because the refractive index of silicon has a similar temperature variation to that of InP, this passband is sufficient to ensure low transmission loss is maintained over a wide temperature change because the mux passband will track the drift in the emission wavelength of the DFB laser. Figure 8 shows expected temperature variations for typical InP/InGaAsP DFB lasers from two different manufacturers compared with the calculated variation for a silicon multiplexer device. For comparison, the much smaller temperature variation expected for a silica-based device is included. A large channel spacing ensures that only very coarse and thus low-cost heater-based temperature control solution is required for stable operation over normal ambient conditions (typically 0–70°C). The demux device shown in Figure 7(b) demonstrated 4 dB insertion loss over a passband of 12 nm, $<0.5 \text{ dB}$ PDL, and better than 22 dB crosstalk.

Although a 10 channel device has been demonstrated, the design can be readily extended to higher channel counts. The optimum channel count for a given application will depend on multiple factors including per channel modulation speed, laser wavelength range, required bandwidth over a given temperature range, and minimum chip footprint.

3. HYBRID INTEGRATION

3.1. Laser

To produce an interface for the highly efficient optical transition between a semiconductor laser and the silicon waveguide, the mode profile mismatch and surface reflection between the laser and the waveguide should be reduced as much as possible. This modal mismatch can be improved by appropriate tailoring of the laser structure.

The silicon ridge waveguide structure can be optimized to obtain low coupling loss to the laser. Even at $5 \mu\text{m}$ separation between the two facets, the coupling loss can potentially

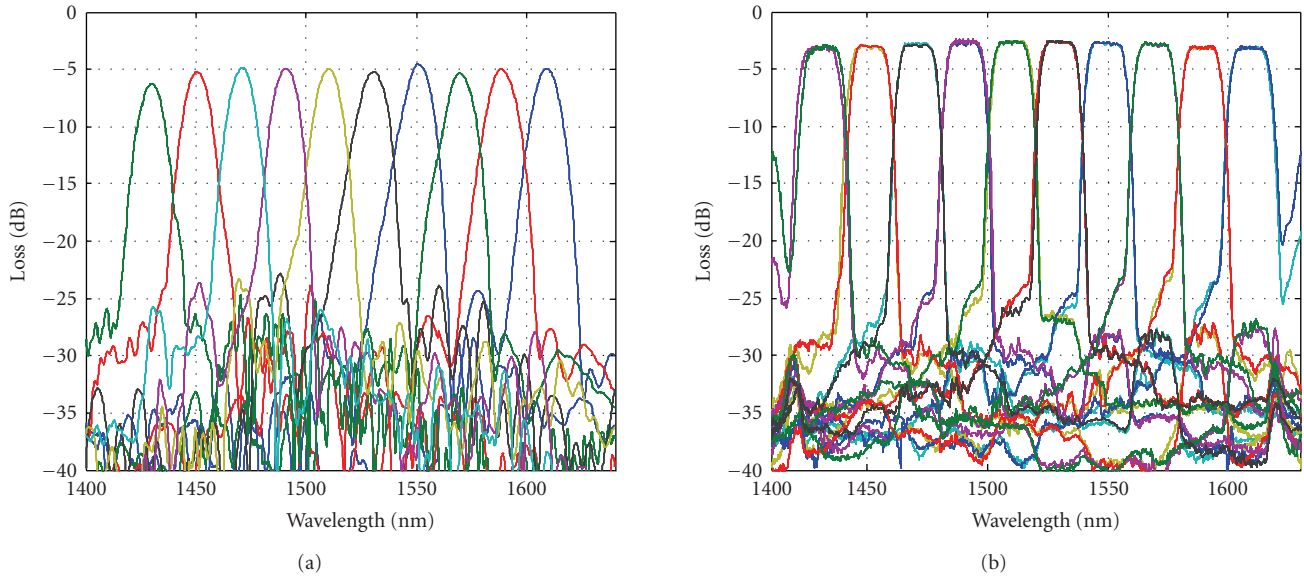


FIGURE 7: (a) Multiplexer TE transmission spectra; (b) demultiplexer transmission spectra for TE and TM polarization states.

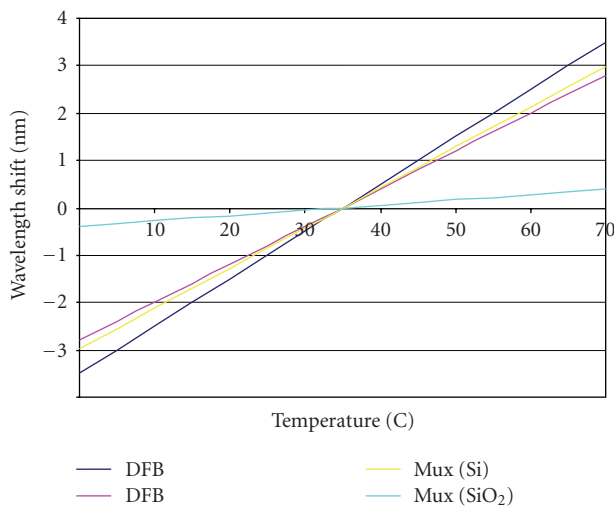


FIGURE 8: Wavelength shift as a function of temperature for typical DFB lasers compared to that of the passband of silicon- and silica-based multiplexers.

be lower than 3 dB for silicon waveguides with different ridge width ranging from 3 to 7 μm . A specific ridge width within this range can thus be chosen to well match the diverging laser mode and provide some tolerance to alignment errors for a targeted gap size. Coupling loss can theoretically be less than 1 dB if the gap size (z -direction gap) is smaller than 2 μm . However, the coupling of the laser to the waveguide in the direction perpendicular to the plane of the chip (y) and along the plane of the chip (x) requires alignment to a few tenths of a micron to obtain low coupling loss. Figure 9 shows the calculated coupling loss taking into account possible alignment errors as a function of silicon waveguide width (W) for a typical DFB laser.

To reduce the amount of reflected light coupled back into the laser cavity, the waveguide facet can be etched in such a way so that it is tilted at an angle ($>10^\circ$) away from the optical axis of the laser beam. A nitride film of thickness ~ 200 nm on the waveguide surface further reduces the reflectivity of the facet. When the laser facet is 4 μm away, the total reflected light coupled back into the laser can be kept below -30 dB over a wavelength range of 200 nm (Figure 10).

3.2. Photodetector

The effective aperture of a high-speed (≥ 10 Gbps) detector is typically smaller than 30 μm in diameter to obtain low capacitance and large bandwidth. To prevent large beam divergence and achieve high detection efficiency, the gap between the output facet of a waveguide and the detector surface must be as small as possible.

The electronic connection employing conventional wire bonds between the detector die to the transimpedance amplifier (TIA) circuits may introduce too much unwanted parasitic capacitance and inductance that limits the speed of the receiver, especially for higher than 10 Gbps detection speed. Two possible methods of hybridization can be considered: edge coupling and flip-chip coupling.

When the detector is vertically attached to the edge of the waveguide chip, the waveguide facet can be almost in direct contact with the detector surface. The detector to waveguide alignment is relatively simple because the effective detection area can be a few times larger than the waveguide mode size. The relatively large aperture of the photodiode covers the entire mode profile at the waveguide facet and ensures high optical detection efficiency. A ceramic submount can be used to fasten the detector (e.g., at the p-side) with necessary metal contacts and traces that can readily be connected to a separated amplifier IC chip through wire bonding. The main disadvantage of this

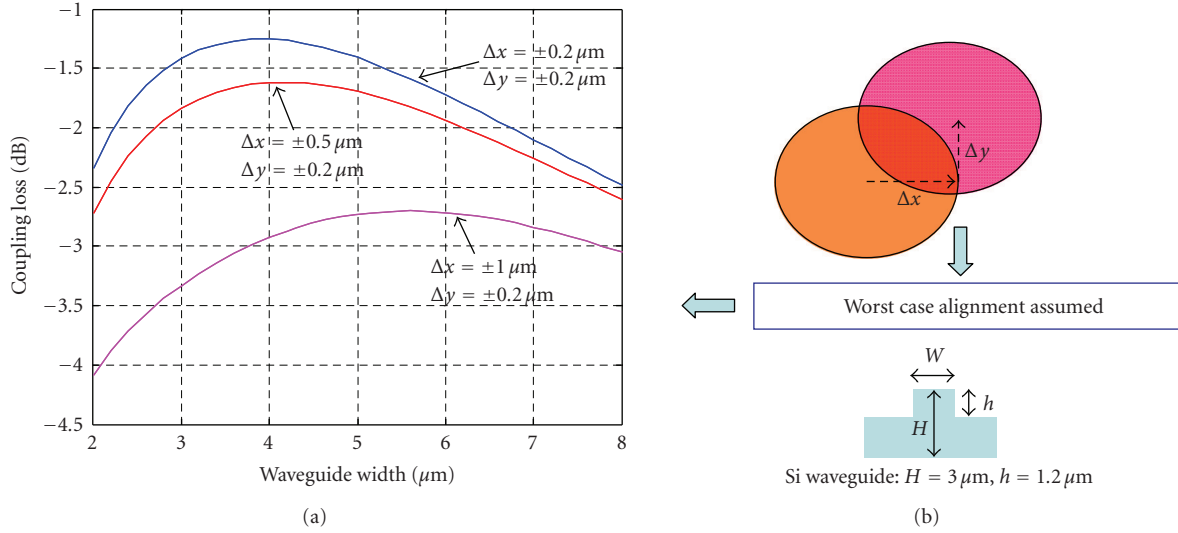


FIGURE 9: Calculated DFB laser coupling loss as a function of silicon waveguide width W for various alignment errors in x and y .

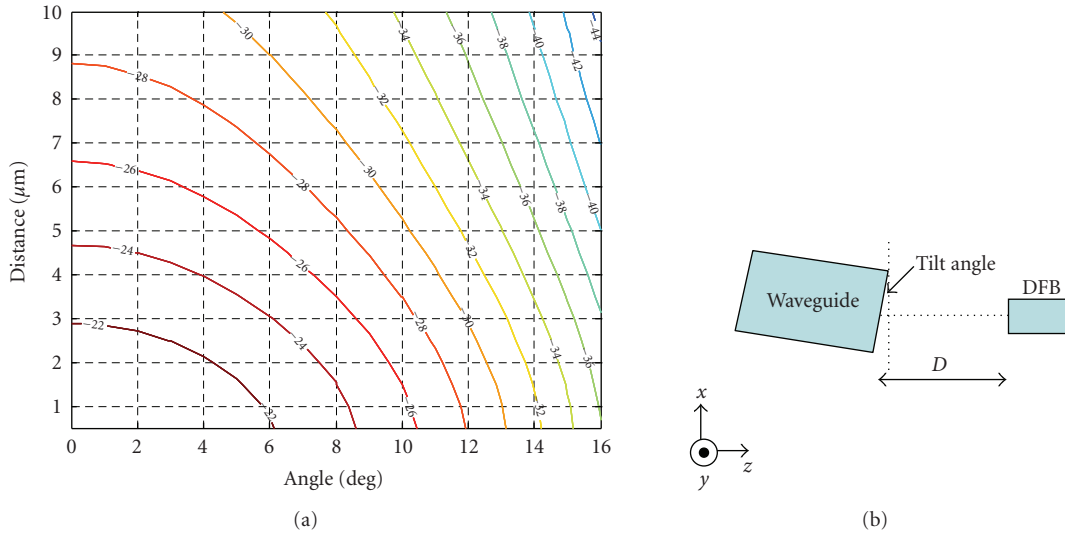


FIGURE 10: Calculated back-reflection of light into the laser as a function of waveguide tilt angle and z -separation (D).

approach is that the waveguide edge needs to be polished, and hence it is not suitable for low-cost, high-volume manufacture.

A more manufacturable approach is to flip-chip bond the detector onto the silicon chip surface (p-side up), where an etched reflective mirror redirects the output beam to the detector surface, as shown in Figure 11. A smooth $\langle 111 \rangle$ direction crystal plane with a 54.7° angle results from the anisotropic etching on the silicon surface; it is coated with aluminum to enhance reflectivity. The etched waveguide facet is coated with a thin nitride antireflection film to minimize the reflection loss at the silicon-to-air interface.

All electronic contacts can be made through the solder pads and metal traces directly plated on the silicon surface. A separate amplifier IC chip with conducting via holes can

be attached onto the silicon chip surface to facilitate low parasitic electronic contact for high-speed operation. Alternatively, the detector can be integrated with the amplifier circuits before being mounted on the silicon chip.

4. POWER BUDGET

The available power budget for a point-to-point transmission system determines the optical loss performance targets for the components making up the system. The maximum optical loss permissible for the system is determined by the output power of the laser source and the sensitivity of the detector. However, the sensitivity of the detector is not only dependent upon the speed, but also on the extinction of the source signal. For example, if the output power of a DFB laser is $+6$ dBm and the maximum sensitivity of a PIN detector

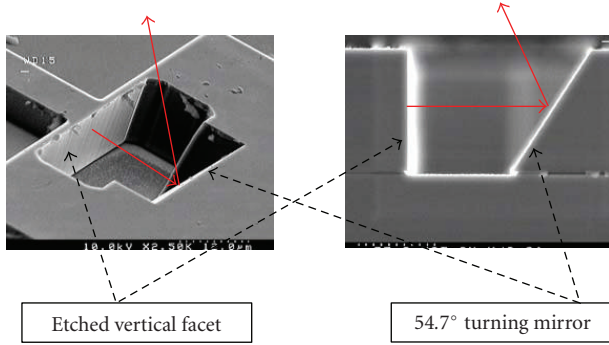


FIGURE 11: SEM photos of an etched waveguide facet and turning mirror.

TABLE 1: Loss budget estimation for a 2 km transmission link.

Source of loss	10×10 Gbps DFB
Laser chip power	6 dBm
To Mux	-3
In Mux	-6.5
Mux to fiber	-1.5
Fiber to DeMux	-1.5
DeMux	-4
DeMux to PD	-0.5
Maximum fiber loss (2 km)	-2
Signal quality (CDP/PMD)	-2
Power to detector	-15 dbm
Detector sensitivity	-17 dbm
Margin	2 db

is -17 dBm at 10 Gbps at an extinction of ~ 5 dB, then the maximum optical loss budget is $+23$ dB for 10×10 Gbps transmission. Table 1 summarizes the projected loss budget assuming use of the mux/demux components demonstrated in this paper.

5. CONCLUSIONS

We have discussed the feasibility of using the silicon photonics platform to provide a viable route to low-cost and compact single-fiber transmission solutions through hybridization of actives with low coupling loss and high-performance mux-demux capability. Although this work concentrated on a 10-channel solution and 10 Gbps data rate per channel, implementation with a greater number of channels and higher data rates is readily achievable.

ACKNOWLEDGMENTS

The authors would like to thank Bob Hartman and Uzi Koren of CyOptics Inc. for technical discussions on the performance of active devices and loss budget. A portion of this work is being funded by the Advanced Technology Program managed by NIST.

REFERENCES

- [1] B. T. Smith, H. Lei, C.-C. Kung, D. Feng, J. Yin, and H. Liang, "Integrated silicon photonic circuit: monolithic 8-channel modulator, tap, vertical coupler, and flip-chip mounted photodetector array," in *Silicon Photonics*, vol. 6125 of *Proceedings of SPIE*, San Jose, Calif, USA, January 2006.
- [2] A. P. Knights, J. D. B. Bradley, S. H. Gou, and P. E. Jessop, "Silicon-on-insulator waveguide photodetector with self-ion-implantation-engineered-enhanced infrared response," *Journal of Vacuum Science & Technology A*, vol. 24, no. 3, pp. 783–786, 2006.
- [3] B. Jalali and S. Fathpour, "Silicon photonics," *Journal of Lightwave Technology*, vol. 24, no. 12, pp. 4600–4615, 2006.
- [4] S. Bidnyk, D. Feng, A. Balakrishnan, et al., "Silicon-on-insulator-based planar circuit for passive optical network applications," *IEEE Photonics Technology Letters*, vol. 18, no. 22, pp. 2392–2394, 2006.

Review Article

On-Chip All-Optical Switching and Memory by Silicon Photonic Crystal Nanocavities

Masaya Notomi, Takasumi Tanabe, Akihiko Shinya, Eiichi Kuramochi, and Hideaki Taniyama

NTT Basic Research Laboratories, NTT Corporation, 3-1 Morinosato-Wakamiya, Atsugi 2430198, Japan

Correspondence should be addressed to Masaya Notomi, notomi@will.brl.ntt.co.jp

Received 23 December 2007; Accepted 13 April 2008

Recommended by D. Lockwood

We review our recent studies on all-optical switching and memory operations based on thermo-optic and carrier-plasma nonlinearities both induced by two-photon absorption in silicon photonic crystal nanocavities. Owing to high- Q and small volume of these photonic crystal cavities, we have demonstrated that the switching power can be largely reduced. In addition, we demonstrate that the switching time is also reduced in nanocavity devices because of their short diffusion time. These features are important for all-optical nonlinear processing in silicon photonics technologies, since silicon is not an efficient optical nonlinear material. We discuss the effect of the carrier diffusion process in our devices, and demonstrate improvement in terms of the response speed by employing ion-implantation process. Finally, we show that coupled bistable devices lead to all-optical logic, such as flip-flop operation. These results indicate that a nanocavity-based photonic crystal platform on a silicon chip may be a promising candidate for future on-chip all-optical information processing in a largely integrated fashion.

Copyright © 2008 Masaya Notomi et al. This is an open access article distributed under the Creative Commons Attribution License, which permits unrestricted use, distribution, and reproduction in any medium, provided the original work is properly cited.

1. INTRODUCTION

It used to be a great challenge to tightly confine light in a wavelength-scale volume, which had limited the capability of photonics technologies in various aspects. Recently, however, an optical resonator with ultrahigh- Q (~ 1 million) and small volume ($\sim (\lambda/n)^3$) becomes possible by employing the state-of-the-art photonic crystal technologies [1–6]. Figure 1 shows an example of high- Q nanocavities, which we have recently demonstrated in silicon photonic crystals. This particular cavity shows a theoretical Q of over 10^8 and an experimental Q of 1.3 million with a mode volume of $1.5(\lambda/n)^3$ [4, 7]. These values are hardly available in optical systems other than photonic crystals. Various forms of light-matter interactions are expected to be enhanced in such high- Q nanocavities having large Q/V ratio [8]. Among them, in this article, we focus on application to all-optical switching and memory operations based on optical nonlinear interaction. Especially for this, we investigate all-optical operations based on carrier-induced nonlinearity and examine the features of photonic crystal nanocavities for such applications.

As has been studied in various forms, all-optical switches can be realized using optical resonators, where a control optical pulse induces a resonance shift via optical nonlinear effects. For such a resonator-based switch, there is a two-fold enhancement in terms of the switching power if a small cavity with a high- Q is employed. First, the light intensity inside the cavity should be proportional to Q/V . Second, the required wavelength shift is proportional to $1/Q$. In total, the switching power should be reduced by (Q^2/V) , which can be significantly large for photonic crystal nanocavities [9]. Although the switching mechanism itself is basically similar to that of previous resonator-based switches, such as nonlinear etalons [10], this large enhancement has had an important impact on optical integration since most optical switching components require too much power for realistic integration. Furthermore, in the case of carrier-induced nonlinearity or thermo-optic nonlinearity, the smallness of the device naturally leads to fast operation speed, since the relaxation time of such processes normally depends on the size. As we will show below, this advantage is significant for wavelength-sized cavities.

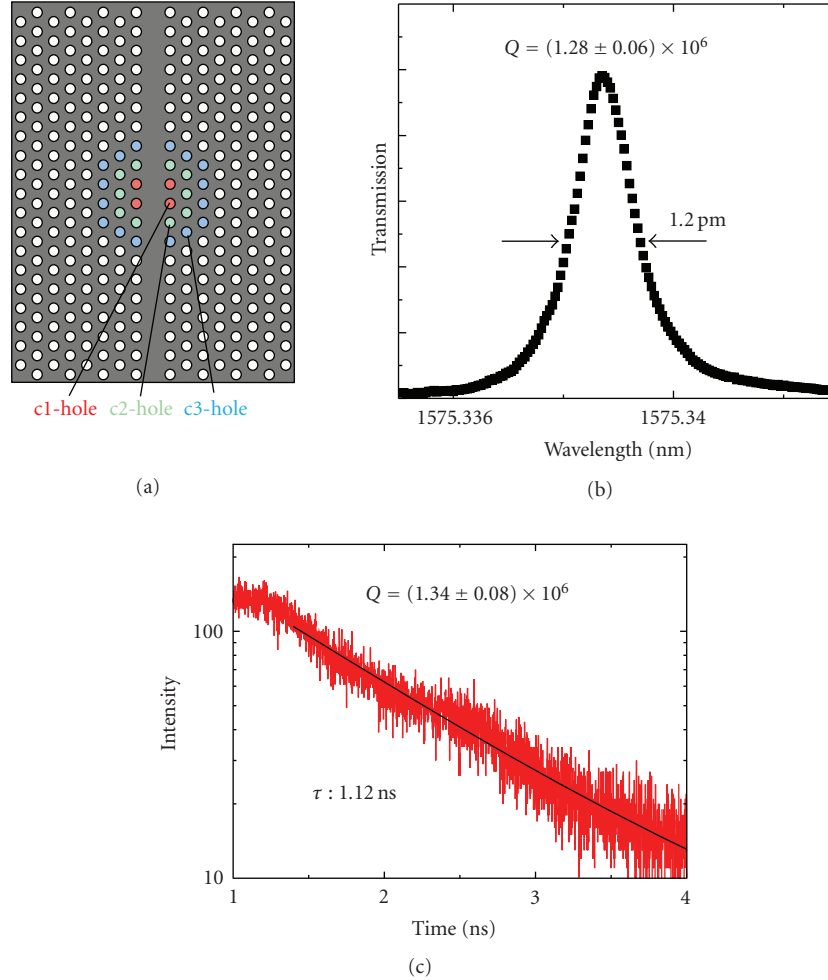


FIGURE 1: Width-modulated, line-defect photonic crystal cavities. (a) Cavity design. The cavity has the theoretical Q . The hole shifts are typically 9 nm (red holes), 6 nm (green holes), and 3 nm (blue holes). (b) Spectral measurement of a nanocavity fabricated in a silicon hexagonal air-hole photonic slab with $a = 420$ nm and $2r = 216$ nm. The transmission spectrum of a cavity with a second-stage hole-shift. The inner and outer hole-shifts are 8 and 4 nm, respectively. (c) Time-domain ring-down measurement. The time decay of the output light intensity from the same cavity as (b). Details can be found in the reference.

In addition, resonator-based optical switches are well known to exhibit optical bistability [10] and thus they can be used for optical memory and all-optical logic [11]. Such functionality is one of the most important functions missing from existing photonic devices. Thus, we believe that all-optical bistable switches based on photonic crystal cavities are important candidates for future optical integration.

In this paper, we investigate all-optical switching and memory action in silicon photonic crystal nanocavity devices. First, we study the switching action using thermo-optic nonlinearity. Next, we investigate similar switching action using much faster carrier-plasma nonlinearity. Thirdly, we analyze the effect of carrier relaxation process in the switching action and made an attempt to further decrease the relaxation time by ion implantation. Furthermore, we demonstrate bistable memory action employing basically the same nanocavity devices and present an example of design for on-chip all-optical logic circuits consisting of two bistable nanocavities.

2. ALL-OPTICAL BISTABLE SWITCHING BY THERMO-OPTIC NONLINEARITY

As described above, photonic crystal nanocavities have a promising potential for all-optical switching applications. To experimentally confirm this, we have investigated all-optical bistable switching operations employing the thermo-optic nonlinearity induced by two-photon absorption (TPA) in silicon [12]. For this study, we employed an end-hole shifted four-point Si photonic crystal cavity integrated with input/output photonic crystal waveguides (shown in Figure 2(a)) [13, 14]. Figure 2(b) shows transmission spectra with various input power at $1.5\mu\text{m}$ wavelength region. As clearly seen in the graph, the transmission spectrum is shifted to longer wavelength (red-shifted). This shift is due to thermo-optic nonlinearity induced by two-photon absorption in the cavity. At input power higher than $10\mu\text{W}$, there is an abrupt kink in the spectrum. This kink corresponds to bistable switching. To see this more

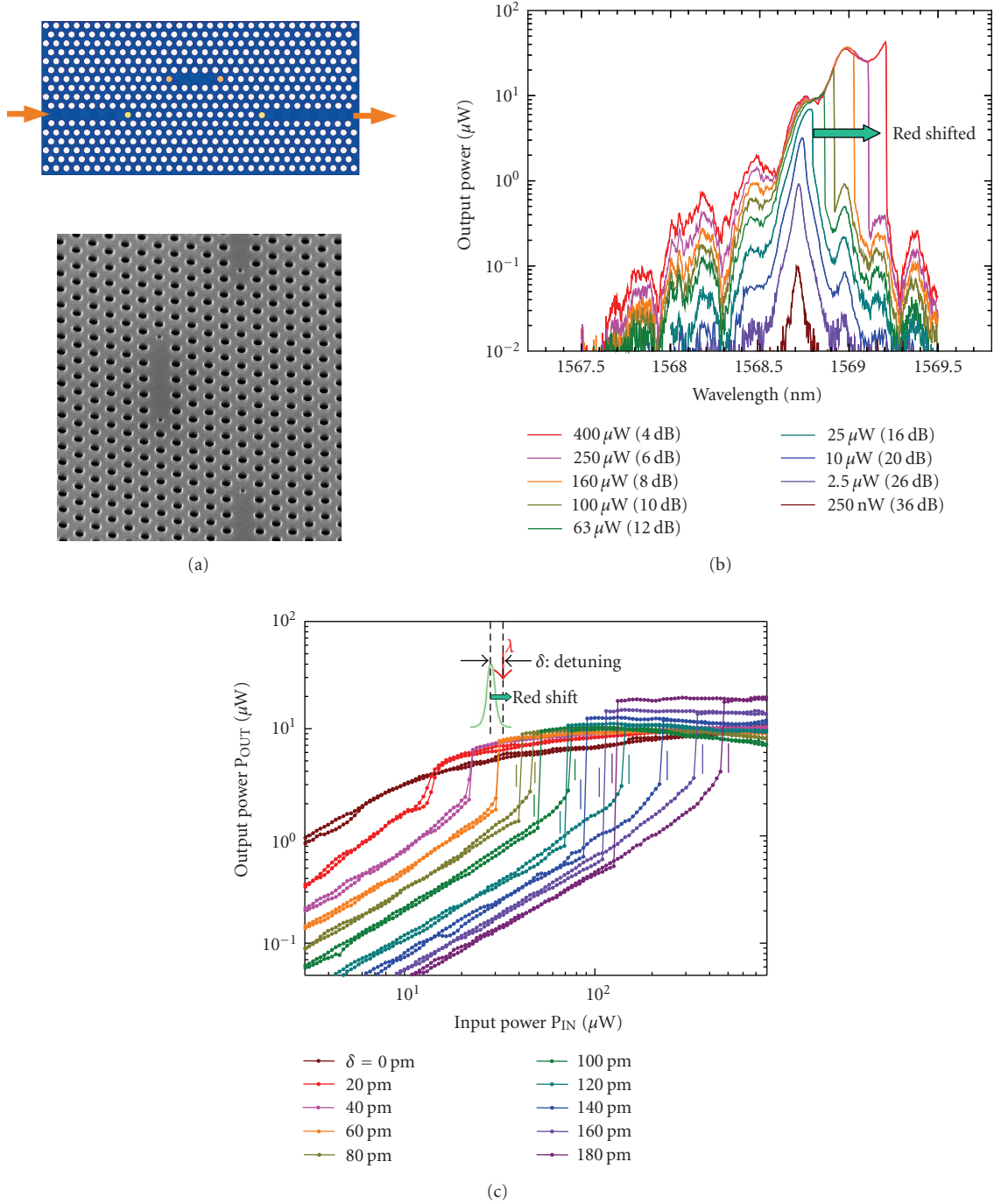


FIGURE 2: All-optical bistable switching in a silicon hexagonal air-hole photonic crystal nanocavity (end-hole shifted four-point defect cavity) realized by the thermo-optic nonlinearity induced by two-photon absorption in silicon. (a) Schematic of the sample and a scanning electron micrograph of the sample. $a = 420 \text{ nm}$, $2r = 0.55a$. The radius of end-holes of the cavity is $0.125a$. $V = 0.102 \mu\text{m}^3$. The radius of end-holes of the waveguide is $0.15a$. (b) Intensity-dependent transmission spectra taken by a tunable laser in the up-sweep condition. Q in the linear regime is 33400. (c) Output power versus input power for various detuning values. The nonlinear regime starts from $10 \mu\text{W}$, and the bistable regime starts from $40 \mu\text{W}$.

directly, we measured the output power as a function of the input power at various detuning conditions, as shown in Figure 2(c). Now, it is clear that this device exhibits bistable switching. The most noteworthy point regarding this switching is its switching power, which is as small as $40 \mu\text{W}$.

This value is remarkably smaller than that of bulk-type thermo-optic nonlinear etalons (a few to several tens mW) [15] and also smaller than that of recent miniature-sized thermo-optic silicon microring resonator devices ($\sim 0.8 \text{ mW}$) [16]. In addition, it is important to note that TPA occurs only in the

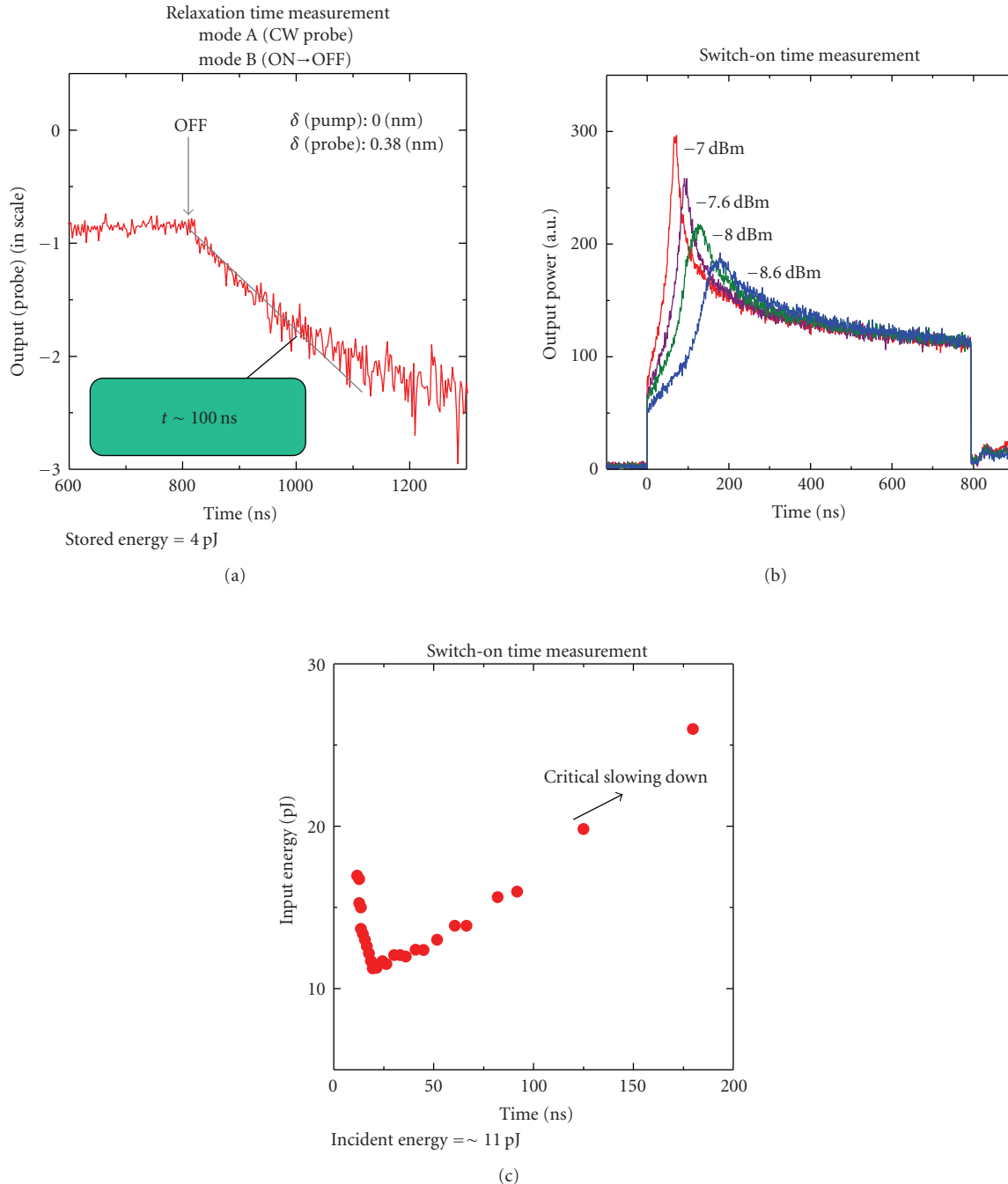


FIGURE 3: Temporal response of thermo-optic switching. (a) Switch-off. Temporal response of the probe output. At $t = 800$ nanoseconds, the pump signal was switched off. The input instantaneous power for the pump is $64 \mu\text{W}$. The pulse width and period are 400 nanoseconds and 40 microseconds. The exponential fit gives a decay time of approximately 100 nanoseconds. (b) Switch-on operation for various input power. (c) Incident energy required for the switch-on operation estimated from the product of the incident energy and the time required for switch-on in (b).

cavity (the linear absorption of silicon at this wavelength is negligible), and, therefore, we can easily integrate this device with transparent waveguides in the same chip.

Our cavity shown in Figure 2(a) was intentionally designed to have two resonant modes, and, therefore, we can perform all-optical switching using independent two inputs with different wavelengths (signal and control),

which is normally required for signal processing. Since bistable switching for one resonant mode should influence the transmission intensity of the other resonant mode in the same cavity, we can easily realize such operation. As we reported in [12], we observe basically similar bistable switching behavior in the relation between the input power for the control mode and the output power for the signal

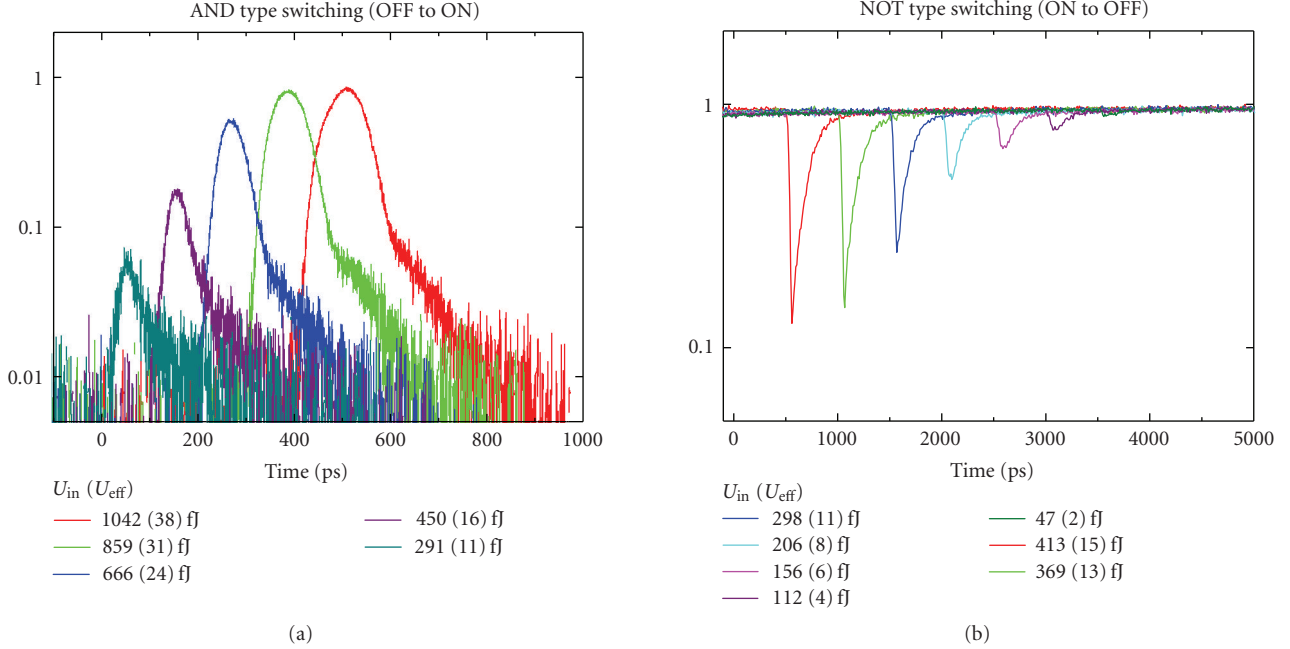


FIGURE 4: All-optical switching in a silicon photonic crystal nanocavity (end-hole shifted four point cavity) realized by carrier-plasma nonlinearity induced by two-photon absorption in silicon. Q for the control mode is 11500, and Q for the signal mode is 23000. (a) AND-type switching at various control pulse energies with the detuning of -0.3 nm. (b) NOT-type switching at various control pulse energies with no detuning. Each line is shifted by 500 picoseconds.

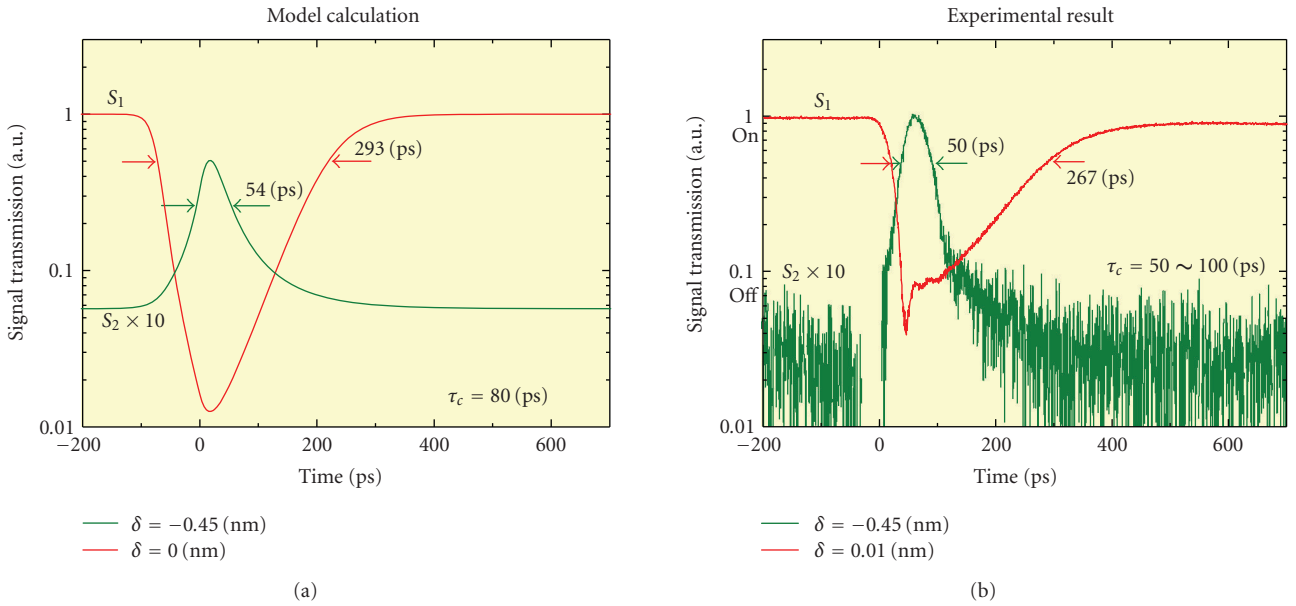


FIGURE 5: Comparison between the rate-equation analysis and measurement result. We modeled the cavity resonance as a Lorentzian function whose center wavelength is shifting in proportion to the carrier density. (a) Calculation. (b) Experiment.

mode. This operation is basically what we expect for the so-called all-optical transistors, and will be basis for various logic functions. The detail of this operation is described in [12]. For example, we demonstrated that we can amplify an AC signal using this device.

Although the bistable operation itself is similar to that of nonlinear etalon switches, these photonic crystal switches can be clearly distinguished in terms of the operating power and capability for integration. The mode volume of this cavity is only approximately $0.1 \mu\text{m}^3$. This small footprint

itself is of course advantageous for integration, but it is also beneficial for reducing the switching speed because our device is limited by the thermal diffusion process. To demonstrate these characteristics, we measured temporal response of the operation for switch-off and switch-on processes, as shown in Figures 3(a) and 3(b). The relaxation time of our switch is approximately 100 nanoseconds, which is much shorter than that of conventional thermo-optic switches (\sim milliseconds). This amazingly fast thermo-optic switching is primarily due to the smallness of our cavity. In addition, we can estimate the required switching energy from the switch-on measurement. The deduced smallest value is as small as 11 pJ as shown in Figure 3(c).

3. ALL-OPTICAL SWITCHING BY CARRIER-PLASMA NONLINEARITY

These thermo-optic nonlinear bistable switches clearly demonstrate that large Q/V photonic crystal cavities are very effective in improving the operation power and speed. However, the speed itself is still not very fast, which is limited by the intrinsically slow thermo-optic effect. To realize much faster all-optical switches, here we employ another nonlinear effect, namely, the carrier-plasma effect [17]. This process is also based on the same TPA process in silicon. Thus most of the arguments concerning their advantages are similar to that for thermo-optic nonlinearity. For this experiment, we used similar photonic crystal cavity devices with a control pulse input. If the duration of the control pulse is sufficiently short, we can avoid thermal heating and may be able to observe only carrier-plasma nonlinearity. In fact, we observed a clear blue shift in the resonance when we injected a 6-picosecond pulse into this device, which is consistent with the expected shift induced by the carrier-plasma nonlinearity. Figure 4 shows the time-resolved output intensity for the signal mode when a 6-picosecond control pulse is input [17]. We observed clear all-optical AND-type switching from OFF to ON for the detuning of 0.45 nm (Figure 4(a)) and NOT-type switching from ON to OFF for the detuning of 0.01 nm (Figure 4(b)). The required switching energy is only a few hundred fJ, which is much smaller than that of ring-cavity-based silicon all-optical switches [18]. If we take the coupling efficiency between the cavity and waveguide into account, the actual pulse energy used for the switching is less than 10 fJ. This extremely small switching energy is attributed to large Q/V ratio in our cavity.

The switching time of our device is approximately from 50 picoseconds to 300 picoseconds depending on the detuning and control pulse energy. Considering the fact that the carrier lifetime in silicon is normally very long (\sim microseconds), this switching time is also surprisingly fast. This apparently indicates that the switching time is not limited by the carrier recombination time of bulk silicon. We analyzed the switching behavior employing simplified rate equations for the photon and carrier density in a photonic-crystal nanocavity incorporating the effective carrier relaxation time. We found that this simple model can reproduce the experimental result fairly well. Figure 5 shows simulated and experimental results for the same

parameter condition. In this calculation, we assumed the carrier relaxation time of 80 picoseconds. This suggests that the effective carrier relaxation time for this all-optical switch is in the range between 50 to 100 picoseconds. This fast carrier relaxation may be attributed to the short diffusion time for generated carriers. Note that the photon lifetime of our cavity is approximately 10 picoseconds, and thus the operation speed of our device is limited by the carrier relaxation time. This carrier relaxation time is much shorter than that in other silicon photonic microdevices [18]. That is, the small footprint of the device is again effective in improving the operating speed.

4. EFFECT OF CARRIER RELAXATION PROCESS ON SWITCHING OPERATION

In Section 3, we demonstrate that silicon all-optical switches based on carrier-plasma nonlinearity can operate at a significantly fast speed, which is attributed to the fast carrier relaxation process. We regard that this fast carrier relaxation is possibly due to the fact that the diffusion process is an efficient relaxation channel for nanocavities. To verify this explanation, we performed numerical simulations for the carrier diffusion process in silicon photonic crystal cavities [19]. In this simulation, we assumed an initial carrier distribution determined from the optical intensity distribution of the cavity mode, and numerically solved two-dimensional diffusion equations with assuming a realistic photonic crystal cavity structure which is the same as that used in the experiment. The side-wall nonradiative recombination process at the air-hole surface is incorporated in the equation as effective surface recombination rate (S), and the effect of the top-surface nonradiative recombination process is incorporated as an effective carrier lifetime parameter which is determined from another calculation for a simple slab. We calculated the time-dependent resonance wavelength shift using instantaneous carrier concentration in the cavity. The calculated snapshots of the carrier distribution at $t = 0, 8,$ and 24 picoseconds are shown in Figures 6(a), 6(b), and 6(c). These snapshots clearly show that the initial distribution is rapidly spread as a result of diffusion. This rapid diffusion results rapid switching recovery. Figure 6(d) shows the calculated shift of the resonance wavelength for the cavity. The initial wavelength shift caused by the carrier plasma shift is recovered quickly. As shown in the figure, the nonradiative recombination does not seriously affect the initial recovery. Therefore, we believe that the fast operation of our optical switches is explained by the rapid carrier diffusion process.

If we wish to increase the operation speed further, we have to somehow decrease the carrier relaxation time. Although there are several ways to do so, we have recently employed an Ar-ion implantation process in order to introduce extremely fast nonradiative recombination centers into silicon. If the carrier recombination time becomes faster than the diffusion time, we can expect an improvement in the operation speed. When we implanted silicon photonic crystal nanocavity switches with Ar⁺ dose of 2.0×10^{14} cm⁻² and an acceleration voltage of 100 keV, we observed a significant

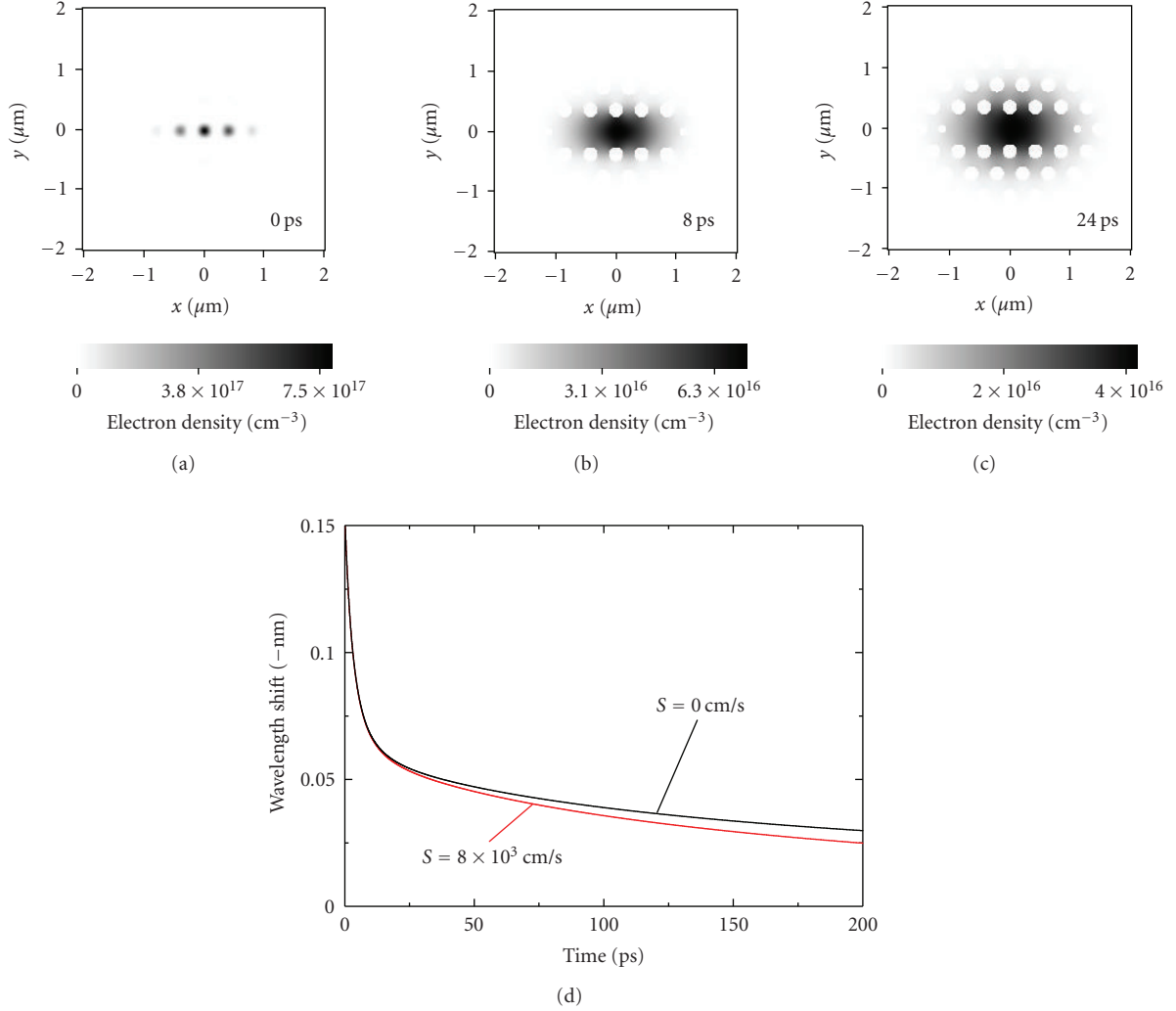


FIGURE 6: Numerical simulation of carrier diffusion process for a silicon end-hole-shifted photonic crystal cavity. (a), (b), (c) snapshots of the carrier distribution at $t = 0, 8, 24$ picoseconds. (c) Shift of the resonance wavelength for the cavity as a function of time with the sidewall nonradiative recombination rate $S = 0$ and $S = 8 \times 10^3$ cm/s.

improvement in switching speed as shown in Figures 7(a), 7(b). The implantation condition was carefully determined so as to keep almost the same cavity Q but to significantly decrease the carrier lifetime in the cavity. In the case of detuning for an NOT gate (Figure 7(a)), it was reduced from 110 picoseconds to 50 picoseconds. In the case of detuning for an AND gate, the switching time was reduced from 220 picoseconds to 70 picoseconds (Figure 7(b)) [20]. As shown in Figure 7(c), the ON/OFF ratio is mostly the same between two conditions. In addition, the required switching energy was almost the same as that without the implantation. Although the reduction of the carrier lifetime may lead to increase in the switching energy, this change is not significant as far as the carrier lifetime is longer than the photon lifetime and the control pulse length (which was the case in our experiment). These results clearly demonstrate the effect of ion-implantation on the improvement in the switching speed.

5. ALL-OPTICAL MEMORY OPERATION AND LOGIC CIRCUIT

In the same way as thermo-optic switching, carrier-plasma switching also provides bistable operation. Figure 8 shows bistable operations realized by employing a pair of set and reset pulses [21]. When a set pulse is fed into the input waveguide, the output signal is switched from OFF to ON and remains ON even after the set pulse exits (green curve). When a pair of set and reset pulses is applied (as shown in Figure 8(a)), the output is switched from OFF to ON by the set pulse and then ON to OFF by the reset pulse (blue curve). This is simply a memory operation using optical bistability. The energy of the set pulse is less than 100 fJ, and the DC bias input for sustaining the ON/OFF states is only 0.4 mW. These small values are primarily the results of the large Q/V ratio of the photonic crystal cavity. It is worth noting that the largest Q/V should always result in the smallest switching power,

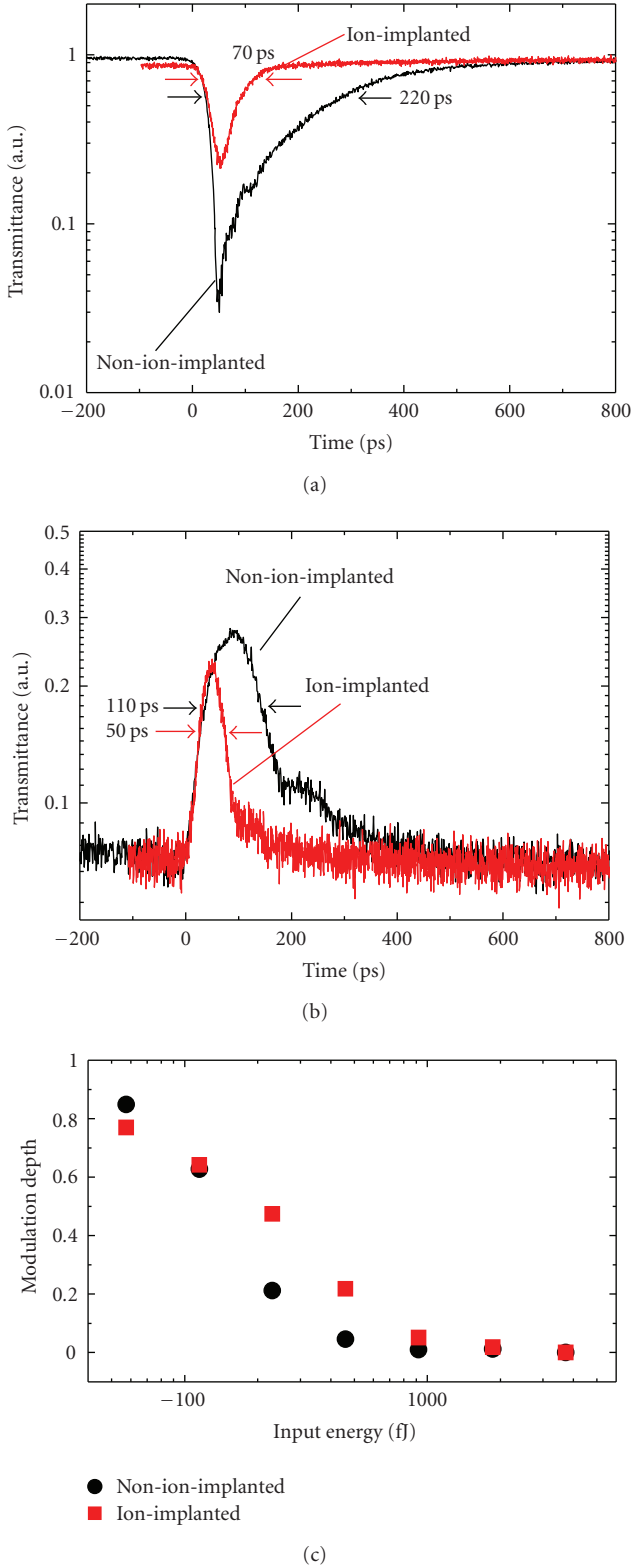


FIGURE 7: All-optical switching for samples with and without ion-implantation. (a) NOT-type switching. (b) AND-type switching. (c) Signal transmission at the time when the control pulses enters the cavity. The ON/OFF contrast of the signal is shown in relation to the input control pulse energy. The circles are the minimal transmission for the nonimplanted sample, and the squares are for the implanted sample.

but the operation speed can be limited by Q . In the present situation, the switching speed is still limited by the carrier relaxation time, and thus a large Q/V is preferable. In the case when the photon lifetime limits the operation speed, we have to choose appropriate loaded Q for the required speed. Even in such a case, it is better to have high unloaded Q because loaded Q can be controlled by changing the cavity-waveguide coupling, and high unloaded Q means low loss of the device. The best design of our device would be a device with the smallest volume, the lowest transmission loss, and the designated *loaded* Q (depending on the operation speed). The lowest loss with the designated *loaded* Q can be obtained only when we employ an ultrahigh *unloaded* Q cavity. Compared with other types of all-optical memories, this device has several advantages, such as small footprint, low-energy consumption, and the capability for integration. The fact that all the light signals used for the operation are transparent in waveguides is important for the application, which is fundamentally different from bistable-laser-based optical memories.

In the above, we showed that a single photonic crystal cavity coupled to waveguides functions as a bistable switch or a memory. If we couple two or more bistable cavities, we can create much more complex logic functions [11], in the same way as with transistor-based logic in electronics. As an example, here we show our numerical design for an all-optical flip-flop consisting of two bistable cavities integrated in a photonic crystal. It has been proposed that all-optical flip-flops be realized by using two nonlinear etalons with appropriate cross-feedback [22], but this proposal is unsuitable for on-chip integration. Here, we propose a different design using two photonic crystal nanocavities [23].

A typical example of flip-flop operation in the high-speed information processing is a retiming circuit, which corrects the timing jitter of an information bitstream and synchronizes it with the clock pulses. This function is normally accomplished by high-speed electronic circuits, but if it can be done all optically, it will be advantageous for future ultrahigh-speed data transmission. Here, we propose a simple flip-flop design for realizing the retiming function. Figure 9(a) shows a design for the retiming circuit. The coupled cavities (C1 and C2) have one common resonant mode ($\lambda_2 = 1548.48$ nm, $Q_2 = 4500$) extended to both cavities and two modes ($\lambda_1 = 1493.73$ nm, $Q_1 = 6100$, and $\lambda_3 = 1463.46$ nm, $Q_3 = 4100$) localized in each cavity. Here, we use two bistable switching operations for C1 and C2. The cross-feedback is realized as follows. C1 is switched ON only when λ_1 and λ_2 are both applied (P_{IN1} and P_{IN2} are ON). C2 is ON only when λ_3 are applied (P_{IN3} is ON) and simultaneously λ_2 is supplied from C1 (which means C1 is ON). Thus the output signal of λ_3 (P_{OUT3}) becomes ON only if P_{IN3} is turned ON when C1 is already ON in advance. These results achieve retiming process. We set P_{IN1} and P_{IN3} as two different clock signals as shown in Figure 9(b), and assume P_{IN2} to be bit-stream NRZ (nonreturn-to-zero) data with finite timing jitter. The resultant P_{OUT3} is precisely synchronized to the clock signals and is actually an RZ (return-to-zero) data stream converted from P_{IN2} with jitter corrected.

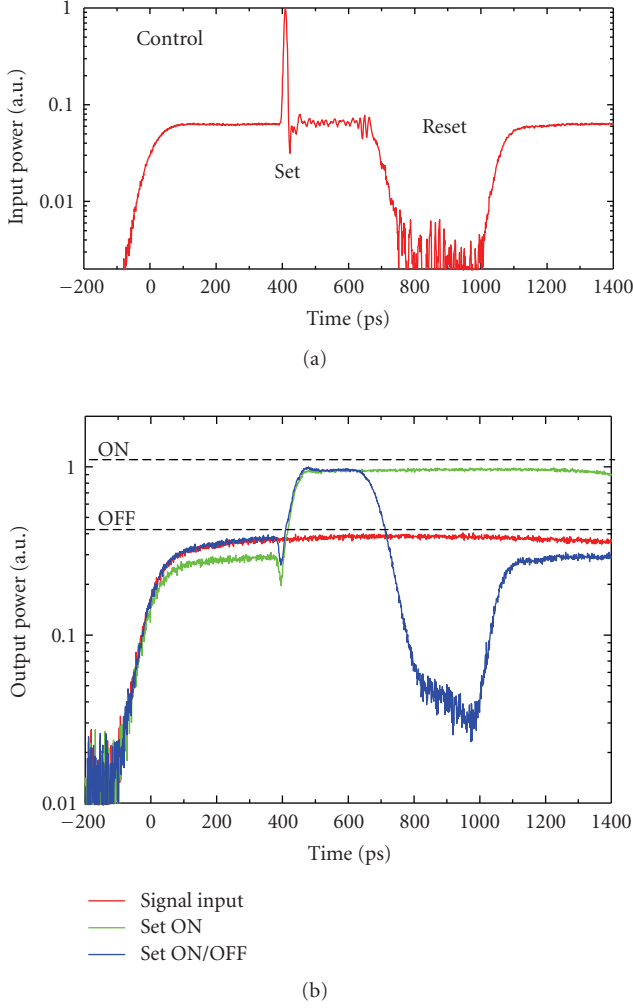


FIGURE 8: All-optical bistable memory operation in a silicon photonic crystal nanocavity (end-hole shifted four-point defect cavity) realized by the carrier-plasma nonlinearity induced by two-photon absorption in silicon. Q for the control mode is 7640, and Q for the signal mode is 12400. (a) Injected control light consisting of a pair of set and reset pulses. (b) Output signal intensity as a function of time for three different cases: with no set/reset pulses (red curve), with set pulse only (green curve), and with set and reset pulses (blue curve).

We designed this function in a photonic crystal slab system, and numerically simulated its operation using the FDTD method. The structural parameters are shown in the figure caption. We assumed realistic material parameters (with a Kerr coefficient $\chi^{(3)}/\epsilon_0 = 4.1 \times 10^{-19} \text{ (m}^2/\text{V}^2)$, a typical value for AlGaAs) and the instantaneous driving power is assumed to be 60 mW for all three inputs. Figure 9(b) shows three input signals (a data stream with jitter, and two clock pulses), and the output from P_D (P_{OUT3}). As seen in this plot, P_{OUT3} is the RZ signal of the input with the jitter corrected. We confirmed that the operation speed corresponds to 50 GHz operation. Note that this work was intended to demonstrate the operation principle and the structure has not yet been optimized. We expect \sim mW

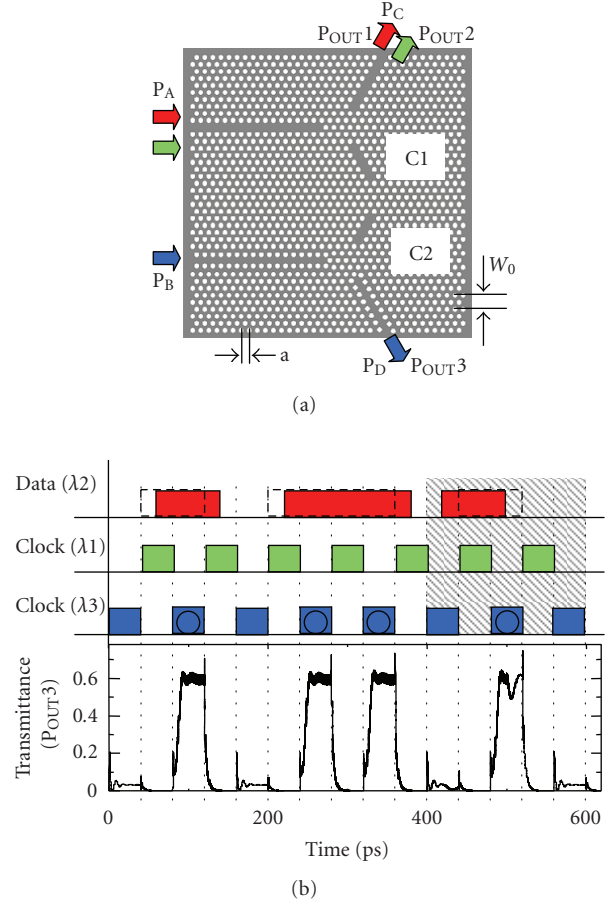


FIGURE 9: All-optical retiming circuit based on two bistable cavities. (a) Design based on a hexagonal air-hole 2D photonic crystal with $a = 400 \text{ nm}$ and $2r = 0.55 a$. Two waveguides in the upper area (P_A and P_C) are W_1 and the other two in the lower area (P_B and P_D) are $W_0.8$. (b) Simulated operation.

operation may be possible after the optimization since our rough estimation shows that a single cavity switch can operate at sub-mW input power for the similar condition. In addition, if we manage to employ the carrier-plasma effect for this operation (as was done in Figure 8), we can expect further decrease in terms of the input power.

In addition to this work, we have reported another design of all-optical logic circuit which is mostly equivalent to an SR flip-flop employing two bistable cavities [8].

6. SUMMARY

Recent rapid progress in photonic crystal nanocavities is enabling low-power, all-optical switching and memory actions on a silicon chip. We have shown that our experimental demonstration of all-optical switching operation using thermo-optic nonlinearity and carrier-plasma nonlinearity, both based on two-photon absorption in silicon. For both cases, we observed significant decrease in the switching power (energy) and also significant increase in the switching speed. In this article, we numerically investigated the

diffusion process concerning photonic-crystal nanocavities, which is fundamentally different from that in conventional optical devices with much larger size. Moreover, we have demonstrated their potential for optical logic by a combination of bistable elements. For the application in all-optical processing, a photonic crystal has several important advantages, such as small footprint, small energy consumption, high speed, and significant integratability. Thus we believe that it may be a promising candidate for all-optical information processing on a silicon chip.

REFERENCES

- [1] B.-S. Song, S. Noda, T. Asano, and Y. Akahane, "Ultra-high-Q photonic double-heterostructure nanocavity," *Nature Materials*, vol. 4, no. 3, pp. 207–210, 2005.
- [2] S. Noda, M. Fujita, and T. Asano, "Spontaneous-emission control by photonic crystals and nanocavities," *Nature Photonics*, vol. 1, no. 8, pp. 449–458, 2007.
- [3] E. Kuramochi, M. Notomi, S. Mitsugi, A. Shinya, T. Tanabe, and T. Watanabe, "Ultra-high-Q photonic crystal nanocavities realized by the local width modulation of a line defect," *Applied Physics Letters*, vol. 88, no. 4, Article ID 041112, 3 pages, 2006.
- [4] T. Tanabe, M. Notomi, E. Kuramochi, A. Shinya, and H. Taniyama, "Trapping and delaying photons for one nanosecond in an ultrasmall high-Q photonic-crystal nanocavity," *Nature Photonics*, vol. 1, no. 1, pp. 49–52, 2007.
- [5] R. Herrmann, T. Sünner, T. Hein, A. Löffler, M. Kamp, and A. Forchel, "Ultra-high-quality photonic crystal cavity in GaAs," *Optics Letters*, vol. 31, no. 9, pp. 1229–1231, 2006.
- [6] T. Tanabe, A. Shinya, E. Kuramochi, S. Kondo, H. Taniyama, and M. Notomi, "Single point defect photonic crystal nanocavity with ultrahigh quality factor achieved by using hexapole mode," *Applied Physics Letters*, vol. 91, no. 2, Article ID 021110, 3 pages, 2007.
- [7] T. Tanabe, M. Notomi, E. Kuramochi, and H. Taniyama, "Large pulse delay and small group velocity achieved using ultrahigh-Q photonic crystal nanocavities," *Optics Express*, vol. 15, no. 12, pp. 7826–7839, 2007.
- [8] M. Notomi, T. Tanabe, A. Shinya, et al., "Nonlinear and adiabatic control of high-Q photonic crystal nanocavities," *Optics Express*, vol. 15, no. 26, pp. 17458–17481, 2007.
- [9] M. Soljačić and J. D. Joannopoulos, "Enhancement of nonlinear effects using photonic crystals," *Nature Materials*, vol. 3, no. 4, pp. 211–219, 2004.
- [10] H. M. Gibbs, *Optical Bistability: Controlling Light with Light*, Academic Press, Orlando, Fla, USA, 1985.
- [11] S. D. Smith, "Optical bistability, photonic logic, and optical computation," *Applied Optics*, vol. 25, no. 10, pp. 1550–1564, 1986.
- [12] M. Notomi, A. Shinya, S. Mitsugi, G. Kira, E. Kuramochi, and T. Tanabe, "Optical bistable switching action of Si high-Q photonic-crystal nanocavities," *Optics Express*, vol. 13, no. 7, pp. 2678–2687, 2005.
- [13] S. Mitsugi, A. Shinya, E. Kuramochi, M. Notomi, T. Tshchizawa, and T. Watanabe, "Resonant tunneling wavelength filters with high Q and high transmittance based on photonic crystal slabs," in *Proceedings of the 16th Annual Meeting of IEEE Lasers and Electro-Optics Society (LEOS '03)*, vol. 1, pp. 214–215, Tucson, Ariz, USA, October 2003.
- [14] M. Notomi, A. Shinya, S. Mitsugi, E. Kuramochi, and H.-Y. Ryu, "Waveguides, resonators and their coupled elements in photonic crystal slabs," *Optics Express*, vol. 12, no. 8, pp. 1551–1561, 2004.
- [15] G. R. Olbright, N. Peyghambarian, H. M. Gibbs, H. A. MacLeod, and F. Van Milligen, "Microsecond room-temperature optical bistability and crosstalk studies in ZnS and ZnSe interference filters with visible light and milliwatt powers," *Applied Physics Letters*, vol. 45, no. 10, pp. 1031–1033, 1984.
- [16] V. R. Almeida and M. Lipson, "Optical bistability on a silicon chip," *Optics Letters*, vol. 29, no. 20, pp. 2387–2389, 2004.
- [17] T. Tanabe, M. Notomi, S. Mitsugi, A. Shinya, and E. Kuramochi, "All-optical switches on a silicon chip realized using photonic crystal nanocavities," *Applied Physics Letters*, vol. 87, no. 15, Article ID 151112, 3 pages, 2005.
- [18] V. R. Almeida, C. A. Barrios, R. R. Panepucci, and M. Lipson, "All-optical control of light on a silicon chip," *Nature*, vol. 431, no. 7012, pp. 1081–1084, 2004.
- [19] T. Tanabe, H. Taniyama, and M. Notomi, "Carrier diffusion and recombination in photonic crystal nanocavity optical switches," *Journal of Lightwave Technology*, vol. 26, no. 11, pp. 1396–1403, 2008.
- [20] T. Tanabe, K. Nishiguchi, A. Shinya, et al., "Fast all-optical switching using ion-implanted silicon photonic crystal nanocavities," *Applied Physics Letters*, vol. 90, no. 3, Article ID 031115, 3 pages, 2007.
- [21] T. Tanabe, M. Notomi, S. Mitsugi, A. Shinya, and E. Kuramochi, "Fast bistable all-optical switch and memory on a silicon photonic crystal on-chip," *Optics Letters*, vol. 30, no. 19, pp. 2575–2577, 2005.
- [22] H. Tsuda and T. Kurokawa, "Construction of an all-optical flip-flop by combination of two optical triodes," *Applied Physics Letters*, vol. 57, no. 17, pp. 1724–1726, 1990.
- [23] A. Shinya, S. Mitsugi, T. Tanabe, et al., "All-optical flip-flop circuit composed of coupled two-port resonant tunneling filter in two-dimensional photonic crystal slab," *Optics Express*, vol. 14, no. 3, pp. 1230–1235, 2006.

Research Article

Optical Filters Utilizing Ion Implanted Bragg Gratings in SOI Waveguides

M. P. Bulk,¹ A. P. Knights,¹ P. E. Jessop,¹ P. Waugh,² R. Loiacono,² G. Z. Mashanovich,²
G. T. Reed,² and R. M. Gwilliam²

¹Department of Engineering Physics, McMaster University, 1280 Main Street West, Hamilton, ON, Canada L8S 4J1

²Advanced Technology Institute, University of Surrey, Guildford, Surrey GU2 4EL, UK

Correspondence should be addressed to A. P. Knights, aknight@mcmaster.ca

Received 6 January 2008; Accepted 13 March 2008

Recommended by Pavel Cheben

The refractive index modulation associated with the implantation of oxygen or silicon into waveguides formed in silicon-on-insulator (SOI) has been investigated to determine the feasibility of producing planar, implantation induced Bragg grating optical filters. A two-dimensional coupled mode theory-based simulation suggests that relatively short grating lengths, on the order of a thousand microns, can exhibit sufficient wavelength suppression, of > 10 dB, using the implantation technique. Fabricated planar implanted slab-guided SOI waveguides demonstrated an extinction of -10 dB for TE modes and -6 dB for TM modes for the case of oxygen implantation. Extinctions of -5 dB and -2 dB have been demonstrated with silicon implantation.

Copyright © 2008 M. P. Bulk et al. This is an open access article distributed under the Creative Commons Attribution License, which permits unrestricted use, distribution, and reproduction in any medium, provided the original work is properly cited.

1. INTRODUCTION

The preliminary work of Soref et al. and the subsequent study by Pogossian et al. demonstrated the ability to produce single mode optical waveguides in silicon at telecommunication wavelengths with cross-sectional dimensions compatible with standard photolithography [1, 2]. Immediate interest pursued as this structure was a suitable candidate for low-loss, high-index-contrast waveguides capable of routing optical signals at the wafer scale. The integration of optical components on a silicon platform also had the added benefits of low-cost large-scale manufacturability utilizing existing CMOS facilities and the possibility of amalgamating electrical and optical functionality on a single wafer.

Consequently, the miniaturized counterparts of many bulk optical components have been realized in silicon. These include detectors, couplers, filters, and sensors [3–6]. It is of particular interest to control the propagation of individual optical wave-fronts in such devices. One method to achieve wavelength dispersion exploits the unique behavior of optical waves propagating in a medium containing a periodically modulated refractive index. Indeed, this approach has found extensive use in such areas as photonic crystals, distributed

feedback (DFB) lasers and optical spectroscopy. In one-dimension, the perturbation is referred to as a grating and serves as a robust and flexible tool in photonics technology. Depending on the desired outcome, gratings can be implemented to act as couplers, reflectors, mode converters, optical filters among others [7].

In the case of silicon-on-insulator (SOI) waveguides, a surface relief structure provides the most straightforward method for fabrication of an integrated Bragg grating. Such devices are inherently passive, although electrically tuneable gratings based on the plasma dispersion effect have been developed [8] along with those which are thermo-optically tuned [9]. The Bragg grating itself is typically formed through a lithographic patterning technique and an etching sequence, although, relatively recently, focused ion beam milling has been used to realize higher-order mode conversion and filtering in SOI [10]. Perhaps the benchmark for performance of gratings in SOI waveguides remains the work of Murphy et al. [11]. There, surface relief gratings with a period of 223 nm were formed in $3\ \mu\text{m}$ high SOI rib waveguides via interference photolithography and plasma etching to a depth of 150 nm. The authors demonstrated an optical transmission dip of 8 dB at the resonant wavelength

of 1543 nm, for the fundamental TE mode. The device had a transmission loss of nearly 10 dB which the authors attributed to sidewall scattering. The biggest drawback of the fabrication method leading to surface relief is the inherent deviation from a planar surface, limiting the ability of further processing. This is particularly problematic in nanophotonics, where the required thin processing layers are quickly skewed by alterations of wafer topography.

An alternative method which we propose here involves the well-established ion implantation process to introduce dopants and/or structural modifications to the crystalline lattice. By selectively introducing ions using a masking process, the refractive index can be periodically modified to produce a Bragg grating. The implantation process can alter the refractive index through either compound formation, as in the case of oxygen implantation, or chemically inert structural damage as achieved by self-irradiation [12, 13]. Apart from small volumetric changes, the result is a Bragg grating retaining a nearly planar surface. This makes it a very interesting candidate for photonic applications possessing surface sensitive topography, such as wafer-bonding techniques required for three-dimensional photonic circuits. Therefore, this paper investigates the formation of Bragg gratings via implantation of oxygen and silicon into SOI. To the authors' knowledge, this preliminary work is the first report of integrated Bragg gratings in SOI waveguides formed via ion implantation.

2. ION IMPLANTED GRATING DESIGN AND CONSIDERATIONS

Some authors have already pointed out the possibility of fabricating isolated buried oxide regions through a high dose oxygen implantation [14] in order to create hybrid SOI/silicon wafers for CMOS applications in a manner similar to the buried oxide formed in the separation by IMplantation of OXYgen (SIMOX) process [12]. Such formation is generally conducted using doses around 10^{18} ions/cm², with energies of 150–200 keV and at high temperatures (65°C) in order to prevent amorphization [15]. Traditional SIMOX processes need high dose implants in order to obtain a stoichiometric oxide. In the case of grating fabrication, high dose is still a desirable process parameter, whereas the implant energy will be lower as the oxide layer needs not to be buried but close to the wafer surface. For this reason, implantation energy can be lowered to 20–30 keV. Following the implantation process, the substrate generally contains a series of extended defects. Depending on the implant condition these defects may include stacking faults, dislocation loops, amorphous clusters, oxygen precipitates, and columnar defects [16]. In general, SIMOX process requires postimplant annealing treatment up to 1300°C. The postimplant anneal is essential in order to finalize oxide formation, as it stimulates oxygen diffusion and SiO₂ formation via Ostwald Ripening [17], while repairing lattice damage. By this mechanism, small faulty zones and precipitates tend to coalesce into bigger aggregations in order to achieve a more favorable energy configuration. Although the structures reported here have not received such a high-

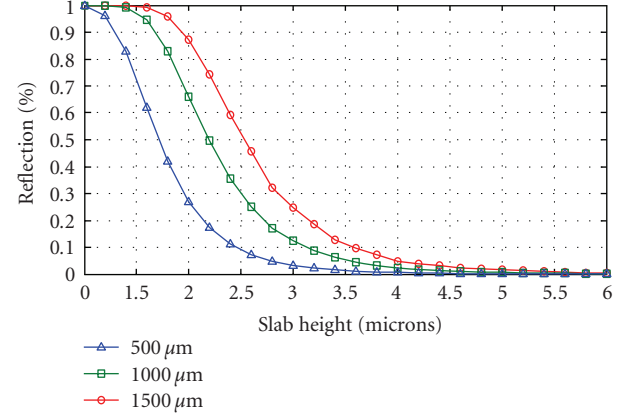


FIGURE 1: Coupled mode theory prediction of peak reflected power as a function of the silicon slab waveguide height for grating lengths of 500, 1000, and 1500 μm. Simulations are performed with regard to amorphous silicon induced via self-implantation. The depth of amorphous silicon is taken to be 100 nm.

temperature anneal, it is likely that isolated precipitates of SiO₂ are formed during the high temperature implantation stage.

In contrast, the low temperature self-irradiation of silicon results in the production and accumulation of point defects, defect complexes, and locally amorphous regions until it becomes thermodynamically favorable for the lattice to undergo a transition from the crystalline to amorphous state [18]. Of particular interest to optical devices is the ensuing increase of the index of refraction as a result of damage accumulation. The increase continues until the amorphous transition, at which point the refractive index saturates to a value approximately 0.27 higher (for a wavelength of around 1550 nm) than that of crystalline silicon [19]. It should be noted that although propagation losses tend to be high, amorphous silicon (*a*-Si) has demonstrated guiding capabilities. Therefore, if applied periodically, *a*-Si serves as a unique candidate for grating structures.

In order to achieve a first-order Bragg grating in silicon, the Bragg condition,

$$\Lambda = \frac{\lambda}{2N_{\text{eff}}}, \quad (1)$$

requires a period (Λ) of 222 nm, assuming a wavelength (λ) of 1550 nm and an effective index (N_{eff}) of approximately 3.48. This poses a fabrication challenge since the lateral damage/straggle must remain below 55 nm in order to achieve adequate modulation. Since the implantation profiles depend on the implantation energy, dose, temperature, implantation angle, and ion mass, the lateral profile can be manipulated by varying these parameters.

The implantation profiles can be construed using ion implantation simulators. In the case of the oxygen implantation, in order to achieve a uniform dopant implantation to a depth of 70 nm and retain adequate lateral modulation, it was determined that a dual implant process was required. The first implant utilized ion energy of 20 keV with a dose

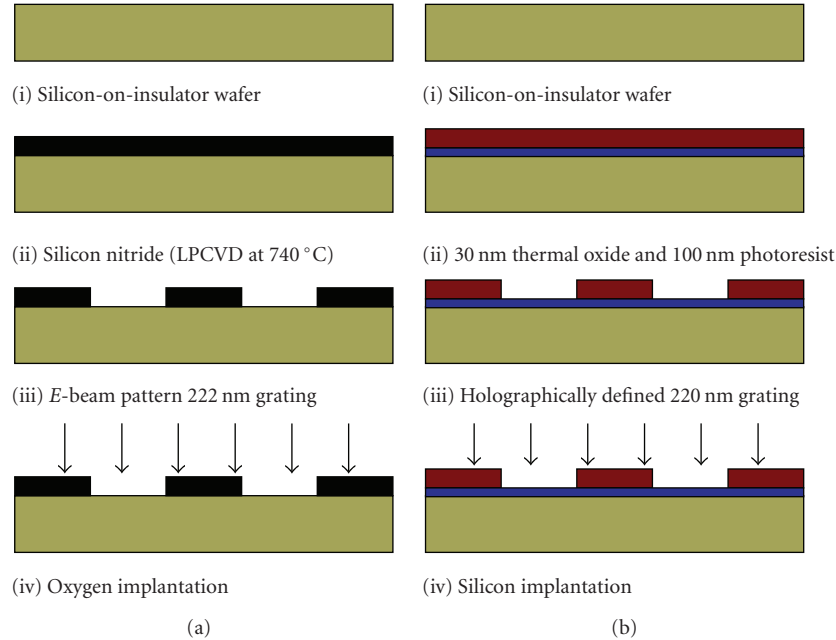


FIGURE 2: Fabrication process of planar SOI gratings for the case of (a) oxygen implantation and (b) silicon implantation.

of 1.6×10^{17} ions/cm². A subsequent surface implant was carried out at 10 keV with a dose of 0.8×10^{17} ions/cm².

For silicon self-irradiation, and implanting at a temperature of 77 K to minimize dynamic annealing, a dose of approximately 10^{15} ions/cm⁻² is required to induce amorphization [18]. The total damage to the lattice is characterized by the number of displacements per unit volume of the crystal. When the defect contributions are higher than a critical value, the substrate can be approximated as amorphous. Although reported values vary, lattice displacement concentrations in the range of 10% to 25% of the silicon density appear to satisfy this condition [20, 21].

Assuming an impenetrable masking layer, it was determined that to provide suitable lateral modulation the implant energy should remain below approximately 60 keV. The 60 keV implant limit also determines the extent of the grating depth. Using similar analysis, a modulated index is expected to exist to a depth of approximately 150 nm. Since the degree of coupling from the forwards to the backwards modes depends directly on the overlap integral of the mode with the grating region, it is important to quantify the suitability of the depth limitation.

A two-dimensional coupled mode theory (CMT) approach assuming TE modes in a slab SOI waveguide, with an upper-cladding of air, was applied to approximate the strength of the grating [22]. Assuming an implantation dose capable of rendering the silicon amorphous and taking the depth of the implant to be fixed at 100 nm, the degree of modal overlap can be altered by varying the slab height. This is analogous to changing the silicon over-layer height. Figure 1 depicts the maximum reflected power for different grating lengths while varying the slab height, assuming a lossless medium for simplicity. From the figure, it is apparent that over 90% of the power is expected to be

reflected at the resonant wavelength for slab heights on the order of $2 \mu\text{m}$ and a grating length of approximately $1500 \mu\text{m}$. Similar analysis was performed assuming a 70-nm deep grating consisting of a periodic oxide (as opposed to amorphous silicon) and grating lengths of $1000 \mu\text{m}$ were found to result in approximately 35 dB reflections.

3. FABRICATION

The fabrication process is depicted schematically in Figure 2 for the cases of the oxygen implant and the silicon implant. For the oxygen implanted samples, a 100-nm layer of silicon nitride was deposited onto a $1.5 \mu\text{m}$ over-layer SOI wafer using LPCVD at 740°C. Electron-beam lithography then provided the necessary resolution to produce the 222 nm gratings in the silicon nitride layer to a length of $1000 \mu\text{m}$. The patterned silicon nitride layer then served as the implantation mask. The samples were subsequently implanted following the dual implantation process formulated above at an elevated temperature such that amorphization was prevented. Following implantation, the nitride mask was removed.

While fabricating oxygen implanted samples, several processing issues have been noticed that can negatively influence the device performance. First and foremost, the necessity of high dose implantation associated with this is sputtering and target erosion problems. In the current case, the nitride hardmask used for pattern definition tends to sputter as the implantation advances. This means that pattern definition becomes more and more uncertain by the termination of the implantation. The sputtering yield is greatest on the mask sidewalls, as the angle between the ion beam and the surface is not zero. Atomic force microscopy (AFM) measurements on the implanted target also showed

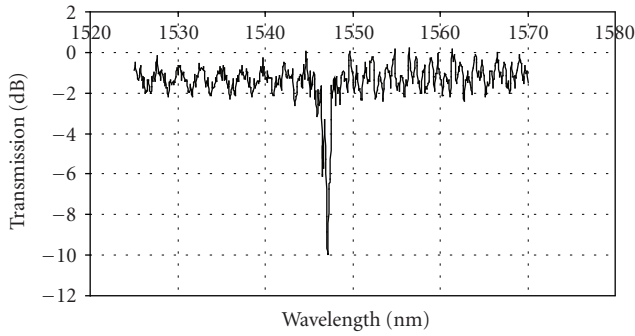


FIGURE 3: Experimental TE response of oxygen implant Bragg grating.

surface erosion of the order of 10 nm. This means that the grating response could also be influenced by the surface modification.

The silicon implanted samples were implemented on a 2.2- μm over-layer SOI wafer. The wafers were subject to a thermal oxidation resulting in a 40-nm silicon dioxide layer. This layer serves as a buffer aiding the removal of the photoresist following implantation. A 7000- μm grating pattern was produced holographically in photoresist using a Lloyd's mirror setup and a 325-nm HeCd laser. The photoresist layer then serves as the low-energy implantation mask. After exposure and development, scanning electron microscopy (SEM) images determined the photoresist thickness to be 100 nm. Si implantation was carried out at energies of 50 and 70 keV and a nominal dose of 1×10^{15} ions/cm² at 77 K. Following implantation, the photoresist mask was removed, followed by the oxide buffer layer.

4. RESULTS

Optical transmission spectra were obtained utilizing a tunable laser operating in the range of 1525 to 1570 nm. For the oxygen implanted samples, the signal was coupled to the waveguides using an objective lens. Light was then measured via a free-space power meter at the output. Prior to the objective lens, a beam splitter and half-wave plate were inserted to provide discrimination between TE and TM modes. The silicon implants were measured in transmission in a similar fashion, except for the use of a low-loss tapered optical fiber to butt couple light into the waveguide.

Figure 3 shows the TE mode of the “as-implanted” oxygen implanted sample, following the removal of the nitride mask. The peak response occurs at approximately 1547 nm for the TE polarized light and shows a discrimination of approximately 10 dB. This appears to be a promising result, considering no post implantation annealing was performed.

Using CMT analysis, the expected result on reflected power of a grating formed of SiO₂ can be overlaid with the previous result to compare the expected and measured grating response. It is also possible to approximate the index of refraction responsible for the response in Figure 3 as a single fit factor, by assuming that the oxygen implant

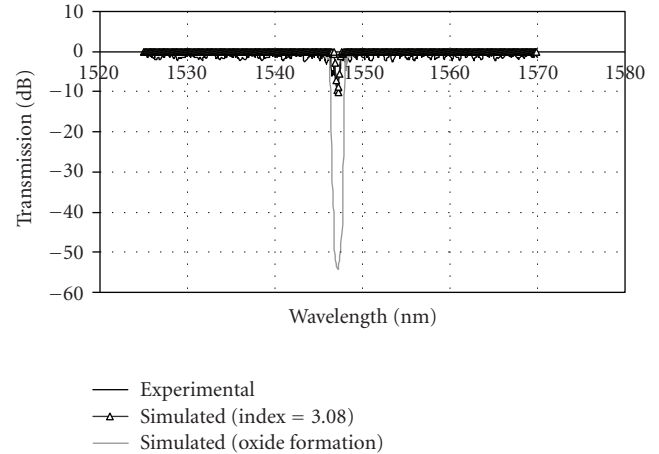


FIGURE 4: Simulated response of oxygen grating corresponding to experimental results.

achieves a depth of approximately 70 nm. The result is shown in Figure 4.

From Figure 4, it is shown that the expected transmission drop, assuming complete oxide synthesis, is on the order of -55 dB, suggesting that the current results could be dramatically improved. Further, we approximate the index of refraction of the “as-implanted” region to lie at around 3.08. What is thus clear in this preliminary work is that the high dose, high temperature oxygen implantation, does not form continuous volumes of SiO₂. In agreement with previous work [17], this should only be expected following postimplant annealing at around 1300°C. An effort to fabricate gratings with fully formed oxide is currently in progress.

The resultant data for the 50 keV and 70 keV silicon implanted samples for TE light are shown in Figures 5 and 6. The 50 keV samples show a wavelength suppression of approximately -5 dB at approximately 1530 nm with the oxide layer intact. Upon removing the oxide layer, the response drops to an extinction of around -3 dB. SEM images determined that no residual photoresist mask remained on the oxide and, therefore, suggested the damage inherent in the oxide layer contributes to the grating response. For the case of the 70 keV implant with the oxide removed, the sample exhibited a -5 dB suppression. The spectral response of the 50 keV response is in agreement with the CMT model for the holographically defined 220 nm gratings, however, a -3 dB suppression corresponds to an implanted index of only 3.493. This value is lower than expected for completely amorphized silicon and is either a result of ion straggle inflicting damage underneath the mask material reducing modulation or is a result of incomplete amorphization. For the 70 keV samples, the implant depth is approximately 170 nm, and the corresponding index to produce the -5 dB extinction is 3.491.

It is noted that for both the oxygen and silicon implanted grating devices there exists a deviation from the anticipated resonant wavelength of 1550 nm. This can be attributed to

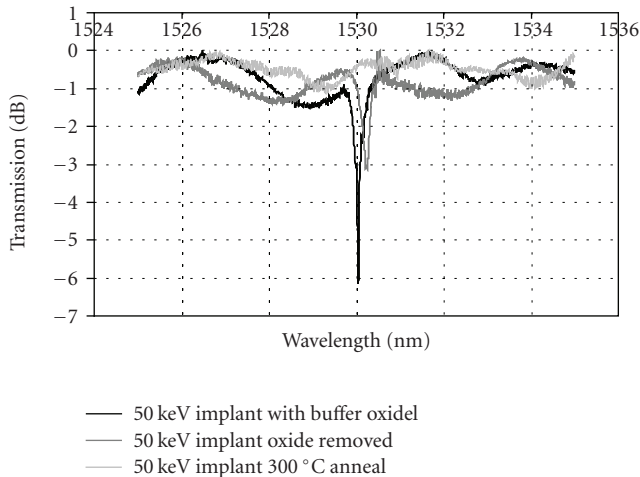


FIGURE 5: Experimental TE response of 50 keV silicon implanted Bragg grating.

an error associated with the lithographical fabrication. In the case of electron-beam lithography, we might anticipate a deviation in Λ on the order of a few nm's, reflected in the small deviation from the resonance at 1550 nm of only ~ 3 nm, while in the holographic lithography process, a slight angular misalignment of the Lloyd's mirror setup of 1° leads to a change in the Bragg wavelength of ~ 25 nm (a direct result of the dependence of Λ on the angle between the two mirrors). The measured resonance of ~ 1530 – 1532 nm reflects a misalignment of the Lloyd's mirror setup of ~ 1 – 2° . For this preliminary work, we find these results encouraging while recognizing that control of the lithographical process is critical to achieve precise resonance wavelengths.

In an attempt to improve the lateral modulation, a 300°C anneal for 10 minutes was performed on the silicon implanted samples. This annealing process was aimed to remove primary defects such as di-interstitials and divacancies (which can be found at the end of the implanted range in ion beam amorphized silicon) while retaining the amorphous structure itself [18]. As a result, amorphous pockets should remain and, in effect, be defined with a sharper amorphous/crystalline boundary. The results of the annealing on the transmission spectra are shown in Figures 5 and 6. It is seen that the grating response is essentially quenched in both cases. This strongly suggests that the implantation conditions were not sufficient to invoke complete amorphization. Hence, the grating comprised of simple point defects in an otherwise crystalline structure. Therefore, the low-temperature anneal was enough to eliminate the point defects and lower the refractive index to near that of c-Si and consequently eliminating the Bragg response. At the present time, further samples are being fabricated using a higher implantation dose, and a report of the annealing will be made in the future on the successful thermal processing of these grating structures.

No attention was paid to minimizing the optical propagation loss in these relatively crude slab waveguides. It is anticipated that Fresnel loss, mode mismatch between the

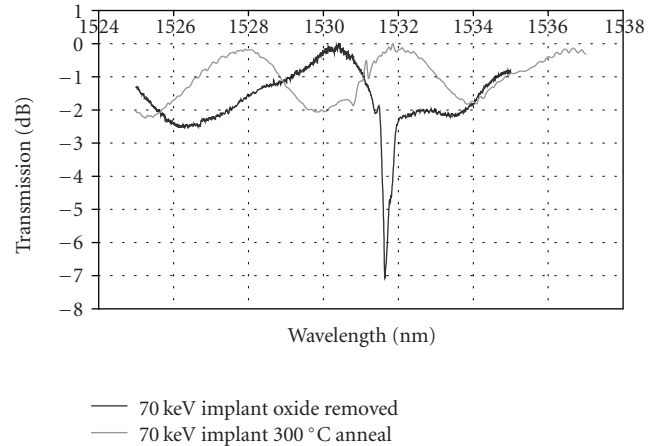


FIGURE 6: Experimental TE response of 70 keV silicon implanted Bragg grating.

input beam and the waveguide, and incomplete collection of the output would introduce a significant “coupling” loss in this system of tens of dB. Of some importance to these specific devices is the excess loss caused by the introduction of implantation induced lattice damage to the SOI (as in the case of the silicon implantation). This has been previously measured to be as much as 1000 dBcm^{-1} for almost completely irradiated rib waveguide structures [23]. Given the shallow depth of the implantation used in this study (on the order of 100 nm) and thus the relatively small overlap of the mode with the lattice damage, we expect an excess loss in the region of 10 dB. Although this is undesirable, it is likely to be reduced significantly following low-temperature annealing [19]. The balance between minimizing optical loss and producing a strong interaction between the propagating mode and the grating will be dealt with in some detail in a future publication.

For this initial study, grating fabrication is limited to slab waveguides, although they will ultimately be of more practical importance when incorporated into rib waveguides. Whereas rib waveguides can be made effectively single mode by suitable choices of rib width and etch depth [2], slab waveguides of the thicknesses used in this study are highly multimode. The resonances shown in Figures 3 to 5 result from the coupling of light in the forward propagating fundamental mode into the reverse propagating fundamental mode. One might also expect to see resonances due to coupling from the forward propagating fundamental mode into higher-order reverse propagating modes or from higher-order forward propagating modes into reverse propagation of the same mode. The former type of higher-order resonance is observed in the case of relief gratings on rib waveguides where the higher-order modes are leaky [11]. We also expect to see this when implanted gratings are used in rib gratings. The higher-order resonances occur at wavelengths that are a few tens of nm lower than that of the fundamental resonance, corresponding to effective index differences of 1–2% between low-order modes in these

structures. In this work, however, we observed neither type of higher-order resonance. We believe that the former type will be much weaker than in the rib waveguide case because of more complete mode orthogonality. The latter case is absent because the input light couples predominantly into the fundamental mode so that any individual higher-order mode has very little power in it to lose to resonant coupling.

5. CONCLUSION

This report demonstrated the viability of utilizing ion induced refractive index change in the manufacture of an optical filter in silicon waveguides. Response curves typical of passive grating filters were achieved, and extinction ratios of -10 dB and -7 dB were found for oxygen implants and -5 dB and -2 dB for silicon implants for TE and TM polarized light, respectively. From CMT analysis, it appears that the current results have the potential to be improved upon significantly. These implanted gratings could serve a useful role in future three-dimensional integrated photonics whose fabrication is contingent on surface sensitive bonding techniques.

ACKNOWLEDGMENTS

The authors would like to thank the Canadian Institute for Photonics Innovation (CIPI), the Natural Sciences and Engineering Research Council of Canada (NSERC), and the Ontario Centres of Excellence (OCE) for partially funding this work. We are also grateful to the members of the Centre for Emerging Device Technologies at McMaster University, and Interface Science Western, University of Western Ontario for assistance with device fabrication.

REFERENCES

- [1] R. A. Soref, J. Schmidtchen, and K. Petermann, "Large single-mode rib waveguides in GeSi-Si and Si-on-SiO₂," *IEEE Journal of Quantum Electronics*, vol. 27, no. 8, pp. 1971–1974, 1991.
- [2] S. P. Pogossian, L. Vescan, and A. Vonsovici, "The single-mode condition for semiconductor rib waveguides with large cross section," *Journal of Lightwave Technology*, vol. 16, no. 10, pp. 1851–1853, 1998.
- [3] J. D. B. Bradley, P. E. Jessop, and A. P. Knights, "Silicon-waveguide-integrated optical power monitor with enhanced sensitivity at 1550 nm," *Applied Physics Letters*, vol. 86, no. 24, Article ID 241103, 3 pages, 2005.
- [4] D. Taillaert, P. Bienstman, and R. Baets, "Compact efficient broadband grating coupler for silicon-on-insulator waveguides," *Optics Letters*, vol. 29, no. 23, pp. 2749–2751, 2004.
- [5] P. D. Trinh, S. Yegnanarayanan, F. Coppinger, and B. Jalali, "Silicon-on-insulator (SOI) phased-array wavelength multi/demultiplexer with extremely low-polarization sensitivity," *IEEE Photonics Technology Letters*, vol. 9, no. 7, pp. 940–942, 1997.
- [6] G. N. Pearson and P. E. Jessop, "Silicon-on-insulator interferometric strain sensor," in *Photonics Packaging and Integration III*, vol. 4997 of *Proceedings of SPIE*, pp. 242–249, San Jose, Calif, USA, January 2003.
- [7] H. Nishihara, M. Haruna, and T. Suhara, *Optical Integrated Circuits*, McGraw-Hill, New York, NY, USA, 1989.
- [8] A. Cutolo, M. Iodice, A. Irace, P. Spirito, and L. Zeni, "An electrically controlled Bragg reflector integrated in a rib silicon on insulator waveguide," *Applied Physics Letters*, vol. 71, no. 2, pp. 199–201, 1997.
- [9] S. Honda, Z. Wu, J. Matsui, et al., "Largely-tunable wideband Bragg gratings fabricated on SOI rib waveguides employed by deep-RIE," *Electronics Letters*, vol. 43, no. 11, pp. 630–631, 2007.
- [10] D. J. Moss, V. G. Ta'eed, B. J. Eggleton, et al., "Bragg gratings in silicon-on-insulator waveguides by focused ion beam milling," *Applied Physics Letters*, vol. 85, no. 21, pp. 4860–4862, 2004.
- [11] T. E. Murphy, J. T. Hastings, and H. I. Smith, "Fabrication and characterization of narrow-band Bragg-reflection filters in silicon-on-insulator ridge waveguides," *Journal of Lightwave Technology*, vol. 19, no. 12, pp. 1938–1942, 2001.
- [12] G. T. Reed and A. P. Knights, *Silicon Photonics: An Introduction*, John Wiley & Sons, Chichester, UK, 2004.
- [13] J. E. Fredrickson, C. N. Waddell, W. G. Spitzer, and G. K. Hubler, "Effects of thermal annealing on the refractive index of amorphous silicon produced by ion implantation," *Applied Physics Letters*, vol. 40, no. 2, pp. 172–174, 1982.
- [14] Y. Dong, M. Chen, J. Chen, X. Wang, and X. Wang, "Comparative study of Sol/Si hybrid substrates fabricated using high-dose and low-dose oxygen implantation," *Journal of Physics D*, vol. 37, no. 13, pp. 1732–1735, 2004.
- [15] K. Kajiyama, "Buried-oxide layer formation by high dose oxygen ion implantation into Si wafers: SIMOX (separation by implanted oxygen)," *Applied Surface Science*, vol. 85, pp. 259–264, 1995.
- [16] A. G. Revesz and H. L. Hughes, "Properties of the buried oxide layer in SIMOX structures," *Microelectronic Engineering*, vol. 36, no. 1–4, pp. 343–350, 1997.
- [17] Y. Li, C. D. Marsh, A. Nejm, R. J. Chater, J. A. Kilner, and P. L. F. Hemment, "SIMOX: processing, layer parameters design, and defect control," *Nuclear Instruments and Methods in Physics Research B*, vol. 99, no. 1–4, pp. 479–483, 1995.
- [18] L. Pelaz, L. A. Marqués, and J. Barbolla, "Ion-beam-induced amorphization and recrystallization in silicon," *Journal of Applied Physics*, vol. 96, no. 11, pp. 5947–5976, 2004.
- [19] M. J. A. de Dood, A. Polman, T. Zijlstra, and E. W. J. M. van der Drift, "Amorphous silicon waveguides for microphotonics," *Journal of Applied Physics*, vol. 92, no. 2, pp. 649–653, 2002.
- [20] L. A. Christel, J. F. Gibbons, and T. W. Sigmon, "Displacement criterion for amorphization of silicon during ion implantation," *Journal of Applied Physics*, vol. 52, no. 12, pp. 7143–7146, 1981.
- [21] W. P. Maszara and G. A. Rozgonyi, "Kinetics of damage production in silicon during self-implantation," *Journal of Applied Physics*, vol. 60, no. 7, pp. 2310–2315, 1986.
- [22] A. Yariv, *Introduction to Optical Electronics*, Holt, Rinehart and Winston, New York, NY, USA, 1976.
- [23] A. P. Knights and G. F. Hopper, "Effect of ion implantation induced defects on optical attenuation in silicon waveguides," *Electronics Letters*, vol. 39, no. 23, pp. 1648–1649, 2003.

Review Article

Tuning of the Optical Properties in Photonic Crystals Made of Macroporous Silicon

Heinz-S. Kitzerow,¹ Heinrich Matthias,¹ Stefan L. Schweizer,² Henry M. van Driel,³ and Ralf B. Wehrspohn²

¹ Department of Chemistry, Faculty of Science, University of Paderborn, 33095 Paderborn, Germany

² Institute of Physics, Martin-Luther-University Halle-Wittenberg, 06099 Halle, Germany

³ Department of Physics and Institute for Optical Sciences, University of Toronto, Toronto, ON, Canada M5S 1A7

Correspondence should be addressed to Heinz-S. Kitzerow, heinz.kitzerow@upb.de

Received 9 January 2008; Accepted 11 April 2008

Recommended by D. Lockwood

It is well known that robust and reliable photonic crystal structures can be manufactured with very high precision by electrochemical etching of silicon wafers, which results in two- and three-dimensional photonic crystals made of macroporous silicon. However, tuning of the photonic properties is necessary in order to apply these promising structures in integrated optical devices. For this purpose, different effects have been studied, such as the infiltration with addressable dielectric liquids (liquid crystals), the utilization of Kerr-like nonlinearities of the silicon, or free-charge carrier injection by means of linear (one-photon) and nonlinear (two-photon) absorptions. The present article provides a review, critical discussion, and perspectives about state-of-the-art tuning capabilities.

Copyright © 2008 Heinz-S. Kitzerow et al. This is an open access article distributed under the Creative Commons Attribution License, which permits unrestricted use, distribution, and reproduction in any medium, provided the original work is properly cited.

1. INTRODUCTION

Artificial structures exhibiting a spatially periodic structure with lattice constants comparable to the wavelength of light [1, 2] are extremely promising materials for integrated optical devices. These structures, referred to as photonic crystals [3–11], are characterized by an unusual dispersion relation which might show a photonic band gap (PBG), that is, a frequency range in which the propagation of light is not permitted. Properly designed defects within these structures may serve, for example, as optical waveguides, frequency filters, optical switches, or resonant microcavities with high quality factor, which can be used for low-threshold lasing. Many excellent works have demonstrated the potential capabilities of these structures, but their fabrication is still elaborate.

Electrochemical etching of silicon turned out to be a very reliable and versatile technique to fabricate two-dimensional periodic arrays of macropores [12–15]. Similarly to the method of electrochemical polishing, silicon wafers are dipped into hydrofluoric acid and a DC voltage between the wafer and a counter-electrode is applied. The generation of free charge carriers in the doped silicon is assisted by

exposure to infrared radiation. However, in contrast to the common polishing process, the parameters are chosen in a narrow range where the etching process does not lead to flattening of the surface, but instabilities cause the self-organized growth of pores. Spontaneously, the pores tend to arrange in a two-dimensional hexagonal lattice with spacings between $0.5\ \mu\text{m}$ and $10\ \mu\text{m}$. Additional pretreatment of the surface by photolithography can be used to alter the symmetry of the lattice, to create extremely high correlation lengths, and to design the arrangement of defects with very high precision. The depth-to-width ratio of the pores can be as large as 500. In addition, it is possible to modulate the width of the pores along the pore axes by controlling the current through the sample during the growth process, thereby creating even three-dimensional structures [13–15].

In addition to utilizing the benefits of the unusual dispersion relation, it is highly desirable to change the dielectric properties and to control them by external parameters, thereby achieving even a tunable dispersion relation [16–18]. This might be necessary in order to compensate for fabrication tolerances and to fine-tune the properties of the produced photonic crystal, or be motivated by targeting active switching devices. An obvious way to achieve tunable

properties is altering the dielectric susceptibility of the silicon. As usual, the dielectric susceptibility can be expanded in a power series as follows:

$$\chi = \chi^{(1)} + \chi^{(2)}E + \chi^{(3)}EE + \dots \quad (1)$$

Thus, linear [$\chi^{(1)}$] or nonlinear effects [$\chi^{(2)}, \chi^{(3)}, \dots$] may be considered. In addition, the macroporous silicon structures can be filled with a dielectric compound. If the silicon ($\epsilon = \epsilon_1$) is infiltrated with a different compound ($\epsilon = \epsilon_2$), the most fundamental change is a shift of the average dielectric constant ϵ_{av} , which is approximately given by the Maxwell-Garnett relation [19]

$$(\epsilon_{av} - \epsilon_1)(\epsilon_{av} + 2\epsilon_1)^{-1} = f_2(\epsilon_2 - \epsilon_1)(\epsilon_2 - 2\epsilon_1)^{-1}, \quad (2)$$

where f_2 is the volume fraction of component 2. If the denominators in (2) are not too different, the effective refractive index of the composed material is approximately given by

$$n_{eff} = (\sum f_i n_i^2)^{1/2}, \quad (3)$$

where f_i is the volume fraction of component i of the heterogeneous system. Thus, changing the refractive index of one of the two components has an effect on the properties of the entire structure. However, the influence on the dispersion relation and on the linear and nonlinear photonic properties is much more subtle than a simple change of the average refractive index. Due to their sensitivity to external parameters, liquid crystals proved to be very efficient as a dielectric liquid yielding addressable photonic properties.

In this paper, we would like to review the methods of tuning by means of liquid crystal infiltration (Section 2) as well as all-optical effects that are due to the properties of the silicon (Section 3). The latter effects can be based on charge carrier injection due to one- or two-photon absorption or on Kerr-like nonlinearities (the latter being described by the real part of $\chi^{(3)}$).

2. TUNING BY MEANS OF LIQUID CRYSTAL INFILTRATION

Liquid crystals [20–24] exhibit very sensitive electro- and thermo-optical properties. Filled into the pores of a photonic crystal, they provide the opportunity of adjusting the effective refractive index by external parameters. This method was proposed by Busch and John [25–28] and experimentally demonstrated for colloidal crystals [29–34] before being applied to macroporous silicon [35–46] and other PBG semiconductor structures, including tunable light sources [47–50]. The sensitivity of liquid crystals is due to a preferred uniform alignment of their typically rod-like molecules, which in turn leads to birefringence. The local structure of the least complicated liquid crystalline mesophase, the nematic phase (Figure 1), can be described by the director \mathbf{n} (a pseudovector) and a scalar order parameter S , which indicate the local molecular alignment (i.e., the optical axis) and the degree of orientational order, respectively. External fields can rotate the optical axis, while an increasing

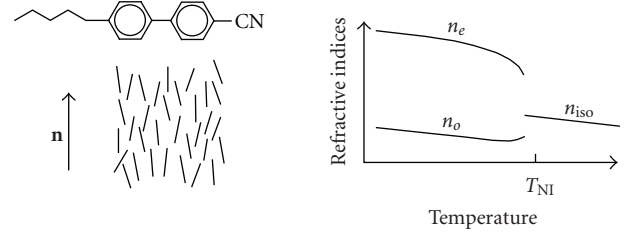


FIGURE 1: The chemical structure of 4-cyano-4'-pentyl-biphenyl, arrangement of rod-like molecules in the (nonchiral) nematic (N), and temperature dependence of the ordinary refractive index n_o (effective for light that is linearly polarized with its electric field perpendicular to the director \mathbf{n}), the extraordinary refractive index n_e (effective for light that is linearly polarized with its electric field parallel to the director \mathbf{n}), and the isotropic refractive index n_{iso} .

temperature results in a decreasing order parameter and thus a decreasing birefringence Δn . Typically, the difference $\Delta n = n_e - n_o$ between the extraordinary refractive index n_e and the ordinary refractive index n_o is of the order $\Delta n \approx 0.2$ if the temperature is several Ks below the nematic-isotropic phase transition (clearing temperature). No birefringence appears above the clearing temperature. Thus, relatively large thermally induced changes of the effective refractive index are observed at this phase transition.

Leonard et al. [35] were the first to infiltrate a two-dimensional structure made of macroporous silicon with a liquid crystal and observed changes of the photonic band edge for light propagating in the plane of the silicon wafer. This effect might be very useful for integrated optical waveguides in silicon. Subsequent experiments were focused on three-dimensional (3D) structures consisting of macroporous silicon that are filled with a liquid crystal. The latter structures show also a stop band for light propagating perpendicular to the plane of the wafer. Two-dimensional hexagonal or rectangular arrays of pores with an extremely high aspect ratio (diameter $\leq 1 \mu\text{m}$, depth $\geq 100 \mu\text{m}$) were fabricated by a light-assisted electrochemical etching process using HF [12, 13], and a periodic variation of pore diameter was induced by variation of the electric current during the etching procedure, thereby yielding in a three-dimensional photonic crystal (PhC) [14, 15]. The macroporous structure was evacuated and filled with a liquid crystal. The photonic properties for light propagation along the pore axis were studied by Fourier transform infrared (FTIR) spectroscopy [36–38]. Deuterium-nuclear magnetic resonance ($^2\text{H-NMR}$) [36, 37] and fluorescence confocal polarizing microscopy (FCPM) [39–42] were used in order to analyze the director field of the liquid crystal inside the pores.

For example, Figure 2 shows the infrared transmission of samples that show a two-dimensional hexagonal array of pores with a lattice constant $a = 1.5 \mu\text{m}$. Along the pore axis, the diameter of each pore varies periodically between $D_{min} = (0.76 \pm 0.10) \mu\text{m}$ and $D_{max} = (1.26 \pm 0.10) \mu\text{m}$ with a lattice constant $b = 2.6 \mu\text{m}$. The pores were filled with the nematic liquid crystal 4-cyano-4'-pentyl-biphenyl (5CB, Figure 1) which shows a clearing temperature of

$T_{\text{NI}} = 34^\circ\text{C}$. For light propagation along the pore axes, the FTIR transmission spectrum of the silicon-air structure shows a stop band centered at $\lambda = (10.5 \pm 0.5)\mu\text{m}$. Filling the pores with 5CB decreases the dielectric contrast to silicon and results in a shift of the stop band to $\lambda \approx 12\mu\text{m}$. The band edge was found to be sensitive to the state of polarization of the incident light. For linearly polarized light, rotation of the sample with respect to the plane of polarization was found to cause a shift of the liquid crystal band edge by $\Delta\lambda \approx 152\text{ nm}$ (1.61 meV). This effect can quantitatively be explained by the square shape of the pore cross-section, which brakes the threefold symmetry of the hexagonal lattice. Due to the presence of the liquid crystal, the band edge at lower wavelengths (“liquid crystal band” edge) can be tuned by more than 140 nm (1.23 meV) by heating the liquid crystal from 24°C (nematic phase) to 40°C (isotropic liquid phase).

The shift of the photonic band edge towards larger wavelengths indicates an increase of the effective refractive index with increasing temperature. This effect can be explained by a predominantly parallel alignment of the optical axis (director) of the nematic liquid crystal along the pore axis. For a uniform parallel alignment, the effective refractive index of the nematic component corresponds to the ordinary refractive index n_o of 5CB. Increasing the temperature above the clearing point causes an increase to the isotropic value $n_{\text{iso}} \approx (1/3n_e^2 + 2/3n_o^2)^{1/2}$, where n_e is the extraordinary refractive index of the liquid crystal ($n_e > n_o$). For a very crude approximation, the average dielectric constant ε_{av} of the heterogeneous structure can be calculated from the respective dielectric constants [$\varepsilon_{\text{LC}}(24^\circ\text{C}) = n_o^2$ and $\varepsilon_{\text{LC}}(40^\circ\text{C}) = n_{\text{iso}}^2$] using the Maxwell-Garnett relation (2) [19]. The relative shift of the stop band edge towards larger wavelengths corresponds approximately to the relative increase of the average refractive index by $\approx 0.65\%$. However, more precise analysis of the data shown in Figure 2 indicates that the shift of the two band edges is not the same (the shift of the left band edge is larger). The reason for the difference is that the overlap of the electric field with the pores is different at the two band edges (it is larger at the short wavelength edge), therefore changes of the refractive index in the pores translate into different shifts of the band edge. This is correctly predicted by the calculated dispersion relation shown in the right part of Figure 2, but cannot be explained by the Maxwell-Garnett relation [36].

Planar microcavities inside a 3D photonic crystal appear when the pore diameter is periodically modulated along the pore axis, stays constant within a defect layer, and is continued to vary periodically. Figure 3 shows a structure where a defect layer is embedded between five periodic modulations of the pore diameter. The pores are arranged in a 2D square lattice with a lattice constant of $a = 2\mu\text{m}$. The pore width varies along the pore axis between $D_{\text{min}} = 0.92\mu\text{m}$ and $D_{\text{max}} = 1.55\mu\text{m}$. The length of a modulation is $b = 2.58\mu\text{m}$. The defect has a length of $l = 2.65\mu\text{m}$ and pore diameters $D_{\text{def}} = 0.82\mu\text{m}$. Within the defect layer, the filling fraction of the liquid crystal is $\xi_{\text{def}} = 0.17$. For infrared radiation propagating along the pore axes, a fundamental stop gap at around $13\mu\text{m}$ and a second stop

gap at around $7\mu\text{m}$ are expected from calculations using the plane wave approximation [51]. The experiment shows a transmission peak at $\lambda = 7.184\mu\text{m}$ in the center of the second stop band, which can be attributed to a localized defect mode. Filling the structure with the liquid crystal 4-cyano-4'-pentyl-biphenyl (5CB, Merck) at 24°C causes a spectral red-shift of the stop band. Together with the stop band, the wavelength of the defect state is shifted by 191 nm to $\lambda = 7.375\mu\text{m}$. An additional shift of $\Delta\lambda = 20\text{ nm}$ to $\lambda = 7.395\mu\text{m}$ is observed when the liquid crystal is heated from 24°C (nematic phase) to 40°C (isotropic liquid phase). Again, the shift towards larger wavelengths indicates an increase of the effective refractive index n_{eff} of the liquid crystal with increasing temperature and can be attributed to the transition from an initially parallel aligned nematic phase ($n_{\text{LC,eff}} = n_o$) to the isotropic state ($n_{\text{LC,eff}} = n_{\text{iso}}$). During continuous variation of the temperature, a distinct step by 20 nm is observed at the phase transition from the nematic to the isotropic phase. The quality factor Q of the investigated structure, $Q = \lambda/\delta\lambda = 52$, is rather small and thus the shift by 20 nm appears to be small compared to the spectral width of the defect mode. However, the same order of magnitude of the temperature-induced wavelength shift can be expected for structures with a much higher quality factor and might be quite large compared to the band width of the defect mode.

Comparison of experimental $^2\text{H-NMR}$ results and calculated spectra (Figure 4) confirms a parallel (P) alignment of the director along the pore axis for substrates that were treated like the samples described above. However, also an anchoring of the director perpendicular to the silicon surfaces (“homeotropic” anchoring) can be achieved if the silicon wafer is cleaned with an ultrasonic bath and a plasma-cleaner and subsequently pretreated with *N,N*-dimethyl-*n*-octadecyl-3-aminopropyl-trimethoxysilyl chloride (DMOAP). NMR data indicate the appearance of an escaped radial (ER) director field in the latter case.

For the first time, optical microscopic studies of the director field in pores with a spatially periodic diameter variation could be achieved by means of a nematic liquid crystal polymer that shows a glass-like nematic state at room temperature [39, 40]. For fluorescence polarizing microscopy, the polymer was doped with *N,N'*-bis(2,5-di-*tert*-butylphenyl)-3,4,9,10-perylene-carboximide (BTBP). After filling the photonic crystal in vacuum, the sample was annealed in the nematic phase at 120°C for 24 hours and subsequently cooled to room temperature, thereby freezing the director in the glassy state. The silicon wafer was dissolved in concentrated aqueous KOH solution and the remaining isolated polymer rods were washed and investigated by fluorescence confocal polarizing microscopy (FCPM). The transition dipole moment of the dichroic dye BTBP is oriented along the local director of the liquid crystal host. The incident laser beam (488 nm, Ar⁺) and the emitted light pass a polarizer, which implies that the intensity of the detected light scales as $I \propto \cos^4\alpha$ for an angle α between the local director and the electric field vector of the polarized light. Thus, the local fluorescence intensity indicates the local orientation of the liquid crystal director with very high sensitivity. For a template with homeotropic anchoring and

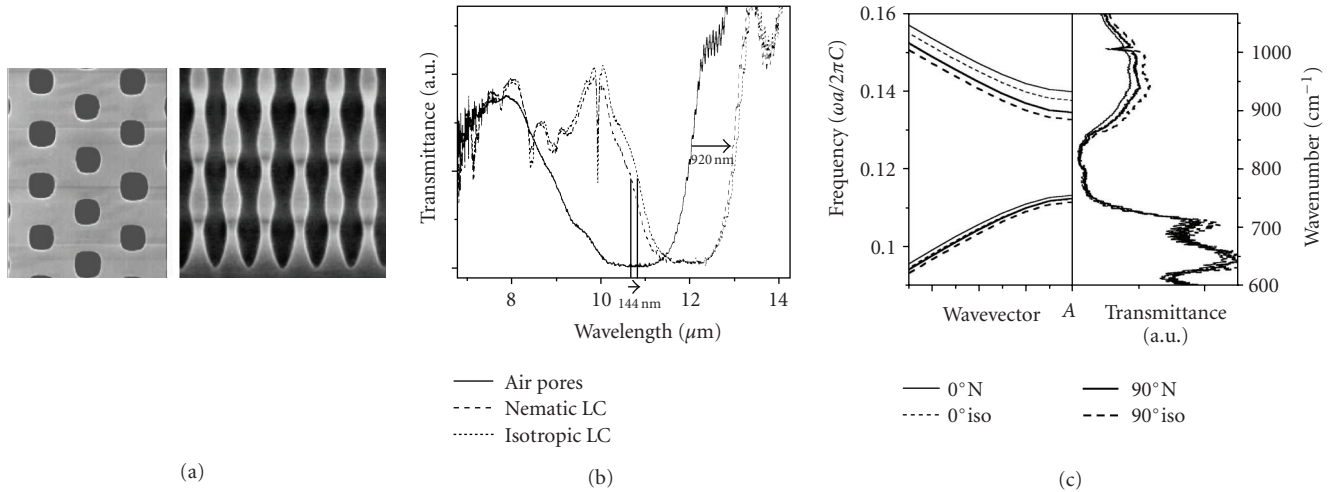


FIGURE 2: (a) SEM top-view and side-view of a photonic crystal made of macroporous silicon containing a two-dimensional hexagonal array of pores with periodically modulated diameter. (b) Transmission spectra of the same photonic crystal for light propagation along the pore axes if the sample is filled with (—) air, (---) 5CB in its nematic phase, and ($\cdot\cdot\cdot$) 5CB in its isotropic liquid state, respectively. (c) Comparison of the calculated dispersion relation using the plane wave approximation and the experimental spectra. For details, see [36].

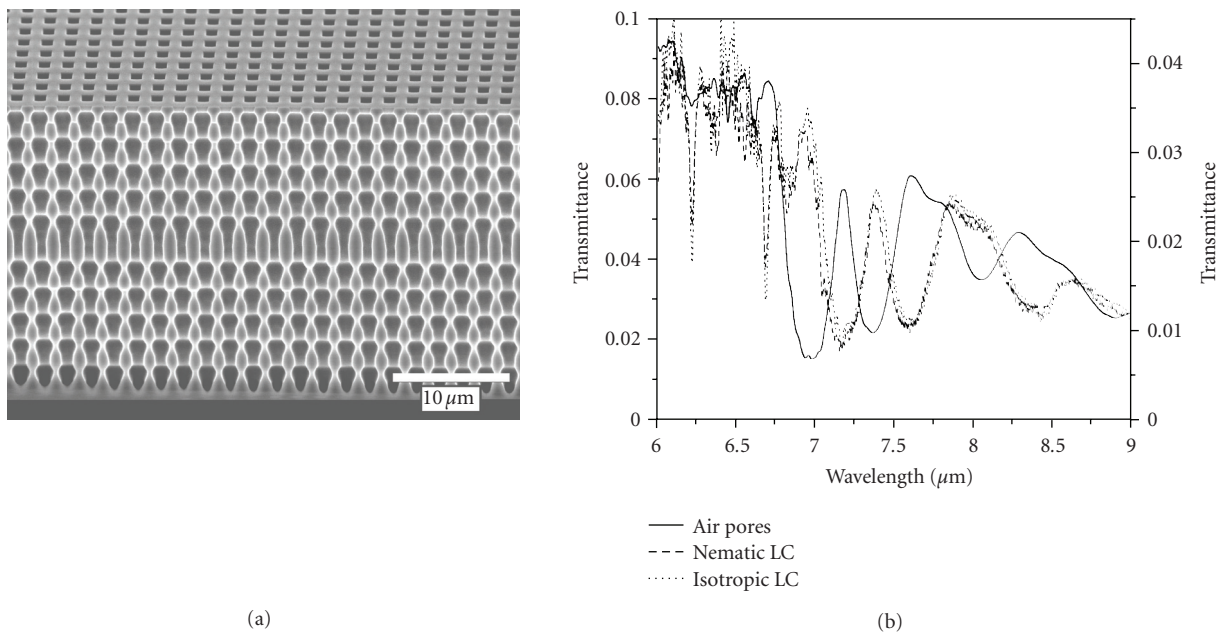


FIGURE 3: (a) SEM image (bird's eye view) of a silicon structure with modulated pores including a planar defect layer without modulation. (b) Transmission spectra of this structure if the sample is filled with (—) air, (---) 5CB in its nematic phase, and ($\cdot\cdot\cdot$) 5CB in its isotropic liquid state, respectively. For details, see [38].

a sine-like variation of the pore diameter between $2.2 \mu\text{m}$ and $3.3 \mu\text{m}$ at a modulation period of $11 \mu\text{m}$, the FCPM images of the nematic glass needles (Figure 5) indicate an escaped radial director field. Comparison with numerical calculations based on a tensor algorithm [52, 53] reveals some characteristic features that differ from nonmodulated pores. In the cylindrical cavities studied previously, point-like hedgehog and hyperbolic defects appear at random positions and tend to disappear after annealing, due to the attractive forces between defects of opposite topological

charges. In contrast, the modulated pores stabilize a periodic array of disclinations. Moreover, disclination loops appear instead of point-like disclinations.

3. ALL-OPTICAL TUNING

Altering the optical properties by optical irradiation has been the subject of intense research efforts related to the potential development of active photonic crystal components. Here, the impact of an optical pump beam on a photonic crystal

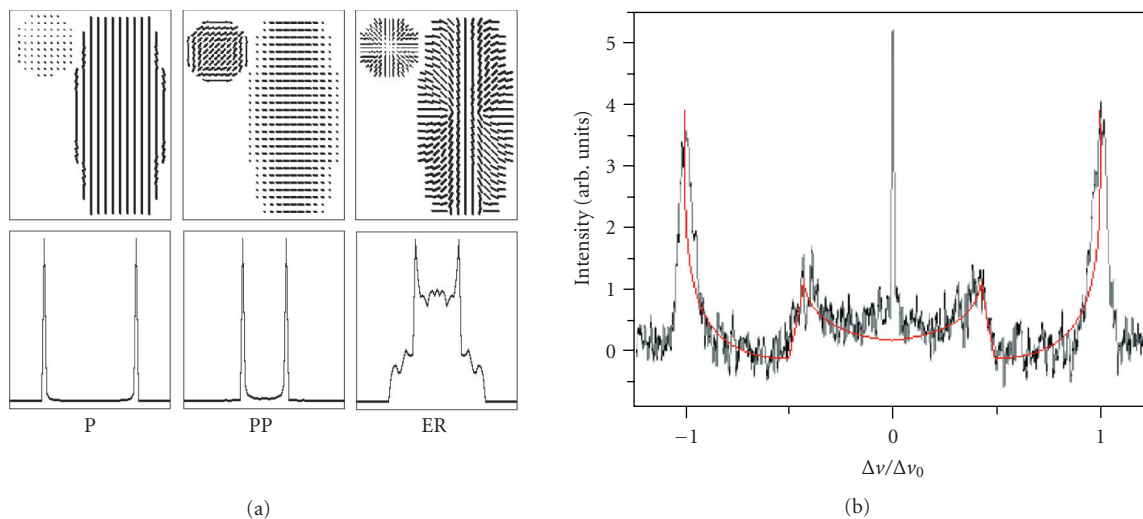


FIGURE 4: (a) Schematic relation between parallel (P), planar polar (PP), or escaped radial (ER) director fields and the respective ^2H -NMR-lineshapes. (b) ^2H -NMR spectrum of α -deuterated 5CB in cylindrical pores with perpendicular anchoring [thin line: spectrum expected for an escaped radial (ER) structure with weak anchoring]. For details, see [36, 37].

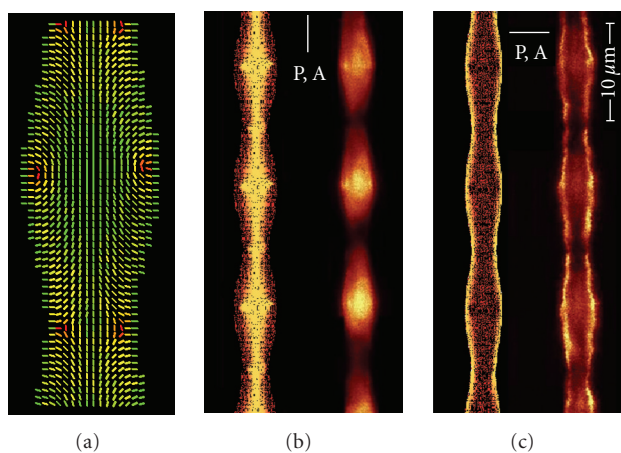


FIGURE 5: (a) Nematic escaped radial (ER) director field, calculated using the algorithm described in [52, 53]. (b) Theoretical and experimental fluorescent confocal polarizing microscopy (FCPM) images for polarized light with its electric field parallel to the tube axis. (c) Theoretical and experimental FCPM images for polarized light with its electric field perpendicular to the tube axis. For details, see [39].

consisting of a two-dimensional array of macropores in silicon [54–59] is reviewed. Figure 7(a) shows a sketch of such a crystal with photo-electrochemically etched straight pores with an aspect ratio of 100 [8, 12, 14]. If the photon energy ($\hbar\omega_p$) of the pump beam is larger than the electronic band gap of silicon, absorption causes a free charge carrier generation in the semiconductor which in turn changes the dielectric constant due to the Drude relation [54] (Section 3.1). These free carriers, generated by photon absorption, can be injected either by a single photon absorption or, in the presence of very high pump

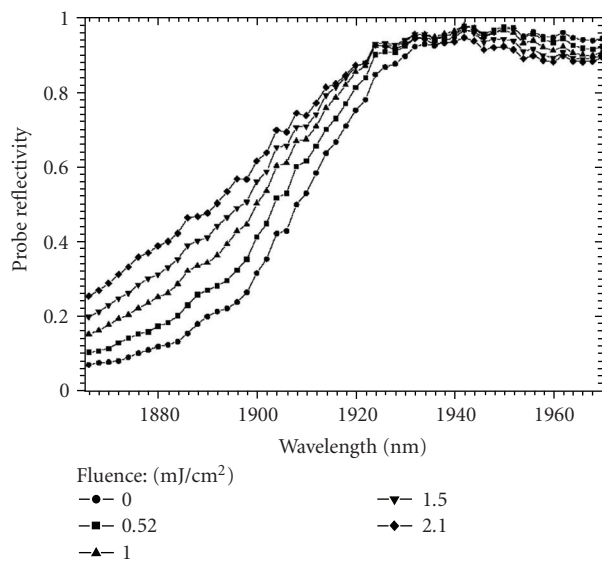


FIGURE 6: Variation of the air band edge of the silicon photon crystal following optical pumping by a 300 fs, 800 nm pulse of variable fluence.

intensities, by two-photon absorption. In contrast to the changes achieved by liquid crystal reorientation, this direct optical addressing of the silicon is very fast. Whereas the former occurs on time scales ranging from milliseconds to seconds, the optical tuning takes place in the subpicosecond regime.

Because of the centrosymmetric space group of silicon, bulk-contributions corresponding to the second-order nonlinear susceptibility $\chi^{(2)}$ are ruled out, but surface effects and third-order, that is, Kerr-like nonlinearities, corresponding to $\chi^{(3)}$ can be found. In addition, two-photon absorption of photons with low energy can cause a charge carrier injection

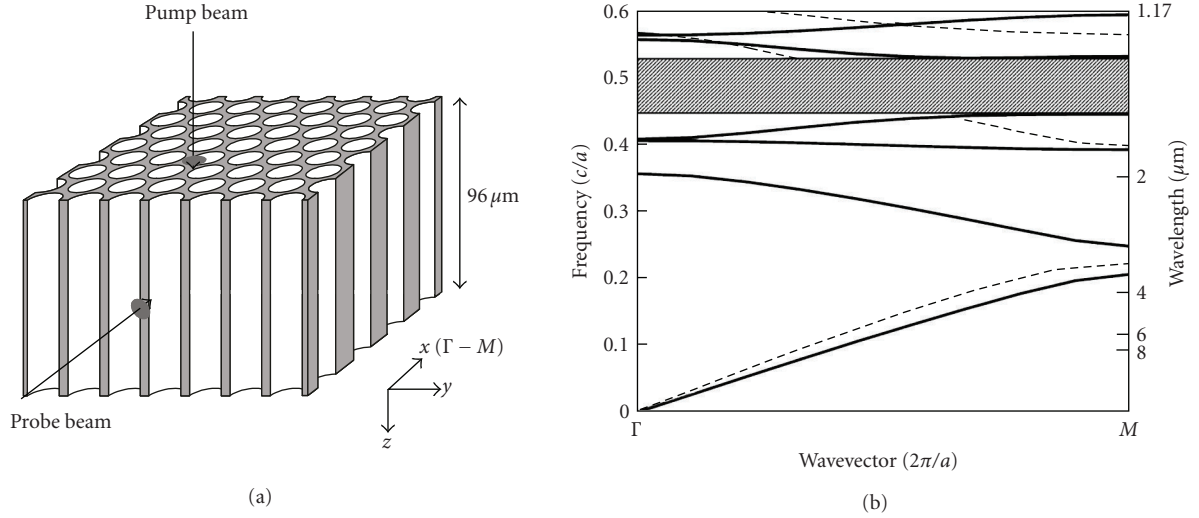


FIGURE 7: (a) The 2D Si photonic crystal showing pump-probe beam geometry. The probe beam is incident along the Γ - M direction. (b) Band structure of the photonic crystal for the Γ - M direction. The solid and dashed lines correspond to E and H polarized lights, respectively.

like the one-photon absorption of photons with high energy. Silicon has an indirect band gap of 1.1 eV ($\lambda = 1.1 \mu\text{m}$) at 295 K and a direct band gap of 3.5 eV ($\lambda = 355 \text{ nm}$). Thus, a relatively weak phonon-assisted linear absorption or a two-photon one occurs across the visible and near infrared. If the pump intensity is sufficiently high, nonlinear optical effects can cause changes of the dielectric constant even for photon energies that are smaller than the electronic band gap of silicon [55].

3.1. Charge carrier injection by one-photon absorption

To explore the influence of an electron-hole-plasma, a high density of carriers in a native macroporous silicon sample had been optically injected using optical techniques and by this monitoring the shift of a stop-gap edge [54]. As the (indirect band gap) absorption edge of silicon is at $1.1 \mu\text{m}$ for room temperature, electron-hole pairs can be efficiently produced at shorter wavelengths. The presence of the high density (N) carriers is expected to alter the real part of the dielectric constant ϵ at probe frequency ω through the expression

$$\epsilon = \epsilon_{\text{Si}} - \frac{Ne^2}{\epsilon_0 \omega^2 m^*}, \quad (4)$$

where ϵ_{Si} (11.9) is the quiescent dielectric constant of silicon, ϵ_0 is the permittivity of free space, and m^* is the optical effective mass of the electrons and holes. The carrier relaxation rate ($\sim 6 \text{ THz}$) has been neglected in comparison with the probing frequencies of interest. In the infrared region of the spectrum for wavelengths between $1 \mu\text{m}$ and $5 \mu\text{m}$, this is a reasonable approximation. Similarly, the influence of the imaginary part of the dielectric constant that would contribute to loss was neglected. From the frequency dependence in (1) one observes that for probing wavelengths in the near infrared region, changes in the dielectric constant

of the order of 10% can be obtained for our peak carrier densities. These substantial changes are expected to modify the location of the band gaps. For the experiments, the lowest stop band was investigated, which occurs in the photonic crystal described above between $1.9 \mu\text{m}$ and $2.3 \mu\text{m}$ for E -polarized light propagating along the Γ - M direction. In particular, the shift of the shorter wavelength band edge was measured. Similar shifts are expected for the longer wavelength band edge. The experimental results were obtained with a parametric generator pumped by a 250 kHz repetition rate Ti-sapphire oscillator/regenerative amplifier which produces 130 fs pulses at 800 nm at an average power of 1.1 W. The signal pulse from the parametric generator is tunable from $1.2 \mu\text{m}$ to $1.6 \mu\text{m}$ and the idler pulse is tunable from $2.1 \mu\text{m}$ to $1.6 \mu\text{m}$. Reflection measurements were made using 150 fs pulses with center wavelength of $1.9 \mu\text{m}$ and of sufficient bandwidth to probe the dynamical behavior of this edge. The pulses were focused onto the silicon photonic crystal with fluence per pulse up to $\sim 2 \text{ mJ cm}^{-2}$. Simple estimates based on anticipated absorption properties of the photonic crystal at this wavelength indicate that the peak density of electron hole pairs is $> 10^{18} \text{ cm}^{-3}$. The focal spot diameter of the probe beam was $30 \mu\text{m}$, reasonably small compared to the $\sim 100 \mu\text{m}$ spot diameter of the H-polarized pump beam. Figure 6 shows how the probe reflection characteristics change with the fluence of the pump beam.

The major effect of the optical pumping is to shift the band edge to shorter wavelengths as expected since the Drude contribution decreases the dielectric constant of the silicon. Detailed calculations based on absorption characteristics of the photonic crystal at the pump wavelength and the variation of the photonic crystal dispersion curves with injected carrier density are in agreement with the maximum shift of about 30 nm (at the 3 dB point) that is observed here. Indeed, the shift of the edge scales linearly with the pump fluence, or injected carrier density, as expected theoretically. It should be noted however that the shift of the edge is not

rigid. The shift is less for higher values of the reflectivity. This is presumably related to the fact that the 800 nm pump radiation is inhomogeneously absorbed, with an absorption depth of a few microns. In the spectral range near the peak value of the reflectivity associated with a stop gap, the reflectivity originates from lattice planes over a considerable depth within the crystal. In contrast, Fresnel reflectivity of the surface region dictates the reflection characteristics in the spectral range with higher transmission. To overcome this problem, other pumping schemes have to be used.

It was also possible to time resolve the reflectivity behavior by monitoring the probe reflectivity of the band edge as a function of delay between the probe and pump beams. Not surprisingly, the probe reflectivity change is virtually complete within the duration of the pump beam as charge carriers accumulate in the silicon. However, the recovery of the induced change occurs on a much longer time scale (at least nanoseconds) in our photonic crystal reflecting the electron-hole carrier recombination characteristics.

3.2. Tuning by Kerr-like optical nonlinearities

The Kerr effect was used to tune the short wavelength edge of a photonic band gap. In these experiments, a 2D photonic crystal was used to demonstrate the all optical tuning. Both the short wavelength edge (1.3 μm) and the long wavelength edge (1.6 μm) could be redshifted by the Kerr effect ($\chi^{(3)}$). But for high pump intensities, the two-photon absorption was significantly generating free carriers, leading to a blueshift of the photonic band edge via the Drude contribution to $\chi^{(1)}$.

The 2D silicon PhC sample has a triangular lattice arrangement of 560 nm diameter, 96 μm deep air holes with a pitch, a , equal to 700 nm. Figure 7(a) shows a real space view of the sample while Figure 7(b) illustrates the photonic band structure for the Γ - M direction, which is normal to a face of the PhC. Of particular interest is the third stop gap for E -polarized (E -field parallel to the pore axis) light. Lying between 1.3 μm and 1.6 μm , this gap falls between two dielectric bands that are sensitive to changes in the silicon refractive index. The purpose was to optically induce changes to the two edges with idler pulses from the parametric generator and probe these changes via time-resolved reflectivity of the signal pulses. Note that, because of the link between the signal and idler wavelengths, different pump wavelengths (2.0 μm for a 1.3 μm probe; 1.76 μm for a 1.6 μm probe) must be used when the probe wavelength is changed. However, as will be shown in what follows, small changes in the pump wavelength can lead to significant changes in the induced optical processes.

Figure 8 shows the time-dependent change in reflectivity at 1.3 μm for a 2.0 μm pump pulse and the cross-correlation trace of both pulses. The pump and probe intensities are 17.6 and 0.5 GW/cm^2 , respectively. The decrease in reflectivity is consistent with a redshift of the band edge due to a positive nondegenerate Kerr index. The FWHM of the reflectivity trace is 365 ± 10 fs which is 1.83 times larger than the pump-probe cross-correlation width as measured by sum frequency generation in a beta-barium borate (BBO) crystal.

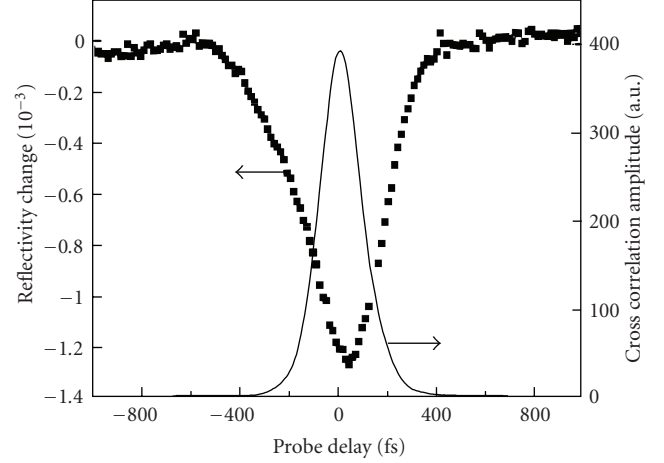


FIGURE 8: Temporal response of reflectivity change at the 1.3 μm band edge when the PhC is pumped with a 2.0 μm pulse at 17.6 GW/cm^2 . Also shown is the cross-correlation trace of the pump and probe pulses.

This difference can be explained in terms of pump and probe beam transit time effects in the PhC as discussed above. Indeed, from the pump group velocity and probe spot size, one can deduce that the reflected probe pulse is delayed by 110 fs within the PhC sample. After these effects are taken into account, the intrinsic interaction times are essentially pulse width limited, consistent with the Kerr effect.

One can estimate a value for the nondegenerate Kerr coefficient n_2 in the silicon PhC from the relation [55]

$$\Delta R = \frac{dR}{d\lambda} \frac{d\lambda}{dn} n_2 \frac{1 - R_u}{f} I_0, \quad (5)$$

where I_0 is the incident intensity, f is the filling fraction, and R_u is the reflectivity of the sample. The experimental values of the steepness of the band edge reflectivity, $dR/d\lambda = 0.04 \text{ nm}^{-1}$, and the differential change in band edge wavelength with refractive index, $d\lambda/dn = 174 \text{ nm}$, are relatively large. Thus, induced reflectivity changes in the vicinity of the 1.3 μm band edge are found to be 70 times more sensitive than that in bulk materials for the same refractive index change, a degree of leverage also noted by others [54, 60]. Indeed, when the PhC is replaced by bulk crystalline silicon, *no change* in reflectivity is observed for the range of pump intensity.

The inset to Figure 9 shows there is good correlation between the change in probe reflectivity and the steepness of the band edge reflectivity (measured separately) at different wavelengths and for a range of pump intensities. Figure 9 shows the change in reflectivity with pump intensity at zero time delay. The linear dependence is consistent with the Kerr effect and the nondegenerate Kerr index is estimated to be $5.2 \times 10^{-15} \text{ cm}^2/\text{W}$. This is within an order of magnitude of the degenerate Kerr index reported [61, 62] at 1.27 μm and 1.54 μm and represents reasonable agreement considering uncertainty in the lateral position (x) of the pump pulse and its intensity at the probe location. It should also be noted that

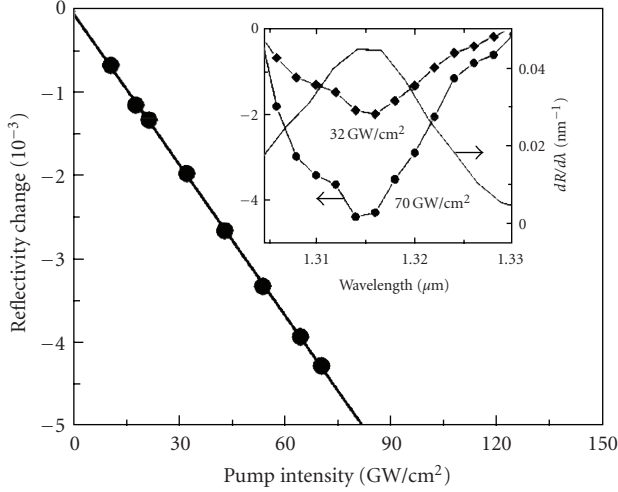


FIGURE 9: Dependence of probe reflectivity change at $1.316 \mu\text{m}$ on pump intensity at zero delay. The inset shows the spectral characteristic of reflectivity change at the $1.3 \mu\text{m}$ band edge at zero delay for different pump intensities at $2.0 \mu\text{m}$. Also shown in the inset is the $dR/d\lambda$ curve, which measures the steepness of the band edge reflectivity.

linear scattering losses as the pump pulse propagates through the PhC along the pore axis have not been taken into account.

3.3. Tuning by Kerr-like nonlinearities and two-photon absorption

In general, overall pulse-width limited response can only be achieved using nonresonant, nonlinear induced changes to material optical properties such as the optical Kerr effect (a third-order nonlinearity). In this case, the change in refractive index for a probe beam is given by

$$\Delta n = n_2 I, \quad (6)$$

where I is the intensity of the pump beam and n_2 is the Kerr coefficient associated with the pump and probe frequencies. If the probe light intensity is limited to values like in the experiment of Leonard et al. [54], the imaginary terms in the dielectric function arising from free-carrier absorption and intervalence-band absorption are very small.

Results from experiments used to probe the $1.6 \mu\text{m}$ band edge when the sample is pumped with $1.76 \mu\text{m}$ pulses are illustrated in Figure 10, which shows the temporal response of the change in probe reflectivity at different pump intensities for a probe intensity of 0.13 GW/cm^2 . There is an initial increase and decrease in probe reflectivity on a subpicosecond time scale followed by a response that decays on a time scale of 900 picoseconds and partially masks the Kerr effect near zero delay. At this band edge, the subpicosecond behavior is consistent with a Kerr effect similar to the previous experiments. The long time response could possibly be due to thermal or Drude contributions to the dielectric constant due to the generation of free carriers. Using a peak pump intensity of 120 GW/cm^2 and a 0.8 cm/GW two-photon absorption coefficient [61, 62] for $1.55 \mu\text{m}$ as an upper limit, one can estimate the surface

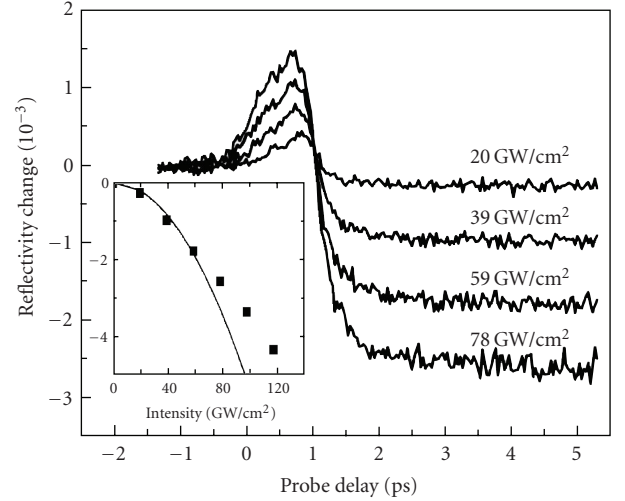


FIGURE 10: Temporal response of the reflectivity change at the $1.6 \mu\text{m}$ band edge for different pump intensities at $1.76 \mu\text{m}$. The inset shows the dependence of the carrier-induced reflectivity change on pump intensity for low pump powers.

peak carrier density to be $<10^{19} \text{ cm}^{-3}$ and the maximum change in temperature to be $<0.15 \text{ K}$. From the thermo-optic coefficient $\partial n/\partial T \approx 1 \times 10^{-4} \text{ K}^{-1}$ at the probe wavelength [63], the change in silicon refractive index is on the order of 10^{-5} and the (positive) induced change in reflectivity is expected to be about the same. From free carrier (Drude) contributions to the refractive index at the probe wavelength, changes to the imaginary part of the dielectric constant are about 2 orders of magnitude smaller than that of the real part [64], which is about -10^{-3} . Hence, free carrier absorption of the probe pulse as well as thermally induced changes can be neglected in what follows and the change in reflectivity is ascribed to changes in the real part of the dielectric constant due to Drude effects.

At low pump powers, the change in probe reflectivity scales quadratically with pump intensity. This can be explained by free carrier generation due to two-photon absorption, with the charge carrier density N being given by

$$N(z) = \frac{\sqrt{\pi}\beta\tau_p}{4\hbar\omega_p\sqrt{\ln 2}} I^2(z), \quad (7)$$

where β is the two-photon absorption coefficient, τ_p is the temporal FWHM pulse width of the pump pulses, and ω_p is the pump frequency. However, at higher pump intensities, there is an apparent deviation from this quadratic dependence (see inset in Figure 10) due to pump saturation effects, since the pump intensity I varies along the z -direction as

$$I(z) = \frac{(1 - R_u)I_0}{f + \beta z(1 - R_u)I_0}, \quad (8)$$

according to attenuation by two-photon absorption. With increasing intensity in a two-photon absorption process, an increasing fraction of the carriers are created closer to the

TABLE 1: Spectral shifts and switching speeds of the different effects described in Sections 2 and 3.

Effect	Initial frequency ν (Hz)	Frequency shift $\delta\nu$ or refractive index shift δn /control parameter	Relative frequency shift $ \delta\nu /\nu$	Time constant (s)
Temperature-induced shift of the “silicon” band edge in a liquid crystal-infiltrated structure [36].	$2.32 \cdot 10^{13}$	$\delta\nu/\delta T = -1.68 \cdot 10^{11} \text{ Hz}/16^\circ\text{C}$	0.72%	
Temperature-induced shift of the “liquid crystal” band edge in a liquid crystal-infiltrated structure [36].	$2.81 \cdot 10^{13}$	$\delta\nu/\delta T = -3.74 \cdot 10^{11} \text{ Hz}/16^\circ\text{C}$	1.33%	$\approx 10^{-3}$
Temperature-induced shift of the microcavity resonance in a liquid crystal-infiltrated structure [38].	$4.05 \cdot 10^{13}$	$\delta\nu/\delta T = -1.56 \cdot 10^{11} \text{ Hz}/1^\circ\text{C}$	0.39%	
Temperature-induced shift of the PL emission frequency in an Er-doped liquid crystal-infiltrated structure [46].	$1.93 \cdot 10^{14}$	$\delta\nu/\delta T = -8.70 \cdot 10^{11} \text{ Hz}/23^\circ\text{C}$	0.45%	
Free charge carrier injection induced by one-photon absorption [54].	$1.58 \cdot 10^{14}$	$\delta\nu/\delta T = -2.53 \cdot 10^{12} \text{ Hz}/(2.1 \pm 0.4) \text{ m J}/\text{cm}^2$	1.60%	$\approx 10^{-6}$
Tuning by Kerr-like nonlinearities [55].		$\delta n \approx 10^{-3}$		Instantaneous (10^{-13})

surface where the pump pulse enters and the probe region develops a reduced and increasingly nonuniform carrier density. It can be estimated that at a depth of $60 \mu\text{m}$, the expected saturation pump intensity is about an order of magnitude larger than the maximum pump intensity used in this setup. The carrier lifetime of 900 picoseconds is most likely associated with surface recombination within the PhC sample with its large internal surface area.

The reflectivity change due to the Drude effect is given by

$$\Delta R = \frac{dR}{d\lambda} \frac{d\lambda}{dn} \frac{e^2}{2n_0\omega_r^2 m^* \varepsilon_0} \frac{\sqrt{\pi}\beta\tau_p}{4\hbar\omega_p \sqrt{\ln 2}} I^2(z), \quad (9)$$

where ω_r is the probe frequency, m^* is the effective optical mass of the electrons and holes ($= 0.16 m_0$), and ε_0 is the permittivity of free space. Thus, from the low intensity behavior in the inset to Figure 10, the two-photon absorption coefficient, β , can be estimated to be $0.02 \text{ cm}/\text{GW}$, which is within an order of magnitude but smaller than that reported [61, 65] for wavelengths near $1.55 \mu\text{m}$. For the $2 \mu\text{m}$ pump wavelength, the upper limit for β is estimated to be $2 \times 10^{-3} \text{ cm}/\text{GW}$ from the signal to noise and the fact that no measurable long-lived response at the highest pump intensity used is observed. This value is an order of magnitude smaller than what is determined at $1.76 \mu\text{m}$ and it is not a surprise since β is expected to decrease rapidly with increasing wavelength as the indirect gap edge is approached.

4. SUMMARY

In conclusion, either the infiltration of macroporous silicon with liquid crystals and subsequent control of the thermo-

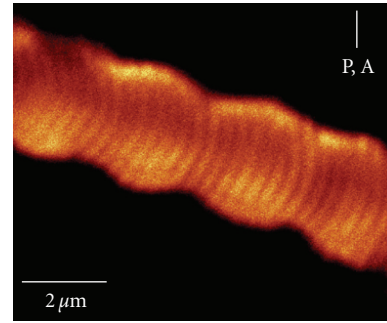


FIGURE 11: FCPM image of a cholesteric cylinder with perpendicular anchoring and a helix pitch smaller than the cylinder diameter. The regular fringes are perpendicular to the pitch axis and their distance corresponds to one half of the pitch. For further details, see [41].

dynamic variables or the use of light absorption of Kerr-like optical nonlinearities can be used to achieve tunable properties in photonic crystals made of macroporous silicon. For both methods, the relative frequency shift of photonic bands, band edges, or resonance frequencies of microcavities is roughly of the order of 1% of the absolute frequency (Table 1). The effect is limited, but can nevertheless be much larger than the linewidth of modes to be tuned, since microresonators with very large Q factors can be fabricated. The methods summarized in Sections 2 and 3 may find different applications. The use of liquid crystals has the advantage that the control parameters temperature and electric fields are easily available. However, the greatest disadvantage is probably the limited speed of director

reorientation, which corresponds to time constants in the millisecond range. In contrast, absorption and nonlinear effects lead to very fast changes of the photonic properties (with time constants below 1 picosecond) and can be used for all-optical switching. However, very large intensities are required for the nonlinear optical effects.

Besides further technical developments that make use of the effects studied, so far, a couple of novel, fundamentally interesting systems deserve to be explored in more detail:

(1) Chiral liquid crystals: cholesteric phases and blue phases [20–24] show a helical superstructure of the local alignment, thereby leading to a spatially periodic director field $\mathbf{n}(\mathbf{r})$. This intrinsic periodicity can be combined with two-dimensional arrays of pores, thereby leading to novel three-dimensional heterogeneous structures [41]. As an example, Figure 11 shows the FCPM image of a sample which shows an inherent periodicity within the pores. Such structures may show enhanced nonlinear optical effects or may be used for switching between a three-dimensional and a two-dimensional periodicity of the optical density. Additional work on these systems is in progress.

(2) Liquid crystals can exhibit both second- and third-order optical nonlinearity. Thus, infiltration of photonic crystals with liquid crystals that exhibit large $\chi^{(2)}$ - or $\chi^{(3)}$ -values may be used for frequency conversion or all-optical switching, respectively. A considerable enhancement of second harmonic generation (SHG) intensity is known to appear in spatially periodic structures, where both the fundamental frequency and the second harmonic are close to photonic stop bands [66, 67]. In addition, suitable liquid crystals are known for their giant optical nonlinearity (GON) [68], that is, a huge Kerr effect which is due to collective reorientation of the liquid crystal molecules induced by the optical electric field strength.

Fundamental studies of these effects in the environment of a silicon photonic crystal appear to be challenging. In conclusion, the development of tunable photonic crystals based on silicon is still in progress.

ACKNOWLEDGMENTS

This work was supported by the company E. Merck (Darmstadt) with liquid crystals. Also, the funding by the German Research Foundation (KI 411/4 and SPP 1113) and the European Science Foundation (EUROCORES/05-SONS-FP-014) is gratefully acknowledged.

REFERENCES

- [1] E. Yablonovitch, "Inhibited spontaneous emission in solid-state physics and electronics," *Physical Review Letters*, vol. 58, no. 20, pp. 2059–2062, 1987.
- [2] S. John, "Strong localization of photons in certain disordered dielectric superlattices," *Physical Review Letters*, vol. 58, no. 23, pp. 2486–2489, 1987.
- [3] J. D. Joannopoulos, R. D. Meade, and J. N. Winn, *Photonic Crystals: Molding the Flow of Light*, Princeton University Press, Princeton, NJ, USA, 1995.
- [4] C. M. Soukoulis, Ed., *Photonic Crystals and Light Localization in the 21st Century*, vol. 563 of *NATO Science Series C: Mathematical and Physical Sciences*, Kluwer Academic Publishers, Dordrecht, The Netherlands, 2001.
- [5] S. G. Johnson and J. D. Joannopoulos, *Photonic Crystals: The Road from Theory to Practice*, Kluwer Academic Publishers, Boston, Mass, USA, 2002.
- [6] R. E. Slusher and B. J. Eggleton, Eds., *Nonlinear Photonic Crystals*, vol. 10 of *Springer Series in Photonics*, Springer, Berlin, Germany, 2003.
- [7] K. Inoue and K. Ohtaka, Eds., *Photonic Crystals: Physics, Fabrication and Applications*, vol. 94 of *Springer Series in Optical Sciences*, Springer, Berlin, Germany, 2004.
- [8] K. Busch, S. Lölkes, R. B. Wehrspohn, and H. Föll, Eds., *Photonic Crystals: Advances in Design, Fabrication and Characterization*, Wiley-VCH, Weinheim, Germany, 2004.
- [9] K. Sakoda, *Optical Properties of Photonic Crystals*, vol. 80 of *Springer Series in Optical Sciences*, Springer, Berlin, Germany, 2nd edition, 2005.
- [10] J.-M. Lourtioz, H. Benisty, V. Berger, J.-M. Gerard, D. Maystre, and A. Tchebnokov, *Photonic Crystals: Towards Nanoscale Photonic Devices*, Springer, Berlin, Germany, 2005.
- [11] K. Yasumoto, Ed., *Electromagnetic Theory and Applications for Photonic Crystals*, vol. 102 of *Optical Science and Engineering*, CRC Press, Boca Raton, Fla, USA, 2006.
- [12] F. Müller, A. Birner, U. Gösele, V. Lehmann, S. Ottow, and H. Föll, "Structuring of macroporous silicon for applications as photonic crystals," *Journal of Porous Materials*, vol. 7, no. 1, pp. 201–204, 2000.
- [13] J. Schilling, F. Müller, S. Matthias, R. B. Wehrspohn, U. Gösele, and K. Busch, "Three-dimensional photonic crystals based on macroporous silicon with modulated pore diameter," *Applied Physics Letters*, vol. 78, no. 9, pp. 1180–1182, 2001.
- [14] A. Birner, R. B. Wehrspohn, U. M. Gösele, and K. Busch, "Silicon-based photonic crystals," *Advanced Materials*, vol. 13, no. 6, pp. 377–388, 2001.
- [15] S. Matthias, R. Hillebrand, F. Müller, and U. Gösele, "Macroporous silicon: homogeneity investigations and fabrication tolerances of a simple cubic three-dimensional photonic crystal," *Journal of Applied Physics*, vol. 99, no. 11, Article ID 113102, 5 pages, 2006.
- [16] P. V. Braun and S. M. Weiss, Eds., *Tuning the Optic Response of Photonic Bandgap Structures III*, vol. 6322 of *Proceedings of the SPIE*, San Diego, Calif, USA, August 2006.
- [17] P. M. Fauchet and P. V. Braun, Eds., *Tuning the Optical Response of Photonic Bandgap Structures II*, vol. 5926 of *Proceedings of the SPIE*, San Diego, Calif, USA, July-August 2005.
- [18] P. M. Fauchet and P. V. Braun, Eds., *Tuning the Optical Response of Photonic Bandgap Structures*, vol. 5511 of *Proceedings of the SPIE*, Denver, Colo, USA, August 2004.
- [19] J. C. M. Garnett, "Colours in metal glasses and in metallic films," *Philosophical Transactions of the Royal Society of London A*, vol. 203, pp. 385–420, 1904.
- [20] P. G. de Gennes and J. Prost, *The Physics of Liquid Crystals*, Clarendon Press, Oxford, UK, 2nd edition, 1993.
- [21] S. Chandrasekhar, *Liquid Crystals*, Cambridge University Press, Cambridge, UK, 2nd edition, 1992.
- [22] S. Kumar, Ed., *Liquid Crystals: Experimental Study of Physical Properties and Phase Transitions*, Cambridge University Press, Cambridge, UK, 2001.
- [23] G. P. Crawford and S. Žumer, Eds., *Liquid Crystals in Complex Geometries Formed by Polymer and Porous Networks*, Taylor & Francis, London, UK, 1996.

- [24] H.-S. Kitzerow, "The effect of electric fields on blue phases," *Molecular Crystals and Liquid Crystals*, vol. 202, no. 1, pp. 51–83, 1991.
- [25] K. Busch and S. John, "Photonic band gap formation in certain self-organizing systems," *Physical Review E*, vol. 58, no. 3, pp. 3896–3908, 1998.
- [26] K. Busch and S. John, "Liquid-crystal photonic-band-gap materials: the tunable electromagnetic vacuum," *Physical Review Letters*, vol. 83, no. 5, pp. 967–970, 1999.
- [27] S. John and K. Busch, "Photonic bandgap formation and tunability in certain self-organizing systems," *Journal of Lightwave Technology*, vol. 17, no. 11, pp. 1931–1943, 1999.
- [28] S. John and K. Busch, "Electro-actively tunable photonic bandgap materials," US patent 6813064, November 2004.
- [29] K. Yoshino, Y. Shimoda, Y. Kawagishi, K. Nakayama, and M. Ozaki, "Temperature tuning of the stop band in transmission spectra of liquid-crystal infiltrated synthetic opal as tunable photonic crystal," *Applied Physics Letters*, vol. 75, no. 7, pp. 932–934, 1999.
- [30] K. Yoshino, S. Satoh, Y. Shimoda, Y. Kawagishi, K. Nakayama, and M. Ozaki, "Tunable optical stop band and reflection peak in synthetic opal infiltrated with liquid crystal and conducting polymer as photonic crystal," *Japanese Journal of Applied Physics*, vol. 38, no. 8, pp. L961–L963, 1999.
- [31] D. Kang, J. E. MacLennan, N. A. Clark, A. A. Zakhidov, and R. H. Baughman, "Electro-optic behavior of liquid-crystal-filled silica opal photonic crystals: effect of liquid-crystal alignment," *Physical Review Letters*, vol. 86, no. 18, pp. 4052–4055, 2001.
- [32] G. Mertens, T. Röder, R. Schweins, K. Huber, and H.-S. Kitzerow, "Shift of the photonic band gap in two photonic crystal/liquid crystal composites," *Applied Physics Letters*, vol. 80, no. 11, pp. 1885–1887, 2002.
- [33] H.-S. Kitzerow, A. Hoischen, G. Mertens, et al., "Polymer / liquid crystal composites: from polymer-dispersed liquid crystals to tunable photonic crystals," *Polymer Preprints*, vol. 43, no. 2, pp. 534–535, 2002.
- [34] H.-S. Kitzerow, "Tunable photonic crystals," *Liquid Crystals Today*, vol. 11, no. 4, pp. 3–7, 2002.
- [35] S. W. Leonard, J. P. Mondia, H. M. van Driel, et al., "Tunable two-dimensional photonic crystals using liquid-crystal infiltration," *Physical Review B*, vol. 61, no. 4, pp. R2389–R2392, 2000.
- [36] G. Mertens, T. Röder, H. Matthias, et al., "Two- and three-dimensional photonic crystals made of macroporous silicon and liquid crystals," *Applied Physics Letters*, vol. 83, no. 15, pp. 3036–3038, 2003.
- [37] G. Mertens, *Anwendung von Flüssigkristallen für abstimmbare photonische Kristalle*, Ph.D. dissertation, University of Paderborn, Paderborn, Germany, 2004.
- [38] G. Mertens, R. B. Wehrspohn, H.-S. Kitzerow, S. Matthias, C. Jamois, and U. Gösele, "Tunable defect mode in a three-dimensional photonic crystal," *Applied Physics Letters*, vol. 87, no. 24, Article ID 241108, 3 pages, 2005.
- [39] H. Matthias, T. Röder, R. B. Wehrspohn, H.-S. Kitzerow, S. Matthias, and S. J. Picken, "Spatially periodic liquid crystal director field appearing in a photonic crystal template," *Applied Physics Letters*, vol. 87, no. 24, Article ID 241105, 3 pages, 2005.
- [40] H.-S. Kitzerow, G. Mertens, H. Matthias, et al., "Director fields of nematic liquid crystals in tunable photonic crystals," in *Tuning the Optical Response of Photonic Bandgap Structures II*, vol. 5926 of *Proceedings of SPIE*, pp. 25–34, San Diego, Calif, USA, July–August 2005.
- [41] H. Matthias, S. L. Schweizer, R. B. Wehrspohn, and H.-S. Kitzerow, "Liquid crystal director fields in micropores of photonic crystals," *Journal of Optics A*, vol. 9, no. 9, pp. S389–S395, 2007.
- [42] H.-S. Kitzerow, A. Lorenz, and H. Matthias, "Tuneable photonic crystals obtained by liquid crystal infiltration," *Physica Status Solidi (A)*, vol. 204, no. 11, pp. 3754–3767, 2007.
- [43] S. M. Weiss, M. Haurylau, and P. M. Fauchet, "Tunable photonic bandgap structures for optical interconnects," *Optical Materials*, vol. 27, no. 5, pp. 740–744, 2005.
- [44] S. M. Weiss, H. Ouyang, J. Zhang, and P. M. Fauchet, "Electrical and thermal modulation of silicon photonic bandgap microcavities containing liquid crystals," *Optics Express*, vol. 13, no. 4, pp. 1090–1097, 2005.
- [45] M. Haurylau, S. P. Anderson, K. L. Marshall, and P. M. Fauchet, "Electrically tunable silicon 2-D photonic bandgap structures," *IEEE Journal on Selected Topics in Quantum Electronics*, vol. 12, no. 6, pp. 1527–1532, 2006.
- [46] S. M. Weiss, J. Zhang, P. M. Fauchet, V. V. Seregin, and J. L. Coffey, "Tunable silicon-based light sources using erbium doped liquid crystals," *Applied Physics Letters*, vol. 90, no. 3, Article ID 031112, 3 pages, 2007.
- [47] Ch. Schuller, F. Klopff, J. P. Reithmaier, M. Kamp, and A. Forchel, "Tunable photonic crystals fabricated in III-V semiconductor slab waveguides using infiltrated liquid crystals," *Applied Physics Letters*, vol. 82, no. 17, pp. 2767–2769, 2003.
- [48] H.-S. Kitzerow and J. P. Reithmaier, "Tunable photonic crystals using liquid crystals," in *Photonic Crystals: Advances in Design, Fabrication and Characterization*, K. Busch, H. Föll, S. Lölkes, and R. B. Wehrspohn, Eds., chapter 9, pp. 174–197, Wiley-VCH, Weinheim, Germany, 2004.
- [49] B. Maune, M. Lončar, J. Witzens, et al., "Liquid-crystal electric tuning of a photonic crystal laser," *Applied Physics Letters*, vol. 85, no. 3, pp. 360–362, 2004.
- [50] K. A. Piegdon, H. Matthias, C. Meier, and H.-S. Kitzerow, "Tunable optical properties of photonic crystals and semiconductor microdisks using liquid crystals," in *Emerging Liquid Crystal Technologies III*, vol. 6911 of *Proceedings of SPIE*, pp. 6911–1619, San Jose, Calif, USA, January 2008.
- [51] S. G. Johnson and J. D. Joannopoulos, "Block-iterative frequency-domain methods for Maxwell's equations in a planewave basis," *Optics Express*, vol. 8, no. 3, pp. 173–190, 2001.
- [52] S. Dickmann, *Numerische Berechnung von Feld und Molekülausrichtung in Flüssigkristallanzeigen*, Ph.D. thesis, University of Karlsruhe, Karlsruhe, Germany, 1994.
- [53] H. Mori, E. C. Gartland Jr., J. R. Kelly, and P. J. Bos, "Multidimensional director modeling using the Q tensor representation in a liquid crystal cell and its application to the π cell with patterned electrodes," *Japanese Journal of Applied Physics*, vol. 38, no. 1, pp. 135–146, 1999.
- [54] S. W. Leonard, H. M. van Driel, J. Schilling, and R. B. Wehrspohn, "Ultrafast band-edge tuning of a two-dimensional silicon photonic crystal via free-carrier injection," *Physical Review B*, vol. 66, no. 16, Article ID 161102, 4 pages, 2002.
- [55] H. W. Tan, H. M. van Driel, S. L. Schweizer, R. B. Wehrspohn, and U. Gösele, "Nonlinear optical tuning of a two-dimensional silicon photonic crystal," *Physical Review B*, vol. 70, no. 20, Article ID 205110, 5 pages, 2004.

- [56] H. W. Tan, H. M. van Driel, S. L. Schweizer, and R. B. Wehrspohn, "Influence of eigenmode characteristics on optical tuning of a two-dimensional silicon photonic crystal," *Physical Review B*, vol. 72, no. 16, Article ID 165115, 8 pages, 2005.
- [57] S. L. Schweizer, R. B. Wehrspohn, H. W. Tan, and H. M. van Driel, "Nonlinear optical tuning in a 2-D silicon photonic crystal," in *Tuning the Optical Response of Photonic Bandgap Structures II*, vol. 5926 of *Proceedings of SPIE*, pp. 48–56, San Diego, Calif, USA, July-August 2005.
- [58] H. W. Tan, H. M. van Driel, S. L. Schweizer, and R. B. Wehrspohn, "Phase and envelope characteristics of ultrashort pulses reflected from a two-dimensional silicon photonic crystal," *Physical Review B*, vol. 74, no. 3, Article ID 035116, 6 pages, 2006.
- [59] A. D. Bristow, N. Rotenberg, and H. M. van Driel, "Two-photon absorption and Kerr coefficients of silicon for 850–2200 nm," *Applied Physics Letters*, vol. 90, no. 19, Article ID 191104, 3 pages, 2007.
- [60] A. D. Bristow, J.-P. R. Wells, W. H. Fan, et al., "Ultrafast nonlinear response of AlGaAs two-dimensional photonic crystal waveguides," *Applied Physics Letters*, vol. 83, no. 5, pp. 851–853, 2003.
- [61] M. Dinu, F. Quochi, and H. Garcia, "Third-order nonlinearities in silicon at telecom wavelengths," *Applied Physics Letters*, vol. 82, no. 18, pp. 2954–2956, 2003.
- [62] H. K. Tsang, C. S. Wong, T. K. Liang, et al., "Optical dispersion, two-photon absorption and self-phase modulation in silicon waveguides at 1.5 μm wavelength," *Applied Physics Letters*, vol. 80, no. 3, pp. 416–418, 2002.
- [63] K.-H. Hellwege, Ed., *Landolt-Bornstein 17-a*, Springer, Berlin, Germany, 1982.
- [64] M. I. Gallant and H. M. van Driel, "Infrared reflectivity probing of thermal and spatial properties of laser-generated carriers in germanium," *Physical Review B*, vol. 26, no. 4, pp. 2133–2146, 1982.
- [65] R. W. Boyd, *Nonlinear Optics*, Academic Press, San Diego, Calif, USA, 2003.
- [66] V. A. Belyakov, "Efficient nonlinear-optical frequency conversion in periodic media in the presence of diffraction of the pump and harmonic fields," *JETP Letters*, vol. 70, no. 12, pp. 811–818, 1999.
- [67] K.-C. Shin, H. Hoshi, D.-H. Chung, K. Ishikawa, and H. Takezoe, "Enhanced second-harmonic generation by use of the photonic effect in a ferroelectric smectic C* liquid crystal," *Optics Letters*, vol. 27, no. 2, pp. 128–130, 2002.
- [68] P. Palffy-Muhoray, "The nonlinear optical response of liquid crystals," in *Liquid Crystals: Applications and Uses, Vol 1*, B. Bahadur, Ed., chapter 18, World Scientific, Singapore, 1990.

Review Article

Silicon-Based Light Sources for Silicon Integrated Circuits

L. Pavesi

Nanoscience Laboratory, Department of Physics, University of Trento, 38050 Povo, Trento, Italy

Correspondence should be addressed to L. Pavesi, pavesi@science.unitn.it

Received 15 January 2008; Accepted 30 April 2008

Recommended by D. Lockwood

Silicon the material per excellence for electronics is not used for sourcing light due to the lack of efficient light emitters and lasers. In this review, after having introduced the basics on lasing, I will discuss the physical reasons why silicon is not a laser material and the approaches to make it lasing. I will start with bulk silicon, then I will discuss silicon nanocrystals and Er^{3+} coupled silicon nanocrystals where significant advances have been done in the past and can be expected in the near future. I will conclude with an optimistic note on silicon lasing.

Copyright © 2008 L. Pavesi. This is an open access article distributed under the Creative Commons Attribution License, which permits unrestricted use, distribution, and reproduction in any medium, provided the original work is properly cited.

1. INTRODUCTION

Recently, a large research effort has been dedicated to the development of compact optoelectronic platforms. The increasing interest in conjugating optical functionality to integrated circuits stems not only from the potential of optics to overcome interconnect bottlenecks imposed on electronic circuits by speed, power, and space demands, but also from their flexibility for human interface devices (e.g., displays and image recognition) and for a large set of specific applications (including, e.g., biological sensors and compact optical tomography apparatus). Optical signals are generally interesting in connection to low power consumption, a key issue in the context of general trends such as increased miniaturization and wireless and autonomous operation.

From the industrial perspective, the preferred route towards optoelectronic platforms is the upgrade of existing electronic technology, in which Si has had no competitors since the 1960's. Compared to Ge, Si has larger bandgap (1.12 eV), which allows higher operating temperature, can be naturally structured with a companion insulator (SiO_2), and is cheap and easily available. On the other hand, compound semiconductor technologies, such as InP or GaAs, are not competitive with Si essentially because of cost issues.

While monolithic Si-compatible solutions have been known since several years for many devices such as light detectors, waveguides, and modulators, the lack of monolithic energy-efficient and cost-effective CMOS-compatible light sources has hampered the development of optoelectronic and photonic platforms. In this paper, we consider

the state of the art of Si-based light-emitting devices for Si integrated circuits. The reader is encouraged to consult also the various review articles or books which have been published on the topic of light emission in Si [1–8] as well as on hybrid technology [9]. It is worth to note that in this paper we will not discuss the hybrid approach based on III–V semiconductors either bonded or heteroepitaxied on silicon, though hybrid lasers have been integrated in silicon with very promising performances.

2. BASICS OF LIGHT AMPLIFICATION AND GAIN

A laser requires three main components: an active material which is able to generate and amplify light by stimulated emission of photons, an optical cavity which provides the optical feedback to sustain the laser action, and a pumping mechanism to supply energy to the active material. In the case of lasers based on first-order optical processes, the pumping mechanism must be able to produce a population inversion in the material. In an injection diode laser, the pumping mechanism is provided by carrier injection via a p-n junction and the optical feedback is usually provided by a Fabry-Perot cavity, [10, 11] although recently whispering gallery resonators (microdisks) and photonic crystals are receiving increasing attention.

The light generation by electron-hole recombination in semiconductors is quantified by the internal quantum efficiency η_{int} , which is the ratio between the number of generated photons and the number of electron-hole pairs that

recombine. This number is given by the ratio of the electron-hole (e-h) radiative recombination probability over the total e-h recombination probability, that is, by the fraction of all excited e-h pairs that recombine radiatively. It is easy to demonstrate that $\eta_{\text{int}} = \tau_{nr}/(\tau_{nr} + \tau_r)$, where τ_{nr} and τ_r are the nonradiative and radiative lifetimes, respectively. Thus, in order to have a high η_{int} , either the radiative lifetime should be short (as in direct bandgap semiconductors) or the non-radiative lifetime should be long (as in color center systems).

The property of amplifying light is given by the gain spectrum of the material. For a bulk semiconductor, it is related to the joint density of states $\rho(\hbar\omega)$, the Fermi inversion factor $f_g(\hbar\omega)$, and the radiative lifetime:

$$\begin{aligned} d\Phi(\hbar\omega) &= dr_{\text{stim}}(\hbar\omega) - dr_{\text{abs}}(\hbar\omega) \\ &= \frac{\lambda^2}{8\pi\tau_r} \rho(\hbar\omega) f_g(\hbar\omega) \Phi(\hbar\omega) dz \\ &= g(\hbar\omega) \Phi(\hbar\omega) dz, \end{aligned} \quad (1)$$

where $g(\hbar\omega)$ is the gain coefficient, $d\Phi$ is the change in the photon flux, dr_{stim} or dr_{abs} is the rate of stimulated emission or absorption at a given photon energy $\hbar\omega$, respectively, $f_g(\hbar\omega, E_F^e, E_F^h, T) = [f_e(\hbar\omega, E_F^e, T) - (1 - f_h(\hbar\omega, E_F^h, T))]$, f_e and f_h are the thermal occupation functions for electrons and holes, and Φ is the photon flux density. E_F^e and E_F^h are the quasi-Fermi levels for electrons and holes, respectively. When no external pumping is present, the Fermi inversion factor reduces to the simple Fermi statistics for an empty conduction band and a filled valence band ($f_g < 0$), and the gain coefficient reduces to the absorption coefficient α . When an external pump excites a large density of free carriers, the splitting of the quasi-Fermi levels increases, and when $E_F^e - E_F^h > \hbar\omega$ the condition of population inversion is satisfied and $f_g > 0$. This means that (1) is positive and hence the system shows positive net optical gain ($g > 0$). Note that in (1) a critical role is played by the radiative lifetime: the shorter the lifetime, the stronger the gain.

For an atomic system, the expression of the gain coefficient reduces to

$$g(\hbar\omega) = \sigma_{\text{em}}(\hbar\omega)N_2 - \sigma_{\text{abs}}(\hbar\omega)N_1, \quad (2)$$

where σ_{em} is the emission cross-section, σ_{abs} is the absorption cross-section, and N_2 and N_1 represent the density of active centers in the excited and ground states, respectively. If $\sigma_{\text{em}} = \sigma_{\text{abs}}$, the condition to have positive optical gain is that $N_2 > N_1$, that is, the condition of population inversion.

If a piece of active material of length L is used to amplify light, one achieves light amplification whenever the material gain g is positive and larger than the propagation losses α_p of the light through the material, that is, $g > 0$ and $g > \alpha_p$. If the system is forged as a waveguide of length L , and we call I_T and I_0 the intensity of the transmitted and the incident beams, the amplification factor of the light is then

$$G = \frac{I_T}{I_0} = \exp[(\Gamma g - \alpha_p)L] > 1, \quad (3)$$

where Γ is the optical confinement factor of the optical mode in the active region.

In a laser, optical feedback is usually provided by a Fabry-Perot cavity so that the round-trip gain (the overall gain experienced by a photon traveling back and forth across the cavity) can be larger than 1. This condition is expressed by the relation $G^2 R_1 R_2 > 1$, where R_1 and R_2 are the back and front mirror reflectivities.

3. LIMITATION OF SI FOR LIGHT EMISSION AND AMPLIFICATION

Among the various semiconductor materials which have been used to form LEDs and lasers, the absence of Si is striking. Let us review why Si has not been used as a light-emitting material [4, 5, 7, 8]. Si is an indirect bandgap semiconductor (see Figure 1). As a consequence, the probability for a radiative recombination is low, which in turn means that the e-h radiative lifetime is long (of the order of some milliseconds). An e-h pair has to wait on average a few milliseconds to recombine radiatively. During this time, both the electron and the hole move around and cover a volume of the order of $10 \mu\text{m}^3$. If they encounter a defect or a trapping center, the carriers might recombine nonradiatively. Typical nonradiative recombination lifetimes in Si are of the order of some nanoseconds. Thus, in electronic grade Si, the internal quantum efficiency η_{int} is about 10^{-6} . This is the reason why Si is a poor luminescent material, that is, the efficient nonradiative recombinations which rapidly deplete the excited carriers. Many strategies have been researched over the years to overcome this Si limitation, and some of which are based on the spatial confinement of the carriers, and others on the introduction of impurities, the use of quantum confinement, and the use of Si-Ge alloys or superlattices [4]. The fact that a slow emission, that is, a long radiative lifetime, is also associated with low brightness of the source and with the requirement of an external modulation scheme for high-speed data transmission is to be noticed.

In addition, two other phenomena limit the use of Si for optical amplification (see Figure 1). The first is a non-radiative three-particle recombination mechanism where an excited electron (hole) recombines with a hole (electron) by releasing the excess energy to another electron (hole). This is called nonradiative Auger recombination mechanism (Figure 1). This recombination mechanism is active as soon as more than one carrier is excited. The probability of an Auger recombination is proportional to the square of the number of excited carriers Δn and inversely proportional to the bandgap energy [12]. For our discussion, this is a very relevant mechanism because the more excited the semiconductor is, the more the Auger recombination is effective. The probability for an Auger recombination in a bulk material is proportional to Δn^2 ; we can thus write a nonradiative recombination lifetime due to Auger as $\tau_A = 1/C\Delta n^2$, where C is a constant which depends on the doping of the material. For Si $C \sim 10^{-30} \text{ cm}^6 \text{ s}^{-1}$ [7]. For $\Delta n \sim 10^{19} \text{ cm}^3$, $\tau_A = 10$ nanoseconds. The Auger recombination is the dominant recombination mechanism for high carrier injection rate in Si.

The second phenomenon is related to free-carrier absorption (see Figure 1). Excited carriers might absorb photons and thus deplete the inverted population and, at

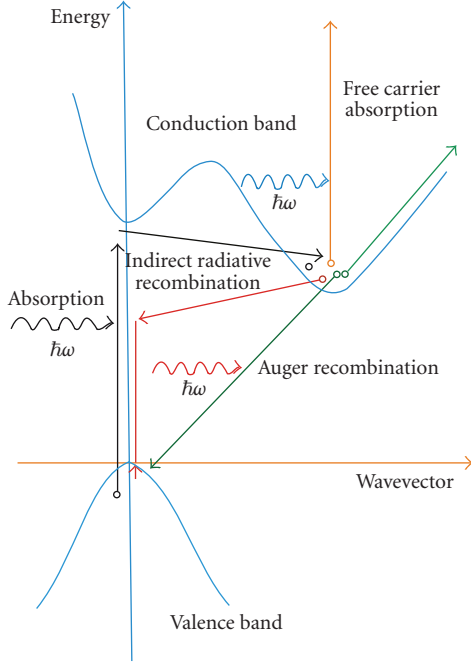


FIGURE 1: Band structure of bulk Si with the various possible transitions for an electron-hole pair: radiative recombination, Auger recombination, and free-carrier absorption.

the same time, increase the optical losses suffered by the signal beam. The free-carrier absorption coefficient can be empirically related to the Si free-carrier density n_{fc} and to the light wavelength λ as $\alpha_n \sim 10^{-18} n_{fc} \lambda^2$ at 300 K [7]. For $n_{fc} = 10^{19} \text{ cm}^{-3}$ and $\lambda = 1.55 \mu\text{m}$, $\alpha_n = 24 \text{ cm}^{-1}$. For heavily doped Si, these are the main limitations to lasing, while for intrinsic Si this contribution can be exceedingly small unless n_{fc} is very high as in a laser. In confined systems, such as Si nanocrystals, this recombination mechanism is due to confined carriers, and hence it is called confined carrier absorption.

4. APPROACHES TO SI LIGHT-EMITTING SOURCES

In early 2000's, a series of papers appeared, which questioned the common belief that Si cannot be used to form a laser [13–19]. In October 2004, the first report on an Si laser appeared [20–22], while in February 2005 the first CW Raman laser integrated in Si was reported [23–25]. Hybrid approaches became effective in 2006–2007 [9]. We summarize the most relevant approaches towards light emission in Si in the following list.

High-quality bulk Si inserted in a forward biased solar cell. This approach has a demonstrated emission wavelength of $1.1 \mu\text{m}$, and its system features include LED. The advantages of such approach are demonstrated through a power efficiency of $>1\%$ at 200 K and through the highly efficient electrical injection, and the disadvantages are demonstrated by a wavelength in an unsuitable wavelength region.

Evidence of optical gain has never been reported in Si [15, 26].

Stimulated Raman scattering in Si waveguides. The demonstrated emission wavelength of such system is $1.6 \mu\text{m}$, and its system features include CW optically pumped Raman laser. Its advantages are demonstrated by the fact that it is the only system where lasing has been clearly demonstrated in a cavity, and the continuously tunable wavelength in near infrared. The disadvantage is that no electrical injection is achievable according to fundamental mechanism [24, 25].

Nanopatterned Si. The demonstrated emission wavelength of the system is $1.28 \mu\text{m}$, and its system features include optically pumped stimulated emission at cryogenic temperature. The advantages include significant line narrowing and threshold behaviour at low pumping power, and the disadvantages are manifested by a wavelength in an unsuitable wavelength region, and the fact that the effect is demonstrated only at cryogenic temperature and that electrical injection seems prohibitive [16].

Dislocation loops formed by ion implantation in an Si p-n junction. The demonstrated emission wavelength is $1.1 \mu\text{m}$. The system features include LED with a significant efficiency. The advantages are demonstrated through simple fabrication method and efficient electrical injection, and the disadvantages through a wavelength in an unsuitable wavelength region. The evidence of optical gain has never been reported in Si [27].

Si nanocrystals in dielectric (SiO₂) matrix. The system's demonstrated emission wavelength is $0.75 \mu\text{m}$, and its system features include optical gain at room temperature and efficient LED demonstrated in AC electrical pumping regime. The advantages lie in the fact that it is CMOS-compatible and easy to fabricate, as well as its demonstrated optical microcavity and electrical injection scheme (AC). The disadvantages lay in the fact that a wavelength does not match standard optical communication, and that efficient bipolar electrical injection has not been yet achieved [13, 28].

Er coupled to Si nanocrystals in a dielectric. The demonstrated emission wavelength is $1.535 \mu\text{m}$. The system features include internal gain demonstrated in waveguides. The advantages lie in the fact that it is CMOS-compatible and easy to fabricate, in addition to its demonstrated optical cavity and wavelength being suitable for optical communication. The disadvantages lie in the fact that overall gain has not been yet demonstrated in waveguides, and that efficient electrical injection has not been yet achieved [29].

Strained germanium on Si. The system's demonstrated emission wavelength is $1.55 \mu\text{m}$. The system features are demonstrated by a theory being able to predict high gain. The advantages lie in the fact that

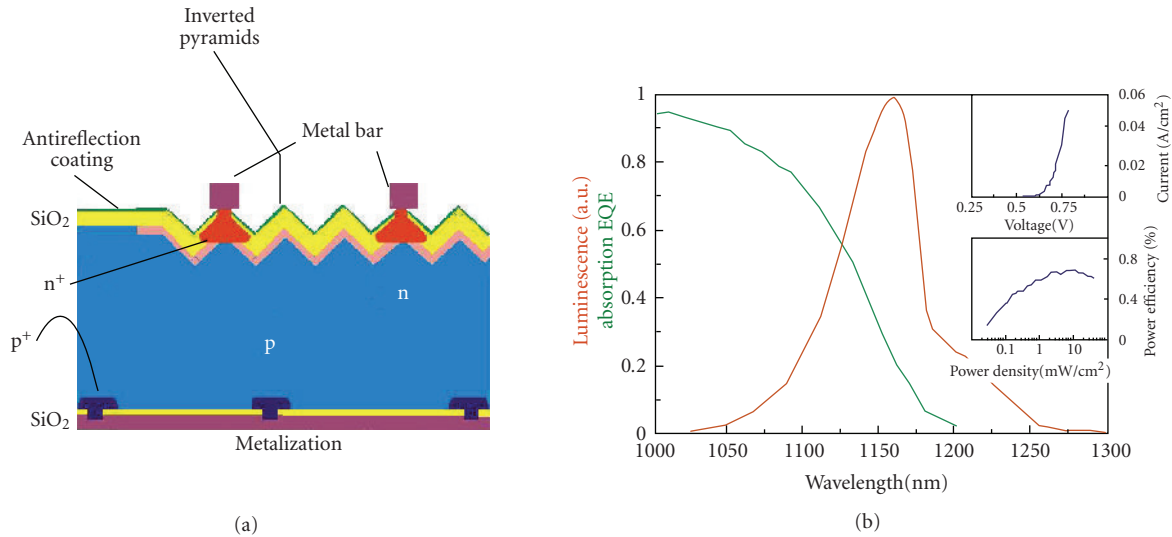


FIGURE 2: Summary of the results of the Australian group on a bulk Si LED. (a) Sketch of the LED geometry. (b) Luminescence spectrum (red), absorption spectrum (green), power efficiency versus injected electrical power density (blue), and I-V characteristics (inset) at room temperature, adapted from [15, 26].

it is easy to fabricate and has a wavelength suitable for optical communication. The disadvantages are manifested by the fact that no experiments are in support of the theory till now [30].

On considering the CMOS compatibility, one should mention that annealing procedure to nucleate the Si nanocrystals requires high temperatures (usually in excess of 1000°C). In a CMOS run, such high-temperature steps can only be introduced at the beginning of the process. This implies that the standard CMOS steps are to be performed after the nanocrystal fabrication. While this is an obviously tight constraint, compatibility with standard CMOS is in principle possible within this limitation. Otherwise one needs to consider other kinds of processing such as layer bonding.

4.1. Bulk Si light-emitting diodes

The common belief that bulk Si cannot be a light-emitting material has been severely questioned in a series of recent works. An Australian group noticed that top-quality solar cells are characterized by extremely long carrier recombination lifetimes of the order of some milliseconds. That is, the recombination lifetime is of the order of the radiative lifetime; hence η_{int} is of the order of 1. Then, if the solar cell is biased in the forward regime instead of the usual reverse regime, the solar cell could behave as a very efficient light-emitting diode [15, 26].

Figure 2 shows a schematic of the device and a room temperature emission spectrum. To increase the light extraction efficiency, the LED surface was texturized so that most of the internally generated light was impinging on the external surface of the cell with an incident angle lower than the critical angle for total internal refraction. Thus, the light extraction efficiency was increased from a few

% being typical of a flat surface to almost 100% for the texturized LED. Finally, to reduce free-carrier absorption to a minimum, the electrodes, that is, the heavily doped regions, were confined in very thin and small lines. By using these three practices, a plug-in efficiency (ratio of the optical power emitted from the LED to the electrical driving power) larger than 1% at 200 K was achieved. Most interestingly, the turn-on voltage of the device was the same as the forward bias of the solar cell, that is, less than 1 V.

The same research group published also a theoretical paper [31], which questioned one common belief that indirect bandgap materials could not show optical gain because of parasitic absorption processes due to free carriers [32]. Indeed they demonstrated that optical gain is theoretically possible, and pointed out that the most suitable energy region is the sub-bandgap region where processes involving photons could help in achieving gain.

These theoretical arguments have been partially confirmed in a recent study where stimulated emission has been observed (see Figure 3) [33]. As the limit to efficient light generation in Si is the short nonradiative lifetime, the idea was to avoid carrier diffusion and to spatially localize free carriers in a small device region where nonradiative recombination centers can be easily saturated.

Carrier localization was achieved by spin-on doping of small silica nanoparticles at the junction of a p-n diode (Figure 3) [33]. The current-voltage I-V characteristic of the diode shows rectifying behavior with a clear threshold in the light-current L-I characteristic. A change from a broad emission spectrum below threshold to sharp peaks due to stimulated emission above threshold is observed too. Stimulated emission is observed for a two-phonon indirect transition as it was theoretically predicted. Furthermore, when the injection current significantly exceeds the threshold, a single peak dominates. All these results are very encouraging since

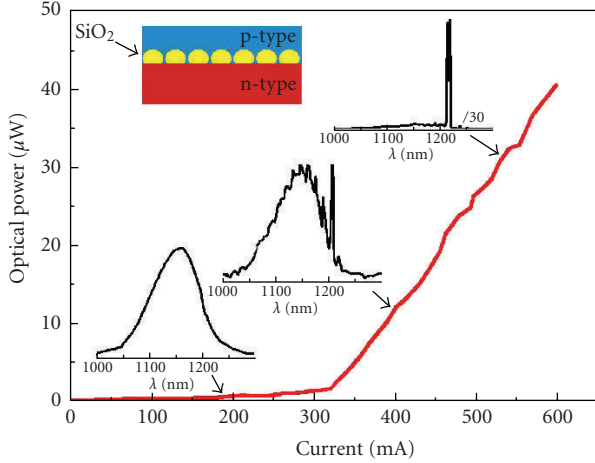


FIGURE 3: Optical power versus injected current for an LED containing SiO_2 nanoclusters in the junction region (inset). Also shown are a few electroluminescence spectra for different injection rate (arrows), adapted from [33].

the proposed systems have excellent electrical qualities as they are p-n junctions. One puzzling question is about the reproducibility of this work since no other papers were appearing after this result. The crucial question about the nature of the stimulated emission (bulk- or defects-related) is still unanswered.

Recently, another report of stimulated emission in bulk Si has appeared [16]. Nanopatterning of a thin Si on insulator layer allows to have a large effective Si surface, where a sizable density of A' centers could pile up. These defect centers are believed to play the role of active optical centers which can be optically inverted. Indeed, very convincing experimental data of gain in these nanopatterned films have been reported. The major caveat is that the gain is vanishing as the temperature is raised; sizable gain is observed only for temperatures lower than 80 K.

Strong efficiency improvement of electroluminescence has been independently reported by two groups. They have used carrier confinement in extremely thin Si layers (few nm). In one work [17], lateral p^+-p-n^+ junctions have been developed where the p-layer has been thinned down to 5 nm. Electroluminescence peaked at 1130 nm due to carrier confinement in the thin p-region, and an efficiency of 1.4×10^{-4} was reported ($0.1 \mu\text{W}$ optical power for mA injection current). In another approach [18, 19], a light-emitting field-effect transistor with lateral p-n junction was used to inject carrier into an active layer made by ultrathin intrinsic Si layer, thinned down using LOCOS processing. Performances similar to the one shown in [17] have been achieved.

4.2. Optical gain in Si nanocrystals

Another interesting approach to form light emitters and amplifiers in Si is to use small Si nanoclusters (Si-nc) dispersed in a dielectric matrix, most frequently SiO_2 [4]. With this approach, one maximizes carrier confinement, improves the radiative probability by quantum confinement,

shifts the emission wavelength to visible and controls the emission wavelength by Si-nc dimension, decreases the confined carrier absorption due to the decreased emission wavelength, and increases the light extraction efficiency by reducing the dielectric mismatch between the source materials and the air. Various techniques are used to form Si-nc whose size can be tailored in the few nm range (Figure 4).

Starting with an Si rich oxide, which can be formed by deposition, sputtering, ion implantation, cluster evaporation, and so on, a partial phase separation is induced by thermal annealing. The duration of the thermal treatment, the annealing temperature, the starting excess Si content are all determining the final sizes of the clusters, their dispersion in size which can be significant, and the Si-nc crystalline nature. The size dispersion is usually claimed as the source of the broad emission lineshape that at room temperature is typical of the Si-nc emission spectra. In addition to size dispersion, both size-selected deposition [34] and single Si-nc luminescence experiments [35] demonstrate that Si-nc emission is intrinsically broad due to the indirect nature of the emission. The active role of the interface region in determining the optical properties of Si-nc has been highlighted in a joint theoretical and experimental paper [36]. The origin of the luminescence in Si-nc is still unclear; many authors believe that it comes from confined exciton recombination in the Si-nc [37], while others support a defect-assisted recombination mechanism where luminescence is due to recombination of carriers trapped at radiative recombination centers which form at the interface between Si-nc and the dielectric [38] or even in the dielectric [39]. One candidate for these centers is the silanone bond which is formed by double Si-O bonds [40]. The most probable nature of the luminescence in Si-nc is a mechanism which involves both recombination paths: excitons at about 800 nm and trapped carriers on radiative interface state, which form in small sized nanocrystals, at about 700 nm. Indeed, passivation experiments show that the intensity and lineshape of the emission can be influenced by exposition to hydrogen gas or by further oxidation [41].

A number of papers reported observation of optical gain in these systems [13, 42–49]. The observations of gain by several different groups and on several differently prepared materials make the observation solid. Figure 5 reports a summary of the most relevant data taken on Si-nc formed by plasma-enhanced chemical vapor deposition (PECVD) [44, 45, 47]. Two techniques are reported here: the variable stripe length method (VSL) which is sketched in the inset of Figure 5 and is based on the one-dimensional amplifier model [45], and the pump-probe technique which is based on the probe amplification in presence of a high-energy and high-intensity pump beam [47]. In the VSL method, by varying the extent of the pumped region (whose length is z), one measures the amplified spontaneous emission (I_{ASE}) signal coming out from an edge of a waveguide whose core is rich in Si-nc:

$$I_{\text{ASE}}(z) = \frac{J_{\text{sp}}(\Omega)}{g_{\text{mod}}} (e^{g_{\text{mod}} z} - 1), \quad (4)$$

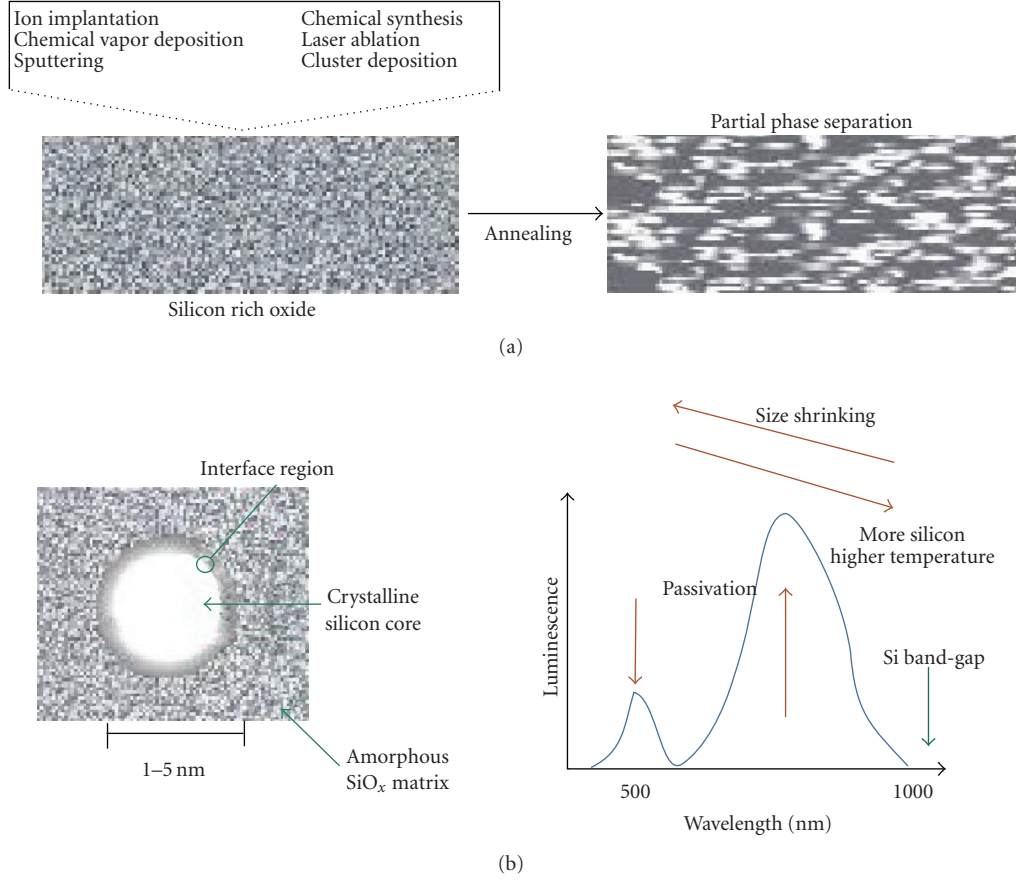


FIGURE 4: Si nanocrystals formation, structure, and luminescence spectrum.

where $J_{sp}(\Omega)$ is the spontaneous emission intensity emitted within the solid angle Ω , and g_{mod} is the *net modal gain* of the material, defined as $g_{mod} = \Gamma g_m - \alpha$.

Data reported in Figure 5 show that the ASE intensity increases sublinearly with the pumping length when the pumping power is lower than a threshold. For pumping power higher than threshold, the ASE signal increases more than exponentially. This is a consequence of the pump-induced switching from absorption ($g_{mod} < 0$) to gain ($g_{mod} > 0$).

In addition, if time-resolved measurements are performed (Figure 5(c)), [45] the ASE decay lineshape shows two time regimes: a fast decay within the first nanosecond, and a slow time decay with typical time constant of few microseconds. It is well known that Si-nc has time decay constant of some microseconds, so the appearance of a nanosecond time decay is at first surprising. What is important is the fact that the fast decay appears only if the pumping power and the excitation volume are both large. If one decreases the excitation volume at high power or the pumping power at large excitation volume, the fast decay disappears. This can be understood if the fast decay is due to stimulated emissions. In fact, at high pumping rate, three competitive paths open: stimulated emission, Auger recombination, and confined carrier absorption. All of these could be the cause of the fast decay. In particular, the Auger

lifetime τ_A and the confined carrier absorption lifetime τ_{CC} can be modeled in an Si-nc by

$$\tau_A = \frac{1}{C_A N_{ex}}, \quad \tau_{CC} = \frac{1}{2C_{CC} N_{ex}}, \quad (5)$$

where C_A and C_{CC} are coefficients, and N_{ex} is the density of excited recombination centers. N_{ex} is directly proportional to the pumping power and not to the pumping volume. Thus, by decreasing the pumping length, the ASE lineshape should be unchanged. On the other hand, by a simple rate equation modeling [50], the stimulated emission lifetime τ_{se} turns out to be

$$\tau_{se} = \frac{4}{3} \pi (R_{NS})^3 \frac{1}{\xi \sigma_g c n_{ph}}, \quad (6)$$

where R_{NS} is the average radius of the Si-nc, ξ is their packing density, σ_g is the gain cross-section, and n_{ph} is the photon flux density. Note that τ_{se} depends not only on the material properties (R_{NS} , ξ , σ_g) but also on the photon flux density n_{ph} which exists in the waveguide. Also, n_{ph} depends in turn on the waveguide losses, the Si-nc quantum efficiency, and the pumping rates. In addition, if the sample shows gain, by increasing the excitation volume, n_{ph} exponentially increases; that is, τ_{se} decreases. τ_{se} shortens when either the pumping length or the pumping power increases as both increase n_{ph} .

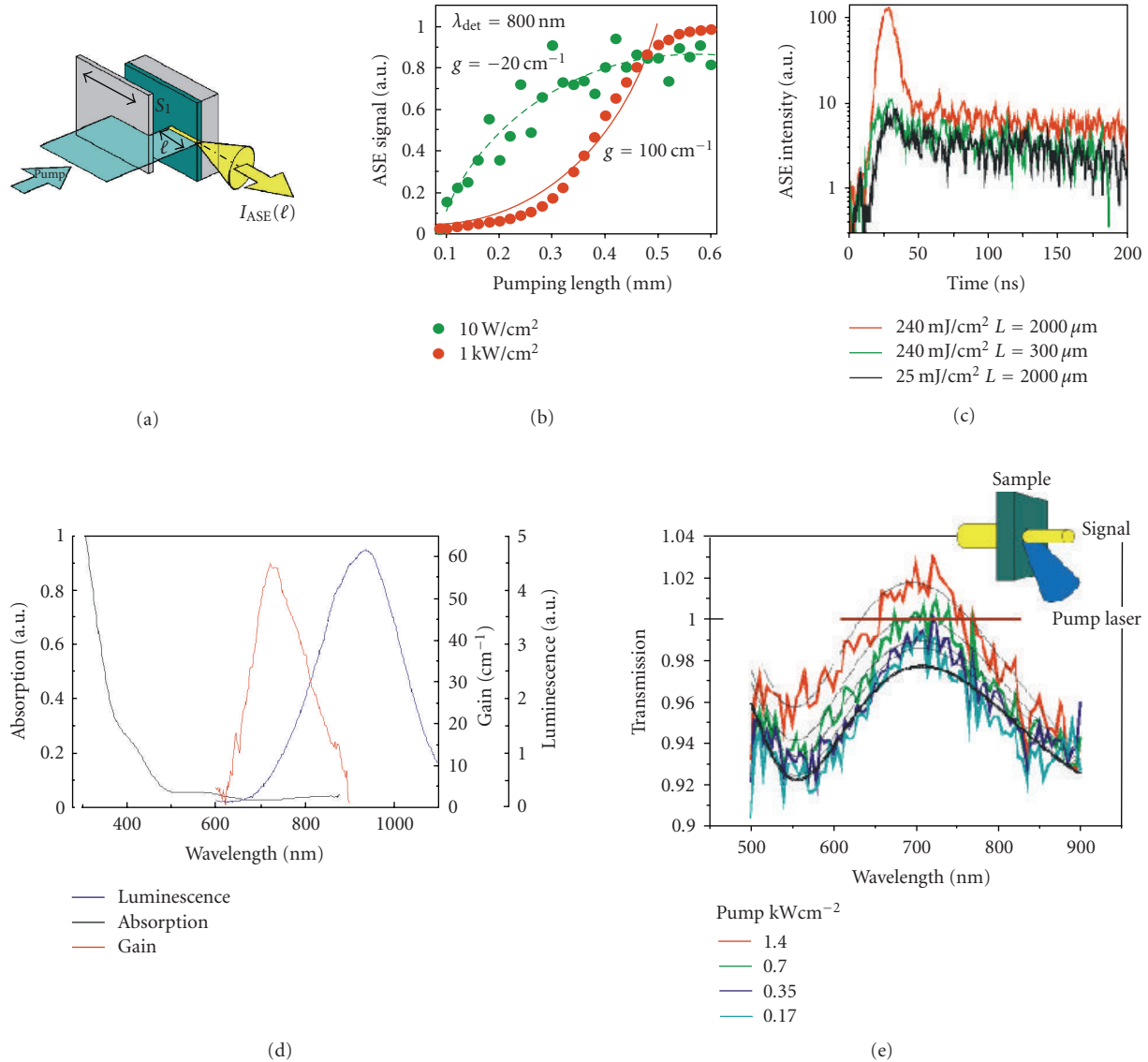


FIGURE 5: Summary of various experimental proofs of gain in Si-nc. (a) Geometry used to measure the amplified spontaneous emission (ASE); (b) ASE versus the pumping length for two pumping powers; (c) ASE time decay for the various pumping conditions indicated in the inset (L is the pumping length); (d) luminescence, absorption, and gain spectra at room temperature for an Si-nc rich waveguide; (e) transmission spectra for various pumping powers (the inset shows the experimental geometry used). Data have been redrawn from [44, 45, 47].

It is important to note that calculations show that the Auger lifetime in Si-nc is in the interval of 0.1–10 nanoseconds [51], which means that Auger recombination is a strong competitive process which should be always considered. In some Si-nc systems, due to either material problems or poor waveguide properties or even both, Auger recombination and confined carrier absorption might prevail, and no optical gain could be observed.

Figure 5(d) shows a summary of the wavelength dependence of the luminescence, absorption, and gain spectra in a sample with 4 nm Si-nc [44]. It is seen that the gain spectrum is on the high-energy side of the emission band and that absorption is negligible in the region of gain and luminescence. These facts suggest a four-level model to

explain the gain where the levels can be associated with both different Si-nc populations or with a radiative state associated with an Si=O double bond for which optical excitation causes a large lattice relaxation of the Si=O bond [52, 53] as in the silanone molecule. A recent paper shows that oxide is needed to observe gain [54]. Indeed, Si nanocrystals formed in Si nitride do not show gain, while Si nanocrystals formed in Si oxide do show gain.

Pump-probe measurements were attempted with contradictory results [47, 55]. Our group was able to show probe amplification under pumping conditions (see Figure 5(e)) [47], while another group reported pump-induced absorption probably associated with confined carrier absorption [55]. Literature results show that the confined carrier

absorption cross-section σ_{fc} in Si-nc is at least one order of magnitude reduced with respect to bulk Si [56]: $\sigma_{fc} \approx 10^{-18} \text{ cm}^2$ at $1.55 \mu\text{m}$ in P-doped Si-nc. This cross-section should be further reduced at 700 nm due to the λ^2 dependence of the confined carrier absorption. Transmission measurements of a probe beam through an Si-nc slab deposited on a quartz substrate show the typical interference fringes due to multiple reflection at the slab interfaces (Figure 5). When the pump power is raised, the transmission is increased and, at the maximum power used, net probe amplification with respect to the input probe intensity in air is observed in a narrow wavelength interval. Note that the probe amplification spectrum overlaps the fast luminescence spectrum measured by time-resolved technique. Based on these results, design of optical cavity for an Si-nc laser has been published [57].

In addition, very favorable results have been published with respect to Si-nc-based LED, where turn-on voltage as low as few volts can be demonstrated by using thin Si-nc active layers [58]. Electroluminescence in these LEDs was due to impact excitation of electron-hole pairs in the Si-nc. Improvements in the electroluminescence efficiency have been achieved by using Si nanocrystals dispersed within a polymer matrix [59].

Another recent work reports on an FET structure where the gate dielectric is rich in Si-nc [28]. In this way, by changing the sign of the gate bias, separate injection of electrons and holes in the Si-nc is achieved. Luminescence is observed only when both electrons and holes are injected into the Si-nc. By using this pulsing bias technique, high efficiency in the emission of the LED is achieved due to the copresence of electrons and holes. Channel optical waveguide with a core layer rich in Si-nc shows optical losses of only a few dB/cm mainly due to direct Si-nc absorption and to scattering caused by the composite nature of the guiding medium [60]. All these different experiments have still to be merged into a laser cavity structure to demonstrate an Si-nc-based laser.

4.3. Light amplification in Er-coupled Si nanoclusters

The radiative transitions in the internal 4f shell of erbium ions (Er^{3+}) are exploited in the erbium-doped fiber amplifier (EDFA) [61], an all optical amplifier which has revolutionized the optical communication technology. During the nineties, several experimental efforts have been exerted in order to develop an efficient and reliable light source by using Er^{3+} in Si [4]. The idea was to excite the Er^{3+} , which emits $1.535 \mu\text{m}$ photons, by an energy transfer from the electrically injected e-h pairs in a p-n Si diode. The most successful results have been shown by the demonstration of room temperature emission with an external quantum efficiency of 0.1% in an MHz modulated Er^{3+} -doped Si LED [62]. The main problem associated with Er^{3+} in Si is the back transfer of energy from the Er^{3+} ions to the Si host, which causes a lowering of the emission efficiency of the diode [63]. This is due to a resonant level which appears in the Si bandgap due to the Er^{3+} doping and which couples with the Er^{3+} levels. In order to reduce this back-transfer process, it was proposed to

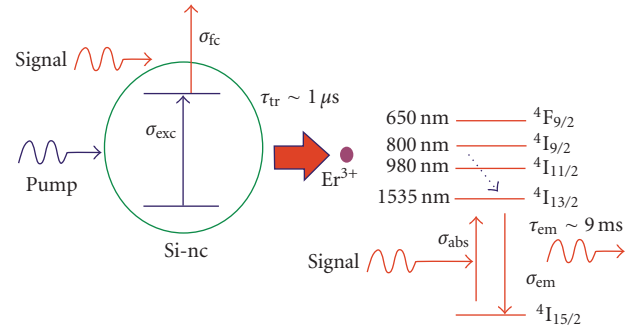


FIGURE 6: Diagram of the excitation process of Er^{3+} ions via an Si-nc, with the main related cross-sections. On the right, the main internal energy levels of the Er^{3+} are shown.

enlarge the bandgap of the Er^{3+} host so that the resonance between the defect level and the internal Er^{3+} levels is lost [64]. Si-nc in an SiO_2 dielectric were thus proposed as the host [65]. Indeed, it turns out that Si-nc are very efficient sensitizers of the Er^{3+} luminescence with typical transfer efficiency as high as 70% and with a typical transfer time of 1 microsecond [66]. In addition, the Er^{3+} are dispersed in SiO_2 , where they found their most favorable chemical environment. Quite interestingly, the transfer efficiency gets maximized when the Si-nc are not completely crystallized but still in the form of Si nanoclusters [67]. Some reports claim even that the Er^{3+} can be excited through defects in the matrix [68]. Still under debate is the number of Er ions that can be excited by a single Si-nc: a few or many ions.

Figure 6 summarizes the various mechanisms, and defines the related cross-sections for this system. Excitation of Er^{3+} occurs via an energy transfer from photoexcited e-h pairs which are excited in the Si-nc; the overall efficiency of light generation at $1.535 \mu\text{m}$ through direct absorption in the Si-nc is described by an effective Er^{3+} excitation cross-section σ_{exc} . On the other hand, the direct absorption of the Er^{3+} ions, without the mediation of the Si-nc, and the emission from the Er ions are described by absorption σ_{abs} and emission σ_{em} cross-sections, respectively. The typical radiative lifetime of Er^{3+} is of the order of 1 millisecond, with values as high as 7 milliseconds in carefully prepared samples, which is similar to the one of Er^{3+} in pure SiO_2 [69]. Figure 7(a) reports the luminescence and absorption spectra measured in an Er^{3+} -coupled Si-nc ridge waveguide at room temperature [70, 71].

Table 1 summarizes the results for the various cross-sections which are the results of an intensive study [72]. It is important to note the five orders of magnitude increase in σ_{exc} and the fact that this value is conserved also when electrical injection is used to excite the Si-nc [73]. If one places the Er^{3+} ions in an Si-nc ridge waveguide (see inset of Figure 7(b)), one can perform experiments on signal amplification at $1.535 \mu\text{m}$ with the aim of demonstrating an Er-doped waveguide amplifier (EDWA). The main advantage of an EDWA with respect to an EDFA is the reduced size, the decreased pump power to achieve the same gain, and the

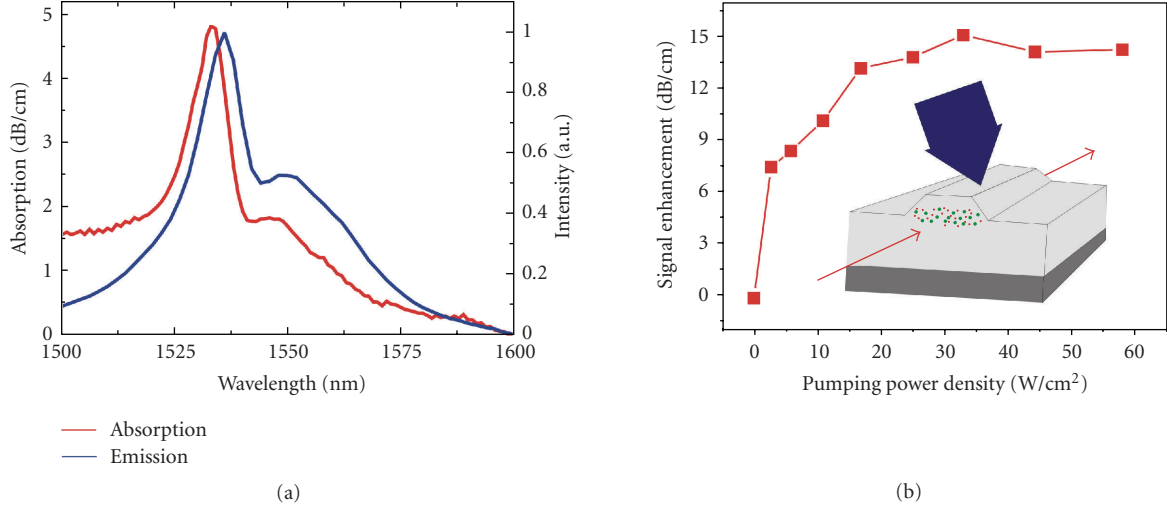


FIGURE 7: (a) Absorption and luminescence spectra of an Er^{3+} -coupled Si-nc waveguide. Adapted from [71]. (b) Signal enhancement at $1.535 \mu\text{m}$ in an Er^{3+} -coupled Si-nc waveguide versus the pumping power density by using top pumping as shown in the inset. Adapted from [74].

TABLE 1: Summary of the various cross-sections related to Er^{3+} coupled to Si-nc. These values are the results of the LANCER collaboration [71].

Erbium absorption cross-section at 1530 nm	$\sigma_{\text{abs}} = 6.6 \times 10^{-21} \text{ cm}^2$
Erbium emission cross-section at 1530 nm	$\sigma_{\text{em}} = 5.7 \times 10^{-21} \text{ cm}^2$
Erbium effective cross-section at 470 nm	$\sigma_{\text{exc}} = 2 \times 10^{-16} \text{ cm}^2$
Erbium metastable level lifetime	3 ms
Erbium decay time ${}^4I_{11/2}$ to ${}^4I_{13/2}$ transition	2.38 μs
Upconversion coefficient C_{up} for $N_{\text{Er}} < 3 \times 10^{20} \text{ cm}^{-3}$	$7 \times 10^{-17} \text{ cm}^3/\text{s}$
Si-nc absorption cross-section at 470 nm	$\sigma_{\text{Si}} = 2 \times 10^{-16} \text{ cm}^2$
Si-nc exciton lifetime τ_{ab}	50 μs
Transfer coefficient	$C_{b1} = 2 \times 10^{-15} \text{ cm}^3/\text{s}$

wide spectrum range to optically pump the system. A few groups have performed such an experiment [70, 71, 74–76].

The most successful result was reported in [76] (see Figure 7(b)). In this work, a very low Si-nc concentration has been used, and an internal gain of 7 dB/cm has been deduced. A successful experiment of pumping the EDWA with LED was also reported [76]. In other experiments, with a large Si-nc concentration, no or weak signal enhancement has been observed [70, 71, 75]. The reason is attributed to the presence of a strong confined carrier absorption which introduces a loss mechanism at the signal wavelength, and prevents the sensitizing action of the Si-nc. Indeed, the energy transfer is in competition with confined carrier absorption at the signal wavelength (see Figure 6). A confined carrier cross-section of 10^{-18} cm^2 is usually assumed [66]. Propagation losses, saturation of Er^{3+} excitation, upconversion, and confined carrier absorption make the proper design of EDWA difficult, where optical amplification can be observed. The most relevant problem in the realization of an amplifier is related to the fact that the coupling of Er with Si-nc is not complete. Indeed, most of the reported works show that only up to 5%

of the Er ions are coupled to the Si-nc, while the other can be excited only through direct Er absorption [72]. This is the main problem limiting the achievement of a net overall gain in the waveguide amplifier. In addition, a flux-dependent effective excitation cross-section has been demonstrated due to the distance-dependent coupling coefficient. Higher flux yields lower excitation cross-section due to the saturation of the strongly coupled ions. Thus, the main problem to obtain overall gain with this system concerns the nanoengineering of the material composition, allowing the production of materials with a high density of small sized Si-nc coupled effectively to all the Er ions in the system. The small size is needed to minimize the confined carrier absorption, while the high density is necessary to increase the coupling with the Er ions [72]. Having obtained internal gain, electrically injected LED [63, 77], and optical cavities [78], a laser which uses the Er^{3+} -coupled Si-nc system as active material seems feasible. With this respect, it is worth noticing that toroidal microcavities formed in silica doped with Er^{3+} have demonstrated optically pumped lasing at room temperature [79].

5. CONCLUSIONS

After seven years from the first observation of optical gain in Si nanocrystals, a first Si laser has been demonstrated, though not using Si-nc but the Raman effect. Various different approaches have been however suggested to achieve electrically pumped lasing in Si. These cover a wide spectral range from visible to infrared. These facts show that the perspectives to achieve an injection laser in Si are nowadays more solid than ever. We are quite optimistic that a laser will be realized in the near future by using one of the various approaches presented here.

ACKNOWLEDGMENTS

The collaboration with the MTLab of FBK-irst (Dr. Bellutti and Dr. Pucker) has allowed us to reach a detailed view of the field. The supports of EC (LANCER: FP6-033574; PHOLOGIC: FP6-017158), INTEL, and PAT are gratefully acknowledged.

REFERENCES

- [1] S. S. Iyer and Y.-H. Xie, "Light emission from silicon," *Science*, vol. 260, no. 5104, pp. 40–46, 1993.
- [2] L. C. Kimerling, K. D. Kolenbrander, J. Michel, and J. Palm, "Light emission from silicon," *Solid State Physics*, vol. 50, p. 333, 1997.
- [3] O. Bisi, S. U. Campisano, L. Pavesi, and F. Priolo, *Silicon-Based Microphotonics, From Basics to Applications*, IOS Press, Amsterdam, The Netherlands, 1999.
- [4] S. Ossicini, L. Pavesi, and F. Priolo, *Light Emitting Silicon for Microphotonics*, Springer, Berlin, Germany, 2003.
- [5] L. Pavesi, S. Gaponenko, and L. Dal Negro, *Towards the First Silicon Laser*, NATO Science, Kluwer Academic Publishers, Dordrecht, The Netherlands, 2003.
- [6] G. Reed and A. Knights, *Silicon Photonics: An Introduction*, John Wiley & Sons, New York, NY, USA, 2004.
- [7] L. Pavesi and D. Lockwood, *Silicon Photonics, Vol. 94 of Topics in Applied Physics*, Springer, Berlin, Germany, 2004.
- [8] L. Pavesi and G. Guillot, *Optical Interconnects: The Silicon Route*, Springer, Berlin, Germany, 2006.
- [9] "Shining light on Silicon," *Materials Today*, vol. 10, no. 7-8, 2007.
- [10] O. Svelto, *Principles of Lasers*, Springer, Berlin, Germany, 4th edition, 1998.
- [11] W. S. C. Chang, *Principles of Lasers and Optics*, Cambridge University Press, Cambridge, UK, 2005.
- [12] P. Jonsson, H. Bleichner, M. Isberg, and E. Nordlander, "The ambipolar Auger coefficient: measured temperature dependence in electron irradiated and highly injected n-type silicon," *Journal of Applied Physics*, vol. 81, no. 5, pp. 2256–2262, 1997.
- [13] L. Pavesi, L. Dal Negro, C. Mazzoleni, G. Franzò, and F. Priolo, "Optical gain in silicon nanocrystals," *Nature*, vol. 408, pp. 440–444, 2000.
- [14] G. Dehlinger, L. Diehl, U. Gennser, et al., "Intersubband electroluminescence from silicon-based quantum cascade structures," *Science*, vol. 290, no. 5500, pp. 2277–2280, 2000.
- [15] M. A. Green, J. Zhao, A. Wang, P. J. Reece, and M. Gal, "Efficient silicon light-emitting diodes," *Nature*, vol. 412, no. 6849, pp. 805–808, 2001.
- [16] S. G. Cloutier, P. A. Kosyrev, and J. Xu, "Optical gain and stimulated emission in periodic nanopatterned crystalline silicon," *Nature Materials*, vol. 4, no. 12, pp. 887–891, 2005.
- [17] T. Hoang, P. LeMinh, J. Holleman, and J. Schmitz, "Strong efficiency improvement of SOI-LEDs through carrier confinement," *IEEE Electron Device Letters*, vol. 28, no. 5, pp. 383–385, 2007.
- [18] S.-I. Saito, D. Hisamoto, H. Shimizu, et al., "Silicon light-emitting transistor for on-chip optical interconnection," *Applied Physics Letters*, vol. 89, no. 16, Article ID 163504, 3 pages, 2006.
- [19] S.-I. Saito, D. Hisamoto, H. Shimizu, et al., "Electroluminescence from ultra-thin silicon," *Japanese Journal of Applied Physics*, vol. 45, pp. L679–L682, 2006.
- [20] R. Claps, D. Dimitropoulos, V. Raghunathan, Y. Han, and B. Jalali, "Observation of stimulated Raman amplification in silicon waveguides," *Optics Express*, vol. 11, no. 15, pp. 1731–1739, 2003.
- [21] O. Boyraz and B. Jalali, "Demonstration of a silicon Raman laser," *Optics Express*, vol. 12, no. 21, pp. 5269–5273, 2004.
- [22] O. Boyraz and B. Jalali, "Demonstration of directly modulated silicon Raman laser," *Optics Express*, vol. 13, no. 3, pp. 796–800, 2005.
- [23] A. Liu, H. Rong, M. Paniccia, O. Cohen, and D. Hak, "Net optical gain in a low loss silicon-on-insulator waveguide by stimulated Raman scattering," *Optics Express*, vol. 12, no. 18, pp. 4261–4268, 2004.
- [24] H. Rong, A. Liu, R. Jones, et al., "An all-silicon Raman laser," *Nature*, vol. 433, no. 7023, pp. 292–294, 2005.
- [25] H. Rong, R. Jones, A. Liu, et al., "A continuous-wave Raman silicon laser," *Nature*, vol. 433, no. 7027, pp. 725–728, 2005.
- [26] J. Zhao, M. A. Green, and A. Wang, "High-efficiency optical emission, detection, and coupling using silicon diodes," *Journal of Applied Physics*, vol. 92, no. 6, pp. 2977–2979, 2002.
- [27] W. L. Ng, M. A. Lourenço, R. M. Gwilliam, S. Ledain, G. Shao, and K. P. Homewood, "An efficient room-temperature silicon-based light-emitting diode," *Nature*, vol. 410, no. 6825, pp. 192–194, 2001.
- [28] R. J. Walters, G. I. Bourianoff, and H. A. Atwater, "Field-effect electroluminescence in silicon nanocrystals," *Nature Materials*, vol. 4, no. 2, pp. 143–146, 2005.
- [29] N. Daldosso, D. Navarro-Urrios, M. Melchiorri, et al., "Er-coupled Si nanocluster waveguide," *IEEE Journal on Selected Topics in Quantum Electronics*, vol. 12, no. 6, pp. 1607–1617, 2006.
- [30] J. Liu, X. Sun, D. Pan, et al., "Tensile-strained, n-type Ge as a gain medium for monolithic laser integration on Si," *Optics Express*, vol. 15, no. 18, pp. 11272–11277, 2007.
- [31] T. Trupke, M. A. Green, and P. Würfel, "Optical gain in materials with indirect transitions," *Journal of Applied Physics*, vol. 93, no. 11, pp. 9058–9061, 2003.
- [32] W. P. Dumke, "Interband transitions and maser action," *Physical Review*, vol. 127, no. 5, pp. 1559–1563, 1962.
- [33] M. J. Chen, J. L. Yen, J. Y. Li, J. F. Chang, S. C. Tsai, and C. S. Tsai, "Stimulated emission in a nanostructured silicon pn junction diode using current injection," *Applied Physics Letters*, vol. 84, no. 12, pp. 2163–2165, 2004.
- [34] M. Zacharias, J. Heitmann, R. Scholz, U. Kahler, M. Schmidt, and J. Blasing, "Size-controlled highly luminescent silicon nanocrystals: a SiO/SiO₂ superlattice approach," *Applied Physics Letters*, vol. 80, no. 4, pp. 661–663, 2002.
- [35] J. Valenta, R. Juhasz, and J. Linnros, "Photoluminescence spectroscopy of single silicon quantum dots," *Applied Physics Letters*, vol. 80, no. 6, pp. 1070–1072, 2002.

- [36] N. Dalbosso, M. Luppi, S. Ossicini, et al., "Role of the interface region on the optoelectronic properties of silicon nanocrystals embedded in SiO₂," *Physical Review B*, vol. 68, no. 8, Article ID 085327, 8 pages, 2003.
- [37] J. Heitmann, F. Müller, L. Yi, M. Zacharias, D. Kovalev, and F. Eichhorn, "Excitons in Si nanocrystals: confinement and migration effects," *Physical Review B*, vol. 69, no. 19, Article ID 195309, 7 pages, 2004.
- [38] L. Khriachtchev, M. Räsänen, S. Novikov, O. Kilpelä, and J. Sinkkonen, "Raman scattering from very thin Si layers of SiO/SiO₂ superlattices: experimental evidence of structural modification in the 0.8–3.5 nm thickness region," *Journal of Applied Physics*, vol. 86, no. 10, pp. 5601–5608, 1999.
- [39] L. Khriachtchev, M. Räsänen, S. Novikov, and L. Pavesi, "Systematic correlation between Raman spectra, photoluminescence intensity, and absorption coefficient of silica layers containing Si nanocrystals," *Applied Physics Letters*, vol. 85, no. 9, pp. 1511–1513, 2004.
- [40] Y. J. Chabal, K. Raghavachari, X. Zhang, and E. Garfunkel, "Silanone (Si=O) on Si(100): intermediate for initial silicon oxidation," *Physical Review B*, vol. 66, no. 16, Article ID 161315, 4 pages, 2002.
- [41] J. S. Biteen, N. S. Lewis, H. A. Atwater, and A. Polman, "Size-dependent oxygen-related electronic states in silicon nanocrystals," *Applied Physics Letters*, vol. 84, no. 26, pp. 5389–5391, 2004.
- [42] L. Khriachtchev, M. Räsänen, S. Novikov, and J. Sinkkonen, "Optical gain in SiO/SiO₂ lattice: experimental evidence with nanosecond pulses," *Applied Physics Letters*, vol. 79, no. 9, pp. 1249–1251, 2001.
- [43] M. H. Nayfeh, S. Rao, N. Barry, et al., "Observation of laser oscillation in aggregates of ultrasmall silicon nanoparticles," *Applied Physics Letters*, vol. 80, no. 1, pp. 121–123, 2002.
- [44] L. Dal Negro, M. Cazzanelli, N. Dalbosso, et al., "Stimulated emission in plasma-enhanced chemical vapour deposited silicon nanocrystals," *Physica E*, vol. 16, no. 3-4, pp. 297–308, 2003.
- [45] L. Dal Negro, M. Cazzanelli, L. Pavesi, et al., "Dynamics of stimulated emission in silicon nanocrystals," *Applied Physics Letters*, vol. 82, no. 26, pp. 4636–4638, 2003.
- [46] J. Ruan, P. M. Fauchet, L. Dal Negro, M. Cazzanelli, and L. Pavesi, "Stimulated emission in nanocrystalline silicon superlattices," *Applied Physics Letters*, vol. 83, no. 26, pp. 5479–5481, 2003.
- [47] L. Dal Negro, M. Cazzanelli, B. Danese, et al., "Light amplification in silicon nanocrystals by pump and probe transmission measurements," *Journal of Applied Physics*, vol. 96, no. 10, pp. 5747–5755, 2004.
- [48] M. Cazzanelli, D. Kovalev, L. Dal Negro, Z. Gaburro, and L. Pavesi, "Polarized optical gain and polarization-narrowing of heavily oxidized porous silicon," *Physical Review Letters*, vol. 93, no. 20, Article ID 207402, 4 pages, 2004.
- [49] K. Luterová, K. Dohnalová, V. Švrček, et al., "Optical gain in porous silicon grains embedded in sol-gel derived SiO₂ matrix under femtosecond excitation," *Applied Physics Letters*, vol. 84, no. 17, pp. 3280–3282, 2004.
- [50] V. I. Klimov, A. A. Mikhailovsky, S. Xu, et al., "Optical gain and stimulated emission in nanocrystal quantum dots," *Science*, vol. 290, no. 5490, pp. 314–317, 2000.
- [51] C. Delerue, M. Lannoo, G. Allan, et al., "Auger and coulomb charging effects in semiconductor nanocrystallites," *Physical Review Letters*, vol. 75, no. 11, pp. 2228–2231, 1995.
- [52] F. Zhou and J. D. Head, "Role of Si=O in the photoluminescence of porous silicon," *Journal of Physical Chemistry*, vol. 104, no. 43, pp. 9981–9986, 2000.
- [53] A. B. Filonov, S. Ossicini, F. Bassani, and F. Arnaud d'Avitaya, "Effect of oxygen on the optical properties of small silicon pyramidal clusters," *Physical Review B*, vol. 65, no. 19, Article ID 195317, 9 pages, 2002.
- [54] H. Chen, J. H. Shin, P. M. Fauchet, J.-Y. Sung, J.-H. Shin, and G. Y. Sung, "Ultrafast photoluminescence dynamics of nitride-passivated silicon nanocrystals using the variable stripe length technique," *Applied Physics Letters*, vol. 91, no. 17, Article ID 173121, 3 pages, 2007.
- [55] R. G. Elliman, M. J. Lederer, N. Smith, and B. Luther-Davies, "The fabrication and properties of silicon-nanocrystal-based devices and structures produced by ion implantation—the search for gain," *Nuclear Instruments and Methods in Physics Research Section B*, vol. 206, pp. 427–431, 2003.
- [56] A. Mimura, M. Fujii, S. Hayashi, D. Kovalev, and F. Koch, "Photoluminescence and free-electron absorption in heavily phosphorus-doped Si nanocrystals," *Physical Review B*, vol. 62, no. 19, pp. 12625–12627, 2000.
- [57] S. L. Jaiswal, J. T. Simpson, S. P. Withrow, C. W. White, and P. M. Norris, "Design of a nanoscale silicon laser," *Applied Physics A*, vol. 77, no. 1, pp. 57–61, 2003.
- [58] G. Franzò, A. Irrera, E. C. Moreira, et al., "Electroluminescence of silicon nanocrystals in MOS structures," *Applied Physics A*, vol. 74, no. 1, pp. 1–5, 2002.
- [59] R. K. Ligan, L. Mangolini, U. R. Kortshagen, and S. A. Campbell, "Electroluminescence from surface oxidized silicon nanoparticles dispersed within a polymer matrix," *Applied Physics Letters*, vol. 90, no. 6, Article ID 061116, 3 pages, 2007.
- [60] P. Pellegrino, B. Garrido, C. Garcia, et al., "Low-loss rib waveguides containing Si nanocrystals embedded in SiO₂," *Journal of Applied Physics*, vol. 97, no. 7, Article ID 074312, 8 pages, 2005.
- [61] E. Desurvire, *Erbium-Doped Fiber Amplifiers: Principles and Applications*, John Wiley & Sons, New York, NY, USA, 1994.
- [62] G. Franzò, S. Coffa, F. Priolo, and C. Spinella, "Mechanism and performance of forward and reverse bias electroluminescence at 1.54 μm from Er-doped Si diodes," *Journal of Applied Physics*, vol. 81, no. 6, pp. 2784–2793, 1997.
- [63] F. Priolo, G. Franzò, S. Coffa, and A. Carnera, "Excitation and nonradiative deexcitation processes of Er³⁺ in crystalline Si," *Physical Review B*, vol. 57, no. 8, pp. 4443–4455, 1998.
- [64] A. J. Kenyon, P. F. Trwoga, M. Federighi, and C. W. Pitt, "Optical properties of PECVD erbium-doped silicon-rich silica: evidence for energy transfer between silicon microclusters and erbium ions," *Journal of Physics: Condensed Matter*, vol. 6, no. 21, pp. L319–L324, 1994.
- [65] M. Fujii, M. Yoshida, Y. Kanzawa, S. Hayashi, and K. Yamamoto, "1.54 μm photoluminescence of Er³⁺ doped into SiO₂ films containing Si nanocrystals: evidence for energy transfer from Si nanocrystals to Er³⁺," *Applied Physics Letters*, vol. 71, no. 9, pp. 1198–1200, 1997.
- [66] D. Pacifici, G. Franzò, F. Priolo, F. Iacona, and L. Dal Negro, "Modeling and perspectives of the Si nanocrystals-Er interaction for optical amplification," *Physical Review B*, vol. 67, no. 24, Article ID 245301, 13 pages, 2003.
- [67] G. Franzò, S. Boninelli, D. Pacifici, F. Priolo, F. Iacona, and C. Bongiorno, "Sensitizing properties of amorphous Si clusters on the 1.54-μm luminescence of Er in Si-rich SiO₂," *Applied Physics Letters*, vol. 82, no. 22, pp. 3871–3873, 2003.

- [68] D. Kuritsyn, A. Kozanecki, H. Przybylińska, and W. Jantsch, "Defect-mediated and resonant optical excitation of Er^{3+} ions in silicon-rich silicon oxide," *Applied Physics Letters*, vol. 83, no. 20, pp. 4160–4162, 2003.
- [69] M. Wojdak, M. Klik, M. Forcales, et al., "Sensitization of Er luminescence by Si nanoclusters," *Physical Review B*, vol. 69, no. 23, Article ID 233315, 4 pages, 2004.
- [70] N. Daldosso, D. Navarro-Urrios, M. Melchiorri, et al., "Absorption cross section and signal enhancement in Er-doped Si nanocluster rib-loaded waveguides," *Applied Physics Letters*, vol. 86, no. 26, Article ID 261103, 3 pages, 2005.
- [71] N. Daldosso, D. Navarro-Urrios, M. Melchiorri, et al., "Refractive index dependence of the absorption and emission cross sections at $1.54 \mu\text{m}$ of Er^{3+} coupled to Si nanoclusters," *Applied Physics Letters*, vol. 88, no. 16, Article ID 161901, 3 pages, 2006.
- [72] V. Toccafondo, F. Di Pasquale, S. Faralli, N. Daldosso, L. Pavesi, and H. E. Hernandez-Figueroa, "Study of an efficient longitudinal multimode pumping scheme for Si-nc sensitized EDWAs," *Optics Express*, vol. 15, no. 22, pp. 14907–14913, 2007.
- [73] F. Priolo, G. Franzò, D. Pacifici, V. Vinciguerra, F. Iacona, and A. Irrera, "Role of the energy transfer in the optical properties of undoped and Er-doped interacting Si nanocrystals," *Journal of Applied Physics*, vol. 89, no. 1, pp. 264–272, 2001.
- [74] H.-S. Han, S.-Y. Seo, J. H. Shin, and N. Park, "Coefficient determination related to optical gain in erbium-doped silicon-rich silicon oxide waveguide amplifier," *Applied Physics Letters*, vol. 81, no. 20, pp. 3720–3722, 2002.
- [75] P. G. Kik and A. Polman, "Gain limiting processes in Er-doped Si nanocrystal waveguides in SiO_2 ," *Journal of Applied Physics*, vol. 91, no. 1, pp. 534–536, 2002.
- [76] J. Lee, J. Shin, and N. Park, "Optical gain in Si-nanocrystal sensitized, Er-doped silica waveguide using top-pumping 470 nm LED," in *Proceedings of Optical Fiber Communication Conference*, Los Angeles, Calif, USA, February 2004.
- [77] M. E. Castagna, S. Coffa, M. Monaco, et al., "High efficiency light emitting devices in silicon," *Materials Science and Engineering: B*, vol. 105, no. 1–3, pp. 83–90, 2003.
- [78] F. Iacona, G. Franzò, E. C. Moreira, and F. Priolo, "Silicon nanocrystals and Er^{3+} ions in an optical microcavity," *Journal of Applied Physics*, vol. 89, no. 12, pp. 8354–8356, 2001.
- [79] A. Polman, B. Min, J. Kalkman, T. J. Kippenberg, and K. J. Vahala, "Ultralow-threshold erbium-implanted toroidal microlaser on silicon," *Applied Physics Letters*, vol. 84, no. 7, pp. 1037–1039, 2004.

Research Article

Stress Induced Effects for Advanced Polarization Control in Silicon Photonics Components

D.-X. Xu,¹ W. N. Ye,² S. Janz,¹ A. Del  ge,¹ P. Cheben,¹ B. Lamontagne,¹ E. Post,¹ and P. Waldron¹

¹*Institute for Microstructural Sciences, National Research Council Canada (NRC), Ottawa, ON, Canada K1A 0R6*

²*Department of Electronics, Carleton University, 1125 Colonel By Drive, Ottawa, ON, Canada K1S 5B6*

Correspondence should be addressed to D.-X. Xu, danxia.xu@nrc-cnrc.gc.ca

Received 24 January 2008; Accepted 11 March 2008

Recommended by D. Lockwood

We review the use of the oxide cladding stress-induced photoelastic effect to modify the polarization dependent properties in silicon-on-insulator (SOI) waveguide components, and highlight characteristics particular to this high index contrast (HIC) systems. The birefringence in SOI waveguides has its origin in the electromagnetic boundary conditions at the waveguide boundaries, and can be further modified by the presence of stress in the waveguiding materials. With typical stress levels in SiO₂ films, which are often used as the upper cladding, the waveguide effective index can be altered anisotropically up to the order of 10⁻³ for ridges with heights ranging from 1 μm to 5 μm. This effect can be used effectively to counter the waveguide geometrical birefringence, allowing the waveguide cross-section profiles to be optimized for design criteria other than null geometrical birefringence. Design strategies are developed for using stress engineering to achieve a variety of functions. Polarization insensitive arrayed waveguide gratings (AWGs), polarization insensitive ring resonators, and polarization splitters and filters are demonstrated using these design principles.

Copyright   2008 D.-X. Xu et al. This is an open access article distributed under the Creative Commons Attribution License, which permits unrestricted use, distribution, and reproduction in any medium, provided the original work is properly cited.

1. INTRODUCTION

Silicon photonics is a rapidly growing research field with many important advances in recent years [1–9]. Primarily motivated by the potential of high-integration density and compatibility with mature CMOS technologies, silicon-on-insulator (SOI) has been the main material platform for silicon photonic waveguide components [1, 9]. Along with these benefits, control and utilization of polarization-dependent properties arise as a challenge, as well as open new possibilities in advanced designs and functionalities [10–15].

Polarization-dependent properties have long been an important issue in integrated optics systems. In applications such as wavelength demultiplexing and high resolution spectroscopy, the shift in channel wavelength with the polarization state of the incoming optical signal often compromises the device spectral resolution [8]. One approach to handle this issue is to produce devices with polarization insensitive performance. In some cases this approach may not be practical, and then polarization diversity may be adopted where the signal is divided into orthogonal polarization states using a polarization splitter and processed

separately. In this paper, we review the characteristics of modal birefringence in SOI waveguides, with regard to the two main sources of polarization anisotropy, namely, the geometrical and the stress-induced birefringence [13, 16]. Design methodologies and experimental demonstrations for using the stress-induced birefringence to achieve polarization-insensitive arrayed waveguide gratings (AWGs) [13, 17], polarization insensitive ring resonators [18, 19], and zero-order AWG-based broadband polarization splitters [20] are presented.

2. WAVEGUIDE BIREFRINGENCE: GEOMETRICAL EFFECTS

In planar waveguides, the modal birefringence (the difference in the effective index for the TM and TE polarizations $\Delta n_{\text{eff}} = n_{\text{eff}}^{\text{TM}} - n_{\text{eff}}^{\text{TE}}$) results from the combination of geometrical, compositional, and stress-induced effects. In low index contrast glass waveguides, the geometrical effect is negligible and the birefringence is primarily controlled by the residual stress in the waveguide layers. A large body of research has been devoted to this subject, where the main

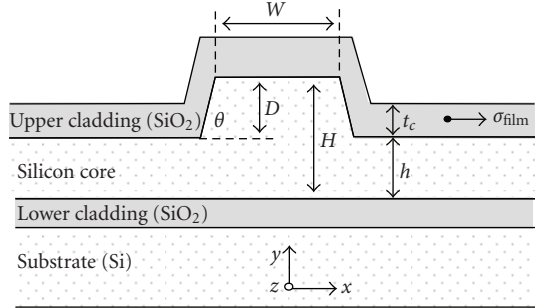


FIGURE 1: Schematic cross-section of an SOI ridge waveguide.

goal is to reduce the stress anisotropy in the waveguide core region by adjusting the thermal expansion coefficients of the cladding and core layers or creating stress relief features [21, 22]. In high-index contrast waveguides such as SOI where the light confinement is strong, electromagnetic boundary conditions dictated by the cross-section geometry of the waveguides have the largest impact on the waveguide effective index and consequently the birefringence. These geometrical dependencies have been used to obtain single mode waveguides with large cross-sections, and to adjust the waveguide geometrical birefringence Δn_{geo} to desired values. In an SOI ridge waveguide as illustrated in Figure 1, it is possible to minimize the birefringence by tailoring the waveguide aspect ratio, particularly for waveguides with relatively large cross-sections [10–13]. As the core size is reduced, typically to $\sim 2 \mu\text{m}$ and less, it becomes increasingly difficult to attain the designed birefringence values [13, 16, 17]. Since ridge dimensions also determine the number of waveguide modes, the minimum usable bend radius, the mode size, and the coupling between adjacent waveguides, it is often impossible to meet these different design objectives simultaneously.

As an example, Figure 2(a) (dashed lines) shows the dependence of waveguide geometrical birefringence Δn_{geo} on the etch depth D for waveguides with vertical sidewalls, ridge height $H = 2.2 \mu\text{m}$, and widths of 1.6 and $2.5 \mu\text{m}$, respectively. Results for waveguides under stress (solid lines) will be discussed in Section 3. For a given waveguide width W , the polarization degeneracy ($\Delta n_{\text{geo}} = 0$) may be achieved at a specific value of etch depth D . At the birefringence-free point for $W = 1.6 \mu\text{m}$ near $D = 1.3 \mu\text{m}$ the change of Δn_{geo} with the fluctuation in the etch depth is $\sim 1.5 \times 10^{-4}$ for $\Delta D = \pm 10 \text{ nm}$. When $W = 2.5 \mu\text{m}$, Δn_{geo} is less sensitive to the fluctuations in the etch depth ($\sim 2 \times 10^{-5}$ for $\Delta D = \pm 10 \text{ nm}$ near $D = 1.5 \mu\text{m}$), however the birefringence-free condition cannot be achieved. To reduce the birefringence below the level required for the state-of-the-art photonic devices ($\Delta n_{\text{eff}} < 10^{-4}$) by selecting and attaining the ridge aspect ratio W/D , dimension control on the order of 10 nm is required for these waveguides [13, 16, 17], which is very difficult in fabrication.

The effect of changing the waveguide width on the geometrical birefringence Δn_{geo} is shown in Figure 2(b) (dashed curves), for sidewall angles of 90° and 54° , which represent the profiles typically obtained by dry and

anisotropic wet etching, respectively. Waveguide sidewall angles strongly affect the mode properties, especially as the sidewall approaches vertical. With decreasing ridge width for $\theta = 90^\circ$, Δn_{geo} shifts towards positive values initially, until the waveguide is so narrow that the modes mainly reside in the etched slab section and the birefringence changes to negative values rapidly. The birefringence of a trapezoidal ridge waveguide is less susceptible to changes in the ridge geometry (width and etch depth) as compared to a rectangular waveguide (i.e., $\theta = 90^\circ$) with similar cross-section area, as can be observed from the data for a sidewall angle of 54° shown in Figure 2(b). The geometrical birefringence, however, remains negative for the entire waveguide width range. For the rectangular waveguides, an optimal width can be found to satisfy the birefringence-free condition (zero birefringence at $W \sim 2 \mu\text{m}$). Detailed discussions on the influence of geometrical parameters can be found in previous publications [16, 17].

Even though waveguide geometries satisfying both the single-mode and birefringence-free conditions can be found in principle, it is important to be able to implement the designs using existing fabrication technologies. Using contact-print lithography, waveguide-width variations on the order of 100 nm can be expected. Using state-of-the-art high resolution lithography methods such as e-beam direct write or deep UV steppers, dimensional control on the order of 10 nm is possible but still very challenging. These techniques, however, are expensive and are not widely available. Because it is difficult to precisely control the waveguide dimensions due to limitations of the fabrication techniques, methods of controlling birefringence other than modifying waveguide geometries are desirable.

3. PHOTOELASTIC EFFECT AND THE STRESS-INDUCED BIREFRINGENCE

Cladding layer such as silicon dioxide is usually deposited or grown at elevated temperatures on the silicon substrate. A (compressive) stress is often found in the silicon dioxide (SiO_2) films, due to the different thermal expansion coefficients of Si ($3.6 \times 10^{-6} \text{ K}^{-1}$) and oxide ($5.4 \times 10^{-7} \text{ K}^{-1}$) as well as intrinsic stress that may exist in the oxide film. When a material is subjected to a stress, the material refractive index is altered due to the photoelastic effect. The stress-induced changes in the *material* refractive index are given by [13, 14, 23]

$$\begin{aligned} n_x - n_0 &= -C_1 \sigma_x - C_2 (\sigma_y + \sigma_z), \\ n_y - n_0 &= -C_1 \sigma_y - C_2 (\sigma_z + \sigma_x). \end{aligned} \quad (1)$$

Here σ_i ($i = x, y, z$) is the stress tensor, n_i is the material refractive index in the corresponding directions, n_0 is the (isotropic) refractive index in the absence of stress, and C_1 and C_2 are the stress-optic constants. If a stress (tensor) with axial anisotropy is imposed on an originally optically isotropic material, a *material* birefringence is induced:

$$n_y - n_x = (C_2 - C_1)(\sigma_y - \sigma_x). \quad (2)$$

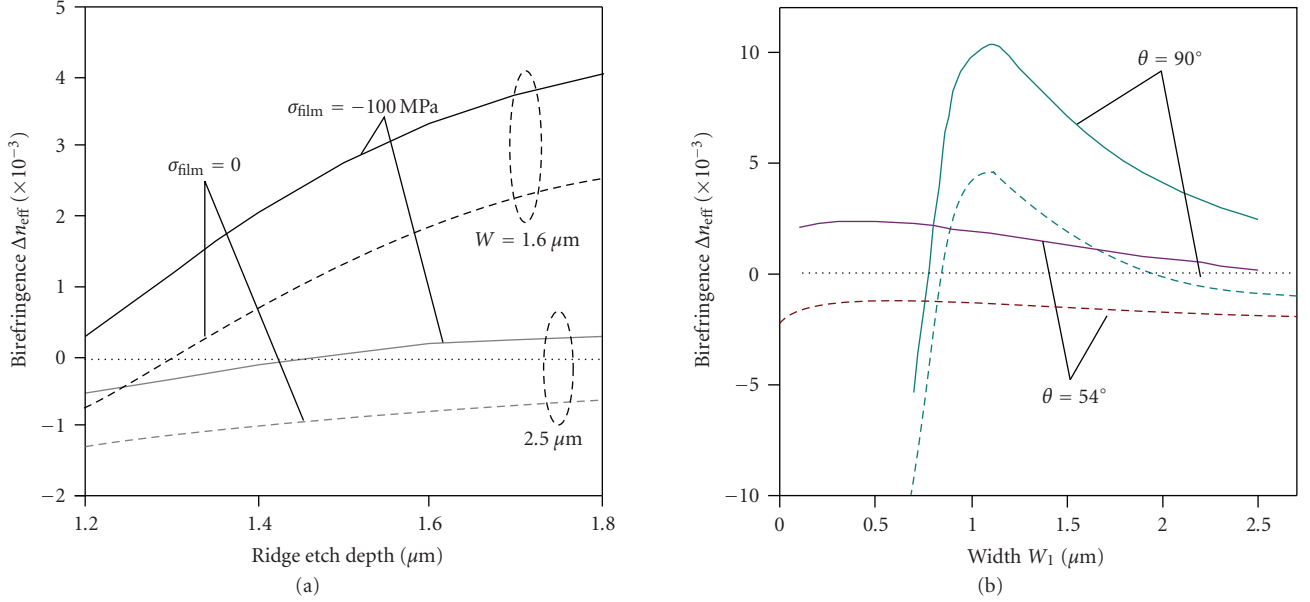


FIGURE 2: (a) Calculated modal birefringence Δn_{eff} for waveguides with $H = 2.2 \mu\text{m}$. (a) Δn_{eff} in ridge waveguides with vertical sidewalls ($\theta = 90^\circ$) as a function of etch depth D . Waveguide width $W = 1.6$ and $2.5 \mu\text{m}$, cladding thickness $t_c = 0.7 \mu\text{m}$, and film stress $\sigma_{\text{film}} = -100 \text{ MPa}$. (b) Δn_{eff} in vertical ($\theta = 90^\circ$) and trapezoidal ($\theta = 54^\circ$) waveguides as a function of the ridge top width W_1 , for $D = 1.5 \mu\text{m}$, $t_c = 0.7 \mu\text{m}$, and $\sigma_{\text{film}} = -300 \text{ MPa}$. The dashed curves show the geometrical birefringence Δn_{geo} (i.e., in the absence of stress), the solid curves show Δn_{eff} including both the geometrical and stress-induced components.

TABLE 1: Stress-optic constants of some materials.

Material	λ (μm)	C_1 (10^{-12} Pa^{-1})	C_2 (10^{-12} Pa^{-1})
Si	1.15	-11.04	4.04
Silica	0.633	0.65	4.5
GaAs	1.15	-18.39	-10.63

Stress-optic constants of silicon and glass are listed in Table 1, as well as those of GaAs for comparison.

The stress-induced *material* birefringence in turn causes a stress contribution Δn_s to the modal birefringence. The total modal birefringence can be expressed as $\Delta n_{\text{eff}} = n^{\text{TM}} - n^{\text{TE}} = \Delta n_{\text{geo}} + \Delta n_s$. The stress distributions in an SOI ridge waveguide are shown in Figures 3(a) and 3(b), for SiO_2 upper and lower claddings under a compressive stress of $\sigma_{\text{film}} = -320 \text{ MPa}$ (σ_{film} is the in-plane stress component in the uniform cladding film far from the ridge), calculated using a finite-element multiphysics solver (FEMLAB). The primarily in-plane stress (Figure 3, x -direction) in the oxide film compresses the Si ridge and results in a compressive stress in the x -direction (Figure 3(a)) and a higher tensile stress in the y -direction (Figure 3(b)) in the silicon core. For the waveguide example shown in Figure 3, $\sigma_x \approx -70 \text{ MPa}$ and $\sigma_y \approx 180 \text{ MPa}$ at the waveguide center. This stress anisotropy is the fundamental reason for the stress-induced birefringence. The corresponding local *material* birefringence ($n_y - n_x$) is shown in Figure 3(c), with values as large as 4×10^{-3} . These modifications in the *material* index cause the modal index $n_{\text{eff}}^{\text{TM}}$ to increase and $n_{\text{eff}}^{\text{TE}}$ to decrease with the oxide thickness and the stress level (Figure 4(a)). The corresponding stress-induced birefringence thus can be controlled with two parameters:

the oxide thickness t_c and the film stress level σ_{film} , as shown in Figure 4(b). The stress-induced index variations resulting from commonly used oxide cladding films are of comparable magnitude to the geometrical birefringence found in typical SOI ridge waveguides. Depending on the specific value of the geometrical birefringence Δn_{geo} , the total modal birefringence may be designed to be zero or other desired values. Figure 5 shows the calculated results for maximum birefringence that can be induced by a cladding with $\sigma_{\text{film}} = -300 \text{ MPa}$ in waveguides with $2 \mu\text{m}$ ridge height and different aspect ratios. These characteristics are the bases for stress engineering in SOI waveguides, and they can be advantageously employed in many applications.

4. EXPERIMENTAL IMPLEMENTATIONS

In the following, we present several examples of using stress engineering for the control of polarization-dependent properties of SOI waveguide devices. First, we present polarization insensitive AWG demultiplexers, where the birefringence in the waveguide array is eliminated by the proper selection of the oxide cladding stress and thickness [13, 17]. Then we introduce polarization insensitive ring resonators using multimode interference (MMI) couplers to achieve polarization insensitive coupling between the bus waveguide and the ring cavity [18, 19]. Stress-induced birefringence is used to compensate the round-trip phase difference between the two polarizations. The last example is a polarization splitter in a zero-order AWG configuration, where a prism-shaped oxide patch is placed in the arrayed waveguide section to disperse the TE and TM modes into

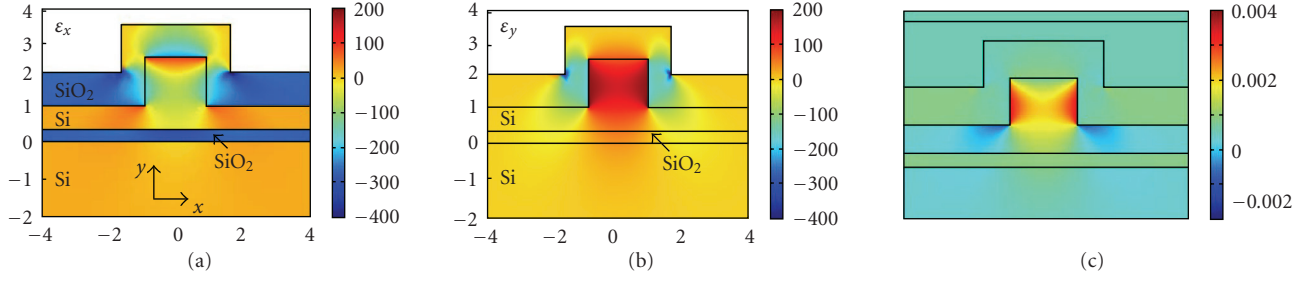


FIGURE 3: Stress distributions in the (a) x -direction and (b) y -direction. The ridge height is $2.2 \mu\text{m}$, the width is $1.8 \mu\text{m}$, and the etch depth is $1.47 \mu\text{m}$. The cladding oxide is $1 \mu\text{m}$ thick with a compressive stress of $\sigma_{\text{film}} = -320 \text{ MPa}$. (c) Stress-induced material birefringence ($n_y - n_x$) corresponding to the stress distributions shown in Figures 3(a) and 3(b).

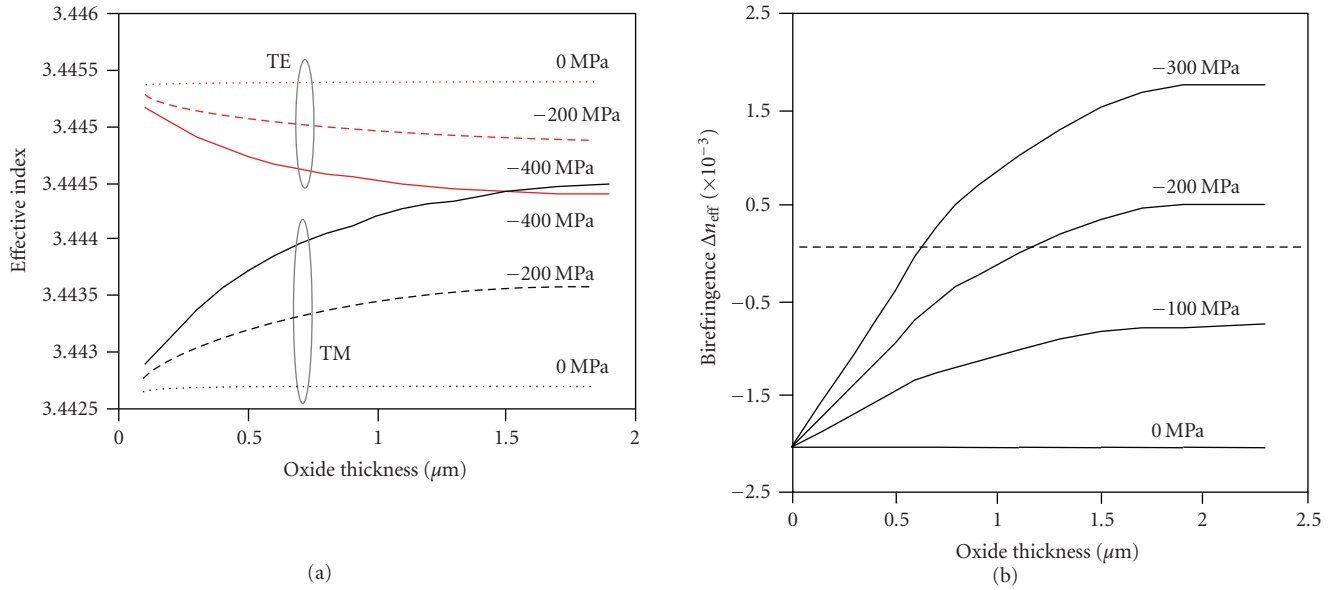


FIGURE 4: (a) Effective index as a function of the oxide upper-cladding thickness t_c , for different cladding stress levels σ_{film} of 0, -200 , and -400 MPa , respectively; (b) total modal birefringence Δn_{eff} as a function of t_c and σ_{film} .

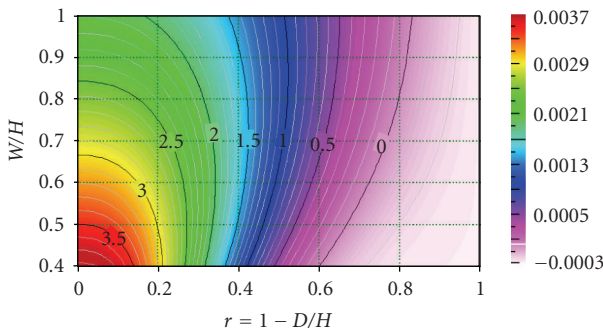


FIGURE 5: Stress-induced modal birefringence Δn_s for ridge waveguides with different aspect ratios, with $H = 2 \mu\text{m}$, $t_c = 2 \mu\text{m}$, and $\sigma_{\text{film}} = -300 \text{ MPa}$.

separate output waveguides. Since this AWG operates at near zero-order, broadband performance is achieved [20].

4.1. Polarization-independent AWGs

In AWGs, the polarization-dependent wavelength shift $\Delta\lambda = \lambda_{\text{TM}} - \lambda_{\text{TE}}$ mainly arises from the birefringence of the arrayed

waveguides and can be expressed as $\Delta\lambda \approx \lambda \Delta n_{\text{eff}} / n_g$, where n_g is the waveguide group index and λ is the operating wavelength in vacuum. The AWGs used for this demonstration of polarization compensation using stress engineering were made on SOI substrates with a silicon thickness of $2.2 \mu\text{m}$, with 9 output channels spaced at 200 GHz , and centered at 1550 nm [8, 13, 17] (see Figure 6(a)). The arrayed waveguide gratings of order 40 were formed by 100 waveguides of width $2 \mu\text{m}$. Waveguides were produced using both wet and dry etching methods, yielding $\sim 54^\circ$ and nearly vertical sidewall angles, respectively. Waveguide birefringence simulations were performed using measured waveguide dimensions. Upper cladding oxide films of different thicknesses were deposited at $\sim 400^\circ\text{C}$ using PECVD, with a film stress of $\sigma_{\text{film}} = -320 \text{ MPa}$ in the blank films, measured from wafer bowing. Figure 6(b) shows the calculated and measured dependence of $\Delta\lambda$ on the cladding thickness t_c , for both trapezoidal and rectangular waveguides. Calculated results agree well with experiments for both types of waveguides, showing that $\Delta\lambda$ can be modified over $\sim 2 \text{ nm}$ wavelength range [16]. Figures 6(c) and 6(d) show the TE and TM spectra of a wet-etched AWG before and after

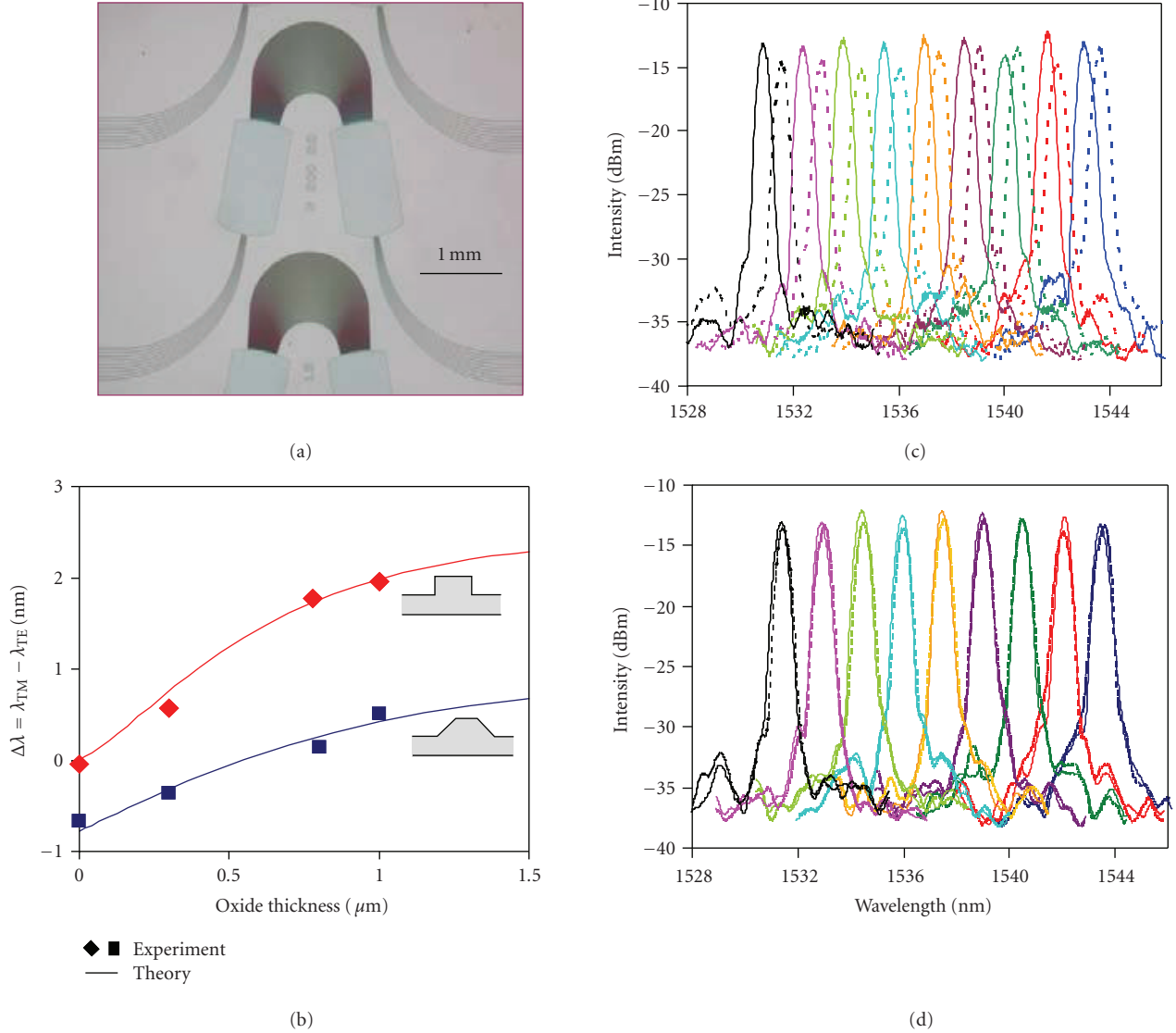


FIGURE 6: (a) Optical image of a fabricated AWG. (b) Polarization-dependent wavelength shift $\Delta\lambda$ as a function of the cladding thickness t_c , for AWGs fabricated using wet (waveguide top width $W_1 = 1.1 \mu\text{m}$ and bottom width $W_2 = 3.8 \mu\text{m}$) and dry ($W_1 = 1.85 \mu\text{m}$ and $W_2 = 2.0 \mu\text{m}$) etching to a depth of $D = 1.47 \mu\text{m}$. The cladding stress is $\sigma_{\text{film}} = -320 \text{ MPa}$. Measured spectra for an SOI AWG. (c) Measured spectrum for an SOI AWG without the oxide upper cladding. (d) Compensated using a $0.6 \mu\text{m}$ thick SiO_2 claddings with $\sigma_{\text{film}} = -320 \text{ MPa}$. TM (solid) and TE (dashed).

polarization compensation. The adjacent channel cross-talk is less than -25 dB . The noncompensated AWG device has a polarization-dependent wavelength shift of $\Delta\lambda \sim 0.6 \text{ nm}$ (Figure 6(c)), arising from the geometrical birefringence of $\Delta n_{\text{geo}} \sim -1.3 \times 10^{-3}$ in the arrayed waveguide. With an oxide upper cladding film of -320 MPa in stress and $0.6 \mu\text{m}$ in thickness, the $\Delta\lambda$ was then reduced to below 0.04 nm for all channels (corresponding to $\Delta n_{\text{eff}} < 1 \times 10^{-4}$) (Figure 6(d)). The polarization dependent loss (PDL) was also found to be negligible in these devices after the compensation.

4.2. MMI-coupled polarization-independent ring resonators

We also applied the stress engineering technique to achieve polarization-insensitive ring resonators [18, 19]. Ring res-

onators have been used as the building blocks in applications including add-drop, switching, modulation, and sensing [24–27]. However, polarization sensitivity is often an obstacle that limits their practical use [12, 15, 18].

The power transmission in the bus waveguide of a single coupler ring resonator (Figure 7(a)) can be obtained by a generalization of the ring resonator equations to incorporate the coupler loss [18, 28]:

$$|T|^2 = \alpha_{\text{MMI}}^2 \left[\frac{\alpha^2 - 2\alpha t \cos\phi + t^2}{1 - 2\alpha t \cos\phi + \alpha^2 t^2} \right], \quad (3)$$

where ϕ is the total round trip phase accumulation, and $\alpha^2 = \alpha_{\text{MMI}}^2 \cdot \alpha_{\text{ring}}^2$ is the combined power loss factor including both the ring loss and the coupler loss. The self-coupling

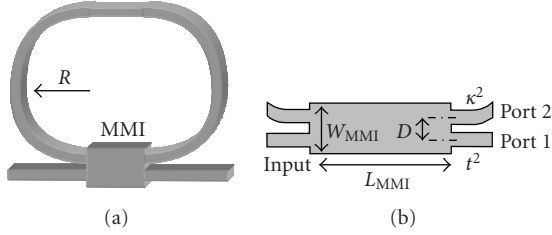


FIGURE 7: (a) A ring resonator with an MMI coupler. (b) A schematic of the MMI structure.

coefficient t^2 is the ratio of power transfer from the input to the output port 1 of the multimode interference (MMI) coupler, as indicated in Figure 7(b). The resonance extinction ratio is maximum at $\alpha^2 = t^2$, which is referred to as the critical coupling condition. A series of transmission minima occur at wavelengths λ_m for which the round-trip phase accumulation is integer multiple of 2π . It is apparent that a polarization dependence in the coupling coefficient t and/or the loss factor α lead to different resonance quality factors and linewidths for TE and TM input polarizations. If the waveguides are birefringent, the round trip phase accumulation ϕ varies with the polarization, and the resonance wavelengths and free spectral range (FSR) are polarization sensitive. To achieve polarization independence in a ring resonator, all these factors need to be addressed.

Polarization-independent ring resonator designs using directional couplers have been investigated [12], but showed long coupler length and very stringent fabrication requirements. We proposed the use of MMI couplers to achieve polarization-independent light transfer between the resonator bus and the ring waveguides (Figures 7(a) and 7(b)). For simplicity, we have chosen the commonly used 2×2 restricted interference coupler with a 50:50 splitting ratio between the two output ports [29]. The coupler width is $W_{\text{MMI}} = 3D$, where D is the center-to-center separation between the access waveguides (Figure 7(b)). The resonators are designed with the following ring and access waveguide dimensions: ridge height $H = 1.5 \mu\text{m}$, width $W = 1.5 \mu\text{m}$ and $1 \mu\text{m}$, and etch depth $H - h = 0.9 \mu\text{m}$. A separation of $D = 2.5 \mu\text{m}$ between the access waveguides is used in the MMI design, based on the considerations of a compact footprint and ease of fabrication, yielding an MMI width of $W_{\text{MMI}} = 7.5 \mu\text{m}$. The quality factor of a resonator is determined by the coupler splitting ratio and the loss in the resonator cavity. MMI designs with variable splitting ratios have been proposed and demonstrated by other groups and may be used for high-quality factor resonators [30, 31].

The optical field distribution in the 2×2 MMI coupler is shown in Figure 8(a), while Figure 8(b) shows the MMI coupler transfer characteristics in terms of the normalized power coupled to the fundamental mode in ports 1 and 2, respectively, as a function of the coupler length. For each polarization, a splitting ratio close to 50:50 is achieved over the range of coupler length L_{MMI} from 82 to $86 \mu\text{m}$, with a coupler imbalance of ≤ 0.05 dB. The combined power in the two outputs is the total transmitted power α_{MMI}^2 ,

which indicates the loss through the coupler (with $\alpha_{\text{MMI}}^2 = 1$ being lossless). The optimum coupling length differs by $\sim 2.5 \mu\text{m}$ (or $\sim 3\%$) between the two polarizations. As a first approximation, a coupler length of $L_{\text{MMI}} = 84 \mu\text{m}$ at the crossing point is used in all our resonator designs, where a similar excess loss of ~ -0.2 dB is found for both polarizations. This choice is based on the assumption that losses from all other mechanisms are similar for TE and TM, which is not necessarily the case. In addition to the coupler excess loss, there are several other mechanisms contributing to the overall resonator loss. For example, the waveguide propagation loss due to scattering depends on the optical mode overlap with the roughness at the waveguide boundaries and is generally polarization dependent. This loss is proportional to the propagation distance, and therefore to the cavity length of a ring resonator. Another source is the radiation loss in waveguide bends, as well as possible losses at discontinuities such as the junctions between the straight and curved waveguides. These factors need to be considered in the device design, and detailed discussions can be found in [19].

Since the stress in SOI waveguides caused by the cladding layer can be used effectively to control the birefringence over a wide range, it can be applied to eliminate the polarization dependence in the ring phase accumulation ϕ . The phase change in the MMI section is $2\pi n_{\text{eff}}^{\text{MMI}} L_{\text{MMI}}/\lambda$, plus a constant correction factor which is a multiple integer of $\pi/2$ [32]. Since the stress-induced birefringence in the ring waveguide Δn_s^{ring} is much larger than that in the wider MMI section [16] (i.e., $\Delta n_s^{\text{MMI}} \ll \Delta n_s^{\text{ring}}$), the difference in the phase accumulation $\Delta\phi$ between TM and TE polarizations can be expressed as [18]:

$$\Delta\phi = \frac{2\pi}{\lambda} [\Delta n_{\text{geo}}^{\text{MMI}} L_{\text{MMI}} + \Delta n_{\text{geo}}^{\text{ring}} L_1 + \Delta n_s^{\text{ring}} L_1]. \quad (4)$$

Here L_1 is the total length of the narrower ring waveguide sections, $L_1 = L - L_{\text{MMI}} = 2\pi R + L_{\text{MMI}}$. Figure 9 shows the ring resonator phase difference $\Delta\phi = \phi^{\text{TM}} - \phi^{\text{TE}}$ as a function of the oxide cladding thickness for two cladding stress levels. Obviously, various combinations of cladding stress and thickness can be found to adjust $\Delta\phi$ to zero.

We have fabricated MMI-based ring resonators in SOI wafers with $1.5 \mu\text{m}$ thick silicon at the Canadian Photonics Fabrication Center (CPFC). SEM images of a fabricated device are shown in Figures 10(a) and 10(b). Standard inhouse PECVD process produces oxide films with -250 MPa stress. Measured transmission spectra for a MMI-coupled ring resonator with a radius of $200 \mu\text{m}$ are shown in Figure 10(c) for TE and TM polarizations. Over the 4 nm scan range, the polarization-dependent wavelength shift is below 2 pm, which is the laser scan step used in these measurements. The measured free spectral range (FSR) is ~ 0.46 nm, and the quality factor is $Q \sim 15,000$. Polarization insensitive operation is achieved in these resonators, demonstrating the effectiveness of the proposed method for polarization control.

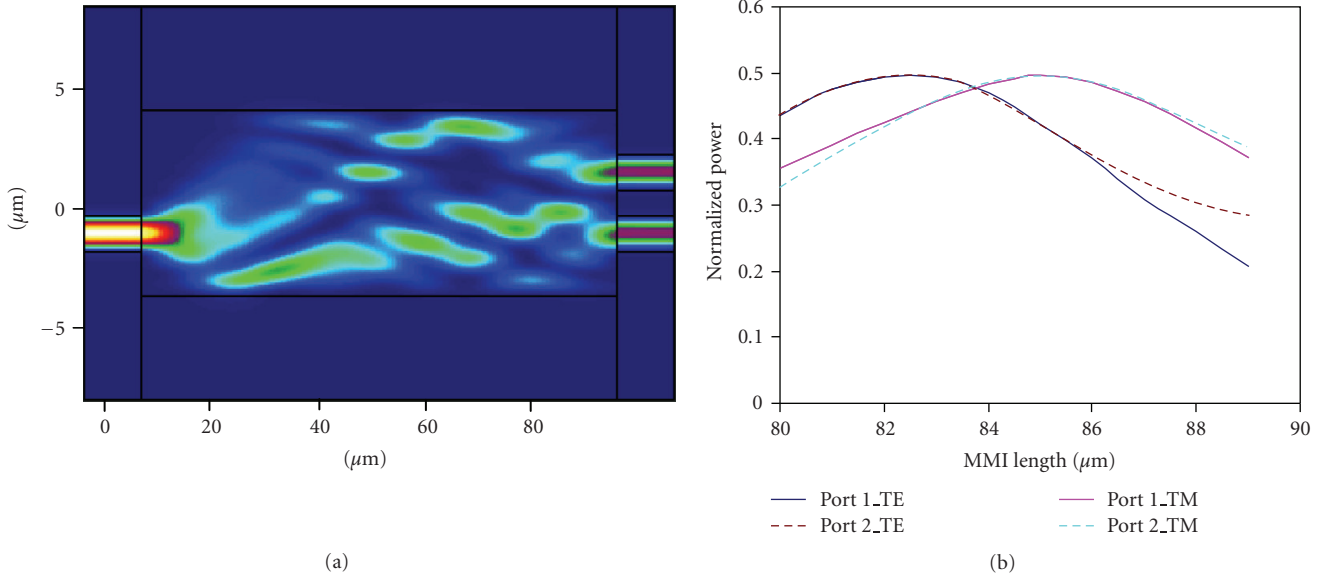


FIGURE 8: (a) Optical field distribution in the SOI MMI coupler of $7.5 \mu\text{m} \times 84 \mu\text{m}$ in dimensions, with an etch depth of $1 \mu\text{m}$. (b) Corresponding normalized power in the fundamental mode in ports 1 and 2, for the TE and TM polarizations.

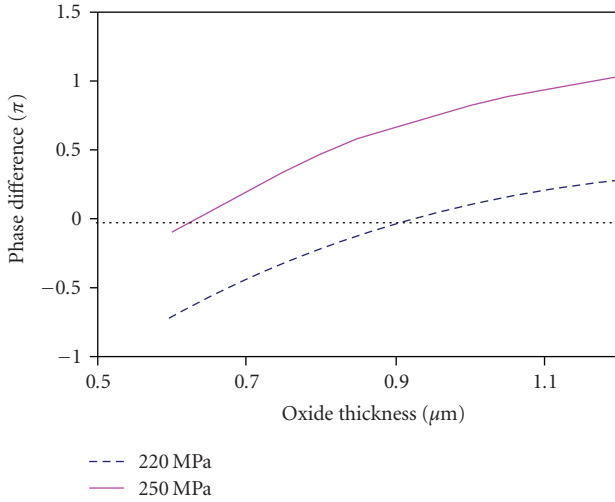


FIGURE 9: Phase difference $\Delta\phi = \phi^{\text{TM}} - \phi^{\text{TE}}$ as a function of the oxide cladding thickness for an MMI-coupled ring resonator with a radius R of $200 \mu\text{m}$ and an oxide cladding stress of -220 and -250 MPa, respectively.

4.3. Broadband polarization splitter in a zero-order AWG configuration

Stress-induced effects can also be used to produce high level of birefringence in selected waveguide areas. Since the stress-induced index modifications are several orders of magnitude smaller than the core-cladding refractive index contrast in SOI, the effect of a SiO_2 cladding on mode shape is negligible. Thus there is little mode mismatch loss or polarization-dependent loss at the junctions between waveguide sections with and without the cladding. Figure 11 shows a zero-order AWG where all of the arrayed waveguides have

identical geometrical path lengths [20]. A triangular patch of oxide cladding is placed in the arrayed waveguide section with a constant length increment ΔL between the adjacent waveguides. The stress in the waveguide cladding induces a polarization-dependent phase difference in the light signal propagating in the waveguide array (see Figure 4(a)), causing a polarization-dependent tilt in the phase front of the light in the free propagation region (FPR) (see Figure 11(b)). Since all waveguides have the same physical length, the phase difference for light propagating in the adjacent waveguides of the arrayed section depends solely on the cladding stress-induced index change and the patch-length increment. Since the stress-induced index change in the TE and TM polarization modes has opposite signs for silicon waveguides, the two modes are spatially displaced in the opposite directions in the focal region relative to the free propagation region centerline, as shown in Figure 11(b). With proper placement of the two receiver waveguides along the focal plane, the two polarizations are spatially separated.

Zero-order AWG-based polarization splitters were designed and fabricated on SOI wafers, with a $2.2 \mu\text{m}$ thick silicon core layer. The deposited oxide cladding film had a thickness of $1 \mu\text{m}$, and the measured cladding film stress was approximately -340 MPa. The overall device size is $\sim 12 \text{ mm} \times 4 \text{ mm}$. Figure 12(a) shows several fabricated AWG devices with triangular cladding regions of varied patch sizes. Based on the measured cladding film stress and thickness, the cladding patch-length increment ΔL between the adjacent waveguides was set to $16.4 \mu\text{m}$ to produce the required polarization-dependent phase front tilt at the output of the waveguide array. Since stress-induced effects do not vary with wavelength appreciably, and the AWG operates close to zero order, the performance of the splitter is expected to be wavelength independent over a large application bandwidth, which was experimentally

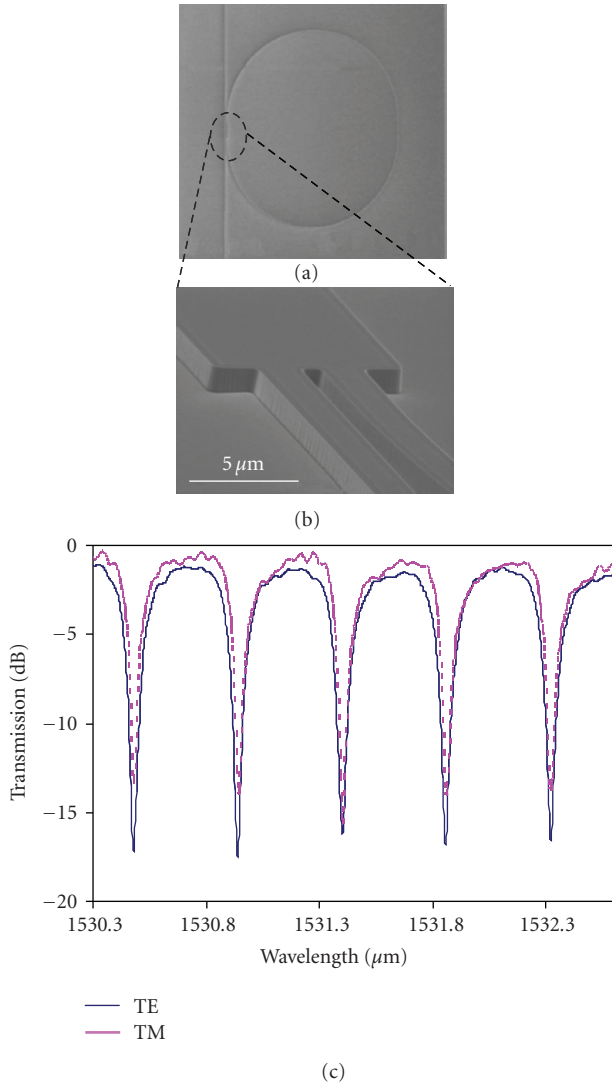


FIGURE 10: (a) SEM image of an MMI-coupled ring resonator. (b) A closeup of the MMI section. (c) TE and TM transmission spectra of the ring resonator, with an upper SiO₂ cladding of 0.8 μm thick and film stress of $\sigma_{\text{film}} = -250$ MPa.

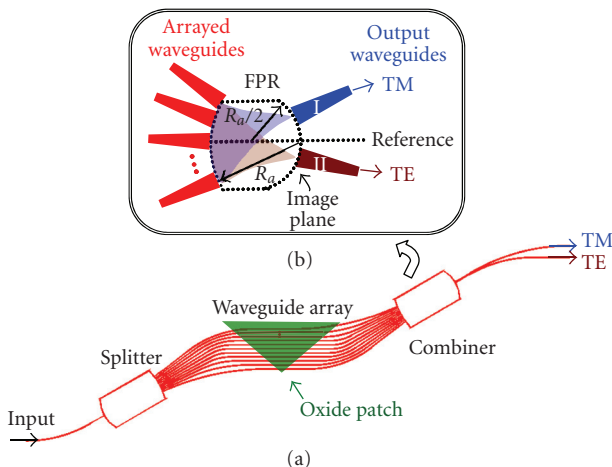


FIGURE 11: (a) Schematic layout of a broadband zero-order AWG polarization splitter. (b) Geometry of the output FPR with a Rowland circle configuration.

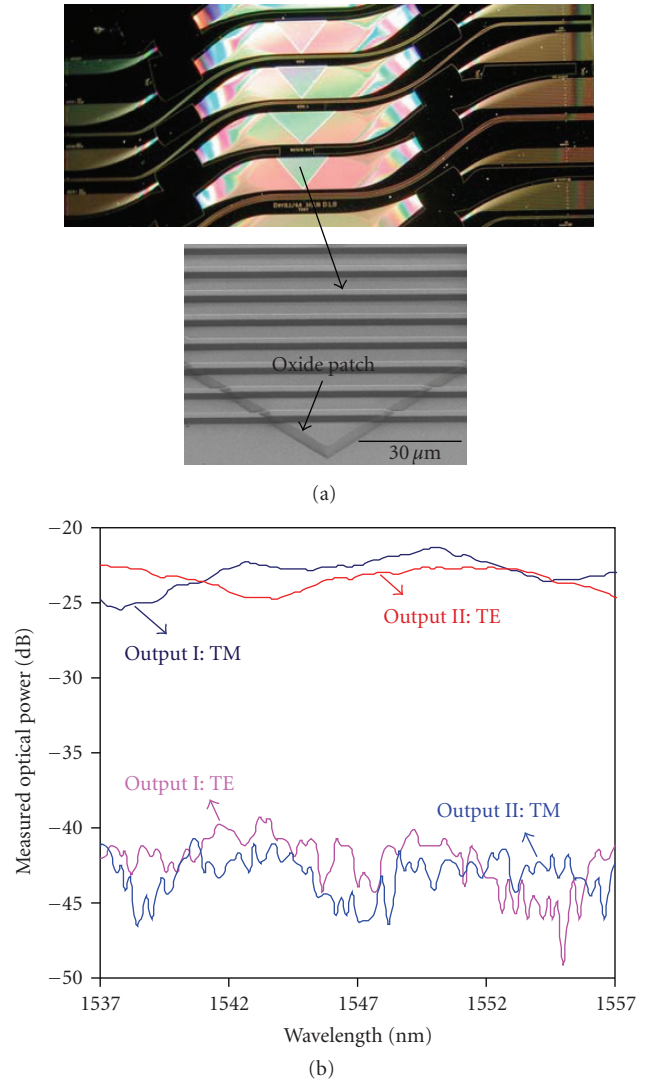


FIGURE 12: (a) A top view of the fabricated wavelength-independent zero-order AWG polarization splitters and insert an expanded SEM image of the oxide cladding patch in the waveguide array. (b) Measured transmission as a function of wavelength of a zero-order AWG-based polarization splitter.

confirmed. The measured extinction ratio of the polarization splitter was better than -10 dB for both output polarizations over the entire tuning range of our laser (1465–1580 nm). Figure 12(b) shows the measured polarization splitter transmission for a wavelength range of $\lambda = 1537$ to 1557 nm. Over this range, the splitter extinction ratio is < -15 dB. The best extinction ratio achieved was -20 dB. Similar birefringence modification method was also applied in a Mach-Zehnder interferometer configuration to form polarization splitters and filters [33].

5. SUMMARY

We have reviewed the stress-induced modifications of the waveguide effective index for the TE and TM modes and the associated birefringence which are important for a wide

range of commonly employed SOI waveguide geometries. The significance of these stress-induced effects is now being recognized in the research community and applied in component development. If not taken into consideration, these effects can lead to large deviations in device characteristics from the designed specifications. Fortunately, the use of cladding stress to correct the waveguide birefringence allows a considerable degree of freedom in designing SOI waveguides to meet other performance criteria such as relaxed dimensional tolerance, reduced loss at waveguide bends, and overall improved device performance. This technique is simple to implement, and there are no additional process steps required other than the conventional cladding layer deposition. The stress-induced modifications to the effective index in SOI waveguides are readily controlled by the stress level and the thickness of the upper-oxide cladding. We have demonstrated that cladding stress engineering can be used to achieve polarization insensitivity in AWGs, spectrometers, and ring resonators, leaving the freedom of optimizing the waveguide geometry for considerations other than the birefringence. Since the effect of the SiO₂ cladding on the mode profile is negligible, there is little mode mismatch loss or polarization-dependent loss at the junctions between waveguide sections with and without the cladding. Therefore, tailored cladding patches can be applied at discrete locations in a planar waveguide circuit with negligible insertion loss and PDL penalty, as we demonstrated in the example of a broadband polarization splitter. The applications of cladding stress-induced effects can be envisioned in a variety of situations to enhance device functionality, simplify fabrication, and improve operation tolerance.

ACKNOWLEDGMENT

The authors gratefully acknowledge the contribution of Canadian Photonics Fabrication Center (CPFC) (<http://cpfc-ccfdp.nrc-cnrc.gc.ca/>) in fabricating the MMI-based polarization insensitive ring resonators.

REFERENCES

- [1] L. Pavesi and D. Lockwood, Eds., *Silicon Photonics*, Springer, Berlin, Germany, 2004.
- [2] Q. Xu, S. Manipatruni, B. Schmidt, J. Shakya, and M. Lipson, "12.5 Gbit/s carrier-injection-based silicon micro-ring silicon modulators," *Optics Express*, vol. 15, no. 2, pp. 430–436, 2007.
- [3] A. Liu, R. Jones, L. Liao, et al., "A high-speed silicon optical modulator based on a metal-oxide-semiconductor capacitor," *Nature*, vol. 427, no. 6975, pp. 615–618, 2004.
- [4] O. Boyraz and B. Jalali, "Demonstration of a silicon Raman laser," *Optics Express*, vol. 12, no. 21, pp. 5269–5273, 2004.
- [5] A. Densmore, D.-X. Xu, P. Waldron, et al., "A silicon-on-insulator photonic wire based evanescent field sensor," *IEEE Photonics Technology Letters*, vol. 18, no. 23, pp. 2520–2522, 2006.
- [6] P. Cheben, A. Bogdanov, A. Del age, et al., "A 100-channel near-infrared SOI waveguide microspectrometer: design and fabrication challenges," in *Optoelectronic Devices and Integration*, vol. 5644 of *Proceedings of SPIE*, pp. 103–110, Beijing, China, November 2004.
- [7] R. R. Whiteman, A. P. Knights, D. George, et al., "Recent progress in the design, simulation and fabrication of small cross-section silicon-on-insulator VOAs," in *Photonics Packaging and Integration III*, vol. 4997 of *Proceedings of SPIE*, pp. 146–156, San Jose, Calif, USA, January 2003.
- [8] P. Cheben, "Wavelength dispersive planar waveguide devices: echelle gratings and arrayed waveguide gratings," in *Optical Waveguides: From Theory to Applied Technologies*, M. L. Calvo and V. Lakshminarayanan, Eds., chapter 5, p. 173, CRC Press, London, UK, 2007.
- [9] S. Janz, P. Cheben, D. Dalacu, et al., "Microphotonic elements for integration on the silicon-on-insulator waveguide platform," *IEEE Journal on Selected Topics in Quantum Electronics*, vol. 12, no. 6, pp. 1402–1414, 2006.
- [10] L. Vivien, S. Laval, B. Dumont, S. Lardenois, A. Koster, and E. Cassan, "Polarization-independent single-mode rib waveguides on silicon-on-insulator for telecommunication wavelengths," *Optics Communications*, vol. 210, no. 1–2, pp. 43–49, 2002.
- [11] D. Dai and S. He, "Analysis of the birefringence of a silicon-on-insulator rib waveguide," *Applied Optics*, vol. 43, no. 5, pp. 1156–1161, 2004.
- [12] W. R. Headley, G. T. Reed, F. Gardes, A. Liu, and M. Paniccia, "Enhanced polarisation-independent optical ring resonators on silicon-on-insulator," in *Optoelectronic Integration on Silicon II*, vol. 5730 of *Proceedings of SPIE*, pp. 195–202, San Jose, Calif, USA, January 2005.
- [13] D.-X. Xu, P. Cheben, D. Dalacu, et al., "Eliminating the birefringence in silicon on insulator ridge waveguides using the cladding stress," *Optics Letters*, vol. 29, no. 20, pp. 2384–2386, 2004.
- [14] M. Huang, "Stress effects on the performance of optical waveguides," *International Journal of Solids and Structures*, vol. 40, no. 7, pp. 1615–1632, 2003.
- [15] I. Kiyat, A. Aydinli, and N. Dagli, "Polarization characteristics of compact SOI rib waveguide racetrack resonators," *IEEE Photonics Technology Letters*, vol. 17, no. 10, pp. 2098–2100, 2005.
- [16] W. N. Ye, D.-X. Xu, S. Janz, et al., "Birefringence control using stress engineering in silicon-on-insulator (SOI) waveguides," *Journal of Lightwave Technology*, vol. 23, no. 3, pp. 1308–1318, 2005.
- [17] D.-X. Xu, W. N. Ye, A. Bogdanov, et al., "Design of polarization-insensitive components using geometrical and stress-induced birefringence in SOI waveguides," in *Optoelectronic Integration on Silicon II*, vol. 5730 of *Proceedings of SPIE*, pp. 158–172, San Jose, Calif, USA, January 2005.
- [18] D.-X. Xu, S. Janz, and P. Cheben, "Design of polarization-insensitive ring resonators in silicon-on-insulator using MMI couplers and cladding stress engineering," *Photonics Technology Letters*, vol. 18, no. 2, pp. 343–345, 2006.
- [19] D.-X. Xu, P. Cheben, A. Del age, et al., "Polarization-insensitive MMI-coupled ring resonators in silicon-on-insulator using cladding stress engineering," in *Silicon Photonics II*, vol. 6477 of *Proceedings of SPIE*, pp. 1–11, San Jose, Calif, USA, January 2007.
- [20] W. N. Ye, D.-X. Xu, S. Janz, P. Waldron, P. Cheben, and N. G. Tarr, "Passive broadband silicon-on-insulator polarization splitter," *Optics Letters*, vol. 32, no. 11, pp. 1492–1494, 2007.
- [21] A. Kilian, J. Kirchhof, B. Kuhlow, G. Przyrembel, and W. Wischmann, "Birefringence free planar optical waveguide made by flame hydrolysis deposition (FHD) through tailoring of the overcladding," *Journal of Lightwave Technology*, vol. 18, no. 2, pp. 193–198, 2000.

- [22] C. K. Nadler, E. K. Wildermuth, M. Lanker, W. Hunziker, and H. Melchior, "Polarization insensitive, low-loss, low-crosstalk wavelength multiplexer modules," *IEEE Journal on Selected Topics in Quantum Electronics*, vol. 5, no. 5, pp. 1407–1412, 1999.
- [23] T. S. Narasimhamurthy, *Photoelastic and Electro-Optic Properties of Crystals*, Plenum Press, New York, NY, USA, 1981.
- [24] B. E. Little, S. T. Chu, H. A. Haus, J. Foresi, and J.-P. Laine, "Microring resonator channel dropping filters," *Journal of Lightwave Technology*, vol. 15, no. 6, pp. 998–1005, 1997.
- [25] C. K. Madsen, "Efficient architectures for exactly realizing optical filters with optimum bandpass designs," *IEEE Photonics Technology Letters*, vol. 10, no. 8, pp. 1136–1138, 1998.
- [26] Q. Xu, B. Schmidt, S. Pradhan, and M. Lipson, "Micrometer-scale silicon electro-optic modulator," *Nature*, vol. 435, pp. 325–327, 2005.
- [27] D.-X. Xu, A. Densmore, P. Waldron, et al., "High bandwidth SOI photonic wire ring resonators using MMI couplers," *Optics Express*, vol. 15, no. 6, pp. 3149–3155, 2007.
- [28] A. Yariv, "Universal relations for coupling of optical power between microresonators and dielectric waveguides," *Electronics Letters*, vol. 36, no. 4, pp. 321–322, 2000.
- [29] L. B. Soldano and E. C. M. Pennings, "Optical multi-mode interference devices based on self-imaging: principles and applications," *Journal of Lightwave Technology*, vol. 13, no. 4, pp. 615–627, 1995.
- [30] P. A. Besse, E. Gini, M. Bachmann, and H. Melchior, "New 2×2 and 1×3 multimode interference couplers with free selection of power splitting ratios," *Journal of Lightwave Technology*, vol. 14, no. 10, pp. 2286–2292, 1996.
- [31] T. Saida, A. Himeno, M. Okuno, A. Sugita, and K. Okamoto, "Silica-based 2×2 multimode interference coupler with arbitrary power splitting ratio," *Electronics Letters*, vol. 35, no. 23, pp. 2031–2033, 1999.
- [32] M. Bachmann, P. A. Besse, and H. Melchior, "General self-imaging properties in $N \times N$ multimode interference couplers including phase relations," *Applied Optics*, vol. 33, no. 18, pp. 3905–3911, 1994.
- [33] W. N. Ye, D.-X. Xu, S. Janz, P. Waldron, and N. G. Tarr, "Stress-induced SOI polarization splitter based on Mach-Zehnder Interferometers (MZI)," in *Proceedings of the 3rd IEEE International Conference on Group IV Photonics (GFP '06)*, pp. 249–251, Ottawa, Canada, September 2006.

Research Article

Silicon Photonic Biosensors for Lab-on-a-Chip Applications

**Kirill Zinoviev,¹ Laura G. Carrascosa,² José Sánchez del Río,² Borja Sepúlveda,²
Carlos Domínguez,¹ and Laura M. Lechuga²**

¹*Instituto de Microelectrónica de Barcelona, CNM-CSIC, Campus UAB, Bellaterra 08193, Barcelona, Spain*

²*Nanobiosensors and Molecular Nanobiophysics Group, Research Center on Nanoscience and Nanotechnology (CIN2: CSIC-ICN), Campus UAB, Bellaterra 08193, Barcelona, Spain*

Correspondence should be addressed to Laura M. Lechuga, laura.lechuga@cin2.es

Received 13 February 2008; Accepted 24 April 2008

Recommended by Pavel Cheben

In the last two decades, we have witnessed a remarkable progress in the development of biosensor devices and their application in areas such as environmental monitoring, biotechnology, medical diagnostics, drug screening, food safety, and security, among others. The technology of optical biosensors has reached a high degree of maturity and several commercial products are on the market. But problems of stability, sensitivity, and size have prevented the general use of optical biosensors for real field applications. Integrated photonic biosensors based on silicon technology could solve such drawbacks, offering early diagnostic tools with better sensitivity, specificity, and reliability, which could improve the effectiveness of in-vivo and in-vitro diagnostics. Our last developments in silicon photonic biosensors will be showed, mainly related to the development of portable and highly sensitive integrated photonic sensing platforms.

Copyright © 2008 Kirill Zinoviev et al. This is an open access article distributed under the Creative Commons Attribution License, which permits unrestricted use, distribution, and reproduction in any medium, provided the original work is properly cited.

1. INTRODUCTION

The progressive demand for the rapid and precise detection of any type of substances has speed up the development of a large variety of biosensors. For most of the applications, it is desirable to have a compact biosensor with high sensitivity, fast response, and able to perform real-time measurements. These requirements can be achieved mainly with optical sensors [1] due to the own nature of the optical measurements that endow a great number of different techniques, as emission, absorption, fluorescence, refractometry, or polarimetry. Among them, photonic biosensors based on evanescent wave detection have demonstrated its outstanding properties, such as an extremely high sensitivity for the direct measurement of biomolecular interactions, in real time and in label-free schemes [1].

In the evanescent wave detection, a receptor layer is immobilized onto the core surface of the waveguide. The exposure of the functionalized surface to the complementary analyte molecules and the subsequent biochemical interaction between them induces a local change in the optical properties of the biological layer. This change is detected via the evanescent field of the guided light and its amplitude can

be correlated to the concentration of the analyte and to the affinity constant of the interaction, yielding a quantitative signal of the interaction.

The wide variety of optical sensing platforms is spread over sensors based on optical fibers [2], planar waveguide structures [3], microresonators [4–6], resonant waveguide diffractive structures [7, 8], light addressable potentiometric devices (LAPS) [9, 10], micromechanical structures with optical readout [11], porous silicon [12, 13], and so forth.

The advantages of optical sensing are significantly improved when this approach is used within an integrated optics context. Integrated optics technology allows the integration of passive and active optical components (including fibres, emitters, detectors, waveguides, and related devices) onto the same substrate, allowing the flexible development of miniaturized compact sensing devices, with the additional possibility to fabricate multiple sensors on a single chip. The integration offers additional advantages such as miniaturization, robustness, reliability, potential for mass production with consequent reduction of production costs, low energy consumption, and simplicity in the alignment of the individual optical elements.

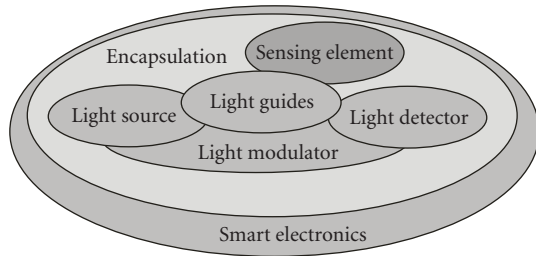


FIGURE 1: The main research areas in the development of photonics biosensors based on silicon technology.

Several technologies are available for the fabrication of photonic biosensors, but the well-developed silicon technology is one of the most useful and promising tools. Much work on silicon photonic devices has been done in the telecommunications field, and some results have been successfully applied for sensor development. In “siliconized” photonics, the fabrication of the devices is performed with silicon or silicon-related materials using microelectronics technologies, with the aim of integrating all the sensing components in a single chip. In order to “siliconize” photonics, there are several building blocks for investigation, including light generation and coupling, selectively guiding and transporting within the waveguides, light encoding, detection, packaging the devices, and, finally, “smart” electronic control of all these photonic functions (see Figure 1). Biofunctionalization of the sensing element is a subject of special research beyond photonics, thus the element has been highlighted in a separate block on the diagram of Figure 1.

In particular, light guiding for sensing applications can be based on total internal reflection (TIR) planar or rib waveguides [3, 14, 15], hollow waveguides [16–19], antiresonant reflecting optical waveguides (ARROW) [20–22], or slot [4, 23] waveguides. Interestingly, complex waveguide structures developed for telecommunications with the purpose of further miniaturization of photonics devices, which show potential sensing applications, have been reported recently [24].

In this paper, we will discuss the photonic biosensing platforms based on silicon technology, which are investigating in our laboratory, such as interferometric Mach-Zehnder (MZI), bimodal waveguides devices, and optomechanical microcantilevers. The three devices have advantages and disadvantages and depending on the specific biological application one is more suitable than the others. The interferometric MZI sensors show extremely high sensitivity; however, the existing light coupling methods frequently limit their application to laboratory use only. High thermal stability is required for the bimodal waveguide interferometers but this device is simpler in operation than the MZI. The optical microcantilevers also require a high mechanical and thermal stability for operation but this device is easily scalable to dozens or hundreds of sensors in the same chip opening the way to high-throughput screening using label-free biosensors. The main aim of this article is to describe the use of silicon technology for the implementation

of integrated optical biosensor rather than to perform a sensitivity comparison between the different devices.

2. INTEGRATED MACH-ZEHNDER INTERFEROMETER (MZI) SENSOR

Interferometric biosensors constitute one of the most sensitive integrated-optic alternatives as compared to other optical biosensor (i.e., plasmonic biosensors) for label-free detection. In these sensors, the guided light interacts with the analyte through its evanescent field or, alternatively, the analyte can propagate in the core of the waveguide if hollow or slot waveguides are employed. The most common Mach-Zehnder and Young interferometers [3, 25, 26] are composed of an incident waveguide that is split in two single mode waveguide branches, in which one of them contains a sensing window.

We have developed integrated Mach-Zehnder interferometers based on TIR waveguides ($\text{Si}/\text{SiO}_2/\text{Si}_3\text{N}_4$) of micro/nanodimensions, as it is shown on Figure 2. For biosensing applications, the optical waveguides of the MZI must have high surface sensitivity and single mode behavior. For that reason, we have chosen Si_3N_4 core layers ($n_c = 2.00$) over a SiO_2 substrate ($n_s = 1.46$). In this waveguide configuration (and wavelength in the visible range), the single mode behavior is obtained for core thickness below 300 nm. In order to provide single mode operation in the lateral direction, rib structures several nanometers high (below 5 nm) and rib widths of $4\ \mu\text{m}$ were fabricated. To achieve single mode behavior, the waveguide could be designed to be narrower and with a higher rib but this will depend on the tolerances of the equipment available for the fabrication. With the equipment of our facilities, we can ensure the reproducibility of the rib height at a nanometric scale which allows us to make relatively wide waveguides which are more convenient for experimental work. Figure 2 shows a schematic of the waveguide configuration. In the MZI, Y-shape divisors with circular arms of $R = 80\ \text{nm}$ were designed to direct light in the two branches of the MZI with 3 dB split ratio. To protect the device from temperature fluctuations, the waveguide branches are placed very close to each other ($100\ \mu\text{m}$), thus the temperature changes affect both waveguides simultaneously.

The devices are fabricated in our clean room facilities. The final device has a length of 3 cm and the sensor area is 1.5 cm long and $50\ \mu\text{m}$ wide. The experimental evaluation of the device was performed in an optical bench, where polarized light from an He-Ne laser ($\lambda = 0.633\ \mu\text{m}$) was end-fire coupled to the sensor. The propagation losses of the waveguides were measured by the Fabry-Perot resonance technique, and the optical coupling losses were measured by the cutback method. Propagation losses, in the case of MZI of 200 nm core thickness, vary between 0.13 and 0.15 dB/cm for TE polarization and between 0.27 and 0.30 dB/cm for TM polarization. Insertion losses are 5.84 dB for TM polarization and 8.3 dB for TE polarization. The sensitivity of the sensor for both polarizations was analyzed in the same way as in previous reports [3]. The evaluation was done flowing solutions of water and ethanol of varying concentration

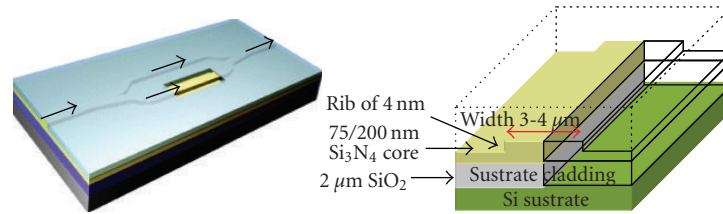


FIGURE 2: (left). Mach-Zehnder interferometer (MZI) configuration. (right) Cross-section schematic of the TIR waveguides employed in the integrated MZI device.

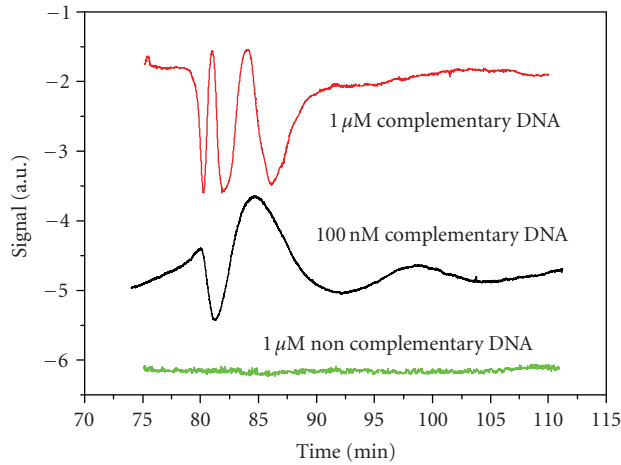


FIGURE 3: Real-time DNA hybridization signal corresponding to 1 μM and 100 nM complementary oligonucleotide and 1 μM noncomplementary oligonucleotide.

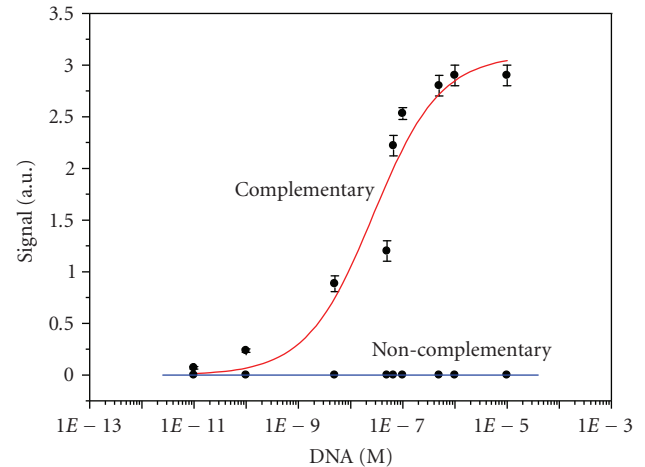


FIGURE 4: Calibration curve for the hybridization of complementary (red line) and noncomplementary (blue line) DNA (58 mers). Limit of detection is 10 pM.

(refractive index steps of 10^{-3}) and measuring the output signal in real time. Taking into account the signal-to-noise ratio of our system, the lowest detection limit in the variation of the refractive index (n_0) for the TM polarization was found to be $\Delta n_{0,\min} = 1 \cdot 10^{-7}$.

The relatively simple design, high integration level, well developed read out techniques, and the high sensitivity make these devices very attractive for bio/chemical applications. The MZI device has been used for the direct detection of DNA hybridization and for the detection of single mutations at the BRCA-1 gene, involved in breast cancer development, without target labelling [27]. The oligonucleotide probe is immobilized by covalent attachment to the sensor surface through silanization procedures. A silane (3-mercaptopropyltrimethoxysilane) with a thiol group at the free end was employed for the chemical modification of the surface. A thiol-derivatized oligonucleotides (28 mer) used as receptors can bind to the silanized Si₃N₄ surface through a disulphide bond. The DNA probe has also a 15-tiamine tail which is employed as a vertical spacer chain to increase the accessibility to the complementary DNA to the sensor surface.

After DNA immobilization, complementary oligonucleotides (58 mer) were flowed in the sensor for hybridization experiments. The hybridization was performed for different DNA target concentrations from 1 pM to 1 μM.

Regeneration after each hybridization was achieved flowing deionized water and HCl 3.2 mM. Figure 3 shows examples of the real-time detection of DNA hybridization for several concentrations. The calibration curve as a function of the DNA concentration can be seen in Figure 4. In these measurements, a 10 pM-concentration of complementary non-labelled DNA in buffer solution was the lowest hybridization limit achieved, which means an average DNA growth layer of $1 \cdot 14^{-4}$ nm, corresponding to an estimation of $2 \cdot 10^5$ DNA molecules/cm² hybridized at the sensor area of the MZI. In contrast, noncomplementary oligonucleotides did not show any significant signal.

More importantly, we have detected the hybridization of 100 nM DNA target with two mismatching bases corresponding to a mutation of the BRCA-1 gene (data not shown). These results place the Mach-Zehnder interferometer as one of the most sensitive optical biosensor for label-free mismatch and DNA hybridisation detection.

3. BIMODAL WAVEGUIDE SENSOR

This sensor is comprised by a single straight bimodal waveguide (BiMW), which supports the zero- and first-order transversal modes (see Figure 5). These modes propagate with different velocities depending, among other factors, on the refractive index of the cladding layer. The interference

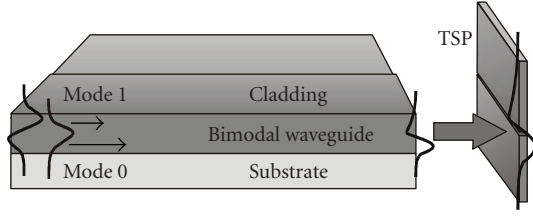


FIGURE 5: Schematic view of the bimodal waveguide sensor device. The modes are propagating with different velocities. The interference pattern, created at the exit and projected onto a two-sectional photodetector (TSP), varies as a function of the refractive index of the cladding layer.

pattern formed at the exit of the waveguide changes if the refractive index varies. The pattern is projected on a two-sectional photodetector (TSP), then the intensity maximum moves between the lower and the upper sections of the photodetector. The signals generated by the photodetector sections are recalculated into a parameter S_r , according to the expression

$$S_r = \frac{U_{\text{up}} - U_{\text{down}}}{U_{\text{up}} + U_{\text{down}}}, \quad (1)$$

where U_{up} , U_{down} are the signals generated by the upper and the lower sections of the photodetector, respectively.

The difference between U_{up} , and U_{down} can reach 17 dB, which means a variation of S_r from 0 to 0.96. These values were calculated assuming a silicon nitride waveguide with thickness of 400 nm operated at 633 nm. The total output signal, which can be represented by the denominator in the right part in (1), is proportional to the light power coupled into the waveguide, except for minor changes due to reflection at the output facet, which slightly depends on the intensity distribution at the exit, according to the simulations. Using the parameter S_r , the ambiguities due to coupling efficiency variations can be significantly reduced. However, as the monitoring of light power coupled into the waveguide is still desirable, a part of the incoupled light can be tapped off and measured with a conventional photodetector. The sensitivity of the device is given by

$$\text{Sens} = \frac{\partial S_r}{\partial \phi} \left(\frac{\partial n_{\text{eff}}^1}{\partial n_{\text{cl}}} - \frac{\partial n_{\text{eff}}^0}{\partial n_{\text{cl}}} \right) \frac{2\pi}{\lambda} L, \quad (2)$$

where L is the length of the sensing window, λ is the wavelength, n_{eff}^0 , n_{eff}^1 are the effective refractive index of the zero- and first-order modes, respectively, ϕ is the phase shift between the modes, and n_{cl} is the refractive index of the cladding layer.

For the experiments, we employed a 3 μm -wide, 400 nm thick Si_3N_4 waveguide deposited on a silicon dioxide buffer layer, and the length of the sensing area was 3 mm. The waveguide was excited by direct focusing of light from an He-Ne laser (633 nm, 10 mW). A slight misalignment of the objective with respect to the waveguide in the vertical direction allows for excitation of both modes simultaneously. Light was collected by an objective lens, and the image of the waveguide facet was projected on the photodetector (TSP).

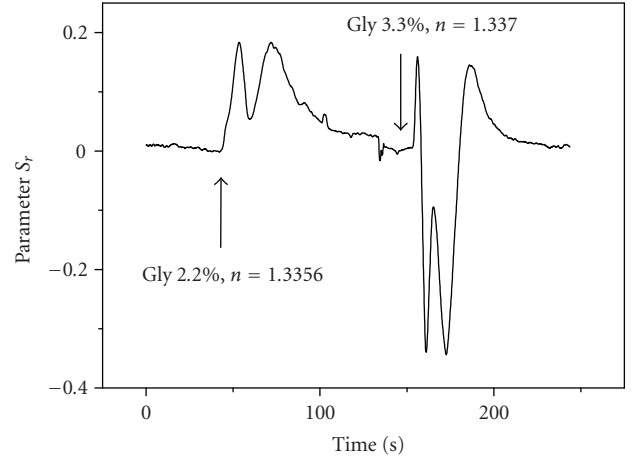


FIGURE 6: Response of the BiMW sensor to the injection of glycerin solutions with concentrations of 2.2% and 3.3% (v).

The detection of the refractive index changes was performed by injecting varying concentrations of water/glycerin solutions into a microfluidic channel formed over the sensing area. An example of the changes of the interferogram due to refractive index variation is shown in Figure 6. The sensitivity, defined as the relative change in the output signal per RIU change, can reach a value of better than 1×10^4 per RIU on a 1 cm-long waveguide with thickness less than 400 nm. A sensitivity of 2×10^3 per RIU was demonstrated experimentally on a silicon nitride waveguide with thickness of 400 nm. The obtained sensitivity was limited mostly by the thickness of the waveguide and by the coupling technique which allowed for only 25% modulation of the output signal. Biosensing experiments with this device are in progress.

4. OPTICAL MICROCANTILEVER BIOSENSOR

The development of microprobes for atomic force microscopy (AFM) was an important milestone for the establishment of efficient technological approaches to MEMS sensors. The principle of operation of the microcantilever sensor is based on the bending induced in the cantilever when a biomolecular interaction takes place in one of its surfaces. In this way, microcantilevers translate the molecular reaction into a nanomechanical motion, which is commonly detected using optical or piezoresistive readout [28].

In order to achieve highly integrated microsystem with microcantilever transducers, we have recently introduced a new type of readout technique. The combination of photonics and mechanics has been demonstrated in an optical waveguide cantilever sensor. The sensor can work in static or dynamic modes, either by monitoring the deflection or the changes in the resonance frequency of the cantilever. The principle of operation is based on the sensitivity of energy transfer between two butt-coupled waveguides to their misalignment with respect to each other as it is represented in Figure 7. The advantage of the device is that the transducer is integrated with the receptor in the same chip and the external photodetector is only used for optical

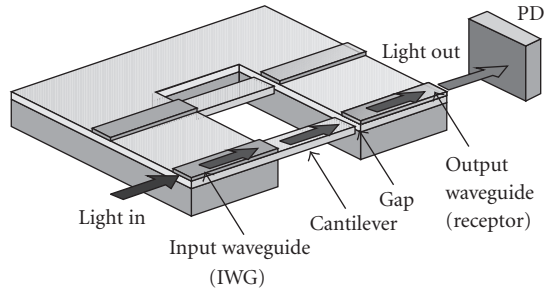


FIGURE 7: Sketch of the sensor based on optical waveguide microcantilevers.

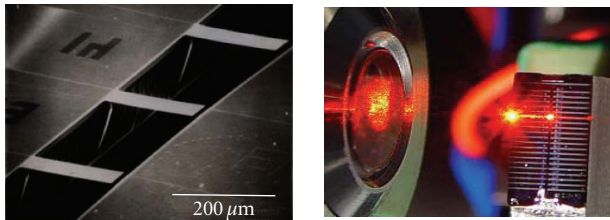


FIGURE 8: Photographs of the optical cantilevers and the light coupling inside them.

power readout. No preliminary alignment or adjustment is needed, except for light coupling into the chip.

We have fabricated arrays of 20 optical microcantilevers. Each of them is $200\ \mu\text{m}$ long, $40\ \mu\text{m}$ wide, and $500\ \text{nm}$ thick with a spring constant of $0.050\ \text{N/m}$. Fabrication of the sensor is done using standard microelectronic technology. The cantilevers are made of thermal silicon dioxide, transparent in visible range. Input and output waveguides are made of silicon nitride and are $140\ \text{nm}$ -thick and $40\ \mu\text{m}$ -wide. The cantilever has low stress gradient and is practically flat, the misalignment between the output waveguide and the cantilever free end is around $1\ \mu\text{m}$. Some photographs of the fabricated devices can be seen in Figure 8. Coupling of the light in the cantilever is achieved through the evanescent field of the input waveguide.

In order to characterize the sensor, an experimental setup was used to measure the amplitude of modulation of the output signal induced by the vibration of the cantilever at the resonance frequency. Light from He-Ne laser ($632.8\ \text{nm}$, $7.5\ \text{mW}$) was coupled into the chip using direct focusing with an objective lens ($40\times$, $\text{NA } 0.65$) and was collected upon exiting by another objective ($40\times$, $\text{NA } 0.65$) before being directed to a silicon photodetector connected to an oscilloscope and an acquisition system for spectrum analysis through a low-noise amplifier with bandwidth 5 to $45\ \text{kHz}$, at FWHM. Light from the same laser source after splitting was focused by a lens with a focal distance of $75\ \text{mm}$ on the cantilever near its free end. The reflected beam was projected on to a two-sectional position sensitive photodetector to monitor the displacement of the cantilever. Clear resonance behavior near $13\ \text{kHz}$ with a Q -factor of 12 was observed [11]. The change in the output voltage per unit cantilever

displacement was calculated to be $15\ \mu\text{V/nm}$, thus nanometre resolution of the system was demonstrated.

Taking account in this configuration that the minimum detectable deflection is limited by the shot noise of the photodetector, the Johnson noise of the load resistor, the noise in the acquisition system, the cantilever vibration due to the thermal noise, and the noise produced by the laser source, we have estimated that, for a $1\ \mu\text{m}$ wide gap, the cantilever displacement can be detected with a resolution of $18\ \text{fm}/\sqrt{\text{Hz}}$ [11], showing similar performances for biosensing than the standard microcantilevers.

One of the advantages of this device is that real-time parallel monitoring of several channels can be done simultaneously, opening the way for multisensing. The cantilever can be metallized with gold (and then it is possible to use the well-known thiol chemistry for bioreceptors immobilization) and its initial displacement can be adjusted by varying the power of light coupled inside [29]. This new device has shown good performances for biosensing and offers an interesting approach for further integration in lab-on-a-chip microsystems. The integration with the light source and the biofunctionalization of the device is a subject of our current research.

5. INTEGRATION IN “LAB-ON-A-CHIP” MICROSYSTEMS

For the development of a complete photonic lab-on-a-chip microsystem device, several units must be incorporated on the same platform: (i) the micro/nanodevices, (ii) the flow cells and the flow delivery system, (iii) for interferometric sensors, a phase modulation system to convert the periodic output signal in direct phase measurements, (iv) integration of the light sources and the photodetectors, and (v) CMOS processing electronics. For achieving this goal, our first step has been the development of a novel low temperature (100°C) CMOS compatible microfluidic technology to create 3D embedded interconnected microfluidic channels between different substrates. The microfluidic channels have a height from 40 to $60\ \mu\text{m}$ and a width between 100 to $250\ \mu\text{m}$. More details can be found in [30].

6. CONCLUSIONS

We have presented the development of different integrated optical biosensor platforms based on silicon technologies: a Mach-Zehnder integrated interferometer, a bimodal waveguide sensor, and a waveguided microcantilever device. The feasibility of the different platforms for biosensing has been proved. In the case of the MZI device, we have achieved a lowest limit of detection of $10\ \text{pM}$ for the DNA hybridization of the BRCA-1 gene, involved in breast cancer development. These results place the Mach-Zehnder interferometer as one of the most sensitive optical biosensor for label-free DNA detection.

All the described sensing configurations look ahead the possibility of the integration of optic, fluidic, and electrical functions on one platform to obtain lab-on-a-chip microsystems. These results open the way for further

development of portable and multianalyte sensors for the detection of several biological molecules of interest in situ and in real-time.

ACKNOWLEDGMENTS

Authors would like to thank the financial support of the Spanish Ministry of Education and Science (project TEC2005-13604) and M. Botín Foundation.

REFERENCES

- [1] L. M. Lechuga, "Optical biosensors," in *Biosensors and Modern Biospecific Analytical Techniques*, L. Gorton, Ed., vol. 44 of *Comprehensive Analytical Chemistry Series*, pp. 209–250, Elsevier Science BV, Amsterdam, The Netherlands, 2005.
- [2] B. Culshaw, "Optical fiber sensor technologies: opportunities and-perhaps-pitfalls," *Journal of Lightwave Technology*, vol. 22, no. 1, pp. 39–50, 2004.
- [3] F. Prieto, B. Sepúlveda, A. Calle, et al., "An integrated optical interferometric nanodevice based on silicon technology for biosensor applications," *Nanotechnology*, vol. 14, no. 8, pp. 907–912, 2003.
- [4] C. A. Barrios, "Ultrasensitive nanomechanical photonic sensor based on horizontal slot-waveguide resonator," *IEEE Photonics Technology Letters*, vol. 18, no. 22, pp. 2419–2421, 2006.
- [5] T. M. Benson, S. V. Boriskina, P. Sewell, A. Vukovic, S. C. Greedy, and A. I. Nosich, "Micro-optical resonators for microlasers and integrated optoelectronics: recent advances and future challenges," in *Frontiers of Planar Lightwave Circuit Technology: Design, Simulation and Fabrication*, S. Janz, J. Ctyroky, and S. Tanev, Eds., pp. 39–70, Springer, Berlin, Germany, 2005.
- [6] H.-C. Ren, F. Vollmer, S. Arnold, and A. Libchaber, "High-Q microsphere biosensor-analysis for adsorption of rodlike bacteria," *Optics Express*, vol. 15, no. 25, pp. 17410–17423, 2007.
- [7] Y. Fang, A. M. Ferrie, N. H. Fontaine, J. Mauro, and J. Balakrishnan, "Resonant waveguide grating biosensor for living cell sensing," *Biophysical Journal*, vol. 91, no. 5, pp. 1925–1940, 2006.
- [8] M. Wiki, R. E. Kunz, G. Voirin, K. Tiefenthaler, and A. Bernard, "Novel integrated optical sensor based on a grating coupler triplet," *Biosensors & Bioelectronics*, vol. 13, no. 11, pp. 1181–1185, 1998.
- [9] D. G. Hafeman, J. W. Parce, and H. M. McConnell, "Light-addressable potentiometric sensor for biochemical systems," *Science*, vol. 240, no. 4856, pp. 1182–1185, 1988.
- [10] W. J. Parak, M. George, J. Domke, et al., "Can the light-addressable potentiometric sensor (LAPS) detect extracellular potentials of cardiac myocytes?" *IEEE Transactions on Biomedical Engineering*, vol. 47, no. 8, pp. 1106–1113, 2000.
- [11] K. Zinoviev, C. Domínguez, J. A. Plaza, V. J. C. Busto, and L. M. Lechuga, "A novel optical waveguide microcantilever sensor for the detection of nanomechanical forces," *Journal of Lightwave Technology*, vol. 24, no. 5, pp. 2132–2138, 2006.
- [12] L. De Stefano, P. Arcari, A. Lamberti, et al., "DNA optical detection based on porous silicon technology: from biosensors to biochips," *Sensors*, vol. 7, no. 2, pp. 214–221, 2007.
- [13] J. J. Saarinen, S. M. Weiss, P. M. Fauchet, and J. E. Sipe, "Optical sensor based on resonant porous silicon structures," *Optics Express*, vol. 13, no. 10, pp. 3754–3764, 2005.
- [14] A. Densmore, D.-X. Xu, S. Janz, et al., "Spiral-path high-sensitivity silicon photonic wire molecular sensor with temperature-independent response," *Optics Letters*, vol. 33, no. 6, pp. 596–598, 2008.
- [15] B. J. Luff, J. S. Wilkinson, J. Piehler, U. Hollenbach, J. Ingenhoff, and N. Fabricius, "Integrated optical Mach-Zehnder biosensor," *Journal of Lightwave Technology*, vol. 16, no. 4, pp. 583–592, 1998.
- [16] V. J. Cadarso, I. Salinas, A. Allobera, and C. Domínguez, "Multimode interference devices based on silicon," in *Integrated Optics: Theory and Applications*, vol. 5956 of *Proceedings of SPIE*, pp. 1–8, Warsaw, Poland, August 2005.
- [17] R. Bernini, S. Campopiano, L. Zeni, and P. M. Sarro, "ARROW optical waveguides based sensors," *Sensors and Actuators B*, vol. 100, no. 1-2, pp. 143–146, 2004.
- [18] S. Campopiano, R. Bernini, L. Zeni, and P. M. Sarro, "Microfluidic sensor based on integrated optical hollow waveguides," *Optics Letters*, vol. 29, no. 16, pp. 1894–1896, 2004.
- [19] D. Yin, J. P. Barber, E. Lunt, et al., "Planar single-molecule sensors based on hollow-core ARROW waveguides," in *Silicon Photonics*, vol. 6125 of *Proceedings of SPIE*, pp. 1–13, San Jose, Calif, USA, January 2006.
- [20] F. Prieto, A. Llobera, D. Jiménez, A. Calle, C. Domínguez, and L. M. Lechuga, "Design and analysis of silicon antiresonant reflecting optical waveguides for highly sensitive sensors," *Journal of Lightwave Technology*, vol. 18, no. 7, pp. 966–972, 2000.
- [21] F. Prieto, L. M. Lechuga, A. Calle, A. Llobera, and C. Domínguez, "Optimised silicon antiresonant reflecting optical waveguides for sensing applications," *Journal of Lightwave Technology*, vol. 19, no. 1, pp. 75–83, 2001.
- [22] A. Llobera, J. A. Plaza, I. Salinas, et al., "Technological aspects on the fabrication of silicon-based optical accelerometer with ARROW structures," *Sensors and Actuators A*, vol. 110, no. 1–3, pp. 395–400, 2004.
- [23] T. Fujisawa and M. Koshiba, "Guided modes of nonlinear slot waveguides," *IEEE Photonics Technology Letters*, vol. 18, no. 14, pp. 1530–1532, 2006.
- [24] S. V. Boriskina, "Spectral engineering of bends and branches in microdisk coupled-resonator optical waveguides," *Optics Express*, vol. 15, no. 25, pp. 17371–17379, 2007.
- [25] A. Ymeti, J. S. Kanger, R. Wijn, P. V. Lambeck, and J. Greve, "Development of a multichannel integrated interferometer immunosensor," *Sensors and Actuators B*, vol. 83, no. 1–3, pp. 1–7, 2002.
- [26] A. Densmore, D.-X. Xu, P. Waldron, et al., "A silicon-on-insulator photonic wire based evanescent field sensor," *IEEE Photonics Technology Letters*, vol. 18, no. 23, pp. 2520–2522, 2006.
- [27] B. Sepúlveda, J. Sánchez del Río, M. Moreno, et al., "Optical biosensor microsystems based on the integration of highly sensitive Mach-Zehnder interferometer devices," *Journal of Optics A*, vol. 8, no. 7, pp. S561–S566, 2006.
- [28] L. G. Carrascosa, M. Moreno, M. Álvarez, and L. M. Lechuga, "Nanomechanical biosensors: a new sensing tool," *Trends in Analytical Chemistry*, vol. 25, no. 3, pp. 196–206, 2006.
- [29] K. Zinoviev, C. Domínguez, J. A. Plaza, and L. M. Lechuga, "Optical waveguide cantilever actuated by light," *Applied Physics Letters*, vol. 92, no. 1, Article ID 011908, 3 pages, 2008.
- [30] F. J. Blanco, M. Agirregabiria, J. Berganzo, et al., "Microfluidic-optical integrated CMOS compatible devices for label-free biochemical sensing," *Journal of Micromechanics and Microengineering*, vol. 16, no. 5, pp. 1006–1016, 2006.

Review Article

Silicon Nanocrystals: Fundamental Theory and Implications for Stimulated Emission

V. A. Belyakov,¹ V. A. Burdov,¹ R. Lockwood,² and A. Meldrum²

¹Department of Theoretical Physics, University of Nizhniy Novgorod, pr. Gagarina 23, Nizhniy Novgorod 603950, Russia

²Department of Physics, University of Alberta, Edmonton, AB, Canada T6G2G7

Correspondence should be addressed to A. Meldrum, ameldrum@ualberta.ca

Received 18 February 2008; Accepted 9 May 2008

Recommended by D. Lockwood

Silicon nanocrystals (NCs) represent one of the most promising material systems for light emission applications in microphotonics. In recent years, several groups have reported on the observation of optical gain or stimulated emission in silicon NCs or in porous silicon (PSi). These results suggest that silicon-NC-based waveguide amplifiers or silicon lasers are achievable. However, in order to obtain clear and reproducible evidence of stimulated emission, it is necessary to understand the physical mechanisms at work in the light emission process. In this paper, we report on the detailed theoretical aspects of the energy levels and recombination rates in doped and undoped Si NCs, and we discuss the effects of energy transfer mechanisms. The theoretical calculations are extended toward computational simulations of ensembles of interacting nanocrystals. We will show that inhomogeneous broadening and energy transfer remain significant problems that must be overcome in order to improve the gain profile and to minimize nonradiative effects. Finally, we suggest means by which these objectives may be achieved.

Copyright © 2008 V. A. Belyakov et al. This is an open access article distributed under the Creative Commons Attribution License, which permits unrestricted use, distribution, and reproduction in any medium, provided the original work is properly cited.

1. INTRODUCTION

Silicon is the most widespread semiconductor in modern microelectronics technologies. Its natural abundance, low cost, and high purity, as well as the high electronic quality of the Si/SiO₂ interface, have led to its overwhelming dominance in microelectronic devices. Nevertheless, the use of silicon in optoelectronics remains highly limited. This state of affairs has remained, in fact, almost unchanged because of a fundamental property of the silicon band structure—the indirect band gap.

The indirect radiative interband transitions in bulk Si are strongly suppressed because an emitted photon cannot satisfy the momentum conservation law for transitions from the conduction-band minimum (Δ -point) to the top of the valence band (Γ -point). The photon wave vector is about three orders of magnitude less than that required for the transition between the Δ - and Γ -points. This difference in k -space is $k_{\Delta} = 0.86 \times 2\pi/a_0$, with a_0 being the lattice constant of silicon, equal to 5.43 Å. The electron-hole radiative recombination in the bulk material is exactly forbidden unless additional mechanisms allowing the momentum to

be conserved are involved in the recombination process. The most probable means to have a radiative indirect transition without breakdown of the momentum conservation law is via phonon absorption or emission. However the electron-phonon interaction is weak; consequently, phonon assistance is a low-probability (and hence slow) process. This leads to a substantial increase of the total recombination time, and a decrease of the recombination probability compared to the direct no-phonon $\Gamma - \Gamma$ radiative transitions in direct-gap semiconductors. In this sense, we call such transitions in Si “strongly suppressed.”

The discovery of visible-range emission from nanocrystalline [1] and porous [2–4] silicon in the early 1990s suggested that some of the problems associated with the silicon band structure might be overcome in nanoscale crystallites hosted in a widegap dielectric matrix like SiO₂, in order to create a strong confining potential for carriers inside the nanocrystal. Electronic states become localized within the NC and the momentum distribution spreads due to the Heisenberg uncertainty relations. In other words, the wave functions consist of plane waves with all possible wave vectors including both $k \sim k_{\Delta}$ for holes and $k \sim 0$ for electrons,

respectively. Thus, the momentum conservation law is not violated in this case, which yields a nonzero probability of the $\Delta - \Gamma$ radiative transition even in the absence of phonons.

Indeed, some time later, efficient visible photoluminescence (PL) from silicon nanocrystals was experimentally demonstrated, (e.g., [5]) and attributed to the transitions between confined electron and hole states inside the nanocrystal [6, 7] (the so-called quantum confinement effect) or between interface states [8, 9]. However, the emission quantum efficiency in Si nanocrystals remains low compared to the direct gap III-V or II-VI materials. This is naturally explained by the small “weights” of the plane waves with $k \sim k_{\Delta}$ for the valence states and $k \sim 0$ for the conduction states. Thus, improvement of the light emission efficiency of Si quantum dots remains a challenge for optoelectronic technologies.

As a means to modify the optical properties of silicon crystallites, doping with shallow impurities has been suggested [10–18]. In some cases (depending on the conditions and methods of preparation), the emitting properties of the dots were improved significantly. In particular, the PL intensity was several times greater when the nanocrystals were doped with phosphorus [10–12, 14] or codoped with phosphorus and boron [15, 17]. The origin of this phenomenon is not fully understood at the present time, and we will touch on the problem of impurity states in silicon nanocrystals in this review.

PL experiments are not usually carried out with a single quantum dot but rather with large ensembles. As a result, interpretation of the experimental data is attendant with difficulties because of the associated inhomogeneous broadening and various collective effects that can occur as a result of the mutual influence of the nanocrystals in the ensemble. Some recent studies have reported on the PL spectra of individual silicon quantum dots [19, 20] and this is shedding new light on the physics involved in the light emission process. A principal distinction in the emission of a single NC and a nanocrystal ensemble lies in the various mechanisms of interaction amongst the nanocrystals in an ensemble. In particular, in solid nanocrystal arrays, some collective effects caused by electron, photon, and phonon transfer between the dots can strongly influence the luminescence dynamics of the nanocrystals in comparison with the case of isolated NCs. The size distribution of the nanocrystals can play an essential role in the excitation exchange between the clusters.

One possible mechanism of the NC-NC interaction is the direct tunneling of excited carriers from one quantum dot to another [21–23]. As an example, we can imagine two (or more) closely separated quantum dots with different sizes. Presumably, excited carriers in the smaller nanocrystal, having higher quantized energy levels, may relax either to the valence band of this nanocrystal or to the conduction band of the adjacent nanocrystal with a larger size. The transition to the valence band is indirect, and therefore suppressed. Meanwhile, the transfer to the neighboring quantum dot occurs as if within the same (conduction) band, and may be more probable in the case where the nanocrystals are sufficiently close. If so, then the smaller nanocrystals will

inject their own excited carriers into the larger nanocrystals, in which radiative interband transition will subsequently take place. This idea implies the possibility of an optical nanofountain [24]—a device emitting photons from the area where quantum dots with larger sizes are concentrated.

An additional nonradiative mechanism of energy transfer between adjacent nanocrystals becomes possible in dense arrays. This is the so-called Forster mechanism originating from the dipole-dipole (or higher-order multipole) interaction between excitons in different quantum dots [25–27]. Because of the dipole-dipole interaction, the electron-hole excitations can “travel” throughout the nanocrystals without charge transfer. Such transitions have been observed in solid arrays of CdSe nanocrystals [28, 29]. Some theoretical aspects of the Forster transfer in silicon quantum dots were recently discussed by Allan and Delerue [30].

Various collective effects in quantum-dot arrays can result in a complicated time dependence of the experimental PL decay. As a rule, the decay is described by the stretched exponential function $\exp\{-(t/\tau)^{\beta}\}$ with β less than unity [31–35]. Evidently, the value of β can be due to a size distribution of the nanocrystals (and hence a distribution of the recombination rates). Theoretical explanations of the stretched exponential from the point of view of the multiexponential decay and associated Laplace transforms have been given in [36].

This is, in short, the framework in which we will address the present review. At first we will briefly describe the experimental situation in this field in Section 2. Then the single-particle electronic structure and many-body corrections will be considered in Section 3 for a single silicon quantum dot as a basis for treatment of more complicated problem of solid quantum-dot ensembles. The latter will be reviewed in Section 4. Finally, Section 5 presents a general conclusion and a commentary on the potential for stimulated emission in silicon nanocrystal ensembles.

2. EXPERIMENTAL RESULTS: OVERVIEW

Different methods can be used for preparation of silicon nanocrystals, for instance, Si ion implantation [37–41], chemical vapor deposition [42], magnetron sputtering [43, 44], colloidal synthesis [45], electron beam evaporation [46, 47], and some others. A high-temperature thermal treatment is generally required in order to precipitate the crystallites. All these techniques allow one to form silicon NCs with sizes predominantly ranging from 2–6 nm. Their electronic structure and optical properties depend, of course, on the preparation conditions and method of fabrication. However, there are some common properties typical for silicon NCs, independent of the fabrication technique employed. In particular, the nanocrystals’ surroundings, either vacuum or some host material like silicon dioxide, represent a high potential barrier for carriers of both kinds. Such a barrier is often referred to as a confining potential that mainly defines the energy spectrum of the nanocrystal. In what follows we will discuss some manifestations of the quantum-confinement effect in experiments and theoretical models.

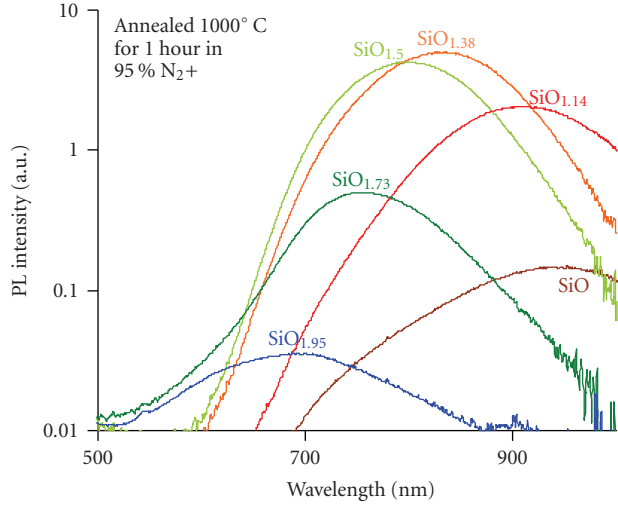


FIGURE 1: PL spectra of silicon NCs in SiO_2 . The 200-nm-thick samples were approximately identical except for the amount of excess silicon.

First, let us briefly discuss experimental data on the PL spectra in silicon quantum dots.

2.1. Size dependence

As has been mentioned above, silicon NCs are capable of emitting electromagnetic energy in the visible spectrum. This is in contrast with bulk silicon, in which energy of the interband transition corresponds to the silicon bandgap energy of 1.12 eV. The increase (decrease) of the photon frequency (wavelength) in nanocrystals compared to the bulk material is a universal phenomenon taking place in various semiconductor materials and quantum dots. In the general case one may say that the energy of the emitted photon increases as the nanocrystal size decreases. Such an increase is usually called a “blueshift” because the photon energy shifts toward the shorter-wavelength side of the visible spectrum. This blueshift is illustrated for Si NCs in Figure 1. Here, the mean NC size is controlled via the excess Si concentration, with the smallest NCs occurring in the most silicon deficient samples. The PL intensity has not been normalized here; the drop in intensity on the silicon-poor side of the compositional map is due to the lower number density of NCs, and on the silicon-rich side it is due to the opening of nonradiative pathways in large and highly interconnected nanoclusters.

In the simplest model of an infinitely strong confining potential (i.e., infinitely high potential barriers at the dot boundary) it is possible to estimate the energies of electrons and holes localized inside the nanocrystal as proportional to R^{-2} , where R is the nanocrystal radius. Thus, the optical gap may be calculated as $\varepsilon_g(R) = \varepsilon_g + A/R^2$, where ε_g is the bandgap of bulk silicon, A is some positive constant, and A/R^2 represents the total energy of the non-interacting electron-hole pairs inside the dot. It is obvious that: (i) the nanocrystal gap must be always greater than the bulk

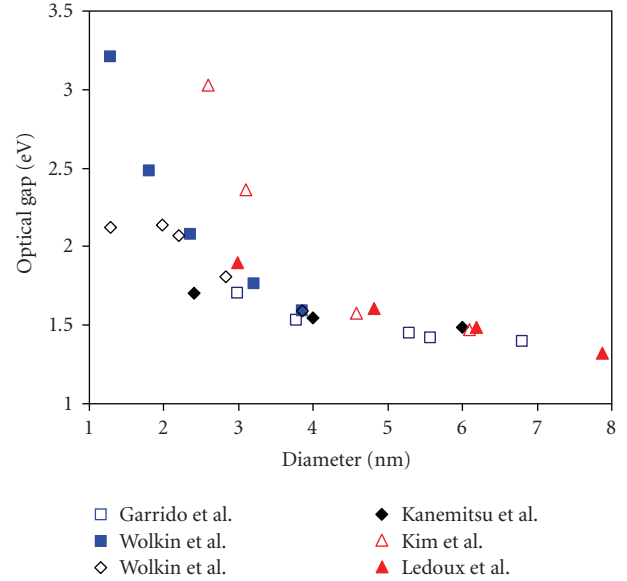


FIGURE 2: Experimental data on the size dependence of the optical gap of silicon crystallites. Hydrogen-passivated surface—Wolkin et al. [8] and Garrido et al. [53] (blue squares); SiO -bonds at the surface—Wolkin et al. [8], Kanemitsu et al. [51] (diamonds); deposition on quartz substrate—Ledoux et al. [48] (filled triangles); nanocrystals embedded in Si_3N_4 matrix—Kim et al. [49] (empty triangles).

one due to the additional positive term A/R^2 , and (ii) the photon energy, equal to the energy of the lowest electron-hole transition, increases as the dot size decreases.

In experimental work carried out over the past fifteen years with silicon nanocrystals, the optical-gap dependence on the dot size was measured and discussed extensively. Although it is impractical to cite all the papers dealing with this topic, a sampling is given in [8, 23, 48–56]. The data in these papers is summarized in Figure 2. There is a fairly large spread in the calculated values of the optical gaps as a function of NC diameter. Presumably, several factors influencing the accuracy of the optical-gap measurements are as follows. First, it is difficult to determine exactly the dot sizes and the size distribution in a luminescent ensemble of NCs. Second, using the mean size in an ensemble of NCs in a diagram like Figure 2 can be misleading, since it is possible that the observed PL peak does not correspond exactly to the mean size but instead to the largest PL rate. Third and more practically, the nanocrystals studied by different research groups have been prepared by different methods. As a result, the NCs have different surroundings, surface bonds, and shapes, all of which could lead to scatter in the experimental data. Finally, as shown in later sections, NC-NC interactions can play a dominant role in the emission spectrum.

Furthermore, the blue-shift energy $\Delta\varepsilon_g(R)$, determined from the experiments, does not obey the law A/R^2 following from the simplest quantum-mechanical model. This dependence is rather $\Delta\varepsilon_g(R) \sim R^{-b}$ with $1 < b < 1.5$ or an even weaker dependence on R in some cases. Such behavior has been a reason for supposing a key role for interface states in

the radiative recombination process [51]. The question about the origin of the radiative electron-hole transitions in the nanocrystals is remains under extensive debate even today.

Nevertheless, employing the principle of Occam's razor, the deviations from the simplest model predictions for high-energy luminescence (when the peak-position energy exceeds the bulk gap ε_g) may be explained within the quantum confinement framework without necessarily the need to invoke sub-gap radiative centers. Let us, first, take into account the finiteness of the potential barriers, leading to some weakening of the quantum confinement and, as a consequence, to a more complicated and less steep size-dependence of $\Delta\varepsilon_g(R)$ other than R^{-2} . In addition, electron-hole Coulomb interaction contributes a further $-R^{-1}$ dependence in the blue-shift energy. Both these mechanisms result in a more gradual dependence of the optical gap on the dot radius, which is in fact observed in experiments.

At the same time, low-energy PL with photon energies less than the gap of bulk silicon are also observed in experiments, see, for example, [57]. In this work an extra luminescence peak arose at about 0.9 eV at low temperatures, and its position remained almost unchanged for nanocrystals of various sizes. This may be indeed treated as an attribute of the surface states which can appear inside the band gap of bulk silicon. This possibility and the associated pair-wise trapping rates have been discussed and derived theoretically by Lannoo et al. [58].

2.2. Decay rate

Time-resolved studies of the PL of silicon NCs demonstrate near-exponential decays of the photoluminescence intensity. Typical decay times τ_{PL} vary within a wide range of about 1 to 1000 μ s depending on the particle size, temperature, detected wavelength, method of preparation, and so forth [31, 32, 51, 59–62]. Such lifetimes are indeed large, and this is an explicit indication of an indirect-band-gap material. Contrary to direct-gap III-V or II-VI compounds, the drop of luminescence intensity for silicon crystallites is sufficiently slow to result in a low PL irradiance compared to direct-gap NCs, even for comparable quantum efficiencies.

The characteristic time of the PL decay is determined by two different recombination mechanisms: radiative, with typical time τ_R ; and nonradiative, with typical time τ_{NR} . The rate of the photoluminescence decay is the sum of the radiative and nonradiative recombination rates: $1/\tau_{PL} = 1/\tau_R + 1/\tau_{NR}$. In the case where one of the two times is much less than the other, the photoluminescence lifetime coincides with the smallest time. Usually in silicon, the nonradiative channel turns out to be faster compared to the radiative one (see, e.g., [31]), so that the PL lifetime equals τ_{NR} . The quantum yield η , which is proportional to the PL intensity, may be defined as the “weight” of the radiative channel in the recombination process: $\eta = \tau_{NR}^{-1}/\tau_{PL}^{-1}$. If $\tau_R \gg \tau_{NR}$, then $\eta = \tau_{NR}/\tau_R \ll 1$. Obviously, one can use two physically different ways to increase η . The first one is an increase of the radiative transitions, while the second is a decrease of the nonradiative processes. The second

way appears easier in practice because the nonradiative processes can be influenced by preparation conditions, as has been recently demonstrated by Miura et al. [62]. On the contrary, according to [62], radiative recombination cannot be controlled by the preparation conditions. Therefore, control of the radiative channel efficiency seems to be fairly difficult to achieve in practice.

Sometimes, both radiative and nonradiative channels contribute comparably in the interband recombination in silicon nanocrystals. In these cases the quantum efficiency becomes very high—possibly on the order of tens of percent [62]. It should be noted, however, that these situations are possible, presumably, at pumping levels corresponding to no more than one excited carrier in every quantum dot. Then, traps such as surface defects may be the main sources of nonradiative recombination. Alternatively, when the excitation power is very high and several electrons are excited in the dots, the Auger process becomes possible. Since Auger interactions are fast, the radiative channel will be “shunted” in this case. Accordingly, η tends to some small value, on the order of a fraction of a percent.

In cases when the nonradiative channel is mostly “closed,” that is, $\tau_R \ll \tau_{NR}$, silicon nanocrystals demonstrate strong temperature dependence of the PL lifetime [23, 33, 57, 63, 64]. In particular, the lifetime becomes smaller as the temperature decreases from ~ 300 to 4 K. This behavior is explained within the framework of the singlet-triplet two-level model suggested by Calcott et al. [3, 4] for porous silicon. According to this model the exciton state splits due to the electron-hole exchange interaction into the upper singlet with relatively short lifetime τ_1 , and lower triplet with about 2–3 orders-of-magnitude longer lifetime τ_1 . The decay rate is then defined by

$$\frac{1}{\tau_{PL}} \approx \frac{1}{\tau_R} = \frac{(3/\tau_1) + (1/\tau_1) \exp[-(\Delta_{S-T}/kT)]}{3 + \exp[-(\Delta_{S-T}/kT)]}, \quad (1)$$

where Δ_{S-T} is the energy of the singlet-triplet splitting, k is the Boltzmann constant, and T is the temperature. The energy of the singlet-triplet splitting depends on the nanocrystal size and increases from a few meV to 10–20 meV for photon energies increasing from 1.4 eV to 2.2 eV [57, 64]. At low temperature, when $\Delta_{S-T} \gg kT$ the decay of the singlet state is strongly suppressed, and the total lifetime τ_{PL} coincides with the longer time τ_1 . In the opposite case (when $\Delta_{S-T} \ll kT$), τ_{PL} is close to $4\tau_1$. As a result, the PL decay occurs substantially faster at low temperature. More rigorous theoretical analysis [65–68] reveals a rich fine structure in the excitonic spectrum of silicon NCs. Exciton states with different symmetry may be ascribed to so-called bright and dark excitons which have essentially different recombination lifetimes.

2.3. Enhancement and quenching of photoluminescence due to impurities

During the past decade, doping Si NCs with shallow impurities has been explored as a potential route for modifying the luminescent properties of silicon nanocrystals. The main

questions are the following: are we able to improve the emission of silicon quantum dots by incorporating donors or acceptors (or both)? If so, then the next question is what is the mechanism for the improvement? The results obtained by different research groups indicate that the PL spectra of silicon nanocrystals are, indeed, sensitive to doping. However, both an increase [10–13] and a decrease [18] of the PL intensity have been observed. This, again, depends on the sample fabrication method and the type of doping.

Silicon NCs doped with phosphorus [10–13, 16, 69], boron [18], or co-doped with P and B [14, 15, 17] have recently been investigated. At the same time, the authors of [70–72] reported on experiments with silicon NCs doped not only with phosphorus or boron but also with hydrogen and nitrogen. Summarizing the results, one can conclude that doping with phosphorus or codoping with phosphorus and boron can enhance the PL intensity of the nanocrystals by several times, as initially reported in [10]. Meanwhile, no enhancement is observed for NCs doped with boron, hydrogen, or nitrogen. Moreover, the degree of quenching of the luminescence depends on the annealing procedure [18, 70–72].

In accordance with the results of Miura et al. [12], Fujii et al. [13], and Mikhaylov et al. [72] reported that an increase of the phosphorus concentration leads to an initial rise of the photoluminescence peak, whereupon the PL intensity subsequently decreases with a further increase in doping. Moreover, the P concentration corresponding to the maximum intensity becomes greater with decreasing NC size [11–13]. Therefore, in some cases, where the NCs had small sizes of about 3–4 nm [11, 70], only a monotonic rise of the PL peak was observed as P concentration increased. One possible reason for this phenomenon lies in the passivation of dangling bonds (i.e., neutral or charged P_b centers) at the NC surfaces. The absence of the enhancement effect for heavily P-doped crystallites at a given size has been explained by more extensive Auger recombination [14, 15, 17] or a coalescence mechanism [72]. The authors of [72] also pointed out the essential distinction in the photoluminescence of the P-doped nanocrystals formed by ion implantation at 1000°C and 1100°C. The former demonstrate up to 5 to 6 times intensity enhancement, while for the latter only PL quenching was found (Figure 3).

As a method to reduce the Auger recombination, simultaneous codoping with phosphorus and boron, thereby compensating the numbers of donors and acceptors inside the crystallite, has been proposed [14, 15, 17]. PL enhancement was successfully obtained for larger nanocrystals of ~6–8 nm in diameter. In this case, a large shift of the PL peak, even below the optical gap of bulk silicon, takes place when increasing P concentration with fixed concentration of boron [14]. This may be evidence of the formation of bulk-like impurity states. At the same time, codoping with high concentration of both donor- and acceptor-type impurities result in a strong chemical shift of the ground-state energy levels in the conduction and valence bands [73], which may substantially reduce the NC optical gap. In the latter case no assumptions on the bulk-like form of electron states

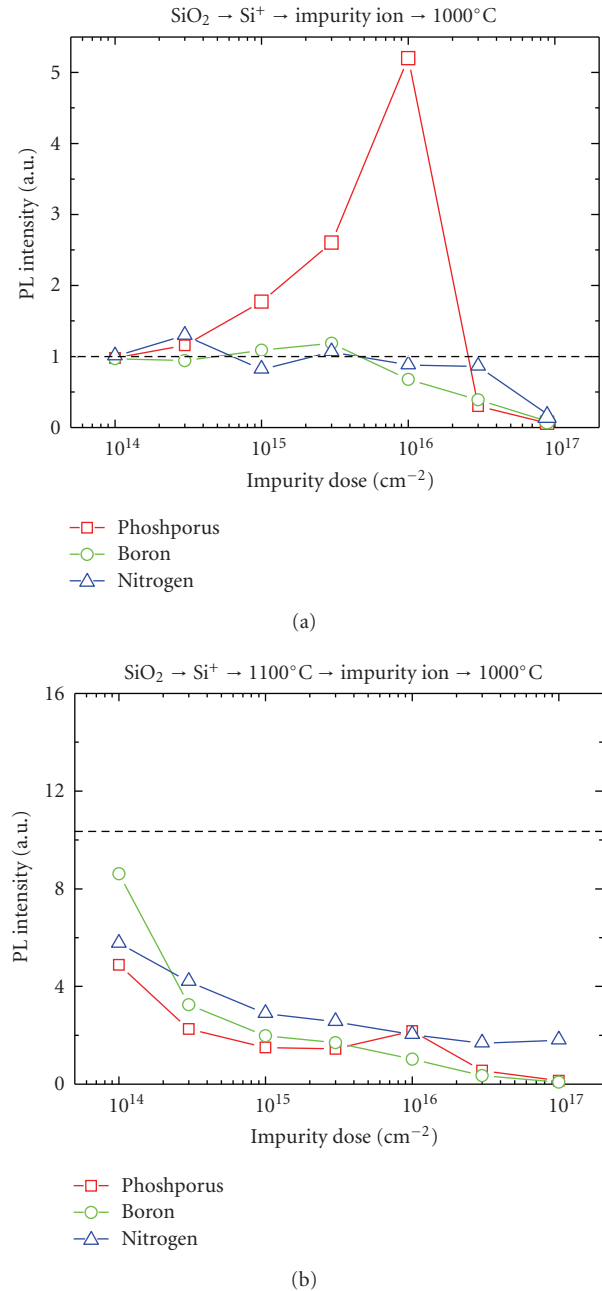


FIGURE 3: Influence of doping with P, B, N on the PL intensity at 750 nm in Si NC layers synthesized by ion implantation and annealed at either 1000 or 1100°C. Samples were subsequently implanted with impurity ions and then re-annealed. The dashed line represents the intensity of the undoped reference sample. (The figures have been kindly provided by D. I. Tetelbaum, A. N. Mikhaylov, O. N. Gorshkov, D. I. Kambarov, V. K. Vasiliev, and A. I. Belov, who did the experiments).

in silicon quantum dots are required, because the effect of the strong chemical shift is exclusively due to the confining potential of the dot.

3. SINGLE-DOT PROBLEM

We next turn to the quantum-mechanical analysis of various aspects of light emission in silicon nanocrystals. It is quite clear, of course, that a consideration of electronic structure, electron-hole recombination, and the role of impurities in a single quantum dot provides a basis for understanding optical properties of the quantum-dot ensembles. Therefore the present chapter first discusses some theoretical models concerning the interband transitions in an individual quantum dot. First, we will discuss the optical gap and energy spectra of undoped nanocrystals. Then the “band” structure and charge distribution in doped dots will be analyzed. Finally, the recombination lifetimes will be calculated for undoped and doped crystallites.

3.1. Electronic structure of perfect silicon nanocrystals

The first step is a calculation of the ground-state energies both for the conduction and valence bands of a nanocrystal. Note that here and throughout the paper we will use terminology that is typical for the bulk material. Of course, no genuine energy bands exist in the nanocrystal because of its finite size. Nevertheless, the states above and below the NC optical gap originate from the size-quantized states of conduction and valence bands of the bulk crystal, respectively. Moreover, in the following we mainly intend to employ the envelope-function approximation ($\mathbf{k}\cdot\mathbf{p}$ method) to describe electronic states of the nanocrystals. Consequently, such the terminology is convenient and should not lead to any misunderstandings. The states above and below the optical gap will be further referred to as conduction and valence bands, as in the bulk. Different approaches are used when calculating the gap of silicon nanocrystals. Among them, the simplest is the single-particle approximation. Usually, the single-particle gap exceeds real optical gap because the electron-hole Coulomb interaction reduces the total energy of the system. For this reason, the values of the single-particle gap may be treated as an upper bound for the optical gap. In this section we discuss electron and hole states of a “pure” crystallite, which has no defects and a perfect diamond lattice all over its whole volume. The results are compared with the simpler approximations discussed in the introduction.

3.1.1. Optical gap. Numerical results

It is possible to separate all calculation methods applied for computation of the electronic spectra in pure NCs into two groups. In the first group we have the numerical first-principles, empirical, and semi-empirical methods, such as density functional theory (DFT) [68, 74–78], pseudopotential (PP) method (or various combinations of PP and DFT) [79–82], tight-binding (TB) models [83–86], combined Green’s function (GW-approximation), and the Bethe-Salpeter equation (BSE) technique [87–89]. All these methods require considerable computational time, a problem that worsens as the nanocrystal size is increased. Analytical methods such as the effective mass approximation or $\mathbf{k}\cdot\mathbf{p}$ method [67, 90–95] may be ascribed to the second

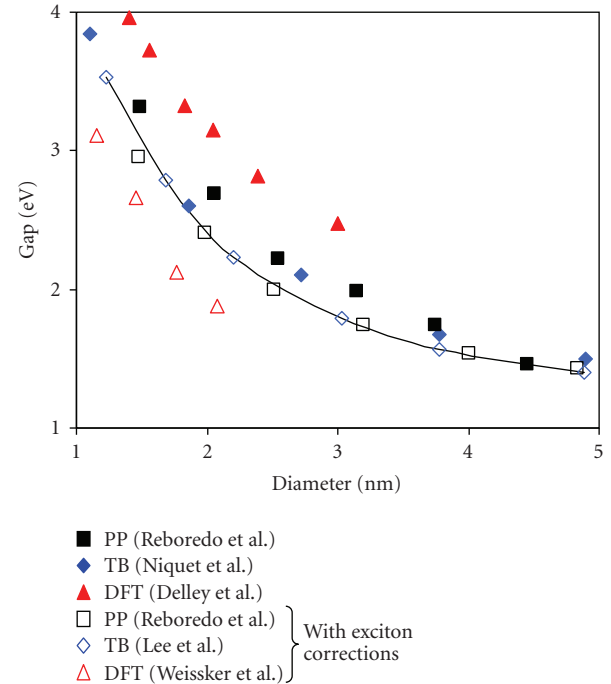


FIGURE 4: Optical gap calculated by PP [65], TB [85, 86], and DFT [68, 74] methods. Solid line: EFA calculations, see (22) below [93].

group. In following we combine these two methods into a single envelope function approximation (EFA). The latter allows one to perform calculations without any restrictions on cluster sizes. Additionally, this approach can be used to find the higher excited states of the nanocrystal.

In the present subsection, we summarize the results of some of the methods discussed above, which illustrate dependence of the optical gap on the nanocrystal size (Figure 4). In all calculations, any dangling bonds at the nanocrystal surface were considered to be H-passivated. As is seen in the figure, there is some scatter of data due to the different computational methods and different approximations utilized in the computational procedure.

In particular, taking into account the self-energy correction or electron-hole interaction can considerably change the magnitude of the nanocrystal optical gap, in opposite directions, as has been pointed out by many authors (see, e.g., [81, 88, 89]). In particular, it is known that the local density approximation of the DFT tends to underestimate the optical-gap (similar results happen for silicon nanowires) [96, 97] compared to those obtained in experiments. For a more accurate account of the self-energy corrections and excitonic effects, the GW+BSE approach is often applied. The combination of the GW and BSE methods yields almost complete compensation of the exciton and the self-energy corrections to the single-particle optical gap [88]. The same effect was also found by Franceschetti and Zunger [81] within the framework of the PP method. Unfortunately, the GW+BSE approach is employed for nanocrystals whose diameters do not exceed 1 nm [87–89]. Therefore, we did not depict the results of this approach in Figure 4.

3.1.2. Electron and hole spectra in a dot

Let us now discuss electronic spectra in both the valence and conduction bands of the quantum dot. As has been pointed out, for this purpose it is convenient to use the EFA. Here we describe in more detail not only the lowest but also the higher excited electronic states as a function of size.

We assume the total potential energy of the electron inside the quantum dot to be of the following form

$$U(\mathbf{r}) = U_0(r) + V_{\text{sp}}(r). \quad (2)$$

Here $U_0(r)$ is the confining potential equal to zero inside and infinity outside the dot. The second part $V_{\text{sp}}(r)$ describes an interaction between the electron and its image, arising due to the charge polarization on the boundary between the silicon nanocrystal and its dielectric surrounding. $V_{\text{sp}}(r)$ is often referred to as a self-polarization term. It can be represented as

$$V_{\text{sp}}(r) = \frac{e^2(\varepsilon_s - \varepsilon_d)}{2\varepsilon_s R} \sum_{l=0}^{\infty} \frac{l+1}{l\varepsilon_s + (l+1)\varepsilon_d} \frac{r^{2l}}{R^{2l}}, \quad (3)$$

where ε_s and ε_d are the static dielectric constants of silicon and the dielectric matrix, respectively. In order to find the electronic states in the dot, we have to solve the single-particle Schrödinger-like equation for the envelope function vector $|\Phi\rangle$:

$$(H + U(\mathbf{r}))|\Phi\rangle = E|\Phi\rangle. \quad (4)$$

Here, H is the bulk $\mathbf{k}\cdot\mathbf{p}$ Hamiltonian operator acting on the six-dimensional (6D) envelope-function vectors $|\Phi\rangle$, and E is the electron energy. The components of the 6D-vector $|\Phi\rangle$ are slowly varied expansion coefficients $\Phi_j(\mathbf{r})$ of the total wave function in the Bloch-state basis.

The electronic states in the valence and conduction bands can be determined separately. Starting with the valence band, the Bloch-state for the Γ -point is $|YZ\rangle|\uparrow\rangle$, $|XZ\rangle|\uparrow\rangle$, $|XY\rangle|\uparrow\rangle$, $|YZ\rangle|\downarrow\rangle$, $|XZ\rangle|\downarrow\rangle$, $|XY\rangle|\downarrow\rangle$, where $|\uparrow\rangle$ and $|\downarrow\rangle$ are ‘‘up’’ and ‘‘down’’ spinors, respectively, and the Bloch functions $|YZ\rangle$, $|XZ\rangle$, $|XY\rangle$ belong to the irreducible representation $\Gamma_{25'}$. The $\mathbf{k}\cdot\mathbf{p}$ Hamiltonian matrix H in 4 is the sum of three parts: $H = H^{(0)} + H^{(1)} + H^{(\text{so})}$. Here $H^{(0)} = (\mathbf{p}^2/2m_h) \times \mathbf{I}$ is the isotropic part obtained as the average of the total $\mathbf{k}\cdot\mathbf{p}$ matrix over all angles in \mathbf{p} -space. $H^{(1)}$ is the anisotropic part that can be represented by two equivalent 3×3 blocks situated on the main diagonal of the total 6×6 $\mathbf{k}\cdot\mathbf{p}$ matrix:

$$H^{(1)} = \begin{pmatrix} H_3 & 0 \\ 0 & H_3 \end{pmatrix}, \quad (5)$$

$$H_3 = -\frac{1}{2m_0} \begin{pmatrix} Q_1 & Np_x p_y & Np_x p_z \\ Np_x p_y & Q_2 & Np_y p_z \\ Np_x p_z & Np_y p_z & Q_3 \end{pmatrix},$$

where Q_1 denotes $((L - M)/3)(3p_x^2 - \mathbf{p}^2)$, Q_2 denotes $((L - M)/3)(3p_y^2 - \mathbf{p}^2)$, and Q_3 denotes $((L - M)/3)(3p_z^2 - \mathbf{p}^2)$.

Finally, the term

$$H^{(\text{so})} = \frac{1}{3} \begin{pmatrix} 0 & -i\Delta & 0 & 0 & 0 & \Delta \\ i\Delta & 0 & 0 & 0 & 0 & -i\Delta \\ 0 & 0 & 0 & -\Delta & i\Delta & 0 \\ 0 & 0 & -\Delta & 0 & i\Delta & 0 \\ 0 & 0 & -i\Delta & -i\Delta & 0 & 0 \\ \Delta & i\Delta & 0 & 0 & 0 & 0 \end{pmatrix} \quad (6)$$

describes the spin-orbit interaction. We have introduced above the spin-orbit energy Δ equal to 44 meV for silicon, the 6×6 identity matrix \mathbf{I} , and the hole effective mass $m_h = 3m_0/(L+2M)$, where the numbers L, M, N are dimensionless empirical parameters in the $\mathbf{k}\cdot\mathbf{p}$ Hamiltonian operator in the valence band. For silicon they equal 5.8, 3.43, and 8.61, respectively [98].

Because of the isotropic and diagonal form of the operator $H^{(0)} + U_0(r)$, it is possible to classify its eigenstates similarly to atomic systems using common terminology such as s -, p -, and d -type states, and so forth [92]. Accordingly, one may expand the components of the envelope-function vectors over these eigenstates as

$$\Phi_j(\mathbf{r}) = \sum_{\alpha} C_{j\alpha} |\alpha\rangle, \quad (7)$$

where $|\alpha\rangle$ stands for the s -, p -, d -, ... states and $C_{j\alpha}$ are the expansion coefficients. For instance, the $1s$ -, $1p$ -, $1d$ -, (in the following simply s -, p -, and d -) and $2s$ -type states are described by the following functions:

$$|s\rangle = \sqrt{\frac{\pi}{2R^3}} j_0(\pi r/R),$$

$$|p_a\rangle = \sqrt{\frac{3}{2\pi R^3}} \frac{j_1(\mu_1 r/R)}{j_0(\mu_1)} \frac{x_a}{r},$$

$$|d_{ab}\rangle = \sqrt{\frac{15}{2\pi R^3}} \frac{j_2(\mu_2 r/R)}{j_1(\mu_2)} \frac{x_a x_b}{r^2}, \quad a \neq b, \quad (8)$$

$$|d_{x^2-y^2}\rangle = \sqrt{\frac{15}{8\pi R^3}} \frac{j_2(\mu_2 r/R)}{j_1(\mu_2)} \frac{x^2 - y^2}{r^2},$$

$$|d_{3z^2-r^2}\rangle = \sqrt{\frac{15}{8\pi R^3}} \frac{j_2(\mu_2 r/R)}{j_1(\mu_2)} \frac{3z^2 - r^2}{r^2},$$

$$|2s\rangle = \sqrt{\frac{\pi}{2R^3}} j_0(2\pi r/R),$$

where $j_n(x)$ are the spherical Bessel functions of argument x , and μ_n are the first roots of $j_n(x)$. Below, we restrict the basis of envelope functions $|\alpha\rangle$ with these states only, and determine the electron and hole spectra. Substitution of $\Phi_j(\mathbf{r})$ into (4) yields algebraic equations for $C_{j\alpha}$:

$$(E - E_{\alpha})C_{i\alpha} = \sum_{\beta} \langle \alpha | H_{ij}^{(1)} + H_{ij}^{(\text{so})} + V_{\text{sp}}(\mathbf{r}) \delta_{ij} | \beta \rangle C_{j\beta}, \quad (9)$$

where E_{α} denotes the energy of the state $|\alpha\rangle$, δ_{ij} stands for the Kronecker delta, and the Einstein convention has been used

when summing over j . Considering all operators in the right side of (9) as perturbations [92], one can solve the equation and find the energies in the valence band.

Restricting the basis of the envelope states $|\alpha\rangle$ by $1s$, $2s$, $1p$, and $1d$ functions, and neglecting the spin-orbit interaction, we obtain the following ‘‘hierarchy’’ of energies (for convenience, we write down the hole energies differing in the sign from the electron energies, which are determined with (9)). The ground-state energy

$$E_h^{(s)} = \frac{\hbar^2 \pi^2}{2m_h R^2} \quad (10)$$

is triply degenerate (or sixfold, if spin is taken into account). It is the energy of the $1s$ state. Hybridization of the p -type states yields four different levels with the energies

$$\begin{aligned} E_{h1}^{(p)} &= \frac{\hbar^2 \mu_1^2}{2m_h R^2} \left[1 - \frac{3N + 2L - 2M}{5L + 10M} \right], \\ E_{h2}^{(p)} &= \frac{\hbar^2 \mu_1^2}{2m_h R^2} \left[1 - \frac{3N - 4L + 4M}{5L + 10M} \right], \\ E_{h3}^{(p)} &= \frac{\hbar^2 \mu_1^2}{2m_h R^2} \left[1 + \frac{3N - 2L + 2M}{5L + 10M} \right], \\ E_{h4}^{(p)} &= \frac{\hbar^2 \mu_1^2}{2m_h R^2} \left[1 + \frac{6N + 4L - 4M}{5L + 10M} \right], \end{aligned} \quad (11)$$

where $\mu_1 = 4.4934$. The energies of the d - d hybridized states are as follows:

$$\begin{aligned} E_{h1}^{(d)} &= \frac{\hbar^2 \mu_2^2}{2m_h R^2} \left[1 - \frac{6N}{7L + 14M} \right], \\ E_{h2}^{(d)} &= \frac{\hbar^2 \mu_2^2}{2m_h R^2} \left[1 - \frac{3N + 4L - 4M}{7L + 14M} \right], \\ E_{h3}^{(d)} &= \frac{\hbar^2 \mu_2^2}{2m_h R^2} \left[1 + \frac{3N - 2L + 2M}{7L + 14M} \right], \\ E_{h4}^{(d)} &= \frac{\hbar^2 \mu_2^2}{2m_h R^2} \left[1 + \frac{6N - 4L + 4M}{7L + 14M} \right], \end{aligned} \quad (12)$$

where $\mu_2 = 5.7634$. Finally, the energies of the $1d$ - $2s$ hybrids are written as

$$\begin{aligned} E_{h1}^{(2sd)} &= \frac{\hbar^2}{2m_h R^2} \left[\frac{4\pi^2 + \mu_2^2}{2} + \frac{3\mu_2^2}{14} \frac{N + 2L - 2M}{L + 2M} \right. \\ &\quad \left. - \frac{12\sqrt{6}}{\sqrt{5}} \frac{\pi\mu_2}{4\pi^2 - \mu_2^2} \frac{N}{L + 2M} \right], \\ E_{h2}^{(2sd)} &= \frac{\hbar^2 \mu_2^2}{2m_h R^2}, \\ E_{h3}^{(2sd)} &= \frac{\hbar^2}{2m_h R^2} \left[\frac{4\pi^2 + \mu_2^2}{2} + \frac{3\mu_2^2}{14} \frac{N + 2L - 2M}{L + 2M} \right. \\ &\quad \left. + \frac{12\sqrt{6}}{\sqrt{5}} \frac{\pi\mu_2}{4\pi^2 - \mu_2^2} \frac{N}{L + 2M} \right]. \end{aligned} \quad (13)$$

The contribution of the self-polarization term from (10)–(13) has been omitted since it represents, in fact, a common shift of all the levels by $e^2(1/\epsilon_d - 1/\epsilon_s)/2R$.

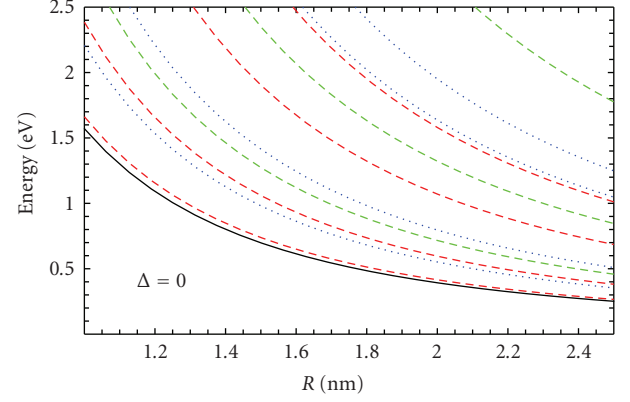


FIGURE 5: Hole energy spectrum according to (10)–(13) in case of no spin-orbit interaction. Solid line: s -type level. Short dashed lines: p - p hybridized levels. Dots: d - d hybridized levels. Long dashed lines: $2s$ - d hybridized levels. All energies are counted deep into the valence band with respect to the valence band maximum. The degeneracy degree including spin (from bottom to top) is 6; 6; 6; 4; 6; 4; 6; 6; 2; 6; 2; 6.

In Figure 5 the energy levels from (10)–(13) have been plotted as functions of the NC radius. The two lowest hole levels have very similar energies. The lowest level, being sixfold degenerate, corresponds to six electron states with an s -type envelope function. These states have an isotropic macroscopic (averaged over the unit-cell volume) charge distribution inside the dot. The second level corresponds to six electron states with p -type envelope functions. Correspondingly, the macroscopic charge has an anisotropic distribution for these states (see [92] for details).

In the conduction band the Bloch-state basis consists of six Bloch functions of three different X -points in the Brillouin zone [99]. We denote three pairs of these functions as $|X\rangle$, $|X'\rangle$; $|Y\rangle$, $|Y'\rangle$; $|Z\rangle$, $|Z'\rangle$. Each pair belongs to the twofold degenerate irreducible representation X_1 of the corresponding X -point. The unprimed Bloch functions have a nonzero value at the lattice site, while the primed functions are zero at those points. The choice of the X_1 -functions as the Bloch basis allows us to describe correctly a dispersion-law nonparabolicity that originates mainly from the energy-branch crossing in the X -points.

The $\mathbf{k} \cdot \mathbf{p}$ Hamiltonian operator in the conduction band represents a 6×6 matrix having the form

$$H = \begin{pmatrix} H_x & 0 & 0 \\ 0 & H_y & 0 \\ 0 & 0 & H_z \end{pmatrix}. \quad (14)$$

Each element of the matrix H is a block 2×2 matrix defined by the following expressions [99]:

$$H_a = \begin{pmatrix} \frac{p_a^2}{2m_l} + \frac{\mathbf{p}^2 - p_a^2}{2m_t} & \left(\frac{1}{m_t} - \frac{1}{m_0} \right) p_b p_c + i \frac{p_0}{m_l} p_a \\ \left(\frac{1}{m_t} - \frac{1}{m_0} \right) p_b p_c - i \frac{p_0}{m_l} p_a & \frac{p_a^2}{2m_l} + \frac{\mathbf{p}^2 - p_a^2}{2m_t} \end{pmatrix}. \quad (15)$$

Here $p_0 \approx 0.14(2\pi\hbar/a_0)$ is the distance in \mathbf{p} -space from any of the energy minima to the nearest X -point, a_0 is the lattice constant of silicon. $m_l = 0.92m_0$ and $m_t = 0.19m_0$ are the “longitudinal” and “transverse” effective masses. The origin of the E -axis coincides with the X -point energy. Each of the small indices (a, b, c) runs over the values x, y , or z and always differs from the others.

Solving (4) for the conduction band is done in the same way as for the valence band, as in (9)–(13) above. One can then obtain the following groups of energies. The ground states, as well as the second excited ones, are the $1s$ - $1p$ hybrids. Their energy levels are given by

$$\begin{aligned} E_{e1}^{(sp)} &= \frac{E_s + E_p - 2H_{pp}}{2} - \sqrt{\left(\frac{E_p - E_s - 2H_{pp}}{2}\right)^2 + H_{sp}^2}, \\ E_{e2}^{(sp)} &= \frac{E_s + E_p - 2H_{pp}}{2} + \sqrt{\left(\frac{E_p - E_s - 2H_{pp}}{2}\right)^2 + H_{sp}^2}, \end{aligned} \quad (16)$$

where

$$\begin{aligned} H_{sp} &= \frac{ip_0}{m_l} \langle s | p_z | p_z \rangle \\ &= \frac{2\pi\hbar\mu_1 p_0}{[\sqrt{3}m_l R(\mu_1^2 - \pi^2)]}, \\ H_{pp} &= \frac{1}{12} \left(\frac{1}{m_t} - \frac{1}{m_l} \right) \langle p_z | \mathbf{p}^2 - 3p_z^2 | p_z \rangle \\ &= \frac{\hbar^2 \mu_1^2 (m_l - m_t)}{15m_t m_l R^2} \end{aligned} \quad (17)$$

are s - p and p - p type matrix elements of anisotropic part H_a , $E_s = \hbar^2 \pi^2 / 2m_e R^2$, and $E_p = \hbar^2 \mu_1^2 / 2m_e R^2$ are the energies of the s - and p -type states of the isotropic unperturbed Hamiltonian operator. The isotropic average electron effective mass is defined by $m_e^{-1} = (2m_t^{-1} + m_l^{-1})/3 \approx (0.26m_0)^{-1}$. The p - p hybridization forms states with energies:

$$E_{e1,2}^{(p)} = E_p + H_{pp} \mp H_{xy}. \quad (18)$$

Here $H_{xy} = \hbar^2 \mu_2^2 (m_0 - m_t) / 5m_t m_0 R^2$. The next three levels are the result of the d - d hybridization:

$$\begin{aligned} E_{e1}^{(d)} &= \frac{\hbar^2 \mu_2^2}{2m_e R^2} \left(1 - \frac{2}{7} \frac{m_l - m_t}{2m_l + m_t} - \frac{6}{7} \frac{m_l}{m_0} \frac{m_0 - m_t}{2m_l + m_t} \right), \\ E_{e2}^{(d)} &= \frac{\hbar^2 \mu_2^2}{2m_e R^2} \left(1 + \frac{4}{7} \frac{m_l - m_t}{2m_l + m_t} \right), \\ E_{e3}^{(d)} &= \frac{\hbar^2 \mu_2^2}{2m_e R^2} \left(1 - \frac{2}{7} \frac{m_l - m_t}{2m_l + m_t} + \frac{6}{7} \frac{m_l}{m_0} \frac{m_0 - m_t}{2m_l + m_t} \right). \end{aligned} \quad (19)$$

Finally, the $2s$ - d hybridized energies are obtained numerically:

$$\begin{aligned} E_{e1}^{(2sd)} &= \frac{\hbar^2}{2m_e R^2} \left(\frac{4\pi^2 + 2\mu_2^2}{3} - 0.477\mu_2^2 \right), \\ E_{e2}^{(2sd)} &= \frac{\hbar^2}{2m_e R^2} \left(\frac{4\pi^2 + 2\mu_2^2}{3} - 0.455\mu_2^2 \right), \\ E_{e3}^{(2sd)} &= \frac{\hbar^2}{2m_e R^2} \left(\frac{4\pi^2 + 2\mu_2^2}{3} + 0.932\mu_2^2 \right). \end{aligned} \quad (20)$$

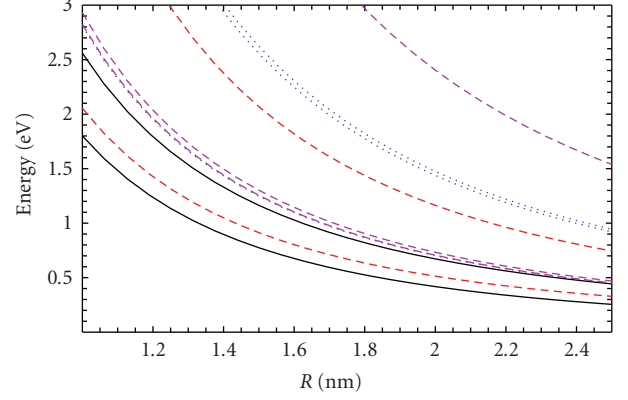


FIGURE 6: The lowest energy levels in the conduction band as functions of the NC radius, from (16)–(20). The energies are counted from the X -point energy. Solid line: s - p type levels. Short dashed lines: p - p hybridized levels. Dots: d - d hybridized levels. Long dashed lines: $2s$ - d hybridized levels. All the levels are 12-fold degenerate including spin degeneracy.

The results for the single-particle electron spectrum in the conduction band are shown in Figure 6.

The wave function of the ground state turns out to be a superposition of the terms with s - and p -type envelope functions (see [92] for details). The “weight” of the s -type envelope function is greater than that of the p -type function. Therefore the macroscopic charge for the ground state has a distribution close to isotropic.

From the above calculations, the optical gap of the NC can be obtained as the sum of the lowest energies in both bands and the energy difference between X - and Γ -points in bulk $\Delta_{X\Gamma} = 1.24$ eV:

$$\varepsilon_g(R) = \Delta_{X\Gamma} + E_{el}^{(sp)} + E_h^{(s)}. \quad (21)$$

This energy somewhat overestimates value compared to that obtained with the numerical methods, as indicated by the solid line in Figure 7. This is a consequence of two main factors.

The first factor is that we have assumed infinitely high potential barriers at the interface. The authors of [91, 93, 95] calculated the carrier energies supposing the potential barriers to be finite and equal to approximately 3 eV (or a little more) for electrons and 4-5 eV for holes. Moreover, the discontinuity of the effective mass has been taken into account. In Figure 7 we have plotted the optical gap of silicon nanocrystal versus the confining parameter $1/R$ for three models differing according to the nanocrystal’s surroundings. The solid line corresponds to infinitely high potential barriers. Circles represent the finite barriers and constant effective mass throughout the sample. Finally, in case of the mass discontinuity with effective mass outside the dot coinciding with free electron mass, the optical gap has been represented by disks. For the last two cases, the dependence $\Delta\varepsilon_g(R)$ becomes weaker than R^{-2} , especially for the case of the discontinuous effective mass where the dependence is

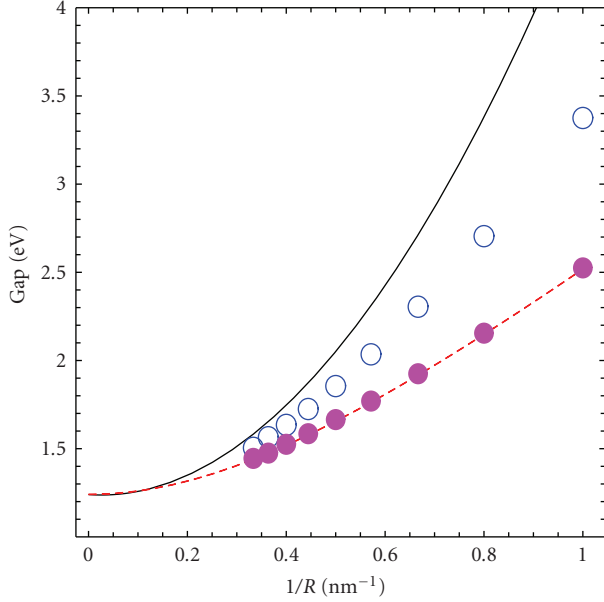


FIGURE 7: NC gap versus reciprocal dot radius. Solid line: infinite barriers (21). Circles: finite barriers (3.2 eV for electrons and 4.3 eV for holes, which corresponds to Si/SiO₂ interface) and constant effective mass. Disks—finite barriers and free electron mass outside the dot. Both of the latter are numerical results by EFA [92]. The dashed line is a guide to the eye.

closer to $1/R$. In the last case the gap dependence is well fitted by the function:

$$\varepsilon_g^{(1)}(R) = \sqrt{\varepsilon_g^2 + \frac{D_1}{R^2}} \quad (22)$$

with $D_1 = 4.8 \text{ eV}^2 \cdot \text{nm}^2$. In general, one may conclude that the calculated values of the optical gap are reduced due to the barrier finiteness and mass discontinuity, and agree better with those shown in Figure 4.

The second factor, strongly influencing the dot gap, is electron-hole Coulomb interaction. Its contribution to the optical gap will be discussed in the next subsection.

3.1.3. EFA calculations: exciton corrections

The electron-hole interaction reduces the energy of the electron-hole pair. As a result, the exciton optical gap is also reduced. In order to estimate the exciton correction to the total electron-hole single-particle energy one must solve the two-particle problem. This has been done for silicon NCs embedded in an infinitely wide-band-gap material [67, 90, 94]. The exciton corrections were found to be about 0.4 eV [67], 0.25 eV [90], and 0.3 eV [94] for 2-nm-diameter NCs, with the correction decreasing approximately as R^{-1} with increasing size.

Meanwhile, as has been pointed out in the preceding section, the finiteness of the potential barriers and effective mass discontinuity can appreciably influence the electron and hole energies. Therefore, it is possible to expect the same for the excitonic energies. Ferreyra and Proetto [91]

have studied excitonic states for a quantum dot in vacuum. Accordingly, they accepted the barrier heights equal to the electron affinity of the corresponding bulk material for electrons and infinity for holes, and the effective mass being m_0 . They found an exciton correction of the order of 0.2 eV for a 2-nm-diameter dot. As the nanocrystal size increases, the magnitude of this correction decreased as $R^{-0.7}$.

The authors of some of the previous work (e.g., [67, 90, 91]) treated the Coulomb potential energy as $V_C = -e^2/\varepsilon_s r_{eh}$ similar to bulk silicon. However, in a quantum dot the electron and hole interact not only with each other but also with their “images” due to the difference in the permittivity of the materials inside and outside the dot. These are the so-called polarization fields arising because of the charge polarization at the dot boundary. The interaction with the polarization fields has been taken into account in [94]. Nevertheless, the polarization fields did not lead to any significant corrections to the optical gap. As mentioned above, the correction does not exceed 0.3 eV, which is close to the values obtained by other authors.

Evidently, the calculations carried out with the EFA [67, 90, 91, 94] provide sufficiently good coincidence with both experimental and theoretical data. For comparison, we have depicted in Figure 4 with the solid line the EFA single-particle gap according to (22). The gap values $\varepsilon_g^{(1)}(R)$ agree well with those computed by PP, TB, and DFT methods. Obviously, a small exciton correction of about 0.3–0.1 eV for 2 to 5 nm diameter crystallites, respectively, does not significantly change the single-particle gap values.

It should be noted, in conclusion, that all the authors employed the perturbation theory considering the electron-hole interaction to be weak compared to the typical quantum confinement energies in the dot. Such an approach is justified if the exciton Bohr radius is significantly larger than the dot radius. This requirement remains valid for small quantum dots with the sizes of about 5–6 nm or less.

3.1.4. Interface states

We have already emphasized in the introduction that radiative transitions between interface states are also often considered as the origin of NIR, or even visible, emission from silicon nanocrystals. In a certain sense, this point of view is alternative to the idea of quantum confinement. Description of the interface states with EFA is difficult because the real potential existing in the vicinity of the nanocrystal surface has in principle a microscopic nature that manifests itself at a distance on the order of a bond length. Meanwhile, the EFA is, in fact, a “macroscopic” method which is not able to distinguish the spatial structure on scales smaller than the size of the primitive cell. Therefore TB and DFT methods are essentially more suitable for this goal.

As a rule, interface states originate from various-type defects existing at the surface of the crystallite. These include, mainly, dangling bonds (P_b centers) which can be neutral, positively, or negatively charged, and different SiO bonds (backbonded and double bonded oxygen) arising at Si/SiO₂ interface. Charged dangling bonds corresponding to zero or two electrons in the bond level, respectively, produce deep

levels inside the band gap of bulk silicon. Their energies are approximately 0.3 eV below the conduction band minimum for the negatively charged bond, and 0.3 eV above the valence band maximum if the bond is positively charged [100]. Consequently, the effective gap between these levels is about 0.5–0.6 eV [101]. For nanocrystals, the effective gap gradually rises as the nanocrystal size decreases. In particular, for a 5-nm-diameter NC this shift equals approximately 0.6 eV, while for a 2 nm crystallite it is 1.3–1.4 eV [100]. Thus, we see that the dangling bond levels are sensitive to the NC size.

Nanocrystal oxidation has been studied theoretically by TB [8, 102], DFT [103, 104], and GW+BSE [89] methods. The role of the so-called backbonded (Si–O–Si) and double bonded (Si=O) oxygen atoms has been examined for the case where the spherical NC surface is passivated with hydrogen. In the first case (Si–O–Si), oxygen forms two bonds with two different silicon atoms which already have four bonds with other silicon or hydrogen atoms. In the second case (Si=O), oxygen replaces two hydrogen atoms bonded with one silicon atom. It is natural to suppose that the system perturbation in the second case should be more significant because of the stronger distortions of the structure. In fact, it was found that the presence of one Si=O bond at the NC surface provides an optical gap almost independent of the dot size [8]. At the same time, the nanocrystal with a Si–O–Si bond has a gap that gradually decreases with increasing size. Nevertheless, this gap remains smaller, and varies more slowly than the gap of perfect nanocrystal with hydrogen passivated surfaces. The calculations carried out by different methods [89, 102, 103] for oxidized crystallites show an essential difference in the energy of the ground electron-hole transition in crystallites with Si–O–Si and Si=O bonds. All the methods used exhibit the smallest gap for the case of double-bond oxidation, while the crystallites with backbonded oxygen have the greater gap. In turn, the latter is less than the gap of a perfect NC. The authors of [89] have found that only the bridge-type bond (Si–O–Si) can provide a satisfactory agreement with experiments on the photoluminescence in nc-Si/SiO₂ system. This fact may be explained by the considerably different oscillator strengths of the ground transitions for NCs with Si=O and Si–O–Si defects. As has been shown by Nishida [102], the oscillator strength for Si–O–Si case is several orders of magnitude greater than that for Si=O case, especially for NCs smaller than 1 nm in diameter. This is precisely the case studied by Luppi et al. [89], where NCs of 0.5 nm and 0.9 nm in diameter were considered. However, according to [102] the difference between the size-quantized energy levels and those of the Si=O and Si–O–Si defects, as well as the difference in the oscillator strengths of the ground electron-hole transitions, are essential only for NC diameters less than 2 to 2.5 nm [8, 102]. For larger sizes, the energies and the transition intensities for perfect and oxidized crystallites almost coincide.

Finally, nonradiative trapping rates are also critical in the light emission properties of silicon NCs. The group of neutral or charged P_b centers at silicon dangling bonds is the most important nonradiative trap in bulk silicon [105], and acts also in the case of Si NCs [58]. In a detailed theoretical investigation, Lannoo et al. [106] found that the

carrier trapping at neutral P_b centers is nonradiative, whereas capture at charged centers can lead to photon emission at energies smaller than the bandgap of bulk silicon. The rate for carrier trapping at a neutral dangling bond defect at the Si–SiO₂ interface in a NC with a single P_b center was established theoretically as a function of the NC size [106]:

$$w_{nr} = \frac{\sigma_0 v}{V} \frac{1}{\sqrt{2\pi}} \left(\left(\frac{E_0}{\hbar\omega} \right)^2 + z^2 \right)^{-0.25} \times \exp \left[-S \coth \left(\frac{\hbar\omega}{2kT} \right) + \frac{E_0}{2kT} + \left(\left(\frac{E_0}{\hbar\omega} \right)^2 + z^2 \right)^{0.5} - \frac{E_0}{\hbar\omega} a \sinh \left(\frac{E_0}{\hbar\omega z} \right) \right]. \quad (23)$$

In (23), σ_0 is the capture cross section given by c_0/v where c_0 is the capture coefficient and v is the thermal velocity equal to $\sqrt{8kt/\pi m^*}$, E_0 is the ionization energy of the defect (approximately equal to the Franck-Condon energy plus the carrier confinement energy), S is the Huang-Rhys factor ($S \sim 15$) [107], $\hbar\omega$ is the average phonon energy, V is the nanocrystal volume, and $z = S/[\sinh(\hbar\omega/2kT)]$. The capture rate increases strongly as a function of NC size due to the decreasing defect ionization energy, until eventually the volume term begins to dominate the trapping rate, which then begins to decrease again. Since, the calculated rate is for a single isolated defect, in practice the rate should be modified for the likelihood of multiple defects on larger clusters, as discussed in Section 4.

3.2. Shallow impurities in silicon nanocrystals

There is one more type of defect which can play an important role in the optical and transport properties of bulk semiconductors and their low-dimensional counterparts (in particular, silicon). These are impurity centers, of which some experimental results were discussed previously. Let us now consider NCs doped with shallow impurities and discuss impurity states in silicon quantum dots.

Various aspects of the problem have been explored. One of them—the central-cell effect [108–111]—causes splitting of the sixfold degenerate ground energy level in bulk silicon into a singlet, doublet, and triplet with a typical energy splitting of about 10–20 meV for various donors [112]. According to a number of theoretical studies [73, 113–119], in quantum dots doped with donors or acceptors the central-cell potential strengthens the level splitting compared to (i) bulk silicon, and (ii) undoped dots [66, 85, 120, 121]. Investigations of the spatial charge distribution [122, 123], the formation of impurity centers inside silicon nanocrystals from the energy point of view [114–117, 124, 125], intervalley scattering [126], hyperfine splitting and optical gap effects [127], and the screening of the point-charge field [123, 128–136] have been performed. Below, we present EFA calculations of the electronic structure of both donor- and acceptor-doped silicon quantum dots and examine the dependence on the impurity position inside the dot within

the framework of the hydrogenic-impurity model. Also, we discuss the effect of the central-cell potential in screening the point charge in NCs.

3.2.1. Screening in quantum dots

In order to solve accurately the Schrodinger-like equation for the envelope functions in the dot in the presence of an impurity ion, we need the correct expression for the Coulomb potential energy V_C . Its determination in the quantum dot is not a simple task because of the complicated character of screening in NCs. Some authors described the screening properties in an NC with a modified dielectric constant $\epsilon(R)$ that depends on the dot radius [137–139]. Such a simple model, indeed, gives a moderate increase of the dielectric properties due to the finite size of the crystallite but it does not reflect correctly the local structure of the electric field.

The correct description of such a structure requires first-principles calculations [123, 129–136]. Nevertheless, the microscopic picture permits a clear qualitative macroscopic interpretation using the local dielectric function $\epsilon(r)$ depending on electron position vector, r . Taking into account the short-range field and charge polarization at the dot boundary due to different static dielectric constants ϵ_s and ϵ_d of an NC and its surroundings, one can in principle obtain $\epsilon(r)$ (Figure 8) [73].

An overall decrease of $\epsilon(r)$ in a nanocrystal takes place compared to the bulk value of $\epsilon_s = 12$. As was pointed out earlier [123, 128, 129], this decrease is mainly due to the polarization charges at the dot boundary. The monotonic decrease of $\epsilon(r)$ extends to the nanocrystal boundary, where the value of the dielectric function becomes equal to ϵ_d . At the same time, the sharp reduction of $\epsilon(r)$ toward unity occurring at small r is exclusively due to the short-range central-cell potential.

3.2.2. Donor states in silicon crystallite

First, we consider electronic states in a silicon NC with a hydrogenlike donor placed in some arbitrary position inside the dot. The total electron potential energy described by (2) transforms into $U(\mathbf{r}, \mathbf{h}) = U_0(r) + V_C$ where \mathbf{h} stands for the impurity position vector, and V_C is a Coulomb potential energy, including not only the direct electron-ion interaction but also the interaction with polarized charges arising at the dot boundary. Solving the eigenstate and eigenvalue problem for the conduction band [140] yields the ground-state energy splitting shown in Figure 9 at $n_x = 0.8$, $n_y = 0.5$, and $n_z = 0.33$, where $\mathbf{n} = \mathbf{h}/h$, and h stands for the absolute value of \mathbf{h} .

In Figure 10, the envelope-function correction $\Delta\Phi$ is shown for the ground state due to the hydrogen-like donor, as a function of the angles θ and φ on the spherical surface $r = h$ for the former values of n_a . Angles θ and φ are the spherical coordinates. The maximal values of $\Delta\Phi$ (light areas in the figure) are located around the donor site marked with the cross. This is a natural result in that the electron density shifts towards the donor site.

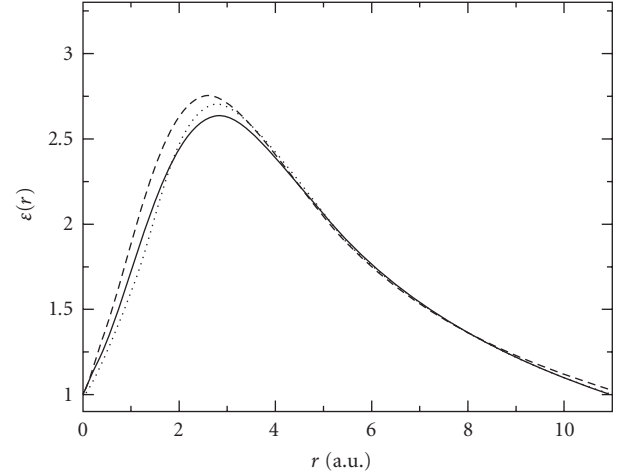


FIGURE 8: Dielectric function of silicon NCs in silicon dioxide matrix ($\epsilon_d = 3$) for (1) $R = 1$ nm; (2) $R = 1.75$ nm; (3) $R = 2.5$ nm.

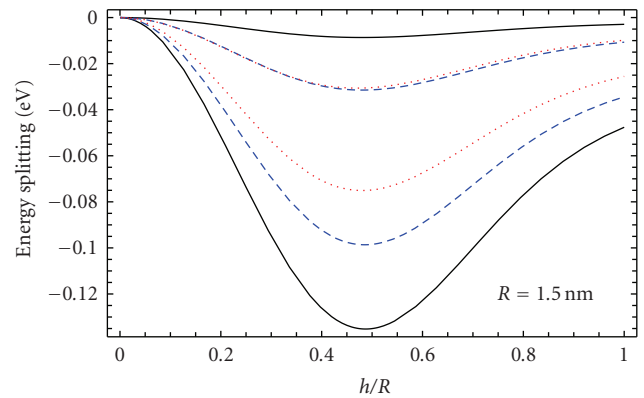


FIGURE 9: Fine structure of the energy spectrum with respect to the unperturbed sixfold degenerate energy level. Solid lines correspond to two states located in the Brillouin zone at the X-point (001). Dashed line: X-point (010). Dots: X-point (100). The direction of the donor's position vector is defined by $n_x = 0.8$, $n_y = 0.5$, and $n_z = 0.33$. The NC radius is indicated in the figure.

3.2.3. Acceptor states in silicon crystallite

It is interesting to compare the fine structure of the spectrum for donor- and acceptor-doped dots. Obviously, the fine structure in the valence band occurs because of the spin-orbit interaction and the asymmetry of the Coulomb field inside the dot, when the acceptor occupies some noncentral position. The energy splitting has been presented in Figure 11. Similarly to the donor case, the splitting turns out to be large compared to the magnitudes of chemical shifts in bulk silicon [141–144].

The Coulomb and spin-orbit interactions remove the sixfold degeneracy of both lowest levels shown in Figure 5, keeping only the double spin degeneracy of each the levels. Furthermore the splitting increases with decreasing the

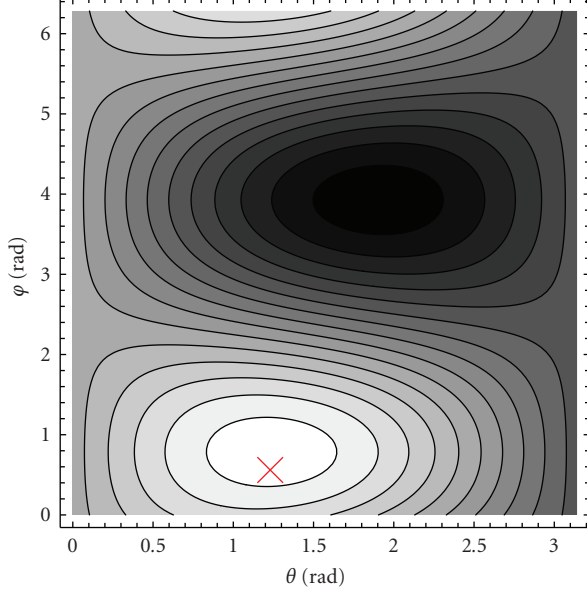


FIGURE 10: Contour plot of the first-order correction to the envelope function for a 3-nm-diameter quantum dot. The value of the correction rises from dark to light. The cross indicates the donor position defined by: $n_x = 0.8$, $n_y = 0.5$, and $n_z = 0.33$. $h/R = 0.46$.

nanocrystal size. This is evidence in favor of a quantum confinement effect, as was the case in the donor-doped dots.

The spatial distribution of the hole density in B-doped crystallite for all the six doublets is shown in Figure 12 for $h/R = 0.1$ (upper panels) and $h/R = 0.46$ (lower panels). We have plotted the average of the squared absolute value of the total wave function over the unit cell. In this case the Bloch-function oscillations do not appear in the electron density, which reduces to the “density of envelope function” $\rho_{\text{env}}(\mathbf{r}) = \sum_{j=1}^6 |\Phi_j(\mathbf{r})|^2$, where $\Phi_j(\mathbf{r})$ is the j th element of the 6D envelope function vector $|\Phi\rangle$ as before.

As the calculations show, for all the six doublets the envelope-function density has an axial symmetry with respect to the line drawn through the NC center and the acceptor. Therefore $\rho_{\text{env}}(\mathbf{r})$ has the same distribution in any dot cross-section to which the acceptor position-vector belongs. Figure 12 shows such a central cross-section of the electron density averaged over the unit cell for all the doublets. Brighter areas in the density plots correspond to higher values of $\rho_{\text{env}}(\mathbf{r})$. The circle represents the nanocrystal boundary, and the bold point situated at the vertical axis indicates the acceptor location.

It should be noted that the general trends in the location of the electron density under the action of the acceptor electric field are, in fact, similar for all the doublets in both cases $h/R = 0.1$ and $h/R = 0.46$. In particular, the ground-state electron density shifts to the acceptor site, while for the excited states, as the energy of the state increases and the electron density gradually moves into the areas free of the acceptor.

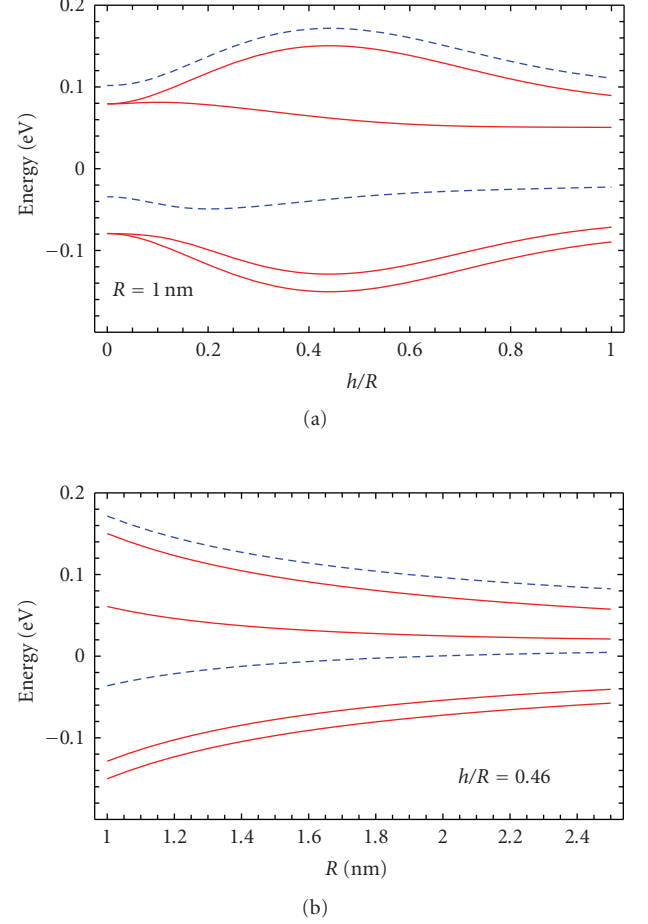


FIGURE 11: Splitting of the two lower hole levels shown in Figure 5 as function of the dimensionless acceptor displacement from the dot center in (a), and with respect to the NC radius in (b). The direction of the acceptor position-vector is defined by $n_x = 0.8$, $n_y = 0.5$, and $n_z = 0.33$. Dashed and solid lines represent the energies originating from doublet and quadruplet at $h = 0$, respectively. All the energies are counted from the mean quadruplet energy at $h = 0$.

3.3. Interband recombination in silicon nanocrystals

The PL intensity and quantum efficiency is defined by the relative contribution $\tau_R^{-1}/\tau_{\text{PL}}^{-1}$ of a radiative recombination channel in an interband transition. In turn, the total decay rate is defined by both radiative and nonradiative recombination rates: $1/\tau_{\text{PL}} = 1/\tau_R + 1/\tau_{\text{NR}}$. Consequently, in order to discuss possible means of increasing the quantum efficiency of silicon crystallites, we should understand what factors influence the radiative and nonradiative rates. For this purpose in this section we analyze theoretically both radiative and nonradiative recombination processes.

3.3.1. Radiative recombination times in undoped Si NCs

In bulk silicon, no-phonon radiative transitions between the conduction-band Δ -point and the valence-band Γ -point are forbidden because of indirect band-gap of silicon. In

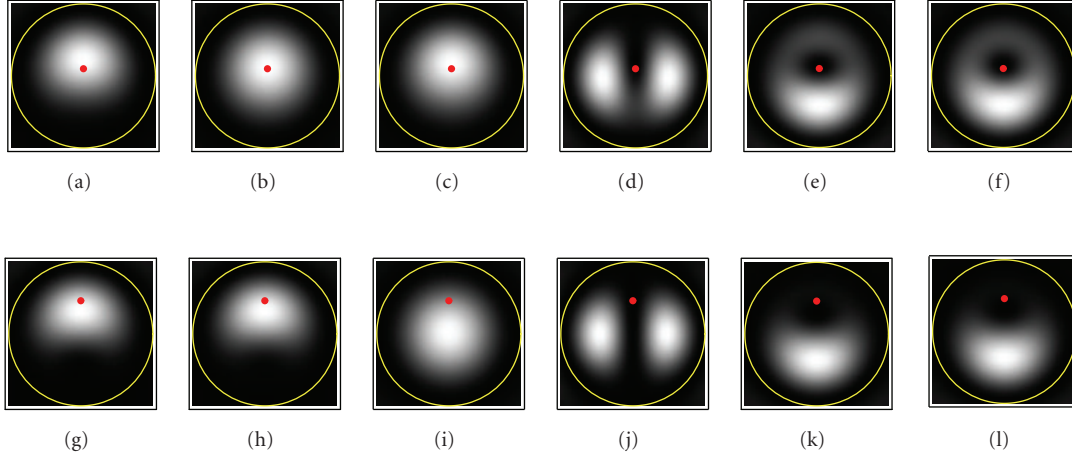


FIGURE 12: Density plot of the probability distribution $\rho_{\text{env}}(\mathbf{r})$ of all the six doublets at $h/R = 0.1$ (upper images), and $h/R = 0.46$ (lower images) for NCs containing a hydrogenic acceptor. The acceptor position is indicated with a red point. (a): ground state; (b) to (f): first to fifth excited states. For each state the hole density is normalized to its maximum in the state, and rises from dark to light. The nanocrystal boundary is marked by the yellow circle, with $R = 1.5$ nm.

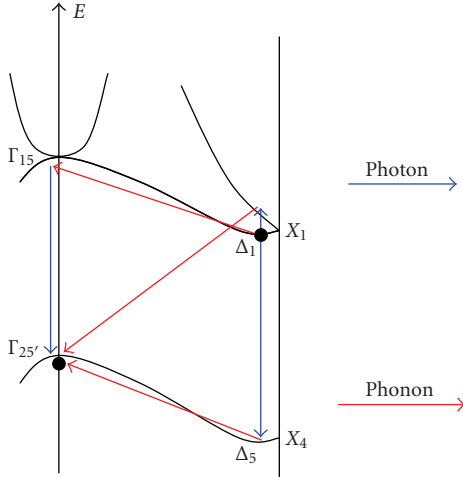


FIGURE 13: Schematic representation of the silicon band structure with phonon-assisted radiative transitions from the conduction-band minimum to the valence-band maximum indicated by arrows.

this case, only phonon-assisted transitions may take place, as shown in Figure 13. In a quantum dot no-phonon emission becomes possible but remains a low probability process for reasons discussed below. Meanwhile, the phonon-assisted radiative transitions have much greater rate. Here, we calculate both no-phonon and phonon-assisted radiative lifetimes in silicon nanocrystal.

We first calculate the rate τ_0^{-1} of the no-phonon radiative recombination. Using Fermi's golden rule in the first-order perturbation theory, one can write the decay rate for the transition between initial (I) and final (F) states in the

conduction and valence bands, respectively, in the following form:

$$\tau_{0,IF}^{-1} = \frac{2\pi}{\hbar} \sum_{\mathbf{Q},\sigma} |W_{IF}|^2 \delta(\varepsilon_g(R) - \hbar\omega_\sigma(\mathbf{Q})). \quad (24)$$

Here, $\omega_\sigma(\mathbf{Q})$ and \mathbf{Q} stand for the photon frequency and wave vector. The Dirac delta-function reflects the energy conservation law for the electron transition. The operator W describes the electron-photon interaction, and has the form:

$$W = \sum_{\mathbf{k},\sigma} \sqrt{\frac{2\pi\hbar e^2 \kappa(\varepsilon_s; \varepsilon_d)}{m_0^2 \omega_\sigma(\mathbf{Q}) V_0 \varepsilon_s}} (c_{\mathbf{Q}\sigma} + c_{\mathbf{Q}\sigma}^\dagger) \mathbf{e}_{\mathbf{Q}\sigma} \mathbf{p}, \quad (25)$$

where $\mathbf{p} = -i\hbar\nabla$ is the electron momentum operator, $\mathbf{e}_{\mathbf{Q}\sigma}$ is the polarization vector, the operator $c_{\mathbf{Q}\sigma}$ annihilates and $c_{\mathbf{Q}\sigma}^\dagger$ creates a photon with the wave vector \mathbf{Q} and polarization σ , and V_0 stands for the volume of the electromagnetic resonator. The function $\kappa(\varepsilon_s; \varepsilon_d)$ is written as [145]

$$\kappa(\varepsilon_s; \varepsilon_d) = \sqrt{\frac{\varepsilon_d}{\varepsilon_s} \left(\frac{3\varepsilon_d}{2\varepsilon_d + \varepsilon_s} \right)^2}. \quad (26)$$

This function represents the correction factor in the field magnitude due to the replacement of homogeneous media with bulk permittivity ε_s by a spherical silicon nanocrystal surrounded by silicon dioxide with a dielectric constant ε_d .

The initial state in (24) corresponds to an electron-hole pair being in its ground state, and an ensemble of photons whose distribution over \mathbf{Q} is described by the Bose-Einstein statistics. In the final state, the valence band is completely occupied and the conduction band is empty. The number of photons in the final state always increases by one.

As has already been mentioned (see Section 3.1.2), the ground spinless electron state in the conduction band is sixfold degenerate. However, TB [85, 120], PP [66], and DFT

[121] calculations revealed a weak splitting of the ground state into the singlet, doublet, and triplet states due to the tetrahedral symmetry of the spherical silicon nanocrystal. The authors pointed out that as the NC size varies, A_1 -, E -, or T_2 -type states alternately become the ground level. Correspondingly, in order to take into account tetrahedral symmetry of the quantum dot, we build the six ground states in accordance with the symmetric transformations of the irreducible representations A_1 (singlet), E (doublet), and T_2 (triplet) of the tetrahedral group. These functions are defined as follows [73]:

$$\begin{aligned}
\Psi_S &= \cos(\lambda) |A_1\rangle |s\rangle \\
&\quad + \sin(\lambda) \frac{|X'\rangle |p_x\rangle + |Y'\rangle |p_y\rangle + |Z'\rangle |p_z\rangle}{\sqrt{3}}, \\
\Psi_D^{(1)} &= \cos(\lambda) |E^{(1)}\rangle |s\rangle \\
&\quad + \sin(\lambda) \frac{|X'\rangle |p_x\rangle - |Y'\rangle |p_y\rangle}{\sqrt{2}}, \\
\Psi_D^{(2)} &= \cos(\lambda) |E^{(2)}\rangle |s\rangle \\
&\quad + \sin(\lambda) \frac{|X'\rangle |p_x\rangle + |Y'\rangle |p_y\rangle - 2|Z'\rangle |p_z\rangle}{\sqrt{6}}, \\
\Psi_T^{(1)} &= \cos(\lambda) |X'\rangle |s\rangle \\
&\quad - \sin(\lambda) \frac{\sqrt{2}|A_1\rangle + \sqrt{3}|E^{(1)}\rangle + |E^{(2)}\rangle}{\sqrt{6}} |p_x\rangle, \\
\Psi_T^{(2)} &= \cos(\lambda) |Y'\rangle |s\rangle \\
&\quad - \sin(\lambda) \frac{\sqrt{2}|A_1\rangle - \sqrt{3}|E^{(1)}\rangle + |E^{(2)}\rangle}{\sqrt{6}} |p_y\rangle, \\
\Psi_T^{(3)} &= \cos(\lambda) |Z'\rangle |s\rangle \\
&\quad - \sin(\lambda) \frac{|A_1\rangle - \sqrt{2}|E^{(2)}\rangle}{\sqrt{3}} |p_z\rangle.
\end{aligned} \tag{27}$$

Here, the parameter λ is defined by the relationships [92]

$$\begin{aligned}
\cos(2\lambda) &= \frac{E_p - E_s - 2H_{pp}}{\sqrt{(E_p - E_s - 2H_{pp})^2 + 4H_{sp}^2}}, \\
\sin(2\lambda) &= \frac{2H_{sp}}{\sqrt{(E_p - E_s - 2H_{pp})^2 + 4H_{sp}^2}},
\end{aligned} \tag{28}$$

where vectors $|s\rangle$ and $|p_\alpha\rangle$ stand for the s - and p -type envelope functions as before. The Bloch states $|A_1\rangle = (|X\rangle + |Y\rangle + |Z\rangle)/\sqrt{3}$, $|E^{(1)}\rangle = (|X\rangle - |Y\rangle)/\sqrt{2}$, $|E^{(2)}\rangle = (|X\rangle + |Y\rangle - 2|Z\rangle)/\sqrt{6}$, and $|T_2\rangle = |X'\rangle$, $|Y'\rangle$, or $|Z'\rangle$ belong to the representations A_1 , E , and T_2 of the tetrahedral group. In what follows, when computing the interband matrix elements of W we will choose one of the states given by (27) as the initial one. For convenience, one can rewrite the wave functions of the initial states in a general form:

$$\Psi_I = \sum_{\alpha,j} B_I^{\alpha j} F_\alpha(\mathbf{r}) \psi_j(\mathbf{r}), \tag{29}$$

where the index α indicates the “values” of the s , p_x , p_y , and p_z , functions, and $\psi_j(\mathbf{r})$ stands for the six Bloch functions $|X\rangle$, $|Y\rangle$, $|Z\rangle$, $|X'\rangle$, $|Y'\rangle$, $|Z'\rangle$ of the irreducible representation X_1 . The s - and p -type envelope functions are denoted as $F(r)$, and $F_x(\mathbf{r})$, $F_y(\mathbf{r})$, $F_z(\mathbf{r})$, respectively. Selecting expansion coefficients $B_I^{\alpha j}$, we can construct any of the states defined by (27).

The final state is one of the three degenerate states (neglecting the spin-orbit coupling) in the valence band [92] with the s -type envelope function:

$$\Psi_F = F(r) \psi_F(\mathbf{r}), \tag{30}$$

where $\psi_F(\mathbf{r})$ stands for the Bloch state basis functions $|YZ\rangle$, $|XZ\rangle$, or $|XY\rangle$ of the irreducible representation $\Gamma_{25'}$.

After some algebra, one can obtain recombination rate $\tau_{0,IF}^{-1}$ in the form:

$$\tau_{0,IF}^{-1} = \frac{4e^2 \sqrt{\epsilon_s} \kappa(\epsilon_s; \epsilon_d) \epsilon_g(R)}{3m_0^2 \hbar^2 c^3} |\mathbf{p}_{IF}|^2, \tag{31}$$

where $\mathbf{p}_{IF} = \langle \Psi_I | \mathbf{p} | \Psi_F \rangle$. In order to compute the momentum matrix element, we expand the Bloch functions $\psi_j(\mathbf{r})$ and $\psi_F(\mathbf{r})$ over the reciprocal lattice vectors \mathbf{g}_n as follows:

$$\begin{aligned}
\psi_j(\mathbf{r}) &= \sum_{\mathbf{m}} C_{j\mathbf{m}} \exp [2\pi i (\mathbf{g}_m + \mathbf{e}_j) \mathbf{r} / a_0], \\
\psi_F(\mathbf{r}) &= \sum_{\mathbf{n}} V_{F\mathbf{n}} \exp [2\pi i \mathbf{g}_n \mathbf{r} / a_0],
\end{aligned} \tag{32}$$

where a_0 is the lattice constant of silicon, and unit vectors \mathbf{e}_j define the X -point. We set $\mathbf{e}_{1,4} = \mathbf{e}_x$, $\mathbf{e}_{2,5} = \mathbf{e}_y$, and $\mathbf{e}_{3,6} = \mathbf{e}_z$. Expansion coefficients $C_{j\mathbf{m}}$ and $V_{F\mathbf{n}}$ are determined with the local pseudopotential method. They satisfy the normalizing condition $\sum_{\mathbf{n}} |C_{j\mathbf{n}}|^2 = \sum_{\mathbf{n}} |V_{F\mathbf{n}}|^2 = 1$. As a result, the momentum matrix element is given by

$$\mathbf{p}_{IF} = \frac{\hbar}{4\pi a_0} \mathbf{b}_{IF}(R) \left(\frac{a_0}{R} \right)^4, \tag{33}$$

where $\mathbf{b}_{IF}(R) = \sum_{\alpha,j} B_I^{\alpha j} \mathbf{J}_\alpha(R)$ with $\mathbf{J}_\alpha(R)$ being oscillating vector functions [146] of the dot radius. For s - and p -type subscripts, respectively, these functions are

$$\begin{aligned}
\mathbf{J}(R) &= \sum_{\mathbf{n},\mathbf{m}} \frac{C_{j\mathbf{m}}^* V_{F\mathbf{n}} \mathbf{d}_{\mathbf{n}+\mathbf{m}}}{d_{\mathbf{n}-\mathbf{m}}^4} \cos \left(2\pi d_{\mathbf{n}-\mathbf{m}} \frac{R}{a_0} \right), \\
\mathbf{J}_\alpha(R) &= -i \frac{\sqrt{3} \mu_1}{\pi} \sum_{\mathbf{n},\mathbf{m}} \frac{C_{j\mathbf{m}}^* V_{F\mathbf{n}} \mathbf{d}_{\mathbf{n}+\mathbf{m}} d_{\mathbf{n}-\mathbf{m}}^{(a)}}{d_{\mathbf{n}-\mathbf{m}}^5} \sin \left(2\pi d_{\mathbf{n}-\mathbf{m}} \frac{R}{a_0} \right).
\end{aligned} \tag{34}$$

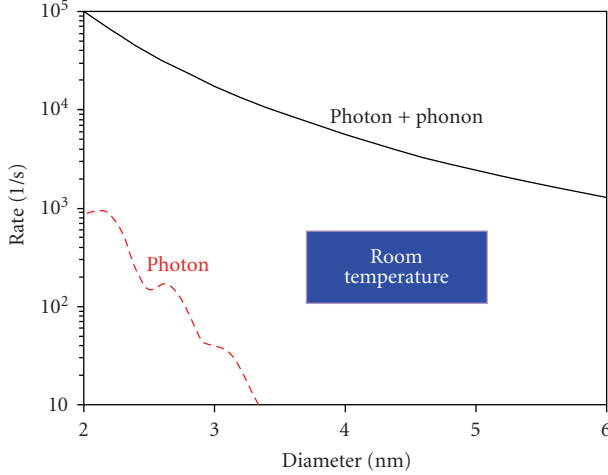


FIGURE 14: Recombination rates of no-phonon and phonon-assisted radiative transitions between the ground electron and hole states in silicon NCs, after averaging over all degenerate initial and final states.

Here, $a = x, y, z$, $\mathbf{d}_{n\pm m} = \mathbf{g}_n \pm \mathbf{g}_m \pm \mathbf{e}_j$, and $d_{n-m}^{(a)}$ represents an a th component of \mathbf{d}_{n-m} . The nonzero value of \mathbf{p}_{IF} is exclusively due to the Heisenberg uncertainty relations which cause the wide distribution of the wave function in \mathbf{p} -space.

Averaging (31) over all possible initial and final states yields

$$\tau_0^{-1} = \frac{e^2 \sqrt{\epsilon_s} \kappa(\epsilon_s; \epsilon_d) \epsilon_g(R)}{12\pi^2 m_0^2 c^3 a_0^2} \left(\frac{a_0}{R}\right)^8 \langle |\mathbf{b}_{IF}(R)|^2 \rangle. \quad (35)$$

In Figure 14 we show the no-phonon recombination rate τ_0^{-1} as function of the dot size. Although the no-phonon decay rate has a nonzero value, its magnitude remains small (less than 10^3 s^{-1}) within the range of the NC sizes shown in the figure.

Next, we calculate the phonon-assisted recombination rate [95, 147–149]. The total phonon-assisted rate of the radiative electron-hole recombination is determined in the second-order perturbation theory as

$$\begin{aligned} \tau_{R,IF}^{-1} &= \frac{2\pi}{\hbar} \sum_{\mathbf{Q}, \sigma} \sum_{\mathbf{q}, \ell} \left| \sum_a \frac{W_{FA} U_{AI} + U_{FA} W_{AI}}{\epsilon_I - \epsilon_A} \right|^2 \\ &\times [\delta(\epsilon_g(R) - \hbar\omega_\sigma(\mathbf{Q}) - \hbar\nu_\ell(\mathbf{q})) \\ &+ \delta(\epsilon_g(R) - \hbar\omega_\sigma(\mathbf{Q}) + \hbar\nu_\ell(\mathbf{q}))]. \end{aligned} \quad (36)$$

Here the matrix elements of the electron-photon (W) and electron-phonon (U) interaction operators are calculated between the initial I , the final F , and an intermediate state A ; ϵ_A and ϵ_I are the total energies of the intermediate and initial states, respectively, including not only the energies of the electrons (or holes) but also the energies of the photons and phonons. The phonon frequency of ℓ th polarization is denoted as $\nu_\ell(\mathbf{q})$ with \mathbf{q} being the dimensionless phonon wave vector taken in units of $2\pi/a_0$.

The electron-phonon interaction operator is treated within the framework of the rigid-ion model and is given by

$$\begin{aligned} U &= - \sum_{\mathbf{q}, \ell} \sum_{\mathbf{n}, s} \sqrt{\frac{\hbar}{2MN\nu_\ell(\mathbf{q})}} \nabla V_{\mathbf{n}s} \\ &\times \left(\mathbf{e}_{\mathbf{q}\ell s} \exp \left\{ \frac{i2\pi\mathbf{q}\mathbf{R}_n}{a_0} \right\} b_{\mathbf{q}\ell} \right. \\ &\left. + \mathbf{e}_{\mathbf{q}\ell s}^* \exp \left\{ -\frac{i2\pi\mathbf{q}\mathbf{R}_n}{a_0} \right\} b_{\mathbf{q}\ell}^+ \right). \end{aligned} \quad (37)$$

Here, N is the number of primitive cells in the crystal, M is the mass of a silicon atom, $V_{\mathbf{n}s} = V_{\text{at}}(\mathbf{r} - \mathbf{R}_n - \boldsymbol{\tau}_s)$ is the atomic potential, where \mathbf{R}_n stands for the position vector of the n th unit cell, and $\boldsymbol{\tau}_s$ represents the position vectors of two atoms within the unit cell: $\boldsymbol{\tau}_1 = 0$, and $\boldsymbol{\tau}_2 = (1, 1, 1) \times a_0/4$, $b_{\mathbf{q}\ell}^+$ and $b_{\mathbf{q}\ell}$ are the phonon creation and annihilation operators, and the phonon polarization vectors are denoted as $\mathbf{e}_{\mathbf{q}\ell s}$. Making the Fourier transformation of the atomic potential: $V_{\text{at}}(\mathbf{r}) = N^{-1} \sum_{\mathbf{p}} V_{\mathbf{p}} \exp\{i\mathbf{p}\mathbf{r}\}$, one can rewrite the operator U in the form (see also [150, 151]):

$$\begin{aligned} U &= \frac{2\pi i}{a_0} \sum_{\mathbf{q}, \ell, s, m} \sqrt{\frac{\hbar}{2MN\nu_\ell(\mathbf{q})}} (\mathbf{q} + \mathbf{g}_m) \\ &\times \left[\mathbf{e}_{\mathbf{q}\ell s}^* V_{\mathbf{q}+\mathbf{g}_m}^* \exp \left\{ -\frac{i2\pi(\mathbf{q} + \mathbf{g}_m)(\mathbf{r} - \boldsymbol{\tau}_s)}{a_0} \right\} b_{\mathbf{q}\ell}^+ \right. \\ &\left. - \mathbf{e}_{\mathbf{q}\ell s} V_{\mathbf{q}+\mathbf{g}_m} \exp \left\{ \frac{i2\pi(\mathbf{q} + \mathbf{g}_m)(\mathbf{r} - \boldsymbol{\tau}_s)}{a_0} \right\} b_{\mathbf{q}\ell} \right]. \end{aligned} \quad (38)$$

Calculations of the electron-photon and electron-phonon matrix elements yield

$$\begin{aligned} \tau_{R,IF}^{-1} &= \frac{4\pi^2 \hbar^2 e^2 \sqrt{\epsilon_s} \kappa(\epsilon_s; \epsilon_d) \epsilon_g(R)}{3Mm_0^2 c^3 a_0^4} \left(\frac{a_0}{R}\right)^3 \\ &\times \sum_{\ell} \frac{P_{IF}(\ell)}{\hbar\nu_\ell} \coth \left[\frac{\hbar\nu_\ell}{2kT} \right], \end{aligned} \quad (39)$$

where

$$\begin{aligned} P_{IF}(\ell) &= B_I^{am} (B_I^{\beta n})^* x_{Fm}(\ell) x_{Fn}(\ell) 2\pi^2 R^3 \\ &\times \int d\mathbf{r} F_\alpha(\mathbf{r}) F_\beta(\mathbf{r}) F^2(r), \\ x_{Fm}(\ell) &= \sum_A \frac{\langle \psi_F | w | \psi_A \rangle \langle \psi_A | u | \psi_m \rangle + \langle \psi_F | u | \psi_A \rangle \langle \psi_A | w | \psi_m \rangle}{\epsilon_I - \epsilon_A}. \end{aligned} \quad (40)$$

ψ_A represents the Bloch functions of the intermediate states and the operators w and u are directly proportional to W and U :

$$\begin{aligned} W &= w \frac{2\pi\hbar}{a_0} \sqrt{\frac{2\pi\hbar^2 \kappa(\epsilon_s; \epsilon_d)}{m_0^2(\mathbf{Q}) V_0 \epsilon_s}}, \\ U &= u \frac{2\pi}{a_0} \sqrt{\frac{\hbar}{2MN\nu_\ell(\mathbf{q})}}. \end{aligned} \quad (41)$$

As has been shown earlier, the electron subsystem in silicon nanocrystals interacts more efficiently with TO and LO phonons [147, 148] similarly to bulk silicon [150, 151]. The contribution of TA phonons is negligibly small. Therefore, in the sum over the phonon modes in (39), only TO and LO modes may be taken into account.

For convenience, we have again averaged the calculated rates over all the possible initial and final degenerate states and obtained the recombination rate in the following form:

$$\begin{aligned} \tau_R^{-1} = & \frac{\pi^2 \hbar^2 e^2 \varepsilon_g(R) \sqrt{\varepsilon_s} \kappa(\varepsilon_s, \varepsilon_d)}{9Mm_0^2 c^3 a^4} \left(\frac{a_0}{R}\right)^3 \\ & \times \left(\frac{7.527 \coth[\hbar\nu_{\text{LO}}/2kT]}{\hbar\nu_{\text{LO}}} + \frac{32.768 \coth[\hbar\nu_{\text{TO}}/2kT]}{\hbar\nu_{\text{TO}}} \right) \\ & \times (4\cos^2\lambda + 9.26). \end{aligned} \quad (42)$$

Here: $\hbar\nu_{\text{LO}} = 0.051$ eV and $\hbar\nu_{\text{TO}} = 0.0576$ eV represent the energies of LO and TO phonons and the numbers 7.527, 32.768 come from numerical integration of electron-phonon matrix elements. The size dependence of the recombination rate has been presented in Figure 14. The dependence of τ_R^{-1} on the dot radius is close to R^{-3} . This is much slower than the rate obtained for no-phonon transitions (R^{-8}).

The results presented here agree well both qualitatively and quantitatively with those obtained by other authors [95, 147, 148] for similar systems. In particular, according to their results, the recombination rates for NCs from 2 to 6 nm in diameter do not exceed 10^5 s $^{-1}$ and are never less than 5×10^2 s $^{-1}$. It should be noted, however, that the TB calculations [148] produce a considerably slower decrease of the radiative decay rate than the EFA (as developed here and in [95, 147, 149]) predicts.

Finally, concluding this subsection, we would like to discuss briefly the relation between our single-particle calculations and the singlet-triplet model which gives a reduction of the radiative lifetime with increasing temperature, as in (1). It is, of course, not applicable in the frame of a single-particle treatment to obtain the state splitting caused by the exchange electron-hole interaction. Therefore, the temperature dependence of τ_R^{-1} (42) is defined exclusively by the phonons. As a result, no sharp rise of the decay rate appears in our model as the temperature increases up to the room values. At temperatures higher than about 150–200 K, both models nevertheless should give similar results because the upper excitonic states become highly populated. Thus, the single-particle model remains valid for $T > 200$ K. As well, it should be noted that the separation of dark and bright excitons is not always possible. The spin-orbit coupling transforms forbidden exciton transitions into suppressed ones due to the entanglement of single-particle states with different spin projections. The entanglement can be crucially strengthened by imperfections of the crystallite structure such as shape nonsphericity or, especially, by various point defects such as P_b centers, SiO bonds, and impurities. In the presence of the latter effects, all the transitions can become allowed and consequently the single-particle model is acceptable.

3.3.2. Radiative recombination in doped dots

Experimental evidence of shallow impurity effects in the PL of silicon NCs (see Section 2.3) has no corresponding rigorous theoretical grounds. Usually, when discussing various changes in optical properties of the NCs due to doping, the nonradiative recombination channel is considered more closely. For instance, doping may passivate dangling bonds, and, as a consequence, essentially reduce the effectiveness of the nonradiative channel. On the other hand, a large number of donors or acceptors in the nanocrystal leads to the appearance of extra carriers that can recombine through the Auger process. Thus, doping is an important factor influencing the nonradiative recombination (a more detailed description of the nonradiative recombination mechanisms can be found in the next subsection). The nonradiative lifetime τ_{NR} can be varied by doping, which leads to the change of the emission efficiency.

The impact of doping on the radiative channel has not yet reported. However, it is interesting to examine also the possibility of increasing the quantum yield via enhancement of the radiative rate τ_R^{-1} . This is exclusively a quantum effect that can be explained by the reconstruction of the wave functions in different symmetry (or asymmetry), and changing selection rules for the interband transitions. We would like to touch upon this question in the present subsection and compute the radiative recombination rates in a silicon NC doped with a hydrogen-like donor and acceptor.

In order to compute the decay rates for the doped dot we follow (36). The main reason for the rate changes compared to the case of the undoped dot lies in some corrections to the electronic wave functions of both initial and final states (27), (30) due to the existence of a shallow impurity in the dot. In the following, we discuss two different cases.

The first case corresponds to an off-center position for the impurity inside the dot. In the valence band such an impurity location creates a field asymmetry in the system, which entangles the three spinless s -type states (30) with the three spinless p -type states [92]

$$\begin{aligned} \Psi_{p1} &= \frac{F_x(\mathbf{r})|XZ\rangle - F_y(\mathbf{r})|YZ\rangle}{\sqrt{2}}, \\ \Psi_{p2} &= \frac{F_z(\mathbf{r})|YZ\rangle - F_x(\mathbf{r})|XY\rangle}{\sqrt{2}}, \\ \Psi_{p3} &= \frac{F_y(\mathbf{r})|XY\rangle - F_z(\mathbf{r})|XZ\rangle}{\sqrt{2}}. \end{aligned} \quad (43)$$

These states (30) and (43) correspond to the closely spaced lowest triply degenerate energy levels shown in Figure 5. As a result, the ground hole state becomes a superposition of the states with s - and p -type envelope functions. In the conduction band, the ground electron states are the s - p combinations even without impurities, as seen from (27). Embedding the impurity into some arbitrary position within the NC raises the number of the p -type envelope functions in the ground states as well as in the valence band. However, $P_{IF}(\ell)$ becomes smaller if the integrated envelope functions are p -type. Consequently, the squared transition matrix element, proportional to $P_{IF}(\ell)$, and the rate itself decrease

relative to the case of an undoped NC, as shown in Figure 15 for two different displacements of the impurity from the dot center.

The ratio $h/R = 0.46$ corresponds to the greatest possible mix of s - and p -type states with maximal weight of the p -type envelope functions in the ground states both in the conduction and valence bands. The strong mixing results in maximal decrease of the decay rate independently of the impurity type. When the impurity is situated near the nanocrystal boundary, $h/R = 0.9$, the weight of the p -type envelope functions reduces in the ground state of both bands. As a consequence, the rate rises with respect to the case $h/R = 0.46$, but remains smaller than that for the undoped NC.

The second case we consider is the case of the central-located impurity. If $h = 0$, no s - p entanglement takes place in the valence band. The functions with the s -type envelope (30) describe the ground states of both donor- and acceptor-doped NCs.

The situation is different for the conduction band. Formally, the wave functions of the six spinless ground states are described by (27) as before. However, for doped dots, parameter λ has a form which differs from that given by (28). In the presence of an impurity center, λ is defined as:

$$\begin{aligned} \cos(2\lambda) &= \frac{E_p - E_s + \delta V - 2H_{pp}}{\sqrt{(E_p - E_s + \delta V - 2H_{pp})^2 + 4H_{sp}^2}}, \\ \sin(2\lambda) &= \frac{2H_{sp}}{\sqrt{(E_p - E_s + \delta V - 2H_{pp})^2 + 4H_{sp}^2}}, \end{aligned} \quad (44)$$

where $\delta V = V_{pp} - V_{ss}$ is the difference between the p - p and s - s type matrix elements of the Coulomb potential energy V_C . The appearance of this term in the definition of λ is explained by the shift of the energy levels of the s - and p -states E_s and E_p , respectively, due to the Coulomb interaction. The relative shift δV turns out to be positive for donors, and negative for acceptors. Consequently, $\cos(\lambda)$ increases and $\sin(\lambda)$ decreases for donors, and vice versa for acceptors.

This implies that the weight of the s -type envelope function in the electron ground state increases for the donor-doped dot and shrinks for the dot doped with acceptor, with respect to its value in the undoped dot. Hence, the coefficient $P_{IF}(\ell)$ for the donor-doped dot is greater than that for the undoped dot. In turn, the latter exceeds $P_{IF}(\ell)$ for the acceptor-doped dot. Precisely the same relationships take place for the recombination rates, as shown in Figure 15.

Note in conclusion, that the central-symmetric case $h = 0$ qualitatively corresponds to some real situation, where the NC has been highly doped with donors or acceptors. It is natural to assume a homogeneous impurity distribution within the nanocrystal in this case. Obviously, such a homogeneous density of charge induces a spherically symmetric electric field that cannot mix the s - and p -type states. Moreover, the relative Coulomb shift δV remains positive for donors and negative for acceptors, as in the above case of a single impurity center in the dot [73]. Therefore, one can expect similar behavior of τ_R^{-1} for highly doped NCs.

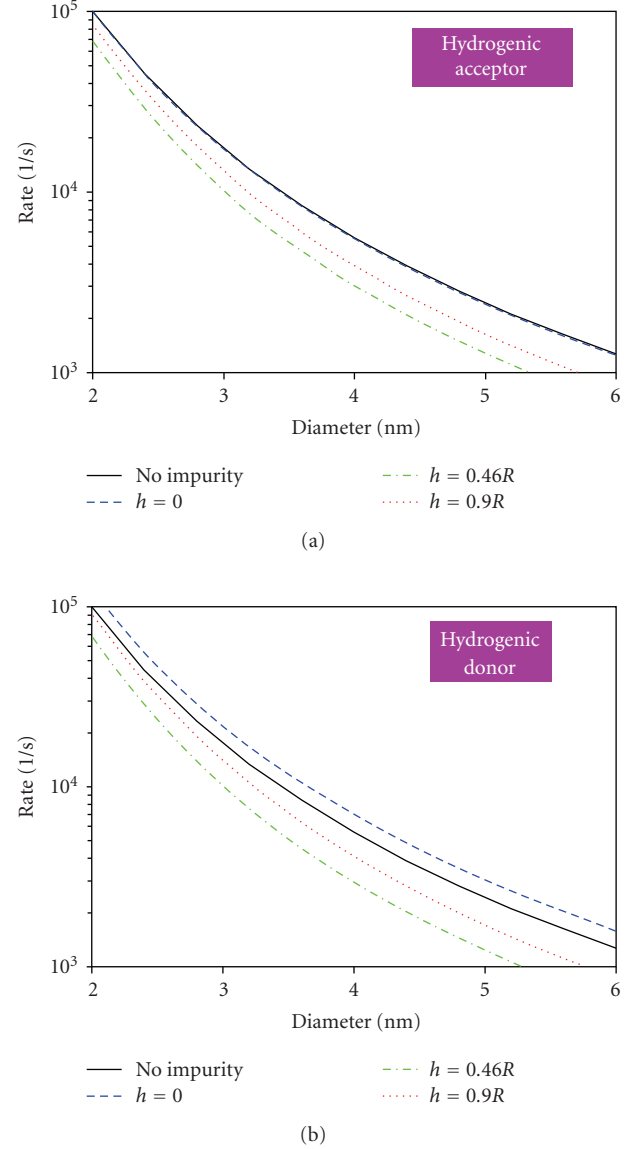


FIGURE 15: The rates of the phonon-assisted ground radiative transition as functions of the dot radius for a doped dot. For $h \neq 0$, we have $n_x = 0.8$, $n_y = 0.5$, and $n_z = 0.33$.

3.3.3. Nonradiative recombination

In parallel with radiative transitions, nonradiative processes occur in silicon nanocrystals. As a rule, nonradiative processes play a problematic role in silicon crystallites, due to their high recombination rates which substantially exceed the rates of the radiative transitions. Among the possible nonradiative processes, capture on dangling bonds and Auger recombination are the most efficient. Both processes are phonon-assisted, possibly even multi-phonon. The first one takes place both at low and high pumping levels, while Auger recombination becomes possible exclusively at high excitation power when more than one excited electron (hole) exist in the conduction (valence) band of the nanocrystal.

The capture on a neutral dangling bond has been studied earlier by TB method [100, 106]. It was shown that excited electron-hole pairs can recombine on a neutral dangling bond in two stages. First, the electron (hole) is trapped on a neutral P_b center making it negatively (positively) charged. Then, the hole (electron) is trapped on the charged dangling bond. According to estimations [100], the capture rate on the neutral dangling bond for holes is always much greater than that for electrons. In turn, the electron capture rate at room temperature increases sharply as the nanocrystal gap decreases from 2.7 eV to 1.5 eV (see (23)). Within the same range of energy gaps, the hole capture rate also increases but less sharply. We should emphasize the presence of two main features of the capture process. First, there is a very strong dependence of the capture rates (even for holes) on the energy gap, that is, the NC size. The second feature is the overall high capture rates, which are much greater than the radiative decay rates. Evidently, the presence of a dangling bond in silicon crystallite drastically reduces the quantum efficiency of photon generation. Therefore the passivation of dangling bonds is required for achievement of relatively efficient luminescence.

Let us now touch briefly on the role of SiO defects in the photoluminescence. The calculations of Nishida [102] showed that the oscillator strength is almost independent of the existence of Si–O–Si bonds. In contrast, the Si=O bonds reduce the oscillator strength by several orders of magnitude. Recently, however, Sa’ar et al. [64] demonstrated experimentally that both back-bonded and double-bonded oxygen atoms can enhance the PL intensity due to formation of coupled states of electrons (holes) and SiO vibrations. Such vibrations induce electric polarization fields generating long-lived coupled states named “vibrons”. Usually, the surface vibrations scatter the carriers; however, vibrons, being coupled states, do not scatter the carriers and thereby exclude one of possible nonradiative channels from the recombination process.

For highly excited nanocrystals, Auger recombination may take place. It is sufficient to have only three particles (two electrons and a hole, or vice versa) for this process to occur. It is well known that Auger recombination has high efficiency in bulk silicon. Therefore, it is natural to expect a similar behavior in silicon crystallites. Calculations of the Auger-recombination rate in crystallites carried out with TB [58, 152] and EFA [153] techniques confirm, indeed, the fast character of this mechanism. In particular, the characteristic times have been found to be of the order 0.1 to 10 ns⁻¹ and gradually rise with decreasing nanocrystal size. Thus, Auger recombination, as well as dangling bonds, can strongly quench the luminescence in silicon crystallites, as confirmed experimentally [152].

4. ENSEMBLES OF QUANTUM DOTS

4.1. Size distributions

As discussed in detail in the previous sections, the recombination energy for Si NCs is dependent on the NC size. In order to achieve optical gain and stimulated emission,

therefore, a narrow size distribution would be beneficial in order to narrow the gain profile. In ensembles of silicon nanocrystals grown by various thin film methods or by ion implantation, it is so far not possible to obtain the narrow size distributions that can be achieved with chemical methods, where post-synthesis size selection methods are routinely employed [154]. However, there is hope for better size selectivity, as will be discussed toward the end of this section.

The nucleation and growth behavior of nanocrystals in ion implanted systems, in particular, has been extensively characterized [155, 156]. The lognormal size distribution results in general when multiple microscopic processes govern the nucleation and growth kinetics, as is typical in these systems. The lognormal distribution is found even in cases where the “memory” of the specific initial conditions is lost, for example, after annealing of ion implanted samples [156]. In such cases, the nanocrystal size distribution is governed by the standard lognormal curve:

$$P(x) = \frac{1}{Sx\sqrt{2\pi}} \exp \left[-\frac{(\ln(x) - M)^2}{2S^2} \right], \quad (45)$$

where the mean and variance can be related to the M and S parameters by $\mu = \exp(M + S^2/2)$ and $\text{var} = \exp(S^2 + 2M)[\exp(S^2) - 1]$.

For thin films also, a lognormal distribution is predicted on the basis of random nucleation and growth in a homogeneous medium, regardless of the growth temperature, specific method of crystallization, and the mean grain size [157, 158], which is consistent with previous theories on cluster growth in metals and ceramics [159]. Lognormal distributions in the case of silicon grains crystallizing in amorphous silicon have been reported [157], and the lognormal size distribution has also been observed in silicon NCs over the range of annealing temperatures from 400 to 1100°C [47, 160]. Figure 16 shows the size distributions obtained from TEM data for two samples available in the literature. In Figure 16(a), the data from Vinciguerra et al. [161] are reproduced along with a Gaussian least squares fit ($\mu_{\text{radius}} = 1.68$ nm, $\sigma = 0.65$ nm) which is similar to the fit in the original publication (quoted as $\mu = 1.7 \pm 0.6$ nm), and a lognormal fit with $S = 0.27$ and $M = 0.54$). The data look decidedly lognormal with a skew toward large radii; the lognormal fitting matches the data better on both the high and low tails of the distribution, has a better correlation ($R^2 = 0.94$ versus 0.86), and is naturally equal to zero for negative radii. Figure 16(b) shows the original data from Glover and Meldrum [162], along with a lognormal fit with $S = 0.29$, $M = 0.22$. This latter data and fit will be used in the model in the following subsections. Obviously, the exact numbers obtained for M and S depend on the histogram binning and on the quantity of the data.

Size distributions can potentially be different than lognormal whenever the nucleation and growth processes are not random but are controlled in some way, such as via irradiation-induced nucleation [163], or through nonuniformities in the concentration of silicon, or when size selection is built into the process as, for example, in the formation

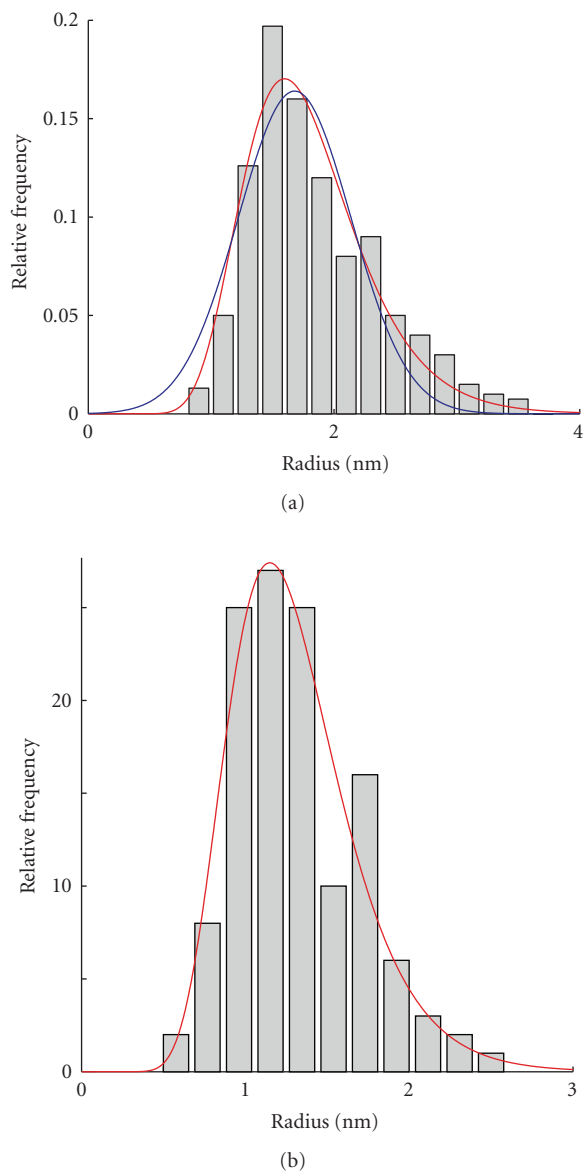


FIGURE 16: (a) Experimental size histogram from [161], with a Gaussian fit (blue line) and a lognormal fit (red line). Panel (b) shows the data from [162] with a lognormal fit.

of silicon nanocrystals by laser pyrolysis [164], or when size selection is done after crystal formation in solution, or when there is a mechanism for producing nonuniform (i.e., bimodal) distributions. Nevertheless, in numerous studies of silicon nanocrystals a Gaussian distribution is assumed. It can be mentioned that in most cases where a Gaussian fit is used to model the silicon NC size distribution, there is in fact no theoretical basis for it. In fact, it can predict unphysical results (e.g., the Gaussian function does not go to zero when its argument—the radius or diameter—is negative).

The lognormal function should, therefore, be used in cases except those in which there are reasons to expect a different distribution. Since there is a strong dependence of the bandgap energy on the cluster size, accurate modeling of

the behavior of ensembles of Si NCs does imply that the size distributions should be well known and correctly modeled. For modeling luminescent properties of ensembles of silicon nanocrystals, as discussed below, the lognormal distribution will be used in every case.

4.2. PL spectra and dynamics

Silicon NCs are characterized by a broad emission spectrum typically peaked between 800 and 900 nm, with a full-width-at-half-maximum (FWHM) of as much as 200 nm, even in “monodispersed” multilayered samples [165]. Although the size distributions for the monodispersed samples in [165] were not actually reported, it seems likely that they would nevertheless be much wider than typically obtained for CdSe NCs due to the lack of post-synthesis size selection methods. Therefore, the broad emission band could simply be due to the range of confined carrier energies in clusters of different sizes, or to the random nature of the interface states that may affect the PL spectrum. Single quantum dots may show homogeneous broadening up to ~ 150 meV at room temperature [19], although this is still narrower than the overall inhomogeneous broadening due to the size distribution. Below, we will investigate the spectral effects of broadening and nonradiative defects on the emission spectrum of an ensemble of Si NCs.

In order to investigate the theoretical luminescence spectrum and dynamics, the NC size distribution for SiO films annealed at 1000°C from [47] (lognormal radius parameters $S = 0.21$, $M = 0.74$) was used along with the theory developed in Sections 1–3. First, the effect of inhomogeneous broadening was investigated by plotting one spectrum in which the energies of 10^6 NCs produced with a lognormal probability function were binned in histogram form. In this case, for simplicity the NCs were treated as isolated, and energy transfer between them was not permitted (purple curve, Figure 17). The effect of homogeneous broadening was determined by assigning each cluster a Gaussian range of emission energies with standard deviations ranging from 0 to 200 meV and adding all the resulting curves (Figure 17). As the homogeneous broadening increases, the emission spectrum became broader, effectively similar to a “Gaussian smoothing” of the spectrum. Additionally, the spectrum was observably wider even for small levels of homogeneous broadening, and the peak shifts to slightly shorter wavelengths due to the overall shape of the lognormal function. The spectrum maximizes at shorter wavelengths than actually observed for a real specimen with this size distribution because NC-NC interactions were not yet turned on in the simulation. At this stage, the intent is simply to demonstrate the effect of homogeneous broadening on the observed PL spectrum. One may furthermore propose that the term “monodisperse” may only be used rigorously in situations in which the width of the PL spectra is governed primarily by homogeneous rather than inhomogeneous spectral broadening.

Next, the effect of nonradiative interface defects on the emission spectra and dynamics was estimated. Two size

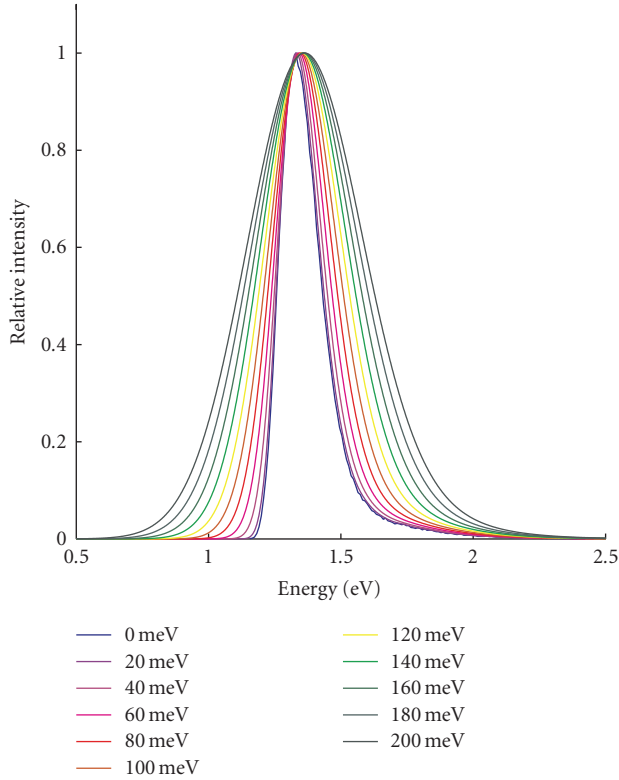


FIGURE 17: Effect of homogeneous broadening on the simulated (normalized) PL spectrum. The FWHM of the Gaussian homogeneous broadening is shown in the legend.

distributions corresponding to those in [47] ($S = 0.21$; $M = 0.74$) and [162] ($S = 0.29$; $M = 0.22$) were used, and for the present evaluation NC-NC energy transfer was not permitted. Several different concentrations of nonradiative defects ranging from 0 to 10^{20} cm^{-3} were assigned to the clusters with probabilities weighted proportionally to the surface areas. Clusters were checked in random order and a defect was assigned to a cluster if the random number was smaller than $A_{\text{NC}}/A_{\text{all NCs}}$. The process was continued until all defects had been assigned, allowing for multiple defects on a single particle (Figure 18). Every cluster was then given an electron-hole pair with a lowest excited-state energy calculated according to (22). The radiative and nonradiative rates were calculated from (42) and (23), respectively. Using a simple Monte Carlo procedure, the probabilities of radiative and nonradiative decay were calculated for each NC and a random number generator used to determine whether either type of decay occurred. This process continued until no excited carriers remained.

The resulting PL spectra were characterized by an asymmetric curve shape, tailing toward higher energies due to the form of the equations leading up to (22) (Figure 19). The effect of various concentrations of nonradiative surface defects is clearly observable in the simulated PL spectra. In addition to decreasing the overall PL intensity, the effect of the nonradiative centers is to blueshift the peak wavelength. The spectral blueshift occurs because the larger

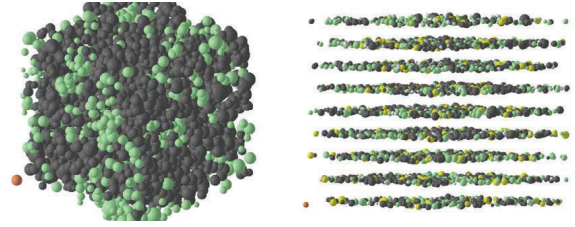


FIGURE 18: Left: Plot of a simulation box, 4000 NCs, initial state. Dark clusters contain one or more defects. Right: multilayered sample in a time window between 50–100 μs after the end of the pump pulse. Yellow NCs had a radiative recombination event during this time period and white NCs have no charge carriers remaining. Interaction effects were turned off for these simulations. The orange NC in the lower left corner of both images is 5 nm in diameter.

clusters are statistically more likely to contain defects, and the effect would be even stronger if defects were assigned with a volume rather than surface-area weighting (e.g., for volume defects). If extended annealing periods can remove nonradiative centers without increasing the NC size [166], then the effect would be to cause an increased intensity and a redshift of the PL peak, exactly as reported experimentally [53]. This redshift is not due to increasing cluster size, but is due to the removal of nonradiative traps. Finally, the high-energy skewness of the simulated spectra is due to a combination of effects, including the lognormal size distribution, and the lack of carrier transfer from small to large clusters.

As discussed in Section 1, PL decay dynamics in ensembles of Si NCs are characterized by the “stretched exponential” function $I_t/I_0 = \exp[-(t/\tau)^\beta]$, with values of the exponent β often between 0.7–0.8. The stretched exponential has been suggested to be due to a hopping mechanism in which excitons are temporarily trapped and delayed at sites in the oxide matrix or at the cluster-oxide interfaces [32, 167, 168]. However, the stretched exponential decay could also be due to the distribution of lifetimes in NCs of different sizes, as has been indicated by a few groups [35, 169]. In the absence of radiative centers, the recombination energy is given by (22), and the size-dependent radiative rates were developed in (42). Here we found that when the defect concentration was set to zero (uppermost line in Figure 20), values of $\beta = 0.58$ and $\tau = 33 \mu\text{s}$ emerged naturally. The small lifetime is due to the small size of the clusters used in this simulation. Also, since interactions were not enabled, there is no energy transfer from small to large clusters which would also affect the time constant (and the value of β). Including defects changed these values considerably: with increasing defect concentration, the decays are more precipitous (Figure 20). The stretched exponential function with low β values can, therefore, be obtained naturally as a result of the lifetime distribution. Approximately 100-microsecond-timescale carrier hopping, as suggested in previous work [168] as an explanation for the stretched exponential decay, while not ruled out by this

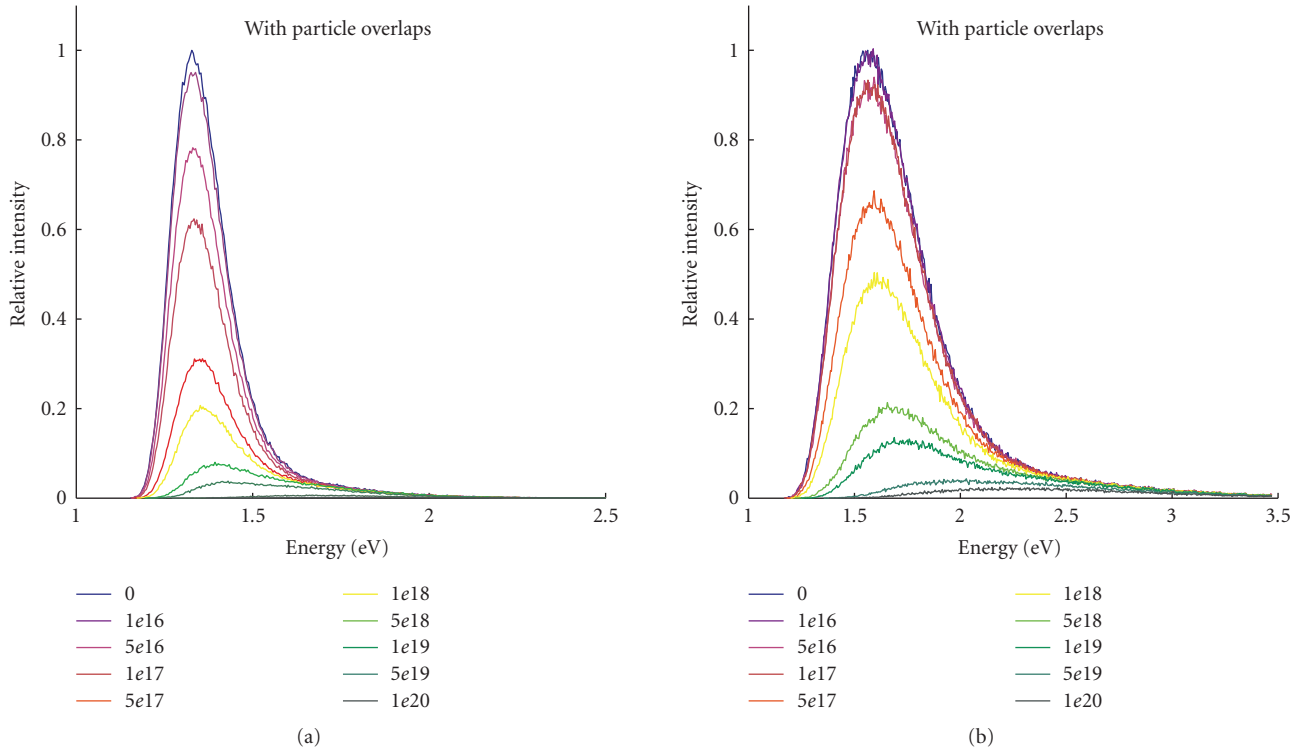


FIGURE 19: PL spectra as a function of surface defect concentration for non-interacting NCs. The spectra in the top panel correspond to $\mu_{\text{radius}} = 2.1 \text{ nm}$, $\text{var}_{\text{radius}} = 0.21 \text{ nm}^2$; the bottom panel is for $\mu_{\text{radius}} = 1.3 \text{ nm}$, $\sigma_{\text{radius}} = 0.38 \text{ nm}$. The legends show the defect concentration in cm^{-3} .

analysis, is not required in order to generate the stretched exponential dynamics, a conclusion that is in agreement with recent experimental results [169].

This is not meant to imply that energy transfer does not occur—in fact, it certainly does occur in most samples as discussed below—but that the shape of the decay curve is in fact governed by the size distribution even in the presence of energy transfer. However, energy transfer will also affect the shape of the decay curve—in the absence of nonradiative processes shifting the decay to longer lifetimes and larger β . In fact, in the absence of nonradiative decay, it is in theory possible to work back from the observed decay to the lifetime distribution using the inverse Laplace transform for the stretched exponential function [170]. From the lifetime distribution one could in principle then work back to the size distribution if $\tau_{pl} \approx \tau_{\text{rad}}$ and the radiative rate model is accurate. If nonradiative processes are included, the values of β and τ are sensitive to the size distribution, filling fraction, and defect concentration. In the discussion below, the first interaction simulation including Forster transfer and tunneling will be performed and its effect on the PL spectrum investigated.

4.3. Interactions

In order to achieve better size control, several studies have formed silicon nanocrystals using a thin film multilayering

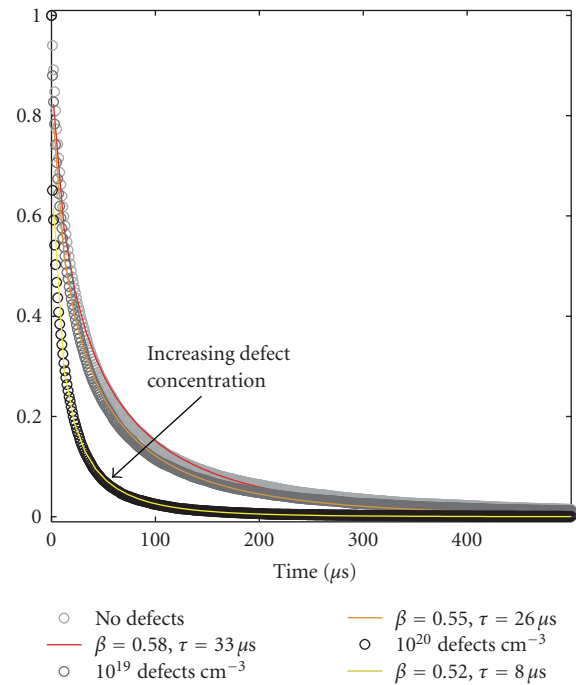


FIGURE 20: Simulated PL decays for a specimen with $\mu_{\text{radius}} = 1.3 \text{ nm}$, $\text{var}_{\text{radius}} = 0.15 \text{ nm}^2$. The lines correspond to defect concentrations of 0 , 10^{19} cm^{-3} , 10^{20} cm^{-3} . Interactions were not permitted, which minimizes the effect of defects.

approach. Instead of depositing a single thick layer of SiO_x , alternating thin layers of SiO_x and SiO_2 were used. In this way, the thin SiO_x layers are isolated from one another by the SiO_2 buffer layers. Upon annealing, silicon clusters crystallize in the SiO_x layers, but the cluster growth occurs only by diffusion within the layer as opposed to three-dimensionally. Although the resulting cluster sizes should clearly be *smaller* than for three-dimensional diffusion in a thick layer of the same composition, it is not immediately clear without more detailed modeling whether the distribution should, in theory, be more narrowly distributed with respect to the mean value. However, narrower distributions have been reported in many cases [171]. Nevertheless, even in apparently monodispersed multilayered samples [165] the PL peak is nearly 200 nm wide at the half maximum.

Through investigating the effect of multilayering of the Si NCs on the luminescence spectrum, it has been observed that the PL spectrum and dynamics from silicon nanocrystals depends on the thickness of both the SiO_2 buffer layers and the active nanocrystal layers, even if the size distributions remain approximately constant [23, 32, 162]. This is evidence of an interaction mechanism operating between the clusters: as the NCs become more isolated—in one direction at least—by the buffer layers, the PL peak shifts to shorter wavelengths and there is a change in the decay dynamics as well, with a possible trend toward higher values of the exponent β . As already discussed, this has been widely interpreted in terms of a kind of excitonic hopping or migration (e.g., see [23]) between clusters, although only more recently have the mechanisms for carrier transfer among Si NCs been more clearly elucidated [30, 160].

There are at least two fundamental means by which closely spaced nanocrystals can exchange charge carriers. The first mechanism is via tunneling of individual electrons or holes from one cluster to another. If the two clusters are approximately the same size (or if the higher levels of a larger cluster overlap with lower levels of a smaller one), then the tunneling is resonant, it is equally probable in either direction, and its rate depends on the negative exponent of the separation distance. Tunneling is well known to occur in silicon clusters and forms the basis of silicon nanocrystal memories [172, 173]. Accurate calculation of the tunneling rate in ensembles of nanocrystals with different energies and spacings is a difficult problem, however. The tunneling rate can be approximated by the Wentzel-Kramers-Brouillain (WKB) approximation, as has been established for the case of double quantum wells [174–176]:

$$w_t = \frac{1}{t_{\text{tunnel}}} = \left(\frac{1}{2d_p} \right) \left(\frac{2E}{m_p} \right)^{1/2} \frac{16E(V-E)(m_p/m_b)}{[V + (m_p/m_b - 1)E]^2} \times \exp \left[-2d_b \left(\frac{2m_b(V-E)}{\hbar^2} \right)^{1/2} \right], \quad (46)$$

where m_b and m_p are the carrier effective masses in the barrier and the particle, d_p and d_b are the particle diameter and barrier thickness, V is the barrier height, and E is the carrier energy. This equation (using the corrected form

shown in [160]) has previously been employed to estimate tunneling rates between *asymmetric* quantum wells [176], despite the fact that (46) is strictly applicable only to the resonant case.

If the energy levels of adjacent clusters are mismatched, then tunneling must be “assisted” by emission or absorption of phonons. The tunneling rate dependence on the energy gap, ΔE , and the phonon energies (within the clusters and in the SiO_2 matrix) for these mechanisms is not well known and may need to be estimated experimentally if sufficiently narrow size distributions can be obtained. Recently, computer simulations showed [160] that a large Stokes shift between absorption and emission in the specimen as a whole can occur as a result of tunneling between nanocrystals although, as for the quantum well case, (46) was used without accounting for phonon-assisted tunneling.

The second fundamental interaction mechanism is resonance energy transfer, or “Forster transfer” [177]. In this mechanism, electron-hole pairs may “migrate” from particle to particle by a dipole-dipole or higher-order multipole coupling, that is, the Forster process—which has already been established for the case of CdSe nanocrystals [178]. Others have shown that it applies to silicon nanocrystals also [30], although due to the indirect gap the rates can be much different (typically smaller) than for CdSe. Forster transfer is the basis for fluorescence resonance energy transfer (FRET) microscopy, and has been widely investigated in the case of interactions amongst the rare earth ions [179]. The distance dependence of the transition dipole transfer rate, w_d , is given by $w_d = w_{\text{PL}}(R_0/r)^6$, where w_{PL} is the PL rate, R_0 is the distance at which the transfer rate and the PL rate are equal, and r is the distance between the edges of the particles. R_0 itself depends on the spectral overlap integral between the donor (D) and acceptor (A) clusters, and is, therefore, technically different for any pair of nanocrystals undergoing this process. Previous work in CdSe nanocrystals has assumed that the energy levels must be resonant for the Forster transfer to occur [178], however this is not strictly true: phonon-assisted Forster transfer has been calculated for the rare earth ions and should apply to nanocrystals as well. In the Miyakawa-Dexter theory [180], the resonant Forster rate is modified by considering the electron-phonon coupling parameters in the density-of-states function for the donor and activator ions. In this way, one obtains [180]:

$$w_{\text{dip}} = w_{\text{pl}} \left(\frac{R_0}{r} \right)^6 \exp(-\beta \Delta E), \quad (47)$$

where β depends on the electron-phonon coupling strength, and its value can be extracted from a plot of the transfer rate versus ΔE in silicate glass. From the data provided in [181], a rough estimate gives $\alpha = 0.0018$ for rare earth ions embedded in SiO_2 , where α indicates internal transitions and is about twice the value of β [180]. Unfortunately, the value of β is much more difficult to obtain experimentally for silicon NCs, as a result of the size distributions (i.e., every NC is slightly different; whereas all rare earth ions of the same type have identical properties).

The Miyakawa-Dexter model has been widely discussed and applied extensively in the case of transfer between

different rare earth ions [182–184]. In the present case, one may assume that the energy difference is lost to phonons in the surrounding silicate glass, as would be the case for isolated “point” dipoles such as the rare earth ions. As the energy gap grows, the transfer rate decreases exponentially, and experimentally, for rare earth ions at least, this trend shows little variation despite the many simplifications in the Miyakawa-Dexter model [185]. The effective Forster distance, R_0 , is more difficult to obtain, since it is not practical to calculate the overlap integral (including phonon sidebands) for every possible pair of interacting particles in a sample. Therefore, an experimental approach is taken to approximate a single R_0 value for all pairs of particles. By varying the distance between layers of interacting particles and using the geometrical constraints imposed by interacting layers (as opposed to two point dipoles) [186], an estimated value of $R_0 = 5$ nm was used in the simulations. Obviously, this is a significant simplification and it must be stressed that the results remain approximate until phonon-assisted multipole transfer between all possible pairs of NCs can be calculated in a reasonable way.

The simulation setup was done exactly as described previously: every particle was populated with a single electron-hole pair at time $t = 0$. This time, the effect of nonradiative traps was not included in order to show only the energy migration effects. Next, for every nanocluster the probabilities associated with each of the four processes described above (radiative decay, nonradiative decay, tunneling, and Forster transfer) were calculated in random order (the NCs themselves are also checked randomly) and compared to a flat-probability random number between 0 and 1 to determine whether one of these four events occurred. When the calculation started, the simulation timestep was 1×10^{-12} s. After iterating through all the particles, the time increments by one picosecond and the process repeats. If ten complete iterations through all the clusters (in randomized order each time) produce no events of any kind, the timestep is multiplied by a factor of ten. In this way, it is possible to overcome the otherwise impossible computational limits associated with the vastly different rates for the different processes. The simulation ends when there are no electron-hole pairs left. When a particle radiates, the energy of the outgoing photon is stored for the spectral output function, and the time is recorded in order to plot the decay of the luminescence. Finally, a set of tests were performed to find the minimum sample size for which edge effects (due to the finite box size) became unobservable. A simulation of 5,000 particles was found to provide sufficiently short computation time (~ 12 hours on a 2.6 GHz CPU) and no observable edge effects. Auger effects were not simulated, which effectively approximates the behavior of a lightly pumped ensemble.

Figure 21 shows the PL spectrum with and without the Forster and tunneling “energy migration” interactions. In the first few nanoseconds, numerous tunneling events and dipole-dipole interactions occurred. The rates for these processes for adjacent nanocrystals are many orders of magnitude faster than the radiative decay processes. Some nonradiative trapping can also occur early on in the simulation. Even after only a few picoseconds, there was already

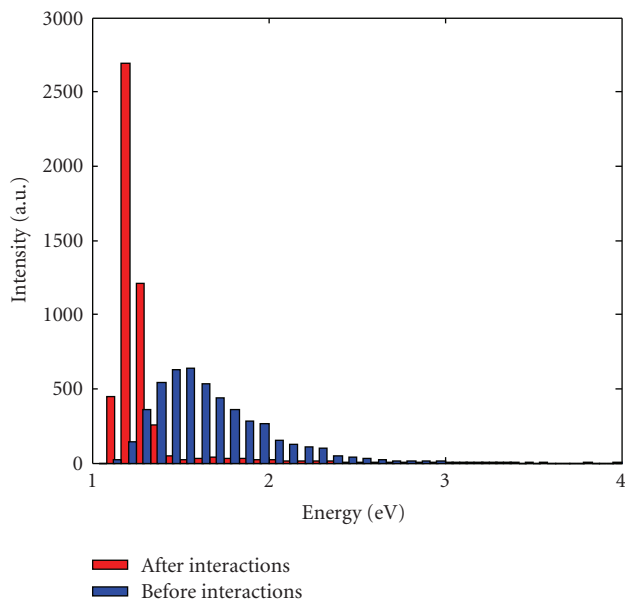


FIGURE 21: Effect of carrier migration on the PL histogram of a silicon NC ensemble with a lognormal distribution $S = 0.21$, $M = 0.74$, and volume fill = 35%. The PL spectrum is strongly redshifted as a result of tunneling and Forster transfer in this densely packed ensemble. For this simulation, there were no non-radiative defects and infinite barriers were assumed. The “after interactions” result agrees reasonably well with the observed CW PL from a specimen with the same size distribution and volume fill [47].

a small fraction of charged nanocrystals due to electron or hole tunneling events. Many nanocrystals had no remaining charge carriers, and many others—predominantly the larger ones—had multiple electron-hole pairs. After 500 ns, many thousands of tunneling and dipole events occurred and most of the smaller clusters were devoid of charge carriers. In the microsecond timescale, radiative decay joins the longer-range energy transfer events, and by 100 microseconds only a few excited nanocrystals remained. The long wavelength of the emitting states (compared to absorption)—as well as a decrease in the overall skewness of the PL peak—in dense ensembles of Si NCs can originate predominantly from energy migration, indicating that the large Stokes shift in ensembles of Si NCs can be attributed, at least in part, to these effects. We have also found that the degree of “stretching” of the PL decay depends on the resulting ensemble of particles with electron-hole pairs; in the absence of nonradiative effects the PL lifetime is longer but if defects are introduced the PL lifetime can be dramatically shorter in the presence of energy migration, due to the greater statistical probability for defects to occur on larger NCs. Based on the initial results presented here, it would seem that the combination of theory with computational simulations may be one of the best tools to obtain a more thorough understanding of the complicated and controversial luminescence behavior of ensembles of silicon clusters.

At this point, although instructive, the simulations have obvious limitations that we are currently working to overcome. For example, we have not incorporated the

effects of Si=O surface bonds, which again may cause the simulated spectra to peak at wavelengths slightly too short, especially for smaller NCs. An obvious limitation of the model is the estimate of a single value of R_0 for all Forster interactions. The fact that phonon-assisted Forster processes among silicon NCs remain beyond theoretical scope [30], required a further assumption that the phonon-assisted rate had a similar dependence on ΔE as for the case for rare-earth ions in silicate glass. Higher-order multipole interactions were also ignored. Finally, unlike the case in which infinite barriers were assumed [160], here the resulting spectra are narrower and redder than observed experimentally.

Nevertheless, the implications of these simulations are clear. First, the two energy transfer mechanisms dominate the PL spectrum when the clusters are separated by less than 2 nm, and can still be significant in the case of Forster transfer over distances of 5 nm or more. Therefore, in most of the experimental work reported to date, NC-NC interactions strongly affect the PL spectrum. Multilayer simulations such as that shown in Figure 18 have also been performed, and the results are consistent with the experimentally observed spectral blueshift and increased lifetime in multilayered samples. The decay exponent β shows a more complicated behavior however; its value depends on the distribution of lifetimes which in turn depends on the size distribution and the nonradiative defect concentration. Next, in most samples the largest clusters act as depressions in the energy landscape and can attract numerous charge carriers. Under high pump rates, therefore, the Auger problem can become significant when the clusters are reasonably closely separated. Next, the simulations can easily be extended to model the sensitizing action of the NCs on erbium ions; this work is currently ongoing and uses the Forster mechanism of energy transfer. The results seem consistent with the reports of optical gain (ASE) in very short timescales before significant amount of energy transfer can occur (as long as the size distribution is sufficiently narrow to have a narrow enough gain profile) but for CW stimulated emission the NCs must be sufficiently well separated to prevent carrier migration and buildup on the largest clusters. The largest NCs are also the ones most likely to contain a defect, so their effects on the emission spectrum and gain profile are extremely strong in most samples where carrier interactions occur. Therefore, in the final section of this paper we briefly discuss the controversial observations of optical gain in silicon nanocrystals, and the implications of the theoretical results in Sections 1–3 and the simulations of Section 4 for the development of photonic devices relating to stimulated emission in silicon nanocrystals.

4.4. Stimulated emission in Si NCs

There have been numerous recent reports of optical gain in silicon nanocrystals [165, 187–189], and stimulated emission was reported in [190], although to our knowledge the results are not fully understood. Many of these studies deduced the presence of gain by analyzing data from the variable strip length (VSL) technique [191]. This method has been discussed in great detail in the literature, owing to the many possible sources of error. In general, a planar waveguide film

containing silicon nanocrystals is optically pumped from above (parallel to the specimen surface normal). The pump laser beam is first incident on a variable-length slit, such that only a diffraction-limited strip of the sample is pumped. The waveguided PL signal is then collected from the edge of the specimen in the direction parallel to the axis of the excitation strip. The signature of optical gain is a superlinear increase in the PL intensity (marked by a distinct transition) for constant pump flux as the strip is lengthened. This is due to the stimulated emission from excited nanocrystals interacting with photons originally emitted at the farther end of the excitation strip. This method, along with some corrections, has been one of the most widely used methods to support optical gain in Si NCs. The other method that has been used, although somewhat less extensively, is the standard pump-probe technique. In that case, the transmission of a probe beam is measured as a function of the probe power, with the transition from loss to gain marked by a shift from positive to negative absorption of the pump. This method has been used both for Si NC waveguides and in single-pass measurements.

The presence (or absence) of SE in Si NCs is a subject of much debate. After the initial report [5], which used both the VSL and the single-pass pump-probe methods to report a net modal gain for a silicon nanocrystal film of 100 cm^{-1} , a net material gain of 10^4 cm^{-1} , and a gain cross section per NC of $\sim 10^{-16} \text{ cm}^2$, numerous groups have searched for optical gain in ensembles of Si NCs. The results of these investigations have not been entirely consistent. Currently, there seems to be some possible evidence in favor of SE in an Auger-limited time window of a few ns after intense pulsed excitation, with gain cross sections per NC of $\sim 10^{-16} \text{ cm}^2$ in the extreme short wavelength side of the broad emission band [189]. However, in comparison to the case for CdSe NCs, where there is clear and unequivocal observations of SE (e.g., marked by a sudden superlinear increase of PL intensity with pumping power in a narrow wavelength range), in the case of Si NCs the signatures of SE have been extracted from fairly elaborate and complicated experiments, and the results have shown significant specimen-to-specimen variation. A brief examination of the limiting factors and key specimen requirements for SE in ensembles of silicon NCs would be of use with the ultimate objective demonstrating, unequivocally, stimulated emission in nanocrystalline silicon.

Gain profile

The calculations discussed in Sections 1–3 indicate several key factors relating to optical gain in Si NCs. First, for size distributions produced by standard physical vapor deposition or ion implantation methods (including multilayering) the gain profile becomes extremely wide. This reduces the gain coefficient and the gain cross section per NC in the sample. Dal Negro et al. [187], for example, reported a gain coefficient of $1600 \pm 300 \text{ cm}^{-1}$ at $\lambda = 750 \text{ nm}$, with a gain cross section at this wavelength of $3 \times 10^{-16} \text{ cm}^2$ per NC. Since the overall PL spectra generally peak at longer wavelengths, only a small fraction of the NCs may actually emit within the reported gain window. Most of the nanocrystals, therefore, may not contribute to SE

and are in fact, detrimental as a result of confined carrier absorption, scattering, and other loss mechanisms they can cause. If Si NCs could be prepared with a size distribution similar to that for CdSe (e.g., 5% standard deviation), the theoretical gain coefficient per nanocrystal in the specimen as a whole could increase by a fairly large factor, simply because a greater number of NCs could contribute to the overall gain at the peak wavelength. Therefore, true monodispersity (i.e., overall emission profile controlled by homogeneous broadening) is likely to be a requirement for producing SE in ensembles of Si NCs.

Secondly, the size distribution presents an inherent problem for laser excitation of the specimen. With the exception of erbium doped waveguides that used LED excitation [192], SE or gain is reported as a result of pumping the sample with a laser. Laser excitation implies a narrow excitation energy window, and only NCs that happen to have a transition within that window will be absorbing. In a given sample with a wide distribution, therefore, many of the NCs may not absorb and cannot contribute to the overall specimen gain. Furthermore, these “unexcited” NCs can enhance the energy migration or other undesired effects discussed above.

The cluster-cluster energy transfer mechanisms found to be important in the overall luminescence spectrum also have implications for the presence of SE in ensembles of Si NCs. Generally, a high-pump rate is necessary to observe the transition from loss to gain. Under such high rates, one can assume a relatively large number of excitons per NC (we hesitate somewhat to suggest a number as high as 100) [5] but at least 1 exciton per NC is readily possible. In this case, charge carriers will be rapidly redistributed through the tunneling and Forster mechanisms, on the sub-nanosecond time scale for a typical volume filling fraction of NCs (the volume fraction ultimately controls the average NC-NC spacing). Therefore, in a short time after the initial pump pulse, one has the accumulation of charge carriers on the largest NCs as a result of tunneling and Forster interactions. This drastically decreases the number of NCs that can contribute to the gain spectrum and can lead to enhanced nonradiative trapping and undesirable Auger interactions. This may be one reason that gain may only occur in very short timescales, as suggested in several recent experimental works [189], and only in certain specimens but not in others. In such cases, gain may only build up before the energy migration processes have occurred, and will be very susceptible to the average NC-NC spacing (and size distribution, as above) from specimen to specimen. The fact that the gain, if present, occurs on the short-wavelength side of the PL band is also consistent with the idea that the gain occurs before the charge carriers transfer to the larger and “redder” nanoclusters. By increasing the NC-NC spacing it should be possible to limit the energy migration problem, due to the strong distance dependence of the main processes. This may be accomplished by, for example, freeing the Si NCs via an HF etch and redepositing them at a known (low) filling fraction, an idea we are currently exploring. Other methods are also possible.

Additionally, the level degeneracies calculated in Section 3 imply a further key limiting factor for SE in silicon

nanocrystals. With a two-fold degeneracy or more, more than 1 exciton per NC must be present, on average, in order to switch from loss to gain, which in turn raises the problem of the Auger interactions. This number becomes higher as the degeneracy of the electron and hole levels increases. In the case of CdSe NCs, Klimov et al. [193] have shown that one way to avoid this problem is to separate electrons and holes in a core-shell nanostructure, thereby creating a large crystal-field shift of the absorption spectrum. Such problems (and solutions) may well apply to Si NCs also.

5. CONCLUSION

There is now an enormous wealth of data on ensembles of silicon nanoclusters. The difficulties in understanding the optical properties of these materials are caused by the indirect gap of silicon, the large homogeneous, and inhomogeneous broadening, the possible effects of radiative centers and nonradiative traps, the cluster size dependence of the lifetimes, and energy transfer. All these processes must be considered when evaluating a luminescence spectrum; it is insufficient to study the luminescence as a function of cluster size only, although size undoubtedly plays a role. Unfortunately, owing to the complexity of the materials, there are many contradictory observations and much uncertainty in the literature. We hope that, with this paper, we have been able to summarize some of the main theoretical and computational results that should help to work out the problems and issues with our understanding of ensembles of silicon NCs. We hope that the combination of theory and simulation, new single particle spectroscopies [20], and new synthesis methods [194] will eventually lead to unequivocal and readily reproducible reports of stimulated emission in Si NCs.

ACKNOWLEDGMENTS

A. Meldrum and R. Lockwood acknowledge and thank iCORE and NSERC. V. A. Belyakov and V. A. Burdov acknowledge RFBR, Russian Ministry of Education and Science (“Development of Scientific Potential of the High School” program), and the “Dynasty” foundation (Russia) for the partial financial support of this work.

REFERENCES

- [1] H. Takagi, H. Ogawa, Y. Yamazaki, A. Ishizaki, and T. Nakagiri, “Quantum size effects on photoluminescence in ultrafine Si particles,” *Applied Physics Letters*, vol. 56, no. 24, pp. 2379–2380, 1990.
- [2] L. T. Canham, “Silicon quantum wire array fabrication by electrochemical and chemical dissolution of wafers,” *Applied Physics Letters*, vol. 57, no. 10, pp. 1046–1048, 1990.
- [3] P. D. J. Calcott, K. J. Nash, L. T. Canham, M. J. Kane, and D. Brumhead, “Identification of radiative transitions in highly porous silicon,” *Journal of Physics: Condensed Matter*, vol. 5, no. 7, pp. L91–L98, 1993.
- [4] P. D. J. Calcott, K. J. Nash, L. T. Canham, M. J. Kane, and D. Brumhead, “Spectroscopic identification of the

- luminescence mechanism of highly porous silicon,” *Journal of Luminescence*, vol. 57, no. 1–6, pp. 257–269, 1993.
- [5] L. Pavesi, L. Dal Negro, C. Mazzoleni, G. Franzò, and F. Priolo, “Optical gain in silicon nanocrystals,” *Nature*, vol. 408, no. 6811, pp. 440–444, 2000.
 - [6] D. Kovalev, H. Heckler, G. Polisski, and F. Koch, “Optical properties of Si nanocrystals,” *Physica Status Solidi B*, vol. 215, no. 2, pp. 871–932, 1999.
 - [7] L. Khriachtchev, M. Räsänen, S. Novikov, O. Kilpelä, and J. Sinkkonen, “Raman scattering from very thin Si layers of Si/SiO₂ superlattices: experimental evidence of structural modification in the 0.8–3.5 nm thickness region,” *Journal of Applied Physics*, vol. 86, no. 10, pp. 5601–5608, 1999.
 - [8] M. V. Wolkin, J. Jorne, P. M. Fauchet, G. Allan, and C. Delerue, “Electronic states and luminescence in porous silicon quantum dots: the role of oxygen,” *Physical Review Letters*, vol. 82, no. 1, pp. 197–200, 1999.
 - [9] A. B. Filonov, S. Ossicini, F. Bassani, and F. Arnaud d’Avitaya, “Effect of oxygen on the optical properties of small silicon pyramidal clusters,” *Physical Review B*, vol. 65, no. 19, Article ID 195317, 9 pages, 2002.
 - [10] D. I. Tetelbaum, I. A. Karpovich, M. V. Stepikhova, V. G. Shengurov, K. A. Markov, and O. N. Gorshkov, “Characteristics of photoluminescence in SiO₂ with Si nanoinclusions produced by ion implantation,” *Surface Investigation X-Ray, Synchrotron and Neutron Techniques*, vol. 14, no. 5, pp. 601–604, 1998.
 - [11] M. Fujii, A. Mimura, S. Hayashi, and K. Yamamoto, “Photoluminescence from Si nanocrystals dispersed in phosphosilicate glass thin films: improvement of photoluminescence efficiency,” *Applied Physics Letters*, vol. 75, no. 2, pp. 184–186, 1999.
 - [12] A. Miura, M. Fujii, S. Hayashi, D. Kovalev, and F. Koch, “Photoluminescence and free-electron absorption in heavily phosphorus-doped Si nanocrystals,” *Physical Review B*, vol. 62, no. 19, pp. 12625–12627, 2000.
 - [13] M. Fujii, A. Mimura, S. Hayashi, Y. Yamamoto, and K. Murakami, “Hyperfine structure of the electron spin resonance of phosphorus-doped Si nanocrystals,” *Physical Review Letters*, vol. 89, no. 20, Article ID 206805, 4 pages, 2002.
 - [14] M. Fujii, K. Toshikiyo, Y. Takase, Y. Yamaguchi, and S. Hayashi, “Below bulk-band-gap photoluminescence at room temperature from heavily P- and B-doped Si nanocrystals,” *Journal of Applied Physics*, vol. 94, no. 3, pp. 1990–1995, 2003.
 - [15] M. Fujii, Y. Yamaguchi, Y. Takase, K. Ninomiya, and S. Hayashi, “Control of photoluminescence properties of Si nanocrystals by simultaneously doping *n*- and *p*-type impurities,” *Applied Physics Letters*, vol. 85, no. 7, pp. 1158–1160, 2004.
 - [16] G. A. Kachurin, S. G. Cherkova, V. A. Volodin, et al., “Implantation of P ions in SiO₂ layers with embedded Si nanocrystals,” *Nuclear Instruments and Methods in Physics Research B*, vol. 222, no. 3–4, pp. 497–504, 2004.
 - [17] M. Fujii, Y. Yamaguchi, Y. Takase, K. Ninomiya, and S. Hayashi, “Photoluminescence from impurity codoped and compensated Si nanocrystals,” *Applied Physics Letters*, vol. 87, no. 21, Article ID 211919, 3 pages, 2005.
 - [18] G. A. Kachurin, S. G. Cherkova, V. A. Volodin, D. M. Marin, D. I. Tetelbaum, and H. Becker, “Effect of boron ion implantation and subsequent anneals on the properties of Si nanocrystals,” *Semiconductors*, vol. 40, no. 1, pp. 72–78, 2006.
 - [19] J. Valenta, R. Juhasz, and J. Linnros, “Photoluminescence spectroscopy of single silicon quantum dots,” *Applied Physics Letters*, vol. 80, no. 6, pp. 1070–1072, 2002.
 - [20] I. Sychugov, R. Juhasz, J. Valenta, and J. Linnros, “Narrow luminescence linewidth of a silicon quantum dot,” *Physical Review Letters*, vol. 94, no. 8, Article ID 087405, 4 pages, 2005.
 - [21] F. Priolo, G. Franzò, D. Pacifici, V. Vinciguerra, F. Iacona, and A. Irrera, “Role of the energy transfer in the optical properties of undoped and Er-doped interacting Si nanocrystals,” *Journal of Applied Physics*, vol. 89, no. 1, pp. 264–272, 2001.
 - [22] I. Balberg, E. Savir, and J. Jedrzejewski, “The mutual exclusion of luminescence and transport in nanocrystalline silicon networks,” *Journal of Non-Crystalline Solids*, vol. 338–340, pp. 102–105, 2004.
 - [23] J. Heitmann, F. Müller, L. Yi, M. Zacharias, D. Kovalev, and F. Eichhorn, “Excitons in Si nanocrystals: confinement and migration effects,” *Physical Review B*, vol. 69, no. 19, Article ID 195309, 7 pages, 2004.
 - [24] T. Kawazoe, K. Kobayashi, and M. Ohtsu, “Optical nanofountain: a biomimetic device that concentrates optical energy in a nanometric region,” *Applied Physics Letters*, vol. 86, no. 10, Article ID 103102, 3 pages, 2005.
 - [25] T. Förster, “Versuche zum zwischenmolekularen Übergang von elektronenanregungsenergie,” *Zeitschrift für Elektrochemie*, vol. 53, pp. 93–100, 1949.
 - [26] T. Förster, “Experimentelle und theoretische Untersuchung des zwischenmolekularen Übergangs von Elektronenanregungsenergie,” *Zeitschrift für Naturforschung A*, vol. 4, pp. 321–327, 1949.
 - [27] D. L. Dexter, “A theory of sensitized luminescence in solids,” *The Journal of Chemical Physics*, vol. 21, no. 5, pp. 836–850, 1953.
 - [28] C. R. Kagan, C. B. Murray, M. Nirmal, and M. G. Bawendi, “Electronic energy transfer in CdSe quantum dot solids,” *Physical Review Letters*, vol. 76, no. 9, pp. 1517–1520, 1996.
 - [29] S. A. Crooker, J. A. Hollingsworth, S. Tretiak, and V. I. Klimov, “Spectrally resolved dynamics of energy transfer in quantum-dot assemblies: towards engineered energy flows in artificial materials,” *Physical Review Letters*, vol. 89, no. 18, Article ID 186802, 4 pages, 2002.
 - [30] G. Allan and C. Delerue, “Energy transfer between semiconductor nanocrystals: validity of Förster’s theory,” *Physical Review B*, vol. 75, no. 19, Article ID 195311, 8 pages, 2007.
 - [31] Y. Kanemitsu, “Photoluminescence spectrum and dynamics in oxidized silicon nanocrystals: a nanoscopic disorder system,” *Physical Review B*, vol. 53, no. 20, pp. 13515–13520, 1996.
 - [32] J. Linnros, N. Lalic, A. Galeckas, and V. Grivickas, “Analysis of the stretched exponential photoluminescence decay from nanometer-sized silicon crystals in SiO₂,” *Journal of Applied Physics*, vol. 86, no. 11, pp. 6128–6134, 1999.
 - [33] M. Dovrat, Y. Goshen, J. Jedrzejewski, I. Balberg, and A. Sa’ar, “Radiative versus nonradiative decay processes in silicon nanocrystals probed by time-resolved photoluminescence spectroscopy,” *Physical Review B*, vol. 69, no. 15, Article ID 155311, 8 pages, 2004.
 - [34] F. Trojánek, K. Neudert, M. Bittner, and P. Malý, “Picosecond photoluminescence and transient absorption in silicon nanocrystals,” *Physical Review B*, vol. 72, no. 7, Article ID 075365, 6 pages, 2005.
 - [35] R. J. Walters, J. Kalkman, A. Polman, H. A. Atwater, and M. J. A. de Dood, “Photoluminescence quantum efficiency of dense silicon nanocrystal ensembles in Si O₂,” *Physical Review B*, vol. 73, no. 13, Article ID 132302, 4 pages, 2006.
 - [36] C. Delerue, G. Allan, C. Reynaud, O. Guillois, G. Ledoux, and F. Huisken, “Multiexponential photoluminescence decay in

- indirect-gap semiconductor nanocrystals," *Physical Review B*, vol. 73, no. 23, Article ID 235318, 4 pages, 2006.
- [37] A. Meldrum, R. F. Haglund Jr., L. A. Boatner, and C. W. White, "Nanocomposite materials formed by ion implantation," *Advanced Materials*, vol. 13, no. 19, pp. 1431–1444, 2001.
- [38] A. Meldrum, L. A. Boatner, and C. W. White, "Nanocomposites formed by ion implantation: recent developments and future opportunities," *Nuclear Instruments and Methods in Physics Research B*, vol. 178, no. 1–4, pp. 7–16, 2001.
- [39] K. S. Zhuravlev, A. M. Gilinsky, and A. Yu. Kobitsky, "Mechanism of photoluminescence of Si nanocrystals fabricated in a SiO₂ matrix," *Applied Physics Letters*, vol. 73, no. 20, pp. 2962–2964, 1998.
- [40] Y. Kanemitsu, N. Shimizu, T. Komoda, P. L. F. Hemment, and B. J. Sealy, "Photoluminescent spectrum and dynamics of Si⁺-ion-implanted and thermally annealed SiO₂ glasses," *Physical Review B*, vol. 54, no. 20, pp. R14329–R14332, 1996.
- [41] S. Guha, "Characterization of Si⁺ ion-implanted SiO₂ films and silica glasses," *Journal of Applied Physics*, vol. 84, no. 9, pp. 5210–5217, 1998.
- [42] L. Dal Negro, M. Cazzanelli, L. Pavesi, et al., "Dynamics of stimulated emission in silicon nanocrystals," *Applied Physics Letters*, vol. 82, no. 26, pp. 4636–4638, 2003.
- [43] L. Tsybeskov, K. D. Hirschman, S. P. Duttagupta, et al., "Nanocrystalline-silicon superlattice produced by controlled recrystallization," *Applied Physics Letters*, vol. 72, no. 1, pp. 43–45, 1998.
- [44] M. Zacharias, J. Heitmann, R. Scholz, U. Kahler, M. Schmidt, and J. Blasing, "Size-controlled highly luminescent silicon nanocrystals: a SiO/SiO₂ superlattice approach," *Applied Physics Letters*, vol. 80, no. 4, pp. 661–663, 2002.
- [45] M. H. Nayfeh, S. Rao, N. Barry, et al., "Observation of laser oscillation in aggregates of ultrasmall silicon nanoparticles," *Applied Physics Letters*, vol. 80, no. 1, pp. 121–123, 2002.
- [46] A. Meldrum, A. Hryciw, A. N. MacDonald, et al., "Photoluminescence in the silicon-oxygen system," *Journal of Vacuum Science and Technology A*, vol. 24, no. 3, pp. 713–717, 2006.
- [47] J. Wang, X. F. Wang, Q. Li, A. Hryciw, and A. Meldrum, "The microstructure of SiO thin films: from nanoclusters to nanocrystals," *Philosophical Magazine*, vol. 87, no. 1, pp. 11–27, 2007.
- [48] G. Ledoux, J. Gong, F. Huisken, O. Guillois, and C. Reynaud, "Photoluminescence of size-separated silicon nanocrystals: confirmation of quantum confinement," *Applied Physics Letters*, vol. 80, no. 25, pp. 4834–4836, 2002.
- [49] T.-Y. Kim, N.-M. Park, K.-H. Kim, et al., "Quantum confinement effect of silicon nanocrystals in situ grown in silicon nitride films," *Applied Physics Letters*, vol. 85, no. 22, pp. 5355–5357, 2004.
- [50] P. M. Fauchet, "Light emission from Si quantum dots," *Materials Today*, vol. 8, no. 1, pp. 26–33, 2005.
- [51] Y. Kanemitsu, S. Okamoto, M. Otobe, and S. Oda, "Photoluminescence mechanism in surface-oxidized silicon nanocrystals," *Physical Review B*, vol. 55, no. 12, pp. R7375–R7378, 1997.
- [52] Y. Kanzawa, T. Kageyama, S. Takeoka, M. Fujii, S. Hayashi, and K. Yamamoto, "Size-dependent near-infrared photoluminescence spectra of Si nanocrystals embedded in SiO₂ matrices," *Solid State Communications*, vol. 102, no. 7, pp. 533–537, 1997.
- [53] B. Garrido Fernandez, M. López, C. García, et al., "Influence of average size and interface passivation on the spectral emission of Si nanocrystals embedded in SiO₂," *Journal of Applied Physics*, vol. 91, no. 2, pp. 798–807, 2002.
- [54] T. van Buuren, L. N. Dinh, L. L. Chase, W. J. Siekhaus, and L. J. Terminello, "Changes in the electronic properties of Si nanocrystals as a function of particle size," *Physical Review Letters*, vol. 80, no. 17, pp. 3803–3806, 1998.
- [55] S. Schuppler, S. L. Friedman, M. A. Marcus, et al., "Size, shape, and composition of luminescent species in oxidized Si nanocrystals and H-passivated porous Si," *Physical Review B*, vol. 52, no. 7, pp. 4910–4925, 1995.
- [56] B. Garrido, M. López, O. González, A. Pérez-Rodríguez, J. R. Morante, and C. Bonafos, "Correlation between structural and optical properties of Si nanocrystals embedded in SiO₂: the mechanism of visible light emission," *Applied Physics Letters*, vol. 77, no. 20, pp. 3143–3145, 2000.
- [57] S. Takeoka, M. Fujii, and S. Hayashi, "Size-dependent photoluminescence from surface-oxidized Si nanocrystals in a weak confinement regime," *Physical Review B*, vol. 62, no. 24, pp. 16820–16825, 2000.
- [58] M. Lannoo, C. Delerue, and G. Allan, "Theory of radiative and nonradiative transitions for semiconductor nanocrystals," *Journal of Luminescence*, vol. 70, no. 1–6, pp. 170–184, 1996.
- [59] C. Garcia, B. Garrido, P. Pellegrino, et al., "Size dependence of lifetime and absorption cross section of Si nanocrystals embedded in SiO₂," *Applied Physics Letters*, vol. 82, no. 10, pp. 1595–1597, 2003.
- [60] L. Dal Negro, M. Cazzanelli, N. Daldosso, et al., "Stimulated emission in plasma-enhanced chemical vapour deposited silicon nanocrystals," *Physica E*, vol. 16, no. 3–4, pp. 297–308, 2003.
- [61] M. Fujii, D. Kovalev, B. Goller, S. Minobe, S. Hayashi, and V. Yu. Timoshenko, "Time-resolved photoluminescence studies of the energy transfer from excitons confined in Si nanocrystals to oxygen molecules," *Physical Review B*, vol. 72, no. 16, Article ID 165321, 8 pages, 2005.
- [62] S. Miura, T. Nakamura, M. Fujii, M. Inui, and S. Hayashi, "Size dependence of photoluminescence quantum efficiency of Si nanocrystals," *Physical Review B*, vol. 73, no. 24, Article ID 245333, 5 pages, 2006.
- [63] A. Yu. Kobitski, K. S. Zhuravlev, H. P. Wagner, and D. R. T. Zahn, "Self-trapped exciton recombination in silicon nanocrystals," *Physical Review B*, vol. 63, no. 11, Article ID 115423, 5 pages, 2001.
- [64] A. Sa'ar, M. Dovrat, J. Jedrzejewski, and I. Balberg, "Optical inter- and intra-band transitions in silicon nanocrystals: the role of surface vibrations," *Physica E*, vol. 38, no. 1–2, pp. 122–127, 2007.
- [65] F. A. Reboredo, A. Franceschetti, and A. Zunger, "Excitonic transitions and exchange splitting in Si quantum dots," *Applied Physics Letters*, vol. 75, no. 19, pp. 2972–2974, 1999.
- [66] F. A. Reboredo, A. Franceschetti, and A. Zunger, "Dark excitons due to direct Coulomb interactions in silicon quantum dots," *Physical Review B*, vol. 61, no. 19, pp. 13073–13087, 2000.
- [67] D. H. Feng, Z. Z. Xu, T. Q. Jia, X. X. Li, and S. Q. Gong, "Quantum size effects on exciton states in indirect-gap quantum dots," *Physical Review B*, vol. 68, no. 3, Article ID 035334, 7 pages, 2003.

- [68] H.-Ch. Weissker, J. Furthmüller, and F. Bechstedt, "Structure- and spin-dependent excitation energies and lifetimes of Si and Ge nanocrystals from *ab initio* calculations," *Physical Review B*, vol. 69, no. 11, Article ID 115310, 8 pages, 2004.
- [69] D. I. Tetelbaum, O. N. Gorshkov, S. A. Trushun, D. G. Revin, D. M. Gaponova, and W. Eckstein, "Enhancement of luminescence in ion implanted Si quantum dots in SiO₂ matrix by means of dose alignment and doping," *Nanotechnology*, vol. 11, no. 4, pp. 295–297, 2000.
- [70] D. I. Tetelbaum, S. A. Trushin, V. A. Burdov, A. I. Golovanov, D. G. Revin, and D. M. Gaponova, "Influence of phosphorus and hydrogen ion implantation on the photoluminescence of SiO₂ with Si nano-inclusions," *Nuclear Instruments and Methods in Physics Research B*, vol. 174, no. 1-2, pp. 123–129, 2001.
- [71] D. I. Tetelbaum, O. N. Gorshkov, V. A. Burdov, et al., "The influence of P⁺, B⁺, and N⁺ ion implantation on the luminescence properties of the SiO₂: nc-Si system," *Physics of the Solid State*, vol. 46, no. 1, pp. 17–21, 2004.
- [72] A. N. Mikhaylov, D. I. Tetelbaum, V. A. Burdov, et al., "Effect of ion doping with donor and acceptor impurities on intensity and lifetime of photoluminescence from SiO₂ films with silicon quantum dots," *Journal of Nanoscience and Nanotechnology*, vol. 8, no. 2, pp. 780–788, 2008.
- [73] V. A. Belyakov and V. A. Burdov, "Valley-orbit splitting in doped nanocrystalline silicon: k-p calculations," *Physical Review B*, vol. 76, no. 4, Article ID 045335, 12 pages, 2007.
- [74] B. Delley and E. F. Steigmeier, "Size dependence of band gaps in silicon nanostructures," *Applied Physics Letters*, vol. 67, no. 16, p. 2370, 1995.
- [75] I. Vasiliev, S. Ögüt, and J. R. Chelikowsky, "Ab initio absorption spectra and optical gaps in nanocrystalline silicon," *Physical Review Letters*, vol. 86, no. 9, pp. 1813–1816, 2001.
- [76] C. S. Garoufalidis, A. D. Zdetsis, and S. Grimme, "High level *ab initio* calculations of the optical gap of small silicon quantum dots," *Physical Review Letters*, vol. 87, no. 27, Article ID 276402, 4 pages, 2001.
- [77] H.-Ch. Weissker, J. Furthmüller, and F. Bechstedt, "Optical properties of Ge and Si nanocrystallites from *ab initio* calculations. II. Hydrogenated nanocrystallites," *Physical Review B*, vol. 65, no. 15, Article ID 155328, 7 pages, 2002.
- [78] X.-H. Peng, S. Ganti, A. Alizadeh, P. Sharma, S. K. Kumar, and S. K. Nayak, "Strain-engineered photoluminescence of silicon nanoclusters," *Physical Review B*, vol. 74, no. 3, Article ID 035339, 5 pages, 2006.
- [79] L.-W. Wang and A. Zunger, "Solving Schrödinger's equation around a desired energy: application to silicon quantum dots," *The Journal of Chemical Physics*, vol. 100, no. 3, pp. 2394–2397, 1994.
- [80] S. Ögüt, J. R. Chelikowsky, and S. G. Louie, "Quantum confinement and optical gaps in Si nanocrystals," *Physical Review Letters*, vol. 79, no. 9, pp. 1770–1773, 1997.
- [81] A. Franceschetti and A. Zunger, "Pseudopotential calculations of electron and hole addition spectra of InAs, InP, and Si quantum dots," *Physical Review B*, vol. 62, no. 4, pp. 2614–2623, 2000.
- [82] C. Bulutay, "Interband, intraband, and excited-state direct photon absorption of silicon and germanium nanocrystals embedded in a wide band-gap lattice," *Physical Review B*, vol. 76, no. 20, Article ID 205321, 14 pages, 2007.
- [83] S. Y. Ren and J. D. Dow, "Hydrogenated Si clusters: band formation with increasing size," *Physical Review B*, vol. 45, no. 12, pp. 6492–6496, 1992.
- [84] N. A. Hill and K. B. Whaley, "Size dependence of excitons in silicon nanocrystals," *Physical Review Letters*, vol. 75, no. 6, pp. 1130–1133, 1995.
- [85] Y. M. Niquet, C. Delerue, G. Allan, and M. Lannoo, "Method for tight-binding parametrization: application to silicon nanostructures," *Physical Review B*, vol. 62, no. 8, pp. 5109–5116, 2000.
- [86] S. Lee, L. Jönsson, J. W. Wilkins, G. W. Bryant, and G. Klimeck, "Electron-hole correlations in semiconductor quantum dots with tight-binding wave functions," *Physical Review B*, vol. 63, no. 19, Article ID 195318, 13 pages, 2001.
- [87] M. Rohlfing and S. G. Louie, "Excitonic effects and the optical absorption spectrum of hydrogenated Si clusters," *Physical Review Letters*, vol. 80, no. 15, pp. 3320–3323, 1998.
- [88] C. Delerue, M. Lannoo, and G. Allan, "Excitonic and quasiparticle gaps in Si nanocrystals," *Physical Review Letters*, vol. 84, no. 11, pp. 2457–2460, 2000.
- [89] E. Luppi, F. Iori, R. Magri, et al., "Excitons in silicon nanocrystallites: the nature of luminescence," *Physical Review B*, vol. 75, no. 3, Article ID 033303, 4 pages, 2007.
- [90] T. Takagahara and K. Takeda, "Theory of the quantum confinement effect on excitons in quantum dots of indirect-gap materials," *Physical Review B*, vol. 46, no. 23, pp. 15578–15581, 1992.
- [91] J. M. Ferreyra and C. R. Proetto, "Quantum size effects on excitonic Coulomb and exchange energies in finite-barrier semiconductor quantum dots," *Physical Review B*, vol. 60, no. 15, pp. 10672–10675, 1999.
- [92] V. A. Burdov, "Electron and hole spectra of silicon quantum dots," *Journal of Experimental and Theoretical Physics*, vol. 94, no. 2, pp. 411–418, 2002.
- [93] V. A. Burdov, "Dependence of the optical gap of Si quantum dots on the dot size," *Semiconductors*, vol. 36, no. 10, pp. 1154–1158, 2002.
- [94] A. S. Moskalenko and I. N. Yassievich, "Excitons in Si nanocrystals," *Physics of the Solid State*, vol. 46, no. 8, pp. 1508–1519, 2004.
- [95] A. S. Moskalenko, J. Berakdar, A. A. Prokofiev, and I. N. Yassievich, "Single-particle states in spherical Si/SiO₂ quantum dots," *Physical Review B*, vol. 76, no. 8, Article ID 085427, 9 pages, 2007.
- [96] M. Bruno, M. Palumbo, A. Marini, R. Del Sole, and S. Ossicini, "From Si nanowires to porous silicon: the role of excitonic effects," *Physical Review Letters*, vol. 98, no. 3, Article ID 036807, 4 pages, 2007.
- [97] L. Yang, C. D. Spataru, S. G. Louie, and M. Y. Chou, "Enhanced electron-hole interaction and optical absorption in a silicon nanowire," *Physical Review B*, vol. 75, no. 20, Article ID 201304, 4 pages, 2007.
- [98] M. Voos, Ph. Uzan, C. Delalande, G. Bastard, and A. Halimaoui, "Visible photoluminescence from porous silicon: a quantum confinement effect mainly due to holes," *Applied Physics Letters*, vol. 61, no. 10, pp. 1213–1215, 1992.
- [99] A. A. Kopylov, "Two-hump" structure and parameters of the X minimum of the conduction band of cubic III-V semiconductors," *Soviet Physics. Semiconductors-USSR*, vol. 16, no. 12, pp. 1380–1383, 1982.
- [100] C. Delerue and M. Lannoo, *Nanostructures: Theory and Modeling*, Springer, Berlin, Germany, 2004.
- [101] N. M. Johnson, D. K. Biegelsen, M. D. Moyer, S. T. Chang, E. H. Poindexter, and P. J. Caplan, "Characteristic electronic defects at the Si-SiO₂ interface," *Applied Physics Letters*, vol. 43, no. 6, pp. 563–565, 1983.

- [102] M. Nishida, "Electronic structure of silicon quantum dots: calculations of energy-gap redshifts due to oxidation," *Journal of Applied Physics*, vol. 98, no. 2, Article ID 023705, 6 pages, 2005.
- [103] M. Luppi and S. Ossicini, "Ab initio study on oxidized silicon clusters and silicon nanocrystals embedded in SiO₂: beyond the quantum confinement effect," *Physical Review B*, vol. 71, no. 3, Article ID 035340, 15 pages, 2005.
- [104] L. E. Ramos, J. Furthmüller, and F. Bechstedt, "Reduced influence of defects on oxidized Si nanocrystallites," *Physical Review B*, vol. 71, no. 3, Article ID 035328, 7 pages, 2005.
- [105] D. Vuillaume, D. Deresmes, and D. Stiévenard, "Temperature-dependent study of spin-dependent recombination at silicon dangling bonds," *Applied Physics Letters*, vol. 64, no. 13, pp. 1690–1692, 1994.
- [106] M. Lannoo, C. Delerue, and G. Allan, "Nonradiative recombination on dangling bonds in silicon crystallites," *Journal of Luminescence*, vol. 57, no. 1–6, pp. 243–247, 1993.
- [107] D. Goguenheim and M. Lannoo, "Theoretical calculation of the electron-capture cross section due to a dangling bond at the Si(111)-SiO₂ interface," *Physical Review B*, vol. 44, no. 4, pp. 1724–1733, 1991.
- [108] W. Kohn and J. M. Luttinger, "Theory of donor levels in silicon," *Physical Review*, vol. 97, no. 6, p. 1721, 1955.
- [109] W. Kohn and J. M. Luttinger, "Theory of donor states in silicon," *Physical Review*, vol. 98, no. 4, pp. 915–922, 1955.
- [110] A. Baldereschi, "Valley-orbit interaction in semiconductors," *Physical Review B*, vol. 1, no. 12, pp. 4673–4677, 1970.
- [111] S. T. Pantelides and C. T. Sah, "Theory of localized states in semiconductors. I. New results using an old method," *Physical Review B*, vol. 10, no. 2, pp. 621–637, 1974.
- [112] R. A. Faulkner, "Higher donor excited states for prolate-spheroid conduction bands: a reevaluation of silicon and germanium," *Physical Review*, vol. 184, no. 3, pp. 713–721, 1969.
- [113] Z. Zhou, M. L. Steigerwald, R. A. Friesner, L. Brus, and M. S. Hybertsen, "Structural and chemical trends in doped silicon nanocrystals: first-principles calculations," *Physical Review B*, vol. 71, no. 24, Article ID 245308, 8 pages, 2005.
- [114] S. Ossicini, E. Degoli, F. Iori, et al., "Simultaneously B- and P-doped silicon nanoclusters: formation energies and electronic properties," *Applied Physics Letters*, vol. 87, no. 17, Article ID 173120, 3 pages, 2005.
- [115] L. E. Ramos, E. Degoli, G. Cantele, et al., "Structural features and electronic properties of group-III-, group-IV-, and group-V-doped Si nanocrystallites," *Journal of Physics: Condensed Matter*, vol. 19, no. 46, Article ID 466211, 12 pages, 2007.
- [116] F. Iori, E. Degoli, R. Magri, et al., "Engineering silicon nanocrystals: theoretical study of the effect of codoping with boron and phosphorus," *Physical Review B*, vol. 76, no. 8, Article ID 085302, 14 pages, 2007.
- [117] Q. Xu, J.-W. Luo, S.-S. Li, J.-B. Xia, J. Li, and S.-H. Wei, "Chemical trends of defect formation in Si quantum dots: the case of group-III and group-V dopants," *Physical Review B*, vol. 75, no. 23, Article ID 235304, 6 pages, 2007.
- [118] V. A. Belyakov and V. A. Burdov, "Chemical-shift enhancement for strongly confined electrons in silicon nanocrystals," *Physics Letters A*, vol. 367, no. 1–2, pp. 128–134, 2007.
- [119] V. A. Belyakov and V. A. Burdov, "Anomalous splitting of the hole states in silicon quantum dots with shallow acceptors," *Journal of Physics: Condensed Matter*, vol. 20, no. 2, Article ID 025213, 13 pages, 2008.
- [120] S. Y. Ren, "Quantum confinement of edge states in Si crystallites," *Physical Review B*, vol. 55, no. 7, pp. 4665–4669, 1997.
- [121] B. Delley and E. F. Steigmeier, "Quantum confinement in Si nanocrystals," *Physical Review B*, vol. 47, no. 3, pp. 1397–1400, 1993.
- [122] T. Blomquist and G. Kirczenow, "Poisson-Schrödinger and ab initio modeling of doped Si nanocrystals: reversal of the charge transfer between host and dopant atoms," *Physical Review B*, vol. 71, no. 4, Article ID 045301, 9 pages, 2005.
- [123] F. Trani, D. Ninno, G. Cantele, et al., "Screening in semiconductor nanocrystals: ab initio results and Thomas-Fermi theory," *Physical Review B*, vol. 73, no. 24, Article ID 245430, 9 pages, 2006.
- [124] G. Cantele, E. Degoli, E. Luppi, et al., "First-principles study of n- and p-doped silicon nanoclusters," *Physical Review B*, vol. 72, no. 11, Article ID 113303, 4 pages, 2005.
- [125] F. Iori, E. Degoli, E. Luppi, et al., "Doping in silicon nanocrystals: an ab initio study of the structural, electronic and optical properties," *Journal of Luminescence*, vol. 121, no. 2, pp. 335–339, 2006.
- [126] Y. Hada and M. Eto, "Electronic states in silicon quantum dots: multivalley artificial atoms," *Physical Review B*, vol. 68, no. 15, Article ID 155322, 7 pages, 2003.
- [127] D. V. Melnikov and J. R. Chelikowsky, "Quantum confinement in phosphorus-doped silicon nanocrystals," *Physical Review Letters*, vol. 92, no. 4, Article ID 046802, 4 pages, 2004.
- [128] M. Lannoo, C. Delerue, and G. Allan, "Screening in semiconductor nanocrystallites and its consequences for porous silicon," *Physical Review Letters*, vol. 74, no. 17, pp. 3415–3418, 1995.
- [129] S. Ögüt, R. Burdick, Y. Saad, and J. R. Chelikowsky, "Ab initio calculations for large dielectric matrices of confined systems," *Physical Review Letters*, vol. 90, no. 12, Article ID 127401, 4 pages, 2003.
- [130] C. Delerue, M. Lannoo, and G. Allan, "Concept of dielectric constant for nanosized systems," *Physical Review B*, vol. 68, no. 11, Article ID 115411, 4 pages, 2003.
- [131] X. Cartoixa and L.-W. Wang, "Microscopic dielectric response functions in semiconductor quantum dots," *Physical Review Letters*, vol. 94, no. 23, Article ID 236804, 4 pages, 2005.
- [132] F. Trani, D. Ninno, and G. Iadonisi, "Tight-binding formulation of the dielectric response in semiconductor nanocrystals," *Physical Review B*, vol. 76, no. 8, Article ID 085326, 9 pages, 2007.
- [133] A. Franceschetti and M. C. Tropicovsky, "Screening of point charges in Si quantum dots," *Physical Review B*, vol. 72, no. 16, Article ID 165311, 4 pages, 2005.
- [134] G. Onida, L. Reining, and A. Rubio, "Electronic excitations: density-functional versus many-body Green's-function approaches," *Reviews of Modern Physics*, vol. 74, no. 2, pp. 601–659, 2002.
- [135] M. Shishkin, M. Marsman, and G. Kresse, "Accurate quasiparticle spectra from self-consistent GW calculations with vertex corrections," *Physical Review Letters*, vol. 99, no. 24, Article ID 246403, 4 pages, 2007.
- [136] L.-W. Wang and X. Cartoixa, "Motif-based polarization model: calculations of the dielectric function and polarization in large nanostructures," *Physical Review B*, vol. 75, no. 20, Article ID 205334, 5 pages, 2007.
- [137] L.-W. Wang and A. Zunger, "Dielectric constants of silicon quantum dots," *Physical Review Letters*, vol. 73, no. 7, pp. 1039–1042, 1994.

- [138] R. Tsu and D. Babić, "Doping of a quantum dot," *Applied Physics Letters*, vol. 64, no. 14, pp. 1806–1808, 1994.
- [139] R. Tsu, D. Babić, and L. Ioriatti Jr., "Simple model for the dielectric constant of nanoscale silicon particle," *Journal of Applied Physics*, vol. 82, no. 3, pp. 1327–1329, 1997.
- [140] V. A. Belyakov and V. A. Burdov, "Fine splitting of electron states in silicon nanocrystal with a hydrogen-like shallow donor," *Nanoscale Research Letters*, vol. 2, no. 11, pp. 569–575, 2007.
- [141] N. O. Lipari and A. Baldereschi, "Interpretation of acceptor spectra in semiconductors," *Solid State Communications*, vol. 25, no. 9, pp. 665–668, 1978.
- [142] A. Baldereschi and N. O. Lipari, "Spherical model of shallow acceptor states in semiconductors," *Physical Review B*, vol. 8, no. 6, pp. 2697–2709, 1973.
- [143] A. Baldereschi and N. O. Lipari, "Cubic contributions to the spherical model of shallow acceptor states," *Physical Review B*, vol. 9, no. 4, pp. 1525–1539, 1974.
- [144] N. O. Lipari, A. Baldereschi, and M. L. W. Thewalt, "Central cell effects on acceptor spectra in Si and Ge," *Solid State Communications*, vol. 33, no. 3, pp. 277–279, 1980.
- [145] A. Thränhardt, C. Ell, G. Khitrova, and H. M. Gibbs, "Relation between dipole moment and radiative lifetime in interface fluctuation quantum dots," *Physical Review B*, vol. 65, no. 3, Article ID 035327, 6 pages, 2002.
- [146] D. I. Tetelbaum, V. A. Burdov, A. N. Mikhaylov, and S. A. Trushin, "About the phosphorus sensitization of silicon quantum dots in SiO₂ photoluminescence," in *10th International Symposium on Nanostructures: Physics and Technology*, vol. 5023 of *Proceedings of SPIE*, pp. 186–189, St. Petersburg, Russia, June 2003.
- [147] M. S. Hybertsen, "Absorption and emission of light in nanoscale silicon structures," *Physical Review Letters*, vol. 72, no. 10, pp. 1514–1517, 1994.
- [148] C. Delerue, G. Allan, and M. Lannoo, "Electron-phonon coupling and optical transitions for indirect-gap semiconductor nanocrystals," *Physical Review B*, vol. 64, no. 19, Article ID 193402, 4 pages, 2001.
- [149] V. A. Belyakov, V. A. Burdov, D. M. Gaponova, A. N. Mikhaylov, D. I. Tetelbaum, and S. A. Trushin, "Phonon-assisted radiative electron-hole recombination in silicon quantum dots," *Physics of the Solid State*, vol. 46, no. 1, pp. 27–31, 2004.
- [150] O. J. Glembocki and F. H. Pollak, "Calculation of the γ - δ electron-phonon and hole-phonon scattering matrix elements in silicon," *Physical Review Letters*, vol. 48, no. 6, pp. 413–416, 1982.
- [151] O. J. Glembocki and F. H. Pollak, "Relative intensities of indirect transitions: electron-phonon and hole-phonon interaction matrix elements in Si (TO) and GaP (LA,TA)," *Physical Review B*, vol. 25, no. 2, pp. 1193–1204, 1982.
- [152] I. Mihalcescu, J. C. Vial, A. Bsiesy, et al., "Saturation and voltage quenching of porous-silicon luminescence and the importance of the Auger effect," *Physical Review B*, vol. 51, no. 24, pp. 17605–17613, 1995.
- [153] A. A. Prokofiev, A. S. Moskalenko, and I. N. Yassievich, "Theoretical modeling of excitation and de-excitation processes of Er in SiO₂ with Si nanocrystals," *Journal of Luminescence*, vol. 121, no. 2, pp. 222–225, 2006.
- [154] D. V. Talapin, A. L. Rogach, A. Kornowski, M. Haase, and H. Weller, "Highly luminescent monodisperse CdSe and CdSe/ZnS nanocrystals synthesized in a hexadecylamine-trioctylphosphine oxide-trioctylphosphine mixture," *Nano Letters*, vol. 1, no. 4, pp. 207–211, 2001.
- [155] R. Espiau de Lamaestre and H. Bernas, "Significance of lognormal nanocrystal size distributions," *Physical Review B*, vol. 73, no. 12, Article ID 125317, 9 pages, 2006.
- [156] R. Espiau de Lamaestre and H. Bernas, "Ion beam-induced quantum dot synthesis in glass," *Nuclear Instruments and Methods in Physics Research, Section B*, vol. 257, no. 1-2, pp. 1–5, 2007.
- [157] R. B. Bergmann, J. Köhler, R. Dassow, C. Zaczek, and J. H. Werner, "Nucleation and growth of crystalline silicon films on glass for solar cells," *Physica Status Solidi (A)*, vol. 166, no. 2, pp. 587–602, 1998.
- [158] R. B. Bergmann, J. Krinke, H. P. Strunk, and J. H. Werner, "Deposition and characterization of polycrystalline silicon films on glass for thin film solar cells," in *Materials Research Society Symposium Proceedings*, vol. 467, pp. 325–330, San Francisco, Calif, USA, March 1997.
- [159] S. K. Kurtz and F. M. A. Carpay, "Microstructure and normal grain growth in metals and ceramics—I: theory," *Journal of Applied Physics*, vol. 51, no. 11, pp. 5725–5744, 1980.
- [160] R. Lockwood, A. Hryciw, and A. Meldrum, "Nonresonant carrier tunneling in arrays of silicon nanocrystals," *Applied Physics Letters*, vol. 89, no. 26, Article ID 263112, 3 pages, 2006.
- [161] V. Vinciguerra, G. Franzò, F. Priolo, F. Iacona, and C. Spinella, "Quantum confinement and recombination dynamics in silicon nanocrystals embedded in Si/SiO₂ superlattices," *Journal of Applied Physics*, vol. 87, no. 11, pp. 8165–8173, 2000.
- [162] M. Glover and A. Meldrum, "Effect of "buffer layers" on the optical properties of silicon nanocrystal superlattices," *Optical Materials*, vol. 27, no. 5, pp. 977–982, 2005.
- [163] A. Meldrum, L. A. Boatner, C. W. White, and R. C. Ewing, "Ion irradiation effects in nonmetals: formation of nanocrystals and novel microstructures," *Materials Research Innovations*, vol. 3, no. 4, pp. 190–204, 2000.
- [164] F. Huisken, G. Ledoux, O. Guillois, and C. Reynaud, "Light-emitting silicon nanocrystals from laser pyrolysis," *Advanced Materials*, vol. 14, no. 24, pp. 1861–1865, 2002.
- [165] M. Cazzanelli, D. Navarro-Urriós, F. Riboli, et al., "Optical gain in monodispersed silicon nanocrystals," *Journal of Applied Physics*, vol. 96, no. 6, pp. 3164–3171, 2004.
- [166] I. Y. Choi, K. H. Byoun, M. H. Jung, H.-J. Lim, and H. W. Lee, "Synthesis of cyano cyclic olefins through ring-closing metathesis," *Bulletin of the Korean Chemical Society*, vol. 25, no. 9, pp. 1305–1306, 2004.
- [167] L. Pavesi and M. Ceschini, "Stretched-exponential decay of the luminescence in porous silicon," *Physical Review B*, vol. 48, no. 23, pp. 17625–17628, 1993.
- [168] H. E. Roman and L. Pavesi, "Monte Carlo simulations of the recombination dynamics in porous silicon," *Journal of Physics: Condensed Matter*, vol. 8, no. 28, pp. 5161–5187, 1996.
- [169] O. Guillois, N. Herlin-Boime, C. Reynaud, G. Ledoux, and F. Huisken, "Photoluminescence decay dynamics of noninteracting silicon nanocrystals," *Journal of Applied Physics*, vol. 95, no. 7, pp. 3677–3682, 2004.
- [170] M. N. Berberan-Santos, E. N. Bodunov, and B. Valeur, "Mathematical functions for the analysis of luminescence decays with underlying distributions 1. Kohlrausch decay function (stretched exponential)," *Chemical Physics*, vol. 315, no. 1-2, pp. 171–182, 2005.
- [171] J. Heitmann, F. Müller, M. Zacharias, and U. Gösele, "Silicon nanocrystals: size matters," *Advanced Materials*, vol. 17, no. 7, pp. 795–803, 2005.

- [172] S. Tiwari, F. Rana, H. Hanafi, A. Hartstein, E. F. Crabbé, and K. Chan, "A silicon nanocrystals based memory," *Applied Physics Letters*, vol. 68, no. 10, pp. 1377–1379, 1996.
- [173] T. Z. Lu, M. Alexe, R. Scholz, V. Talelaev, and M. Zacharias, "Multilevel charge storage in silicon nanocrystal multilayers," *Applied Physics Letters*, vol. 78, no. 20, Article ID 202110, 3 pages, 2005.
- [174] S. Muto, T. Inata, A. Tackeuchi, Y. Sugiyama, and T. Fujii, "Longitudinal-optical-phonon assisted tunneling in tunneling bi-quantum well structures," *Applied Physics Letters*, vol. 58, no. 21, pp. 2393–2395, 1991.
- [175] S. Haacke, N. T. Pelekanos, H. Mariette, M. Zigone, A. P. Heberle, and W. W. Rühle, "Tunneling dynamics in CdTe/(Cd,Zn)Te asymmetric double-quantum-well structures," *Physical Review B*, vol. 47, no. 24, pp. 16643–16646, 1993.
- [176] A. Tackeuchi, T. Kuroda, K. Mase, Y. Nakata, and N. Yokoyama, "Dynamics of carrier tunneling between vertically aligned double quantum dots," *Physical Review B*, vol. 62, no. 3, pp. 1568–1571, 2000.
- [177] T. Förster, "Zwischenmolekulare Energiewanderung und Fluoreszenz," *Annalen der Physik*, vol. 2, no. 1-2, pp. 55–75, 1948.
- [178] C. B. Murray, C. R. Kagan, and M. G. Bawendi, "Synthesis and characterization of monodisperse nanocrystals and close-packed nanocrystal assemblies," *Annual Review of Materials Science*, vol. 30, pp. 545–610, 2000.
- [179] G. Liu and B. Jacquier, Eds., *Spectroscopic Properties of Rare Earths in Optical Materials*, Springer, New York, NY, USA, 2005.
- [180] T. Miyakawa and D. L. Dexter, "Phonon sidebands, multiphonon relaxation of excited states, and phonon-assisted energy transfer between ions in solids," *Physical Review B*, vol. 1, no. 7, pp. 2961–2969, 1970.
- [181] R. Reisfeld, "Rare earths complexes in sol gel glasses," *Materials Science*, vol. 20, pp. 5–18, 2002.
- [182] J. L. Kennedy and N. Djeu, "Energy transfer in rare earth doped $Y_3Al_5O_{12}$ at very high temperatures," *Journal of Luminescence*, vol. 101, no. 1-2, pp. 147–153, 2003.
- [183] M. P. Hehlen, N. J. Cockroft, T. R. Gosnell, and A. J. Bruce, "Spectroscopic properties of Er^{3+} - and Yb^{3+} -doped soda-lime silicate and aluminosilicate glasses," *Physical Review B*, vol. 56, no. 15, pp. 9302–9318, 1997.
- [184] F. Pellé, N. Gardant, and F. Auzel, "Effect of excited-state population density on nonradiative multiphonon relaxation rates of rare-earth ions," *Journal of the Optical Society of America B*, vol. 15, no. 2, pp. 667–679, 1998.
- [185] N. Yamada, S. Shionoya, and T. Kushida, "Phonon-assisted energy transfer between trivalent rare earth ions," *Journal of the Physical Society of Japan*, vol. 32, no. 6, pp. 1577–1586, 1972.
- [186] H. Kuhn, "Classical aspects of energy transfer in molecular systems," *The Journal of Chemical Physics*, vol. 53, no. 1, pp. 101–108, 1970.
- [187] L. Dal Negro, M. Cazzanelli, B. Danese, et al., "Light amplification in silicon nanocrystals by pump and probe transmission measurements," *Journal of Applied Physics*, vol. 96, no. 10, pp. 5747–5755, 2004.
- [188] K. Luterová, K. Dohnalová, F. Trojánek, et al., "Porous silicon grains in SiO_2 matrix: ultrafast photoluminescence and optical gain," *Journal of Non-Crystalline Solids*, vol. 352, no. 28-29, pp. 3041–3046, 2006.
- [189] P. M. Fauchet, J. Ruan, H. Chen, et al., "Optical gain in different silicon nanocrystal systems," *Optical Materials*, vol. 27, no. 5, pp. 745–749, 2005.
- [190] M. H. Nayfeh, N. Barry, J. Therrien, O. Akcakir, E. Gratton, and G. Belomoin, "Stimulated blue emission in reconstituted films of ultrasmall silicon nanoparticles," *Applied Physics Letters*, vol. 78, no. 8, pp. 1131–1133, 2001.
- [191] J. Valenta, K. Luterová, R. Tomasiunas, K. Dohnalová, B. Hönerlage, and I. Pelant, "Optical gain measurements with variable stripe length technique," in *Towards the First Silicon Laser*, L. Pavesi, S. Gaponenko, and L. Dal Negro, Eds., vol. 93 of *NATO Science Series*, pp. 223–242, Kluwer Academic Publishers, Dordrecht, The Netherlands, 2003.
- [192] H. Lee, J. H. Shin, and N. Park, "Performance analysis of nanocluster-Si sensitized Er-doped waveguide amplifier using top-pumped 470 nm LED," *Optics Express*, vol. 13, no. 24, pp. 9881–9889, 2005.
- [193] V. I. Klimov, S. A. Ivanov, J. Nanda, et al., "Single-exciton optical gain in semiconductor nanocrystals," *Nature*, vol. 447, no. 7143, pp. 441–446, 2007.
- [194] C. M. Hessel, M. A. Summers, A. Meldrum, M. Malac, and J. G. C. Veinot, "Direct patterning, conformal coating, and erbium doping of luminescent nc-Si/ SiO_2 thin films from solution processable hydrogen silsesquioxane," *Advanced Materials*, vol. 19, no. 21, pp. 3513–3516, 2007.

Research Article

Quantum Electrodynamic Modeling of Silicon-Based Active Devices

Shouyuan Shi, Brandon Redding, Tim Creazzo, Elton Marchena, and Dennis W. Prather

Department of Electrical and Computer Engineering, University of Delaware, Newark, DE 19716, USA

Correspondence should be addressed to Shouyuan Shi, sshi@ee.udel.edu

Received 25 February 2008; Accepted 2 May 2008

Recommended by Pavel Cheben

We propose a time-domain analysis of an active medium based on a coupled quantum mechanical and electromagnetic model to accurately simulate the dynamics of silicon-based photonic devices. To fully account for the nonlinearity of an active medium, the rate equations of a four-level atomic system are introduced into the electromagnetic polarization vector. With these auxiliary differential equations, we solve the time evolution of the electromagnetic waves and atomic population densities using the FDTD method. The developed simulation approach has been used to model light amplification and amplified spontaneous emission in silicon nanocrystals, as well as the lasing dynamics in a novel photonic crystal-based silicon microcavity.

Copyright © 2008 Shouyuan Shi et al. This is an open access article distributed under the Creative Commons Attribution License, which permits unrestricted use, distribution, and reproduction in any medium, provided the original work is properly cited.

1. INTRODUCTION

Silicon, owing to its excellent electronic material properties, availability, and efficient processing, has played major roles in microelectronics during past decades and promises to be the key material in the foreseeable future. However, the rapid progress of microprocessors will soon be limited by the transmission bandwidth capability of electronic connections. To eliminate the bottleneck of electronic circuits and establish interconnection links between circuit boards, between chips on a board, or even with a single chip, research into silicon microphotronics, which merges the power of silicon microelectronics with the advantages of photonics, has attracted increasing attention in recent years [1, 2].

While a wide variety of passive silicon photonic devices have been developed, recent activities have focused on achieving active functionalities, particularly light amplification and generation, in silicon photonic devices [3–5]. However, due to the fundamental limitation related to the indirect nature of the bulk Si band gap, this semiconductor has very low-light emission efficiency. As a result, the development of silicon light emitters, amplifiers, and lasers has become one of the central goals in the advancement of silicon photonics and optoelectronics. Another driving force stimulating research is the need for low-cost photonic devices for applications related to future computing and

communication systems. In the past, a number of different approaches have been taken to overcome silicon's fundamental limitations including silicon nanocrystals, Er-doped Si-Ge, Si-Ge quantum dots, and Er-doped silicon nanocrystals [6–10]. More recently, stimulated Raman scattering has been used to demonstrate light amplification and lasing in silicon, both in pulse and continuous-wave operation [11, 12].

As a result, there is a need for optimal design solutions and physical insight in the field of quantum optics, encompassing applications such as laser systems, amplifiers, laser cooling of atoms, quantum computing, plasmons, polaritons, and enhanced spontaneous emission in microcavities. To address this, various approaches based on quantum electrodynamics, in which the atoms in active systems are treated quantum mechanically but the electromagnetic wave is treated classically, have been developed. In this way, light interaction with an active medium can be studied using a classical harmonic oscillator model and the rate equations of electron population density. Although, simple analytic expressions can be derived for well-defined problems, precise solutions for a realistic system require a numerical solution, particularly in nanophotonic devices.

In addition, over the past several years, numerous methods have been proposed to account for material dispersion, absorption, and gain using the finite-difference and time-domain (FDTD) method [13–17]. One of the most

commonly used and the memory-efficient algorithms is the auxiliary differential equation (ADE) FDTD scheme which accounts for the rate equations that determine the electron energy states' population densities during the propagation of pump and input signals. The approach has been widely used to characterize the absorption in a two-level atomic system [13], gain in a four-level atomic system [14–16, 18], and more complicated lasing dynamics in a four-level two-electron atomic system [19].

In this paper, we present a time-domain analysis of amplification, amplified spontaneous emission (ASE), and lasing dynamics in silicon-based nanophotonic devices based on a coupled quantum mechanical and electromagnetic model. In order to simulate quantum electrodynamics, we incorporate the rate equations of a four-level atomic system to characterize the gain and absorption of an active material. Both amplification and ASE with the assistance of a microcavity are investigated in one-dimensional (1D) and two-dimensional (2D) silicon nanocrystals (Si-ncs). To study lasing dynamics, a novel silicon microcavity based on the unique dispersion properties of photonic crystals is introduced.

2. COUPLED RATE EQUATIONS AND ELECTROMAGNETIC DYNAMICS MODEL

To achieve light amplification and lasing behavior in silicon photonic devices, the development of gain media is essential for the successful design of next generation integrated photonics [4, 5]. As many material systems, such as nanocrystals and Er-doped glasses, have been extensively explored and found to not only experimentally demonstrate photoluminescence for the application of a silicon-based emitter, but also exhibit net gain for the development of a silicon based laser [3, 6–8, 20, 21]. Due to strong coupling between the quantum state and nanoscale electromagnetic waves, a mathematical model is necessary to intimately link quantum mechanical effects to the electromagnetic interaction. To this end, we take both field evolution and material dynamics, such as the dispersive and nonlinear properties, into modeling consideration.

The classical electron oscillator (CEO) model has been widely used to bridge the link between the quantum world and electromagnetic waves. Such quantum-based dynamics are dictated by rate equations which simulate the time evolution of atomic-energy-level populations in the gain medium. The electromagnetic dynamics are dictated by the electromagnetic wave equations [22]. The CEO model allows us to couple these domains and study devices in which the material properties affect the electromagnetic field and vice versa. Depending on the material system, various distinguished energy levels are used to represent its quantum processes, stimulated, and spontaneous emission. As an example, Er-doped glass has been applied as an application of optical amplifier in the field of fiber optics, that is, Er-doped fiber amplifier (EDFA) [18, 23]. A simple four-level model of rate equations is employed to successfully characterize the light amplification. In the presented work,

we will apply a similar model for the design of a silicon photonic microcavity.

Recently, the direct observation of photoluminescence (PL) reveals the potential for optical gain in Si-ncs. Although a full theoretical model for the stimulated emission is still not enough, conventional rate equations can be employed to describe the active and nonlinear properties of Si-ncs [9, 10, 24]. Under the first order of approximation, the Auger process is neglected to phenomenologically study the gain medium. A more general model interested in analyzing gain saturation and other higher-order effects could incorporate additional transitions into the rate equation model to represent Auger-type processes, as discussed in [21]. As a consequence, we can further simplify the rate equations to a four-level atomic system. Coupled with Maxwell's equations, we are able to model the time evolution of the atomic-energy-level population density as well as the optical signal propagation, amplification, and absorption in candidate devices.

As shown in Figure 1, time-domain population dynamics can be expressed with a four-level rate equation formulism:

$$\begin{aligned} \frac{dN_3(t)}{dt} &= -\frac{N_3(t)}{\tau_{32}} + W_p N_0, \\ \frac{dN_2(t)}{dt} &= \frac{N_3(t)}{\tau_{32}} - \frac{N_2(t)}{\tau_{21}} + \frac{1}{\hbar\omega_s} \mathbf{E}(t) \cdot \frac{d\mathbf{P}(t)}{dt}, \\ \frac{dN_1(t)}{dt} &= \frac{N_2(t)}{\tau_{21}} - \frac{N_1(t)}{\tau_{10}} - \frac{1}{\hbar\omega_s} \mathbf{E}(t) \cdot \frac{d\mathbf{P}(t)}{dt}, \\ \frac{dN_0(t)}{dt} &= \frac{N_1(t)}{\tau_{10}} - W_p N_0, \end{aligned} \quad (1)$$

where N_i ($i = 0, 1, 2, 3$) are the transition population densities for different atomic levels, which are related to the total concentration $N_{\text{tot}} = \sum_{i=0}^3 N_i$. τ_{ij} are the lifetimes associated with the transitions from energy E_i to E_j . ω_s is the central frequency of radiation of the materials related to the atomic transition energy levels through $\omega_s = (E_2 - E_1)/\hbar$ and $(1/\hbar\omega_s)\mathbf{E}(t) \cdot d\mathbf{P}(t)/dt$ is the induced radiation rate or excitation rate depending on its sign. The pump rate W_p is defined as $W_p = \sigma_p I_p / \hbar\omega_p$, where σ_p is the absorption cross section, $I_p / \hbar\omega_p$ is the photon flux, and I_p is the intensity of the pumping signal.

Based on the CEO model, the net macroscopic polarization $\mathbf{P}(t)$ induced in the presence of an applied electric field $\mathbf{E}(t)$ for an isotropic medium can be described by the following equations [22]:

$$\frac{d^2\mathbf{P}(t)}{dt^2} + \Delta\omega_s \frac{d\mathbf{P}(t)}{dt} + \omega_s^2 \mathbf{P}(t) = \kappa \Delta N_{12}(t) \mathbf{E}(t), \quad (2)$$

where $\Delta N_{12}(t)$ is the instantaneous population density difference between energy levels 1 and 2 of an atomic transition, given by $\Delta N_{12}(t) = N_1(t) - N_2(t)$. The coupling coefficient, κ , determines the strength of the interaction between the quantum and electromagnetic world. It can be easily derived from the above equation that the amplification line shape is Lorentzian and homogeneously broadened, and can be considered as a quantum mechanically correct equation for the induced polarization density in a real

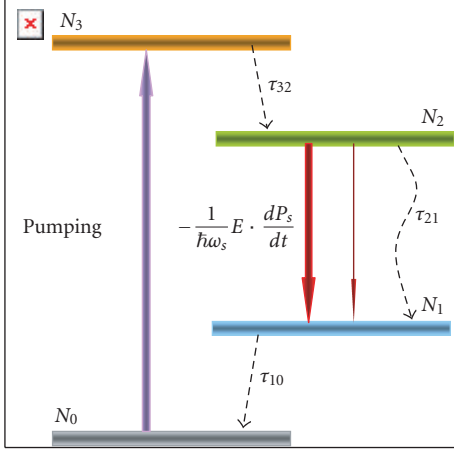


FIGURE 1: An effective four-atomic-level system to qualitatively model the recombination dynamics under the gain condition.

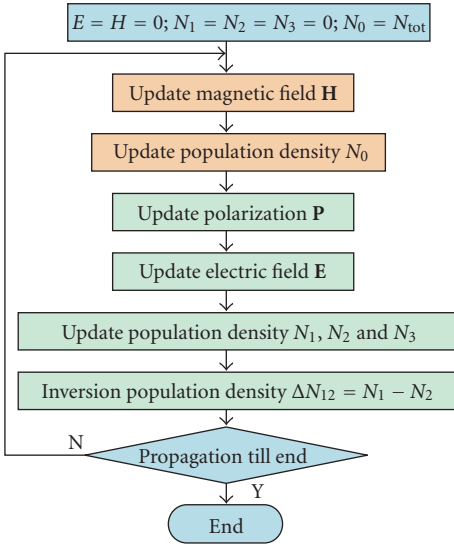


FIGURE 2: Flow chart of time evolution of population density functions and electromagnetic waves.

atomic system. To excite the system, an optical pumping source that is homogeneously distributed across the device is introduced into the system. Amplification takes place when the external pumping mechanism produces a population inversion $\Delta N_{12}(t) < 0$.

In addition, in the frequency domain, the polarization due to the gain or absorption materials can be derived from (2) as

$$[(\omega^2 - \omega_s^2) + j\omega\Delta\omega_s]\mathbf{P} = \kappa\Delta N_{12}\mathbf{E}. \quad (3)$$

The material susceptibility can then be introduced as $\mathbf{P} = \epsilon_0\chi\mathbf{E}$. Assuming the host material has a relative dielectric constant of ϵ_r , the complex dielectric constant can be expressed as

$$\epsilon_s = \epsilon_0(\epsilon_r + \chi_s) = \epsilon_0\left(\epsilon_r + \frac{\kappa\Delta N_{12}/\epsilon_0}{[(\omega^2 - \omega_s^2) + j\omega\Delta\omega_s]}\right). \quad (4)$$

If a plane wave is propagating in such a material, then the imaginary part of the wave vector can be considered as the amplification or absorption coefficient, given by

$$\alpha_s(\omega) = \frac{\pi}{\lambda}\sqrt{\epsilon_r}\text{Im}(\chi_s). \quad (5)$$

On the other hand, if we know the radiative cross-section, σ_s , of the gain medium at peak gain frequency ω_s , the amplification coefficient can be written as

$$\alpha_s = -\frac{\sigma_s\Delta N_{12}}{2}. \quad (6)$$

As a result, we can relate the coupling coefficient with the radiative cross-section through the amplification coefficient as

$$\kappa = c\epsilon_0\sqrt{\epsilon_r}\sigma_s\Delta\omega_s. \quad (7)$$

In this manner, we can obtain a coupling coefficient based on experimental observations.

3. AUXILIARY DIFFERENTIAL EQUATIONS FDTD ANALYSIS

With coupled rate and Maxwell's equations, we introduce FDTD to numerically simulate amplification and lasing dynamics. The central difference method can be applied to discretize the electromagnetic field components, the atomic populations of different levels, and the induced polarizations in space and time. Then time marching of electromagnetic waves in leapfrog fashion can be constructed, and consequently the atomic evolutions can be monitored. The electromagnetic waves are governed by Maxwell's equation as

$$\nabla \times \mathbf{E} = -\mu_0 \frac{\partial \mathbf{H}}{\partial t}, \quad \nabla \times \mathbf{H} = \epsilon_0\epsilon_r \frac{\partial \mathbf{E}}{\partial t} + \frac{\partial \mathbf{P}}{\partial t} + \mathbf{J}. \quad (8)$$

We briefly describe the discretization algorithm as shown in Figure 2, at time $(n + 0.5)\Delta t$, we first update the magnetic field components and population density N_0 . Then, we update the induced polarization based on (2) at time $(n + 1)\Delta t$, where the knowledge of two preceding steps is required. With the known magnetic field and induced polarization, we can calculate the electric field components. At time $(n + 1)\Delta t$, we also update the remaining atomic population densities: N_3 , N_2 , and N_1 . Since the population density at the highest energy level, N_3 , is related only to N_0 which was updated at the half-time step, the population density is computed in order from high to low levels to maintain consistency and minimize the memory storage.

To excite the system, a source, \mathbf{J} , must be introduced. Two different sources are considered, one to investigate spontaneous emission and one to investigate stimulated emission. To characterize the amplification (stimulated emission) of an active medium, we launch a probe signal into the system. With the presence of a pumping signal, population inversion takes place within the active medium. As a result, the probe signal is amplified during propagation through the medium.

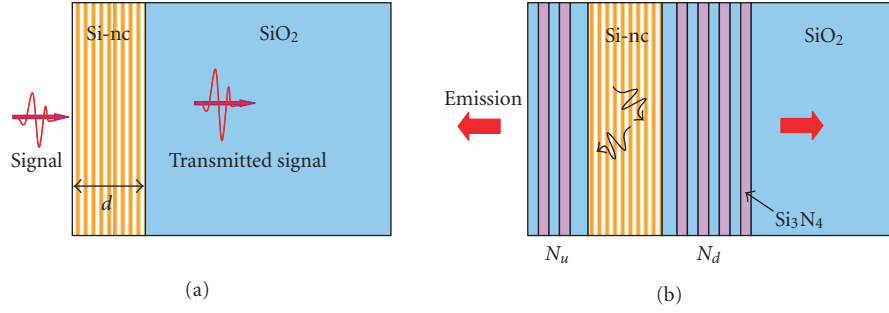


FIGURE 3: (a) 1D Si-nc active device for stimulated emission simulation study. (b) 1D Si-nc active device for amplified stimulated emission simulation study.

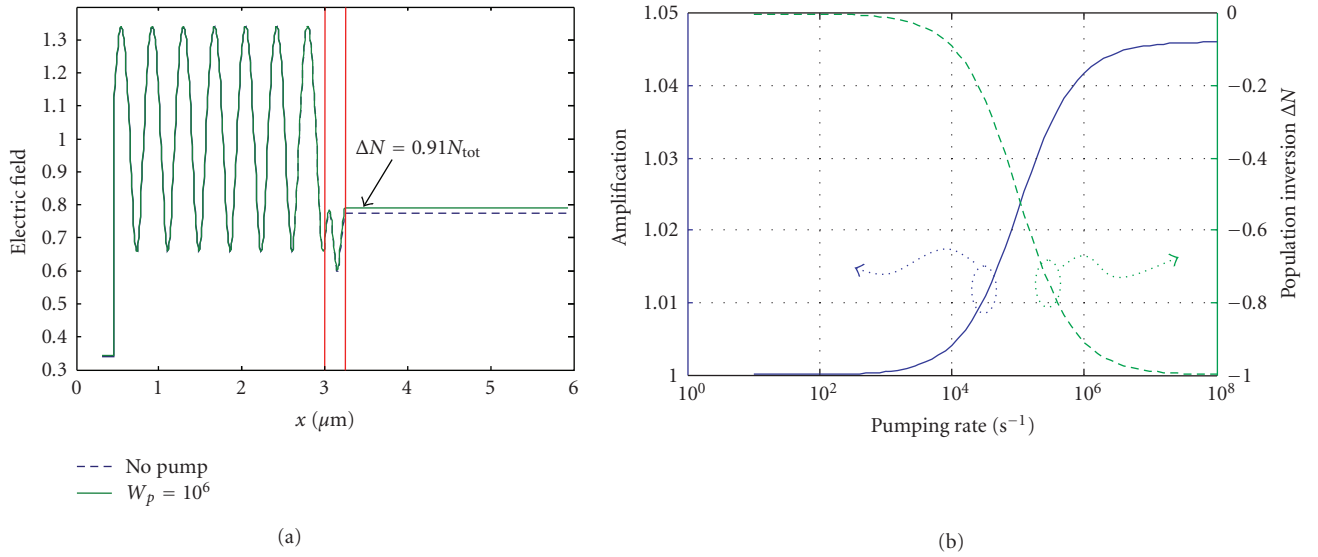


FIGURE 4: (a) Amplitude distributions of electric field across the device, where in the transmitted region, an apparent amplification can be observed under the pump rate of 10^6 compared with no pump case. (b) Amplification of transmitted signal and population inversion ΔN inside the active medium verse the pump rate varying from 10^2 to 10^8 .

To study the PL and lasing dynamics in the active system, we introduce randomly distributed sources within the system to simulate the spontaneous emission. Each source generates waves with a Lorentzian spectrum distribution centered at ω_s and amplitude dependent on the population density of N_2 . Since spontaneous emission is radiated incoherently, the phase associated with the emission is chosen randomly.

4. NUMERICAL SIMULATIONS OF ACTIVE NANOCRYSTAL DEVICES

The demonstration of photoluminescence in Si-ncs under room temperature is a significant step towards the development of Si-based light emitting materials. The indirect nature of the energy band gap is partially resolved due to quantum confinement in lower-dimension silicon such as Si/SiO₂ superlattices, porous silicon, Si-ncs embedded in SiO₂, and rare earth-doped Si-ncs.

Based on the extensive experimental measurements of Si-ncs, the principle structural, and optical parameters, such as

TABLE 1: Optical properties and simulation parameters of Si-ncs.

Pump wavelength (nm)	532
Pump photon flux $I_p/\hbar\omega$ ($\text{cm}^{-2} \text{s}^{-1}$)	$10^{15} \sim 10^{22}$
Absorption cross-section σ_p (cm^2)	10^{-14}
Emission cross-section σ_s (cm^2)	3×10^{-16}
Si-nc concentration N_{tot} (m^{-3})	6×10^{24}
Emission wavelength λ (nm)	750
Emission spectrum linewidth (nm)	200
τ_{10} (s)	10^{-15}
τ_{21} (s)	10^{-5}
τ_{32} (s)	10^{-15}
Refractive index of Si-ncs	$1.9 + i0.0014$
Refractive index of SiO ₂	1.454

emission life time, absorption cross-section, emission cross-section, emission linewidth, and peak wavelength can be deduced, as listed in the following table [10, 21].

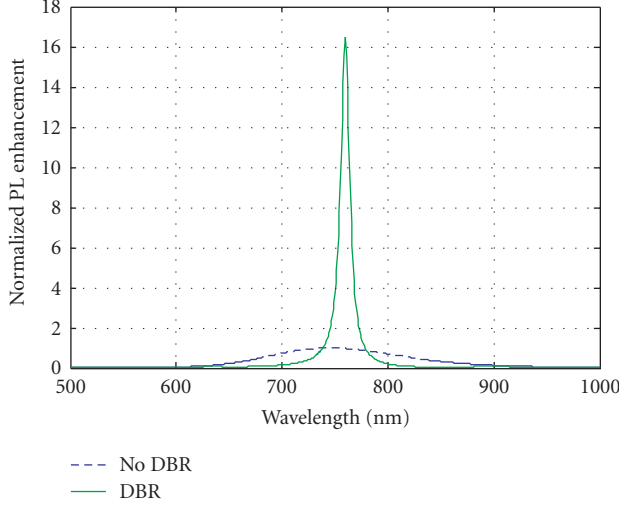


FIGURE 5: Enhanced amplified spontaneous emission (PL) with microcavity consisting of 1D DBRs with the layers of $N_u = 4$ and $N_d = 6$ compared with the one without DBR.

In simulations, the active medium is uniformly pumped with a shorter wavelength source, that is, 457 nm, and the pump photon flux, $I_p/\hbar\omega$, varies from $10^{15} \sim 10^{22} \text{ cm}^{-2} \text{ s}^{-1}$. Then, the pump rate, $W_p = \delta_p I_p/\hbar\omega$, can be determined as $10 \sim 10^8 \text{ s}^{-1}$. The effective index of silicon nanocrystals is calculated using Bruggman's effective medium approximation. In this section, we investigate the gain characteristics of Si-ncs in both 1D stacks [25] and 2D waveguiding structures [26] by incorporating the optical and structural properties above as simulation parameters in the coupled rate and electromagnetic wave equations.

4.1. Light amplification and amplified spontaneous emission in 1D nanocrystals

Based on the theoretical model developed in the previous section, we first consider light amplification in Si-ncs by applying pump and probe signal transmission simulation. The structure investigated is a superlattice of Si/SiO₂ on the top of a quartz substrate, as shown in Figure 3(a). The thickness of Si-nc is 250 nm. In the FDTD simulation, the mesh size is 20 nm, and the time step is 2.25×10^{-17} seconds.

First, we consider a continuous plane wave with a wavelength of 750 nm illuminating the sample from free space. The steady-state results with two different pump rates are shown in Figure 4(a). The red lines indicate interfaces between Si-ncs and their claddings. The solid and dash lines represent the field distributions across the devices with and without a pump rate of 10^6 . In the transmitted region (SiO₂ substrate), an apparent amplification can be identified. To accurately characterize the light amplification of Si-ncs, we calculate the transmittance based on the Poynting vector. Then, the light amplification factor is defined by normalizing the transmitted powers with pump to without pump. In doing so, the interface coupling loss can be subtracted, and consequently, net gain contributed from stimulated

emission can be extracted. We plot both the amplification factor and population inversion in Figure 4(b) for pump rates varying from 10^2 to 10^8 . As we see from the figure, both the amplification factor and normalized population inversion density are nonlinearly dependent on the pump rate. While the pump rate increases to 10^8 , the inversion population density starts to saturate and leads to a maximum amplification factor of 1.046.

In addition to the modeling of stimulated emission for the probe signal amplification through active Si-ncs, we consider photoluminescence and microcavity-based ASE from an Si-nc device, as shown in Figure 3(b). Instead of using an external plane wave, we introduce an artificial source to simulate the spontaneous emission process in an active medium.

The spontaneous emission occurs when electrons spontaneously drop from an upper (N_2) to a lower-energy level (N_1) while emitting electromagnetic radiation at the transition frequency. While atoms emit this kind of fluorescence or spontaneous emission, each individual atom acts exactly like a small random oscillating radiator. Each atom radiates independently, with a temporal phase angle that is independent of all the other radiating atoms. To model this process, we introduce many dipole sources randomly distributed within the system in the FDTD simulation. Each source generates waves in the form of a Lorentzian spectrum distribution centered at 750 nm, with its amplitude dependent on the time varying population density of N_2 . Since the spontaneous emission is incoherent, the phase associated with the photon is random, and thus we code a random phase to each dipole source in the FDTD modeling. To attain the PL characteristics of Si-nc, a few detectors are placed to collect temporal photon luminescence both in free space and the quartz substrate. The recorded temporal electromagnetic waves are Fourier transformed to the frequency domain in order to obtain the PL spectrum.

It is well known that the spontaneous emission is not only determined by the active material, but it also relates to the optical structure. By introducing a microcavity, we can control and manipulate the spontaneous emission. Based on photonic crystal band gap materials, many microcavities have been designed to enhance the spontaneous emission in active material systems [27]. The simplest configuration consists of planar stacks of alternating high- and low-index thin films deposited using conventional planar fabrication processing, such as PECVD [9]. To this end, we designed a Fabry-Perot resonator consisting of one-dimensional photonic crystal structures to confine the optical mode inside the active Si-nc material, as shown in Figure 3(b). The device consists of Si-ncs sandwiched with some variable number of periods of a one-dimensional PhC lattice at both ends, that is, N_u and N_d . To form a band gap within the PL spectrum, Si₃N₄ and SiO₂ are used as alternate high- and low-index materials with their indices of 2.05 and 1.454 at the wavelength of 750 nm. The lattice period is designed as 210 nm and the filling factor of Si₃N₄ is chosen as 50%. Transmission characteristics have been performed to confirm that a band gap opens between 638 and 879 nm. With a 250 nm thick Si-nc medium as a defect, a strong single-cavity

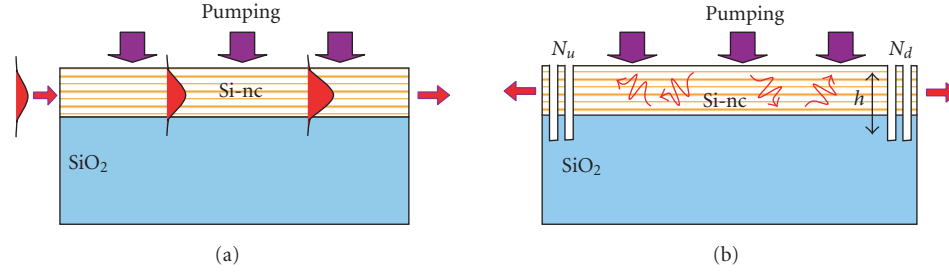


FIGURE 6: (a) Configuration for waveguide amplification study. A Gaussian pulse in air is incident on a pumped Si-nc waveguide. A detector in air at the end of the waveguide measures the amplification by normalizing to the output without pumping. (b) Configuration for amplified spontaneous emission study. Optional DBRs create a microcavity to enhance spontaneous emission of pumped Si-ncs.

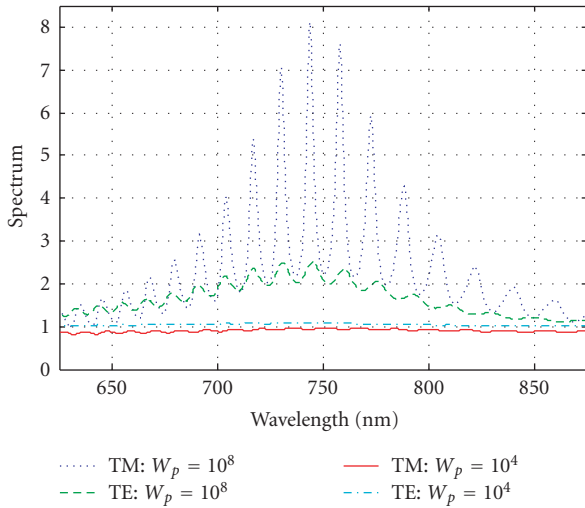


FIGURE 7: Amplification through a pumped Si-nc waveguide for TE and TM cases. Detected signal under pumping is normalized to detected signal without pumping to eliminate loss due to reflection at waveguide interfaces.

mode located at a wavelength of 751 nm can be recognized within the band gap. The Q factor is measured as 85 while the numbers of DBRs are $N_u = 1$ and $N_d = 6$.

Applying the modeling tools developed in this work, we performed numerical simulations to illustrate the enhancement effect of spontaneous emission due to the introduction of a microcavity in an active Si-nc system. During the time evolution of the population densities, the population inversion is found to be $\Delta N = 5.4 \times 10^{24}$ after the system reaches steady state. A comparison of spontaneous emission spectra with and without DBR measured in the free space is illustrated in Figure 5. All the spectra are normalized to the peak PL intensity of Si-nc devices without DBR. As we can see from the figure, the PL spectrum without DBR shows a typical broad emission band of 250 nm centered at 750 nm. By introducing the microcavity, a sharp emission enhancement can be observed. The resonant wavelength is slightly redshifted to a longer wavelength at 760.1 nm and the linewidth becomes smaller (7.2 nm). The peak PL exhibits an enhancement factor of 16.4.

Owing to the large reflectance of DBR mirrors, the optical field at resonance is well confined inside the microcavity. As a consequence, the resonant optical mode has a longer photon lifetime and thus longer interaction with the gain medium resulting in the enhanced PL signal at the resonant wavelength.

In addition to the study of active characteristics in 1D Si-ncs, we are also interested in edge emission from nanocrystals, in which a two-dimensional (2D) system is required. In the following section, we will investigate Si-nc waveguiding structures for this application.

4.2. Light amplification and amplified spontaneous emission in nanocrystal waveguiding structures

In two dimensions, we consider an active planar waveguide made of higher index Si-nc in a SiO₂ matrix on top of a lower index SiO₂ substrate. Both TE and TM propagations are simulated to identify their amplification and ASE characteristics. In cases where we study spontaneous emission, dipole sources representing the spontaneous emission source have freedom to emit in any direction. Gain guiding and total internal reflection (TIR) combine to direct the spontaneous emission along the length of the Si-nc region.

The basic 2D geometry we consider consists of a slab waveguide composed of a 200 nm Si-nc layer on a SiO₂ substrate surrounded by air. We now consider two devices based on this geometry as shown schematically in Figure 6.

The first device is a waveguide amplifier, shown in Figure 6(a). In this case, a Gaussian pulse introduced in air couples into the waveguide, propagates along the length of the waveguide, interacts with the pumped active material, and arrives at the detector, positioned in air at the opposite end. To study the waveguide's behavior as an amplifier, we normalize the detected signal at various pump strengths to the signal when the pumping and material losses are set to zero. This allows us to study amplification without loss due to reflections at the interfaces. The normalized amplification for a 10 μ m waveguide is shown in Figure 7 for the TE and TM cases at two pump rates. Both the TE and TM cases exhibit amplification under sufficient pumping, although the TM case is clearly stronger. This can be understood by considering the TE mode profile which includes a longer evanescent tail, extending into the substrate. The broader

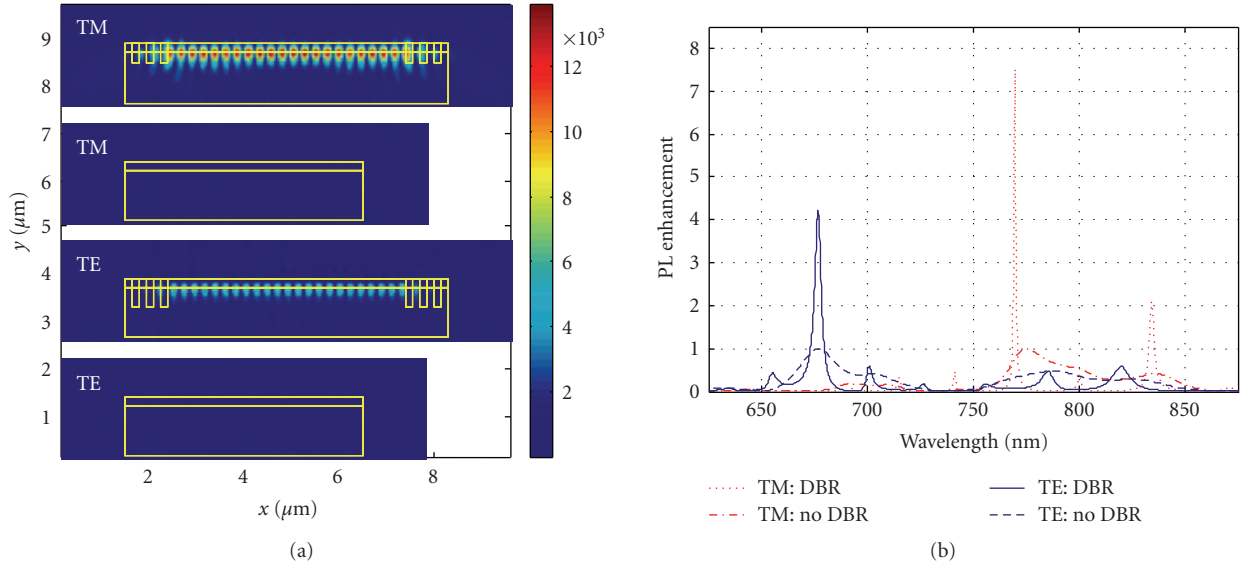


FIGURE 8: DBRs enhance PL signal of Si-ncs by $\sim 4X$ in the TE case and $\sim 8X$ in the TM case. (a) The steady-state amplitude of the E_z component is shown, the TM case corresponds to the peak wavelength of ~ 770 nm while the TE case corresponds to its peak wavelength of 677 nm. (b) The spectral response for TE and TM with 3 periods of DBRs is shown and normalized to the peak PL emission for the no-DBR case.

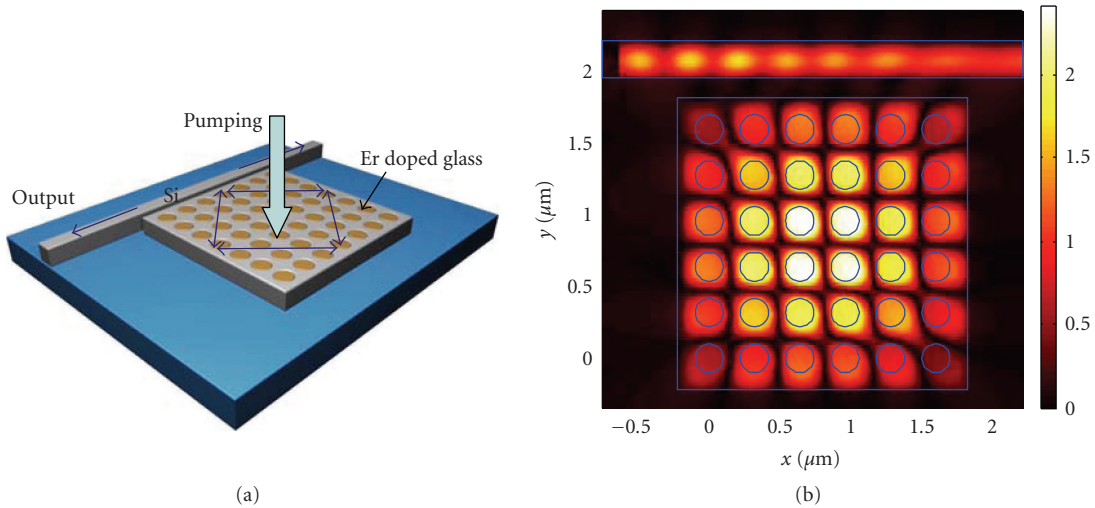


FIGURE 9: (a) Schematic of silicon laser based on dispersion-engineered photonic crystals where the active material is introduced by backfilling the air holes of the PhC. (b) The highest cavity mode below the band edge.

mode results in a reduced modal volume in the Si-nc region where amplification is possible; consequently amplification of the TE mode is reduced relative to the more confined TM mode. The oscillations in the spectral response of both modes are due to Fabry-Perot effects. The high-index contrast Si-nc to air interface introduces enough reflection to create a weak microcavity.

The second device shown in Figure 6(b) employs two DBRs to enhance the Fabry-Perot microcavity which introduced oscillations in the amplification spectrum studied above. The DBR microcavities are considered for their role in an ASE device. Spontaneous emission is modeled as dipole

sources with random phase positioned throughout the Si-nc region. The PL spectrum is detected in air to the right of the waveguide. Each DBR consists of alternating layers of air and Si-nc/SiO₂ with a period of 300 nm, optimized to open a band gap between 650 nm and 900 nm. The air holes are “etched” through the Si-nc region and 200 nm into the SiO₂ region to create the DBR. The detected PL signal with DBR is normalized to the peak PL signal without DBR. A 5 μm Si-nc region is bordered by 3 periods of DBR on either side. The resulting ASE for the TE and TM cases is shown in Figure 8. The steady-state response at the peak wavelength shows the high-optical confinement within the microcavity.

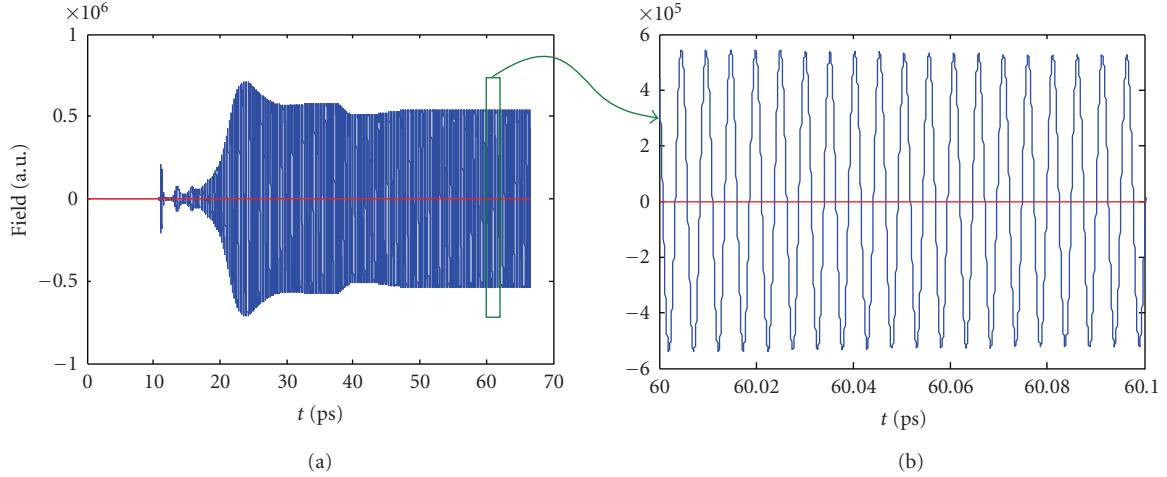


FIGURE 10: (a) Lasing dynamics by monitoring output in the straight dielectric waveguide, (b) steady-state output of single optical mode as shown within the time window in (a).

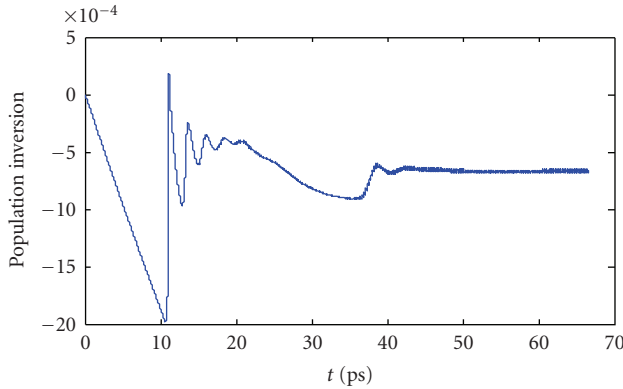


FIGURE 11: Normalized population inversion at pump rate of $2 \times 10^8/\text{s}$.

The inclusion of DBRs enhances the PL signal by a factor of 4 in the TE case and nearly a factor of 8 in the TM case.

5. LASING DYNAMICS IN A PHOTONIC CRYSTAL-BASED SILICON MICROCAVITY

In this section, we employ the developed technique to investigate the time evolution of population density functions and electromagnetic dynamics of a novel photonic crystal-based microcavity. During the lasing activity, the strong feedback of the local light intensity saturates the amplification in the system through the nonlinearity of active material, and eventually leads to a steady optical mode output.

Light propagation in a PhC is most appropriately interpreted through a dispersion diagram, which characterizes the relationship between the frequency of the wave, ω , and its associated wave vector, k . Dispersion surfaces provide the spatial variation of the spectral properties of a certain band within the photonic crystal structure. An electromagnetic wave propagates along the direction normal to the dispersion

surface, which stems from the relation of the group velocity $\mathbf{v}_g = \nabla_k \omega(\mathbf{k})$. The ability to shape the equifrequency contours (EFC), and thereby engineer the dispersion properties of the PhC, opens up a new paradigm for the design of optical devices [28–30]. For the applications of self-collimation, we desire a flat EFC, in which case the wave is only allowed to propagate along those directions normal to the sides of the straight curvatures. As such, it is possible to vary the incident wave vector over a wide range of angles and yet maintain a narrow range of propagating angles within the PhC.

Based on the dispersion waveguiding property in photonic crystals, a novel class of photonic-crystal-embedded microcavity (PCEM) coupled with waveguide [30] has been theoretically investigated using FDTD algorithm, in which both optical resonant mode and quality factor are particularly considered. Figure 9(a) depicts the schematic of our design. A photonic crystal cavity consists of a silicon square slab perforated by an $N \times N$ array of square lattice. The air holes are back-filled with the gain medium, that is, Er-doped glasses, as shown in the inset of Figure 9(a). The hole has a radius of $0.3a$, where a is the lattice constant. The silicon and glass have refractive indices of 3.5 and 1.5, respectively. After the light couples into the resonator from the waveguide, it will propagate along the ΓM direction and then will be reflected at the edge of the resonator. As such, with the assistance of the four clear edges of silicon slab as mirrors, a traveling wave-based cavity can be formed along the optical path indicated by an arrow loop in Figure 9(b), which is similar to a whispering gallery mode in a microdisk resonator. Along one edge of this microcavity, a conventional dielectric waveguide is used for the in-/outcoupling between the cavity and waveguide. To realize the active operation in such a microcavity, we fill the air holes with a certain gain medium to achieve nonlinear gain dynamics. In our design, low-index highly doped Erbium Ion glass is considered as a gain material for the light amplification. The proposed device has several advantages. (1) Since we are working at the first band of the dispersion surface, the self-collimation

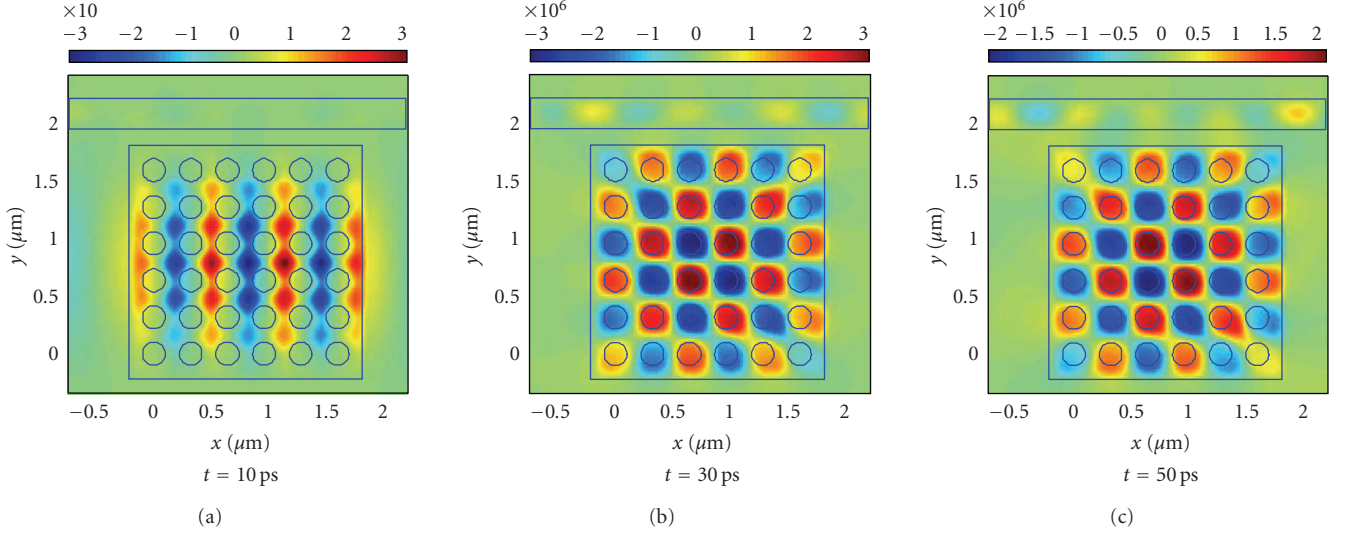


FIGURE 12: Snapshots of 2D field distribution at three time instants: 10, 30, and 50 ps.

mode is far below the light cone, therefore the wave inside the resonator is well confined inside the slab with minimal out-plane propagation loss even with the presence of a substrate. (2) The self-collimation mode is very close to the band edge, so the slow group velocity will enhance the nonlinear interaction between light and gain material.

We simulate the proposed device using the FDTD method. A 6×6 array of glass-filled cylinders is initially simulated; the highest resonant mode below the band edge of the first dispersion band is shown in Figure 9(b). We observe that most optical modes are well confined within the low-index materials. This unique property may benefit the lasing mechanism and lower the optical pumping threshold. The cavity properties are largely dependent on the design parameters, such as gap size between the waveguide and resonator, and array size. An extensive study has been performed to investigate the passive cavity performance. The gap between the cavity and waveguide is a critical design parameter to achieve optimal coupling and Q factor. An optimal gap size of 160 nm is found in the following design. In this case, we measured a Q factor of 520 and drop efficiency of 32.2% for a resonant mode at 1532 nm. We also investigate the Purcell factor as an additional figure of merit for the microcavity. The Purcell factor dictates the enhancement in the radiative recombination rate due to optical confinement provided by the cavity. Based on the mode profile at the resonant wavelength of 1532 nm, the PhC microcavity exhibits an effective mode volume of $3.27 \cdot (\lambda/n)^3$ and a Purcell factor of 10.88.

With the appropriate design of the microcavity based on the dispersion engineering of photonic crystals, we further considered backfilling the air holes in photonic crystals with a gain medium, that is, Er-doped glass, to achieve active operation, as shown in the schematic view of the proposed novel silicon laser in Figure 9(a). For the Er^{3+} Ion, the typical lifetime is on the order of $10^{-3} \sim 10^{-2}$ s. Numerically, using a rigorous EM algorithm in the time domain to

simulate the lasing dynamics, this is far beyond the state-of-the-art computational capability, particularly in a high-dimension system. To phenomenologically investigate the lasing dynamics in the microcavity with the backfilled gain medium, we scale the lifetime of electron population transition accordingly while maintaining a reasonable timescale associated with different relaxation processes. To this end, we shorten the lifetime of atomic transitions to reduce the computation time necessary to achieve the steady state. The lifetimes are given by $\tau_{10} = 10^{-12}$ s, $\tau_{21} = 10^{-10}$ s, and $\tau_{32} = 10^{-13}$ s. The transition frequency associated with the energy levels N_2 and N_1 is chosen as 200 THz and linewidth is taken to be 6 THz. The pump rate into level N_3 is chosen as $W_p = 2 \times 10^8/\text{s}$. The initial state of the simulation is included as follows: all the electrons are in the ground state, so there is no field in the cavity and no spontaneous emission. In this paper, we choose $N_0 = 3 \times 10^{24}/\text{m}^3$. After the electrons are pumped, the system starts to evolve both in terms of population densities and electromagnetic waves. To monitor the EM dynamics, a detector is placed in the waveguide.

In the FDTD simulation, a total time of 66 ps is simulated. The time step Δt is chosen as 3.3×10^{-7} s, so a total of 2 million FDTD iterations are used. The evolution of electromagnetic waves starts from an initial small noise current over the photonic crystal cavity. A detector is placed in the waveguide to monitor the lasing dynamics, and the total field in the output waveguide is illustrated in Figure 10(a). In the figure, we observe the lasing performance. For clarity, we zoom in on a portion of the transient plot near 60 ps as shown in Figure 10(b), which indicates a nearly single lasing mode.

Figure 11 shows the calculated time evolution of the electron population inversion between energy levels 2 and 1 at the position of one of the central holes in the cavity. The plotted population inversion is normalized to total electron concentration. During the simulation, the ground state population density remains relatively unchanged compared

to higher-level populations. In the beginning, the population inversion linearly increases, leading to significant amplification of electromagnetic waves in the cavity. In the meantime, the desired cavity mode is gradually established. Eventually, a convergent population inversion, -6.9×10^{-4} , can be observed. The population dynamics are consistent with the lasing output from the waveguide.

In addition, snapshots of the 2D magnetic fields after the simulation ran for 10, 30, and 50 ps are plotted in Figure 12, where the lasing dynamics of the electromagnetic field is gradually established within the cavity. In the end, the high-intensity distribution of EM field can be observed in the cavity area, particularly in the low-index material region and steady results are output from both ends of the straight waveguide.

6. CONCLUSION

In this paper, a time-domain analysis of active silicon-based photonic devices is proposed. The simulation model couples Maxwell's equations with the rate equations to fully describe the nonlinearity of active medium, and numerically solves them using an ADE-FDTD scheme. Both stimulated and spontaneous emissions are taken into account in the active medium system. Light amplification characteristics due to stimulated emission are investigated under various pump rates in both 1D and 2D waveguiding silicon nanocrystals. To achieve amplified spontaneous emission, microcavities based on photonic band gap materials are carefully designed. These Fabry-Perot microcavities are shown to significantly enhance the spontaneous emission signal. At last, we propose a novel PhC-based microcavity, in which a low-index gain medium is incorporated into the air holes in photonic crystals, to study the lasing characteristics.

ACKNOWLEDGMENT

This work is partially sponsored by the research Contracts FA9550-06-1-0470 and 5710002024 from AFOSR.

REFERENCES

- [1] B. Jalali, M. Paniccia, and G. Reed, "Silicon photonics," *IEEE Microwave Magazine*, vol. 7, no. 3, pp. 58–68, 2006.
- [2] L. Pavesi, "Will silicon be the photonic material of the third millennium?" *Journal of Physics: Condensed Matter*, vol. 15, no. 26, pp. R1169–R1196, 2003.
- [3] M. E. Castagna, S. Coffa, M. Monaco, et al., "Si-based materials and devices for light emission in silicon," *Physica E*, vol. 16, no. 3-4, pp. 547–553, 2003.
- [4] L. Pavesi, L. Dal Negro, C. Mazzoleni, G. Franzò, and F. Priolo, "Optical gain in silicon nanocrystals," *Nature*, vol. 408, no. 6811, pp. 440–444, 2000.
- [5] A. Fojtik, J. Valenta, I. Pelant, M. Kalal, and P. Fiala, "On the road to silicon-nanoparticle laser," *Journal of Materials Processing Technology*, vol. 181, no. 1–3, pp. 88–92, 2007.
- [6] D. J. Lockwood, Z. H. Lu, and J.-M. Baribeau, "Quantum confined luminescence in Si/SiO₂ superlattices," *Physical Review Letters*, vol. 76, no. 3, pp. 539–541, 1996.
- [7] V. Ovchinnikov, A. Malinin, V. Sokolov, O. Kilpelä, and J. Sinkkonen, "Photo and electroluminescence from PECVD grown a-Si:H/SiO₂ multilayers," *Optical Materials*, vol. 17, no. 1-2, pp. 103–106, 2001.
- [8] J. Lee, J. H. Shin, and N. Park, "Optical gain at 1.5 μm in nanocrystal Si-sensitized Er-doped silica waveguide using top-pumping 470 nm LEDs," *Journal of Lightwave Technology*, vol. 23, no. 1, pp. 19–25, 2005.
- [9] T. Creazzo, E. Marchena, B. Redding, T. Hodson, and D. W. Prather, "Fabrication and characterization of silicon/silicon dioxide super lattices for silicon based light emitting devices," in *Nanoengineering: Fabrication, Properties, Optics, and Devices IV*, vol. 6645 of *Proceedings of SPIE*, pp. 1–8, San Diego, Calif, USA, August 2007.
- [10] L. Pavesi, S. Gaponenko, and L. Dal Negro, *Towards the First Silicon Laser*, Kluwer Academic Publishers, Dordrecht, The Netherlands, 2002.
- [11] H. Rong, R. Jones, A. Liu, et al., "A continuous-wave Raman silicon laser," *Nature*, vol. 433, no. 7027, pp. 725–728, 2005.
- [12] O. Boyraz and B. Jalali, "Demonstration of a silicon Raman laser," *Optics Express*, vol. 12, no. 21, pp. 5269–5273, 2004.
- [13] A. S. Nagra and R. A. York, "FDTD analysis of wave propagation in nonlinear absorbing and gain media," *IEEE Transactions on Antennas and Propagation*, vol. 46, no. 3, pp. 334–340, 1998.
- [14] X. Jiang and C. M. Soukoulis, "Time dependent theory for random lasers," *Physical Review Letters*, vol. 85, no. 1, pp. 70–73, 2000.
- [15] P. Sebbah and C. Vanneste, "Random laser in the localized regime," *Physical Review B*, vol. 66, no. 14, Article ID 144202, 10 pages, 2002.
- [16] S. Shi and D. W. Prather, "Lasing dynamics of a silicon photonic crystal microcavity," *Optics Express*, vol. 15, no. 16, pp. 10294–10302, 2007.
- [17] S. Shi, G. Jin, and D. W. Prather, "Electromagnetic simulation of quantum well structures," *Optics Express*, vol. 14, no. 6, pp. 2459–2472, 2006.
- [18] D. Biallo, A. D'Orazio, M. De Sario, V. Petruzzelli, and F. Prudenzeno, "Time domain analysis of optical amplification in Er³⁺ doped SiO₂-TiO₂ planar waveguide," *Optics Express*, vol. 13, no. 12, pp. 4683–4692, 2005.
- [19] S.-H. Chang and A. Taflove, "Finite-difference time-domain model of lasing action in a four-level two-electron atomic system," *Optics Express*, vol. 12, no. 16, pp. 3827–3833, 2004.
- [20] K. K. Lee, D. R. Lim, H.-C. Luan, A. Agarwal, J. Foresi, and L. C. Kimerling, "Effect of size and roughness on light transmission in a Si/SiO₂ waveguide: experiments and model," *Applied Physics Letters*, vol. 77, no. 11, pp. 1617–1619, 2000.
- [21] L. Dal Negro, M. Cazzanelli, N. Daldosso, et al., "Stimulated emission in plasma-enhanced chemical vapour deposited silicon nanocrystals," *Physica E*, vol. 16, no. 3-4, pp. 297–308, 2003.
- [22] A. E. Siegman, *Lasers*, University Science Books, Mill Valley, Calif, USA, 1986.
- [23] J.-Y. Sung, A. Tewary, M. L. Brongersma, and J. H. Shin, "Cavity Q measurements of silica microspheres with nanocluster silicon active layer," *IEEE Journal on Selected Topics in Quantum Electronics*, vol. 12, no. 6, pp. 1388–1392, 2006.
- [24] L. Dal Negro, M. Cazzanelli, B. Danese, et al., "Light amplification in silicon nanocrystals by pump and probe transmission measurements," *Journal of Applied Physics*, vol. 96, no. 10, pp. 5747–5755, 2004.
- [25] S. Shi, T. Creazzo, B. Redding, and D. W. Prather, "Simulation of light amplification and enhanced spontaneous emission in silicon nanocrystals," in review, *Journal of Optics A: Pure and Applied Optics*, 2008.

-
- [26] B. Redding, S. Shi, and D. W. Prather, "Time analysis of active silicon nanocrystal waveguiding structures," *Optics Express*, accepted for publication, 2008.
 - [27] A. Belarouci and F. Gourbilleau, "Microcavity enhanced spontaneous emission from silicon nanocrystals," *Journal of Applied Physics*, vol. 101, no. 7, Article ID 073108, 4 pages, 2007.
 - [28] D. W. Prather, S. Shi, D. M. Pustai, et al., "Dispersion-based optical routing in photonic crystals," *Optics Letters*, vol. 29, no. 1, pp. 50–52, 2004.
 - [29] M. R. Newton, K. A. Morey, Y. Zhang, et al., "Anisotropic diffusion in face-centered cubic opals," *Nano Letters*, vol. 4, no. 5, pp. 875–880, 2004.
 - [30] K. Tsia and A. Poon, "Dispersion-guided resonances in two-dimensional photonic-crystal-embedded microcavities," *Optics Express*, vol. 12, no. 23, pp. 5711–5722, 2004.

Review Article

Three-Dimensional Silicon-Germanium Nanostructures for CMOS Compatible Light Emitters and Optical Interconnects

L. Tsybeskov,¹ E.-K. Lee,¹ H.-Y. Chang,¹ B. V. Kamenev,¹ D. J. Lockwood,² J.-M. Baribeau,² and T. I. Kamins³

¹Department of Electrical and Computer Engineering, New Jersey Institute of Technology, Newark, NJ 07102, USA

²Institute for Microstructural Sciences, National Research Council, Ottawa, Ontario, Canada K1A 0R6

³Quantum Science Research, Hewlett-Packard Laboratories, Palo Alto, CA 94304, USA

Correspondence should be addressed to L. Tsybeskov, tsybesko@adm.njit.edu

Received 1 March 2008; Accepted 2 April 2008

Recommended by Pavel Cheben

Three-dimensional SiGe nanostructures grown on Si (SiGe/Si) using molecular beam epitaxy or low-pressure chemical vapor deposition exhibit photoluminescence and electroluminescence in the important spectral range of 1.3–1.6 μm . At a high level of photoexcitation or carrier injection, thermal quenching of the luminescence intensity is suppressed and the previously confirmed type-II energy band alignment at Si/SiGe cluster heterointerfaces no longer controls radiative carrier recombination. Instead, a recently proposed dynamic type-I energy band alignment is found to be responsible for the strong decrease in carrier radiative lifetime and further increase in the luminescence quantum efficiency.

Copyright © 2008 L. Tsybeskov et al. This is an open access article distributed under the Creative Commons Attribution License, which permits unrestricted use, distribution, and reproduction in any medium, provided the original work is properly cited.

1. INTRODUCTION

Optical interconnects in the form of fiber optics have been used for many years in different long-distance communication applications [1, 2]. With the microprocessor clock speed approaching 10 Gbps, optical interconnects are now being considered for board-to-board and on-chip technology as an alternative to metal wires with their unavoidable RC delay, significant signal degradation, problems with power dissipation, and electromagnetic interference [2–5]. Two major avenues toward optical interconnects on a chip comprise the hybrid approach with III-V optoelectronic components densely packaged into complementary metal-oxide semiconductor (CMOS) architecture [6–9] and the all-group-IV (e.g., Si, SiGe, SiGeC, etc.) approach with the all major components, for example, light emitters, modulators, waveguides, and photodetectors, monolithically integrated into the CMOS environment [10]. There have been great efforts over the past several decades to obtain technologically viable and efficient light emission from group-IV materials. In the visible spectral region, the main emphasis has been on porous silicon [11–13] and other Si nanostructured systems such as silicon/silicon dioxide superlattices [14–17] and silicon nanoprecipitates in silicon dioxide [18, 19]. In the near infrared spectral region, materials and systems such

as erbium in silicon [10, 20], silicon/germanium quantum wells [21, 22], and, more recently, iron disilicide [23] offer potentially useful routes. However, no approach has so far been applied commercially. The reasons for this are the lack of a genuine or perceived compatibility with conventional CMOS technology, the long carrier radiative lifetime in Si-based nanostructures, and, especially in the case of near-infrared emitters, the high thermal quenching leading to extremely poor room-temperature luminescence efficiencies [10].

In the 1990s, an interesting form of semiconductor nanostructure, namely, the three-dimensional (3D) self-assembled system produced by the Stranski-Krastanov or cluster-layer, growth mode in lattice mismatched materials, has been demonstrated [24, 25]. In the case of 3D Si/SiGe nanostructures (NSs), the growth of mostly dislocation-free samples has successfully been achieved using both molecular beam epitaxy (MBE) and chemical vapor deposition (CVD) [26–31]. It has been shown that the nonplanar geometry is mainly responsible for the significant increase of the critical layer thickness in 3D Si/SiGe NSs grown on Si [28, 29]. It has also been found that compared to planar Si/SiGe quantum wells (QWs), the photoluminescence (PL) and electroluminescence (EL) quantum efficiency in 3D Si/SiGe NSs is higher, especially at temperatures $T > 50\text{ K}$

[32–35]. Despite many successful demonstrations of PL and EL in the spectral range of 1.3–1.6 μm , which is important for optical fiber communications, the proposed further development of 3D Si/SiGe NS-based light emitters was discouraged by several studies confirming a type-II energy band alignment at Si/SiGe heterointerfaces [36–40], where the spatial separation of electrons (located in Si) and holes (localized in SiGe) was thought to make carrier radiative recombination very inefficient. Later, it was also shown that 3D Si/SiGe NSs exhibit an extremely long (of the order of 10^{-2} seconds) luminescence lifetime [41], which is of the order of a million times longer than those found in III-V semiconductors. In addition, single crystal Si and Ge are indirect band gap semiconductors and it has been declared that since carrier radiative recombination is an indirect process in these materials, in both real and reciprocal space, this process should be extremely inefficient. Thus, according to this analysis, 3D SiGe NSs cannot be used to achieve efficient and commercially valuable light emitting devices.

In this review paper, we show that despite the fact that bulk Si and Ge are indeed indirect band gap semiconductors and that the Si/SiGe heterointerface most likely exhibits type-II energy band alignment, it is still possible to obtain conditions favorable for efficient carrier radiative recombination. We demonstrate that the recent revised understanding of basic physics in such systems has already helped to achieve nearly constant luminescence intensity at temperatures $4\text{ K} < T < 250\text{ K}$, and that the radiative carrier recombination lifetime can successfully be reduced from 10^{-2} second to 10^{-7} seconds, which is only ~ 10 times longer compared to those found in direct band gap III-V semiconductors.

2. GROWTH AND STRUCTURAL PROPERTIES OF Si/SiGe THREE-DIMENSIONAL NANOSTRUCTURES

The standard approach to the fabrication of a 3D Si/SiGe NS, which for most experiments discussed here is a multilayer Si/SiGe cluster system, is based on the sequential physical sputtering of Si and Ge (SiGe) in MBE or the thermal decomposition of SiH_4 and GeH_4 in CVD at a temperature in the range $T = 550\text{--}650^\circ\text{C}$. At that temperature, both a high Ge solid solubility in Si as well as strain induced SiGe interdiffusion due to the $\sim 4\%$ lattice mismatch between Si and Ge are important. The MBE growth provides better control over the average SiGe cluster composition, although, because of interdiffusion during growth, the composition is not uniform within the cluster volume [42–45]. Figure 1 shows typical transmission electron micrographs (TEMs) together with a summary of analytical TEM studies confirming both the 3D geometry of the SiGe NSs and the complex atomic composition. In general, SiGe cluster growth commences with the spontaneous development of a $\text{Si}_{1-x}\text{Ge}_x$ planar, $<1\text{ nm}$ thick, wetting layer where x varies, mainly due to uncontrolled SiGe interdiffusion. With the further influx of Ge and Si, the growth mode then switches from two dimensional (a layer) to 3D (a cluster), which helps release some of the lattice-mismatch induced strain [44]. The fully grown 3–10 nm high and initially nearly pyramidal-shaped SiGe clusters have a Ge-rich ($\sim 50\%$ depending on the Ge

flux) core, although the exact final cluster shape and composition strongly depends on the fabrication conditions [45]. If the SiGe cluster is covered by a Si cap, the initial pyramid-like cluster top is smoothed out (Figure 1(a)), and the capping Si layer is locally strained, mostly near the top of the SiGe cluster. In multilayer Si/SiGe cluster samples, this strain field propagates in the growth direction, and it induces vertical SiGe cluster self-ordering (Figure 1(a)). Detailed structural analysis also indicates that the Si in the valleys between SiGe clusters is slightly compressed [30, 44]. To summarize, buried SiGe clusters with the highest Ge composition of near 50% in the middle of the clusters are surrounded by Si, which is tensile strained above each cluster and compressed laterally between clusters to maintain a low overall strain. Each SiGe cluster consists of $\text{Si}_{1-x}\text{Ge}_x$ crystalline alloys with x increasing toward the cluster center [43–45]. Thus, despite being fully crystalline alloys, 3D Si/SiGe NSs with a high ($\sim 50\%$) Ge atomic concentration exhibit significant embedded strain and compositional disorder [46]. These conclusions regarding the structural properties of 3D Si/SiGe NSs are critically important in understanding their optical characteristics and light-emitting properties.

3. OPTICAL PROPERTIES OF Si/SiGe THREE-DIMENSIONAL NANOSTRUCTURES

In a system with strong selection rule relaxation, quasidirect carrier recombination is possible, and it should provide a higher PL quantum efficiency compared to that in an indirect band gap semiconductor, for example, single crystal Si and Ge. In fact, many PL measurements in SiGe bulk alloys and Si/SiGe NSs reveal a significantly enhanced intensity ratio between no-phonon (NP) luminescence and phonon-assisted luminescence, as shown in Figure 2(a). On the other hand, in undoped bulk crystalline Si (*c*-Si), the NP PL line intensity is negligible compared to the transverse optical (TO) and transverse acoustic (TA) phonon-assisted radiative transitions (see Figure 2(b)). Thus, systematic studies of the PL spectra in 3D $\text{Si/Si}_{1-x}\text{Ge}_x$ NSs with control over the average Ge atomic concentration x provide very important information regarding changes in the carrier recombination mechanism (e.g., selection rule relaxation, conduction and valence band alignment, etc.) as x increases from 0 (*c*-Si) to $\sim 55\%$.

Figure 3(a) compares PL spectra in MBE samples with $x = 0.096, 0.16,$ and 0.53 . In addition to PL related to *c*-Si, we observe for $x = 0.096$ relatively narrow PL bands at 1.05 and 1.11 eV (Figure 3(a)) attributed to NP and TO phonon PL bands in Si-rich SiGe alloys [33–35, 47, 48]. Note that these PL bands are in the vicinity of *c*-Si luminescence, and that the intensities of these two sets of PL bands are comparable. Therefore, we conclude that a small amount of Ge ($<10\%$) slightly reduces the SiGe band gap and mainly relaxes selection rules, increasing the ratio of NP/TO PL band intensities. The observed broadening of these two PL bands, compared to *c*-Si related PL, is, apparently, due to the composition disorder resulting from the introduction of substitutional Ge atoms ($\sim 10\%$) into the *c*-Si matrix.

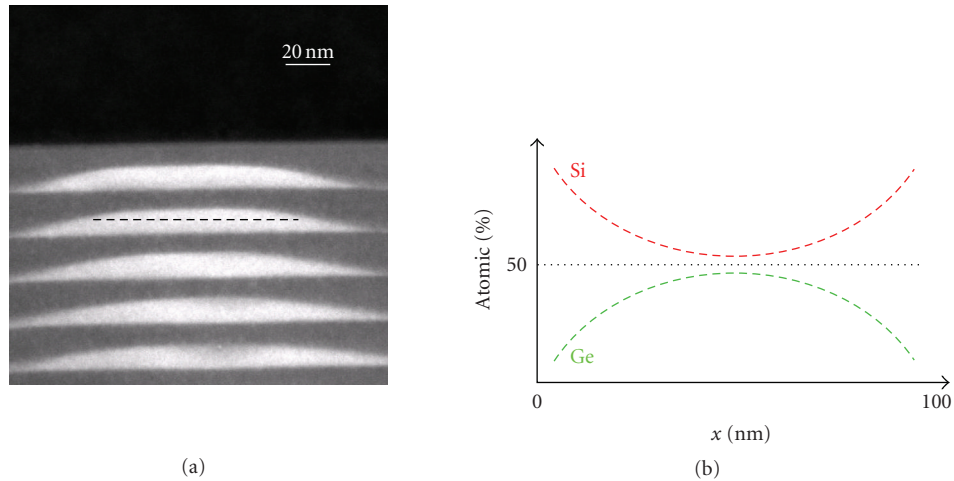


FIGURE 1: (a) Transmission of electron micrograph showing a cross-section of an MBE grown, vertically self-aligned Si/SiGe cluster (or 3D) multilayer structure. (b) Schematic showing typical Si and Ge atomic concentrations within an SiGe cluster measured along a horizontal axis running through the middle of the cluster (see the dashed line in Figure 1(a)).

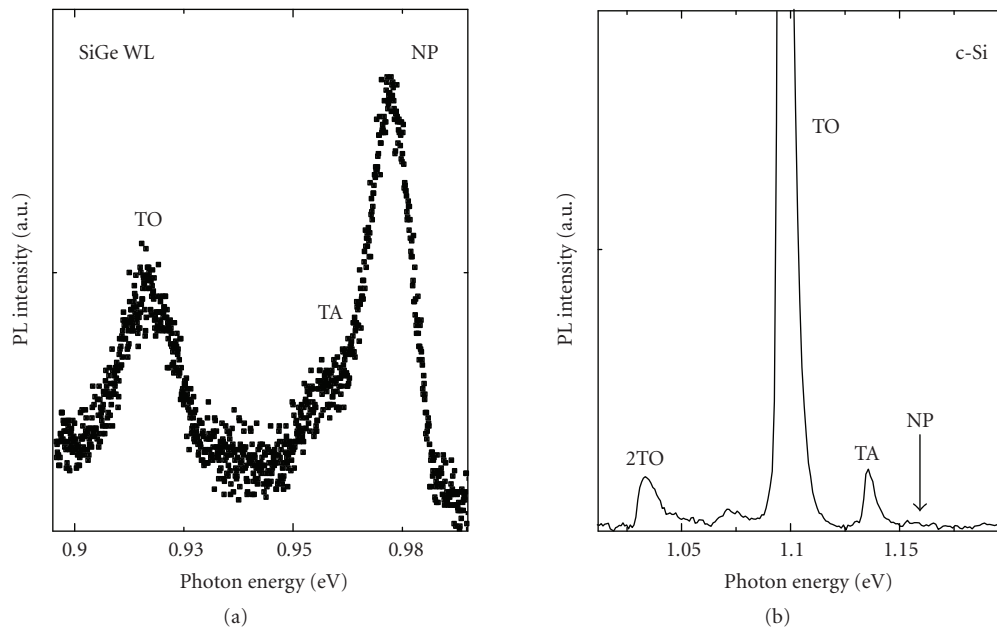


FIGURE 2: Comparison between low temperature ($T = 4$ K) PL spectra in (a) an SiGe wetting layer with $\sim 20\%$ Ge concentration and (b) undoped crystalline Si (c -Si). Note the dramatically different intensity ratios between the NP and TO phonon PL lines of each sample.

Increasing the average Ge composition within $\text{Si}_{1-x}\text{Ge}_x$ clusters up to $x = 0.16$ results in significant changes in the PL spectrum (Figure 3(b)). An intense PL band peaked at 0.95 eV has appeared, showing an effective SiGe band gap reduction of ~ 150 meV compared to c -Si. This broad and featureless PL band with a full width at half maximum (FWHM) of ~ 70 meV indicates a much stronger compositional disorder compared to 3D Si/SiGe NC samples with $x = 0.096$.

The PL spectrum in the samples with an average Ge composition close to 53% (Figure 3(c)) depicts a broad feature with a major PL peak centered at a photon energy

of 0.75 eV, and this peak energy is close to the band gap of crystalline Ge (c -Ge) at 4 K [49]. A second PL peak is found at ~ 0.85 eV. Such samples have the highest PL quantum efficiency as compared to other samples with lower x values. Both PL bands are quite broad, most likely due to compositional disorder, which is in an agreement with the Raman scattering measurements (discussed below).

In contrast to MBE grown samples, CVD growth of 3D Si/SiGe NSs does not provide precise control over the Ge atomic composition, and, most likely, it produces more Si/SiGe interdiffusion at heterointerfaces [42–44, 50]. This is well reflected in PL spectra, where no fine structure has been

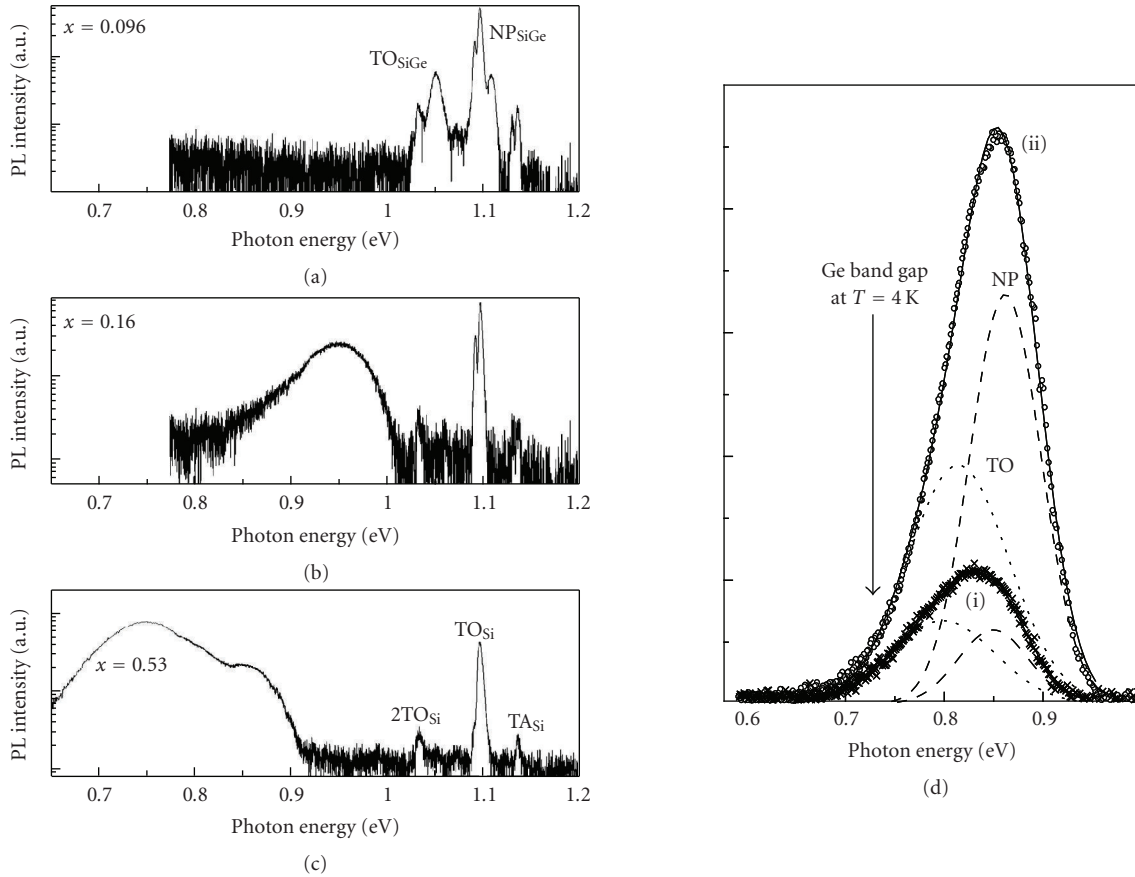


FIGURE 3: (a) Low temperature ($T = 4$ K) PL spectra in (a) MBE grown $\text{Si}/\text{Si}_{1-x}\text{Ge}_x$ 3D NSs with the indicated average Ge atomic concentration x and (d) in Si/SiGe 3D NSs grown by CVD. The characteristic phonon-assisted transitions are indicated. PL spectra in CVD samples show a strong spectral shift toward higher photon energy when the excitation intensity is increased by approximately 5 times from trace (i) to trace (ii) (note the linear intensity scale).

found (see Figure 3(d)). However, the broad and asymmetric PL peak is well fitted by two Gaussian bands often identified as the NP and TO phonon lines [46, 47] that are separated by ~ 48 meV, which is close to the energy of characteristic SiGe phonons. Thus, there is at least a qualitative similarity between PL spectra in MBE and CVD grown 3D Si/SiGe NSs.

Figure 4 summarizes the PL intensity as a function of excitation intensity in MBE samples having different average Ge atomic concentrations. The same linear dependence (on a log-log plot) for PL associated with c-Si and a sublinear (close to square root) dependence for PL associated with a Ge-rich SiGe cluster core has been found in nearly all 3D Si/SiGe NSs grown by both CVD and MBE [35, 51–53].

Studies of the PL temperature dependence show that at low temperatures the PL intensity is nearly temperature independent. At higher temperatures the PL intensity drops exponentially, and the activation energies of PL thermal quenching are shown in Figure 5. There is a clear correlation between the Ge composition in $\text{Si}_{1-x}\text{Ge}_x$ 3D nanostructures and the PL intensity temperature dependence. For samples with a low ($x = 0.096$) Ge composition, the activation energy E_a is ~ 10 meV, and the PL has almost vanished by 40 K. This result could be explained by the thermal dissociation of a

nearly free exciton: a localization mechanism associated with SiGe stoichiometric fluctuations has been proposed in [53–55]. Figure 4(a) shows that the PL intensity as a function of the excitation intensity is linear (again, on a log-log scale), and that is consistent with the assumption of nearly free exciton PL.

In samples with a higher ($x = 0.16$) Ge composition, the activation energy of PL thermal quenching is increased and the PL is observable up to ~ 100 K (Figure 5(b)). The broad PL band observed at 0.95 eV for the $\text{Si}/\text{Si}_{1-x}\text{Ge}_x$ sample of $x = 0.16$ exhibits an activation energy of ~ 25 meV, which combined with a sublinear dependence in PL intensity as a function of excitation intensity (Figure 4(b)) is in contrast with the $x = 0.096$ sample. This observation suggests that the nonequilibrium carriers are spatially localized and that Auger recombination contributes to the overall recombination mechanism even at very low (~ 100 mW/cm²) excitation intensity [54, 55]. Most likely, in 3D $\text{Si}/\text{Si}_{1-x}\text{Ge}_x$ NSs with $x = 0.16$, the carriers (possibly holes) are localized within 3D SiGe quasiwells.

In 3D $\text{Si}/\text{Si}_{1-x}\text{Ge}_x$ nanostructures with $x = 0.53$, the PL spectrum contains two bands peaked at 0.85 eV and 0.75 eV (Figure 3(c)). There are no characteristic phonons in the

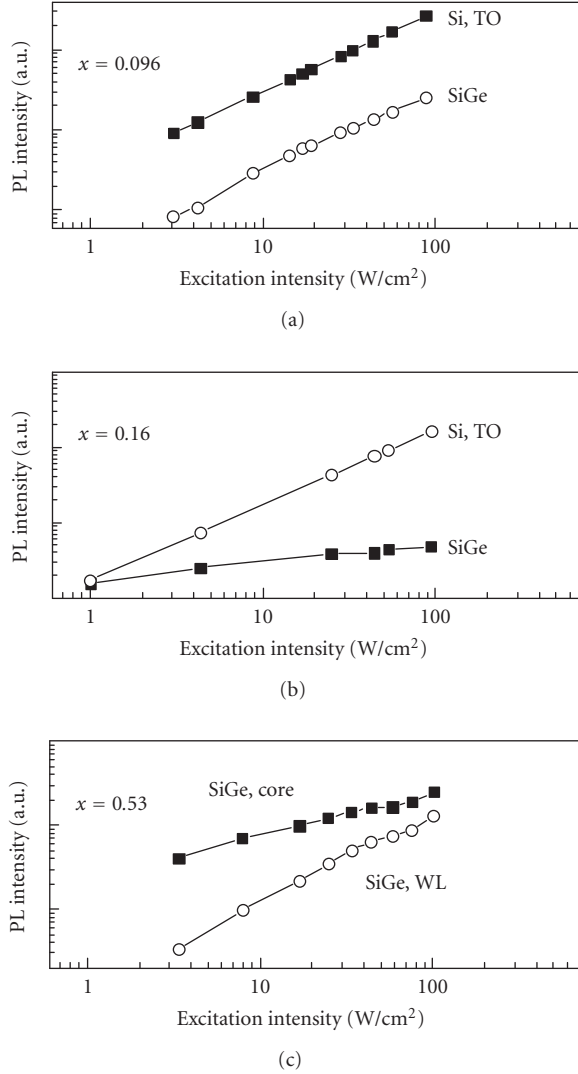


FIGURE 4: The PL intensity as a function of excitation intensity in MBE grown $\text{Si/Si}_{1-x}\text{Ge}_x$ 3D NS samples with the indicated average Ge concentration x . The PL bands associated with the cluster core, wetting layer (WL), and characteristic TO phonons are indicated.

Si/SiGe system having an energy of ~ 100 meV, and it is thus reasonable to assume that the observed PL bands are associated with carrier recombination within two different regions of the 3D SiGe nanostructures. The PL band peaked at 0.85 eV has almost the same PL quenching activation energy (~ 20 meV) as in the sample with $x = 0.16$, while the PL intensity as function of excitation intensity is linear over a wide range of excitation intensities. The second PL band peaked at 0.75 eV has an activation energy of ~ 60 meV (Figure 5(c)) and is nearly temperature independent up to 100 K. Because of its high quantum efficiency, it can be monitored almost up to room temperature. This data suggests that 3D $\text{Si/Si}_{1-x}\text{Ge}_x$ nanostructures with $x = 0.53$ contain coupled subsystems with different (lower and higher) Ge concentrations. It is quite possible that a spatial localization of electron-hole pairs within 3D regions of

higher Ge concentration and thus having a lower band gap could be responsible for the observed sublinear excitation dependence of the PL band at 0.75 eV (Figure 4(c)). The remaining 3D regions with a lower Ge concentration (e.g., having a higher band gap) have a lower carrier concentration and the PL band (peaked at 0.85 eV) exhibits a linear excitation dependence.

A continuous shift of the PL band from ~ 1 to 0.75 eV has been found previously in SiGe alloys with increasing Ge concentration [56]. Instead, in these 3D $\text{Si/Si}_{1-x}\text{Ge}_x$ samples with a Ge concentration higher than 50%, a simultaneous threshold-like appearance of two clearly resolved PL peaks at 0.85 and 0.75 eV is observed. This suggests that Ge segregation might take place as x increases up to ~ 0.5 . Since the PL peak at 0.75 eV essentially matches the value of the band gap in pure $c\text{-Ge}$, we propose that such a segregation results in a Ge-rich core within an SiGe shell forming the 3D $\text{Si/Si}_{1-x}\text{Ge}_x$ NSs embedded within a pure Si matrix.

The PL thermal quenching observed in 3D $\text{Si/Si}_{1-x}\text{Ge}_x$ samples grown by MBE could be associated with different mechanisms. As mentioned earlier, the activation energies of the PL thermal quenching in samples with $x = 0.096$ and $x = 0.16$ are close to the observed exciton binding energy in SiGe alloys and $\text{Si/Si}_{1-x}\text{Ge}_x$ nanostructures [53–57]. In samples with $x = 0.53$, a greater activation energy could be attributed to carrier diffusion from a 3D potential well. This assumption is justified by the expected type-II band alignment in SiGe nanostructures with a deep (>100 meV) potential well for holes and a relatively small potential barrier for electrons [38, 40, 41]. In this model, phonon-assisted carrier tunneling can produce the observed ~ 60 meV activation energy for thermal quenching of the PL intensity. The PL intensity behavior as a function of temperature in CVD grown samples is more complex and will be discussed later.

In 3D Si/SiGe NSs, the PL properties strongly correlate with the sample structural properties, and Raman scattering under excitation conditions similar to PL measurements has been shown to be a very informative characterization technique [35]. In fact, in SiGe materials and systems, Raman spectroscopy is a unique characterization technique due to the multimodal nature of Raman scattering from optical phonons in SiGe , which reveals all three major vibrational modes known, respectively, as the Si–Si vibration at ~ 500 cm^{-1} , the Si–Ge vibration at ~ 400 cm^{-1} , and the Ge–Ge vibration at ~ 300 cm^{-1} (see Figure 6, e.g.). In addition, Raman phonon spectroscopy is a very sensitive probe of global and local embedded strain and of compositional and structural disorder. Figure 6 compares Raman spectra for MBE samples of different Ge composition. In $\text{Si}_{1-x}\text{Ge}_x$ clusters with $x = 0.096$, an intense optical phonon Raman signal associated with Si–Si vibrations is observed at ~ 520 cm^{-1} together with a weaker feature at ~ 300 cm^{-1} related to second-order scattering from Si acoustic phonons [58]. No significant Raman peaks related to Ge–Ge vibrations at ~ 290 cm^{-1} and Si–Ge vibrations at ~ 420 cm^{-1} [59] and to an amorphous Si phase at ~ 480 cm^{-1} [60] were found in this or the $x = 0.16$ sample (see Figure 6, noting that the intensity axis has a log scale).

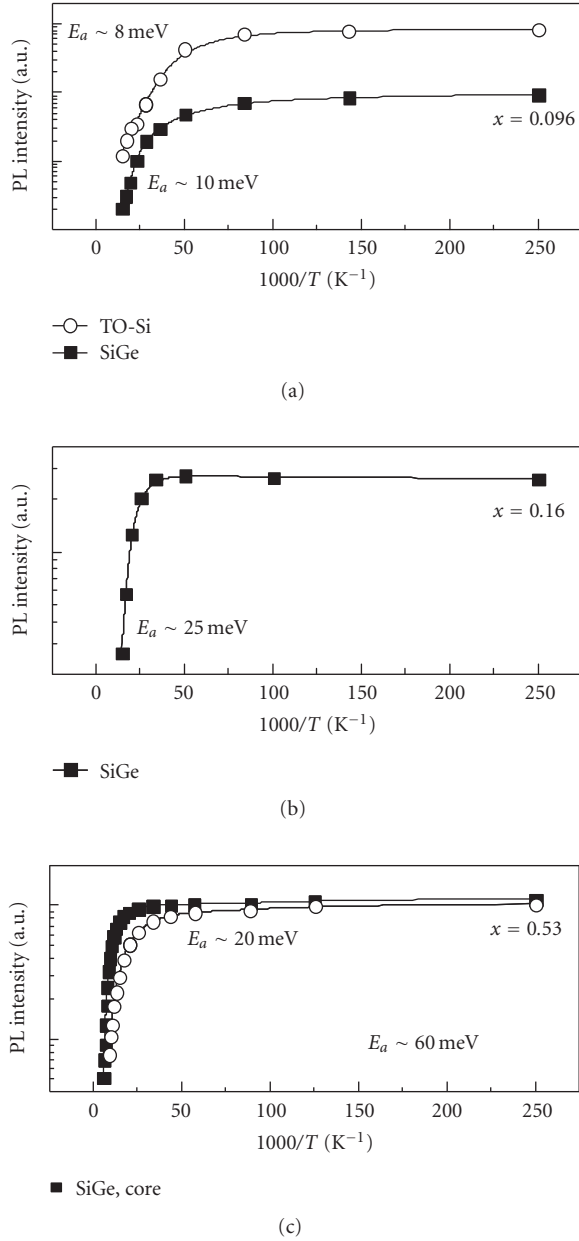


FIGURE 5: The PL intensity temperature dependence in MBE grown $\text{Si}/\text{Si}_{1-x}\text{Ge}_x$ 3D NS samples with the indicated average Ge concentration x measured for different PL bands. Figure 5(c) compares the PL intensity temperature dependencies measured for PL bands with peaks at 0.75 eV (SiGe core) and 0.85 eV.

A further increase in Ge composition to $x = 0.53$ in 3D $\text{Si}_{1-x}\text{Ge}_x$ NSs produces strong Raman signals at ~ 290 cm^{-1} (related to Ge–Ge bonds) and at ~ 420 cm^{-1} (related to Si–Ge bonds), as shown in Figure 6(c). Using a short wavelength photoexcitation (458 nm) and multilayer Si/SiGe 3D samples, the Raman signal from the Si substrate is minimized (see Figure 7). In addition to the major vibrational modes indicated in Figure 7(a), a doublet near 520 cm^{-1} related to compressed (~ 522 cm^{-1}) and strained (~ 507 cm^{-1}) Si is

observed (see Figure 7(b)). The spectrum also exhibits weak and broad (background) Raman peaks in the vicinity of 480 – 490 cm^{-1} and 250 cm^{-1} related to disordered phases of Si and Ge, respectively. Thus, despite the absence of purely amorphous Si and Ge phases in these 3D nanostructured fully-crystalline alloys, compositional disorder and strain-induced lattice distortion combine to produce similar effects in the Raman spectrum.

4. POLARIZED RAMAN SCATTERING IN Si/SiGe THREE-DIMENSIONAL NANOSTRUCTURES

In addition to conventional inelastic light scattering spectroscopy, polarized Raman scattering provides information on Raman scattering intensity as a function of polarization angle. The result is presented employing polar plots and has been shown to be an informative tool for the analysis of local embedded strain in 3D Si/SiGe NSs with larger dome-shaped SiGe clusters grown on Si (100) substrates [61]. In these measurements, the incident light is usually polarized in the plane of the incident and scattered light, and polarization of the scattered light is analyzed using a thin-film polarizer that can be rotated through 360° .

Figure 8 shows angular Raman polarization diagrams for three different alloy vibrational modes (Si–Si at 520 cm^{-1} , Si–Ge at 415 cm^{-1} , and Ge–Ge at 298 cm^{-1}) for multilayer dome/island samples, as well as the Raman polarization dependence for the Si–Si vibration at 520 cm^{-1} measured in $\langle 100 \rangle$ oriented single-crystal Si as a reference. The observed angular dependencies in the polar plots of the Ge–Ge and Si–Ge Raman mode intensities are nearly identical to that in a $\langle 100 \rangle$ Si single crystal. However, a quite different behavior is observed in the Raman polarization dependence for the Si–Si vibration at ~ 519 cm^{-1} .

These different results for the Si–Si mode are emphasized in Figure 8(b), where the Raman spectrum collected at 70° exhibits a major Raman peak at ~ 520 cm^{-1} slightly shifted toward higher wave numbers compared to the data collected at 340° . If this shift is associated with a built-in local strain, the strain can be estimated to be ~ 0.1 GPa [62, 63]. Higher resolution Raman measurements show that the major Raman peak at ~ 520 cm^{-1} is not only just slightly shifted but also broader compared to the spectrum collected from single crystal Si. In addition, we observe a second, much broader peak at ~ 504 cm^{-1} . The angular polarization dependence of the Raman signal at 504 cm^{-1} also deviates from the $\langle 100 \rangle$ oriented single-crystal Si reference, although this deviation is less significant compared to the Raman peak at ~ 520 cm^{-1} . The strong localization of strain observed in the Si matrix is consistent with our understanding of the nature of Stranski-Krastanov growth, where vertical self-ordering is produced by strain propagation through the separating Si layers [64].

5. PHOTOLUMINESCENCE PROPERTIES OF Si/SiGe THREE-DIMENSIONAL NANOSTRUCTURES AS A FUNCTION OF EXCITATION INTENSITY

It has been known for some time that the PL spectra in 3D Si/SiGe NSs, which is similar to that in III-V quantum

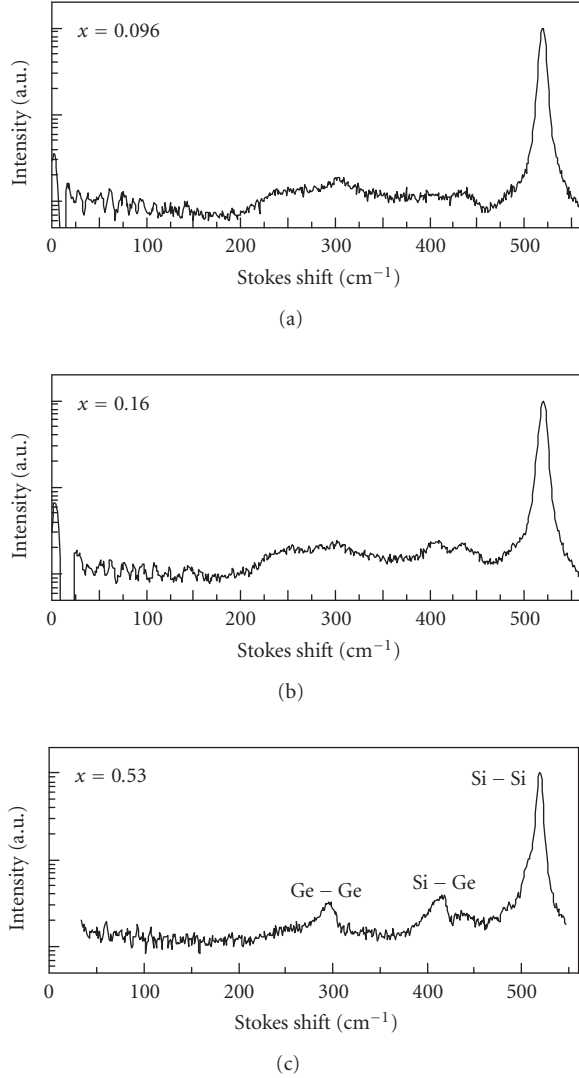


FIGURE 6: Raman spectra measured using 514 nm excitation in MBE grown $\text{Si}/\text{Si}_{1-x}\text{Ge}_x$ 3D NS samples with the indicated average Ge concentration x .

wells with type II energy band alignment [65], exhibit a blue shift as the excitation intensity increases [55, 66]. In our studies, this effect is found in both MBE and CVD grown samples. Figure 9(a) shows PL spectra in a CVD grown sample measured under excitation intensities varied from 0.1 to 100 W/cm^2 . At the lowest excitation intensity used (0.1 W/cm^2), the PL peaks at ~ 0.8 eV. With increasing excitation intensity, a continuous almost parallel PL blue shift of 30–40 meV per decade of excitation intensity increase is observed. At an excitation intensity of 100 W/cm^2 , the PL peak reaches ~ 0.92 eV. Under photoexcitation of 1–10 kW/cm^2 , the low energy part of the PL spectrum does not shift further, while the high energy part continues shifting toward higher energy.

Figure 9(b) compares PL spectra measured with a fixed excitation intensity (~ 5 W/cm^2) for different temperatures

in the range 8–210 K. These measurements clearly show that with increasing temperature, the PL peak associated with SiGe clusters at 0.85–0.9 eV shifts toward lower photon energies. This “red” PL spectral shift is, most likely, associated with the SiGe band gap decrease as the sample temperature increases. Thus, it is opposite to the “blue” PL spectrum shift observed with an excitation intensity increase, and thus this blue shift cannot simply be explained by sample heating due to the intense incident laser beam. There was some sample heating in the measurements, but it was not significant except at the higher laser powers. From the observed broadening of the PL spectral features associated with c-Si, the sample temperature is estimated to increase from 4 to 60 K under the highest excitation intensity used.

Despite the clear shift toward higher photon energy under increasing excitation intensity, the entire set of PL spectra recorded at photon energies < 0.95 eV are well-fitted by two Gaussian peaks (shown in Figure 10(a) for the PL spectrum (1) obtained with 0.1 W/cm^2 excitation). Figure 10(b) summarizes the excitation intensity dependence of the energies of these two PL peak and their widths. For all PL spectra obtained at different excitation intensities, the two PL peaks at photon energies of ≤ 0.95 eV are found to be always separated by ~ 43 meV with a constant FWHM of ~ 78 and ~ 47 meV, respectively. These two PL peaks are attributed to the NP transition and TO phonon replica in the SiGe clusters, respectively, and the separation energy of ~ 43 meV is close to the energy of the TO Si-Ge phonon [30, 32–35, 47, 52–55]. The constant energy separation of the two PL peaks is additional evidence that, at the excitation intensities used, the observed PL blue shift is not due to thermal broadening caused by sample heating with the laser beam, and that the integrated PL intensities measured at different excitation intensities can be directly compared.

Figure 11 shows a modified (note the double logarithmic scale) Arrhenius plot of the normalized integrated PL intensity of a 3D Si/SiGe multilayer sample grown by CVD and measured at different excitation intensities. The normalized PL intensity temperature dependencies are fitted by a standard equation:

$$I_{\text{PL}}(T) = \frac{1}{[1 + C_1 \cdot \exp(-E_1/kT) + C_2 \cdot \exp(-E_2/kT)]^2} \quad (1)$$

(see, e.g., [41]) with two thermal quenching activation energies E_1 and E_2 . Here T is the temperature, k is Boltzmann’s constant, and C_1 and C_2 are scaling coefficients. In all measurements for all samples, the PL thermal quenching activation energy $E_1 \approx 15$ meV and E_1 is independent of excitation intensity. In contrast, the activation energy E_2 depends significantly on the excitation intensity: the PL temperature dependence shows a step-like behavior, and E_2 increases dramatically from ~ 120 to 340 meV as the excitation intensity increases from 0.1 to 10 W/cm^2 .

We start our discussion by noting that the observed excitation-independent PL thermal quenching activation

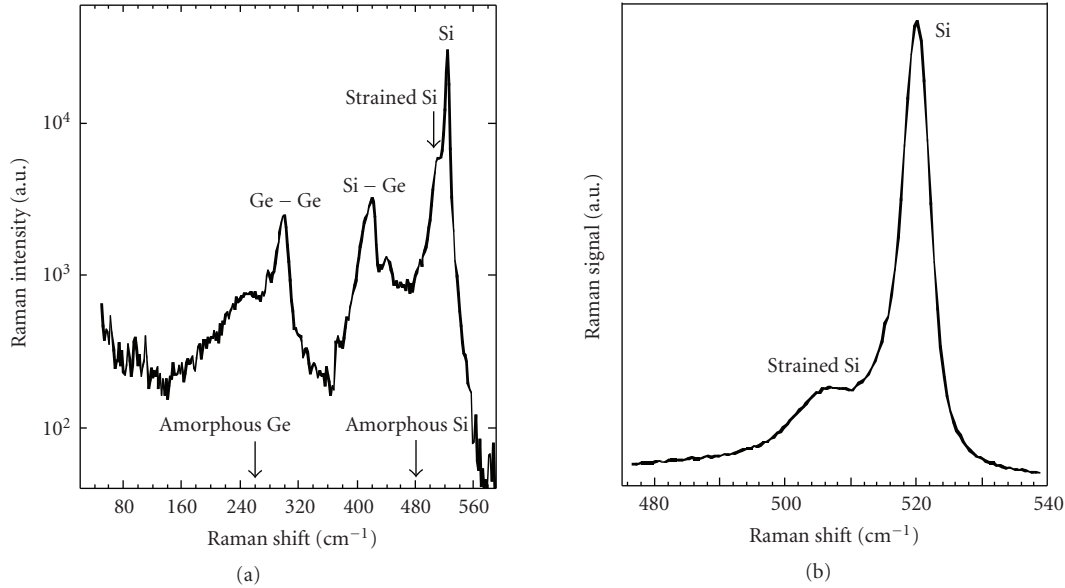


FIGURE 7: Raman spectra measured using 458 nm excitation in MBE grown $\text{Si}/\text{Si}_{1-x}\text{Ge}_x$ 3D NS samples with x approaching 50%. (a) A full-range spectrum comparing the major SiGe Raman modes with the positions of the Raman peaks seen in a-Si and a-Ge. (b) Raman spectrum on a linear intensity scale showing Si-Si vibrational modes including the vibration associated with strained Si at $\sim 507 \text{ cm}^{-1}$.

energy of $\sim 15 \text{ meV}$ is close to the exciton binding energy in SiGe alloys and Si/SiGe superlattices [3, 14]. Thus, we conclude that one of the mechanisms of PL thermal quenching is the thermal dissociation of excitons. The activation energy of $\sim 15 \text{ meV}$ can therefore be associated with exciton localization in specific regions of the clusters associated with variations of the SiGe composition [1, 4]. Hence, the nonuniform SiGe cluster composition and, perhaps, variations in SiGe cluster size and shape could be responsible for the observed relatively broad PL spectra.

It has been proposed previously that 3D Si/SiGe nanostructures can be modeled using type-II energy band alignment, where, depending on the SiGe cluster size, valence band energy quantization is possible [41, 67]. Using the same model, we focus next on nonradiative carrier recombination and the different mechanisms of electron-hole separation. Electron transport in 3D Si/SiGe nanostructures is limited by a small ($\leq 10\text{--}15 \text{ meV}$) conduction band energy barrier and SiGe compositional disorder [41]. Thus, the PL thermal quenching activation energy of $\sim 15 \text{ meV}$ could also be associated with electron diffusion in Si/SiGe 3D NSs.

In contrast, hole diffusion in 3D Si/SiGe multilayer NSs with a high Ge content is controlled by large ($>100 \text{ meV}$) valence band energy barriers at Si/SiGe heterointerfaces [30, 40, 52, 68]. In this system, we consider two major mechanisms of hole transport: (i) hole tunneling and (ii) hole thermionic emission. Hole tunneling in 3D Si/SiGe NSs with thin (5–7 nm) Si separating layers and nearly perfect SiGe cluster vertical self-alignment could be very efficient. These nanostructures are usually grown by MBE and exhibit a PL thermal quenching activation energy of $\sim 60 \text{ meV}$ [41]. The same PL thermal quenching activation energy is

found for the lowest excitation intensity in our CVD-grown samples with 7.5 nm thick Si separating layers. We suggest that in 3D Si/SiGe multilayer NSs with thin Si layers at low excitation intensity, the electron-hole separation and nonradiative carrier recombination are mainly controlled by hole tunneling between SiGe clusters. Due to significant variations in the SiGe cluster size, shape, and chemical composition, the process of hole tunneling could be assisted by phonon emission and/or absorption [69]. Therefore, the observed PL thermal quenching activation energy is close to the Si TO phonon energy [14]. In 3D Si/SiGe multilayer samples with 20 nm thick Si layers, where SiGe cluster vertical self-alignment is practically absent [42], the probability of hole tunneling is reduced, and hole thermionic emission over the Si/SiGe heterointerface barrier is playing a bigger role. Thus, in these samples the PL thermal quenching activation energy is expected to be greater, as has been found in our experiments (see Figure 11).

In this simple model, efficient hole tunneling between adjacent SiGe nanoclusters requires not only reasonably low and thin energy barriers but also a low carrier concentration (i.e., a large enough number of empty adjacent SiGe clusters). By increasing the photoexcitation intensity (i.e., the number of photogenerated carriers), hole tunneling can effectively be suppressed since fewer empty adjacent SiGe clusters can be found. At high excitation intensity, assuming (i) a negligible value of the conduction band offset compared to that in the valence band and (ii) a nearly pure Ge composition in the SiGe cluster core, the maximum anticipated PL thermal quenching activation energy should be $E_2 \leq E_g^{\text{Si}} - E_g^{\text{Ge}} \leq 400 \text{ meV}$. This value sets the upper limit in the activation energy of PL intensity thermal quenching in 3D

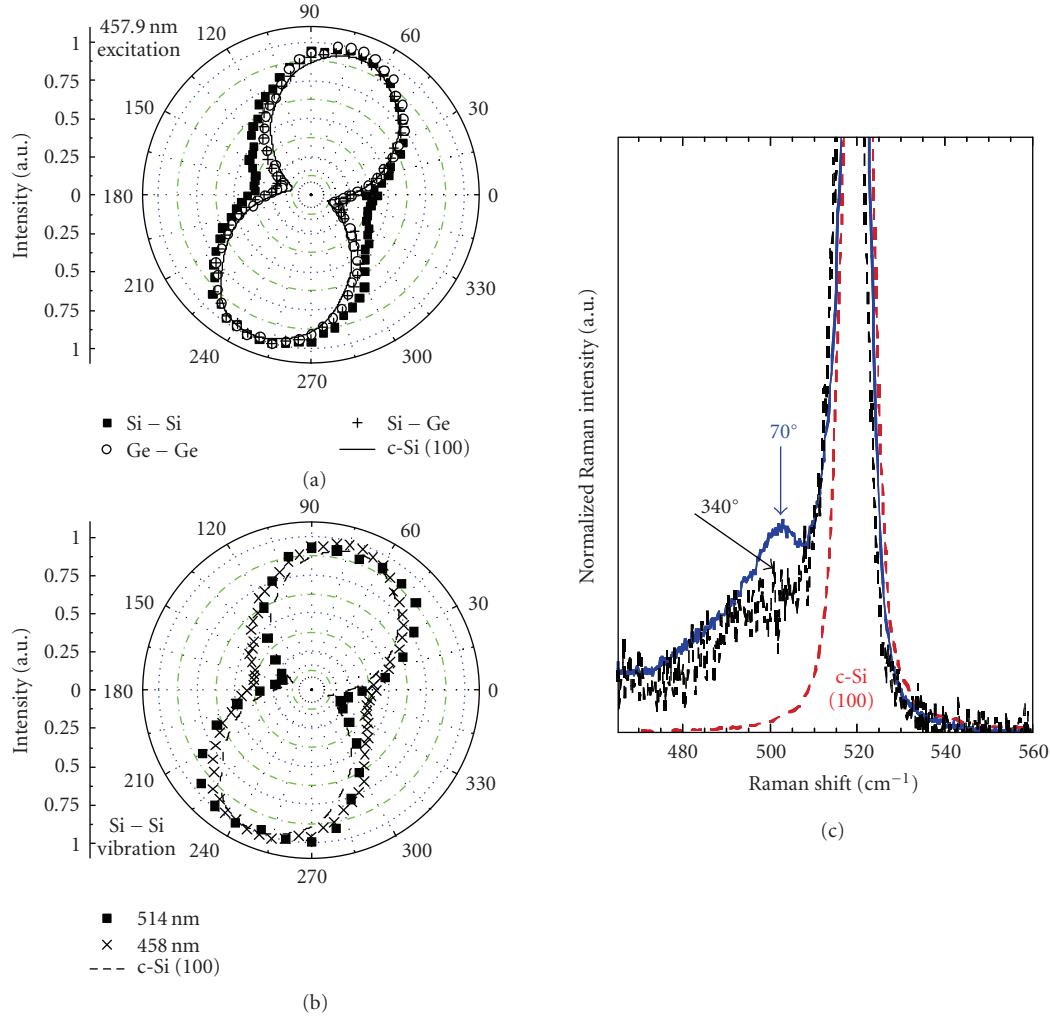


FIGURE 8: Polarization Raman polar diagrams in CVD grown SiGe 3D NS samples measured (a) for Si–Si, Si–Ge, and Ge–Ge vibrational modes using 458 nm excitation and (b) for the Si–Si vibrational mode using 458 and 514 nm excitation. The results obtained are compared with that of *c*-Si. (c) Raman spectra on a linear intensity scale in the vicinity of Si–Si vibrational modes in CVD-grown SiGe 3D NSs measured using two different polarization angles compared with that of *c*-Si.

SiGe multilayer NSs, and it is close to the activation energy of $E_2 \approx 340$ meV that has been found under the highest excitation intensity (see Figure 11).

6. PHOTOLUMINESCENCE DYNAMICS IN Si/SiGe THREE-DIMENSIONAL NANOSTRUCTURES

The PL dynamics, that is, the PL intensity decay under pulsed laser excitation, is an important technique for studying the carrier recombination mechanism. The PL decays discussed here were obtained using excitation by the second harmonic of a Q-switched YAG : Nd laser with photon energy $\hbar\omega = 2.33$ eV, pulse duration $\tau \approx 6$ nanoseconds, and repetition rate $\nu = 10$ Hz. The laser energy density on the sample was of the order of 1 mJ/cm². The PL signal in the 0.77–0.9 eV spectral region was recorded with an InGaAs photomultiplier tube (PMT) and stored in a digital LeCroy oscilloscope. The overall time resolution of the entire system was better than 20 nanoseconds.

Figure 12 shows the normalized PL decays collected from a CVD grown sample at 4 K. The initial PL decay is fast—close to the resolution of our detection system (<20 nanoseconds). The longer-lived PL shows a strong dependence on the detection photon energy, as summarized in Figure 13: the PL lifetime at photon energies below 0.8 eV is found to be ~ 20 microseconds, and it drastically decreases to ~ 200 nanoseconds for the PL component measured at 0.89 eV.

Such a dramatic (100 times) decrease in the PL lifetime provides key information about the carrier recombination mechanism and this will be discussed later.

7. ELECTROLUMINESCENCE IN Si/SiGe THREE-DIMENSIONAL NANOSTRUCTURES

Electroluminescence (EL) in 3D Si/SiGe NSs was found almost simultaneously with the first investigations of the PL [22, 30]. In many of the Si-based nanostructures with

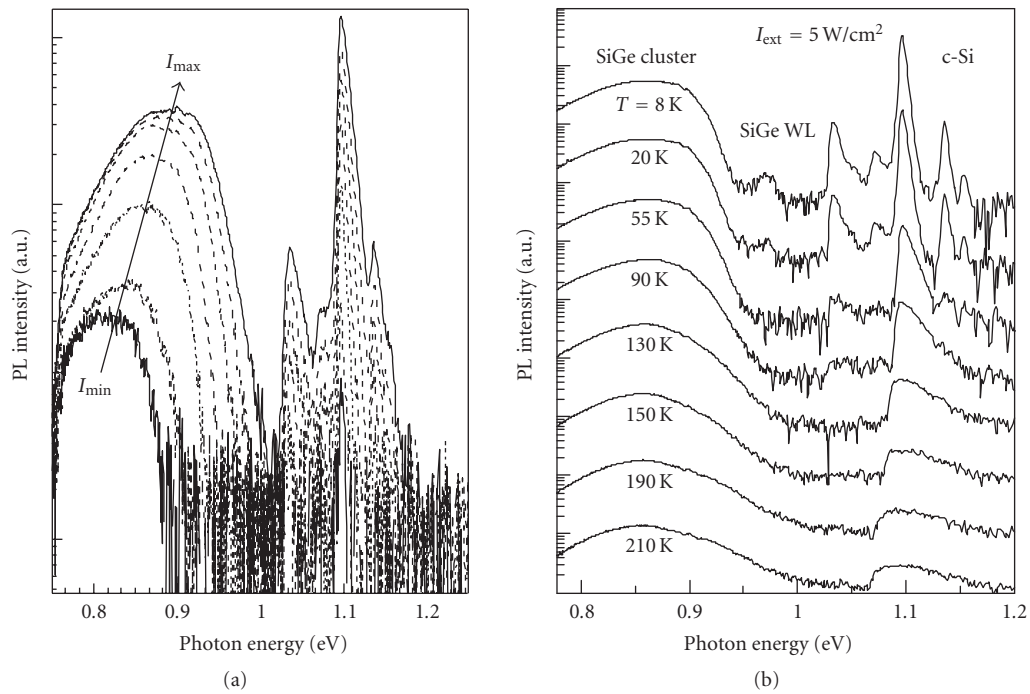


FIGURE 9: PL spectra in CVD grown Si/SiGe 3D NSs (a) measured at $T = 4$ K under different excitation intensities from I_{\min} (0.1 W/cm²) to I_{\max} (100 W/cm²) and (b) under a fixed excitation intensity of 5 W/cm² at the indicated temperatures (the PL spectra have been shifted vertically for clarity).

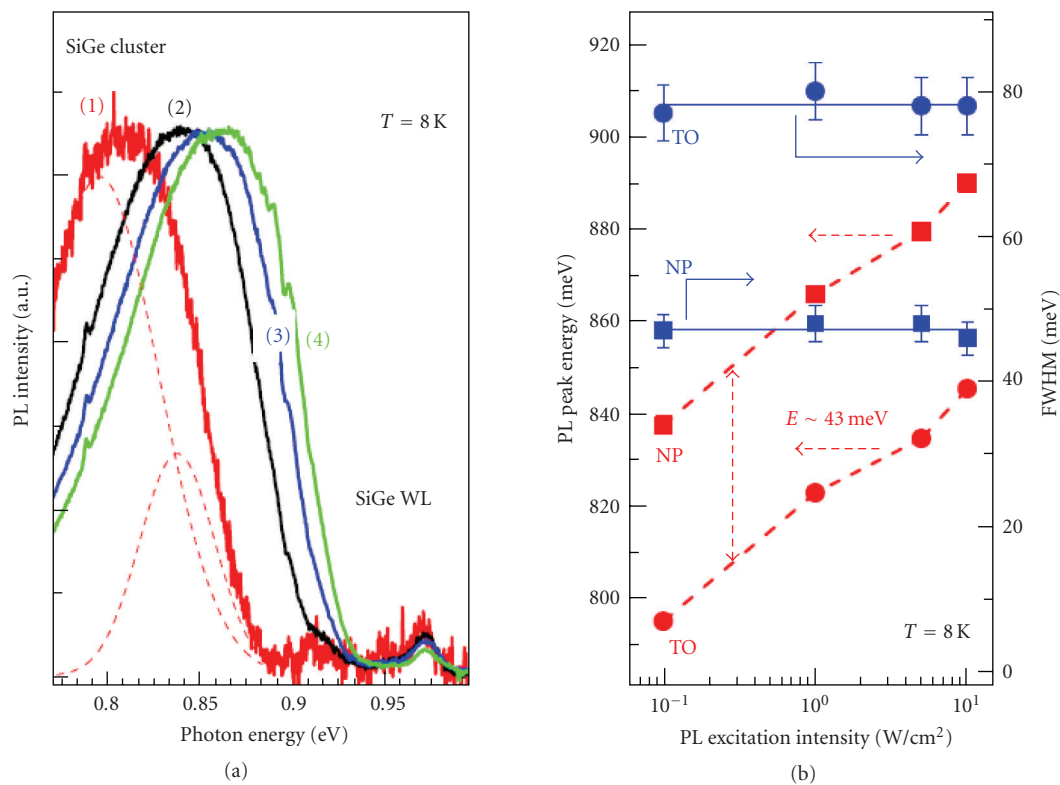


FIGURE 10: (a) Normalized PL spectra in CVD grown Si/SiGe 3D NSs showing the PL spectral shift to higher photon energy under increasing excitation intensity. Each spectrum can be fitted with two (NP and TO) Gaussian spectral bands, as shown, for example, by the dashed lines under trace (1). (b) Summary of PL spectra changes as a function of excitation intensity.

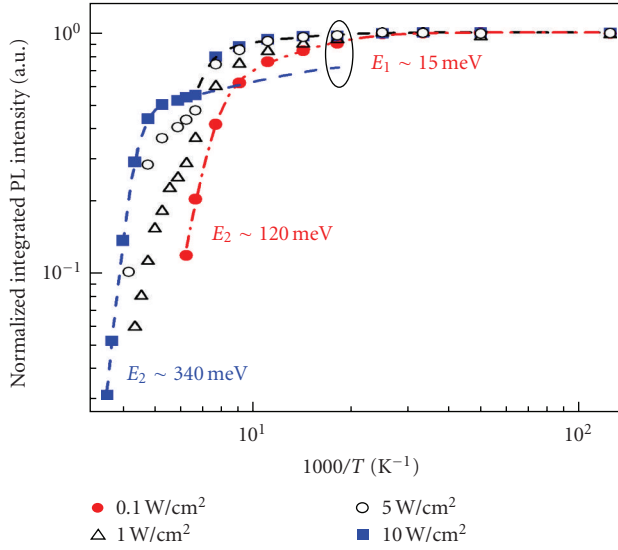


FIGURE 11: Typical integrated PL intensity for CVD grown samples as a function of the reciprocal temperature measured under different excitation intensities, as indicated. The activation energies obtained from fits (shown by the different lines) to the data (shown by the different points) are also given.

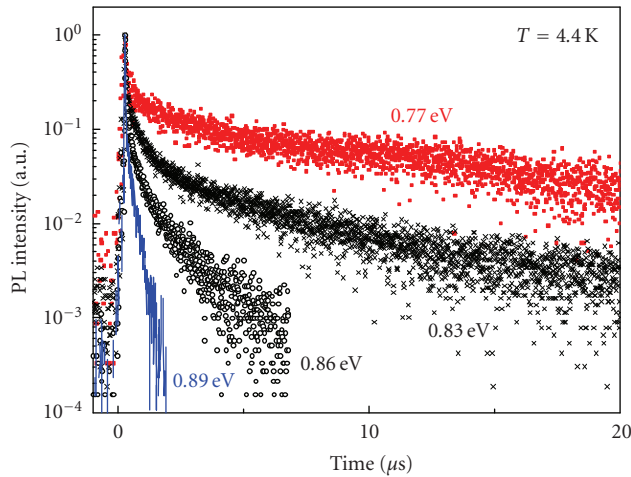


FIGURE 12: Typical low temperature ($T = 4\text{ K}$) PL dynamics for CVD grown samples measured at the indicated photon energies using a short (~ 6 nanoseconds) excitation pulse.

promising PL properties (e.g., Si nanocrystals embedded in silicon oxide, Er⁺ in silicon-rich silicon oxide, etc.), EL is difficult to obtain due to poor carrier transport [11, 15, 20]. In contrast, vertical carrier transport in Si/SiGe multilayers and 3D Si/SiGe NSs is very efficient, and a simple device where Si/SiGe multilayers are embedded into a p-i-n diode or a similar structure can easily be fabricated [22, 33]. Figure 14 proves this statement by showing EL spectra for a CVD grown sample measured under a relatively low value of forward bias of 3–6 V applied to a Schottky-barrier type structure. The measured EL spectrum is broad

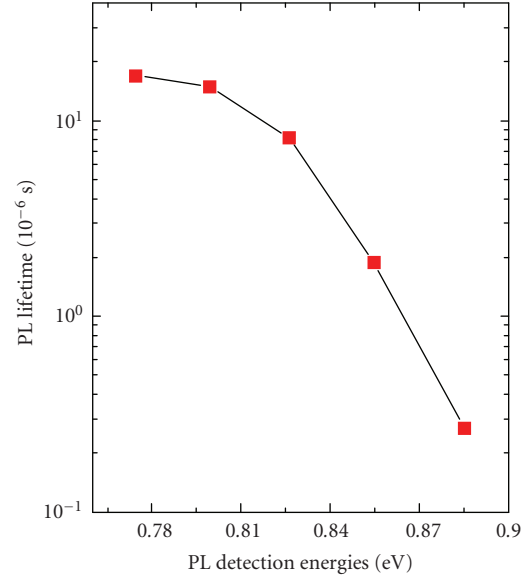


FIGURE 13: Summary of PL lifetimes for CVD grown samples at different photon energies.

with an asymmetric spectral shape, which, similar to the PL spectra, can be well fitted by two Gaussian bands separated by ~ 45 meV. This separation energy is close to an SiGe characteristic phonon energy, proving that the EL mechanism is nearly identical to the PL one, that is, it is due to radiative electron-hole recombination in 3D Si/SiGe layered NSs. On increasing the applied voltage, we observe (similar to that in PL spectra under increasing photoexcitation intensity) a noticeable EL spectral shift toward greater photon energies, that is, a “blue shift” (see Figure 14). The integrated EL intensity is nearly a linear function of the applied voltage (Figure 15). The EL intensity as a function of temperature is also similar to that found in PL, and the EL thermal quenching activation energy is ~ 130 meV (Figure 16(b)). Interestingly, in the same sample, the device current as a function of temperature depicts nearly an exact anticorrelation with the EL intensity and exhibits an activation energy of ~ 140 meV (Figure 16(a)).

8. MECHANISM OF CARRIER RECOMBINATION AND LIGHT EMISSION IN Si/SiGe THREE-DIMENSIONAL NANOSTRUCTURES

In our discussion on carrier recombination in 3D Si/SiGe NSs, we focus on MBE and CVD grown samples with an average Ge atomic composition close to 50%. Several experimental results, including the PL spectral distribution extending well below the band gap of pure Ge [33–35] and the extremely long carrier radiative lifetime of ~ 10 milliseconds [41], as well as the ~ 30 meV per decade PL spectral shift toward higher photon energies as the excitation intensity increases [70], point out strong similarities between the PL in 3D Si/SiGe NSs and the PL in III-V quantum

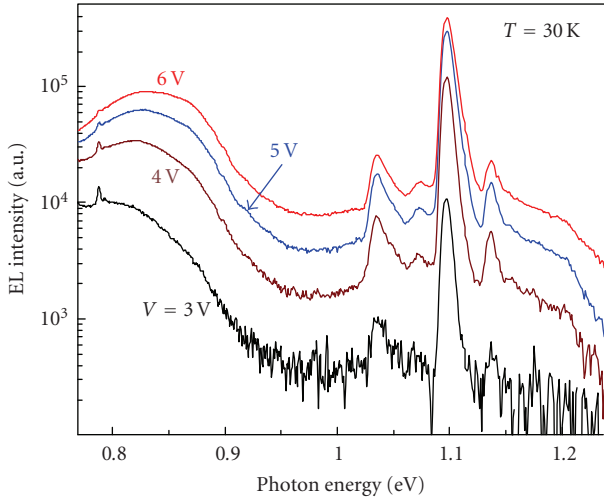


FIGURE 14: EL spectra of a CVD grown sample at $T = 30$ K detected using pulsed electrical excitation at the indicated voltage amplitudes.

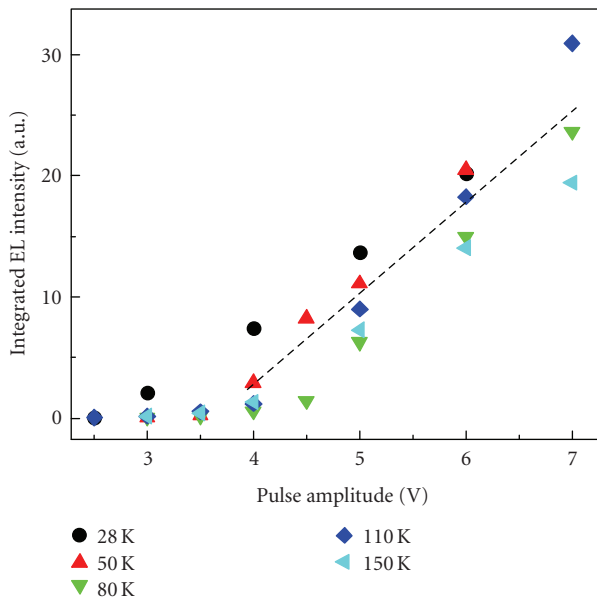


FIGURE 15: Integrated EL intensity over the 0.75–0.95 eV spectral region of a CVD grown sample as a function of the pulsed voltage amplitude measured at the indicated temperatures. The dashed straight line is a guide to the eye.

wells with type-II energy band alignment [65, 66]. Generally, a type-II energy band alignment at the heterointerface is a strong disadvantage for light emitting devices due to a weak overlap between spatially separated electron and hole wave functions. In reality, however, the critical limitation in the efficiency of light-emitting structures is rather the presence of competing nonradiative recombination channels for excess electrons and holes. The most important nonradiative mechanism is carrier recombination via defects, especially heterointerface structural defects such as propagating dislocations and dislocation complexes. The 3D Si/SiGe NSs

investigated here, grown by both MBE and CVD processes, show an almost undetectable density of dislocations [24, 30]. Thus, in these well grown 3D Si/SiGe NSs, we can neglect nonradiative carrier recombination via structural defects, and this explains the experimentally observed high quantum efficiency of PL with photon energy < 0.9 eV, which is associated with SiGe clusters, at low excitation intensities.

It has been suggested that SiGe Stranski-Krastanov (S-K) clusters with a small (3–5 nm) height and greater than 10 : 1 base-to-height aspect ratio can be modeled as nanostructures with a type-II energy band alignment and possibly with SiGe cluster valence-band energy quantization in the direction of growth [39–41, 53]. Strained Si and Si-rich SiGe alloy regions near the base of the clusters (also called SiGe wetting layers) also need to be considered [42]. In our samples, the PL associated with the c-Si separating layers exhibits unusual doublet-like structures (Figure 3), most likely due to the built-in strain. Including the effect of strain, the observed PL bands at 0.916 and 0.972 eV indicate a composition of the $\text{Si}_{1-x}\text{Ge}_x$ transition region, which is presumably located near the bottom of the Ge/Si pyramid-like clusters, to be close to $x \approx 0.2$ [30]. This conclusion is supported by recent direct analytical TEM measurements [42–45].

It has also been proposed that the broad PL band with a peak energy of ~ 0.8 – 0.9 eV is due to the recombination of carriers localized in the Ge-richest areas of the clusters, which is close to the center of “pancake” shaped SiGe clusters [43, 44]. We suggest that at the lowest excitation intensity, the PL arises from electron-hole recombination between holes localized in the Ge-richest regions of the cluster and electrons localized in the strained SiGe alloy region near the cluster base. This immediately explains the extension of the observed PL spectrum below the pure Ge band gap energy.

On increasing the excitation intensity, we find that the high-photon-energy edge of the Ge-rich cluster PL eventually overlaps with PL originating from the $\text{Si}_{1-x}\text{Ge}_x$ alloy region with $x \approx 0.2$. Theoretical calculations predict that strained Si/SiGe two-dimensional NSs with $x \approx 0.2$ might have type-I energy band alignment [36]. The SiGe clusters embedded in the Si matrix can induce local strain mainly in the SiGe alloy region near the bottom of the Ge cluster. We attribute the observed decrease of the PL lifetime (presumably radiative lifetime) detected between 0.8 and 0.9 eV in our experiments to an increasing contribution from fast radiative transitions involving locally strained SiGe regions of lower Ge concentration at the bottom of SiGe clusters.

Figure 17 summarizes in schematic form the proposed model of radiative carrier recombination in 3D Si/SiGe NSs. It illustrates that, at low excitation intensity, the observed PL at photon energies $\hbar\omega < 0.8$ eV is due to slow recombination between electrons localized within a strained Si-rich $\text{Si}_{1-x}\text{Ge}_x$ region with $x \approx 0.2$ and holes occupying the lowest energy states in the Ge-rich cluster core. An increase in the excitation power in PL experiments, as well as the current density in EL experiments, usually leads to changes in the emission spectra; for example, the PL and EL peaks blue shift, that is, they shift toward shorter wavelength (see Figures 9, 10, and 14). At the same time, the PL intensity as a function of excitation

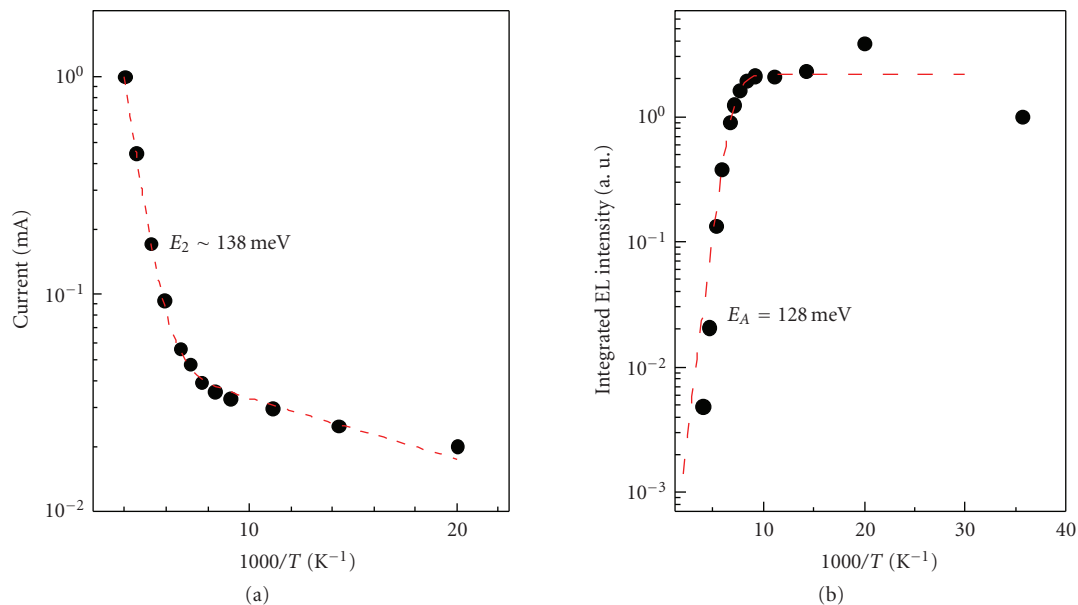


FIGURE 16: (a) Current and (b) EL intensity as a function of the reciprocal temperature for a CVD grown sample. The activation energies obtained from fits to the data (dashed lines) are also shown.

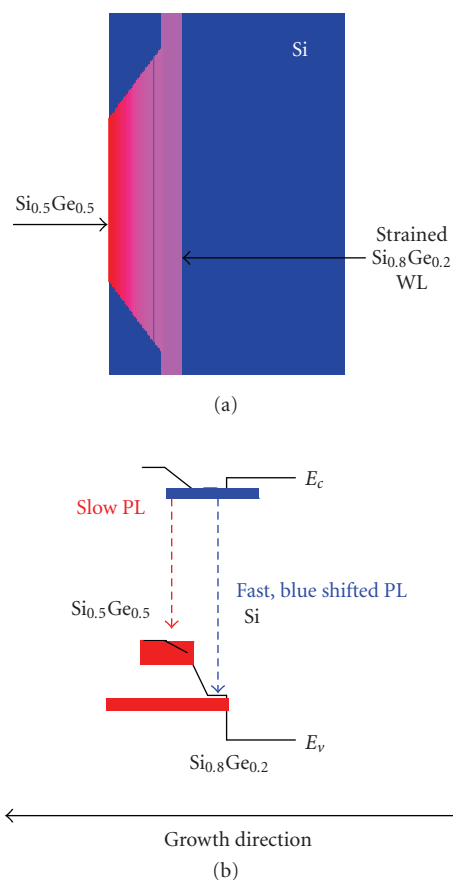


FIGURE 17: (a) Schematic representation of the atomic structure of an SiGe nanocluster on a wetting layer with a core Ge concentration close to 50% embedded into a Si matrix and (b) the corresponding energy band diagram with two possible radiative transitions indicated.

intensity in MBE grown 3D Si/SiGe NSs displays a sublinear dependence on a logarithmic scale (Figure 4). It has been pointed out that possible transformations of hole energy spectra due to quantization and/or strain might dramatically increase the rate of nonradiative Auger recombination, by more than 100 times compared to that in bulk Si and Ge [71]. However, in a quantum well with smoothed (e.g., diffused) heterointerfaces, Auger processes are expected to be less efficient [35, 41]. We find strong evidence that in CVD grown 3D Si/SiGe NSs the reduction of the Auger rate, most likely due to diffused Si/SiGe interfaces, does take place. Thus, on increasing the pumping power in PL experiments on CVD grown samples, we observe a relatively small deviation from a linear function in the PL intensity dependence on excitation (see Figure 9). In addition, we find that the previously mentioned PL spectral blue shift, with the PL peak shifting from a photon energy of 0.78 to 0.88 eV, correlates with a strong (~ 100 times) decrease in the carrier radiative lifetime (Figures 9, 10, 12, and 13). The hole energy barrier between the strained $Si_{0.8}Ge_{0.2}$ transition region and Si is ≥ 200 meV, in good agreement with a larger value of the observed PL thermal quenching activation energy, while the smaller value of 15 meV is closer to the exciton binding energy in SiGe alloys, as has been previously discussed [35, 41, 72].

Figure 17 also proposes an energy band diagram, which takes into account the previously described complex compositional structure of 3D Si/SiGe heterointerfaces. It shows a modified type-II energy band alignment at the SiGe cluster core with a compositional transition toward the Si/SiGe heterointerface and a nearly type-I alignment at the cluster base, mainly due to the strain in the SiGe wetting layer. A continuous change in the Ge atomic concentration is reflected by a gradually increasing energy band gap from the cluster center toward the SiGe wetting layer, where the Ge

atomic concentration is estimated to be $\sim 20\%$. In this band diagram, two types of radiative transitions are shown (Figure 17(b)). First, there is a slow recombination between electrons localized mainly in the SiGe wetting layer and holes localized within SiGe clusters, mostly near the SiGe cluster core. Second, a faster and more efficient radiative recombination is achieved between electrons and holes leaking from the SiGe cluster core toward the cluster base and SiGe wetting layer. This latter recombination mechanism, which becomes dominant under a high photoexcitation intensity when the “slow” recombination channel for spatially separated electrons and holes is saturated, has been called a “dynamic type-I” energy band alignment [41, 70]. It explains very well both the PL spectral blue shift under increasing excitation intensity and the dramatic (~ 100 times) decrease in carrier radiative lifetime measured at photon energies from 0.77 to 0.89 eV. This explanation is also consistent with the previously discussed PL intensity temperature dependence, which shows a different PL thermal quenching activation energy at different excitation intensities (see also [72]).

9. CONCLUSION

In conclusion, we present comprehensive experimental studies on Raman scattering and light-emitting (PL and EL) properties of 3D Si/SiGe NSs. We show that these nanostructures emit light at the technologically important 1.3–1.6 μm wavelength region. The highest PL and EL quantum efficiency is found in SiGe clusters with an $\sim 50\%$ Ge composition near the cluster core. The highest luminescence quantum efficiency is observed at low excitation intensity. However, the PL quantum efficiency decreases as the excitation intensity increases, most likely due to competition with a faster nonradiative Auger recombination. Using time resolved PL measurements, we found that the suspected type-II energy band alignment at the Si/SiGe cluster heterointerface is responsible for the observed long carrier radiative lifetime (10^{-4} – 10^{-3} second). We also found that within the broad PL band, the part of the PL spectra associated with higher photon energies exhibits an ~ 100 times faster radiative transition, which is explained by a proposed “dynamic type-I” energy band alignment, for example, radiative recombination between holes occupying excited states in SiGe clusters and electrons mostly localized close to the $\text{Si}_{1-x}\text{Ge}_x$ wetting layer with $x \approx 0.2$. These experimental observations suggest that a commercially useful SiGe light-emitting device can be fabricated and integrated into the traditional CMOS environment.

ACKNOWLEDGMENTS

The authors would like to thank Xiaohua Wu for the TEM results from an MBE grown sample shown in Figure 1. L. Tsybeskov acknowledges partial support for this project provided by the US National Science Foundation, Intel Corp., Semiconductor Research Corporation, and Foundation at NJIT.

REFERENCES

- [1] N. Savage, “Linking with light,” *IEEE Spectrum*, vol. 39, no. 8, pp. 32–36, 2002.
- [2] B. Mukherjee, “WDM optical communication networks: progress and challenges,” *IEEE Journal on Selected Areas in Communications*, vol. 18, no. 10, pp. 1810–1824, 2000.
- [3] D. V. Plant and A. G. Kirk, “Optical interconnects at the chip and board level: challenges and solutions,” *Proceedings of the IEEE*, vol. 88, no. 6, pp. 806–818, 2000.
- [4] D. A. B. Miller, “Rationale and challenges for optical interconnects to electronic chips,” *Proceedings of the IEEE*, vol. 88, no. 6, pp. 728–749, 2000.
- [5] D. A. B. Miller, “Optical interconnects to silicon,” *IEEE Journal on Selected Topics in Quantum Electronics*, vol. 6, no. 6, pp. 1312–1317, 2000.
- [6] H. Wada and T. Kamijoh, “Room-temperature CW operation of InGaAsP lasers on Si fabricated by wafer bonding,” *IEEE Photonics Technology Letters*, vol. 8, no. 2, pp. 173–175, 1996.
- [7] M. Razeghi, M. Defour, R. Blondeau, et al., “First cw operation of a $\text{Ga}_{0.25}\text{In}_{0.75}\text{As}_{0.5}\text{P}_{0.5}$ -InP laser on a silicon substrate,” *Applied Physics Letters*, vol. 53, no. 24, pp. 2389–2390, 1988.
- [8] H. Park, A. W. Fang, S. Kodama, and J. E. Bowers, “Hybrid silicon evanescent laser fabricated with a silicon waveguide and III-V offset quantum wells,” *Optics Express*, vol. 13, no. 23, pp. 9460–9464, 2005.
- [9] A. W. Fang, H. Park, O. Cohen, R. Jones, M. J. Paniccia, and J. E. Bowers, “Electrically pumped hybrid AlGaInAs-silicon evanescent laser,” *Optics Express*, vol. 14, no. 20, pp. 9203–9210, 2006.
- [10] L. Pavesi and D. J. Lockwood, *Silicon Photonics*, Springer, Berlin, Germany, 2004.
- [11] Y. Kanemitsu, “Light emission from porous silicon and related materials,” *Physics Report*, vol. 263, no. 1, pp. 1–91, 1995.
- [12] K. D. Hirschman, L. Tsybeskov, S. P. Duttagupta, and P. M. Fauchet, “Silicon-based visible light-emitting devices integrated into microelectronic circuits,” *Nature*, vol. 384, no. 6607, pp. 338–341, 1996.
- [13] A. G. Cullis, L. T. Canham, and P. D. J. Calcott, “The structural and luminescence properties of porous silicon,” *Journal of Applied Physics*, vol. 82, no. 3, pp. 909–965, 1997.
- [14] Z. H. Lu, D. J. Lockwood, and J.-M. Baribeau, “Quantum confinement and light emission in SiO_2/Si superlattices,” *Nature*, vol. 378, no. 6553, pp. 258–260, 1995.
- [15] L. Tsybeskov and D. J. Lockwood, “Nanocrystalline silicon-silicon dioxide superlattices: structural and optical properties,” in *Semiconductor Nanocrystals: From Basic Principles to Applications*, A. L. Efros, D. J. Lockwood, and L. Tsybeskov, Eds., pp. 209–229, Kluwer Academics/Plenum Publishers, New York, NY, USA, 2003.
- [16] G. F. Grom, D. J. Lockwood, J. P. McCaffrey, et al., “Ordering and self-organization in nanocrystalline silicon,” *Nature*, vol. 407, no. 6802, pp. 358–361, 2000.
- [17] L. Tsybeskov, K. D. Hirschman, S. P. Duttagupta, et al., “Nanocrystalline-silicon superlattice produced by controlled recrystallization,” *Applied Physics Letters*, vol. 72, no. 1, pp. 43–45, 1998.
- [18] L. Pavesi, L. Dal Negro, C. Mazzoleni, G. Franzò, and F. Priolo, “Optical gain in silicon nanocrystals,” *Nature*, vol. 408, no. 6811, pp. 440–444, 2000.
- [19] S. Schuppler, S. L. Friedman, M. A. Marcus, et al., “Size, shape, and composition of luminescent species in oxidized Si nanocrystals and H-passivated porous Si,” *Physical Review B*, vol. 52, no. 7, pp. 4910–4925, 1995.

- [20] S. Coffa, G. Franzò, and F. Priolo, "High efficiency and fast modulation of Er-doped light emitting Si diodes," *Applied Physics Letters*, vol. 69, no. 14, pp. 2077–2079, 1996.
- [21] S. Fukatsu, N. Usami, Y. Shiraki, A. Nishida, and K. Nakagawa, "High-temperature operation of strained $\text{Si}_{0.65}\text{Ge}_{0.35}/\text{Si}(111)$ *p*-type multiple-quantum-well light-emitting diode grown by solid source Si molecular-beam epitaxy," *Applied Physics Letters*, vol. 63, no. 7, pp. 967–969, 1993.
- [22] L. Vescan and T. Stoica, "Room-temperature SiGe light-emitting diodes," *Journal of Luminescence*, vol. 80, no. 1–4, pp. 485–489, 1998.
- [23] D. Leong, M. Harry, K. J. Reeson, and K. P. Homewood, "A silicon/iron-disilicide light-emitting diode operating at a wavelength of $1.5\ \mu\text{m}$," *Nature*, vol. 387, no. 6634, pp. 686–688, 1997.
- [24] D. J. Eaglesham and M. Cerullo, "Dislocation-free Stranski-Krastanov growth of Ge on Si(100)," *Physical Review Letters*, vol. 64, no. 16, pp. 1943–1946, 1990.
- [25] Y.-W. Mo, D. E. Savage, B. S. Swartzentruber, and M. G. Lagally, "Kinetic pathway in Stranski-Krastanov growth of Ge on Si(001)," *Physical Review Letters*, vol. 65, no. 8, pp. 1020–1023, 1990.
- [26] D. E. Savage, F. Liu, V. Zielasek, and M. G. Lagally, "Fundamental mechanisms of film growth," in *Germanium Silicon: Growth and Materials*, R. Hull and J. C. Bean, Eds., vol. 56 of *Semiconductor and Semimetals*, pp. 49–96, Academic Press, New York, NY, USA, 1999.
- [27] B. Voigtländer and A. Zinner, "Simultaneous molecular beam epitaxy growth and scanning tunneling microscopy imaging during Ge/Si epitaxy," *Applied Physics Letters*, vol. 63, no. 22, pp. 3055–3057, 1993.
- [28] J. A. Flora, E. Chason, L. B. Freund, R. D. Twisten, R. Q. Hwang, and G. A. Lucadamo, "Evolution of coherent islands in $\text{Si}_{1-x}\text{Ge}_x/\text{Si}(001)$," *Physical Review B*, vol. 59, no. 3, pp. 1990–1998, 1999.
- [29] D. E. Jesson, S. J. Pennycook, J. Z. Tischler, J. D. Budai, J.-M. Baribeau, and D. C. Houghton, "Interplay between evolving surface morphology, atomic-scale growth modes, and ordering during $\text{Si}_x\text{Ge}_{1-x}$ epitaxy," *Physical Review Letters*, vol. 70, no. 15, pp. 2293–2296, 1993.
- [30] Y. Shiraki and A. Sakai, "Fabrication technology of SiGe hetero-structures and their properties," *Surface Science Reports*, vol. 59, no. 7–8, pp. 153–207, 2005.
- [31] T. I. Kamins, E. C. Carr, R. S. Williams, and S. J. Rosner, "Deposition of three-dimensional Ge islands on Si(001) by chemical vapor deposition at atmospheric and reduced pressures," *Journal of Applied Physics*, vol. 81, no. 1, pp. 211–219, 1997.
- [32] P. Schittenhelm, M. Gail, J. Brunner, J. F. Nützel, and G. Abstreiter, "Photoluminescence study of the crossover from two-dimensional to three-dimensional growth for Ge on Si(100)," *Applied Physics Letters*, vol. 67, no. 9, pp. 1292–1294, 1995.
- [33] R. Apetz, L. Vescan, A. Hartmann, C. Dieker, and H. Lüth, "Photoluminescence and electroluminescence of SiGe dots fabricated by island growth," *Applied Physics Letters*, vol. 66, no. 4, pp. 445–447, 1995.
- [34] O. G. Schmidt, C. Lange, and K. Eberl, "Photoluminescence study of the initial stages of island formation for Ge pyramids/domes and hut clusters on Si(001)," *Applied Physics Letters*, vol. 75, no. 13, pp. 1905–1907, 1999.
- [35] B. V. Kamenev, L. Tsybeskov, J.-M. Baribeau, and D. J. Lockwood, "Photoluminescence and Raman scattering in three-dimensional $\text{Si}/\text{Si}_{1-x}\text{Ge}_x$ nanostructures," *Applied Physics Letters*, vol. 84, no. 8, pp. 1293–1295, 2004.
- [36] C. G. Van de Walle and R. M. Martin, "Theoretical calculations of heterojunction discontinuities in the Si/Ge system," *Physical Review B*, vol. 34, no. 8, pp. 5621–5634, 1986.
- [37] D. C. Houghton, G. C. Aers, S.-R. Eric Yang, E. Wang, and N. L. Rowell, "Type I band alignment in $\text{Si}_{1-x}\text{Ge}_x/\text{Si}(001)$ quantum wells: photoluminescence under applied [110] and [100] uniaxial stress," *Physical Review Letters*, vol. 75, no. 5, pp. 866–869, 1995.
- [38] M. L. W. Thewalt, D. A. Harrison, C. F. Reinhart, J. A. Wolk, and H. Lafontaine, "Type II band alignment in $\text{Si}_{1-x}\text{Ge}_x/\text{Si}(001)$ quantum wells: the ubiquitous type I luminescence results from band bending," *Physical Review Letters*, vol. 79, no. 2, pp. 269–272, 1997.
- [39] P. Schittenhelm, C. Engel, F. Findeis, et al., "Self-assembled Ge dots: growth, characterization, ordering, and applications," *Journal of Vacuum Science & Technology B*, vol. 16, no. 3, pp. 1575–1581, 1998.
- [40] M. El Kurdi, S. Sauvage, G. Fishman, and P. Boucaud, "Band-edge alignment of SiGe Si quantum wells and SiGe Si self-assembled islands," *Physical Review B*, vol. 73, no. 19, Article ID 195327, 9 pages, 2006.
- [41] B. V. Kamenev, L. Tsybeskov, J.-M. Baribeau, and D. J. Lockwood, "Coexistence of fast and slow luminescence in three-dimensional $\text{Si}/\text{Si}_{1-x}\text{Ge}_x$ nanostructures," *Physical Review B*, vol. 72, no. 19, Article ID 193306, 4 pages, 2005.
- [42] J.-M. Baribeau, N. L. Rowell, and D. J. Lockwood, "Advances in the growth and characterization of Ge quantum dots and islands," *Journal of Materials Research*, vol. 20, no. 12, pp. 3278–3293, 2005.
- [43] J.-M. Baribeau, X. Wu, and D. J. Lockwood, "Probing the composition of Ge dots and $\text{Si}/\text{Si}_{1-x}\text{Ge}_x$ island superlattices," *Journal of Vacuum Science & Technology A*, vol. 24, no. 3, pp. 663–667, 2006.
- [44] J.-M. Baribeau, X. Wu, M.-J. Picard, and D. J. Lockwood, "Characterization of coherent $\text{Si}_{1-x}\text{Ge}_x$ island superlattices on (100) Si," in *Proceedings of the Materials Research Society Fall Meeting, Group IV Semiconductor Nanostructures*, L. Tsybeskov, D. J. Lockwood, C. Delerue, M. Ichikawa, and A. W. van Buuren, Eds., vol. 958, pp. 119–124, Boston, Mass, USA, November-December 2006.
- [45] D. J. Lockwood, X. Wu, and J.-M. Baribeau, "Compositional redistribution in coherent $\text{Si}_{1-x}\text{Ge}_x$ islands on Si(100)," *IEEE Transactions on Nanotechnology*, vol. 6, no. 2, pp. 245–249, 2007.
- [46] B. V. Kamenev, H. Grebel, L. Tsybeskov, et al., "Polarized Raman scattering and localized embedded strain in self-organized Si/Ge nanostructures," *Applied Physics Letters*, vol. 83, no. 24, pp. 5035–5037, 2003.
- [47] L. P. Tilly, P. M. Mooney, J. O. Chu, and F. K. LeGoues, "Near band-edge photoluminescence in relaxed $\text{Si}_{1-x}\text{Ge}_x$ layers," *Applied Physics Letters*, vol. 67, no. 17, pp. 2488–2490, 1995.
- [48] A. Zrenner, B. Fröhlich, J. Brunner, and G. Abstreiter, "Time-resolved photoluminescence of pseudomorphic SiGe quantum wells," *Physical Review B*, vol. 52, no. 23, pp. 16608–16611, 1995.
- [49] M. Chen, D. L. Smith, and T. C. McGill, "Low-temperature photoluminescence spectra of doped Ge," *Physical Review B*, vol. 15, no. 10, pp. 4983–4996, 1977.
- [50] J.-M. Baribeau, X. Wu, N. L. Rowell, and D. J. Lockwood, "Ge dots and nanostructures grown epitaxially on Si," *Journal of Physics Condensed Matter*, vol. 18, no. 8, pp. R139–R174, 2006.

- [51] S. Bozzo, J.-L. Lazzari, G. Bremond, and J. Derrien, "Temperature and excitation power dependencies of the photoluminescence of planar and vertically self-organized $\text{Si}_{0.70}\text{Ge}_{0.30}/\text{Si}$ strained superlattices," *Thin Solid Films*, vol. 380, no. 1-2, pp. 130–133, 2000.
- [52] O. G. Schmidt and K. Eberl, "Multiple layers of self-assembled Ge/Si islands: photoluminescence, strain fields, material interdiffusion, and island formation," *Physical Review B*, vol. 61, no. 20, pp. 13721–13729, 2000.
- [53] K. Brunner, "Si/Ge nanostructures," *Reports on Progress in Physics*, vol. 65, no. 1, pp. 27–72, 2002.
- [54] J. C. Sturm, H. Manoharan, L. C. Lenchyshyn, et al., "Well-resolved band-edge photoluminescence of excitons confined in strained $\text{Si}_{1-x}\text{Ge}_x$ quantum wells," *Physical Review Letters*, vol. 66, no. 10, pp. 1362–1365, 1991.
- [55] L. C. Lenchyshyn, M. L. W. Thewalt, J. C. Sturm, et al., "High quantum efficiency photoluminescence from localized excitons in $\text{Si}_{1-x}\text{Ge}_x$," *Applied Physics Letters*, vol. 60, no. 25, pp. 3174–3176, 1992.
- [56] H. Sunamura, Y. Shiraki, and S. Fukatsu, "Growth mode transition and photoluminescence properties of $\text{Si}_{1-x}\text{Ge}_x/\text{Si}$ quantum well structures with high Ge composition," *Applied Physics Letters*, vol. 66, no. 8, pp. 953–955, 1995.
- [57] J. Weber and M. I. Alonso, "Near-band-gap photoluminescence of Si-Ge alloys," *Physical Review B*, vol. 40, no. 8, pp. 5683–5693, 1989.
- [58] P. A. Temple and C. E. Hathaway, "Multiphonon Raman spectrum of silicon," *Physical Review B*, vol. 7, no. 8, pp. 3685–3697, 1973.
- [59] M. I. Alonso and K. Winer, "Raman spectra of c- $\text{Si}_{1-x}\text{Ge}_x$ alloys," *Physical Review B*, vol. 39, no. 14, pp. 10056–10062, 1989.
- [60] J. E. Smith Jr., M. H. Brodsky, B. L. Crowder, M. I. Nathan, and A. Pinczuk, "Raman spectra of amorphous Si and related tetrahedrally bonded semiconductors," *Physical Review Letters*, vol. 26, no. 11, pp. 642–646, 1971.
- [61] W. L. Henstrom, C.-P. Liu, J. M. Gibson, T. I. Kamins, and R. S. Williams, "Dome-to-pyramid shape transition in Ge/Si islands due to strain relaxation by interdiffusion," *Applied Physics Letters*, vol. 77, no. 11, pp. 1623–1625, 2000.
- [62] F. Cerdeira, C. J. Buchenauer, F. H. Pollak, and M. Cardona, "Stress-induced shifts of first-order Raman frequencies of diamond- and zinc-blende-type semiconductors," *Physical Review B*, vol. 5, no. 2, pp. 580–593, 1972.
- [63] S. C. Jain, B. Dietrich, H. Richter, A. Atkinson, and A. H. Harker, "Stresses in strained GeSi stripes: calculation and determination from Raman measurements," *Physical Review B*, vol. 52, no. 9, pp. 6247–6253, 1995.
- [64] J. Tersoff, C. Teichert, and M. G. Lagally, "Self-organization in growth of quantum dot superlattices," *Physical Review Letters*, vol. 76, no. 10, pp. 1675–1678, 1996.
- [65] J. Hu, X. G. Xu, J. A. H. Stotz, et al., "Type II photoluminescence and conduction band offsets of GaAsSb/InGaAs and GaAsSb/InP heterostructures grown by metalorganic vapor phase epitaxy," *Applied Physics Letters*, vol. 73, no. 19, pp. 2799–2801, 1998.
- [66] T. Baier, U. Mantz, K. Thonke, R. Sauer, F. Schäffler, and H.-J. Herzog, "Type-II band alignment in Si/Si $_{1-x}$ Ge $_x$ quantum wells from photoluminescence line shifts due to optically induced band-bending effects: experiment and theory," *Physical Review B*, vol. 50, no. 20, pp. 15191–15196, 1994.
- [67] J. Wan, G. L. Jin, Z. M. Jiang, Y. H. Luo, J. L. Liu, and K. L. Wang, "Band alignments and photon-induced carrier transfer from wetting layers to Ge islands grown on Si(001)," *Applied Physics Letters*, vol. 78, no. 12, pp. 1763–1765, 2001.
- [68] P. A. Cain, H. Ahmed, D. A. Williams, and J. M. Bonar, "Hole transport through single and double SiGe quantum dots," *Applied Physics Letters*, vol. 77, no. 21, pp. 3415–3417, 2000.
- [69] H. Qin, A. W. Holleitner, K. Eberl, and R. H. Blick, "Coherent superposition of photon- and phonon-assisted tunneling in coupled quantum dots," *Physical Review B*, vol. 64, no. 24, Article ID 241302, 4 pages, 2001.
- [70] B. V. Kamenev, E.-K. Lee, H.-Y. Chang, et al., "Excitation-dependent photoluminescence in Ge/Si Stranski-Krastanov nanostructures," *Applied Physics Letters*, vol. 89, no. 15, Article ID 153106, 3 pages, 2006.
- [71] C. J. Williams, E. Corbin, M. Jaros, and D. C. Herbert, "Auger recombination in strained $\text{Si}_x\text{Ge}_{1-x}/\text{Si}$ superlattices," *Physica B*, vol. 254, no. 3-4, pp. 240–248, 1998.
- [72] E.-K. Lee, L. Tsybeskov, and T. I. Kamins, "Photoluminescence thermal quenching in three-dimensional multilayer SiSiGe nanostructures," *Applied Physics Letters*, vol. 92, no. 3, Article ID 033110, 3 pages, 2008.

Research Article

A New Approach of Electronics and Photonics Convergence on Si CMOS Platform: How to Reduce Device Diversity of Photonics for Integration

Kazumi Wada

Department of Materials Engineering, The University of Tokyo, 7-3-1 Hongo, Bunkyo, Tokyo 113-8656, Japan

Correspondence should be addressed to Kazumi Wada, kwada@material.t.u-tokyo.ac.jp

Received 11 March 2008; Accepted 21 May 2008

Recommended by Pavel Cheben

Integrated photonics via Si CMOS technology has been a strategic area since electronics and photonics convergence should be the next platform for information technology. The platform is recently referred to as “Si photonics” that attracts much interest of researchers in industries as well as academia in the world. The main goal of Si Photonics is currently to reduce material diversity of photonic devices to pursuing CMOS-compatibility. In contrast, the present paper proposes another route of Si Photonics, reducing diversity of photonic devices. The proposed device unifying functionality of photonics is a microresonator with a pin diode structure that enables the Purcell effect and Franz-Keldysh effect to emit and to modulate light from SiGe alloys.

Copyright © 2008 Kazumi Wada. This is an open access article distributed under the Creative Commons Attribution License, which permits unrestricted use, distribution, and reproduction in any medium, provided the original work is properly cited.

1. INTRODUCTION

Electronic and photonic integrated circuits (EPICs) on Si complementary metal oxide semiconductor (CMOS) platform have widely been studied to achieve higher figure-of-merits in communications and computations. A challenging issue is that there are so many kinds of devices in photonics as in Table 1. The photonic devices have been developed for optical communication systems in which integration of these devices on a chip has never been important. Thus, the concurrent photonics consist of various devices (materials) such as light emitters (III-V semiconductors), modulators (LiNbO_3), interconnects (SiO_2), filters (SiO_2), photodetectors (III-V semiconductors), and isolators (YIG). On the contrary, electronics as in Table 1 consists only transistor and interconnect; and the material systems are all compatible to the CMOS fabrication process referred to as “CMOS-compatible.” Si photonics today have focused on reduction of the material diversity by fabricating these photonic devices with CMOS compatible materials. In the present paper we will propose a new approach: functional unification of photonic devices. The enabler of the unification is the materials system of Si waveguide and SiO_2 . The features of the system are as follows:

- (i) polarity and conductivity control of Si waveguides by implementing pin diode structures,
- (ii) high-index contrast to SiO_2 acting as cladding and electrical insulation that reduces device footprints.

To utilize these features, the proposed novel device is based on a microresonator with a built-in pin diode. Physics presenting emitter and modulator functions are the Purcell effect [1] and Franz-Keldysh effect [2].

2. HOW TO REDUCE DEVICE DIVERSITY

The Purcell effect is known to enhance spontaneous emission rate on a resonance wavelength of a microresonator, as schematically shown in Figure 1(a). There have been various papers reporting the effect is actually working based on standing wave resonators [3, 4] and traveling wave resonators [5, 6]. On the other hand, electro-optic effect such as the plasma effect or Franz-Keldysh effect is known to change the complex refractive indices of the resonator materials, which functions to modulate optical amplitudes by shifting the resonance wavelength as also schematically in Figure 1(b). Here, we would propose a new device to unify several photonic functions in Table 1. The device is a resonator with

TABLE 1: Device and material diversity of electronics and photonics.

	Devices	Materials
Electronics	Transistor	Si, SiO ₂
	Interconnect	Al, Cu
Photonics	Light emitter	III-V material
	Modulator	LiNbO ₃
	Interconnect	SiO ₂
	Filter	SiO ₂
	Detector	III-V material
	Amplifier	III-V material
	Isolator	YIG

a pin structure as in Figure 1(c). Forward-biasing of the resonator would function as a light emitter due to the Purcell effect; and reverse-biasing would function as a modulator due to the Franz-Keldysh effect. The device is referred to as a unified functional device (UFD) in the present paper. UFDs should in principle function as a light emitter, an amplifier, a modulator, a switch, as well as a tunable filter. Accordingly the device diversity of photonics in Table 1 is to dramatically shrink and the device set for photonic integration is only UFDs, detectors, and interconnects. Isolator function is not yet available.

3. PHYSICS AND THE REQUIREMENTS TO UNIFY THE DEVICE FUNCTIONS

In this section we will discuss physics, materials, and structures of UFDs.

3.1. Purcell effect and the requirements to ring resonators

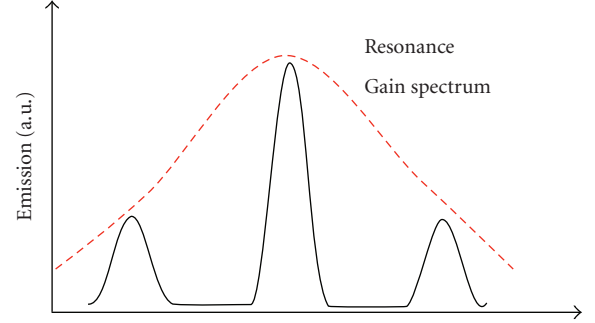
We first consider a single localized radiating dipole; its spontaneous emission rate R can be expressed via the Fermi golden rule;

$$R = \frac{1}{\tau} = \frac{4\pi^2}{h} |\langle \Psi_f | H_i | \Psi_i \rangle|^2 \cdot \rho, \quad (1)$$

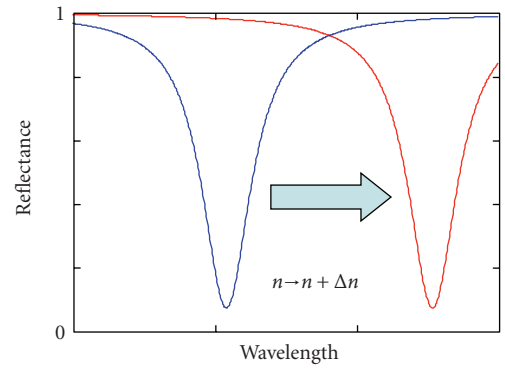
where h is the Planck constant, ρ is the density of optical modes (states) at the emitter's angular frequency. Considering the dipole moment \mathbf{u} , and the electrical vector \mathbf{E} , the term $|\langle \Psi_f | H_i | \Psi_i \rangle|^2$ can be simplified as $|\langle \Psi_f | \mathbf{u} | \Psi_i \rangle|^2$. The matrix element depends on the band structure of the media, we just refer to it as u^2 for simplification later. When \mathbf{E} is parallel to \mathbf{u} , the spontaneous emission rate can be expressed in the following well-known form:

$$R(r) = \int_0^\infty \frac{4\pi^2}{h} u^2(r, \omega) E^2(r, \omega) \cdot f_c(1 - f_v) \rho(\omega) d\omega. \quad (2)$$

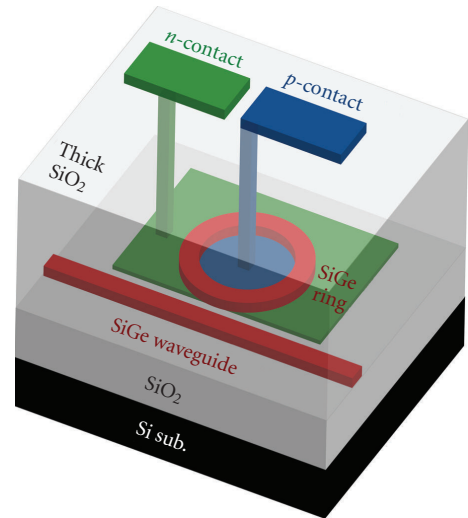
Here, f_c and f_v are the electron density of the conduction band and valence band expressed by Fermi-Dirac statistics.



(a)



(b)



(c)

FIGURE 1: Schematic diagrams of physics of unified function devices and a possible structure.

$\rho(\omega)d\omega$ denotes the mode density in a unit of angular frequency. Equation (2) indicates that R depends on the initial electron—and hole density of states and the final photonic density of states. The quantum confinement focuses on increasing \mathbf{u} while the microresonator on controlling \mathbf{E}^2 .

When the modal volume of the resonator is very large, the optical mode is continuous in the k -space. Assuming

the distribution of the electron is uniform all around the structure, R can be expressed as

$$R_{\text{sp}} \cong \frac{u_0^2 \omega_{\text{sp}}^2 n_{\text{eff}}}{3\pi \epsilon_0 c^3}, \quad (3)$$

where ω_{sp} denotes the center of the spontaneous emission band, u_0 the average dipole momentum, n_{eff} the effective refractive index of the resonator. Considering a small resonator with the scale of the emission wavelength λ_s , the modes will be quantized in the k -space. Meanwhile, the electrical field E will increase with resonator size reduction. The emission rate at the resonance wavelength can be derived as

$$R_{\text{sp}} \cong \frac{4u_0^2 \omega_c \Gamma_r(\omega_c)}{3\epsilon_0 n_{\text{eff}}^2 V_c \Delta\omega_i}, \quad (4)$$

where $\Gamma_r(\omega_c)$ is the relative confinement factor, expressing the overlapping between the optical mode and the resonator structure, and can be 1 in the high-index contrast systems. Here, V_c is the modal volume, and $\Delta\omega_i$ is the larger one of $\Delta\omega_{\text{sp}}$ or the full width at half maximum (FWHM) of resonance mode ($\Delta\omega_c$). Since spontaneous emissions are generally broader than the resonance modes, then $\Delta\omega_i = \Delta\omega_c$; $\Delta\omega_c/\omega_c = Q$. Here, we assumed the resonance frequency is at the center of the spontaneous emission band.

Finally, the enhancement of the spontaneous emission rate usually called Purcell factor F_p can be expressed by comparing the emission rates in the small resonator and space:

$$F_p = \frac{p\Gamma_r}{4\pi^2} \cdot \left(\frac{\lambda}{n_{\text{eff}}}\right)^3 \cdot \frac{Q}{V_c}. \quad (5)$$

In silicon resonators, the other factors except Q and V_c are all state constant. The higher Q/V_c , the higher Purcell factor. According to Zsai et al., we need to get an enhancement factor of nearly 100 to get positive net gain when the loss is due to free-carrier absorption [7]. So, our requirement of the Purcell enhancement is at least 100.

3.2. Franz-Keldysh effect and requirements to unify device functions

Si and Ge have the inversion symmetry in the lattice, prohibiting the existence of a linear electro-optic effect. Thus, the bias applications to the pin diode structures have been employed to change in carrier concentration and/or electric field strength and eventually altering refractive indices of the structures. The Franz-Keldysh (FK) effect is a typical one having been used in III-V semiconductor-based modulators. However, the effect was ignored until recently in Si, since the effect in Si was known very weak. We have recently reported that Ge shows a large electro-optic coefficient induced by the FK effect. The difference from Si can be explained by the difference in the band structure of Ge where the Γ point causing the FK effect is only slightly above the L valley.

The FK effect occurs as follows: the change in dielectric constant ($\Delta\epsilon$) at energy E under the field F is given in terms

of the well-known FK expressions $G(\eta)$ and $F(\eta)$ containing Airy functions and their derivatives [8, 9]:

$$\begin{aligned} \Delta\epsilon(E, F) &= (B/E^2)(\hbar\theta)^{1/2} [G(\eta) + iF(\eta)], \\ \hbar\theta &= \left(\frac{e^2 \hbar^2 F^2}{2\mu}\right)^{1/3}, \quad \eta = \frac{E_g - E}{\hbar\theta}. \end{aligned} \quad (6)$$

Here, B represents transition probability by absorption of photon, containing matrix element E_p and reduced effective mass μ . \hbar is Planck's constant h divided by 2π . In our model, we considered the FK effect from the direct band edge as noted above. The contribution from the indirect band edge was ignored in this treatment.

According to a simple mathematics, the following relations can be derived:

$$Q = \frac{\lambda}{\Delta\lambda} = \frac{n}{\Delta n}. \quad (7)$$

Here, $\Delta\lambda$ denotes the shift of resonance wavelength λ , and Δn denotes the shift of refractive index n . Assuming that Q of the resonator in Figure 1 is 4000, and that Δn should be 10^{-3} when n is 4.0, that is, Ge, the modulation depth can be 50 dB or higher, which is more than enough. However, we will find out that $\Delta n = 10^{-3}$ is the realistic limit in terms of FK effect as shown later. So, we set our goal of index change to be mid 10^{-4} . Thus, Q of 10^4 must be required.

3.3. Ring as a microresonator

There are two kinds of microresonators utilizing traveling waves and standing waves. We have employed traveling wave resonator to demonstrate the feasibility of UFDs since it is expandable to a three-terminal device. In the traveling wave resonator, we have further chosen ring resonators instead of disks because of fewer mode numbers involved in the resonator. In general, the observed Q can be written by [10]

$$\frac{1}{Q_{\text{total}}} = \frac{1}{Q_0} + \frac{1}{Q_{\text{ext}}}. \quad (8)$$

Here, Q_{total} is the observed Q , Q_0 loss Q of the ring itself, and Q_{ext} coupling Q between the waveguide and ring. In case of isolated ring resonators, $Q_{\text{total}} = Q_0$. Thus, Q_{total} can be expressed as

$$Q_{\text{total}} = Q_0 = \frac{\omega_0}{2\alpha v_g}. \quad (9)$$

Here, α denotes the overall attenuation coefficient of the ring, usually consisting of material absorption and attenuation due to light scattering of the ring waveguide.

These are simple explanations to control device functions and requirements for UFDs to function.

4. RESULTS

In this section, we will present the simulation and experimental demonstration of the characteristics of ring resonators functioning as light emitters and modulators. We

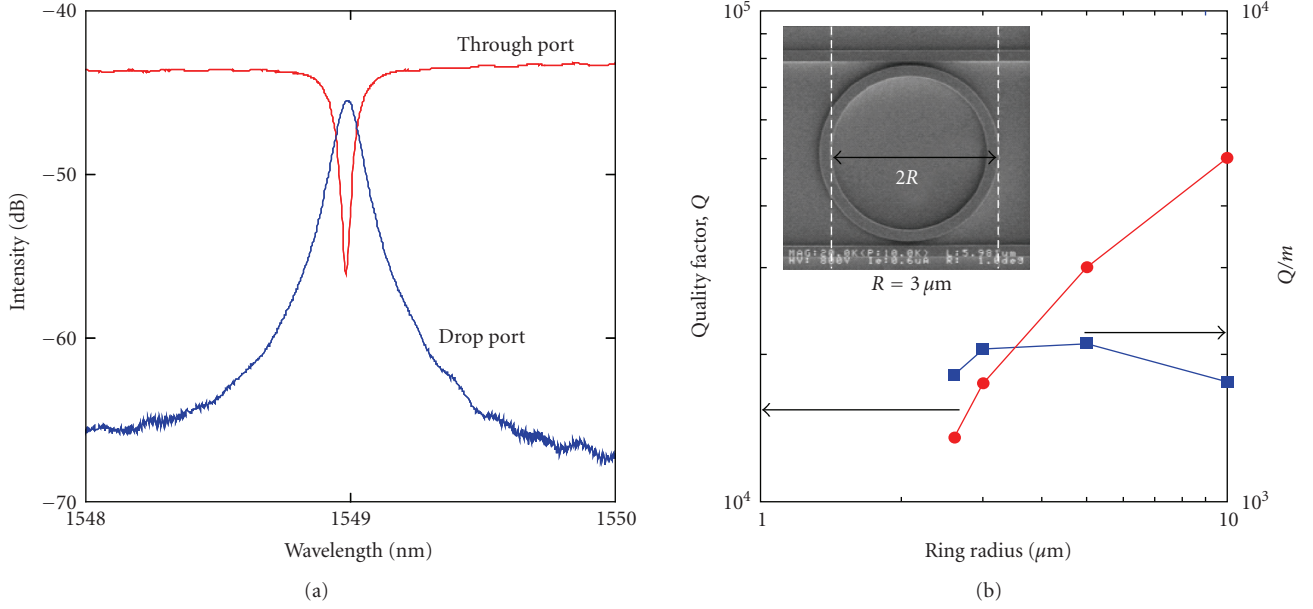


FIGURE 2: Transmission spectra of the ring resonator and Q and Q/m versus ring radii. Q is quality factor and m is the number of wavelengths in the longitudinal ring mode.

have not yet prototyped those with pin diode structure. The resonators were fabricated on Si on insulator (SOI) wafers by means of electron beam (EB) lithography and dry etching (DE) [6, 8, 11]. The SOI wafer has a $3\ \mu\text{m}$ buried oxide (BOX) layer and a $200\ \text{nm}$ top Si layer. The waveguides used to verify the feasibility of UFDs have $400\ \text{nm}$ width and $200\ \text{nm}$ height where the transverse mode is single. The radius ranged from 2.6 to $10\ \mu\text{m}$. The gap between incoming waveguide and the ring was changed from $150\ \text{nm}$ to $350\ \text{nm}$. The gap between outgoing waveguide and the ring is identical to the one between the incoming waveguide and the ring. The SEM image of the fabricated sample is shown as insert in Figure 2. The waveguides for emission function have $250\ \text{nm}$ width and $370\ \text{nm}$ height. The excitation is done by Ar^+ ion laser irradiation focusing on the waveguide. The resonator is isolated, and light escaping from the ring is collected using optical microscope.

4.1. Required characteristics of Si ring resonator and the experimentally obtained data

Figure 2 shows Q and Q/m of the various sizes of rings to check if the requirements described in Section 2 would be met. Q has to be larger than 10^4 for FK requirement for modulator. The cavity volume V is $m(\lambda/n_{\text{eff}})^3$, thus the term of $((\lambda/n_{\text{eff}}))^3 Q/V_c$ in (5) can be simplified by Q/m , where m denotes the number of the wavelength in the longitudinal mode of interest. To meet the requirement of 10–100 time Purcell enhancement, $Q/m > 10^3$. Figure 2(a) shows transmission spectra of the through port and drop port of the ring resonator, $r = 10\ \mu\text{m}$ and gap = $300\ \text{nm}$. From the transmission spectrum of the drop port, Q is determined to be nearly 50 000. It is also clear from Figure 2(b) that the

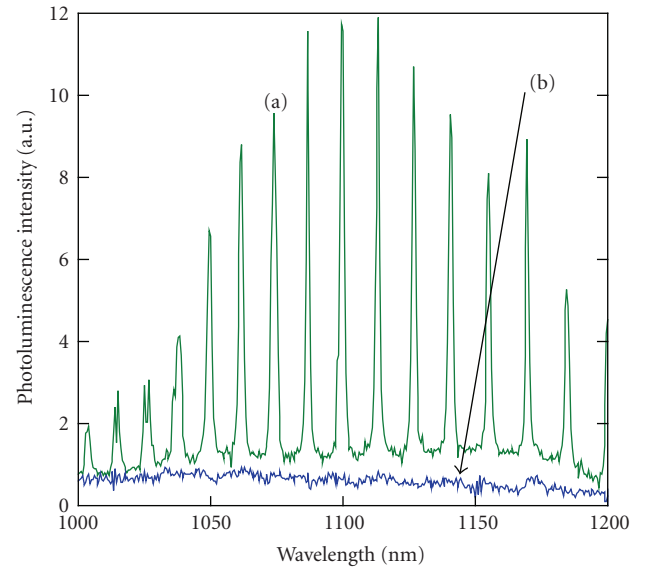


FIGURE 3: Photoluminescence spectra of (a) ring and (b) surrounding slab. The ring is $3.2\ \mu\text{m}$ in radius. The peaks are generated at the resonance wavelengths.

rings fabricated have met the Purcell requirement as well as the FK modulation when the radius is 2.6 – $10\ \mu\text{m}$.

4.2. Purcell enhancement of spontaneous emission of the ring resonator

Figure 3 shows the photoluminescence spectra of (a) the isolated Si ring resonator with the radius of $3.2\ \mu\text{m}$ and the width of $250\ \text{nm}$ and of (b) the slab region surrounding the ring. The luminescence of the slab in Figure 3 is multiplied

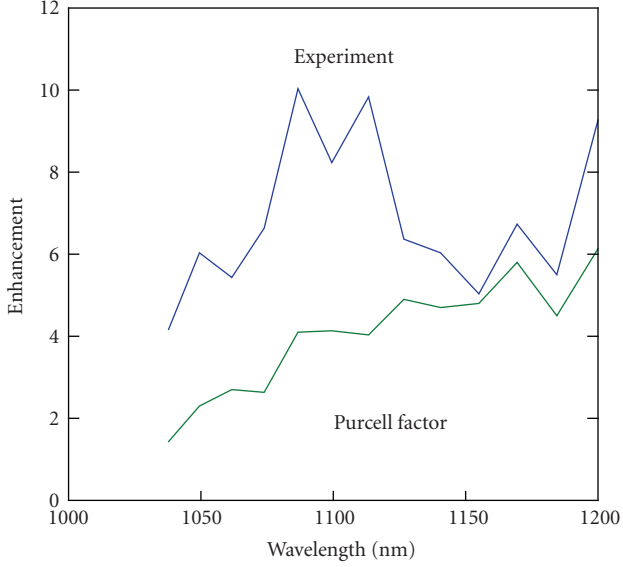


FIGURE 4: Comparison between the experimental enhancements and theoretical enhancement (Purcell factor).

by 10 to show it in this linear scale range. The luminescence consists of many peaks and the highest peak is more than 100-times stronger in intensity than the luminescence of the slab. The wavelengths of all peaks show a clear one-to-one correspondence with the resonance frequencies of the ring. Figure 4 shows the luminescence enhancement observed and the Purcell factors calculated by (5). The experimental data are in a good agreement with the prediction, indicating that the enhancement would occur due to the Purcell Effect. The enhancement is 10 times which is lower than our requirement of ring resonator. We will discuss this point later on.

4.3. Resonance shift using FK effect

The Ge p-i-n photodiodes used in this work were fabricated from 1.3 μm thick undoped Ge epilayers on a p^+ Si(100) substrate with boron concentration $>10^{19} \text{ cm}^{-3}$. The Ge epilayer was under 0.20% tensile strain [12]. Phosphorus was implanted into a poly-Si layer that was deposited on the top of the Ge epilayer to create a pin diode. External biases of 0 and 5 V were applied to the diode, corresponding to electric fields of 14 and 70 kV/cm in the Ge i-layer. The absorption coefficient α was calculated from the photodiode responsivity (R) defined by photocurrent normalized by incoming light power in A/W. Figure 5 shows the absorption coefficients extracted from the spectral responsivity. As predicted by the FK effect, the absorption coefficient increases with the applied electric field.

We have incorporated the strain effect into our Franz-Keldysh model to analyze the data as in Figure 5. The excellent fitting of the experimental data to the model obtained, suggesting that the change in absorption coefficients is due to the Franz-Keldysh effect in the strained Ge epilayer on Si. Based on the Kramers-Kronig relation, we have derived

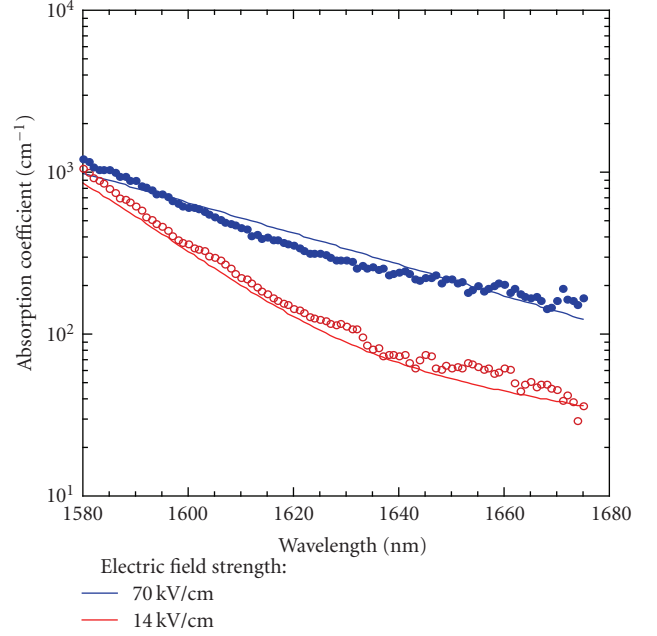


FIGURE 5: Absorption coefficient spectra under electric-field applications. The experiments are well reproduced by the Franz-Keldysh analysis.

the dependences of refractive indices difference Δn and absorption coefficient α as a function of wavelength as in Figure 6. Figure 6(a) shows Δn as a parameter of electric field strength, 20, 50, and 100 kV/cm. It is found that the electric field strength 20 kV/cm is not enough to change refractive index, mid 10^{-4} to enable modulator function. The Ge pin diode for under electric field strength 50 kV/cm can realize such index change in the wavelength range of 1750 nm or shorter. However, the absorption coefficient gets larger in the wavelength range as in Figure 6(b) and it is less likely that Q should exceed 10^4 according to (9). Indeed, Figure 6(c) indicates that Q should be mid 10^3 at 1700 nm that is lower than the requirement discussed above. As in Figure 6(c), Q of the Ge ring under 100 kV/cm can reach $\sim 10^4$ at 1850 nm. This lead us to conclude that the Ge-based ring can be operated as a modulator at 1850 nm under the electric field, 100 kV/cm.

5. DISCUSSION

We have shown the microring resonators can unite the photonic functions ranging from emitter, modulator, as well as filter. This suggests it can function as amplifier, and switch. This substantially reduces device diversity in Photonics. Since materials used in the UFDs are Si or Ge, that is, CMOS-compatible, the presented approach reducing device diversity should be beneficial for large-scale integration of electronics and photonics on a Si chip. However, the presented UFDs require two material systems Si and Ge for resonators although these are on the same materials platform. In this section, we will consider the feasibility of

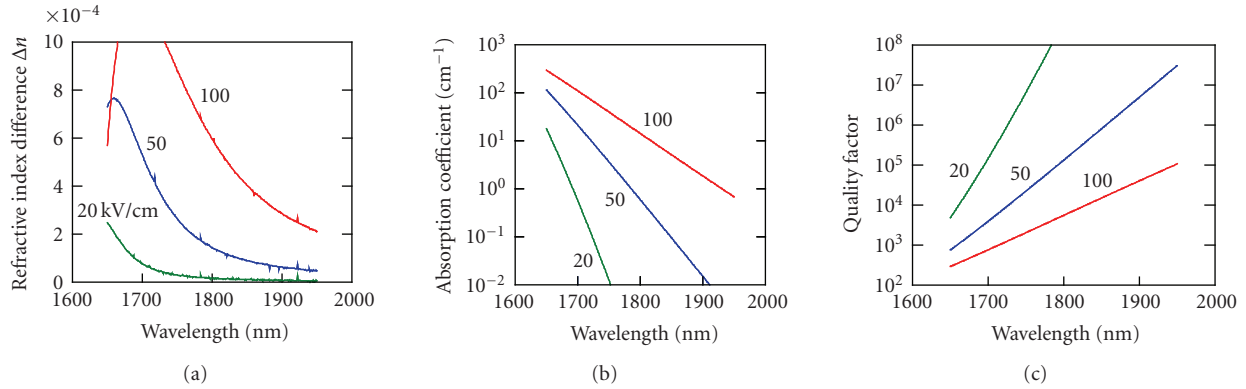


FIGURE 6: Changes in (a) refractive index and (b) absorption coefficient derived by Kramers-Kronig relation. The theoretical dependence of (c) Q versus wavelength.

materials unification via SiGe as the resonator materials to unify the emitter and modulator functions.

5.1. SiGe UFDs

Because of low absorption coefficient resulting in high Q , both of the Purcell enhancement and the FK shift are large at the photon energy slightly below gap, like 1200 nm for Si. According to the literature, Ge-rich SiGe, for example, the Ge composition ~ 0.95 should be of such materials. The indirect bandgap is around 0.8 eV, the communication wavelength band called C- and L-band, and the direct bandgap referencing the FK effect is ~ 1.0 eV [9]. The tensile strain of Ge on Si reduces the direct gap to 0.9 eV, as in Figure 7. The reduction of direct bandgap observed was in a good agreement with the deformation potential calculations [13]. Because of tensile-trained SiGe, we would be able to design UFDs built on the unique material system. This will be reported in a separate paper.

5.2. Increase of luminescence enhancement

The Si ring resonator emits strong light at the resonance wavelengths at the indirect band edge, $1.1 \mu\text{m}$. The enhancement we obtained was about 10 as in Figure 4. To get higher enhancement, we need to increase Q . Although Q of the isolated ring is not ready for measurement, the Purcell analysis leads us to estimate that Q is as low as ~ 500 , corresponding the overall attenuation coefficient to be $\sim 180 \text{ cm}^{-1}$ according to (9), assuming the group velocity is $1 \times 10^{10} \text{ cm/s}$ and wavelength $1.1 \mu\text{m}$. It is clear that the attenuation cannot be material absorption, 1.3 cm^{-1} at $1.1 \mu\text{m}$. It has been pointed that the sidewall roughness should increase the attenuation coefficient and could explain 180 cm^{-1} . According to Soref and Bennett [14], free-electron absorption is $\sim 1 \text{ cm}^{-1}$ at the density of 10^{18} cm^{-3} at $1.1 \mu\text{m}$ and free holes do almost the same. When the ring resonator is excited to measure photoluminescence, a high density of carriers if it is in concentration of 10^{20} cm^{-3} would result in such loss in terms of in free-carrier absorption. Q_0 should be reduced unless otherwise. Therefore, passivation of Si

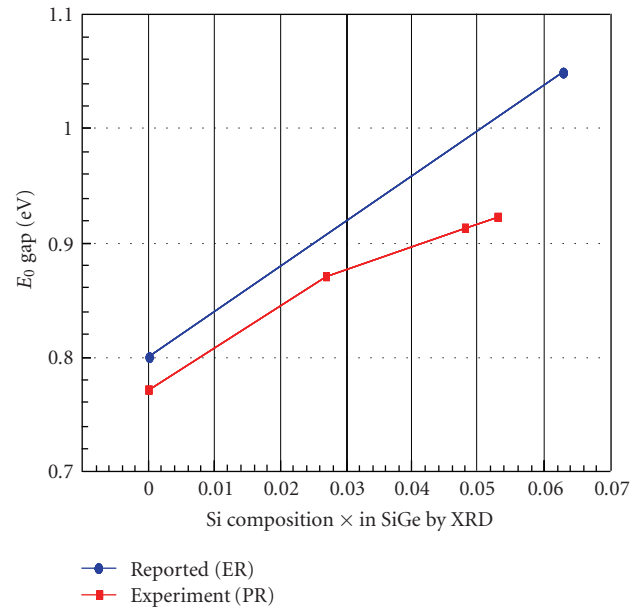


FIGURE 7: The direct bandgap versus SiGe alloy composition. The reported data were taken from bulk Ge using electroreflectance. Our data based on photoreflectance shows smaller direct bandgap in terms of tensile-strain in Ge epi on Si.

waveguides such as hydrogenation, and oxidation should be indispensable for UFDs.

6. CONCLUSION

A new approach on electronics and photonics convergence on Si CMOS platform is proposed; reducing device diversity rather than material diversity in photonics. The device concept unifying functional devices is a microresonator with a pin diode structure, and is theoretically and experimentally studied. It has been shown that the Purcell effect and the Franz-Keldysh effect should enable devising the concept to unite photonic functions such as emitter, amplifier, modulator, switch, and filter. It is further discussed that Ge-rich SiGe would be the material system for UFDs.

The present approach simplifies photonic devices to UFDs, photodetectors, and interconnects, that will be beneficial for large-scale integrated electronics and photonics circuits.

ACKNOWLEDGMENTS

The authors acknowledge Dr. Christina Manolatu in Cornell University for the FDTD simulator code. The work was partly supported by Grant-in-Aid for Creative Scientific Research by Japan Society for the Promotion of Science. The devices were fabricated at the NTT Microsystem Integration Laboratories, by the University of Tokyo VLSI Design and Education Center's (VDEC) 8-inch EB writer F5112+VD01 donated by ADVANTEST Corporation with the collaboration of Cadence Corporation, and at Massachusetts Institute of Technology. The authors are grateful to Drs. K. Yamada, T. Tsuchizawa, T. Watanabe, and S. Itabashi at NTT Microsystem Integration Laboratories, and to Drs. J. F. Liu, S. Jongthammanurak, J. Michel, and L. C. Kimerling at Massachusetts Institute of Technology for their in-depth discussions. The authors also like to thank Dr. Y. Ishikawa, Mr. S. Y. Lin, and Mr. P. H. Lim.

REFERENCES

- [1] E. M. Purcell, "Spontaneous emission probabilities at radio frequencies," *Physical Review*, vol. 69, no. 11-12, p. 681, 1946.
- [2] M. Cardona, *Modulation Spectroscopy*, Academic Press, New York, NY, USA, 1969.
- [3] M. Zelsmann, E. Picard, T. Charvolin, et al., "Seventy-fold enhancement of light extraction from a defectless photonic crystal made on silicon-on-insulator," *Applied Physics Letters*, vol. 83, no. 13, pp. 2542–2544, 2003.
- [4] T. Baba, D. Sano, K. Nozaki, K. Inoshita, Y. Kuroki, and F. Koyama, "Observation of fast spontaneous emission decay in GaInAsP photonic crystal point defect nanocavity at room temperature," *Applied Physics Letters*, vol. 85, no. 18, pp. 3989–3991, 2004.
- [5] J. S. Xia, Y. Ikegami, K. Nemoto, and Y. Shiraki, "Observation of whispering-gallery modes in Si microdisks at room temperature," *Applied Physics Letters*, vol. 90, no. 14, Article ID 141102, 3 pages, 2007.
- [6] S. Lin, Y. Kobayashi, Y. Ishikawa, and K. Wada, "Luminescence enhancement by Si ring resonator structures on silicon on insulator," *Applied Physics Letters*, vol. 92, no. 2, Article ID 021113, 3 pages, 2008.
- [7] C.-Y. Tsai, "Theoretical model for the optical gain coefficient of indirect-band-gap semiconductors," *Journal of Applied Physics*, vol. 99, no. 5, Article ID 053506, 5 pages, 2006.
- [8] Y. Miki, K. Yamada, T. Watanabe, et al., "Design of spontaneous emission enhancement based on Si ring resonators," in *Proceedings of the Electrochemical Society SiGe Symposium*, Pennington, NJ, USA, 2005.
- [9] J. S. Kline, F. H. Pollak, and M. Cardona, "Electroreflectance in the Ge-Si alloys," *Helvetica Physica Acta*, vol. 41, pp. 968–976, 1968.
- [10] H. A. Haus, *Waves and Fields in Optoelectronics*, Prentice-Hall, Englewood Cliffs, NJ, USA, 1984.
- [11] T. Tsuchizawa, K. Yamada, H. Fukuda, et al., "Microphotonics devices based on silicon microfabrication technology," *IEEE Journal on Selected Topics in Quantum Electronics*, vol. 11, no. 1, pp. 232–239, 2005.
- [12] Y. Ishikawa, K. Wada, D. D. Cannon, J. Liu, H.-C. Luan, and L. C. Kimerling, "Strain-induced band gap shrinkage in Ge grown on Si substrate," *Applied Physics Letters*, vol. 82, no. 13, pp. 2044–2046, 2003.
- [13] D. D. Cannon, J. Liu, D. T. Danielson, et al., "Germanium-rich silicon-germanium films epitaxially grown by ultrahigh vacuum chemical-vapor deposition directly on silicon substrates," *Applied Physics Letters*, vol. 91, no. 25, Article ID 252111, 3 pages, 2007.
- [14] R. A. Soref and B. R. Bennett, "Electrooptical effects in silicon," *IEEE Journal of Quantum Electronics*, vol. 23, no. 1, pp. 123–129, 1987.

Research Article

Slow Light with Photonic Crystals for On-Chip Optical Interconnects

Sean P. Anderson,¹ Ashutosh R. Shroff,¹ and Philippe M. Fauchet^{1,2}

¹The Institute of Optics, University of Rochester, Rochester, NY 14627, USA

²Department of Electrical and Computer Engineering, University of Rochester, Rochester, NY 14627, USA

Correspondence should be addressed to Sean P. Anderson, sanderso@optics.rochester.edu

Received 11 March 2008; Revised 21 April 2008; Accepted 3 June 2008

Recommended by Graham Reed

Transistor scaling alone can no longer be relied upon to yield the exponential speed increases we have come to expect from the microprocessor industry. The principle reason for this is the *interconnect bottleneck*, where the electrical connections between and within microprocessors are becoming, and in some cases have already become, the limiting factor in overall microprocessor performance. Optical interconnects have the potential to address this shortcoming directly, by providing an inter- and intrachip communication infrastructure that has both greater bandwidth and lower latency than electrical interconnects, while remaining safely within size and power constraints. In this paper, we review the requirements that a successful optical interconnect must meet, as well as some of the recent work in our group in the area of slow-light photonic crystal devices for on-chip optical interconnects. We show that slow-light interferometric optical modulators in photonic crystal can have not only high bandwidth, but also extremely compact size. We also introduce the first example of a multichannel slow light platform, upon which a new class of ultracompact optical devices can be built.

Copyright © 2008 Sean P. Anderson et al. This is an open access article distributed under the Creative Commons Attribution License, which permits unrestricted use, distribution, and reproduction in any medium, provided the original work is properly cited.

1. INTRODUCTION

Transistor scaling has been the crux of the rapid growth in microprocessor performance over the past forty years [1]. More recently, however, the performance of the electrical interconnects, which are responsible for transporting data within the microprocessor and between the microprocessor and memory, has been unable to keep pace. This is true because as the interconnect is scaled down along with the transistors, resistance and capacitance grow, limiting performance. This not only decreases the bandwidth of the interconnect, but also increases both its latency and power consumption. In fact, in modern microprocessors, over half of the dissipated power is dissipated by the interconnects [2, 3]. These issues will continue to worsen as chip technology continues to scale [3–8]. Optical interconnects can directly address these problems at the system level by replacing electrical interconnects [6–10]. To do so, they must meet the performance requirements of modern and future microprocessors while achieving both compact size and low power consumption.

Implementing optical interconnects in silicon has the advantage of maintaining maximum compatibility with the existing CMOS fabrication infrastructure. Additionally, silicon is transparent in the range of telecom wavelengths ($\lambda \sim 1.5 \mu\text{m}$). However, it is not an ideal choice as an active optical material due to its relatively weak electro-optic response [11]. In general, this results either in large device size or decreased operational bandwidth. The former is true especially for phase-shifting approaches, while the latter applies mostly to resonant approaches. To work around this limitation, it is possible to use some other, extrinsic material as the active medium, such as liquid crystals [12–14], quantum dots [15], or electro-optic polymers [16]. These have the advantage of potentially smaller device size, but at the expense of bandwidth. This is because their response times can be orders of magnitude slower than that of silicon. To date, devices based on such extrinsic materials are unable to meet the bandwidth requirements for optical interconnects. Such hybrid approaches also have the drawback of reduced compatibility with CMOS processing techniques. An all-silicon approach would thus be favorable,

although devices that employ silicon as the active medium have so far been unable to meet the size requirements.

Using slow light, however, it is possible to create a device that meets both of these seemingly contradictory sets of requirements. The advantage of using slow light is that, because the group velocity of light is decreased by two or more orders of magnitude as compared to that in bulk silicon, the effective photon-material interaction length inside an active device is increased [17]. This allows greater use to be made of the small refractive index changes available in silicon, and thus can enable silicon-based photonics to meet the requirements set out by optical interconnects.

In this paper, we first review the rationale behind the push toward optical interconnects, as well as the bandwidth, latency, power, and footprint requirements that an optical interconnect must satisfy in order to be competitive. We then explain how slow light can be used as the basis for an optical interconnect technology that satisfies these requirements. Specifically, we describe how interferometric optical modulators based on slow light in photonic crystals can exhibit not only high bandwidth but also extremely compact size. We also report on recent results regarding a new optical structure that merges slow light with wavelength-division multiplexing to form the first multichannel slow-light platform for silicon photonics. Finally, we outline some of the challenges surrounding the implementation of these novel structures and devices and, more broadly, how a slow-light approach may fit into what has been called “the interconnect era” [18].

2. THE NEED FOR OPTICAL INTERCONNECTS

The electrical interconnects inside modern microprocessors consist of copper wires surrounded by a low- k dielectric [19]. This represents a transition from previous generations of electrical interconnects, which used aluminum wires surrounded by a dielectric. Both the switch from aluminum to copper, and from dielectric to specifically a low- k dielectric, were made to reduce the RC time constant of the interconnect (the former determining the R part, and the latter the C part). Since the RC time constant is essentially a measure of the amount of energy required to operate the interconnect, reducing it allows the interconnect to operate more efficiently. A lower time constant also allows for lower transmission latency and for reduced crosstalk between adjacent wires. Regardless of the materials used, however, the performance of an electrical interconnect, whether measured by bandwidth, latency, power consumption or crosstalk, worsens as its dimensions are scaled down. This is due to the fact that the resistance of a metal wire grows as its cross-sectional area is reduced. The result is a hyperbolic increase in the RC time constant per unit length of interconnect as the chip feature size is scaled down [6]. Optical interconnects, on the other hand, do not suffer from this constraint because they are not subject to an RC time constant.

For this reason, optical interconnects (OIs) offer a number of advantages over electrical interconnects (EIs). The first is a significantly lower signal propagation delay. Figure 1(a) shows the relationship between propagation

delay and interconnect length both for EIs based on copper, and for OIs based on silicon waveguides. Silicon waveguides possess an intrinsic advantage over copper wires because of their higher signal propagation speed, which is in turn due to the absence of RC impedances [10]. Because there is an encoding/decoding penalty associated with optical interconnects (the time spent converting the signal from the electrical domain to the optical, and vice versa), OIs based on silicon waveguides may be best suited for longer length interconnects (i.e., global, as opposed to local, interconnects) [10, 20].

A second metric by which OIs must be compared to EIs is bandwidth density. Although the bandwidth available from a single wire in an EI decreases as the chip feature size is scaled down, the cross-sectional area it occupies also decreases. The net result is that the bandwidth density, as measured by the number of bits that can be transmitted per second per unit lateral width, increases with further chip scaling. Additionally, repeaters can be used to further enhance bandwidth, though at the price of increased size and power consumption [21]. This creates a moving target for OIs to beat. Figure 1(b) compares the bandwidth density of EIs to that of OIs, based on reasonable estimates of the size of and spacing between the silicon waveguides. The bandwidth density of OIs is assumed to scale linearly with the clock speed of the chip, while the bandwidth density of EIs scales at a slightly higher rate. EIs, however, have the disadvantage that they can support only a single data channel at a time. OIs, on the other hand, can employ techniques such as wavelength-division multiplexing (WDM) to support a large number of channels simultaneously. Even at the 22 nm node, only three WDM channels are needed to match the performance of EIs [4]. Although the additional channels come at the price of increased power consumption and footprint, these parameters scale much more weakly for OIs than for EIs. This is due to the fact that the extra space and power are required only by additional modulator/demodulator pairs at the ends of the interconnect. The size of the waveguide itself does not grow (and it consumes no power because, unlike with EIs, it contains no repeaters). This gives WDM OIs a significant advantage over EIs, especially for longer-length interconnects.

An additional metric, the power-delay product, is often used to evaluate interconnect performance because it is a measure of both the power consumed, and the delay introduced, by the interconnect. The power-delay product (PDP) of an OI is dependent on both its length and the technique used to modulate the optical signal. Modulation techniques fall generally into two categories: resonant and interferometric. Figure 2 compares the PDP for these two types of modulators to that of EIs as a function of the achievable index shift Δn . For interferometric modulators, Δn determines the length required to achieve a required phase shift; the lower Δn , the greater the length, and thus the greater the power consumption and delay. A resonator-based modulator has the advantage that its active area can be made much smaller than in an interferometric modulator, resulting in both lower delay and lower power consumption. In fact, the PDP for a resonant modulator is nearly two orders

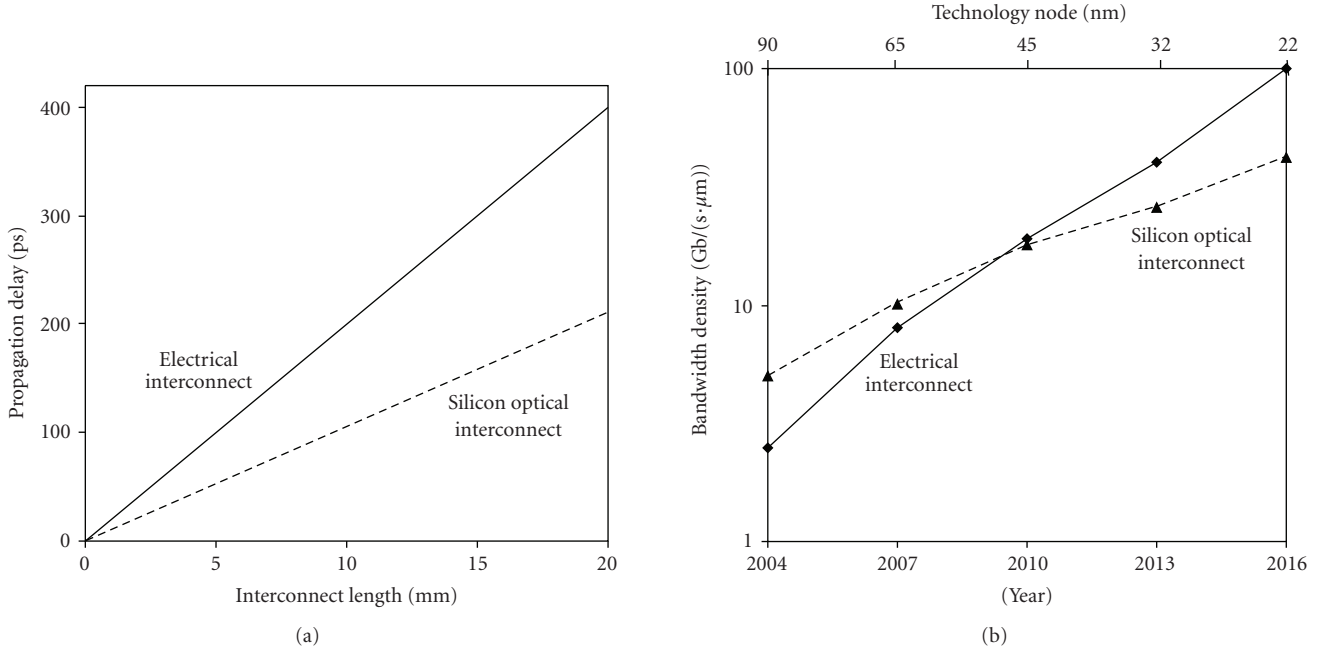


FIGURE 1: (a) Propagation delay of silicon optical waveguides as compared to copper electrical wires (cf. [4]). (b) Comparison of bandwidth density of EIs to that of a single-channel OI as a function of ITRS year and technology node. The use of a multichannel OI can increase bandwidth density over that of EIs (cf. [4]).

of magnitude less than for an interferometric one, assuming each has sufficient bandwidth for a single optical channel. This shows that a resonant approach is generally preferable over one based on interference [4]. Resonant modulators also have the advantage of a smaller footprint, and thus a smaller size penalty for each additional WDM channel. In principle, these advantages come at the price of decreased bandwidth. However, the bandwidth of any interconnect channel is limited by the clock speed of the chip, and that speed is in the range of tens of gigahertz. Therefore, a favorable PDP can still be achieved without using Q-factors so high that they compromise bandwidth.

Optical interconnects thus have advantages in terms of signal propagation delay, power consumption, and bandwidth density. These advantages are especially compelling when the length of the interconnect in question is long. We can then estimate the *critical length* over which OIs are preferable to EIs. This length is plotted in Figure 3 for several technology nodes of the ITRS [22]. The comparison is made separately for three different criteria: signal propagation delay, power consumption, and bandwidth density scaled by delay. In all of these comparisons, OIs are favorable for interconnect lengths over a few millimeters, assuming the use of WDM and resonator-based modulators, with each channel operating at a bit-rate equal to the clock rate of the chip [7, 10, 20].

Therefore, the development of a successful optical interconnect technology must include the development of a compact and low-power modulator, upon which a WDM communication system can be based. However, the size advantage of resonant modulators is not fundamental. In

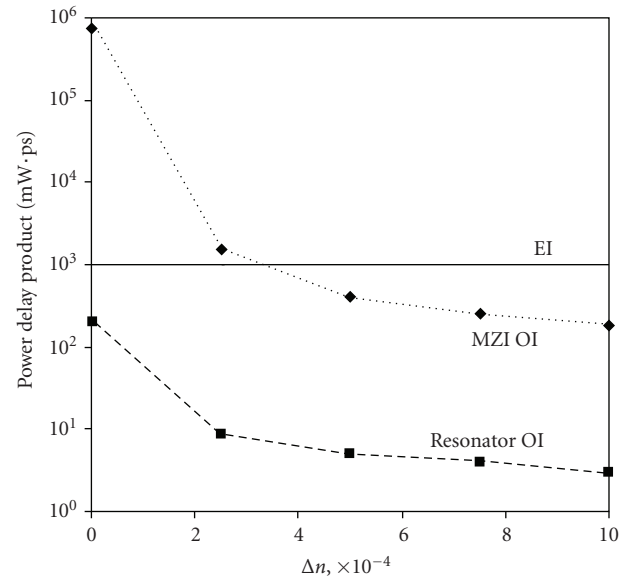


FIGURE 2: Power-delay product of EI and OIs as a function of Δn for the 90 nm technology node, assuming a length of 10 mm. OIs based on resonator-based modulators offer a significant advantage over both EIs and OIs based on interferometric approaches (cf. [4]).

fact, it is possible to produce interferometric modulators with superior power and size characteristics if the group velocity inside the devices can be sufficiently reduced. This is the principle behind *slow-light* devices. We next review recent work in our group in the area of slow-light interferometric devices in silicon.

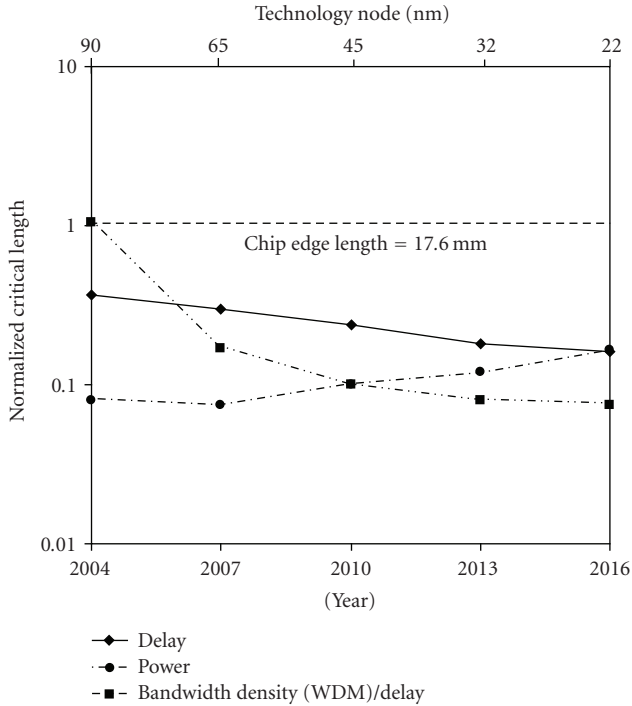


FIGURE 3: Critical length, normalized to the chip edge length, above which OIs (using WDM) are advantageous over EIs in terms of delay, bandwidth density (scaled by delay), and power consumption (cf. [10]).

3. SLOW-LIGHT MACH-ZEHNDER INTERFEROMETERS

Integrated Mach-Zehnder interferometer (MZI) devices are used extensively in optical modulators and switches. Liu et al. demonstrated a silicon high-speed optical modulator with an operational bandwidth of 40 GHz [23]. While the device proves the feasibility of silicon for optoelectronic applications, it suffers from a significant disadvantage: its size is on the order of a millimeter. This is consistent with an earlier analysis presented by Giguere et al. [24]. The large device footprint is a result of the small value of Δn available in silicon. This makes the distance, L_π , required to produce a π phase shift in one arm of the MZI to be very long.

However, Soljačić et al. proposed that by increasing the group index (decreasing the group velocity) of light propagating in the arms of an MZI, the sensitivity to small changes in the material refractive index of the arms could be amplified [17]. More recently, Shi et al. showed experimentally that the sensitivity of an interferometer is dependent on the group index rather than the material index [25]. One way to understand this is that inducing a change δn in the material refractive index in one arm of the interferometer causes the electromagnetic bands to shift in frequency by an amount $d\omega$. Because frequency is kept constant by the choice of the operating wavelength, the propagating wave experiences a change in wavevector magnitude by an amount dk . Therefore, since $n_g = c/v_g = c/(d\omega/dk)$, the larger the group index, the larger the change in wavevector, and thus the shorter the interferometer arms

can be made, because $L_\pi = \pi/dk$. Reducing the device length not only allows for space savings, but also decreases device power consumption. Additionally, the electrodes can be made smaller, thus reducing parasitics and further increasing operating bandwidth.

The photonic crystal platform [26–28] is ideal for implementing such a device because it provides the design flexibility required to increase the group index while allowing the tunability required of an active device. In a photonic crystal coupled-cavity waveguide (PC-CCW), the group velocity can be controlled by changing the spacing between adjacent cavities. This is because the spacing controls the spatial overlap between the optical fields in adjacent cavities, which in turn determines the width (and slope) of the optical miniband and thus its group velocity [29–32]. An MZI based on such a design was proposed and analyzed by Soljačić et al. [17], although that analysis did not include the possibility of optical jitter. The concept of optical jitter in devices is important because it can cause pulse distortion and thus reduced bandwidth. In fact, in MZIs based on slow-light CCWs, deterministic optical jitter is a significant source of pulse distortion at high bit-rates. Further, when multiple devices are cascaded together, uncertainty due to jitter compounds, which can result in asynchronous operation. In slow-light MZIs, deterministic optical jitter grows as the device length is reduced, resulting in a tradeoff between bandwidth and device size reduction. Optical jitter can, however, be minimized by carefully choosing the operating wavelength of the device. This effectively removes the tradeoff between bandwidth and size reduction, but replaces it with a tradeoff between size reduction, and sensitivity of the device to material and fabrication variance. This new tradeoff, however, is a very favorable one because the semiconductor industry excels at minimizing variation.

3.1. Increased sensitivity in slow-light MZIs

Figure 4(a) shows the concept of an MZI in which each arm consists of a PC-CCW. We modeled five different PC-CCWs, denoted by the separation Δ between adjacent cavities, using the MIT Photonic Bands software package [33, 34]. We calculated the TE bands for the structures assuming air holes ($n = 1.0$) of radius $0.3a$ in a silicon slab ($n = 3.4$), where the lattice constant a is chosen to be 400 nm for use at $\lambda = 1.5 \mu\text{m}$. Each cavity consists simply of a missing hole. The Brillouin zone in each case is chosen to include the entire repeat unit cell of length Δ , which determines the distance between adjacent cavities. For ease of comparison, all results are normalized to the lattice constant a . Each PC-CCW has a significant photonic bandgap with a single defect mode (Figure 4(b)). As the separation between adjacent cavities is increased, both the bandwidth and the group velocity of the defect band are reduced because the cavity lifetime of a photon within the defect band is increased. The greater the group index, the shorter the interferometer can be made. For example, if we are able to inject a free carrier concentration of $\Delta N = 10^{18} \text{ cm}^{-3}$ into the silicon, corresponding to an index change of approximately $\delta n = 0.001$ [11], then the length of the MZI can be reduced to approximately $56 \mu\text{m}$

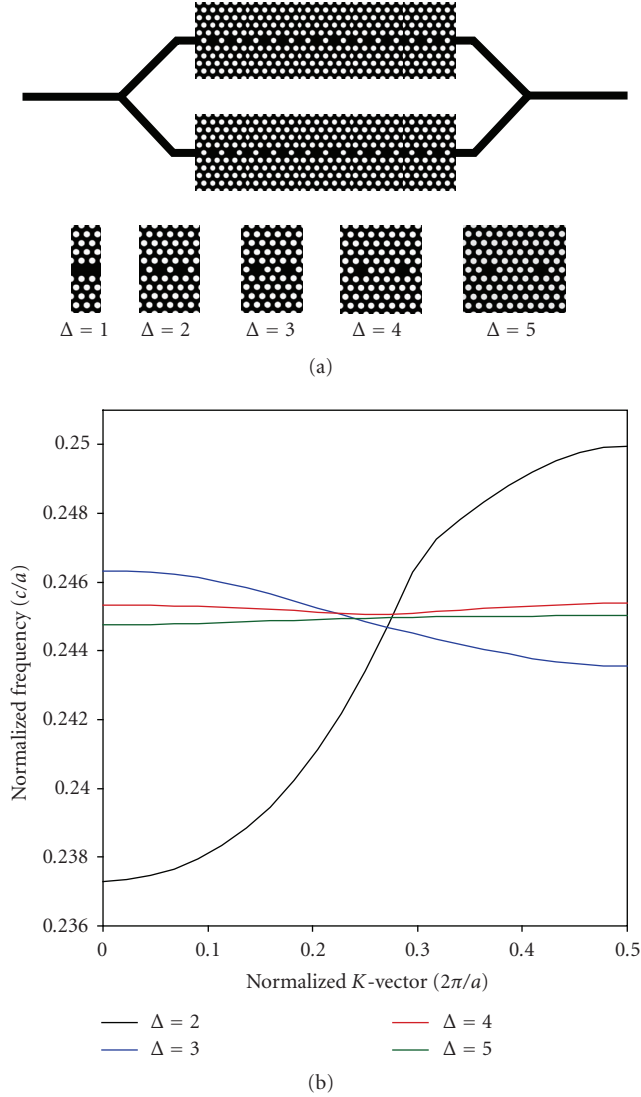


FIGURE 4: (a) Concept of PC-CCWs used to design ultracompact MZIs. Here Δ is the degree of freedom for varying the device structure. (b) The dispersion curves for the CCW defect bands. As the separation Δ between the cavities is increased, the spatial overlap between the fields localized in each cavity is reduced, thus flattening the dispersion curve and reducing group velocity.

(for the $\Delta = 3$ case), as compared to over $600 \mu\text{m}$ for an MZI based on a simple photonic crystal line-defect waveguide (the $\Delta = 1$ case). In fact, the arm length could be reduced even further by using PC-CCWs with greater separations Δ between adjacent cavities.

3.2. Optical jitter

When modeling these PC-CCW structures with a small increase δn in the material refractive index induced in the entire silicon slab, we find, as expected, that the bands shift downward in frequency, causing a change Δk in the magnitude of the corresponding wavevector. Associated with this change in wavevector, however, is a change in group

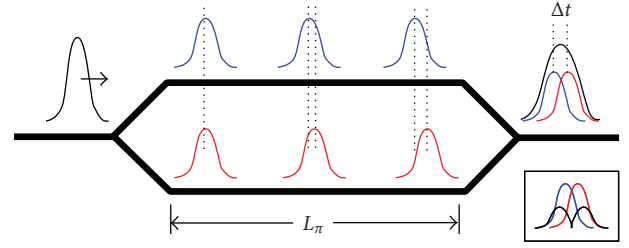


FIGURE 5: When an index shift is induced in one arm of the interferometer, the group velocity in that arm changes. The pulses traveling in the two arms of the interferometer therefore arrive at the output separated in time by Δt , resulting in pulse distortion (broadening). In the worst case, where the pulses interfere destructively, the output pulse can even become double-humped (inset).

velocity. This occurs because the slope of the defect band is not exactly linear at its center, so that when the magnitude of the wavevector changes by Δk , the corresponding point on the dispersion curve has a slightly different slope, and thus a different group velocity. Because the index change is induced in only one arm of the interferometer, the result is that the pulses in the two arms of the MZI do not propagate at the same speed, and thus arrive at the output shifted slightly in time from one another (Figure 5). We have termed this difference in arrival time deterministic optical jitter, Δt . The effect of this type of jitter on the output pulse depends upon both the magnitude of the optical jitter in relation to the pulse width, as well as the bias of the MZI itself. When the optical jitter is comparable to or smaller than the pulse width, the result is pulse broadening in the case of constructive interference, or gross pulse distortion in the case of destructive interference. When the optical jitter is large in comparison to the pulse width, the pulses fail to interfere at all, resulting in two distinct output pulses regardless of the interferometer's bias.

In previous work [17] on slow-light MZI modulators, it was implicitly assumed that $\Delta t = 0$, that is, upon producing a small refractive index shift, δn , in the material, the defect band moves to a higher or lower frequency without changing its slope. While this assumption is true in the case of a single defect in an infinite PC slab, it does not generally hold in the case of PC-CCWs. Because the group velocity is sensitive to changes in the material refractive index, the potential for pulse distortion due to deterministic optical jitter must be taken into account when designing devices based on PC-CCWs. While pulse distortion is insignificant at moderate bit-rates, it becomes more important at higher bit-rates, where Δt becomes significant compared to the FWHM of individual pulses. Depending upon the parameters of the device, jitter can be quite large; over ten picoseconds for the $\Delta = 5$ PC-CCW device, for example. In fact, the amount of optical jitter introduced by the MZI is a function of the separation between adjacent cavities in the PC-CCW. There is thus a tradeoff between the extent to which the arm length can be reduced and the amount of optical jitter introduced (Figure 6). We note also that this behavior is not restricted to the specific geometry used. We have observed the same effect

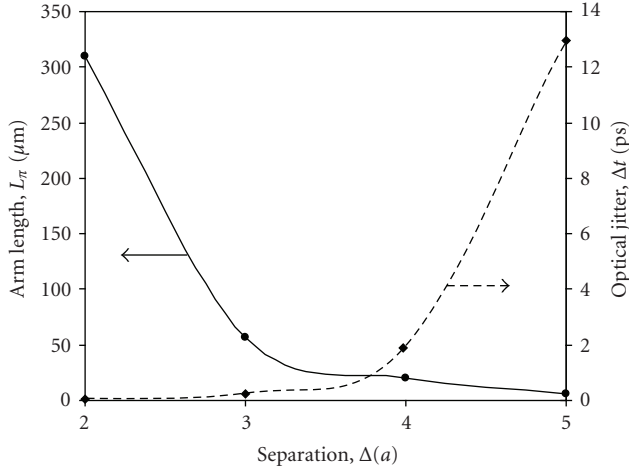


FIGURE 6: Achievable arm length L_π and optical jitter Δt as functions of the separation Δ between the cavities of the PC-CCWs, assuming $\delta n = 0.001$.

in CCWs based on other cavity geometries, including that proposed by Akahane et al. [35, 36].

To characterize the importance of deterministic optical jitter in PC-CCW MZIs, we compared the pulse distortion it causes to that caused by waveguide dispersion. We assumed a 100 Gbits/s Gaussian pulse train, where the pulses have a FWHM of 3.33 picoseconds, and the 10-picosecond bit-slot thus contains 99% of the pulse energy. Because the pulse bandwidth for a 100 Gbits/s signal is significantly smaller than the channel bandwidths of the PC-CCW defect bands, waveguide dispersion should be minimal. To verify this, we calculated the temporal envelope of a single pulse in the 100 Gbits/s pulse train after propagating through an MZI with arm length L_π and optical jitter Δt . We then compared the resulting output pulse to the input pulse using the $(1 - R^2)$ metric, where $0 \leq R^2 \leq 100\%$. This metric is commonly used in regression analysis to calculate the goodness of fit, and is analogous to the mean-squared error metric [37]. In each case, the amount of pulse distortion due to waveguide dispersion was less than 1%. In comparison, approximately the same level of pulse distortion is reached when Δt is only 0.2 picosecond. (This assumes that the pulses interfere constructively at the output; the distortion would be worse for destructive interference.) Because pulse distortion increases rapidly with Δt , deterministic optical jitter has the potential to be the dominant source of pulse distortion in PC-CCW MZIs.

3.3. Design considerations

In previous work, it was assumed that a small change in the material index would result only in a change in the magnitude of the propagating wavevector, and not in the slope of the dispersion curves. Thus, by operating a PC-CCW MZI in the center of the band ($k = 0.25$, where k is the normalized wavevector) where the dispersion curve is approximately linear, no change in group velocity would

be observed. In practice, however, the operating frequency is fixed by the choice of wavelength of the input signal. Therefore, as the dispersion curve shifts up or down, the fixed operating frequency forces a change in the magnitude of the wavevector, and that change may be large enough to shift outside the linear region of the dispersion curve, causing a change in group velocity. This effect is more pronounced in PC-CCWs with larger cavity separations Δ because of the larger changes in k that occur in them. The problem is compounded by the fact that the linear region of the dispersion curve does not necessarily lie exactly at the band center in k -space.

Figure 7 shows the dispersion curves for the $\Delta = 5$ PC-CCW, with and without δn applied. The first operating frequency, ω_1 , was chosen because the dispersion curves crossed the band center at approximately that frequency. While this frequency allows for very large changes in the magnitude of the wavevector (k ranges from 0.23 for the $\delta n = 0$ case to 0.29 for the $\delta n = 0.0005$ case, thus resulting in a very short L_π of only $16 \mu\text{m}$), the slope of the band changes significantly when the index change is induced, causing the group velocity to decrease from $0.0033c$ to $0.0020c$, a reduction of nearly 40%. (Although the example shown in Figure 7 is an extreme one, and the operating frequency ω_1 would not normally be chosen because of its unfavorable dispersion characteristics, it is illustrative of the issue in point.) By shifting the operating frequency down to ω_2 so that it is closer to the linear regions of the dispersion curves, a much smaller change in group velocity can be obtained, thus greatly reducing optical jitter. Figure 8 shows the arm lengths and values of optical jitter that are achievable when these guidelines are applied to MZIs based on other PC-CCWs. While the arm lengths are slightly increased, the amount of optical jitter is reduced by as much as an order of magnitude by optimizing the operating frequency.

Optical jitter can even be eliminated altogether by choosing the appropriate value of δn . For the $\Delta = 5$ PC-CCW, in fact, choosing $\delta n \approx 0.00055$ results in $\Delta t = 0$ picosecond and $L_\pi < 30 \mu\text{m}$ (Figure 9). By slightly varying the operating frequency, the “zero-jitter” point can be shifted to other values of δn . For example, choosing $\omega_2 = 0.24486$ as the operating frequency allows for $\Delta t = 0$ at $\delta n \approx 0.0003$, with $L_\pi < 50 \mu\text{m}$. The arm lengths given here can be further reduced by a factor of two by employing a “push-pull” design for the MZI, where each arm induces a $\pm\pi/2$ phase shift. Figure 9 also shows, however, that Δt is extremely sensitive to the value of δn being used. Thus, a minute variance in the value of δn could increase Δt to be on the order of tenths of a picosecond, severely limiting the operational bandwidth of the resulting device. This sensitivity is more pronounced for shorter device lengths (greater separation Δ between adjacent cavities, and thus lower group velocity), hence the tradeoff between the size of a slow-light MZI and its tolerance to fabrication variances. This new tradeoff is a very favorable one, however, because the semiconductor industry excels at minimizing fabrication variances, and improves at it with each successive generation of technology.

As long as the refractive index change can be tightly controlled, slow-light MZIs can be made very short while

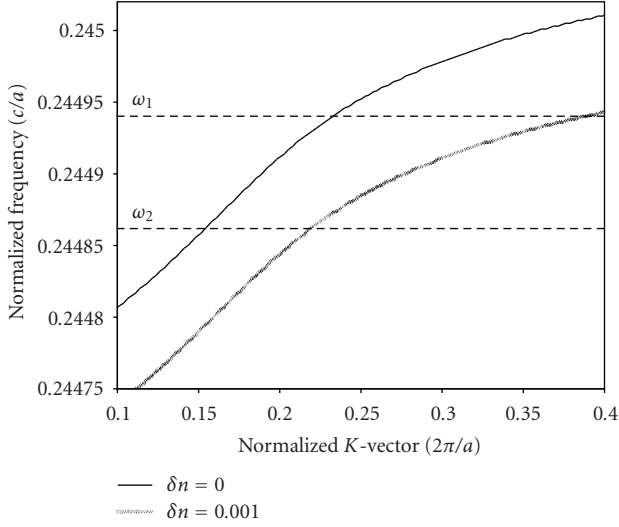


FIGURE 7: When the operating frequency is chosen to correspond to a normalized frequency of $\omega_1 = 0.24494$, the slope of the dispersion curve changes significantly when δn is applied. When the operating frequency is changed to $\omega_2 = 0.24485$, the slopes become more similar, thus reducing Δt .

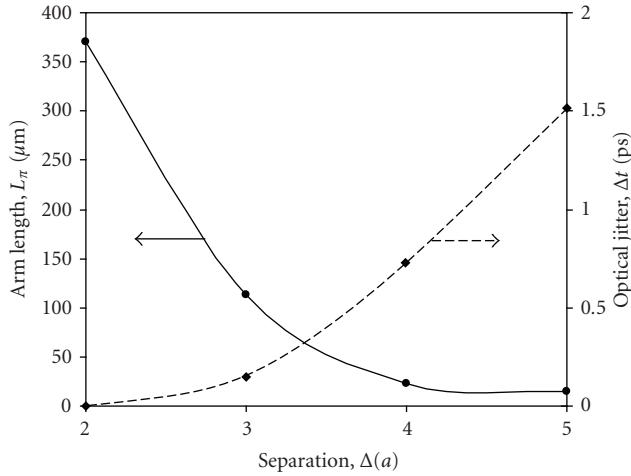


FIGURE 8: Achievable arm length L_π and optical jitter Δt as functions of the separation Δ between the cavities when the optical jitter is minimized by optimizing the operating frequencies for each MZI configuration, assuming $\delta n = 0.001$.

still maintaining the bandwidth necessary for on-chip applications. With an arm length of only $30 \mu\text{m}$ and a width under $10 \mu\text{m}$, slow-light MZIs are competitive with resonant approaches, such as microrings, in terms of on-chip footprint [38]. Furthermore, power consumption scales down along with arm length, so that a $30 \mu\text{m}$ long MZI uses two orders of magnitude less power than, for example, a 3-millimeter long MZI. This brings the power-delay product of slow-light MZIs in line with that of resonator-based modulators, yet with greater bandwidth.

Although the above analysis is specific to slow-light MZIs based on CCWs, the same considerations apply to slow-light

MZI approaches in general, including those based on, for example, line-defect waveguides [39, 40]. Just as the slopes of the dispersion curves must be matched in CCWs to minimize optical jitter, so must the slopes be matched in line-defect waveguides or other slow-light media.

4. INTERLACED COUPLED-CAVITY WAVEGUIDE

Even with the use of these ultracompact, high-speed, slow-light MZIs, it is still desirable to use WDM to increase the net bandwidth density of OIs since, in general, the bandwidth of any device is still limited by the clock speed of the chip. To this end, we have also been investigating a novel type of slow-light structure that may be an ideal platform for WDM. It is the first example of which we are aware, of a *slow-light WDM platform* for silicon photonics.

The interlaced coupled-cavity waveguide (ICCW), as we have named it, is a multiresonant structure. Its operation is analogous to that of a normal CCW, where electromagnetic energy couples from one defect cavity to the next, except that there are now multiple cavities, each of which has a different resonant frequency (Figure 10). Thus, light couples from one cavity to the next of the same size, skipping over the intervening cavities. An ICCW therefore exhibits multiple slow-light bands, each corresponding to cavities of a particular radius.

Simulations of a representative ICCW design, using parameters similar to those used for the slow-light MZI above (slab index 3.4, hole index 1.0, lattice constant 400 nm , $r/a = 0.35$), reveal a significant photonic bandgap. In this particular structure, the radii of the defects increase in steps of $0.075a$ from $r/a = 0.0$ to $r/a = 0.225$. There are 10 TE bands in the bandgap, which includes several coupled-cavity modes as well as several waveguide modes. Each of the coupled-cavity modes is localized to a cavity of a particular radius. Figure 11(a) plots the bandstructure of the ICCW, and Figure 11(b) shows the electric field distributions for three of the localized modes. The exact positions in frequency space of these localized bands, and thus the spacing between them, can be adjusted by fine-tuning the radii of the defect cavities. For example, in Figure 11(a), band 4 can be moved such that it lies exactly between bands 3 and 5 by slightly increasing the radius of the second defect, in which band 4 is localized.

Assuming that only one sixteenth of the bandwidth of each band can be used, centered around the zero-GVD points, this ICCW structure exhibits an aggregate bandwidth above 400 Gbits/s at group velocities below $0.004c$. Several other bands also exhibit good dispersion properties, in addition to low group velocities. However, either their bandwidths are smaller due to band-edge effects or their lowest group velocities are only one to two orders of magnitude lower than c . The use of these additional bands can, however, provide a further boost to the total available bandwidth. Pulse propagation studies, performed using the propagation constant β calculated to the second order from the dispersion curves, show that for short distances the device can support high bandwidths. Figure 12 shows one such study for the fourth

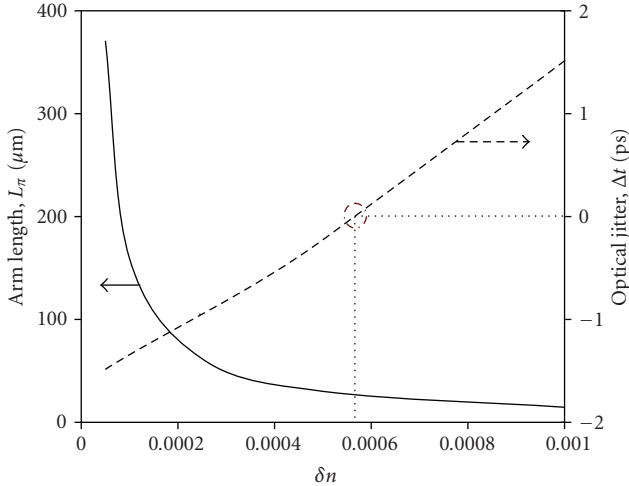


FIGURE 9: Achievable arm length L_π and jitter Δt as functions of δn for the $\Delta = 5$ PC-CCW for the optimized operating frequency of $\omega = 0.24485$. For a material index change of $\delta n \approx 0.00055$, $\Delta t = 0$ picosecond, and $L_\pi < 30 \mu\text{m}$.

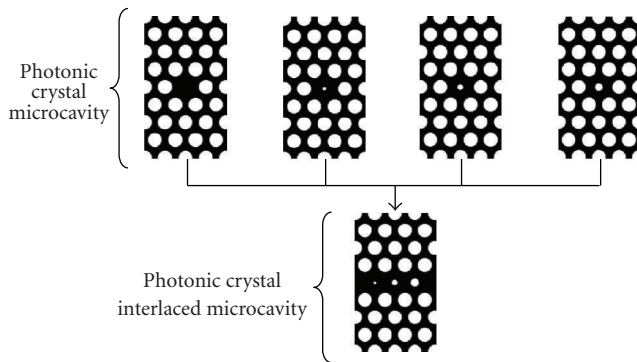


FIGURE 10: Illustration of the concept of a photonic crystal interlaced microcavity. It is a combination of several photonic crystal microcavities into a single waveguide. Repeating the photonic crystal interlaced microcavity yields the ICCW structure.

band in the gap, having an estimated bandwidth of 99 Gbits/s.

4.1. Tuning the slow-light properties of the ICCW

In order to determine the effect of changing the refractive index and radii of the defect cavities, we simulated a second ICCW structure similar to the first but with cavity radii $0.05a$, $0.125a$, $0.20a$, and $0.275a$, corresponding to a $0.05a$ increase over the previous structure. Additionally, the refractive index of the material inside these cavities was set to 1.5 in order to be representative of silicon dioxide, for example, or various active materials such as liquid crystals or electro-optic polymers. This structure exhibits 8 TE bands in its bandgap, which is fewer than the previous structure due to the reduced index contrast. The electric field distributions of the four coupled-cavity modes are shown in Figure 13, and each is localized around a cavity of a particular radius.

We next determined the effect of changing the refractive index of the material in the cavities upon the value of the eigenfrequency of each mode. To do this, we varied the refractive index of the medium in each cavity from 1.5 to 1.501 in steps of 0.0002. Each band exhibits a linear relationship between its eigenfrequency and the refractive index change. This is a very promising feature because it could be exploited to actively tune ICCW-based devices.

The most powerful property of the ICCW, however, is that the cavities can be tuned individually. Figure 14 shows the result of introducing a small index shift (+0.0005) into any cavity. In each case, the mode localized to the cavity in which the index change is introduced experiences a change in frequency on the order of approximately 0.5 GHz (corresponding to a tuning sensitivity df/dn above 1.2 THz/RIU, assuming $1.5 \mu\text{m}$ wavelength), while the other modes experience only a much smaller change. The fact that the multiple slow-light bands of the ICCW structure are each separately accessible may lead to the development of a variety of novel devices including multichannel modulators and switches, multichannel tunable amplifiers and lasers, or multichannel biosensors. Because all of the channels are contained in a single waveguide, these devices could be made no larger than their single-channel counterparts. An optical modulator based on the ICCW platform would have the advantage of being a resonant modulator, but would be able to handle multiple high-bandwidth optical channels simultaneously. Addressing individual cavities will be challenging, but patterning electrical contacts with size and spacing on the order of one lattice period is possible using UV lithography or direct-write methods, for example. Also, work on single quantum dots has shown that it is possible to manipulate the electrical properties of ultrasmall regions of semiconductor, on the order of hundreds of nanometers in size [41, 42]. Although this work has not yet been extended to photonic crystal devices, doing so should not be beyond the capabilities of state-of-the-art nanofabrication techniques.

It is possible to further optimize the performance of the device by changing the number or radii of the cavities, or the refractive indices of the cavities or the surrounding photonic crystal slab. Simulations of an ICCW with three and five different cavity sizes, for example, have also been carried out with similar results to those above, but with three and five localized modes, respectively.

5. IMPLEMENTATION CHALLENGES

Although photonic crystal slow-light devices have considerable potential in the area of optical interconnects, there are still several issues that must be addressed before they can be practically implemented. One challenge applicable to optical interconnects in general is the availability of an effective light source. While it is possible to develop a highly efficient, off-chip source, coupling its output to the chip can add great cost and complexity to chip package design, in addition to counteracting some of the efficiency advantages. A wafer-bonding approach can help to address some of the complexity issues, but still requires an extra

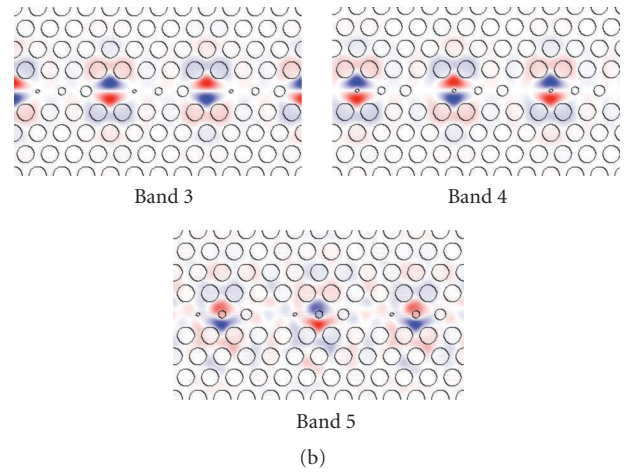
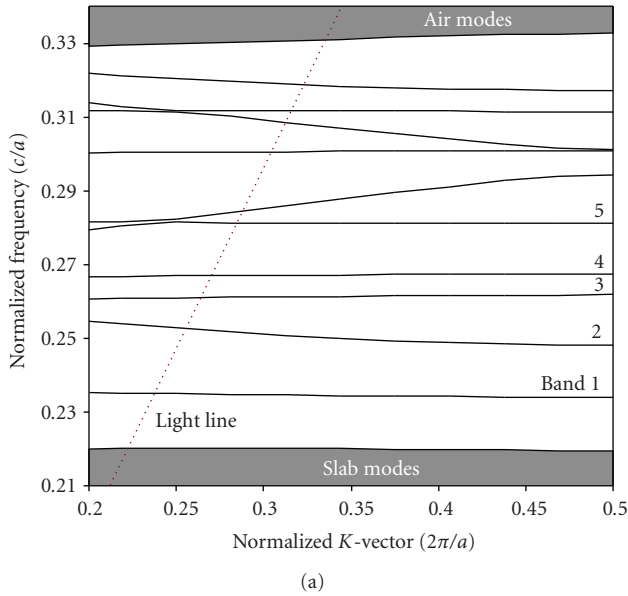


FIGURE 11: (a) Dispersion curves for the photonic crystal modes of the ICCW structure. (b) Electric field distributions for three of the cavity-localized modes.

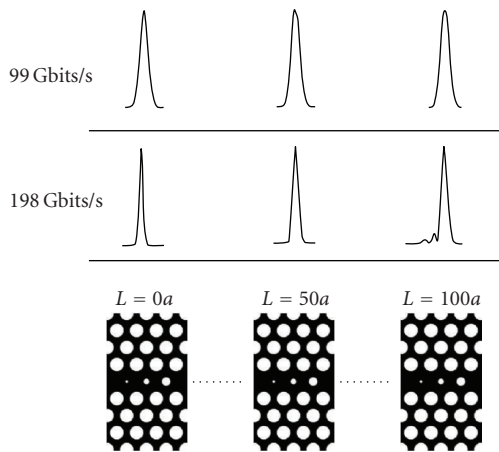


FIGURE 12: Pulse shape evolution for the fourth band in the gap.

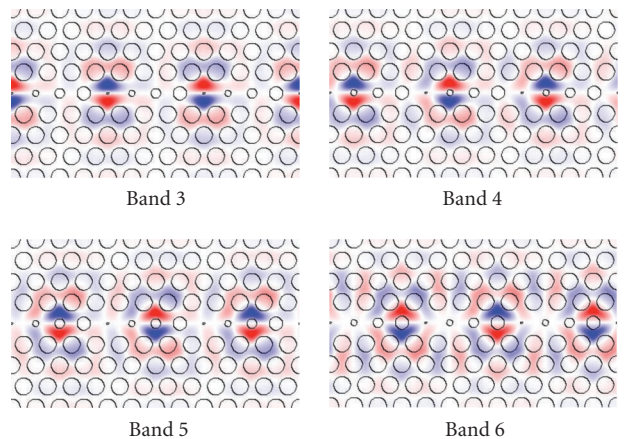


FIGURE 13: Electric field distributions for the four coupled-cavity modes in the ICCW.

layer of fabrication, as well as the inclusion of materials that are not a part of the standard CMOS library [43]. The development of an on-chip light source, however, would eliminate any packaging and output coupling issues, by allowing the light source to be integrated directly on the microprocessor itself [44]. Unfortunately, the constraints of working with silicon (which has an indirect bandgap) in an on-chip platform, where power dissipation, device footprint, and other limitations must be taken into account, complicate the design process. To date, despite evidence for optical gain, there is still no silicon-based laser based on carrier injection [44–46]. Although an optically-pumped silicon laser based on the Raman effect has already been demonstrated [47], an electrically-pumped laser is much more desirable because it would eliminate any need for an off-chip light source. For the

immediate future, a wafer-bonding approach would seem to be the most convenient option, although the inclusion of an electrically-pumped, silicon light source will help to realize the full advantages of optical interconnects.

Several issues specific to the implementation of slow-light devices also exist. The first is that of coupling. In order to maintain the delay and bandwidth density advantages of optical interconnects based on slow-light devices, it is desirable to use silicon wire waveguides as the transmission medium and to use slow-light devices only as the active elements. This is because photonic crystal waveguides, including the ICCW, have a larger cross-section than silicon wire waveguides, the latter of which can have a width under $1 \mu\text{m}$. Additionally, the low group velocities inside coupled-cavity waveguides would increase data propagation delays.

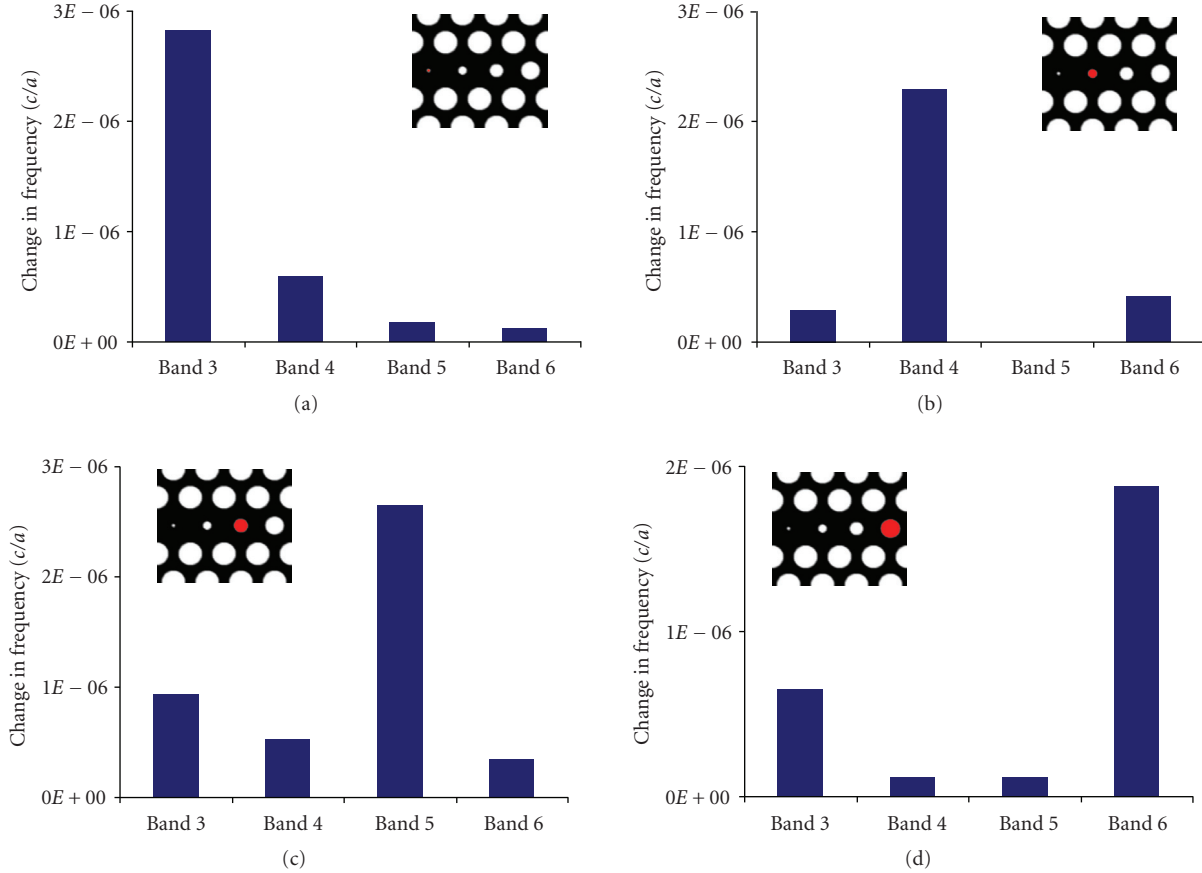


FIGURE 14: Tuning of individual cavities in the ICCW. The cavity tuned in each case is indicated in the schematic.

Therefore, it is necessary to be able to couple the active slow-light devices to traditional silicon wire waveguides. The large mismatch between the group velocities in these two media, however, makes efficient coupling very challenging. An abrupt waveguide-to-CCW interface, for example, causes strong reflection and thus signal loss. Some success has been achieved in coupling silicon ridge waveguides to CCWs [48], although because of the large group velocity difference any approach based on a taper is unlikely to be compact enough for integration [49]. Other methods, such as those based on structural optimization [50, 51] have shown some promise in reducing coupling loss. More recently, another approach based on the use of a photonic crystal waveguide having an intermediate group velocity was demonstrated to have very high coupling efficiency into slow-light modes [49, 52]. While these techniques have so far only been used for coupling into band-edge slow-light modes, they may also prove useful as the basis for coupling into CCW slow-light modes.

A second issue facing slow-light devices is that of insertion loss. Losses in slow-light photonic crystal devices can be divided into two categories: extrinsic loss and intrinsic loss. Extrinsic loss is due to imperfections in the fabricated structure, that is, disorder induced during fabrication. A recent study of slow-light photonic crystal waveguides revealed that extrinsic losses have only a sublinear dependence on group

velocity (proportional to $1/v_g^{1/2}$) [53], which is promising for slow-light devices. However, at very low group velocities (below $0.01c$), extrinsic losses may scale much more strongly and thus may have the potential to become the dominant loss mechanism [53, 54]. Further refinement of fabrication processes can help to control extrinsic losses, though, by reducing the structural disorder that causes it.

Intrinsic loss, on the other hand, exists regardless of fabrication variances. This takes the form of radiation loss, where optical energy leaks out of the structure due to lack of confinement in the vertical direction. In general, these losses grow as the group velocity is decreased. Radiation loss can be controlled, however, by optimizing the quality factor Q of the individual cavities that make up the CCW [55, 56]. Much progress has already been made in the area of ultra-high- Q photonic crystal microcavities [35, 36], and it has been shown that the radiation loss of a CCW can actually be made far lower than that of a single microcavity [55]. This can be accomplished in part by optimizing the spatial distribution of the optical modes in the cavities, such as by using a modified cavity geometry. To that end, we have observed that the analysis presented in Section 3 also holds for other cavity geometries, such as that proposed by Akahane et al. [35, 36]. Finally, because of the extremely short lengths of slow-light devices, even with total losses as high as 20 dB/mm, for example, a $50 \mu\text{m}$ long device would

exhibit only 1 dB of net loss, which is well within acceptable levels for optical interconnects.

6. CONCLUSION

The need for an improved on-chip interconnect technology has brought the possibility of optical interconnects to the fore. Before optical interconnects can replace electrical interconnects, however, they must be able to compete in terms of a variety of parameters, including signal propagation delay, bandwidth density, footprint, and power consumption. In terms of signal propagation delay, optical interconnects have a natural advantage over electrical interconnects because of the absence of RC impedances. Likewise, they have an advantage in terms of bandwidth density if wavelength-division multiplexing is used. The use of photonic crystal slow-light devices has the potential to extend this list of advantages to footprint and power consumption as well.

As we have outlined above, the properties of slow light can be used to vastly shrink the size and power consumption of interferometric optical modulators while maintaining very high bandwidth. Furthermore, the ICCW platform, which is the first example of a slow-light WDM platform, has the potential to be the basis for a variety of ultracompact, low-power, high-bandwidth multichannel devices. With further improvements in coupling and the reduction of intrinsic and extrinsic losses, one can envision an optical interconnect built on slow-light photonic crystal active devices. Because of its unique advantages in terms of low latency and high bandwidth even over large distances, such an interconnect may enable the emergence of a new generation of microprocessors that are no longer interconnect-constrained. These chips would be able to leverage the availability of much longer interconnects than are possible using electrical interconnects. Even before that occurs, optical interconnects based on slow-light photonic crystal active devices will be able to function as a drop-in replacement for electrical interconnects in future microprocessors.

ACKNOWLEDGMENTS

This research is funded by the Air Force Office of Scientific Research (G. Pomrenke) and Intel Corporation.

REFERENCES

- [1] G. Moore, "Cramming more components onto integrated circuits," *Electronics*, vol. 38, no. 8, pp. 114–117, 1965.
- [2] F. J. Pollack, "New microarchitecture challenges in the coming generations of CMOS process technologies," in *Proceedings of the 32nd Annual ACM/IEEE International Symposium on Microarchitecture*, p. 2, Haifa, Israel, November 1999.
- [3] N. Magen, A. Kolodny, U. Weiser, and N. Shamir, "Interconnect-power dissipation in a microprocessor," in *Proceedings of the International Workshop on System Level Interconnect Prediction (SLIP '04)*, pp. 7–13, Paris, France, February 2004.
- [4] M. Haurylau, G. Chen, H. Chen, et al., "On-chip optical interconnect roadmap: challenges and critical directions," *IEEE Journal on Selected Topics in Quantum Electronics*, vol. 12, no. 6, part 2, pp. 1699–1705, 2006.
- [5] N. Nelson, G. Briggs, M. Haurylau, et al., "Alleviating thermal constraints while maintaining performance via silicon-based on-chip optical interconnects," in *Proceedings of the Workshop on Unique Chips and Systems*, pp. 45–52, Austin, Tex, USA, March 2005.
- [6] R. G. Beausoleil, P. J. Kuekes, G. S. Snider, S.-H. Wang, and R. S. Williams, "Nanoelectronic and nanophotonic interconnect," *Proceedings of the IEEE*, vol. 96, no. 2, pp. 230–247, 2008.
- [7] M. J. Kobrinsky, B. A. Block, J.-F. Zheng, et al., "On-chip optical interconnects," *Intel Technology Journal*, vol. 8, no. 2, pp. 129–141, 2004.
- [8] D. A. B. Miller, "Rationale and challenges for optical interconnects to electronic chips," *Proceedings of the IEEE*, vol. 88, no. 6, pp. 728–749, 2000.
- [9] J. W. Goodman, F. J. Leonberger, S.-Y. Kung, and R. A. Athale, "Optical interconnections for VLSI systems," *Proceedings of the IEEE*, vol. 72, no. 7, pp. 850–866, 1984.
- [10] G. Chen, H. Chen, M. Haurylau, et al., "Predictions of CMOS compatible on-chip optical interconnect," *Integration, the VLSI Journal*, vol. 40, no. 4, pp. 434–446, 2007.
- [11] R. A. Soref and B. R. Bennett, "Electrooptical effects in silicon," *IEEE Journal of Quantum Electronics*, vol. 23, no. 1, pp. 123–129, 1987.
- [12] S. M. Weiss, M. Haurylau, and P. M. Fauchet, "Tunable photonic bandgap structures for optical interconnects," *Optical Materials*, vol. 27, no. 5, pp. 740–744, 2005.
- [13] S. M. Weiss, H. Ouyang, J. Zhang, and P. M. Fauchet, "Electrical and thermal modulation of silicon photonic bandgap microcavities containing liquid crystals," *Optics Express*, vol. 13, no. 4, pp. 1090–1097, 2005.
- [14] M. Haurylau, S. P. Anderson, K. L. Marshall, and P. M. Fauchet, "Electrically tunable silicon 2-D photonic bandgap structures," *IEEE Journal on Selected Topics in Quantum Electronics*, vol. 12, no. 6, pp. 1527–1532, 2006.
- [15] M. Haurylau, J. Zhang, S. M. Weiss, et al., "Nonlinear optical response of photonic bandgap structures containing PbSe quantum dots," *Journal of Photochemistry and Photobiology A*, vol. 183, no. 3, pp. 329–333, 2006.
- [16] R. M. de Ridder, A. Driessen, E. Rikkers, P. V. Lambeck, and M. B. J. Diemeer, "Design and fabrication of electro-optic polymer modulators and switches," *Optical Materials*, vol. 12, no. 2-3, pp. 205–214, 1999.
- [17] M. Soljačić, S. G. Johnson, S. Fan, M. Ibanescu, E. Ippen, and J. D. Joannopoulos, "Photonic-crystal slow-light enhancement of nonlinear phase sensitivity," *Journal of the Optical Society of America B*, vol. 19, no. 9, pp. 2052–2059, 2002.
- [18] J. D. Meindl, "Beyond Moore's law: the interconnect era," *Computing in Science and Engineering*, vol. 5, no. 1, pp. 20–24, 2003.
- [19] R. Ho, K. W. Mai, and M. A. Horowitz, "The future of wires," *Proceedings of the IEEE*, vol. 89, no. 4, pp. 490–504, 2001.
- [20] P. Kapur and K. C. Saraswat, "Optical interconnects for future high performance integrated circuits," *Physica E*, vol. 16, no. 3-4, pp. 620–627, 2003.
- [21] V. Adler and E. G. Friedman, "Repeater design to reduce delay and power in resistive interconnect," *IEEE Transactions on Circuits and Systems II*, vol. 45, no. 5, pp. 607–616, 1998.
- [22] <http://public.itrs.net>.
- [23] A. Liu, L. Liao, D. Rubin, et al., "High-speed optical modulation based on carrier depletion in a silicon waveguide," *Optics Express*, vol. 15, no. 2, pp. 660–668, 2007.

- [24] S. R. Giguere, L. Friedman, R. A. Soref, and J. P. Lorenzo, "Simulation studies of silicon electro-optic waveguide devices," *Journal of Applied Physics*, vol. 68, no. 10, pp. 4964–4970, 1990.
- [25] Z. Shi, R. W. Boyd, D. J. Gauthier, and C. C. Dudley, "Enhancing the spectral sensitivity of interferometers using slow-light media," *Optics Letters*, vol. 32, no. 8, pp. 915–917, 2007.
- [26] J. D. Joannopoulos, R. D. Meade, and J. N. Winn, *Photonic Crystals: Molding the Flow of Light*, Princeton University Press, Princeton, NJ, USA, 1995.
- [27] S. John, "Strong localization of photons in certain disordered dielectric superlattices," *Physical Review Letters*, vol. 58, no. 23, pp. 2486–2489, 1987.
- [28] E. Yablonovitch, "Inhibited spontaneous emission in solid-state physics and electronics," *Physical Review Letters*, vol. 58, no. 20, pp. 2059–2062, 1987.
- [29] A. Yariv, Y. Xu, R. K. Lee, and A. Scherer, "Coupled-resonator optical waveguide: a proposal and analysis," *Optics Letters*, vol. 24, no. 11, pp. 711–713, 1999.
- [30] S. Mookherjee and A. Yariv, "Coupled resonator optical waveguides," *IEEE Journal on Selected Topics in Quantum Electronics*, vol. 8, no. 3, pp. 448–456, 2002.
- [31] A. Martínez, A. García, P. Sanchis, and J. Martí, "Group velocity and dispersion model of coupled-cavity waveguides in photonic crystals," *Journal of the Optical Society of America A*, vol. 20, no. 1, pp. 147–150, 2003.
- [32] T. F. Krauss, "Slow light in photonic crystal waveguides," *Journal of Physics D*, vol. 40, no. 9, pp. 2666–2670, 2007.
- [33] S. G. Johnson and J. D. Joannopoulos, "Block-iterative frequency-domain methods for Maxwell's equations in a planewave basis," *Optics Express*, vol. 8, no. 3, pp. 173–190, 2001.
- [34] <http://ab-initio.mit.edu/mpb>.
- [35] Y. Akahane, T. Asano, B.-S. Song, and S. Noda, "High-Q photonic nanocavity in a two-dimensional photonic crystal," *Nature*, vol. 425, no. 6961, pp. 944–947, 2003.
- [36] Y. Akahane, T. Asano, B.-S. Song, and S. Noda, "Fine-tuned high-Q photonic-crystal nanocavity," *Optics Express*, vol. 13, no. 4, pp. 1202–1214, 2005.
- [37] N. R. Draper and H. Smith, *Applied Regression Analysis*, Wiley Series in Probability and Statistics, Wiley-Interscience, New York, NY, USA, 1998.
- [38] M. Lipson, "Compact electro-optic modulators on a silicon chip," *IEEE Journal on Selected Topics in Quantum Electronics*, vol. 12, no. 6, pp. 1520–1526, 2006.
- [39] M. D. Settle, R. J. P. Engelen, M. Salib, A. Michaeli, L. Kuipers, and T. F. Krauss, "Flatband slow light in photonic crystals featuring spatial pulse compression and terahertz bandwidth," *Optics Express*, vol. 15, no. 1, pp. 219–226, 2007.
- [40] L. H. Frandsen, A. V. Lavrinenko, J. Fage-Pedersen, and P. I. Borel, "Photonic crystal waveguides with semi-slow light and tailored dispersion properties," *Optics Express*, vol. 14, no. 20, pp. 9444–9450, 2006.
- [41] S. K. Jung, S. W. Hwang, D. Ahn, J. H. Park, Y. Kim, and E. K. Kim, "Fabrication of quantum dot transistors incorporating a single self-assembled quantum dot," *Physica E*, vol. 7, no. 3, pp. 430–434, 2000.
- [42] S. Sasaki, S. De Franceschi, J. M. Elzerman, et al., "Kondo effect in an integer-spin quantum dot," *Nature*, vol. 405, no. 6788, pp. 764–767, 2000.
- [43] A. W. Fang, H. Park, O. Cohen, R. Jones, M. J. Paniccia, and J. E. Bowers, "Electrically pumped hybrid AlGaInAs-silicon evanescent laser," *Optics Express*, vol. 14, no. 20, pp. 9203–9210, 2006.
- [44] P. M. Fauchet, "Monolithic silicon light sources," in *Silicon Photonics*, L. Pavesi and D. J. Lockwood, Eds., vol. 94 of *Topics in Applied Physics*, pp. 177–198, Springer, Berlin, Germany, month 2004.
- [45] P. M. Fauchet, J. Ruan, H. Chen, et al., "Optical gain in different silicon nanocrystal systems," *Optical Materials*, vol. 27, no. 5, pp. 745–749, 2005.
- [46] L. Pavesi, "Routes toward silicon-based lasers," *Materials Today*, vol. 8, no. 1, pp. 18–25, 2005.
- [47] H. Rong, R. Jones, A. Liu, et al., "A continuous-wave Raman silicon laser," *Nature*, vol. 433, no. 7027, pp. 725–728, 2005.
- [48] D. O'Brien, M. D. Settle, T. Karle, A. Michaeli, M. Salib, and T. F. Krauss, "Coupled photonic crystal heterostructure nanocavities," *Optics Express*, vol. 15, no. 3, pp. 1228–1233, 2007.
- [49] P. Velha, J. P. Hugonin, and P. Lalanne, "Compact and efficient injection of light into band-edge slow-modes," *Optics Express*, vol. 15, no. 10, pp. 6102–6112, 2007.
- [50] E. Miyai and S. Noda, "Structural dependence of coupling between a two-dimensional photonic crystal waveguide and a wire waveguide," *Journal of the Optical Society of America B*, vol. 21, no. 1, pp. 67–72, 2004.
- [51] Y. A. Vlasov and S. J. McNab, "Coupling into the slow light mode in slab-type photonic crystal waveguides," *Optics Letters*, vol. 31, no. 1, pp. 50–52, 2006.
- [52] J. P. Hugonin, P. Lalanne, T. P. White, and T. F. Krauss, "Coupling into slow-mode photonic crystal waveguides," *Optics Letters*, vol. 32, no. 18, pp. 2638–2640, 2007.
- [53] L. O'Faolain, T. P. White, D. O'Brien, X. Yuan, M. D. Settle, and T. F. Krauss, "Dependence of extrinsic loss on group velocity in photonic crystal waveguides," *Optics Express*, vol. 15, no. 20, pp. 13129–13138, 2007.
- [54] S. Hughes, L. Ramunno, J. F. Young, and J. E. Sipe, "Extrinsic optical scattering loss in photonic crystal waveguides: role of fabrication disorder and photon group velocity," *Physical Review Letters*, vol. 94, no. 3, Article ID 033903, 4 pages, 2005.
- [55] M. L. Povinelli and S. Fan, "Radiation loss of coupled-resonator waveguides in photonic-crystal slabs," *Applied Physics Letters*, vol. 89, no. 19, Article ID 191114, 3 pages, 2006.
- [56] D. P. Fussell and M. M. Dignam, "Engineering the quality factors of coupled-cavity modes in photonic crystal slabs," *Applied Physics Letters*, vol. 90, no. 18, Article ID 183121, 3 pages, 2007.